DE-FE0023313

Final Report

CHARACTERIZING AND INTERPRETING THE IN SITU STRAIN TENSOR DURING CO_2 INJECTION

Authors
Larry Murdoch, Scott DeWolf, Leonid Germanovich, Alex Hanna
Robert Moak and Stephen Moysey

Project/Grant Period: 1 October 2014 – 30 September 2018
Report Submission Date: 8 June 2019

Award to

Clemson University
Office for Sponsored Programs
300 Brackett Hall
Clemson, SC 29634-5702
DUNS 04-262-9816

Principal Investigator

Larry Murdoch
864-656-2597
864-656-1041
lmurdoc@clemson.edu

PI Signature: LCMurdoch

Submitted to

U.S. Department of Energy
National Energy Technology Laboratory

CHARACTERIZING AND INTERPRETING THE IN SITU STRAIN TENSOR DURING CO_2 INJECTION

Contributors

Contributors to the Report

This report describes a significant investigation by multiple investigators conducted over the past several years. The investigators describe their contributions in sections, and the sections were combined to create the chapters in the report. Chapter One is an overview of the project and has contributions from all the authors; Scott DeWolf, Leonid Germanovich, Alex Hanna, Rob Moak, Stephen Moysey, and Larry Murdoch. Chapter Two was written by Scott DeWolf with contributions from Leonid Germanovich and Larry Murdoch. Chapter Three was written by Alex Hanna, Leonid Germanovich, Stephen Moysey, and Larry Murdoch. Alex wrote the Python code in the appendix of Chapter Three using an analysis derived by Leonid. Chapter Four was written by Scott, and Larry, and the section describing the work at the Clemson field site was written by Rob Moak. Chapter Five was written by Alex, Scott, Leonid, Stephen and Larry.

Contributors to the Project

This project has benefited from many individuals who were not involved in the writing, and who are therefore not included in the list of authors, but who have nevertheless made important contributions to the project that we would like to acknowledge. Marvin and Scott Robinowitz of Grand Resources are at the top of this list. Marvin and Scott operate the oil field where this research was conducted, so the project would have been impossible without their permission. However, their role goes far beyond simply granting us permission. They contributed their time, and the time of their staff, as well as access to their facilities, equipment, infrastructure and other material resources. This saved considerable costs to the project, but it also improved the quality of the field work. We also appreciate their enthusiastic discussions about improving understanding of the subsurface. June Schmeling, a geologist with Grand Resources, provided unpublished information and insights that helped us understand the geology of the Avant Field, and we also appreciate help in the field from Grand Resources employees, Tim Woodward and Travis Collins. Ken and Gail Bowman own the land where the AVN strainmeters were installed, and we appreciate their permission to allow us to do the drilling and install the surface equipment necessary to measure strain. The job of installing strainmeters required input from a variety of people, and we particularly appreciate the efforts of Wade Johnson, Mike Gottlieb, Liz van Boskirk and colleagues from UNAVCO during installation of the Gladwin strainmeter, and Wade's help during subsequent installations. Graduate students Riley Blais, Grant Plunkett, and Matt Siegler from Clemson, and John Hu from Georgia Tech endured some hot summer weather when they helped install the Clemson strainmeters. Josh Smith of Georgia Tech worked on the project. The instruments developed for the project were crafted from parts made by the skilled machinists at the Clemson Machining and Technical Services group. Field testing at the Clemson site took place on the Simpson Research and Education Center directed by John Andrae, and we appreciate the continued access to this test site.

CHARACTERIZING AND INTERPRETING THE IN SITU STRAIN TENSOR DURING CO_2 INJECTION

Executive Summary

Major Contributions

This project contributes a proof-of-concept demonstration that the strain tensor can be measured during injection into a reservoir, and the data can be interpreted to yield insights into reservoir properties and geometry that would be valuable to CO_2 storage projects.

Specific contributions include:

1. Showed the ability to characterize a strain signal at rates of tens of nanostrain per day that was repeatable over multiple injection tests.
2. Demonstrated feasibility of measuring the strain tensor at shallow depths (30 m) while injecting into a reservoir at 530 m. These data show that horizontal strains are tensile, with the circumferential strain larger than the radial strain. Vertical strain is compressive and similar in magnitude to the average horizontal strain. This appears to be the first time the transient strain tensor caused by injection has been measured.
3. Developed two new strainmeter instruments capable of measuring strains during injection. One instrument measures the vertical strain, the horizontal strain tensor and two tilts using electromagnetic sensors. The other instrument measures areal strain using simple, inexpensive optical fiber sensors.
4. Showed that areal strain data from the optical strainmeter are virtually identical to baseline data from a state-of-the-art Gladwin strainmeter. Low cost, high resolution and verified performance make the optical strainmeter design ideal for during future CO_2 storage projects, or similar applications.
5. Developed four quantitative methods for interpreting strain signals. Derived a new analytical solution for deformation during injection. Developed a stochastic inversion technique well suited to 3D poroelastic problems. Devised a simple graphical method for preliminary interpretation of strain signals.
6. Used four independent interpretation methods to predict material parameters (e.g. permeability, elastic modulus, hydraulic diffusivity, Biot-Willis parameter) and reservoir geometry that are consistent with each other and with independent estimates from the field site. This information would be useful for planning a CO_2 storage project. This appears to be the first time these reservoir parameters were estimated in-situ using a signal measured at a single location at shallow (30 m) depth.
7. Established publication of strain data from a well field in near real time to a publically accessible, archived database maintained by IRIS. Data available at: `http://ds.iris.edu/mda/2J/`.

Project Summary

Injecting fluid into a well creates an evolving strain tensor field that could be used to improve the effectiveness of CO_2 storage, but the strain tensor had never been measured during injection so the value of this technique was unclear. The objective of this project is to evaluate how the strain tensor can be measured

and interpreted to improve the assessment of geomechanical properties and advance an understanding of geomechanical processes that may present risks to CO_2 storage. The project consisted of three primary tasks related to 1) developing instruments for measuring the strain tensor with high precision; 2) developing methods for analyzing strain signals; and 3) demonstrating the approach at a CO_2 storage analog site.

Strain Instruments

The project developed three instruments for measuring strains and tilts caused by injection: 1) Grout-in Eddy Current Tensor Strain and Tilt System, 2) Removeable Eddy Current Strain and Tilt System, 3) Optical Fiber Areal Strainmeter. Two state-of-the-art commercial instruments, a Gladwin Tensor Strainmeter, and an Applied Geomechanics/Jewell Instruments LILY tiltmeter were also used. Gladwin Tensor Strain Meters (GTSM) have been the state of the art in precision strain measurements for three decades, but this project was the first time a GTSM was deployed to measure strain resulting from fluid injection. The resolution of this instrument is 10×10^{-12} strain, or 10 picostrain (least-count) with a linear dynamic range of up to 1×10^{-3} strain when operating with its lowest gain transformer.

The Eddy Current Tensor Strain and Tilt system integrates commercial eddy current displacement sensors to measure three horizontal strains, the vertical strain (in a vertical borehole), and two orthogonal tilts. One of the principle strains is assumed to be vertical, so the horizontal and vertical strains are assumed to resolve the full strain tensor. We demonstrated full functionality of the instrument, but the horizontal strain sensors went off-scale as a result of a small dynamic range. The vertical strain and tilt sensors continue to function as designed. The nominal strain resolution is approximately 10×10^{-9}, or 10 nanostrain in the horizontal and about 1 nanostrain in the vertical, with a dynamic range of up to 2.5×10^{-3} strain ($\sim$0.15 nanostrain per 24-bit least-count).

The Optical Fiber Areal strainmeter uses a Michelson interferometer created with several hundred meters of optical fiber to measure strain. The least-count resolution is approximately 6×10^{-15} strain, or 6 femtostrain, nearly 2,000 times more sensitive than the Gladwin strainmeter. The observed data from the Optical Fiber Areal strainmeter at the field site was essentially identical to the areal strain measurements made with the Gladwin strainmeter. The areal strainmeter was built with several $100 in parts, whereas Gladwin strainmeters cost approximately $100,000 before production was discontinued. The exceptional performance and low cost make the optical fiber areal strainmeter an appealing design for future applications.

Methods of Analysis

Four approaches of varying complexity were developed and evaluated for characterizing and interpreting the strain tensor caused by injection; 1) Strain type curves, 2) Manual parameter estimation with 3D numerical models, 3) Analytical solution to a pressurized poroelastic inclusion, 4) Stochastic inversion of a 3D numerical model.

Field Demonstration at the North Avant Field Site

A field demonstration of measuring and interpreting strain during injection was conducted at the North Avant Field, an oil field in Osage County, north of Tulsa, Oklahoma. Produced water is reinjected in a process analogous to CO_2 storage. Oil occurs in elongated lenses of coarse-grained sand at the bottom of Bartlesville formation at approximately 530 m depth in the North Avant Field. Heterogeneities in the vicinity of an injection well would affect CO_2 storage, so evaluating the properties and geometry of the permeable lenses has applications to CO_2 storage. Three strainmeters and the LILY tiltmeter were installed at 30 m depth approximately 220 m east of well 9A, a water injection well completed in a permeable lens on the

northwestern side of the North Avant Field. The testing program includes three periods of injection at rates between 10 to 15 gpm over periods from 3 to 25 days, followed by periods of recovery.

Field Observations of Strain During Injection

The change in the strain tensor during the three injection tests was similar. The radial and circumferential strains were tensile and the magnitude of the circumferential strain was the greatest, reaching 80 to 250 nε at the end of the tests. The magnitude of the radial strain was 0.2 to 0.5 of the circumferential strain. The vertical strain was compressive and was greater than the radial, but less than the circumferential strain. A principle strain direction was assumed to be vertical because of the shallow depth of the measurement, and this implies that the instruments measure the full strain tensor. Normal strains were detected at the strainmeters almost immediately after the start of injection. The strain rate was as fast as 100 nε/d during the first several hours of injection, but it slowed with time and was approximately 30 nε/d during the first day or two, and 10 nε/d after the first week. The strain signals were approximately proportional to the log of time during the first few days of injection, and the semi-log slope was 50 to 75 nε/log cycle.

Data from the Gladwin strainmeter were processed to give the areal strain and these results were compared to data from the optical fiber areal strainmeter. The results are virtually identical. The eddy current strainmeter provided vertical strains and tilts during the injection tests, and it provided horizontal strain data for approximately 20 days.

Tilt increased to 100 to 200 nrad during the injection tests, but the transient signals were variable and changed significantly during the tests. The signals from the eddy current and LILY tiltmeters were similar in some cases and different in others. In general, it was difficult to identify a consistent tilt signal during the injection tests. The normal strain signals were more consistent, and more interpretable, than the tilt signals.

Interpretation of Strain During Injection

The four methods of interpreting strain signals were evaluated using data from the North Avant Field injection. They give results that are generally consistent with each other, and with independent information characterizing the subsurface in the area. The hydraulic diffusivity of the reservoir in the vicinity of well 9A is approximately 0.5 m^2/s and the permeability is between 100 and 500 mD, according to analysis of the strain signals. This is consistent with measurements of permeability from cores taken in the vicinity of well 9A, and it is consistent with analyses of pressure transients using standard hydraulic well testing interpretation methods. The four methods of analysis indicate that Young's modulus of the reservoir is between 2 and 6 GPa. This is softer than moduli estimated from laboratory tests on cores (approximately 10 GPa), but this is likely because the laboratory tests were biased by preferential selection of the most well indurated intervals in the formation.

Strain interpretations indicate the maximum dimension of the permeable lens is 500 to 1,000 m (Figure 5.47). An isopach map of coarse-grained sand indicates a feature that is roughly 1,000 m in extent, although data constraining the extent is sparse to the north and west (Figure 5.47) and the lens may be larger in those dimensions.

All the interpretations indicate that a boundary of the permeable lens occurs between well 9A and the strainmeters AVN. This interpretation occurs because the boundary is required to explain the relative magnitudes of the radial and circumferential horizontal strains. The boundary reduces the magnitude of the radial strain relative to the circumferential strain, which explains the field data.

Conclusion

This project demonstrated the feasibility of measuring the strain tensor at a depth of 30 m caused by injection into a reservoir at 530 m depth. An injection rate of 10 to 15 gpm caused a strain rate of tens of nanostrain per day. We field demonstrated two new strainmeters. A new optical strainmeter is particularly promising because it has performance that is better than the current state-of-the-art strainmeter, and it could be constructed and deployed at a modest cost. The strain signals measured during a field test are similar to results from theoretical analyses of an idealized reservoir. Four different analyses were used to interpret the strain signal and they give results that are consistent with each other and similar to independent measurements.

These results are a proof-of-concept demonstration that the slow strain caused by injection can be measured and interpreted to obtain useful information.

Contents

Executive Summary **3**

Chapter One
Introduction **11**
1.1 Objectives . . . 11
1.2 Summary of the Project . . . 12
1.2.1 Instruments for Measuring Strain . . . 12
1.2.1.1 Gladwin Tensor Strainmeter . . . 12
1.2.1.2 Grout-in Eddy Current Strain and Tilt System . . . 12
1.2.1.3 Removable Eddy Current Strain and Tilt System . . . 12
1.2.1.4 Optical Fiber Areal Strainmeter . . . 13
1.2.1.5 LILY Electrolytic Tiltmeter . . . 13
1.2.2 Simulating and Interpreting Strain Measurements . . . 13
1.2.2.1 Strain Type Curves . . . 13
1.2.2.2 Manual Parameter Estimation . . . 14
1.2.2.3 Analytical Solution to a Pressurized Poroelastic Inclusion . . . 14
1.2.2.4 Stochastic Inversion using 3D Numerical Model . . . 14
1.2.3 Field Demonstration at a CO_2 Storage Analog Site . . . 15
1.2.3.1 Instruments and Field Tests . . . 15
1.2.3.2 Field Observations During Injection Tests . . . 15
1.2.3.3 Interpretation of Strain During Injection . . . 16
1.3 Project Products . . . 17
1.3.1 Publications . . . 17
1.3.2 Raw and Processed Data . . . 18
1.3.3 Stochastic Inversion Source Code . . . 19
1.3.4 Presentations . . . 19
1.4 Background on the Need and Feasibility of Using In-Situ Deformation to Monitor CO_2 Storage 21
1.4.1 Expected Deformation Field Caused by an Injection Well . . . 21
1.4.1.1 Solution Methods and Codes . . . 24
1.4.1.2 Strain Caused by Injection . . . 24
1.4.1.3 Deformation Pattern . . . 24
1.4.1.4 Radial Deformation in the Vicinity of the Wellbore . . . 27
1.4.1.5 Deformation along the Injection Well . . . 28
1.4.1.6 Deformation Time Series . . . 28
1.4.1.7 Effects of Reservoir Type . . . 30
1.4.1.8 Effects of Injection Rate and Pressure . . . 31
1.4.2 Measuring In-Situ Strain . . . 31
1.4.2.1 Annulus strain sensors . . . 32
1.4.2.2 Portable Strain Instruments . . . 34
1.4.2.3 Portable Extensometers . . . 34
1.4.2.4 Tiltmeters . . . 34
1.4.2.5 Multi-Component Portable Strain Instruments . . . 35
1.4.2.6 Push-in Extensometer . . . 36
1.4.2.7 Grouted Borehole Strainmeters . . . 36
1.4.2.8 Current Geodetic Strainmeters . . . 36
1.4.2.9 Interferometric Optical Fiber Strainmeters . . . 37
1.4.3 Discussion . . . 38
1.4.3.1 Opportunities for Monitoring . . . 38
1.4.3.1.1 Injection well . . . 39
1.4.3.1.2 Reservoir . . . 39

1.4.3.1.3 Overlying confining unit . . . 39
1.4.3.1.4 Heterogeneities . . . 40
1.4.3.2 Interpreting Strain Data . . . 40
1.4.3.3 Overview of the Report . . . 41
References . . . 42

Chapter Two
Instrument Development and Assessment **48**
2.1 Completion and Installation . . . 48
2.1.1 Swaging . . . 49
2.1.2 Grouting . . . 51
2.1.2.1 Field Evaluation of Grout Mix Properties . . . 51
2.1.2.2 Lab Tests of Expanding Grout . . . 51
2.1.2.3 EPA Compliance of Expanding Grout . . . 52
2.2 Multi-Component Eddy Current Strain and Tilt Systems . . . 53
2.2.1 Non-Contact Eddy Current Displacement Transducers . . . 53
2.2.2 Grout-In Multi-Component Eddy Current Strain and Tilt System . . . 55
2.2.2.1 Transducer Integration . . . 55
2.2.2.1.1 Tiltmeters . . . 57
2.2.2.1.2 Strainmeters . . . 58
2.2.2.2 Supporting Electronics . . . 60
2.2.2.3 Field Observations . . . 62
2.2.3 Removable Multi-Component Eddy Current Strain and Tilt System . . . 66
2.2.3.1 Transducer Integration . . . 68
2.2.3.1.1 Tiltmeters . . . 70
2.2.3.1.2 Strainmeters . . . 70
2.2.3.2 Supporting Electronics . . . 74
2.2.3.3 Field Observations . . . 76
2.3 Optical Fiber Areal Strainmeter . . . 76
2.3.1 Optical Fiber Interferometry . . . 76
2.3.2 Down-Hole Package Design . . . 79
2.3.3 Interrogator Design . . . 81
2.3.4 Field Observations . . . 83
2.4 Data Processing . . . 84
2.4.1 Barometric Pressure Fitting and Removal . . . 84
2.4.2 In-Situ Calibration . . . 85
2.4.3 Tide Fitting and Removal . . . 89
2.4.4 Trend Fitting and Removal . . . 90
2.5 Instrument Performance Assessment . . . 90
2.5.1 Tiltmeter Performance . . . 90
2.5.2 Horizontal Strainmeter Performance . . . 91
2.5.3 Vertical Strainmeter Performance . . . 91
2.5.4 Areal Strainmeter Performance . . . 92
2.5.5 Final Instrument Assessment . . . 92
2.6 Data Management and Availability . . . 93
2.6.1 Data Acquisition and Telemetry . . . 94
2.6.2 Raw Data Availability . . . 94
2.6.3 Processed Data Availability . . . 96
References . . . 97

Chapter Three
Theoretical Analysis **99**

3.1 Analysis of a Pressurized Poroelastic Inclusion Resembling a Reservoir . . . 99
3.1.1 Concepts . . . 99
3.1.2 Mathematical Model . . . 101
3.1.3 Results . . . 103
3.1.3.1 Strains and Tilts at the Measurement Location . . . 104
3.1.3.2 Dependence on Material Properties and Normalization . . . 105
3.1.3.3 Simulated Transient Deformation . . . 106
3.1.4 Implementation . . . 108
3.2 Inversion for Interpreting Numerical Poroelastic Analyses . . . 109
3.2.1 Database Design . . . 111
3.2.2 Latin Hypercube . . . 112
3.2.3 NSGA-II: Pareto Rank-Based Fitness, Elitism and Niche Formation . . . 113
3.2.4 Dynamic Parameterization of Heterogeneities . . . 114
3.3 Strain Type-Curve Analysis . . . 115
3.3.1 Analysis . . . 116
3.3.1.1 Geometry and Boundary Conditions . . . 116
3.3.1.2 Scaling . . . 117
3.3.1.3 Comparison to Porous Media Solution . . . 118
3.3.2 Strain Transients . . . 119
3.3.3 Application . . . 122
3.3.4 Results . . . 122
3.3.4.1 Analysis of the Pressure Signal . . . 122
3.3.4.2 Analysis of the Strain Signal . . . 125
3.3.5 Discussion . . . 125
3.3.6 Conclusions . . . 126
3.4 Analysis of Expected Strains at the North Avant Field Site . . . 126
3.4.1 Verification of Simulations with Analytical Solution . . . 127
3.4.2 Injection at 9A . . . 127
3.4.2.1 2D Model of HEC Inclusion . . . 128
3.4.2.2 3D Model of Deformation Pattern . . . 129
3.4.3 Identifying Locations for Strain Instruments . . . 132
Appendix 3.A Python Implementation of the Cuboid Inclusion . . . 135
References . . . 151

Chapter Four
Field Demonstration **154**
4.1 Settings of the Field Sites . . . 154
4.1.1 North Avant Field Site . . . 154
4.1.1.1 Location . . . 154
4.1.1.2 Geology . . . 157
4.1.1.3 Production History . . . 159
4.1.2 Clemson Field Site . . . 160
4.1.2.1 Hydrogeologic Setting and Characterization . . . 160
4.1.2.2 Instrumentation and Ongoing Monitoring . . . 160
4.2 Instrumentation at North Avant Field . . . 161
4.2.1 Gladwin Borehole Tensor Strainmeter . . . 161
4.2.1.1 Installation . . . 163
4.2.2 Grout-In Eddy Current Strain and Tilt System . . . 163
4.2.2.1 Installation at the Simpson Station, SC . . . 167
4.2.2.2 Installation at the North Avant Field, OK . . . 169
4.2.3 Optical Fiber Areal Strainmeter . . . 170
4.2.3.1 Installation at the Simpson Station, SC . . . 170

4.2.3.2 Installation at the North Avant Field, OK . . . 172
4.2.4 Wellhead Instrumentation and Pressure Monitoring . . . 172
4.3 Strain During Transient Well Tests . . . 174
4.3.1 Well Tests at the North Avant Field . . . 174
4.3.1.1 Shut-In Test at Well 1A . . . 178
4.3.1.2 Injection Tests at Well 9A . . . 180
4.3.1.2.1 October 2017 Injection Test . . . 180
4.3.1.2.2 November 2017 Test . . . 184
4.3.1.2.3 July 2018 Test . . . 187
4.3.1.3 Summary of Field Tests at North Avant Field . . . 189
4.3.2 Well Tests at the Clemson Field Site . . . 194
4.3.2.1 Field Site . . . 194
4.3.2.2 In-Situ Strain Measurement . . . 195
4.3.2.3 Field Observations . . . 196
4.3.2.3.1 Fluid Pressure . . . 196
4.3.2.3.2 Vertical Strain . . . 196
4.3.2.3.3 Tilt . . . 198
4.3.2.4 Analysis . . . 198
4.3.2.4.1 Forward Model Results . . . 199
4.3.2.4.2 Sensitivity Analysis . . . 199
4.3.2.5 Summary of Results from Clemson Field Tests . . . 203
References . . . 204

Chapter Five
Interpretation of Field Tests at the North Avant Field **205**
5.1 Strain Type Curve . . . 205
5.2 Manual Calibration using 3D Numerical Model . . . 205
5.2.1 Results . . . 208
5.3 Inversion of Analytical Solution to Poroelastic Inclusion . . . 215
5.3.1 Introduction . . . 215
5.3.2 October and November 2017 injections . . . 216
5.3.3 Discussion . . . 217
5.4 Stochastic Inversion with 3D Poroelastic Model . . . 220
5.4.1 Inversion Methodology . . . 220
5.4.1.1 Forward Model . . . 221
5.4.1.2 Inversion Process . . . 224
5.4.2 Stochastic Inversion of 1A Shut-in . . . 224
5.4.3 Stochastic Inversion of 9A Injection Test, October 2017 . . . 228
5.4.3.1 Results for Lenses with Circular and Elliptical Geometries . . . 228
5.4.3.2 Results for Lenses with Irregular Geometries . . . 231
5.4.3.3 Differences in predicted strain and pressure fields . . . 232
5.4.4 Predicting Future Injection Tests . . . 235
5.4.4.1 Simulation of 9A Injection Test, November 2017 . . . 235
5.4.4.2 Evaluation of 9A Injection Test from July 2018 . . . 236
5.4.5 Summary . . . 236
5.4.5.1 Strain Type Curve . . . 236
5.4.5.2 Pressurized poroelastic inclusion . . . 237
5.4.5.3 Manual fitting of a 3D poroelastic numerical model . . . 237
5.4.5.4 Summary from Stochastic Inversions . . . 238
5.5 Conclusion . . . 239
References . . . 252

Chapter One
Introduction

Injecting CO_2 or other fluids into a well deforms the enveloping rocks in a complex pattern that increases in magnitude and expands outward with time. This evolving strain field holds important information that can be interpreted to improve understanding of geomechanical processes such as fault slip, which could hinder the injection process, or to sharpen estimates of formation properties and pressures, which will reduce risks and costs associated with injection. The in-situ strain field is a tensor with six independent components, and while all of them provide useful information only the tilt component is currently used for monitoring injection (with tiltmeters). The geodetic research community has developed borehole strainmeters that are capable of measuring the horizontal strain tensor with high resolution ($\sim$1 nanostrain).

Several investigators have demonstrated the feasibility of interpreting in situ strain measurements using rigorous numerical inversion methods, and most of this effort has focused on the use of data from tiltmeters. We showed during an earlier study (Murdoch et al., 2015) that it was possible to measure vertical strains with near nanostrain resolution, and that study also demonstrated a reduction in uncertainty that results from using normal strains, in addition to shear strain or tilt during inversion. We also showed with theoretical analyses that it should be feasible to use strain measurements at shallow depths to infer processes and properties in an underlying reservoir, significantly reducing costs compared to using monitoring wells drilled into the formation. While the strains measured at shallow depths are predicted to be small, they are in the range that could be reliably measured with geodetic borehole strainmeters.

This project began with the encouraging backdrop indicating that the in-situ strain tensor could be measured at shallow depths and interpreted using inverse methods (Murdoch et al., 2015). However, instruments with geodetic resolution had, to our knowledge, never been used to measure strain during injection into a reservoir, so the potential value of in-situ strains was unclear.

1.1 Objectives

The objective of the project is to assess the feasibility and value of measuring and interpreting strain caused by CO_2 injection. The goal is to evaluate how subsurface strain measurements can be used to improve the assessment of geomechanical properties and advance an understanding of geomechanical processes that may present risks to CO_2 storage. Objectives by task include:

1. Instrument Development Design instrumentation for measuring the in-situ strain tensor and evaluate performance characteristics relative to the existing state of the art.

2. Theoretical Analysis Develop theoretical analyses for characterizing the strain field associated with injection into a heterogeneous reservoir, and develop and demonstrate methods for inverting strain analyses to provide a quantitative interpretation.

3. Field Demonstration Demonstrate the best available strain measuring instrumentation during a field injection test, interpret the resulting data, and compare the interpretation with currently available information.

The first part of the following chapter provides a summary of important activities and findings during the project. This is followed by a section outlining the background on the need and feasibility of using in-situ deformation to monitor CO_2 storage.

1.2 Summary of the Project

The project consisted of three primary tasks related to developing instruments for measuring strain, analyzing strain signals, and field demonstration.

1.2.1 Instruments for Measuring Strain

The project developed or deployed five instruments for the measuring the subsurface strains and tilts caused by injection; 1) Gladwin Tensor Strainmeter, 2) Grout-in Eddy Current Strain and Tilt System, 3) Removable Eddy Current Strain and Tilt System, 4) Optical Fiber Areal Strainmeter, 5) LILY Electrolytic Tiltmeter. The instruments are summarized below and more details are given in Chapter Two. Data generated during injection tests are described in Chapter Four.

1.2.1.1 Gladwin Tensor Strainmeter

Gladwin Tensor Strainmeters have been the state of the art in high resolution strain measurements for three decades, but this project was the first time a GTSM was deployed to measure strain resulting from injection. A GTSM was grouted in a 30-m-deep boring to measure the horizontal strain tensor, and data from this instrument served as a baseline to evaluate innovations developed for the project. The resolution of this instrument is 10×10^{-12} strain, or 10 picostrain (least-count) with a linear dynamic range of up to 1×10^{-3} strain when operating with its lowest gain transformer.

1.2.1.2 Grout-in Eddy Current Strain and Tilt System

The Eddy Current Tensor Strainmeter integrates commercial eddy current displacement sensors to measure the horizontal strain tensor, the vertical strain, and two orthogonal tilts. One of the principle strains is expected to be vertical, so this instrument measures the full strain tensor. We designed this instrument and built two prototypes, which were deployed in the field. This design was grouted into a borehole using an approach similar to the one used to deploy the Gladwin strainmeter.

We demonstrated full functionality of this instrument, but the horizontal strain sensors went off-scale as a result of a small dynamic range. The vertical strain and tilt sensors continue to function as designed. The nominal strain resolution of these two instrument is approximately 10×10^{-9}, or 10 nanostrain in the horizontal and about 1 nanostrain in the vertical, with a dynamic range of up to 2.5×10^{-3} strain ($\sim$0.15 nanostrain per 24-bit least-count). The tilt resolution is approximately 0.3–0.6 nanoradians with a dynamic range of up to 3 to 6×10^{-3} radians.

1.2.1.3 Removable Eddy Current Strain and Tilt System

The Removable Eddy Current Tensor strainmeter uses components that are similar to the Grout-in version, but this instruments uses retractable anchors to temporarily grip the wall of the borehole during deployment. It is designed to measure the full strain tensor in a vertical hole, along with two components of tilt. This instrument features horizontal strain sensors that are retracted during transport and extended during data gathering in boreholes ranging from 3.25 to just over 4.5 inches in diameter.

A working prototype was designed and fabricated for the project. We tested the components and assembled the prototype, and wrote the software required to achieve functionality. The prototype is essentially ready for field evaluation.

1.2.1.4 Optical Fiber Areal Strainmeter

A strainmeter capable of measuring the areal strain (two times the average horizontal strain) was designed based on an optical fiber Michelson interferometer. Two instruments were built and deployed.

The observed performance of the areal strainmeter deployed at our North Avant Field site was essential identical to the areal strain measurements made with the Gladwin strainmeter. The least-count resolution is approximately 6×10^{-15} strain, or 6 femtostrain, nearly 2,000 times more sensitive than the Gladwin strainmeter. The dynamic range is determined by the maximum strain rate, which is roughly 10^{-4} ε/s, resulting in an effective bit depth of ∼34-bits at 1 Hz.

The areal strainmeter was built with several $100 in parts, whereas Gladwin strainmeters cost approximately $100,000 before production was discontinued. The exceptional performance and low cost make the areal strainmeter an appealing design for future applications.

1.2.1.5 LILY Electrolytic Tiltmeter

A LILY tiltmeter manufactured by Applied Geomechanics uses an electrolytic design that has been the mainstay of precision borehole tiltmeters since the 1990s. We deployed a LILY tiltmeter at our Oklahoma field site to provide baseline data for evaluating the tilt signal from the eddy current instrument. This instrument contains two orthogonal sensors with a resolution of < 5 nanoradians with a dynamic range of up to 330 microradians (∼16-bit resolution).

1.2.2 Simulating and Interpreting Strain Measurements

Four approaches of varying complexity were evaluated for characterizing and interpreting the strain field caused by injection; 1) strain type curves, 2) Manual parameter estimation with 3D numerical models, 3) Analytical solution to a pressurized poroelastic inclusion, 4) Stochastic inversion of a 3D numerical model. The approaches are summarized below and further outlined in Chapter Three. Results of the four approaches applied to field data are given in Chapter Five.

1.2.2.1 Strain Type Curves

The simplest method involves adapting the type-curve approach to analyzing pressure transients during well tests. Dimensionless type curves were developed for various strain components caused by an injection well in a confined reservoir of either infinite or bounded extent. The results indicate that average horizontal strain and the vertical strain become functions of log time at shallow observation points at radial distances further than half the depth to the reservoir. The semi-log slopes of these functions are proportional to the transformational strain, and the 0-strain intercept is approximately proportional to the hydraulic diffusivity in the underlying reservoir. The 0-strain intercept for the vertical strain is equal to the intercept for the average horizontal strain, although the signs and slopes of the two strains are different. The semi-log slope of the strain increases when the pressure in the underlying reservoir interacts with a reservoir boundary, just as the semi-log slope of the pressure record increases as a result of boundary interaction. More information on this interpretation method is in Section 3.3 and field data supporting this finding are in Section 5.1.

1.2.2.2 Manual Parameter Estimation

Parameters and geometries in poroelastic analyses can be adjusted manually to match pressures and strains observed in the field. This approach is capable of identifying sets of parameters that explain field observations, and it can provide some insights into how different parameters affect the resulting predictions. This approach allows more factors to be considered that the type curve methods, and it generally can result in a better match to the field observations. We were able to match both pressures and strains resulting from the field tests (e.g. Section 5.2).

1.2.2.3 Analytical Solution to a Pressurized Poroelastic Inclusion

Only a few analytical solutions are available for poroelastic analyses and none are useful for our applications. In Section 3.1, we derive a new solution to the strains and tilts in the vicinity of a pressurized poroelastic inclusion by building on the work of Eshelby and Midlin and Cheng. The new solution is valid for a thin inclusion of any shape, and in particular, we evaluated cases of circular and rectangular inclusions in a half-space. In the context of this project, a pressurized inclusion is the region of a reservoir where the pressure has been changed by fluid injection or extraction. Rectangular and circular inclusions were evaluated because those shapes resemble high permeability lenses at the North Avant Field site.

The new analyses allow strains and tilts to be calculated for a prescribed pressure distribution in the reservoir. The analytical solution itself is fairly lengthy (e.g 13 pages of code in Appendix 3.A), but it can be solved in a fraction of a second using readily available computers. This approach gives results that explain observed strains quite well when the observed reservoir pressures were used as input (Section 5.3). This method appears to be well suited to quickly identifying parameter suites that explain field data. This could be used as a preliminary step prior to inversion using numerical forward models. Alternatively, this approach could be used to rapidly scan strain data for signatures that could indicate changes in pressure resulting from leaks.

1.2.2.4 Stochastic Inversion using 3D Numerical Model

The most advanced method of interpretation we developed uses a suite of stochastic inversion methods with a poroelastic numerical model. The approach makes use of a highly parallelizable inverse problem solver that distributes computational effort over a large, heterogeneous set of compute nodes. These nodes may be drawn from various resources such as OpenScience Grid, Amazon Web Services, or a university cluster computer. The inverse problem solver includes Monte Carlo, Latin Hypercube, Markov chain Monte Carlo (McMC), gradient descent, and genetic algorithms. We found that the inversion analyses developed for this project worked well using the Latin Hypercube method to broadly search the parameter space, followed by the genetic algorithm NSGA-II to explore promising regions of the parameter space. The inversion method is described in Section 3.2.

The analysis of individual injection tests involved running many tens of thousands of simulations to identify several dozen or more suites of parameters that best explain all the data. These suites of parameters allow mean values and uncertainties of important parameters and reservoir architecture to be evaluated. The application of stochastic inversion methods is described in Section 5.4.

1.2.3 Field Demonstration at a CO_2 Storage Analog Site

A field demonstration of measuring and interpreting strain during injection was conducted at the North Avant Field, an oil field in Osage County, north of Tulsa, Oklahoma. The North Avant Field setting is described in Section 4.1.1. Oil and water are pumped from the Bartlesville Formation, a Pennsylvanian sandstone that occurs at a depth of approximately 500 m. The produced water is re-injected into the same formation in a process analogous to CO_2 storage. Elongate lenses of coarse-grained sand at the bottom of Bartlesville Formation are important oil-bearing units. These permeable lenses are several 100 m wide or more and up to 10 m thick.

The properties and geometry of permeable lenses in the vicinity of an injection well would be affect $C0_2$ storage, so evaluating how these factors could be estimated from strain measurements was a goal of the field tests.

1.2.3.1 Instruments and Field Tests

Three strainmeters were installed at 30 m depth approximately 220 m east of well 9A, a water injection well completed in a permeable lens on the northwestern side of the North Avant Field (Section 4.2). A Gladwin Tensor Strain Meter was installed first, followed 9 months later by the installation of an eddy current strainmeter and an areal strainmeter. The Gladwin strainmeter is the current state-of-the-art instrument used for measuring slow strains for studies involving tectonics or volcano deformation. The eddy current and areal strainmeters were developed for the project. A LILY tiltmeter was also installed.

The testing program includes three periods of injection at a rate of approximately 10 to 15 gpm over 3 to 25 days, followed by periods of recovery. Strain was measured during and following injection, and pore pressure was measured at three monitoring wells completed in the Bartlesville sandstone within several 100 m of well 9A. Another field test consisted of monitoring the strain when well 1A was shut-in for 7 days. Well 1A is approximately 0.8 km east of the strainmeters.

1.2.3.2 Field Observations During Injection Tests

The strain and tilt data were processed by identifying and removing strains associated with Earth tides, barometric pressure change, long-term trends unrelated to injection. The change in the strain tensor during the three injection tests was similar. The radial and circumferential strains were tensile and the magnitude of the circumferential strain was the greatest, reaching 80 to 250 nε at the end of the tests. The circumferential strain is roughly NS and the radial strain is roughly EW during the experiment. The magnitude of the radial strain was 0.2 to 0.5 of the circumferential strain. The vertical strain was compressive and was greater than the radial, but less than the circumferential strain. The field tests are described in Section 4.3.

Normal strains were detected at the strain meters almost immediately at the start of injection. The strain rate was as fast as 100 nε/d over the first several hours of injection, but it slowed with time and was approximately 30 nε/d during the first day or two, and 10 nε/d after the first week.

The strain signals were approximately proportional to the log of time during the first few days of injection, and the semi-log slope was 50 to 75 nε/log cycle (Section 4.3). The semi-log straight segment of the lines intersected the abscissa (0 strain) in the range of 3×10^4 to 5×10^4 s. The semi-log slope of the strain signals increased after $\sim 15 \times 10^4$ to 20×10^4s.

The pressure at the monitoring wells was also approximately a log function of time early in the tests. The semi-log straight segments of the pressure records intersected the abscissa at slightly later than the strain

signals. The slope of the pressure records increased with time, and the change in slope occurred at roughly the same time as it did in the strain records.

Data from the Gladwin strainmeter was processed to give the areal strain and these results were compared to data from the optical fiber areal strainmeter (Section 4.3). The results were virtually identical. The eddy current strainmeter provided vertical strains and tilts during the injection tests, and it provided horizontal strain data for approximately 20 days. These results demonstrate the functionality of the eddy current design, but they also point out the need for an expanded dynamic range on the horizontal strain sensor. A mechanism to increase the dynamic range was created for the removable eddy current strainmeter.

Tilt increased to 100 to 200 nrad during the injection tests, but the transient signals were variable and changed significantly during the tests. The signals from the eddy current and LILY tiltmeters were similar in some cases and different in others. In general, it was difficult to identify a consistent strain signal during the injection tests. The normal strain signals were more consistent, and more interpretable, than the tilt signals (Section 4.3).

A field site was developed at the Simpson Station in the vicinity of Clemson University, where the geology includes biotite gneiss overlain by approximately 30 m of saprolite. The site was used for shakedown testing of prototype strainmeters installed in the biotite gneiss. Strainmeters, extensometers, and wells were installed in the saprolite to characterize pressure change and deformation from pumping. The site is located near Clemson campus, so it was convenient to use for preliminary evaluation of the strainmeters even though the geology differed from conditions typically considered for CO_2 storage. The shakedown tests involved pumping from a well completed in the saprolite and measuring strain and drawdown in the vicinity of the well, and at the underlying strainmeters. The Simpson Station field site is described in Sections 4.1.2 and 4.2.2.1, and the field tests are described in 4.3.2.

1.2.3.3 Interpretation of Strain During Injection

Four independent methods of interpreting strain signals were evaluated using data from the North Avant Field (Chapter Five). They give results (Table 5.6) that are generally consistent with each other, and with independent information characterizing the subsurface in the area. The hydraulic diffusivity of the reservoir in the vicinity of well 9A is approximately 0.5 m^2/s and the permeability is between 100 and 500 mD, according to analysis of the strain signals. This is consistent with measurements of permeability from cores taken in the vicinity of well 9A, and it is consistent with analyses of pressure transients using standard hydraulic well testing interpretation methods. Analysis of strain from a shut-in at well 1A indicates slightly greater permeability, in the range 300 to 1,000 mD, with a mode of 600 mD. The specific capacity (injection rate/pressure) of well 1A is greater than at well 9A, and as a result, it is a preferred well for injecting produced water. This supports the finding that the permeability of the formation in the vicinity of well 1A is greater than it is in the vicinity of well 9A.

The four methods of analysis indicate that Young's modulus of the reservoir is between 2 and 6 GPa. Prior to the project, we conducted triaxial laboratory tests on small core samples of the Bartlesville sandstone from the North Avant Field and found that the Young's modulus was approximately 10 GPa. The small cores were obtained from larger cores stored in a core library operated by Oklahoma Petroleum Information Center (OPIC). The most well indurated sections of the larger core were preferentially selected for the smaller cores, so the samples we tested likely represent the strongest, and stiffest, rock in the formation. The simulations assumed a uniform modulus across the formation, and it seems reasonable that softer interbeds not represented by core samples cause the average Young's modulus to be softer than determined by laboratory tests. As a result, the range of elastic moduli from the strain analyses is a reasonable estimate of field conditions, even though it is softer than measurements made on selected cores.

Some of the interpretation methods, like the pressurized poroelastic inclusion (Section 5.3), only provide estimates of elastic properties, whereas the strain type curve method (Section 5.1) provides estimates of hydraulic properties. These estimates are internally consistent using relationships like equation (5.4). The range of Young's modulus of 2 to 6 GPa is consistent with a range of permeability of 100 to 250 mD using (5.4), $D_h = 0.5$ m^2/s, and typical values for porosity, bulk modulus of the fluid and Poisson's ratio.

None of the interpretation methods was able to provide insights from the tilt data. The tilt data were obtained from two tiltmeters, and the result were more erratic than predicted by the analyses.

Strain interpretations all indicate the reservoir is bounded with a maximum dimension of 500 to 1,000 m (Figure 5.47). Cores and well logs indicate well 9A intersects a permeable lens at the base of the Bartlesville formation. An isopach map of the permeable lens indicates a feature that is roughly 1,000 m in extent, although data constraining the extent is sparse to the north and west (Figure 5.47) and the lens may be larger in those dimensions. The extent of the permeable lens inferred from well data is similar, to larger than the extents estimated from the strain measurements. The strain type curve method predicts the largest extent, but it is only capable of estimating a radial distance from the well. Results from the other methods are remarkably consistent in both size and location. They indicate the maximum dimension is 500 to 600 m and the centroid is to the west of well 9A. The predicted sizes are somewhat smaller than the isopach map, but the differences are small and could be due to internal permeability structure independent of the isopach.

All the interpretations indicate that a boundary of the permeable lens occurs between well 9A and the strainmeters AVN. This interpretation occurs because the boundary is required to explain the relative magnitudes of the radial and circumferential horizontal strains. The boundary reduces the magnitude of the radial (EW) strain relative to the circumferential (NS) strain, which explains the field data.

1.3 Project Products

1.3.1 Publications

We currently have one paper in review covering the feasibility of using in-situ deformation measurements for carbon storage monitoring, which is the primary background and motivation for this project. This paper is summarized in Chapter One, Section 1.4.

Murdoch, L. C., Germanovich, L. N., DeWolf, S., Moysey, S. M., Hanna, A. C., and Kim, S., and Duncan, M. (2019). Feasibility of using in-situ deformation to monitor CO_2 storage. *International Journal of Greenhouse Gas Control*, in review, reference JGGC_2018_541.

The following papers have been prepared and are currently being internally reviewed for submission that cover the stochastic inverse algorithm development and modeling results contained in Chapter Three, Section 3.2 and Chapter Five, Section 5.4.

Hanna, A. C., DeWolf, S., Moysey, S. M., Murdoch, L. C., and Germanovich, L. N. (2019). Development of a cloud computing framework for multiobjective model calibration and decision support in the geosciences. To be submitted to *Geomechanics for Energy and the Environment*, under internal review.

Hanna, A. C., DeWolf, S., Moysey, S. M., Murdoch, L. C., and Germanovich, L. N. (2019). Numerical proof-of-feasibility of using geomechanical measurements to estimate poroelastic parameters. To be submitted to *Geophysical Review Letters*, under internal review.

Hanna, A. C., DeWolf, S., Moysey, S. M., Murdoch, L. C., and Germanovich, L. N. (2019). Using borehole strain tensor measurements to locate and characterize subsurface heterogeneities in the Bartlesville formation in Avant Field, Oklahoma. To be submitted to *Geomechanics for Energy and the Environment*, under internal review.

Hanna, A. C., DeWolf, S., Moysey, S. M., Murdoch, L. C., and Germanovich, L. N. (2019). Using hierarchical inversion to combine fixed and dynamic parameterizations for imaging of heterogeneous ground water systems. To be submitted to *Geomechanics for Energy and the Environment*, under internal review.

These papers form the basis of Alexander C. Hanna's Ph.D. dissertation:

Hanna, A. C. (2019). *Stochastic Parameter Estimation of Poroelastic Processes using Geomechanical Measurements* (Doctoral Dissertation). Clemson University.

Background research into the North Avant Field geology presented in Chapter Four, Section 4.1.1 was performed by Josh Smith as a part of his Ph.D. dissertation:

Smith, J. E. (2017). *Geophysical fluid flow during hydrothermal venting and carbon sequestration* (Doctoral Dissertation). Georgia Institute of Technology.

The following two papers are being prepared for submission that cover the development, installation, field observations and performance of the eddy current strain and tilt systems and optical fiber areal strainmeters presented in Chapter Two, Sections 2.2, 2.3 and 2.5, and Chapter Four, Sections 4.2.2, 4.2.3 and 4.3.

DeWolf, S., and Murdoch, L. C. (2019). Permanent and removable multicomponent borehole tilt and strain measurement using commercial displacement transducers. To be submitted to *Review of Scientific Instruments*, in preparation.

DeWolf, S., and Murdoch, L. C. (2019). New robust borehole optical fiber areal strainmeters for monitoring geophysical and geomechanical deformations. To be submitted to *Geophysical Research Letters*, in preparation.

The following two papers are being prepared for submission that cover the analytical model development of a pressurized poroelastic inclusion presented in Chapter Three, Section 3.1 and its application to the injection test data presented in Chapter Five, Section 5.3.

Germanovich, L. N., Murdoch, L. C., and DeWolf, S. (2019). Simple reservoir analysis based on 2017–2018 injections at the North Avant Field (Osage County, OK). To be submitted to *Journal of Geophysical Research: Solid Earth*, in preparation.

Germanovich, L. N., Murdoch, L. C., and DeWolf, S. (2019). Thin Eshelby inhomogeneity in a bounded or semi-bounded region. To be submitted to *International Journal of Mechanics and Physics of Solids*, in preparation.

The following two papers are in preparation describing the development and application of the type curve method presented in Chapter Three, Section 3.3 and Chapter Five, Section 5.1.

Murdoch, L. C., Germanovich, L. N., and DeWolf, S. (2019). A type curve method for interpreting strain data during well tests. To be submitted to *Water Resources Research*, in preparation.

Murdoch, L. C., Germanovich, L. N., and DeWolf, S. (2019). Field measurements and interpretation of the strain tensor during injection into a reservoir. To be submitted to *Journal of Geophysical Research*, in preparation.

1.3.2 Raw and Processed Data

All raw data from this project are publically available through the Incorporated Research Institutions for Seismology's Data Management Center (IRIS DMC). All data managed by Clemson University are aggregated through the International Federation of Digital Seismograph Networks (FDSN) Network Code 2J, which can be found through the following listing:

DeWolf, S. and Murdoch, L. C. (2016). *Clemson University Subsurface Deformation Monitoring Network*, International Federation of Digital Seismograph Networks, Dataset/Seismic Network, `http://www.fdsn.org/networks/detail/2J_2016/`, DOI: 10.7914/SN/2J_2016.

Metadata (dataless SEED) and waveforms (miniSEED) can be found via the IRIS MetaData Aggregator at:

`http://ds.iris.edu/mda/2J/`

This excludes raw 9A injection pressure and rate data, which are property of Grand Resources. The Gladwin Tensor Strainmeter deployed in AVN2 is operated and maintained by UNAVCO, whose raw data are also publically available under the FDSN Network Code PB. Metadata (dataless SEED) and waveforms (miniSEED) can be found via the IRIS MetaData Aggregator at:

`http://ds.iris.edu/mda/PB/AVN2/`

Processed data from the shut-in and three injection tests discussed in Chapters Four and Five can be found through NETL's Energy Data eXchange (EDX) via the following listings:

Murdoch, L. C., and DeWolf, S. (2019). 1A Shut-In: March 31 thru April 7, 2017. `https://edx.netl.doe.gov/dataset/1a-shut-in-march-2017`, DOI: 10.18141/1505373.

Murdoch, L. C., and DeWolf, S. (2019). 9A Injection: October 11 thru October 17, 2017. `https://edx.netl.doe.gov/dataset/9a-injection-october-2017`, DOI: 10.18141/1505374.

Murdoch, L. C., and DeWolf, S. (2019). 9A Injection: November 28 thru December 1, 2017. `https://edx.netl.doe.gov/dataset/9a-injection-november-28-2017`, DOI: 10.18141/1505375.

Murdoch, L. C., and DeWolf, S. (2019). 9A Injection: June 28 thru July 23, 2018. `https://edx.netl.doe.gov/dataset/9a-injection-june-2018`, DOI: 10.18141/1505376.

These files include 9A injection pressure and rate data, courtesy of Grand Resources, as well as the fully processed, "Level 2" data from the Gladwin Tensor Strainmeter in AVN2, which can be accessed at:

`ftp://bsm.unavco.org/pub/bsm/level2/osageavn2bok2016`

1.3.3 Stochastic Inversion Source Code

The source code for the stochastic inversion algorithm described in Chapter Three, Section 3.2 and implemented in Chapter Five, Section 5.4 is publically available at the following software repository:

`https://github.com/achanna/dmsof`

1.3.4 Presentations

The following is a list of contributed and invited presentations containing activities related to this project given at research conferences. This includes both poster and oral presentations, but excludes oral presentations from the annual DOE NETL progress report meetings.

Moak, R., Murdoch, L. C., DeWolf, S., Germanovich, L. N., Blais, R., and Plunkett, G. (2018). *Characterizing the Subsurface Using Deformation from Pumping and Surface Loading Tests.* 2018 Fall Meeting of the American Geophysical Union, Session H51A, Presentation H51A-07. Washington, DC. December 14, 2018.

Murdoch, L. C., DeWolf, S., Germanovich, L. N., Hua, L., Hanna, A. C., Tang, J., Moysey, S. J., Xiao, H., Moak, R., Plunkett, G., and Blais, R. (2018). *Characterizing Strain During Injection to Reduce Risks During CO2 Storage.* 2018 Fall Meeting of the American Geophysical Union, Session H23M, Presentation S51F-0392. Washington, DC. December 14, 2018.

Hanna, A. C., Moysey, S. J., Murdoch, L. C., DeWolf, S., and Germanovich, L. N. (2018). *A cloud computing approach to massively-parallel distributed stochastic optimization with application to geomechanical reservoir characterization.* 2018 Fall Meeting of the American Geophysical Union, Session H23M, Presentation H23M-2144. Washington, DC. December 11, 2018.

DeWolf, S., Murdoch, L. C., Hua, L., Xiao, H., Germanovich, L. N., Moysey, S. J., and Hanna, A. C. (2018). *New Electromagnetic and Optical Fiber Strainmeters and Tiltmeters for Measuring Deformation.* 2018 Incorporated Research Institutions for Seismology (IRIS) Seismic Instrumentation Symposium, Session 2: Advancements in Instrumentation. Tuscon, AZ. October 30, 2018.

Hanna, A. C., DeWolf, S., Moysey, S. J., and Murdoch, L. C. (2018). *Using strain tensor measurements to locate and characterize subsurface heterogeneities.* European Geophysical Union General Assembly 2018, Session ERE6.1, Presentation EGU2018-19571. Vienna, Austria. April 12, 2018.

DeWolf, S., Murdoch, L. C., Germanovich, L. N., Moysey, S. J., and Hanna, A. C. (2018). *Results from New Tensor and Areal Strainmeters for Monitoring Fluid Injection and Withdrawal.* 2018 Clemson Hydrogeology Symposium. Clemson, SC. April 12, 2018.

DeWolf, S., Murdoch, L. C., Germanovich, L. N., Moysey, S. J., Hanna, A. C., Hu, J., Blais, R., Plunkett, G., and Johnson, W. (2017). *New Tensor and Volumetric Strainmeters for Monitoring Fluid Injection and Withdrawal.* 2017 Fall Meeting of the American Geophysical Union, Session G51B, Presentation G51B-0750. New Orleans, LA. December 15, 2017.

Murdoch, L. C., DeWolf, S., Germanovich, L. N., Moysey, S. J., Hanna, A. C., Hu, J., Blais, R., Plunkett, G., and Johnson, W. (2017). *Forward and Inverse Models Incorporating Strain, Tilt and Pressure Data for Monitoring Deformation During CO2 Injection.* 2017 Fall Meeting of the American Geophysical Union, Session S51C, Presentation S51C-0613. New Orleans, LA. December 15, 2017.

DeWolf, S., Murdoch, L. C., Smith, J., Germanovich, L. N., Moysey, S. J., and Hanna, A. C. (2016). *Results from New Strainmeters and Forward and Inverse Models for Monitoring Deformation During CO2 Injection.* 2016 Fall Meeting of the American Geophysical Union, Session G33A, Presentation G33A-1035. San Francisco, CA. December 14, 2016.

DeWolf, S., Murdoch, L. C., Moysey, S. J., Germanovich, L. N., Hanna, A. C., and Smith, J. (2016). *Two High-Resolution Systems for Measuring Ground Deformation During CO2 Injection.* 2016 Clemson University Research Symposium. Clemson, SC. May 4, 2016.

Smith, J., Murdoch, L. C., Moysey, S. J., Germanovich, L. N., Mattioli, G., DeWolf, S., Hannah, A. C., Robinowitz, M., Robinowitz, S., and Mencin, D. (2016). *Measure and Interpret Deformation During CO2 Injection into a Reservoir.* 2016 Clemson Hydrogeology Symposium. Clemson, SC. March 31, 2016.

DeWolf, S., Murdoch, L. C., Moysey, S. J., Germanovich, L. N., Hanna, A. C., and Smith, J. (2015). *Removable Tensor Strainmeter and Vector Tiltmeter System Coupled with Forward and Inverse Methods for Characterizing Deformation During CO2 Injection.* 2015 Fall Meeting of the American Geophysical Union, Session S21A, Presentation S21A-2673. San Francisco, CA. December 15, 2015.

DeWolf, S., Murdoch, L. C., Moysey, S. J., Germanovich, L. N., Hanna, A. C., and Smith, S. (2015). *Tensor Strainmeter and Vector Tiltmeter Design for Measuring Ground Deformations Associated with Fluid Injection and/or Withdrawal.* 2015 Clemson Hydrogeology Symposium. Clemson, SC. March 26, 2015.

1.4 Background on the Need and Feasibility of Using In-Situ Deformation to Monitor CO_2 Storage

Geologic storage of CO_2 is a promising way to limit the increase of greenhouse gases in the atmosphere (Stocker), and monitoring the injection process is important to ensure CO_2 remains securely stored. A wide range of techniques are being considered for monitoring the injection process (Stocker; Liu, 2012), and one of them involves assessing deformation of the formation caused by changes in fluid pressure (Davis, 2011; Verdon et al., 2013). Deformation during injection can range in magnitude, extent and rate (Rutqvist et al., 2010), causing both opportunities and problems. Deformation at the ground surface may damage infrastructure (Mayuga and Allen, 1969), but even modest deformation forms a pattern that can be interpreted to estimate the distribution of volume change in the reservoir (Vasco et al., 2001, 2010; Germanovich et al., 2012). Surface deformation is typically slow, with rates in the range of mm/yr (Vasco et al., 2010), and the rate and duration of the deformation process are important factors affecting how it is measured (Figure 1.1). Radar interferometry (InSAR) and Global Positioning System (GPS) sensors can measure slow, persistent deformation of the ground surface (Bohloli et al., 2018; Phillips et al., 2003), and these data can be useful for monitoring tectonic processes (Figure 1.1). At the other end of the time scale, rapid deformation in the form of seismicity can cause problems when magnitudes are excessive (Garagash and Germanovich, 2012; Zoback and Gorelick, 2012; Ellsworth, 2013), and small amplitude microseismicity also provides a useful signal for monitoring (Figure 1.1, Maxwell et al. (2008); Rutqvist et al. (2010); Gutierrez et al. (2012)).

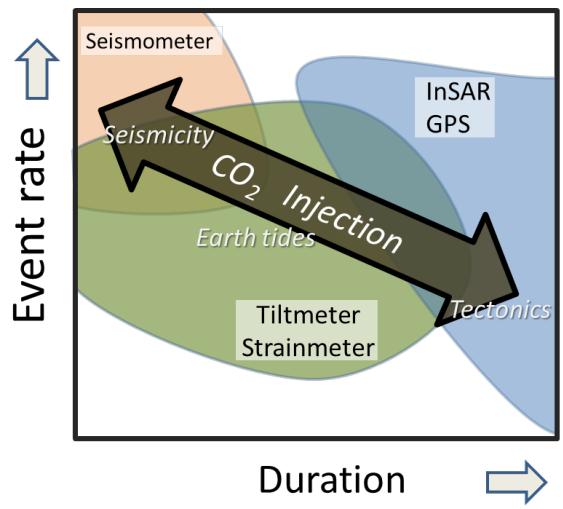

Figure 1.1: Schematic of strain-producing events (seismicity, Earth tides, and tectonics) and techniques for measuring strain (seismometers, strainmeters, and InSAR and GPS). CO_2 injection causes strains that range from fast, short-lived events characterized by seismicity, to slow persistent processes at rates similar to tectonic plate motion.

Deformation during injection also occurs at scales intermediate between the rapid and short-lived seismic events characterized by geophones and the relatively large displacements that can be detected between pairs of measurements made by InSAR and GPS. In-situ sensors are typically required to measure these signals because they can be too small to be distinguished from noise at the ground surface. Borehole tiltmeters that measure the vertical gradient in the horizontal displacement are the most common instrument used for this purpose, and a variety of other strainmeters have been developed for measuring other aspects of in-situ deformation. In general, these instruments offer tradeoffs between the strain resolution, spatial density, logistics of deployment and cost. They were developed for applications other than monitoring CO_2 storage, so their value to this application remains unclear.

The objective of this section is to evaluate the feasibility of using in-situ strain measurements to improve monitoring of CO_2 storage. The section is organized into two subsections. In the first subsection, numerical simulations will be used to evaluate the magnitude and distribution of strains and strain rates related to injection. These are the signals that in-situ sensors would be required to measure. The next subsection is a review of instrumentation for measuring in situ strains.

1.4.1 Expected Deformation Field Caused by an Injection Well

Injection causes the fluid pressure to increase in the vicinity of a well and this deforms the reservoir and overlying confining unit, and the injection wellbore itself. The region of increased fluid pressure expands outward away from the wellbore and this causes the deformation field to change with time.

A simple approach to characterizing the deformation field far from the reservoir is to assume that injection increases the pore pressure in the reservoir, (Δp), over a radial extent, a. The magnitude of a relative to the depth of the reservoir, H, will affect the deformation field. When $a/H \gg 1$, deformation is relatively insensitive to depth, so the confining unit deforms like a thin plate. Whereas when $a/H \ll 1$ deformation is expected to change significantly with vertical distance from the reservoir, and it will resemble the deformation over a point source. The radial extent of the pressurized region expands outward, so a increases with time as $a \sim \sqrt{2D_1 t}$, where D_1 is hydraulic diffusivity. This implies that deformation of the confining unit will resemble that from an underlying a point source early in an injection project, and it will progress toward deformation similar to a thin plate with time.

The magnitude of deformation measured by an instrument will depend on the location of the instrument and a/H at the time of the measurement, and it will also depend on the pressure change in the reservoir, Δp, and mechanical properties of the reservoir and overlying formation. A reference value for deformation is the transformation strain, ε_0, which is related to mechanical properties as $\varepsilon_0 = \alpha \Delta p_c / K$, where K is bulk modulus, and α is the Biot-Willis coefficient, and Δp_c is the characteristic pressure.

The approach used below is to analyze deformation overlying a region where injection is occurring in a geometry and with formation properties resembling those from CO_2 storage projects. Linear elastic poroelasticity (Detournay and Cheng, 1993; Wang, 2000) will be used to describe the distribution of fluid pressure and deformation. Governing equations for poroelasticity are given in Chapter Three. The initial conditions assume there is no fluid flow and the formation is in static mechanical equilibrium. Pressures and displacements are the perturbations determined relative to the initial conditions.

The mechanical boundary conditions assume the ground surface is stress free, and the displacements go to zero in the far field. Continuity of pressure and displacements are preserved across contacts of contrasting material properties. The closed form solution assumes the depth and lateral extents are infinite (a half-space), whereas the numerical analyses uses a lateral boundary that is far (30 km) from the well.

The boundary conditions for the numerical model include the effects of a well where injection is occurring at constant pressure. The mechanical boundary conditions on the well assume the total stress is equal to the fluid pressure. Boundary conditions for the numerical model are given in Table 1.1.

Material properties characterizing formations considered for CO_2 storage span a considerable range, and the magnitudes of these properties affect the resulting response to injection. Results for the closed form solution are scaled to the properties of the reservoir and confining unit, so those results are independent of any particular properties. The numerical analysis was done in two stages to consider effects of variability in properties. We reviewed the properties of different formations (Murdoch et al., 2015) and we used properties typical of a depleted oil reservoir (Table 1.2) to conduct a baseline analysis during the first stage. Additional analyses were conducted during the next stage using distributions of formation properties typical of the geologic settings considered for CO_2 storage.

Table 1.1: Boundary conditions used in analysis

Boundary		Fluid Flow	Elasticity
top ($z = 1,100$ m)		pore pressure = 0 Pa ($P = 0$)	Total normal stress = 0 ($\sigma_n = 0$)
bottom ($z = -100$ m)		impermeable ($\partial P/\partial z = 0$)	roller ($u_z = 0$)
outer ($r = 30,000$ m)		pore pressure = 0 ($P = 0$ Pa)	roller ($u_r = 0$)
Inner (borehole)(r = 0.1m)	lower confining layer ($-100 < z < 0$ m)	impermeable ($\partial P/\partial r = 0$)	roller ($u_r = 0$)
	sand aquifer ($0 < z < 100$ m)	pore pressure = 1 MPa ($P = 1$ MPa)	total normal stress = fluid pressure ($\sigma_n = -P$)
	upper confining layer ($100 < z < 1,100$ m)	impermeable ($\partial P/\partial r = 0$)	total normal stress = fluid pressure ($\sigma_n = -P$)
Interfaces between strati-graphic layers	$z = 0$ and $z = 100$ m	Continuity of pressure	Continuity of displacements

Table 1.2: Representative material properties for a depleted reservoir used for CO_2 storage (from Murdoch et al. (2015)).

	Young's modulus (GPa)	Poisson's ratio	porosity	permeability (mD)	Biot-Willis coefficient
sand reservoir	15	0.25	0.20	100	0.7
shale confining	15	0.25	0.20	0.1	0.7
casing (steel)	200	0.30	0.01	0.0001	0.7
screen (steel)	200	0.30	0.20	100	0.7

1.4.1.1 Solution Methods and Codes

The analyses initially used solutions and three numerical codes (Abaqus, Comsol, and FLAC) designed to solve problems of coupled poroelasticity. The closed-form solution combines asymptotic analysis for thin inclusions (Germanovich and Chanpura, 2002) with the classic Mindlin and Cheng (1950a) and Mindlin and Cheng (1950b) result for a dilation source in a homogeneous elastic half-space, as outlined in Chapter Three. The numerical codes are widely used and readily available.

1.4.1.2 Strain Caused by Injection

The geologic scenarios considered for CO_2 storage are quite variable, and we have tried to select geometries, dimensions and characteristics (Table 1.1 and Table 1.2, Figure 1.2) that are typical. For example, the formation thickness used for CO_2 storage demonstrations ranges from 8 m at the Sleipner project (Chadwick et al., 2004), to more than 300 m of Mt. Simon sandstone at the Decatur project site (Leetaru and Freiburg, 2014). The 100-m thickness used here is between these cases. The lateral extent of formations range from 1 km in the Powder River Basin, Wyoming (Chiaramonte et al., 2008) to several 100 km in the Williston basin, North Datoka (Buursink et al., 2014). The minimum depth for supercritical CO_2 is 800 m, so the depth used in this analysis is on the shallow side of formations that will be considered for CO_2 injection. Nevertheless, some sites, such as the saline aquifer of the Triassic Stuttgart Formation in the northeast Germany Basin, Ketzin, Germany (Forster et al., 2006), are at depths of roughly 1 km.

The fluid injected into the formation is assumed to be at constant temperature and density, both of which are the same as the reservoir fluid. We recognize that the density of supercritical CO_2 is less than that of the brine expected in a reservoir, and the temperature of the CO_2 may differ from that of the subsurface. However, the injection rate and resulting pressure change are expected to dominate the deformation caused by variation in fluid density and temperature, so those variations will be ignored here.

The well is represented as a cylindrical hole lined with a steel tube that represents casing and screen. The properties of cement are assumed to be identical to that of the formation. The casing has properties of steel pipe with a radius of 0.1 m and a wall thickness of 8 mm.

Injection wells may operate at constant rate early in their life, but the formation pressure will increase and later they would probably operate at constant pressure in order to avoid exceeding pore pressures that could damage the formation (Senel and Chugunov, 2013). We have evaluated both constant rate and constant pressure injection scenarios, but the following will be limited to the case of constant injection pressure in order to reduce the number of variables in this initial assessment. The 1 MPa constant pressure at the wellhead results in an injection rate that decreases with time. Most of the change in injection rate occurs in the first few hours, however, and the rate is approximately 0.6 L/s (100 gpm) throughout most of the simulation.

The fluid pressure at the wellbore will be assumed to be fixed at 1 MPa above hydrostatic with injection periods up to several hundred days. These conditions were selected to be between those used for well testing, which could use lower pressures and shorter durations, and those used for sustained operation, which would likely occur at higher pressure during longer periods (Ghomian et al., 2008). For example, injection pressures during CO_2 storage demonstrations were 8 MPa at Ketzin, Germany (Liebscher et al., 2013), 25 MPa at Decatur, Illinois Basin (Senel and Chugunov, 2013) and 45 MPa at Cranfield, Mississippi (Hovorka et al., 2013). As a result, the analyses given here may over-estimate deformations during short-term well testing and under-estimate deformation during operation.

We compared results from preliminary analysis of the configuration in Figure 1.2b using Comsol and Abaqus. The results from the two codes were similar, and progressively finer meshes were evaluated until the results were essentially independent of the mesh density (Murdoch et al. (2016), p. 2–38).

1.4.1.3 Deformation Pattern

The deformation field includes multiple components of strain that change magnitude and sign (Figure 1.2). Some of the strain components go to zero where they change sign from tensile to compressive. This results in a pattern created by three zones; 1) compressive strain, 2) tensile strain, and 3) small strain. Tilt is characterized as a vertical gradient of the horizontal displacement, $\partial u/\partial z$, so leaning away from the well is a positive tilt in axisymmetric coordinates (Figure 1.2).

Strains or tilts with an absolute value less than 0.01 $\mu\varepsilon$ (10^{-8}) were considered to be "small" in Figure 1.2. Earth tides are expected to create strains in the range of 0.01 $\mu\varepsilon$ to 0.1 $\mu\varepsilon$ (10^{-8} to 10^{-7}) in most locations, so "small" strains or tilts are less than those expected to be created by tides.

Results from the simulations show that the pressurized region of the reservoir expands radially outward and upward with time, with the 0.01 MPa contour reaching $r = 800$ m after 1 day, $r = 2,500$ m after 10 days, and $r = 6,000$ m after 100 days of injection (Figure 1.2). The vertical strain is compressive overlying the pressurized zone but it is tensile within the reservoir (Figure 1.2). Tensile vertical strains extend as a bulb ahead of the pressure front in the reservoir, and the edge of the zone of compressive vertical strain in the confining unit overlies or lags slightly behind the pressure front.

Radial normal strain is tensile in the vicinity of the well, but it decreases and becomes compressive with radial distance. The zone of compressive radial strain forms a bulb around the pressure front, which is particularly evident after 1 day of injection (Figure 1.2). The bulb expands with time and reaches the ground surface in a few days. This creates a band of small strain between the two zones that grows outward with time. In general the radial strain is compressive over the pressure front, and the band of small radial strain lags considerably behind the pressure front. Radial strain is particularly large near the well screen, but tensile radial strain occurs near the well throughout the confining unit. The simulation assumes the casing is coupled to the confining unit with cement, so some of the radial strain in the confining unit is from the expansion of the casing itself. Radial strain in the confining unit would be reduced if injection was done through a tubing string that is isolated from the outer casing.

The circumferential strain is tensile everywhere. It is particularly large in the vicinity of the well bore, and it drops off with distance much like the pressure does (Figure 1.2).

The tilt signal is negative (tilt toward the well) overlying the reservoir. The tilt signal expands and a zone of positive tilt develops at the ground surface. Positive surface tilt at the surface is a result of doming caused by injection. The maximum upward displacement of the dome is 0.9 mm for this simulation.

The magnitude and pattern of the numerical results are consistent with the analytical solution in Appendix A, but there are a few differences. The radial strain changes sign with r in both cases, but it does so in the numerical solution closer to the well than in the analytical solution. Vertical strain is compressive over the pressurized zone and it decreases to small values beyond the pressurized zone in the analytical solution. A similar pattern occurs in the numerical results, but the decrease occurs further behind the pressure front. These differences occur because the pressure in the reservoir is assumed to be uniform in the analytical case, whereas it decreases with r in the numerical analysis.

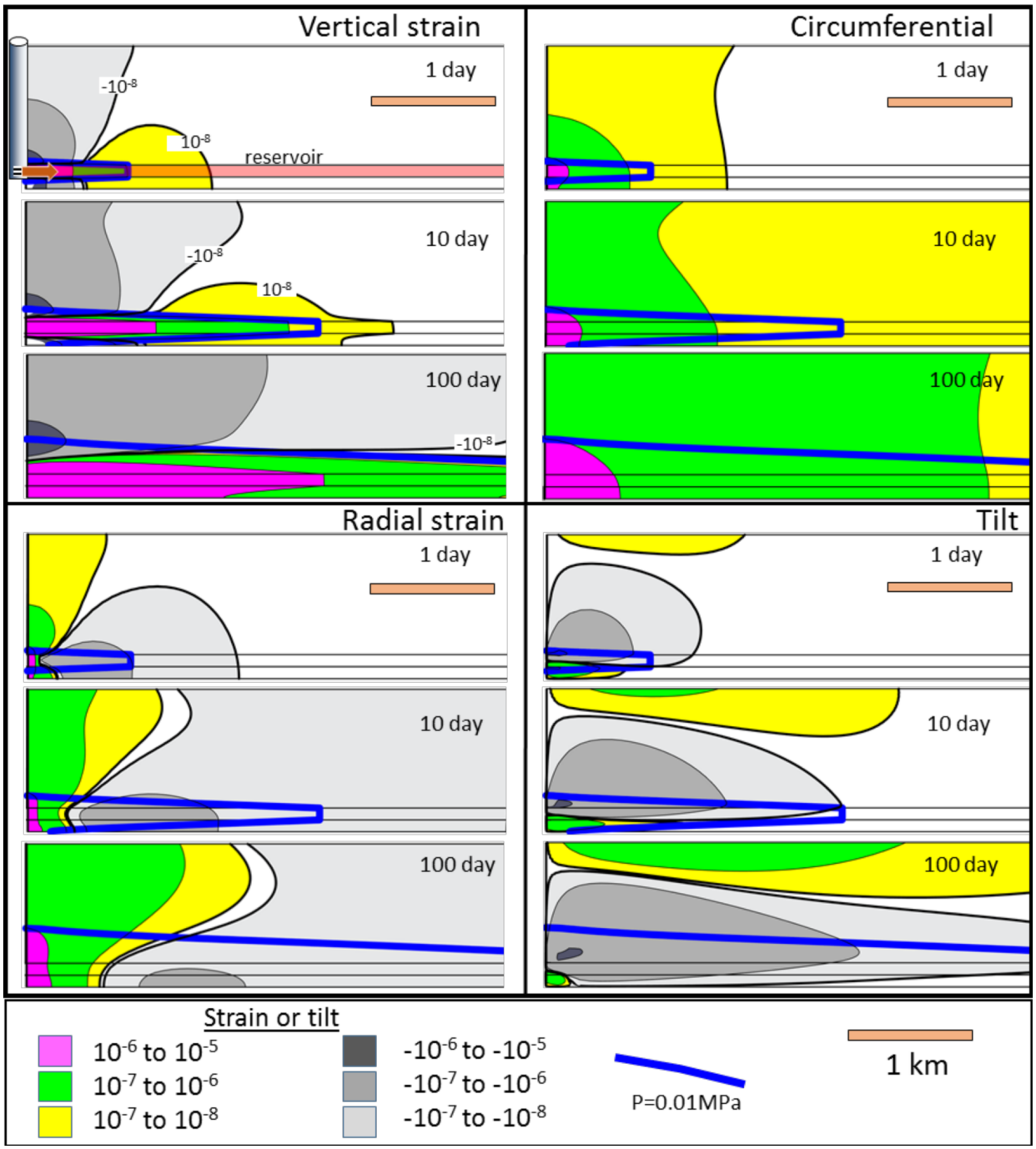

Figure 1.2: Strain or tilt as a function of time during constant pressure (1 MPa) injection. Axially symmetric cross section with well at lower left. The color flood is tensile strain $> 10^{-8}$, or tilt $> 10^{-8}$ rad away from the well. Grey is compressive strain $< -10^{-8}$, or tilt toward well $> 10^{-8}$ rad. Strain and tilt in the white region is small, between $\pm 10^{-8}$. Contours are in log scale. The blue band bounds the region where pore pressure increase is greater than 0.01 MPa.

1.4.1.4 Radial Deformation in the Vicinity of the Wellbore

Radial displacement is generally outward in the vicinity of the well, but details of this process are variable. The magnitude of outward displacement is a few microns at the borehole face, but it increases to more than 10 microns at a radial distance of 1 m in the example (Figure 1.3). The radial displacement results from two effects. One is caused by the stress loading the face of the bore, and it will be called "elastic" loading. The other effect results from changes in the fluid pressure within the formation, and it will be called "pressure" loading. In linear poroelasticity, the total strain (displacement) is the sum of strains (displacements) resulting from the elastic only and pressure only loadings, which, in general, are fully coupled in poroelastic problems.

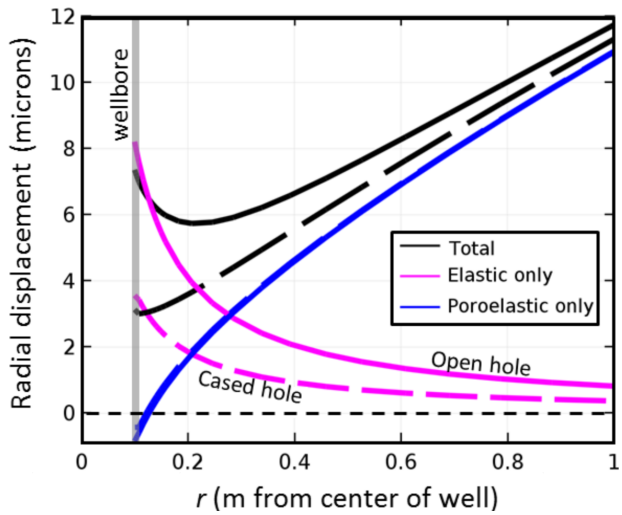

Figure 1.3: Total radial displacement in the vicinity of the well (black lines). Displacements due only to stress on well (elastic, magenta). Displacement due only to fluid pressure (poroelastic, blue). Open hole (solid) and cased hole (dashed). $t = 100$ days, $z = 50$ m. Borehole pressure is 1 MPa.

The elastic-loading case was analyzed by setting the fluid pressures at the inner and outer radial boundaries equal to zero, and keeping the total stress on borehole face equal to the injection pressure. This eliminates flow caused by the fluid boundary conditions, but it is still possible for flow to occur as a result of applying the elastic load. By contrast, an analysis of the pressure-loading case was conducted by setting the total stress on the borehole face equal to zero and keeping the fluid pressure as specified in the original problem.

Total displacement in the vicinity of a pressurized open hole (without casing) is approximately 7.3 microns at the borehole face, it decreases to 5.8 microns at $r = 0.2$ m, and it increases beyond that. Thus, the minimum displacement is in the formation approximately 10 cm from the borehole wall, rather than at the wellbore face itself. This occurs because of the two loading effects. The elastic load creates displacement of approximately 8.2 microns at the borehole face, but it decreases sharply in the formation and is less than 1 micron at $r = 1$ m (Figure 1.3). In contrast, displacement from the pressure-loading case is actually inward by -0.5 micron at the borehole face. It increases with distance and is roughly equal to the displacement from the elastic-only loading at $r \approx 0.3$ m. The total displacement is approximately the sum of the two effects, so it is dominated by the elastic loading of the borehole face at $r < 0.1$ m, and by pressure loading for $r > 1$ m.

Including a perforated casing and/or well screen in the analysis reduces the displacement, but the general effect is retained. The major change occurs because the stiff tubing reduces the elastic loading, so the total displacement in the vicinity of the well bore is reduced to roughly half of the case that considers only an open hole (Figure 1.3). Negative displacements at the well face due to pressure loading also occur when a casing is present.

Displacements from poroelastic processes are small at the borehole face, but they may be significant. Poroelastic effects cause inward displacements in a small region near the borehole where the integrity of the seal between casing and the formation is important. Negative displacements would tend to hold incipient flaws closed, potentially limiting their growth and reducing the onset of leakage.

Details of deformation in the vicinity of a wellbore will vary with material properties, pore pressure, confining stress, and other effects, and the analysis in Figure 1.3 only shows one example. Nevertheless, it

is apparent from this example that monitoring strain or displacements in the annular region could provide useful information about wellbore integrity.

1.4.1.5 Deformation along the Injection Well

The wellbore pressure increases abruptly and is held constant, but the fluid pressure in the confining unit changes with time and this affects the strain near the casing (Figure 1.4a).

The screen is displaced radially outward by approximately 3.5 microns soon after injection starts, and then the displacement decreases with time. In contrast, the outward displacement in the adjacent confining unit is slightly larger at early times, but it increases and then decreases with time (Figure 1.4b).

Vertical strain along the axis of the casing also changes with time, with tensile strain increasing to approximately 10 με ($\varepsilon = 10^{-5}$) in the reservoir. Axial compression occurs in the casing completed in the confining units early in the injection history. The region of axial compression moves into the confining unit with time, roughly tracking the pressure change within the formation (Figure 1.4c).

Strains and displacement in the casing change with time in response to three primary effects: 1) pressure in the casing increases and causes outward radial displacement. 2) Pore pressure adjacent to the casing increases causing inward displacement. This is the same effect that causes inward displacement in the pressure loading case in Figure 1.2. 3) Strains from the deformation of the formation, as shown in Figure 1.2.

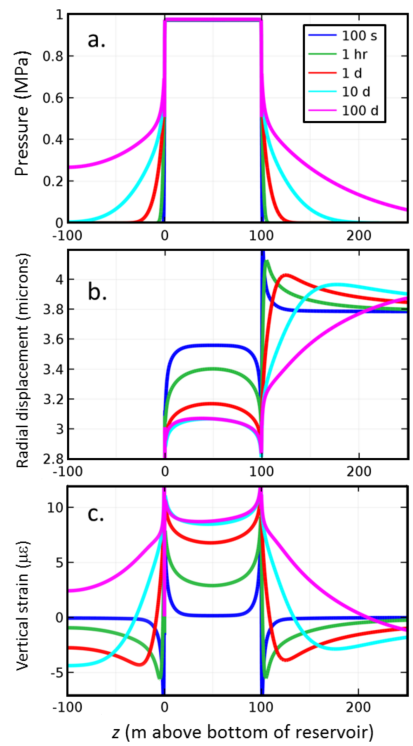

Figure 1.4: Profiles along outside of the casing ($r = 0.1$ m). (a) Fluid pressure. (b) Radial displacement. (c) Vertical (axial) strain.

1.4.1.6 Deformation Time Series

The time series of deformation at selected points is the simulated analog of measurements from an in-situ instrument, so they are valuable when assessing the feasibility of measuring deformation in the field. Two locations were selected as examples (Figure 1.5) of this approach, one representing a monitoring well at a radial distance of 600 m completed at the top of the reservoir (i.e., $z = 100$ m or depth $d = 1,000$ m), and another representing a monitoring well at the same radial location but completed at shallow depth in the confining unit (i.e., $z = 1,000$ m or $d = 100$ m). Time series from other locations are given in (Murdoch et al., 2015).

Deformation at the top of the reservoir at $r = 600$ m is characterized by strain and tilt in the 0.1 με (10^{-7}) range within a few hours after the start of injection (Figure 1.5a). Pore pressure increases to 0.01 MPa by the end of day 1 and it follows a semi-log straight line trend within a few days. In general, the strain signal precedes the pressure signal, although this effect would likely be more significant at greater radial distances where the arrival times are longer. Circumferential and vertical strain both increase with time, and the vertical strain is the largest strain component at this location. The radial strain is initially negative (compressive), but it reaches a maximum compression of -0.2 με and then it starts to increase. The radial strain is zero after approximately 60 days and becomes positive after that (Figure 1.5a).

The strain rates are greatest at the start of injection when they are in the range of 1 to 6×10^{-12} 1/s at the top of the reservoir at $r = 600$ m (Figure 1.5b). The strain rates decrease with time and are less than 10^{-12} 1/s after the first few days. The strain rates are in the range of 10^{-13} to 10^{-12} 1/s for several tens of days (Figure 1.5).

At shallow depth ($d = 100$ m) in the confining unit the strains are smaller and the strain rates are slower than they are at the top of the reservoir (Figure 1.5c and 1.4d). Moreover, the history of strain is considerably different than at depth $d = 1,000$ m. At the shallow location, the strain magnitudes are in the range of tens of nε after the first day and they increase to approximately 100 nε (0.1 με) after 10 to several tens of days. The sign of the response to pressure and strain at shallow depth is opposite to that of the change in the reservoir, with the exception of the circumferential strain, which is tensile at both locations (Figure 1.5). The strain time series follow from the patterns of strain in Figure 1.2.

The decrease in pore pressure in the confining unit (Figure 1.5c) is initially surprising because the pore pressure is increasing in the reservoir. This poroelastic effect occurs because the pore pressure at the shallow monitoring location is isolated from pressure changes in the reservoir over the time scale of the analysis. Instead, the pore pressure drops because the volumetric strain is tensile. A pressure change in a confining unit that opposes the pressure change in an underlying aquifer or reservoir has been observed in a variety of settings (Slack et al., 2013).

Strain rates at the shallow monitoring location are in the range of 10^{-13} s^{-1}, roughly an order of magnitude slower than at the top of the reservoir (Figure 1.5). The rates slow with time, dropping by an order of magnitude within 10 to several tens of days after the start of injection.

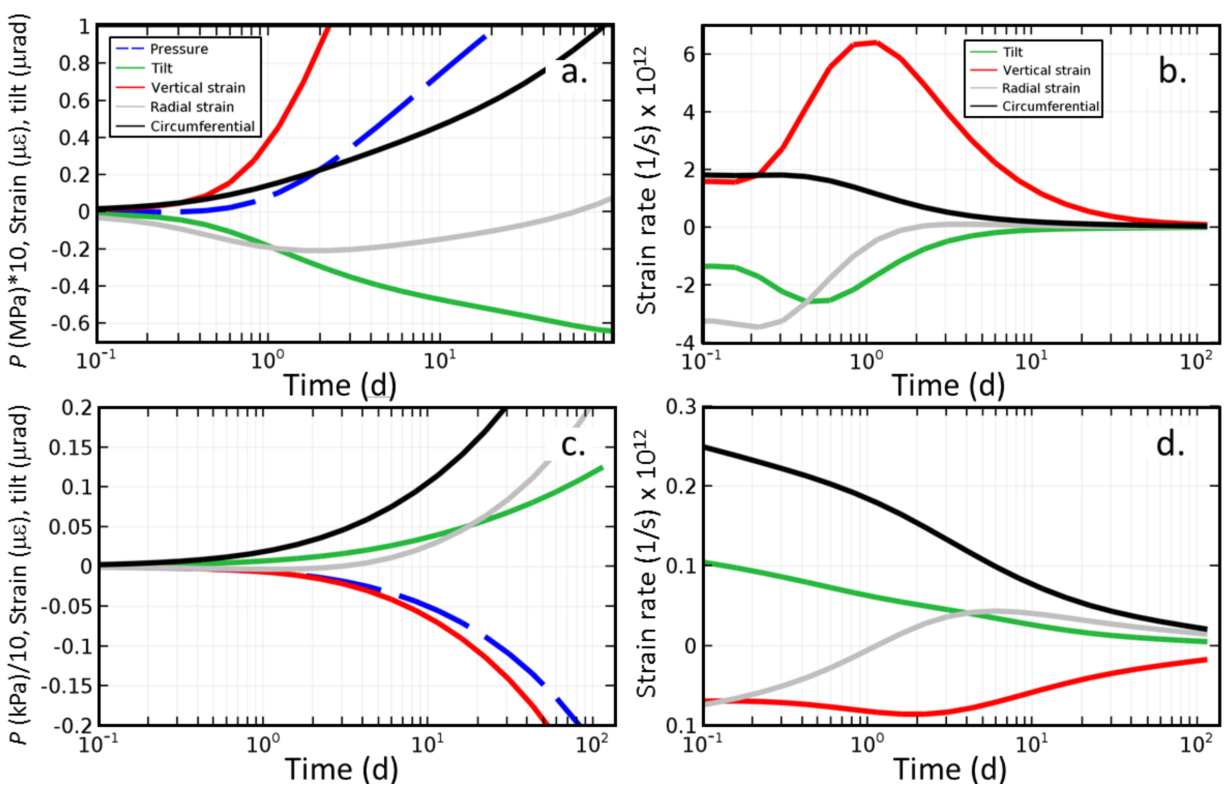

Figure 1.5: Pressure and strain (left column) and strain rate (right column) as functions of time at selected locations. (a) and (b) Deep monitoring well at top of reservoir, $r = 600$ m, $d = 1,000$ m. (c) and (d) Shallow monitoring well; $r = 600$ m, $d = 100$ m.

1.4.1.7 Effects of Reservoir Type

The results outlined above are based on an analysis that uses parameters typical of a depleted reservoir, but results are expected to differ in formations with different properties. CO_2 storage is being considered in several types of formations, including; a) depleted oil-gas reservoirs; b) deep saline aquifers; c) coal beds; d) organic shales; d) basalts. We reviewed the poroelastic properties from approximately 45 locations, including 12 European and 33 US sites used for CO_2 storage and we compiled the results in a database (Murdoch et al., 2015). Three of the formations (depleted gas/oil reservoir, deep saline aquifer and coal beds) were considered for further analysis. We did not consider organic shales because their permeability is extremely low and it will be infeasible to store CO_2 in shales using the conceptual model for flow through porous media adopted here. Basalts were omitted from the analysis because the poroelastic parameters available for basalts were too limited to provide an adequate basis for evaluation.

Results were compiled to evaluate how the ranges of parameters in each geologic setting affected the strains measured at selected points. The data include the transient pressure and strain signals at 16 locations (Murdoch et al. (2015), Figures 2.4–5). This complex set of time series was simplified by selecting representative values for each location and reservoir type at $t = 100$ days (Table 1.3).

Data for the depleted oil/gas reservoir show that the maximum variation in normalized strain is for the vertical strain at the injection well and it ranged from 0.3 to 2.4, and typical values range from 0.5 to 1.5 (normalized values are in parentheses in Table 1.3). The range of normalized strains is larger for the case of saline aquifers and coalbeds, reaching a maximum of 7.7 for radial strain in the confining unit in the coalbed dataset. The minimum normalized strain is negative in some cases. This occurs because the vertical and radial strains change sign with time at some locations, and the range of parameters considered in the analysis affect the timing of when the sign change occurred.

The general result from the analysis of the different combinations of properties is that it will affect the predicted strains by less than a factor of 2 in most locations. Larger relative variations are expected where the predicted strains are small.

Table 1.3: Maximum/mean/minimum strains ($\mu\varepsilon$) at observation points at $t = 100$ days determined using distribution of parameters for a particular reservoir type. Max and min normalized to mean in parentheses. Positive is tensile, negative is compressive strain.

Coord. (m,m)	Location	Radial strain	Circ. strain	Vertical strain
Type: Depleted oil/gas reservoir				
(0.1, 40)	middle of the reservoir at the injection well	-29/ -19/ -12 (1.5/ 0.6)	63/ 43/ 30 (1.4/ 0.7)	44/ 18/ 5 (2.4/ 0.3)
(0.1, 900)	middle of the confining at the injection well	-38/ -38/ -38 (1.0/ 1.0)	103/ 103/ 103 (1.0/ 1.0)	-2.6/ -1.0/ -0.6 (1.6/ 0.6)
(0.1, 1800)	ground surface at the injection well	-38/ -38/ -38 (1.0/ 1.0)	103/ 103/ 103 (1.0/ 1.0)	-1.5/ -1.3/ -1.1 (1.2/ 0.9)
(1000, 40)	middle of the reservoir at monitoring well	0.8/ 0.5/ 0.3 (1.5/ 0.5)	2.4/ 1.3/ 0.6 (1.8/ 0.4)	17/ 7.5/ 2.3 (2.3/ 0.3)
(1000, 900)	middle of the confining at monitoring well	0.8/ 0.5/ 0.2 (1.7/ 0.5)	0.9/ 0.5/ 0.3 (1.7/ 0.5)	-1.7/ -1.0/ -0.5 (1.7/ 0.5)
(1000, 1800)	ground surface at the monitoring well	0.5/ 0.3/ 0.2 (1.6/ 0.5)	0.5/ 0.3/ 0.2 (1.6/ 0.5)	-0.7/ -0.4/ -0.2 (1.6/ 0.5)

continued on next page

continued from previous page

Type: Saline aquifer				
(0.1, 40)	middle of the reservoir at the injection well	-90/ -52/ -33 (1.7/ 0.6)	87/ 68/ 31 (1.3/ 0.5)	246/ 95/ 25 (2.6/ 0.3)
(0.1, 900)	middle of the confining at the injection well	-39/ -38/ -38 (1.0/ 1.0)	104/ 103/ 103 (1.0/ 1.0)	-3.4/ -1.7/ -0.7 (2.1/ -0.4)
(0.1, 1800)	ground surface at the injection well	-38/ -38/ -38 (1.0/ 1.0)	104/ 103/ 103 (1.0/ 1.0)	-2.9/ -1.8/ -1.2 (1.7/ 0.7)
(1000, 40)	middle of the reservoir at monitoring well	0.6/ 0.2/ -0.3 (3.9/ -2.2)	2.5/ 1.5/ 0.8 (1.6/ 0.5)	114/ 46/ 13 (2.5/ 0.3)
(1000, 900)	middle of the confining at monitoring well	0.9/ 0.5/ 0.3 (1.7/ 0.5)	1.3/ 0.7/ 0.3 (1.8/ 0.5)	-1.9/ -1.2/ -0.6 (1.6/ 0.5)
(1000, 1800)	ground surface at the monitoring well	1.0/ 0.5/ 0.2 (1.9/ 0.5)	1.4/ 0.6/ 0.3 (2.2/ 0.4)	-1.6/ -0.8/ -0.3 (2.1/ 0.4)
Type: Coalbed				
(0.1, 5)	middle of the reservoir at the injection well	-100/ -57/ -35 (1.8/ 0.6)	83/ 60/ 17 (1.4/ 0.3)	291/ 120/ 35 (2.4/ 0.3)
(0.1, 380)	middle of the confining at the injection well	-39/ -39/ -38 (1.0/ 1.0)	103/ 103/ 103 (1.0/ 1.0)	-1.1/ -0.5/ -0.1 (2.2/ 0.1)
(0.1, 740)	ground surface at the injection well	-38/ -38/ -38 (1.0/ 1.0)	103/ 103/ 103 (1.0/ 1.0)	-1.6/ -1.2/ -0.9 (1.4/ 0.8)
(1000, 5)	middle of the reservoir at monitoring well	-0.20/ -0.08/ -0.01 (2.6/ 0.1)	0.38/ 0.17/ 0.004 (2.3/ 0.02)	28.0/ 10.0/ 0.01 (2.8/ 0.0009)
(1000, 380)	middle of the confining at monitoring well	0.09/ 0.01/ -0.06 (7.7/ -5.3)	0.23/ 0.11/ 0.005 (2.1/ 0.04)	-0.29/ -0.11/ 0.004 (2.6/ -0.03)
(1000, 740)	ground surface at the monitoring well	0.12/ 0.03/ -0.06 (4.7/ -2.4)	0.23/ 0.11/ 0.008 (2.1/ 0.07)	-0.20/ -0.09/ 0.003 (2.3/ -0.03)

1.4.1.8 Effects of Injection Rate and Pressure

We evaluated a range of injection rates and pressures and compared the resulting strains to the baseline case. The results show that the strain magnitude is proportional to the injection pressure, whereas the strain rate is proportional to the injection rate, a finding consistent with the analytical solution (Appendix A). The baseline case is for injection at constant pressure of 1 MPa. Doubling the injection pressure to 2 MPa will approximately double the strains compared to those shown in cross-section in Figure 1.2, or in the profiles in Figure 1.4 or the time series in Figure 1.5. The injection rate in the baseline simulation decreases with time, but it is approximately 6.3×10^{-3} m^3/s (100 gpm) for most of the simulation. Increasing the injection rate to 1,000 gpm would increase the strain rates by approximately an order of magnitude compared to those shown in Figures 1.2, 1.4 and 1.5.

1.4.2 Measuring In-Situ Strain

The analyses outlined above show that injection will create a richly varied in-situ strain field as pressure changes deform the reservoir and enveloping confining units. At least three classes of in-situ instruments are available for measuring deformation associated with pressure changes in aquifers or reservoirs. The different

classes trade logistics of use for resolution. *Annulus strain sensors* are mounted outside the casing in the annulus between casing and the formation so use of the well is unaffected. These sensors are installed during well completion, so the logistical constraints during use are mild. *Portable strain instruments*, including extensometers and tiltmeters, are temporarily anchored to the inside of a wellbore. This type of anchoring will affect the logistics of well operation, but some operations can continue during deployment and the instrument can be removed afterwards. The other class is *grouted strainmeters*. These instruments were developed by the geodesy community and they are the most sensitive strain instruments available. They are grouted into the bottom of a dedicated boring.

1.4.2.1 Annulus strain sensors

Annulus strain sensors measure deformation outside of the casing (Friefeld, 2017). They typically take advantage of techniques for measuring strain at multiple locations along an optical fiber or electrical cable. While they differ in detail, these techniques typically involve injecting electromagnetic energy and then analyzing the energy that is reflected from various points along an optical fiber or electrical cable. In some cases, Bragg gratings are etched into the fiber (Kreuzer, 2006) or cable (Huang et al., 2013a) and they reflect at a frequency proportional to the spacing of the grating. Changes in the frequency of the reflections are proportional to the strain on the gratings. In other applications, changes in the interference between pairs of reflections can be used to determine the displacement between the two reflectors (Huang et al., 2014).

Another application analyzes small reflections from naturally occurring imperfections in the fiber. This allows distributed strains to be measured using unaltered fibers, instead of requiring fibers with gratings. Brillion scattering within the fiber is shifted in frequency by an amount proportional to strain in the fiber in one application (Galindez-Jamioy and Lopez-Higuera, 2012).

Existing techniques give strain measurements with a resolution of 10^{-7} to 10^{-6} that can be located with a resolution of less than a meter. Equipment to make these measurements is readily available, and a recent example is described by Wu et al. (2015), who used several optical fibers in vertical boreholes to measure distributed vertical strain caused by pumping.

Other applications have focused on measuring strain of the casing, or the annular wellbore region, in an effort to understand wellbore integrity problems. Axial strains can be measured by attaching optical fiber along the axis of the casing. This is the most straightforward configuration, but other strain components can also be important to wellbore integrity and measuring these components requires other sensor configurations. Well casings can be damaged by bending, for example, and a single optical fiber cannot measure bending. One approach is to mount pairs of axial optical fibers at several positions around the circumference of a casing (Jääskeläinen, 2011). One fiber stretches and the opposing one compresses when the casing bends. Casing will dilate when the wellbore is pressurized and this may lead to cracking of wellbore cement or the creation of a micro-annulus, so configurations to monitor radial displacement of casing are also of interest.

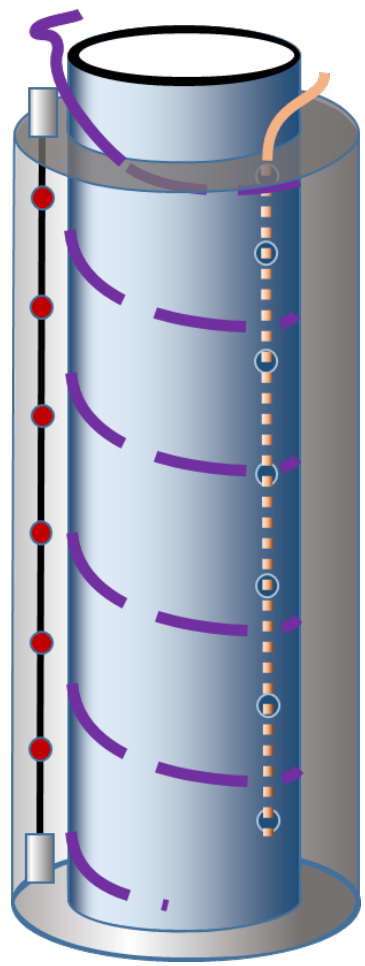

Figure 1.6: Strain sensors in a wellbore annulus. Axial strain sensors embedded in grout (black line with red dots). Distributed sensors along axis (orange) or wrapped helically around casing (purple).

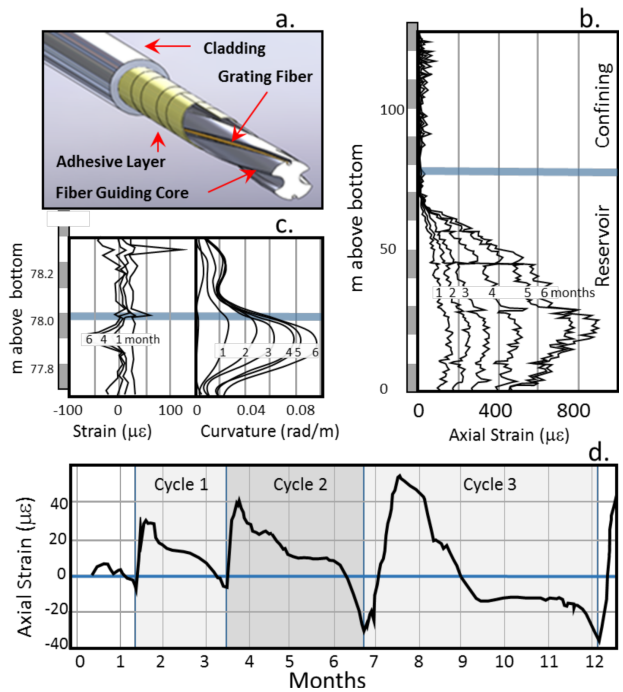

Figure 1.7: (a) Optical fiber wrapped around a helical core in the WIRE strain sensor. (b) Axial strain along the casing measured with WIRE as a function of time in a well completed in a diatomite reservoir. Monthly profiles show strain evolution with time. (c) Axial strain and curvature of the casing as functions of time along the contact between the reservoir and confining unit. Same well as shown in (b). (d) Axial strain along a casing as a function of time in confining unit over a formation undergoing cycles where steam is injected followed by pumping.

One approach for monitoring multiple components of strain, including axial, radial, and bending, is to wrap the the sensors into a helix. Individual strain measurements are made along the axis of the fiber, but the fiber is inclined relative to the axis of the helix, which creates sensitivity to multiple strain components. Measurements from many closely spaced sensors arranged in a helix can be combined to characterize deformation in 3D (Childers et al., 2007), although the sensitivity to the different strain components will vary with the pitch of the helix. Most applications measure strain with optical fibers, but coaxial cables can also be used for distributed strain measurements (Huang et al., 2013b). A coaxial cable wrapped as a helix around casing was evaluated in laboratory by Li et al. (2017), who found that multiple components of strain could be measured during stretching or bending of casing.

Another configuration is to wrap multiple fibers as a helix in a single cable, which is attached to the casing during during completion. The WIRE system uses four optical fibers wrapped as a helix around a central core to create a single cable that can sense 3D deformation (Figure 1.7a). One of the first field applications of the WIRE system was at a well drilled into the Diatomite/Tulare formation in California, a relatively shallow and soft formation that readily deforms during production. Oil and water were being pumped out of this formation, but water was also being injected and these competing processes affected the strain measured at the well. In general, compressive strain increased with time over a 6-month period along a 60-m-long interval within the reservoir, reaching maximum values of approximately 800 με (Figure 1.7b). The strain varied along the casing, and localized strain variations persisted in all the measurements, probably because the strain was responding to local variations in material properties in the formation. The strain is compressive in this example because of a net loss of fluid from the reservoir, and the rate varies with time in response to reservoir activities. The average strain rate was 3×10^{-11} 1/s, but it increased to 8×10^{-11} 1/s when the pumping rate increased, and it decreased to nearly zero when the water injection rate was increased.

Bending strains can be localized along the contact between a reservoir and a confining unit, and it can be strong enough to collapse casing. Bending at the contact between the reservoir and overlying confining unit was measured by the WIRE system using differential strain between adjacent sensors. Bending was particularly large along the contact between the reservoir and the overlying confining unit (Figure 1.7c), with an average rate of approximately 10^{-10} rad/s. At another location, the WIRE instrument was installed along the casing of a well in the confining unit over a reservoir undergoing cycles of steam injection followed by pumping. Steam injection raises the pressure and compresses the confining unit at the beginning of each cycle, much like would occur with CO_2 injection. Subsequent pumping reduces the compressive strain and at the end of each cycle the strain becomes tensile relative to the strain at the beginning of the test (Figure 1.7d).

The WIRE system is designed to characterize relatively high strains that could damage a well casing. It is also possible that this system would detect strains affecting the permeability of the annulus and the integrity of the wellbore seal. An advantage of WIRE, and other annulus monitoring systems is that operation of the well is unaffected, but a disadvantage is that they must be installed when the well is completed so they are unsuitable to existing wells.

1.4.2.2 Portable Strain Instruments

This class of instruments includes extensometers, tiltmeters, and combination instruments. Early investigations of hydromechanical well tests used extensometers that measured displacement over the entire length of a well (Riley, 1969; B. E. Lofgren, 1961; Davis et al., 1969; Pope and Burbey, 2004). These devices provide remarkable insights, but but by spanning a long length so they fall short of characterizing spatial distributions of hydromechanical response. They also require considerable effort to install in a dedicated well. More recent work has led to the development of portable, compact extensometers, which can be moved along a wellbore to characterize hydromechanical responses at many locations (Gale, 1975; Hesler et al., 1990; Martin et al., 1990; Thompson and Kozak, 1991; Cappa et al., 2006a,b, 2007; Svenson et al., 2007; Murdoch et al., 2009; Schweisinger et al., 2011). Axial displacements along a borehole can also be made by anchoring an optical fiber to the borehole wall by pressurizing a flexible sleeve (Becker et al., 2017), which provides additional options for field deployment.

1.4.2.3 Portable Extensometers

Portable extensometers used for well testing measure the change in distance between two anchors set along the borehole. The anchors are spaced 1 to 2 m apart, providing displacement measurements averaged over that length scale. The anchors can be retracted and the device moved to create a profile of properties along a wellbore (Svenson et al., 2007), or the device can be used to characterize known hydraulically active intervals in a borehole (Cappa et al., 2006a, 2007; Schweisinger et al., 2011; Guglielmi et al., 2013). The development of portable extensometers has enabled hydromechanical well tests to be conducted with little additional effort beyond that of a typical straddle packer tests.

1.4.2.4 Tiltmeters

Another approach to conducting a hydromechanical well test is to measure deformation with tiltmeters instead of extensometers. Tiltmeters measure a gradient in displacement, which is a component of shear strain. Tiltmeters have been used for hydrological applications, but according to Agnew (2007) they were initially developed to study Earth tides. Early tiltmeters were water-filled, horizontal

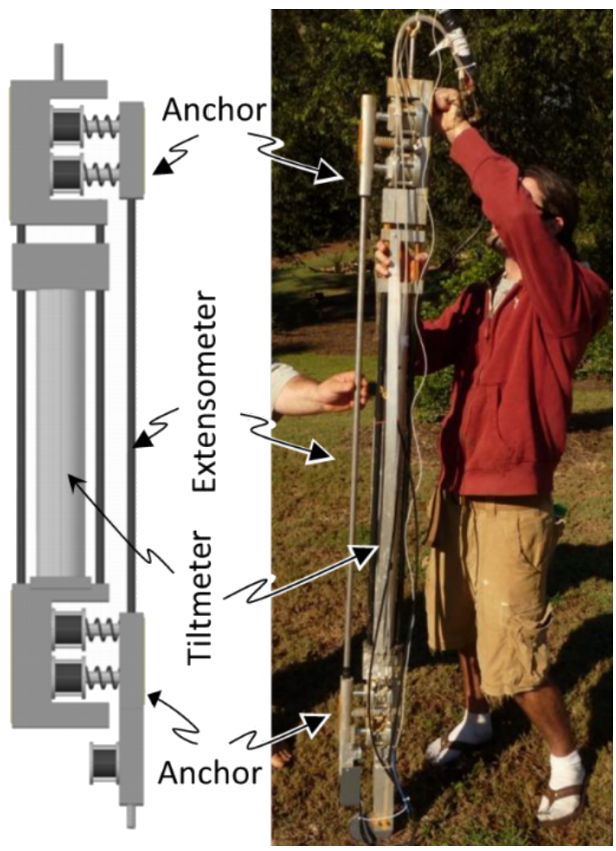

Figure 1.8: Components of a Tilt-X portable borehole tiltmeter and extensometer.

pipes with precision sensors of the water surface at either end (Agnew, 2007). These long-baseline tiltmeters are remarkably accurate, and refined designs continue to be used today for hydrologic studies and other applications (Beavan and Bilham, 1977; Wyatt et al., 1982; Agnew, 1986; Longuevergne et al., 2009; Jacob et al., 2010). The simplicity and high resolution of long baseline tiltmeters makes them attractive for applications in settings where the necessary horizontal access is available (e.g. mines, caves, or similar), but their size and geometry make them cumbersome to deploy.

Tiltmeters using high precision electrolytic bubble sensors developed in compact containers (Agnew, 1986) are readily deployed in boreholes. Refinements in the late 1990s (Castillo et al., 1997; Hunter et al., 2002) have achieved resolution of roughly 10^{-8} rad, which is sufficient to detect deformations associated with changes in pressure during pumping in aquifers or reservoirs (e.g. Figure 1.2; also Fabian and Kümpel (2003); Fabian (2004)). Borehole tiltmeters at depths of less than 50 m have been used to determine deformation caused by aquifer well testing (Vasco et al., 1998; Karasaki et al., 2000; Vasco et al., 2002; Weise et al., 1998; Fabian and Kümpel, 2003; Fabian, 2004) and earth tides (Wyatt and Berger, 1980; Wyatt et al., 1982; Meertens et al., 1989). Borehole tiltmeters have been deployed in several carbon storage demonstration projects (Worth et al., 2014; Verdon et al., 2013), although interpretation of tilt data from these projects remains limited.

1.4.2.5 Multi-Component Portable Strain Instruments

Inversion of tilt (Lecampion et al., 2005) and axial deformation (Svenson et al., 2007; Schweisinger et al., 2011) alone can produce non-unique interpretations, but combining these signals can reduce this ambiguity. This has motivated the development of instruments that measure multiple components of strain at the same location. There are at least two approaches for measuring multiple components of strain, one that uses electromagnetic sensors (Hisz et al., 2013) and and another that uses optical sensors (Guglielmi et al., 2013).

The Tilt-X instrument uses an electrolytic tiltmeter and a differential variable reluctance transducer (DVRT) to measure tilt and axial strain with a resolution of approximately 10^{-8} (Hisz et al., 2013). It has retractable mechanical anchors that grip the borehole wall, so it can be positioned and removed as needed.

The Tilt-X instrument has been field tested at relatively shallow depths (tens of meters). Ambient data obtained deployed across a fracture in crystalline rock resolved an average signal of approximately 15 nm/day during a week-long test. This corresponds to a strain rate of approximately 10^{-13} 1/s, and is probably a result of seasonal changes in groundwater pressure. The ambient data also resolve periodic events where the fracture opens and closes by 20 nm over roughly 8 hours in the morning. Apparently this is largely in response to changes in barometric pressure (Hisz et al., 2013). The ambient tilt signal has a power spectrum with with periods of 12 hr and 24 hr, which are consistent with the O1, K1 and N2, M2 Earth tides (Melchior, 1964). Earth tide tilts are approximately 5×10^{-8} rad and occur at a strain rate of roughly 10^{-12} 1/s.

The ambient field observations show that the Tilt-X instruments can resolve signals expected in the vicinity of CO2 storage wells, which is encouraging. It also points out that hydrologic and atmospheric processes, along with Earth tides, can cause strains of the same magnitude and rate as those expected during CO2 storage. Distinguishing strain signals from different sources will be an important part of the interpretation.

Characterizing formation properties in advance of full-scale CO2 injection is one potential use for portable strain instruments. This application has been evaluated by conducting transient well tests with the Tilt-X in place, and then interpreting the resulting data. An example application conducted at shallow depths shows that the borehole contracts and tilts during pumping. This signal can be explained as a result of a dipping fracture influencing the strain field (details in Hisz et al. (2013)).

Optical sensors can also be used to create a removable, multicomponent strain sensing instruments, and a good example is the SIMFIP probe (Guglielmi et al., 2013). This instrument uses fiber Bragg gratings (FBG) sensors to measure strain within a cage of helical tubes deployed between packers. The helical configuration of sensors allows normal and shear strains to be measured by the instrument, in a manner similar to the configuration used by WIRE. Commercial FBG interrogators use a laser with a wavelength of 1550 nm and a resolution of 1 pm, giving the system the ability to resolve strains slightly better than 10^{-6} (Kreuzer, 2006). This makes the SIMFIP probe well suited to measuring multi-component deformation of boreholes during well tests designed to characterize formations. Guglielmi et al. (2013) describe a step-rate test using the SIMFIP probe that provides a comprehensive suite of hydromechanical characteristics, which would be important for characterizing reservoirs or confining units using for CO2 storage. This instrument has also been used to make the first measurements of shear on a fault as it slips during fluid injection (Guglielmi et al., 2015).

1.4.2.6 Push-in Extensometer

Vertical strain at shallow depths can be measured using a DEL-X extensometer that is pushed into a pilot hole in unlithified material (Murdoch et al., 2016). The frame of the DEL-X consists of a rigid rod with a sleeve around the upper end. The approach is to push or hammer the rod and sleeve to make frictional contact with the pilot hole. The rod and sleeve serve as two anchors separated by approximately 2 m. A Differential Variable Reluctance Transformer (DVRT) displacement transducer is lowered into place after the rod and sleeve are in place, and used to measure the displacement between the two anchors. The DVRT is easily retrieved after use, or for maintenance. The rod and sleeve can also be removed, but they are inexpensive and retrieval may not be cost effective.

The strain resolution of the DEL-X device is less than 10^{-8} (Murdoch et al., 2016) so it is capable of characterizing vertical strains expected at shallow depths above injection scenarios similar to Figure 1.2. The cost of deploying a DEL-X is considerably less than the cost of other strain measuring systems outlined here, so that could make the DEL-X attractive for some applications. It is important to keep in mind, however, that noise from fluctuations in barometric pressure may be greater, and more complicated to remove, at shallow depths than at greater depths. This may impeded interpretation of small strain signals measured by DEL-X.

1.4.2.7 Grouted Borehole Strainmeters

Borehole strainmeters that are grouted in place are the most stable and have the highest resolution of methods for measuring strain at depth. These instruments have been developed to monitor strains caused by tectonics, magmatic intrusion, and other natural processes, and there has been little application to date for monitoring injection. They can resolve strains of 10^{-9} that occur at small rates ($< 10^{-13}$ 1/s), so they have the potential to characterize the strains in much of the colored of shaded regions in Figure 1.1.

1.4.2.8 Current Geodetic Strainmeters

The Sacks-Evertson dilatometer (Sacks et al., 1971) was among the first high-resolution grouted strainmeters to be developed. It was tested in the late 1960s and then it was used for several decades in a variety of geologic applications. This device characterizes strain by measuring the fluid exchange with from one or several oil-filled chambers that are grouted into a borehole. The Gladwin Tensor Borehole Strainmeter (GTSM) was developed in the late 1970s (Gladwin, 1984), and approximately 80 GTSMs were deployed as

a part of the Plate Boundary Observatory (`http://pbo.unavco.org`) in the western U.S. and Canada, and dozens of others are used around the world. The Gladwin strainmeter (Figure 1.8) and similar instruments (e.g. Ishii et al. (2001); Ishii (2002); Ishii and Asai (2015)) have dominated the field of precision strain monitoring for over the last 3 decades, but recent developments have shown that new techniques using optical fiber interferometers have the potential to create an instrument with similar performance and less cost.

1.4.2.9 Interferometric Optical Fiber Strainmeters

Optical fiber interferometers provide one way to measure very small displacements over long baselines or in embedded configurations. These systems operate by dividing laser light into two optical fibers where one is subjected to the desired observable (e.g., strain) while the other is completely isolated or undergoes either an attenuated or opposing strain. The light emerging from each fiber is recombined to form interference fringes whose intensity is proportional to the optical path length difference between the two fibers. This optical interference can be converted into displacements as small as several hundreds of femtometers using fractional fringe counting techniques (Zumberge et al., 2004).

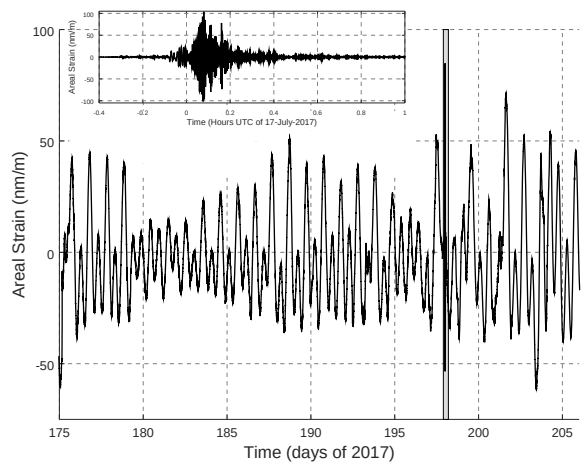

Figure 1.9: Areal strain as a function of time measured with an optical fiber borehole interferometer grouted into biotite gneiss near Clemson, SC, showing the solid Earth tides and surface waves from a teleseismic event (inset).

The high resolution of optical fiber interferometers make them potentially appealing for characterizing small strains and the physical robustness of embedded systems adds to their appeal. The borehole package includes a few simple optical components along with the fiber itself. It is also possible to wrap very long lengths (up to many kilometers) of fiber around metal cylinders to amplify small circumferential strains. This results in a completely passive and rugged package immune to lightning strikes and water incursion known to damage downhole electronics.

Optical fiber interferometers have been used to measure Earth strain over long baselines for decades (Zumberge et al., 1988; Blum et al., 2008; DeWolf, 2014). These instruments consist of stretching one or more fibers in a vertical borehole between an anchor at depth and a clamp near the surface or embedded in the annulus between the formation and well casing (a configuration similar to Figure 1.6). A recent example of the former technique is a triply-redundant, 250-m-long vertical strainmeter in operation at the Piñon Flat Geophysical Observatory (PFO) in Southern California since early 2012. These vertical strainmeters readily measure solid Earth tides, surface waves from teleseismic and microseismic (ocean wave) activity, and dynamic strains and coseismic offsets from regional and local seismicity with a root-mean-squared (RMS) noise of approximately 8 pε.

Unlike their long baseline counterparts, configurations equivalent to existing grout-in borehole strainmeters have only been recently deployed. These systems consist of hundreds of meters of optical fiber wrapped around a pair of nested cylinders, the outermost of which is bonded to the interior of a sealed borehole pressure case and the innermost (reference fiber) is uncoupled (DeWolf, 2014). This configuration measures changes in the cross-sectional area of the pressure case as a result of horizontal strain, as well as the vertical strain due to the off-axis loading of the helically-wrapped fiber. The result is a robust and highly sensitive areal strainmeter capable of measuring strains as small as 10^{-15}. Two of these instruments have been deployed in biotite gneiss near Clemson, SC, and in limestone north of Tulsa, OK, and have

been reliably recording Earth tides and seismicity (Figure 1.9) with a RMS noise equivalent to the PFO instrument.

1.4.3 Discussion

Strain magnitudes decrease with distance from the injection well and increase with time, and a general conceptual model of the strain evolution is useful for anticipating field conditions. For the baseline case analyzed here, strain magnitudes are approximately 10^{-5} in the vicinity of the injection well and they are in the range of 10^{-7} after 10 days of injection within several hundred meters to one km of the injection well. Maximum strain rates are in range of 10^{-11} 1/s near the injection well drop to 10^{-13} 1/s in the confining unit, according to the simulation. Strain rates are relatively rapid soon after injection and they decrease with time, typically slowing by an order of magnitude after 10 days of injection.

Strain caused by injection results from three effects; 1) elastic expansion of the casing; 2) poroelastic deformation of the reservoir and confining units, and 3) mechanical interaction with the ground surface. Elastic expansion of the casing from internal pressure can cause large strains close to the well, but the magnitude decreases sharply with distance (Figure 1.3). Strains in the vicinity of the well are also affected by poroelastic deformation of the reservoir and confining units. Some deformations, like the inward displacement shown in Figure 1.3, are local to the well, whereas others are a result of larger scale deformation, such as the axial compression in the confining unit shown in Figure 1.4c.

Injection causes all three normal strains to be tensile within the pressurized region of the reservoir, and it results in compressive radial strain beyond the pressure front. Radial expansion of the reservoir drags the confining units radially outward, producing negative tilt above the reservoir and positive tilt beneath it. Vertical expansion of the reservoir compresses the overlying confining unit. The increase in pore fluid pressure in the reservoir diffuses upward, causing the confining unit to expand vertically over a zone that grows upward with the pressure change (Figures 1.2 and 1.4).

Stresses are zero at the ground surface and this causes the surface to bulge upward more than it would have in an infinite domain. The resulting shallow strain field is the combination of deformation caused by the expanding reservoir at depth, and additional deformation caused by interaction with the stress free ground surface. This creates a shallow zone where the strain fields are perturbed relative to the fields for an infinite domain. The effect on the tilt is particularly strong because upward bulging causes a significant tilting that is opposite in sign from the underlying tilt field (Figures 1.2, 1.5a and 1.5c). The tilt magnitude goes to zero between the shallow zone and the reservoir zone, and the band of zero tilt creates a convenient boundary between the zones. The depth of the shallow strain zone ranges from 0.2 to 0.35 of the depth of the reservoir. The normal strains are also affected in this shallow zone. For example, the contours of normal strains after 10 days of injection are inclined over the reservoir, but they curve upward and wrap back toward the well as the ground surface is approached (Figure 1.2).

1.4.3.1 Opportunities for Monitoring

Instrumentation is available to measure the strain caused by injection over a wide range of scales, and an effective approach toward deployment would be to match instrumentation with expected signals and logistical constraints. There are at least four primary regions were strain sensing will be of interest, 1) injection well; 2) reservoir or aquifer; 3) overlying confining unit; 4) potential faults.

1.4.3.1.1 Injection well

Strains will be largest in the vicinity of the injection well, so relatively coarse measurement methods can be effective there. This includes distributed strain measurements using optical fibers or electrical cables. These measurements are ideally suited to monitoring relatively large deformations in the cement outside of casing, which could presage damage to the casing. They will be sensitive to changes in pressure in the vicinity of the wellbore, so they could also have applications related to monitoring leaks related to problems with wellbore integrity.

The injection process may cause significant noise and near wellbore effects (e.g. Figure 1.2), which may mask the effects of processes further from the well. However, strain monitoring behind casing above the injection interval may be isolated from the pressure of the injected fluid by the annular space between casing and tubing. Monitoring the axial compression in the confining unit caused by injection in the underlying reservoir could provide useful information on the effects of leaks.

Instrumentation needed to measure strain outside of casing is readily available, and this technology is currently being refined so capabilities are expected to improve. This appears to be an important technology to include in new wells drilled for CO_2 injection.

1.4.3.1.2 Reservoir

Strains in the reservoir are expected to be relatively large near the injection well, and they will decrease with distance. It may be feasible to measure strains in the reservoir using distributed sensors grouted behind the casing of monitoring wells. The vertical strain increases sharply with pressure, and it may be feasible to detect changes in vertical strain in advance of changes in pressure (e.g. Figure 1.4a) using annular sensors in monitoring wells. Shear strains at the contact between a reservoir and confining unit may damage casing in monitoring wells, so annular monitoring would also be useful to warn against this effect. It appears that annular strain monitoring could be useful for both injection wells and monitoring wells drilled into the reservoir.

Portable strain instruments provide the flexibility to monitor strains in wells that were not completed with the instrumentation needed to measure strains in the annulus. Moreover, portable strain instruments can resolve smaller strains than currently available annular sensors, so portable instruments may be useful for monitoring small strain signals that occur during well testing early in program, or at the periphery of an advancing pressure front.

Portable strain instruments have the advantage of being removable for maintenance or redeployment, but the disadvantage is that their anchoring system will likely be less stable than a grouted instrument. This will cause data from portable strain instruments to drift more than grouted instruments. Strain rates are expected to decrease with time during injection (Figure 1.5), so the importance of low drift will increase with time of injection.

1.4.3.1.3 Overlying confining unit

The overlying confining unit will be a good target for strain monitoring because signals resulting from pressure changes in the underlying reservoir can be relatively strong, but costs for drilling and risks of creating leakage pathways will both be less than when sensors are placed in the reservoir. The full strain tensor should provide useful information, but optimal measurement locations will vary with the strain component.

The tilt signal goes from positive to negative at a depth of 0.2 to 0.4 of the depth of the reservoir, so tilt monitoring should either be above or below this depth. In the shallow zone, the tilt is small near the well and reaches a maximum at a radial distance roughly equal to the depth. In contrast, the tilt signal in the lower zone decreases with distance from the well.

Multicomponent portable strain instruments (typically that include a tilt sensor with one or more normal strain sensors) should be capable of resolving strain signals in confining units, particularly early in an injection period when the strain rates are relatively fast.

Relatively small strains make the overlying confining unit an ideal site for grouted strain sensors. These instruments will be well suited to measuring small strains that occur at significant distances from the injection point, or slow strains that occur after injection has been occurring for long periods. Interferometric optical strainmeters are particularly appealing because they offer a robust (no dowhole electronics) way to accurately resolve small strains.

The strain signal at depths of less than a few 100 m should be readily measured using grouted and portable instruments for the scenario simulated here (Figure 1.2). The shallow strain signal will diminish as the depth of the injection increases, and processes above the injection interval (e.g. production from an overlying formation) may mask the underlying strain signal. Nevertheless, costs involved with deploying shallow sensors can be significantly less than costs associated with drilling to reservoir depths and deploying deep sensors, so it may be cost effective for some applications to use shallow strain sensors at many locations instead of one deep one.

The magnitude of drift from measurements made in-situ is likely to eventually exceed that from satellite-based measurements, like InSAR and GPS. That is why in-situ measurements are best suited to characterize changes over moderate time scales (less than weeks to months), whereas satellite-based measurements are better suited to longer time scales (Figure 1.1).

1.4.3.1.4 Heterogeneities

The analyses outlined above have considered the strain field caused by injection into a reservoir and confining unit that differ in properties from each other, but that are otherwise homogeneous. Heterogeneities in elastic properties or permeability may perturb the strain field in important ways. Zones of contrasting stiffness can localize deformation, which may lead to faulting, induced seismicity and leakage. Zones of contrasting permeability may cause leakage in a confining unit, or compartmentalization in a reservoir.

All three types of strain measuring systems have applications in characterizing the strain field resulting from heterogeneities. Grouted sensors are well suited to characterizing strains in the vicinities of heterogeneities, whereas portable systems like SIMFIP (Guglielmi et al., 2013) may be used to monitor creep along a fault itself. Ultimately, however, the value of strain data will be determined by the ability to generate interpretations that can be used for decision making (Vasco et al., 2010; Rutqvist et al., 2010).

1.4.3.2 Interpreting Strain Data

Meaningful quantitative interpretation of strain data will require the calibration of geomechanical models capable of simulating deformation caused by fluid pressure change. There is a long history of analyzing tiltmeter data to characterize hydraulic fractures (Pollard and Holzhausen, 1979; Evans et al., 1982; Castillo et al., 1997; Warpinski et al., 1997), the distribution of hydrocarbon recovery (Dusseault et al., 1993; Vasco et al., 2001, 2002), steam distribution (Holzhausen et al., 1985; Du et al., 2005), and water injection (Kümpel et al., 1996; Vasco et al., 1998; Fabian and Kümpel, 2003; Jahr et al., 2006). More recently, inversions

of strain data at the ground surface have been used to predict the occurrence of a fracture zone above a reservoir receiving CO2 injection at In Salah (Vasco et al., 2010) and the inversion of InSAR data was also an important tool for understanding seismicity accompanying injection (Shirzaei et al., 2016). While studies like these demonstrate the value of deformation data for characterizing subsurface processes, there are relatively few examples where these data have been used to explicitly calibrate poroelastic models of reservoirs (e.g., Vasco et al. (2001); Iglesias and McLaughlin (2012); Hesse and Stadler (2014); Baù et al. (2015); Comola et al. (2016); Jha et al. (2015); Zoccarato et al. (2016b,a)), particularly using in-situ strainmeters.

From the results shown in Figures 1.2–1.6 measurable strain responses are generally expected to occur both within the vicinity of the injection well, but also extend ahead of the pressure front in the reservoir and far up into the cap rock. The implication is that in-situ strain monitoring may provide a valuable compliment to pressure measurements and surface deformations to improve reservoir characterization. The use of strain as a sentinel measurement in regions far from the injection site, such as in shallow wells, is particularly intriguing as it implies monitoring networks can become more flexible to reduce costs and minimize risks associated with creating a pathway for CO_2 release by puncturing the reservoir. Challenges exist, however, in understanding how much information about the reservoir and cap rock such measurements contain. For example, is there an optimal configuration for a shallow network of monitoring wells to provide improved predictive understanding of the interactions between reservoir and cap rock or is detailed information about reservoir mechanics lost with distance, such that multiple shallow measurements simply become redundant? Likewise, how valuable are the different types of strain measurements described in Chapter Four for improving characterization of subsurface properties? Can multi-component measurements at a single monitoring location add information critical for constraining earth model heterogeneity, geometry, anisotropy, or tradeoffs between parameters? Is there unique information contributed by in-situ measurements that is not available in observations of ground surface deformation? Ultimately, many of these issues will be closely tied to the signal to noise ratio of the data. In other words, how does noise in measurements propagate to uncertainty in estimates of reservoir parameters needed to predict and manage reservoir behavior?

1.4.3.3 Overview of the Report

The project described in the following pages is enacted on the stage set in the previous pages. We installed a Gladwin strainmeter as described in Section 1.4.2.8, and we developed several strainmeters of our own design using optical fiber interferometers, motivated by encouraging work outlined in Section 1.4.2.9. The instruments are outlined in Chapter Two. We conducted injection tests, much like those simulated in Section 1.4.1, at the North Avant Field in Oklahoma. The depth and formation properties of the North Avant Field, and the injection rate used in the field test are slightly different from those assumed for the simulation in Section 1.4.1, but the results from the simulation are remarkably similar to the strains measured in the field. The field tests are described in Chapter Four. We expanded on the numerical poroelastic analyses shown above, and we developed a new analytical solution to predict strain in the vicinity of an injection well. We also developed stochastic inversion methods that are well suited to time consuming forward models, like the numerical poroelastic simulations. The theoretical analyses are described in Chapter Three.

References

Agnew, D. C. (1986). Strainmeters and tiltmeters. *Reviews of Geophysics*, 24(3):579–624.

Agnew, D. C. (2007). Before PBO: An overview of continuous strain and tilt measurements in the United States. *Journal of the geodetic Society of Japan*, 53(2):157–182.

B. E. Lofgren, B. (1961). Measurement of compaction of aquifer systems in areas of land subsidence. Technical Report 424-B, United States Geological Survey.

Baù, D., Ferronato, M., Gambolati, G., Teatini, P., and Alzraiee, A. (2015). Ensemble smoothing of land subsidence measurements for reservoir geomechanical characterization. *International Journal for Numerical and Analytical Methods in Geomechanics*, 39(2):207–228.

Beavan, J. and Bilham, R. (1977). Thermally induced errors in fluid tube tiltmeters. *Journal of Geophysical Research*, 82(36):5699–5704.

Becker, M., Coleman, T., Ciervo, C., Cole, M., and Mondanos, M. (2017). Fluid pressure sensing with fiber-optic distributed acoustic sensing. *The Leading Edge*, 36(12):1018–1023.

Blum, J. A., Nooner, S. L., and Zumberge, M. A. (2008). Recording Earth strain with optical fibers. *IEEE Sensors Journal*, 8(7):1152–1160.

Bohloli, B., Bjørnarå, T. I., Park, J., and Rucci, A. (2018). Can we use surface uplift data for reservoir performance monitoring? A case study from In Salah, Algeria. *International Journal of Greenhouse Gas Control*, 76:200–207.

Buursink, M. L., Merrill, M. D., Craddock, W. H., Roberts-Ashby, T. L., Brennan, S. T., Blondes, M. S., Freeman, P. A., Cahan, S. M., DeVera, C. A., and Lohr, C. D. (2014). Geologic framework for the national assessment of carbon dioxide storage resources: Williston Basin, Central Montana Basins, and Montana Thrust Belt study areas. Technical Report 2012–1024–J, United States Geological Survey. Chapter J in *Geologic Framework for the National Assessment of Carbon Dioxide Storage Resources*.

Cappa, F., Guglielmi, Y., Gaffet, S., Lançon, H., and Lamarque, I. (2006a). Use of in situ fiber optic sensors to characterize highly heterogeneous elastic displacement fields in fractured rocks. *International Journal of Rock Mechanics and Mining Sciences*, 43(4):647–654.

Cappa, F., Guglielmi, Y., Rutqvist, J., Tsang, C.-F., and Thoraval, A. (2006b). Hydromechanical modelling of pulse tests that measure fluid pressure and fracture normal displacement at the Coaraze Laboratory site, France. *International Journal of Rock Mechanics and Mining Sciences*, 43(7):1062–1082.

Cappa, F., Guglielmi, Y., and Virieux, J. (2007). Stress and fluid transfer in a fault zone due to overpressures in the seismogenic crust. *Geophysical Research Letters*, 34(5).

Castillo, D., Hunter, S., Harben, P., Wright, C., Conant, R., and Davis, E. (1997). Deep hydraulic fracture imaging: Recent advances in tiltmeter technologies. *International Journal of Rock Mechanics and Mining Sciences*, 34(3–4):47.e1–47.e9.

Chadwick, R. A., Zweigel, P., Gregersen, U., Kirby, G. A., Holloway, S., and P. N. Johannessen, P. (2004). Geological reservoir characterization of a CO2 storage site: The Utsira Sand, Sleipner, northern North Sea. *Energy*, 29(9-10):1371–1381.

Chiaramonte, L., Zoback, M. D., Friedmann, J., and Stamp, V. (2008). Seal integrity and feasibility of CO_2 sequestration in the Teapot Dome EOR pilot: Geomechanical site characterization. *Environmental Geology*, 54(8):1667–1675.

Childers, B. A., Rambow, F. H. K., Dria, D. E., Shuck, M. Y., Homa, D. S., and Poland, S. H. (2007). Downhole fiber optic real-time casing monitor. In *Industrial and Commercial Applications of Smart Structures Technologies 2007*, volume 6527, page 65270J. International Society for Optics and Photonics.

Comola, F., Janna, C., Lovison, A., Minini, M., Tamburini, A., and Teatini, P. (2016). Efficient global optimization of reservoir geomechanical parameters based on synthetic aperture radar-derived ground displacements. *Geophysics*, 81(3):M23–M33.

Davis, E. J. (2011). Interpretation of CO2 sequestration-induced surface deformation over KB-502 at Krechba, Algeria. In *SPE Annual Technical Conference and Exhibition*. Society of Petroleum Engineers.

Davis, S. N., Peterson, F. L., and Halderman, A. D. (1969). Measurement of small surface displacements induced by fluid flow. *Water Resources Research*, 5(1):129–138.

Detournay, E. and Cheng, A. H.-D. (1993). Fundamentals of poroelasticity. In *Analysis and design methods*, pages 113–171. Elsevier.

DeWolf, S. (2014). *Optical Fiber Sensors for Infrasonic Wind Noise Reduction and Earth Strain Measurement*. Doctor of Philosophy in Oceanography, University of California San Diego. `http://roger.ucsd.edu/record=b8191107~S9`.

Du, J., Brissenden, S. J., McGillivray, P., Bourne, S., Hofstra, P., Roadarmel, W. H., Davis, E. J., Wolhart, S. L., and Wright, C. A. (2005). Mapping fluid flow in a reservoir using tiltmeter-based surface-deformation measurements. In *SPE Annual Technical Conference and Exhibition*. Society of Petroleum Engineers.

Dusseault, M. B., Bilak, R. A., and Rothenburg, L. (1993). Inversion of surface displacements to monitor in situ processes. In *International Journal of Rock Mechanics and Mining Sciences and Geomechanics Abstracts*, volume 30, pages 1219–1219. Pergamon Press.

Ellsworth, W. L. (2013). Injection-induced earthquakes. *Science*, 341(6142):1225942.

Evans, K., Holzhausen, G., and Wood, D. M. (1982). The geometry of a large-scale nitrogen gas hydraulic fracture formed in devonian shale: An example of fracture mapping with tiltmeters. *Society of Petroleum Engineers Journal*, 22(5):755–763.

Fabian, M. K. (2004). *Near surface tilt and pore pressure changes induced by pumping in multi-layered poroelastic half-spaces*. PhD thesis, Universitäts-und Landesbibliothek Bonn.

Fabian, M. K. and Kümpel, H.-J. (2003). Poroelasticity: observations of anomalous near surface tilt induced by ground water pumping. *Journal of Hydrology*, 281(3):187–205.

Forster, A., Norden, B., Zinck-Jørgensen, K., Frykman, P., Kulenkampff, J., Spangenberg, E., Erzinger, J., Zimmer, M., Kopp, J., and Borm, G. (2006). Baseline characterization of the CO2SINK geological storage site at Ketzin, Germany. *Environmental Geosciences*, 13(3):145–161.

Friefeld, B. M. (2017). Well instrumentation. In Niemi, A., Bear, J., and Bensabat, J., editors, *Geological Storage of CO2 in Deep Saline Formations*, chapter 8.4, pages 408–419. Springer, Dordrecht, Netherlands.

Gale, J. E. (1975). *A numerical, field and laboratory study of flow in rocks with deformable fractures*. PhD thesis, University of California Berkeley.

Galindez-Jamioy, C. A. and Lopez-Higuera, J. M. (2012). Brillouin distributed fiber sensors: an overview and applications. *Journal of Sensors*, 2012.

Garagash, D. I. and Germanovich, L. N. (2012). Nucleation and arrest of dynamic slip on a pressurized fault. *Journal of Geophysical Research: Solid Earth*, 117(B10).

Germanovich, L. N. and Chanpura, R. A. (2002). Modeling thin inclusions in poroelastic medium by line discontinuities. In *IUTAM Symposium on Analytical and Computational Fracture Mechanics of Non-Homogeneous Materials*, pages 133–142.

Germanovich, L. N., Genc, G., Lowell, R. P., and Rona, P. A. (2012). Deformation and surface uplift associated with serpentinization at mid-ocean ridges and subduction zones. *Journal of Geophysical Research*, 117(B07103).

Ghomian, Y., Pope, G. A., and Sepehrnoori, K. (2008). Reservoir simulation of CO2 sequestration pilot in Frio brine formation, USA Gulf Coast. *Energy*, 33(7):1055–1067.

Gladwin, M. T. (1984). High-precision multicomponent borehole deformation monitoring. *Review of Scientific Instruments*, 55(12):2011–2016.

Guglielmi, Y., Cappa, F., Avouac, J.-P., Henry, P., and Elsworth, D. (2015). Seismicity triggered by fluid injection–induced aseismic slip. *Science*, 348(6240):1224–1226.

Guglielmi, Y., Cappa, F., Lançon, H., Janowczyk, J. B., Rutqvist, J., Tsang, C.-F., and Wang, J. S. Y. (2013). ISRM suggested method for step-rate injection method for fracture in-situ properties (SIMFIP): Using a 3-components borehole deformation sensor. In *The ISRM Suggested Methods for Rock Characterization, Testing and Monitoring: 2007–2014*, pages 179–186. Springer.

Gutierrez, M., Katsuki, D., and Almrabat, A. (2012). Effects of CO2 injection on the seismic velocity of sandstone saturated with saline water. *International Journal of Geosciences*, 3(05):908.

Hesler, G. J., Zheng, Z., and Myer, L. R. (1990). In-situ fracture stiffness determination. In *Rock Mechanics Contributions and Challenges*, pages 405–411, Golden, Colorado. Lawrence Berkeley National Laboratory, 31st U.S. Symposium on Rock Mechanics. `https://escholarship.org/uc/item/9vb4187d`.

Hesse, M. A. and Stadler, G. (2014). Joint inversion in coupled quasi-static poroelasticity. *Journal of Geophysical Research: Solid Earth*, 119(2):1425–1445.

Hisz, D. B., Murdoch, L. C., and Germanovich, L. N. (2013). A portable borehole extensometer and tiltmeter for characterizing aquifers. *Water Resources Research*, 49(12):7900–7910.

Holzhausen, G. R., Card, C. C., Raisbeck, J. M., and Dobecki, T. L. (1985). Hydraulic fracture growth during steam stimulation in a single-well test. In *SPE California Regional Meeting*. Society of Petroleum Engineers.

Hovorka, S. D., Meckel, T. A., and Trevino, R. H. (2013). Monitoring a large-volume injection at Cranfield, Mississippi—Project design and recommendations. *International Journal of Greenhouse Gas Control*, 18:345–360.

Huang, J., Hua, L., Lan, X., Wei, T., and Xiao, H. (2013a). Microwave assisted reconstruction of optical interferograms for distributed fiber optic sensing. *Optics Express*, 21(15):18152–18159.

Huang, J., Lan, X., Luo, M., and Xiao, H. (2014). Spatially continuous distributed fiber optic sensing using optical carrier based microwave interferometry. *Optics Express*, 22(15):18757–18769.

Huang, J., Wang, T., Hua, L., Fan, J., Xiao, H., and Luo, M. (2013b). A coaxial cable Fabry-Pérot interferometer for sensing applications. *Sensors*, 13(11):15252–15260.

Hunter, S. L., Boro, C. O., and Farris, A. (2002). Tiltmeter leveling mechanism. US Patent 6,370,784 B1.

Iglesias, M. A. and McLaughlin, D. (2012). Data inversion in coupled subsurface flow and geomechanics models. *Inverse Problems*, 28(11):115009.

Ishii, H. (2002). Development of multi-component borehole instrument for earthquake prediction study: some observed example of precursory and co-seismic phenomena relating to earthquake swarms and application of the instrument for rock mechanics. *Rock Stress*, page pp 365–377.

Ishii, H. and Asai, Y. (2015). Development of a borehole stress meter for studying earthquake predictions and rock mechanics, and stress seismograms of the 2011 Tohoku earthquake (M 9.0). *Earth, Planets and Space*, 67(1):26.

Ishii, H., Jentzsch, G., Graupner, S., Nakao, S., Ramatschi, M., and Weise, A. (2001). Observatory Nokogiriyama 1 Japan: Comparison of Different Tiltmeters. *Journal of the Geodetic Society of Japan*, 47(1):155–160.

Jääskeläinen, K.-M. (2011). Method for monitoring deformation of well equipment. US Patent App. 13/142,451.

Jacob, T., Chéry, J., Boudin, F., and Bayer, R. (2010). Monitoring deformation from hydrologic processes in a karst aquifer using long-baseline tiltmeters. *Water Resources Research*, 46(9).

Jahr, T., Letz, H., and Jentzsch, G. (2006). Monitoring fluid induced deformation of the Earth's crust: a large scale experiment at the KTB location/Germany. *Journal of Geodynamics*, 41(1-3):190–197.

Jha, B., Bottazzi, F., Wojcik, R., Coccia, M., Bechor, N., McLaughlin, D., Herring, T., Hager, B. H., Mantica, S., and Juanes, R. (2015). Reservoir characterization in an underground gas storage field using joint inversion of flow and geodetic data. *International Journal for Numerical and Analytical Methods in Geomechanics*, 39(14):1619–1638.

Karasaki, K., Freifeld, B., Cohen, A., Grossenbacher, K., Cook, P., and Vasco, D. (2000). A multidisciplinary fractured rock characterization study at Raymond field site, Raymond, CA. *Journal of Hydrology*, 236(1-2):17–34.

Kreuzer, M. (2006). Strain measurement with fiber Bragg grating sensors. *HBM, Darmstadt, S2338-1.0 e.*

Kümpel, H. J., Varga, P., Lehmann, K., and Mentes, G. (1996). Ground tilt induced by pumping—preliminary results from the Nagycenk test site, Hungary. *Acta Geodaetica et Geophysica Hungarica*, 31(1-2):67–79.

Lecampion, B., Jeffrey, R., and Detournay, E. (2005). Resolving the geometry of hydraulic fractures from tilt measurements. *Pure and Applied Geophysics*, 162(12):2433–2452.

Leetaru, H. E. and Freiburg, J. T. (2014). Litho-facies and reservoir characterization of the Mt Simon Sandstone at the Illinois Basin–Decatur Project. *Greenhouse Gases: Science and Technology*, 4(5):580–595.

Li, Y., Cheng, B., Zhu, W., Xiao, H., and Nygaard, R. (2017). Development and evaluation of the coaxial cable casing imager: a cost-effective solution to real-time downhole monitoring for CO2 sequestration wellbore integrity. *Greenhouse Gases: Science and Technology*, 7(5):927–941.

Liebscher, A., Möller, F., Bannach, A., Köhler, S., Wiebach, J., Schmidt-Hattenberger, C., Weiner, M., Pretschner, C., Ebert, K., and Zemkex, C. (2013). Injection operation and operational pressure–temperature monitoring at the CO2 storage pilot site Ketzin, Germany—Design, results, recommendations. *International Journal of Greenhouse Gas Control*, 15:163–173.

Liu, G. (2012). Carbon dioxide geological storage: monitoring technologies review. In *Greenhouse Gases-Capturing, Utilization and Reduction*. IntechOpen.

Longuevergne, L., Florsch, N., Boudin, F., Oudin, L., and Camerlynck, C. (2009). Tilt and strain deformation induced by hydrologically active natural fractures: application to the tiltmeters installed in Sainte-Croix-aux-Mines observatory (France). *Geophysical Journal International*, 178(2):667–677.

Martin, C. D., Davison, C. C., and Kozak, E. T. (1990). Characterizing normal stiffness and hydraulic conductivity of a major shear zone in granite. In Barton and Stephansson, editors, *International Journal of Rock Mechanics and Mining Sciences & Geomechanics Abstracts*, pages 549–556, Balkema, Rotterdam.

Maxwell, S. C., Du, J., and Shemeta, J. (2008). Passive seismic and surface monitoring of geomechanical deformation associated with steam injection. *The Leading Edge*, 27(9):1176–1184.

Mayuga, M. N. and Allen, D. R. (1969). Subsidence in the Wilmington oil field, Long Beach, Calif., USA. *Land Subsidence*, 1(88):6C6–79.

Meertens, C., Levine, J., and Busby, R. (1989). Tilt observations using borehole tiltmeters: 2. Analysis of data from Yellowstone National Park. *Journal of Geophysical Research: Solid Earth*, 94(B1):587–601.

Melchior, P. (1964). Earth tides. *Research in Geophysics*, 2:183–193.

Mindlin, R. D. and Cheng, D. H. (1950a). Nuclei of strain in the semi-infinite solid. *Journal of Applied Physics*, 21(9):926–930.

Mindlin, R. D. and Cheng, D. H. (1950b). Thermoelastic stress in the semi-infinite solid. *Journal of Applied Physics*, 21(9):931–933.

Murdoch, L. C., Freeman, C. E., Germanovich, L. N., Thrash, C., and DeWolf, S. (2015). Using in situ vertical displacements to characterize changes in moisture load. *Water Resources Research*, 51(8):5998–6016.

Murdoch, L. C., Hisz, D. B., Ebenhack, J. F., Fowler, D. E., Tiedeman, C. R., and Germanovich, L. N. (2009). Analysis of hydromechanical well tests in fractured sedimentary rock at the NAWC site, New Jersey. In *43rd US Rock Mechanics Symposium & 4th US-Canada Rock Mechanics Symposium*. American Rock Mechanics Association.

Murdoch, L. C., Moysey, S., Germanovich, L. N., and Hughes, B. (2016). Proof-of-feasibility of using well bore deformation as a diagnostic tool to improve co2 sequestration. Technical Report 1240376, United States Department of Energy. DOI: 10.2172/1240376.

Phillips, S. P., Carlson, C. S., Metzger, L. F., Howle, J. F., Galloway, D. L., Sneed, M., Ikehara, M. E., Hudnut, K. W., and King, N. E. (2003). Analysis of tests of subsurface injection, storage, and recovery of freshwater in Lancaster, Antelope Valley, California. Technical Report 2003-4061, United States Geological Survey. Water-Resources Investigations Report.

Pollard, D. D. and Holzhausen, G. (1979). On the mechanical interaction between a fluid-filled fracture and the Earth's surface. *Tectonophysics*, 53(1-2):27–57.

Pope, J. P. and Burbey, T. J. (2004). Multiple-aquifer characterization from single borehole extensometer records. *Groundwater*, 42(1):45–58.

Riley, F. S. (1969). Analysis of borehole extensometer data from central California. *Land Subsidence*, 2:423–431.

Rutqvist, J., Vasco, D. W., and Myer, L. (2010). Coupled reservoir-geomechanical analysis of CO2 injection and ground deformations at In Salah, Algeria. *International Journal of Greenhouse Gas Control*, 4(2):225–230.

Sacks, I. S., Suyehiro, S., and Evertson, D. W. (1971). Sacks-Evertson strainmeter, its installation in Japan and some preliminary results concerning strain steps. *Proceedings of the Japan Academy*, 47(9):707–712.

Schweisinger, T., Svenson, E. J., and Murdoch, L. C. (2011). Hydromechanical behavior during constant-rate pumping tests in fractured gneiss. *Hydrogeology Journal*, 19(5):963–980.

Senel, O. and Chugunov, N. (2013). CO2 injection in a saline formation: pre-injection reservoir modeling and uncertainty analysis for Illinois Basin–Decatur Project. *Energy Procedia*, 37:4598–4611.

Shirzaei, M., Ellsworth, W. L., Tiampo, K. F., González, P. J., and Manga, M. (2016). Surface uplift and time-dependent seismic hazard due to fluid injection in eastern Texas. *Science*, 353(6306):1416–1419.

Slack, T. Z., Murdoch, L. C., Germanovich, L. N., and Hisz, D. B. (2013). Reverse water-level change during interference slug tests in fractured rock. *Water Resources Research*, 49(3):1552–1567.

Stocker, T. *Climate change 2013: the physical science basis: Working Group I contribution to the Fifth assessment report of the Intergovernmental Panel on Climate Change*. Cambridge University Press.

Svenson, E., Schweisinger, T., and Murdoch, L. C. (2007). Analysis of the hydromechanical behavior of a flat-lying fracture during a slug test. *Journal of Hydrology*, 347(1-2):35–47.

Thompson, P. M. and Kozak, E. T. (1991). In situ measurement of coupled hydraulic pressure/fracture dilation in stiff crystalline rock. *Field Measurements in Geotechnics, Balkema, Rotterdam*, pages 23–31.

Vasco, D. W., Karasaki, K., and Kishida, K. (2001). A coupled inversion of pressure and surface displacement. *Water Resources Research*, 37(12):3071–3089.

Vasco, D. W., Karasaki, K., and Myer, L. (1998). Monitoring of fluid injection and soil consolidation using surface tilt measurements. *Journal of Geotechnical and Geoenvironmental Engineering*, 124(1):29–37.

Vasco, D. W., Karasaki, K., and Nakagome, O. (2002). Monitoring production using surface deformation: the Hijiori test site and the Okuaizu geothermal field, Japan. *Geothermics*, 31(3):303–342.

Vasco, D. W., Rucci, A., Ferretti, A., Novali, F., Bissell, R. C., Ringrose, P. S., Mathieson, A. S., and Wright, I. W. (2010). Satellite-based measurements of surface deformation reveal fluid flow associated with the geological storage of carbon dioxide. *Geophysical Research Letters*, 37(3).

Verdon, J. P., Kendall, J.-M., Stork, A. L., Chadwick, R. A., White, D. J., and Bissell, R. C. (2013). Comparison of geomechanical deformation induced by megatonne-scale CO2 storage at Sleipner, Weyburn, and In Salah. *Proceedings of the National Academy of Sciences*, 110(30):E2762–E2771.

Wang, H. F. (2000). *Theory of linear poroelasticity with applications to geomechanics and hydrogeology*. Princeton Series in Geophysics. Princeton University Press.

Warpinski, N. R., Branagan, P. T., Engler, B. P., Wilmer, R., and Wolhart, S. L. (1997). Evaluation of a downhole tiltmeter array for monitoring hydraulic fractures. *International Journal of Rock Mechanics and Mining Sciences*, 34(3-4):318.e1–318.e13.

Weise, A., Jentzsch, G., Kiviniemi, A., and Kääriäinen, J. (1998). Comparison of long-period tilt measurements: results from the two clinometric stations Metsähovi and Lohja, Finland. *Journal of Geodynamics*, 27(2):237–257.

Worth, K., White, D., Chalaturnyk, R., Sorensen, J., Hawkes, C., Rostron, B., Johnson, J., and Young, A. (2014). Aquistore project measurement, monitoring, and verification: from concept to CO2 injection. *Energy Procedia*, 63:3202–3208.

Wu, J., Jiang, H., Su, J., Shi, B., Jiang, Y., and Gu, K. (2015). Application of distributed fiber optic sensing technique in land subsidence monitoring. *Journal of Civil Structural Health Monitoring*, 5(5):587–597.

Wyatt, F. K. and Berger, J. (1980). Investigations of tilt measurements using shallow borehole tiltmeters. *Journal of Geophysical Research: Solid Earth*, 85(B8):4351–4362.

Wyatt, F. K., Cabaniss, G., and Agnew, D. C. (1982). A comparison of tiltmeters at tidal frequencies. *Geophysical Research Letters*, 9(7):743–746.

Zoback, M. D. and Gorelick, S. M. (2012). Earthquake triggering and large-scale geologic storage of carbon dioxide. *Proceedings of the National Academy of Sciences*, 109(26):10164–10168.

Zoccarato, C., Baù, C., Ferronato, M., Gambolati, G., Alzraiee, A., and Teatini, P. (2016a). Data assimilation of surface displacements to improve geomechanical parameters of gas storage reservoirs. *Journal of Geophysical Research: Solid Earth*, 121(3):1441–1461.

Zoccarato, C., Baù, D., Bottazzi, F., Ferronato, M., Gambolati, G., Mantica, S., and Teatini, P. (2016b). On the importance of the heterogeneity assumption in the characterization of reservoir geomechanical properties. *Geophysical Journal International*, 207(1):47–58.

Zumberge, M. A., Berger, J., Dzieciuch, M. A., and Parker, R. L. (2004). Resolving Quadrature Fringes in Real Time. *Applied Optics*, 43(4):771–775.

Zumberge, M. A., Wyatt, F. K., Yu, D. X., and Hanada, H. (1988). Optical fibers for measurement of Earth strain. *Applied Optics*, 27(19):4131–4138.

Chapter Two
Instrument Development and Assessment

The time evolving strain field contains a wealth of information that can be used to interpret subsurface behavior, however, this is only relevant if these deformations can be reliably measured. The review of down-hole strain monitoring technologies provided in Section 1.4.2 illustrates a number of different potential monitoring technologies, some of which are capable of resolving the deformations anticipated during the injection tests proposed for this project. While we were able to procure and install one of the few remaining Gladwin Tensor Strainmeters (Section 4.2.1.1), additional monitoring required the development of new instruments.

Two instrument designs were completed during this project that are capable of measuring two orthogonal tilts as well as the vertical and three horizontal strains. These systems integrated commercial non-contact eddy current displacement transducers into packages suitable for downhole deformation monitoring. This included the assembly of two permanently installed, or grout-in style instruments (Section 2.2.2) and one removable system (Section 2.2.3). While the reusability of the removable system is quite attractive, the instrument itself is quite complex and expensive and is ideally suited for aluminum casing. The permanent instrument is much simpler to fabricate and assemble, however, it must be abandoned after testing.

Both eddy current systems require successful coupling of the instrument or casing to the formation. This is most commonly acheived using an expanding grout mixture delivered to the bottom of the borehole before lowering the instrument into place, or pumped into the annulus between the casing and formation. In either case the grouting is a critical component governing the success or failure of an installation, which motivated the development of a very low cost, expendable optical fiber areal strainmeter (Section 2.3) as a low-risk method to test the grouting procedure. Results from the first areal strainmeter proved to be the highest resolution borehole strain measurements ever taken, leading to the deployment of a second instrument at the injection site in Oklahoma.

In this chapter we start by investigating the feasibility of swaging in casing and field and laboratory tests of expanding grout mixtures for installing casing and borehole instruments. The main focus of this chapter is detailed descriptions of the design, fabrication and assembly of the instruments developed during this project, along with an exploration of the background field data and an assessment of their relative performance for deformation monitoring. This chapter is concluded with a discussion of how raw data from the instruments are processed and calibrated before being used for modeling and interpretation, as well as a brief discussion of how data are collected, archived and made available.

2.1 Completion and Installation

Borehole strainmeters are designed to measure strain in rock, and methods of well completion and instrument installation play important roles in the coupling between the instrument and the formation. We developed expendable strainmeters designed to be coupled to rock with grout, and a removable instrument designed to measure the deformation of casing, which was coupled to rock. The effectiveness of the strainmeters required that either the instrument themselves, or the casing were well coupled to rock.

Grout is the most widely used method for coupling instruments or casing to rock, and we evaluated this approach. We also evaluated the feasibility of swaging casing in a borehole to couple it to rock. Swaging has some potential advantages over grouting, but it is a more complex and less common procedure, so we conducted a feasibility evaluation.

2.1.1 Swaging

Swaging is a technique where a metal tube is pressurized until it yields and deforms plastically. The concept is to swage a metal tube in a borehole by expanding the tube to a size greater than the diameter of the borehole. This would require applying enough pressure to plastically deform the metal tube and elastically deform the enveloping rock. Swaging is widely used in metal forming and it is used in wells to expand tubing over holes in casing, and other applications. Swaging could be useful for strainmeter applications because the tubing could be used immediately, whereas grouting requires up to several weeks of cure time before it can be used for strain sensing. Moreover, expanding grout is required for proper performance.

A theoretical analysis was performed to examine the feasibility of swaging a metal case into an open borehole. Initial calculations consider a hole drilled in rock using an HQ core barrel that results in a finished hole diameter of 3.779". This size core barrel is commonly available and will create a hole in rock that has a smoother wall than other drilling methods, like a hammer or a tricone bit. Roughness on the wall of the hole will cause perturbations in the deformation of the tube over a region whose size scales with the scale of the roughness. The roughness of a cored hole is difficult to anticipate because it will depend on the rock type, but it will likely be less than 1 mm.

The tubing used for the completion must be capable of stretching under plastic deformation without fracturing by a sufficient amount, and it must be capable of being detected by the eddy current sensors. The eddy current sensor is optimized to measure displacement of an aluminum target, but will also work with a stainless steel target. However, the calibration and potentially the resolution of the sensor will change when materials other than aluminum are used. The extent and consequences of this change are currently unknown, but would need to be evaluated if stainless steel tubing was used. While it is clear that stainless steel would be preferred given its corrosion resistance, it may be possible to use aluminum that has been treated using a deep penetrating anodizing technique like hard anodizing.

The tubing must also small enough to fit in the HQ hole during deployment, but close enough to the size of the hole to minimize the amount of deformation required. This is coupled with the diameter and pressure ratings of available hydraulic packers. One packer that is being considered is the DuraFrac HPC by Inflatable Packers International, whose 70 mm model could be operated at 5,000–6,000 psi over the size range of the tubing. A larger, 89 mm diameter packer can also achieve high pressures but would require a very close match in tubing size. The HQ hole size is 96 mm, and the 89 mm packer is designed to be used in HQ holes, but without an piece of tubing in between.

The swaging process will require 4 stages, which are shown schematically below on the stress-strain diagram for the tubing (Figures 2.1 and 2.2). The concepts behind the stages are outlined first and then analyzed below.

1. Initial inflation to yield: increase internal pressure to reach the yield stress of the tube
2. Expansion: expand the tube plastically until the diameter of the tube contacts the borehole. The metal softens as it deforms plastically, so the slope decreases during this stage (Figure 2.1)
3. Seating: increase pressure to expand both the tube and the hole in the rock. The tube is supported by the hole in the rock, so the slope increases.
4. Unloading: Pressure on the packer is decreased, and the strain on the tube decreases. The objective is that the tube is compressed by the contraction of the rock.

The process can be visualized by tracing the hoop stresses in the tubing and hole as a function of the hoop strain in the tube (Figure 2.1). The stress increases linearly with strain until the yield stress is reached and then the slope flattens as the tube yields plastically in the expansion stage. The seating stage is reached

when the expanding tube contacts the hole wall. The relationship between hoop stress and strain continues on the same trajectory for the tube during seating. The hoop stress in the rock begins to increase with the hoop strain in the tube at the beginning of the expansion stage (green line). The hoop stresses in the rock and tube increase, reach a maximum when the peak internal pressure is reached, and then both stresses decrease as the internal pressure is decreased.

The swaging process is successful if the stresses in the tube remain less than the stresses in the rock during unloading. This could happen if the slope of the unloading curve for the tube is steeper than that of the hole, but this is not required. It could be sufficient for the stresses in the rock to be sufficiently tensile and larger than those in the tube. Swaging will be unsuccessful, however, when the tensile stresses in the rock are less than those in the tube. In this case, the stresses in the rock will go to zero while the stresses in the tube are tensile (Figure 2.2). This means that the rock is unloaded and deformation will stop. However, the tube will continue to contract. This will cause the tube to be separate from the hole in the rock when the pressure in the packer returns to ambient conditions.

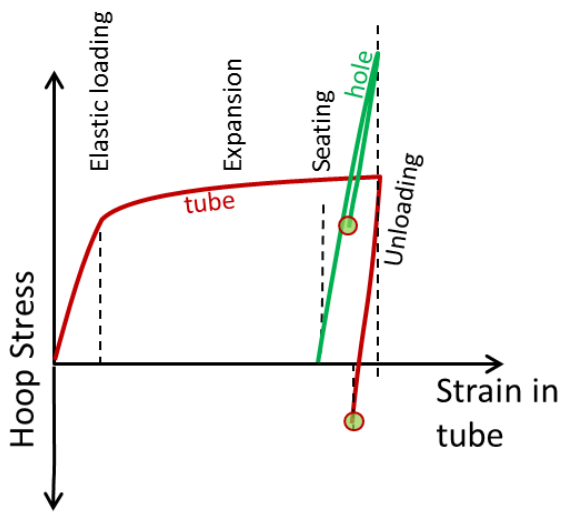

Figure 2.1: Conceptual hoop stress as a function of hoop strain in the tubing when the tubing is being swaged in a hole in rock. Hoop stress in the tube in red and in the rock in green. Circles are the final stresses in the tube and rock. This shows the desired outcome where the tube is put in compression while the hole remains in tension (in a differential sense).

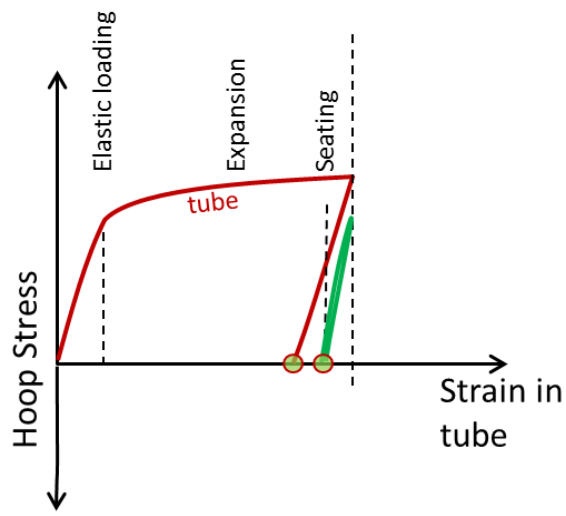

Figure 2.2: This shows the case where strain during seating was insufficient. The hole in the rock returns to zero stress while the tube remains in tension. The tube returns to zero stress in this case. The tube and rock are disconnected at the end of the swaging process in this case.

It appears that the process could work for any modulus of tube or rock, providing sufficient load can be applied to tube and hole during the seating process. However, these analytical and subsequent numerical analyses of the swaging completion method have yielded inconclusive results as to the success or failure of this technique. This is due to the discontinuity in the analytical solution and lack of convergence in the numerical analysis when the plastic deformation of the casing reaches the outer diameter of the material boundary, implying an impractically close fit would be needed between the borehole wall and the casing for this technique to be accurately modeled. We therefore concluded that further investigation of this technique could only proceed on empirical grounds, which was not pursued given the substantial resource commitment of performing such a suite of tests and given the simplicity and success of the grouting method described below.

2.1.2 Grouting

Grout is widely used to seal casing into boreholes, and it is also used to couple strainmeters to rock (UNAVCO). One requirement for grout used in the project is that it must expand slightly during curing. This is because borehole strainmeters must be under compression in order to couple tensile strain in the rock to the instrument. Expansion of the grout during curing is capable of creating the necessary compression. Moreover, wet grout must be pumpable through tubing 1.5 mm in diameter, it and must be capable of standing in a 5-m-high column without separating into different components. For example, some grout contains aggregate grains that can separate by gravity when the grout is placed in a column.

We used BASF Chemical MasterFlow grout to install the strainmeters developed for the project. This grout, or an earlier product with a similar formulation, has been used successfully in the installation of several dozen borehole strainmeters by personnel with UNAVCO. It is capable of meeting the required characteristics when it is mixed in the proper proportions. We developed a recipe for the ratio of solid grout powder to water that would result in the grout with the required characteristics. We found that this recipe could vary slightly with water chemistry, and it was difficult to tightly constrain this recipe during field mixing operations. For that reason, we developed methods for assessing the properties of the grout mix in the field. We also evaluated the characteristics of the solidified grout.

2.1.2.1 Field Evaluation of Grout Mix Properties

We developed tools to evaluate the viscosity and density of grout in the field in order to assess the properties of grout as it was being mixed. BASF Chemical MasterFlow grout was added to water until the desired ratio was achieved. At this point, the density and viscosity of the grout were measured. Apparent viscosity was measured with a flow cone calibrated according to ASTM standard C939 (American Society for Testing and Materials, 2010). Density was measured as the ratio of volume and weight of sample of grout mix.

We also evaluated using a straight-walled cone to estimate viscosity. The effective dynamic viscosity of a fluid flowing in a straight, circular, vertical tube is

$$\mu = \frac{\gamma \pi r^4}{8Q} \tag{2.1}$$

where γ is the unit weight of the fluid, r is the radius of the tube, and Q is the flow rate. A device was developed where a conical funnel was fixed to a straight tube. The funnel and tube were filled with grout while the bottom of the tube was blocked. Then the flow rate was determined by timing the accumulation of a volume of grout and then using (2.1) to calculate viscosity.

2.1.2.2 Lab Tests of Expanding Grout

We performed several controlled tests of the BASF Chemical MasterFlow expanding grout. The most rigorous of these tests consisted of a triplet of concentric cylinders approximately 12" long, with the outermost a 6" Schedule 40 steel pipe (6.63" OD by 6.07" ID), the middle a 4" Schedule 5 aluminum pipe (4.50" OD by 4.42" ID), and the inner-most a 4" diameter, 0.125" wall aluminum tube. The grout mixture was poured into the annulus between the 6" and 4" pipes and the inner diameter of the 4" pipe was measured at three points separated in azimuth by 120° (see Figure 2.3). These displacement measurements were made using one of the 3-channel, single-ended eddy current systems that are being used in the field to estimate the horizontal strain tensor. All cylinders were epoxied to a galvanized steel plate to prevent leakage of the

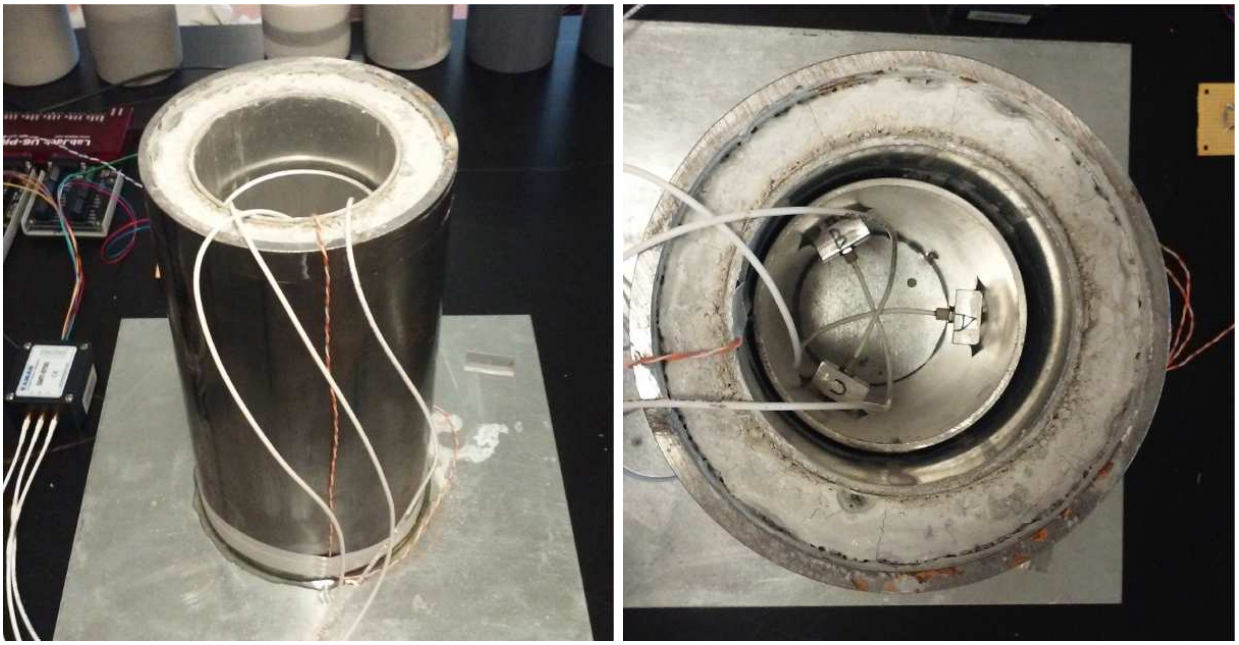

Figure 2.3: Pictures of the enhanced expanding grout laboratory test. (Left) Perspective view of the experimental apparatus showing the outer steel pipe and inner aluminum pipe whose annulus was filled with the expanding grout. (Right) A top view of the same setup to show a more clear view of the inner-most cylinder with the 3 eddy current displacement transducers used to measure the displacement of the inner diameter of the aluminum pipe.

grout and to fix the relative distances between each cylinder. A thermistor was embedded in the annulus between the aluminum pipe and measurement tube to correct for ambient temperature effects.

Results from this test are shown in Figure 2.4. While this test was intended to run for the full duration of the cure time of the grout (approximately 1 month), data after about day 16 are obscured by a serious disturbance to the experimental setup. The results show contraction on all 3 gauges, with a maximum of 40 to 50 microns of total radial compression of the aluminum pipe. These results have also been re-cast in terms of the areal and shear strains that show a clear drop in the areal strain of approximately 4 $\mu\epsilon$.

These results show that curing of the BASF grout around a cylinder will result in compression of the cylinder. This should be sufficient to load the outer pressure case cylinder of both the grout-in instrument and the aluminum casing segment used for the removable instrument.

2.1.2.3 EPA Compliance of Expanding Grout

It is feasible that instruments developed for the project could be used in Class VI injection wells, so we evaluated United States Environmental Protection Agency guidelines for completion of Class VI wells. We believe this grout is acceptable based on p. 27 of *Geologic Sequestration of Carbon Dioxide: Underground Injection Control (UIC) Program Class VI Well Construction Guidance* (Office of Water, 2012), which includes "expanding cements" as an alternative to standard Portland cement for increasing resistance to carbonation by CO_2.

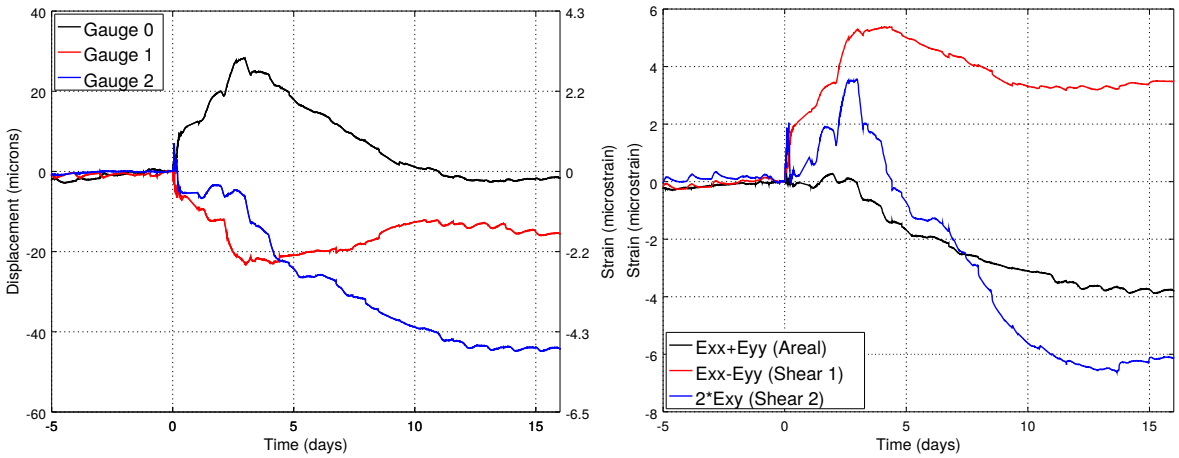

Figure 2.4: Results the enhanced expanding grout laboratory test. (Left) Displacement (and equivalent strain) results from the three gauges. (Right) The same results re-cast in terms of areal and shear strains.

2.2 Multi-Component Eddy Current Strain and Tilt Systems

The high resolution and compact size of eddy current displacement transducers make them a natural choice for integration in a borehole package. While only about one or two orders of magnitude less sensitive than capacitance gauges like those used in the Gladwin Tensor Strainmeter (GTSM) (Gladwin and Wolfe, 1975; Gladwin, 1984), they are commercially available from multiple manufacturers. An eddy current sensor is capable of measuring displacements as small as ∼1 nm in a single-ended configuration, and ∼0.1 nm when using a pair of sensors in a differential arrangement. For comparison, the GTSM capacitance gauge least-count is 0.01 nm. Figure 2.5 shows the Kaman 15N-003 eddy current sensor, which consists of a small coil embedded in the plastic tip extending several mm from its 4 mm diameter, 24 mm long stainless steel housing.

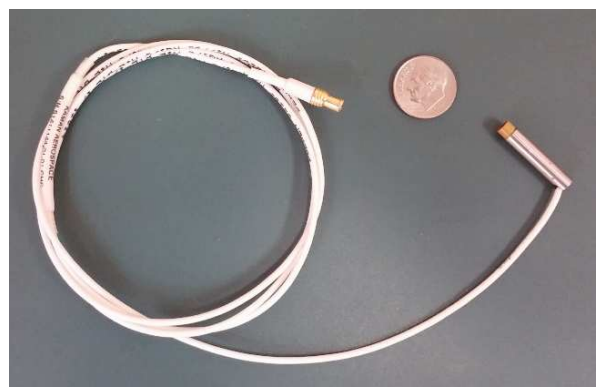

Figure 2.5: Photograph of the Kaman 15N-003 eddy current sensor and cable with a dime for scale.

The following sections present the background of the eddy current sensing technology, as well as two integrations of these transducers for borehole sensing. This includes two iterations of a permanently installed, grout-in style instrument package, as well as one removable system.

2.2.1 Non-Contact Eddy Current Displacement Transducers

The primary configuration of a non-contact eddy current displacement measurement is that of a sensing head facing a conductive target (Figure 2.6). A typical sensor consists of a pair of wire loops referred to as an active coil and a reference coil. The active coil is driven with a high frequency alternating current (AC) which causes the wire loop to emit an alternating magnetic field that induces eddy currents in the surface of a nearby conductive target. These induced currents also produce an alternating magnetic field of the opposite polarity to oppose the field produced by the active coil. The strength of this opposing field

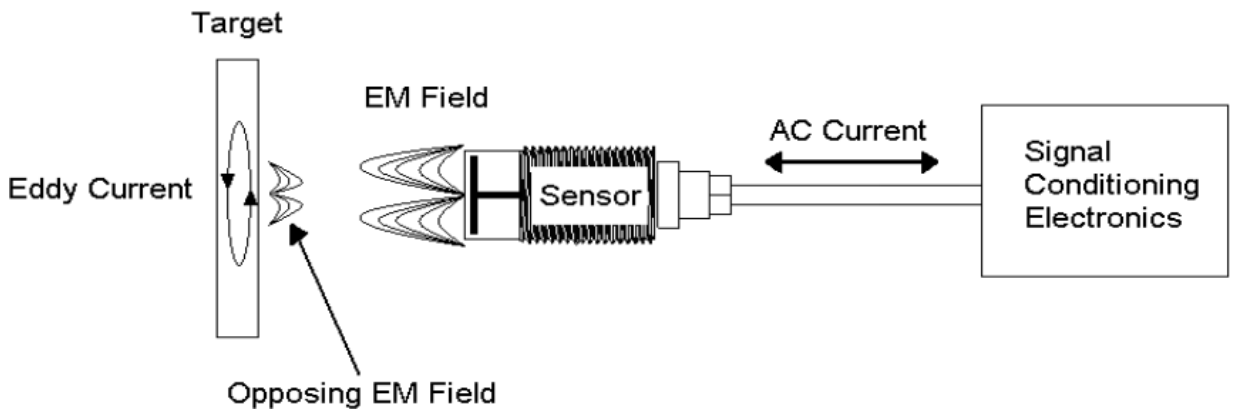

Figure 2.6: Diagram of a typical non-contact measurement setup using a single-ended eddy current sensor and target (from Kaman Precision Products (2011)).

increases or decreases the inductive load, or impedance of the active coil proportional to the distance between the sensor and target. The reference coil, however, remains passive to compensate for thermal and external electromagnetic interference.

An AC bridge circuit is used to measure changes in the impedance of the sensing coil (Figure 2.7). Like its direct-current (DC) counterpart, the active coil impedance is measured against another impedance that is as closely matched as possible to keep the bridge in balance. This comparison can either be done against a fixed reference in the case of a single-ended system (Figure 2.7a), or against another active/reference coil pair in a differential configuration (Figure 2.7b). An imbalance in this circuit causes the frequency of AC current to increase or decrease depending upon the direction of the mismatch, which is then converted to a voltage using a phase-sensitive detection system, or demodulator.

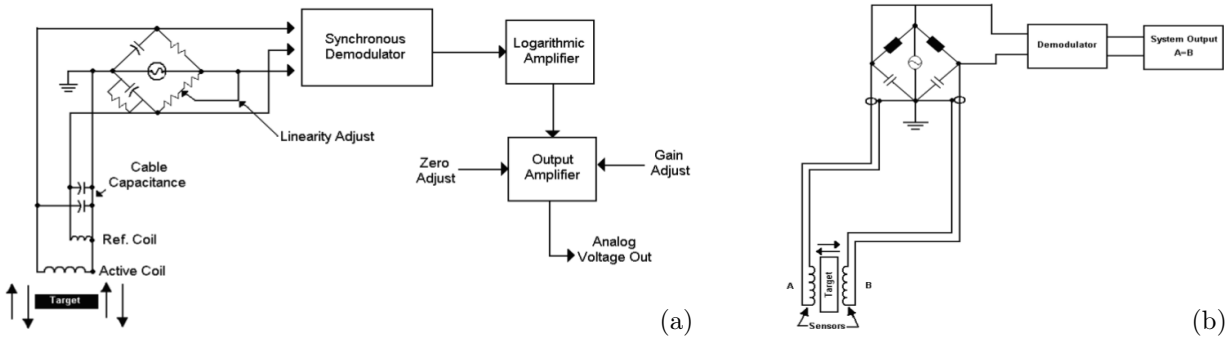

Figure 2.7: Diagrams showing single-ended (a) and differential (b) inductive bridges used to measure impedance changes proportional to the displacement between the sensor(s) and target (from Kaman Precision Products (2011)).

The nanometer and sub-nanometer performance of several single-ended and differential eddy current systems were verified through simple laboratory experiments. This included systems from Kaman Precision Products and Micro-Epsilon, which appear to be the two leading manufacturers of the highest performance eddy current sensors. Multiple systems were tested in the lab and appeared to have similar resolutions and noise performance, but most importantly they were all deemed sufficient for detecting the sub-surface deformations predicted by previous numerical models. It is also critical to note that while these sensors can be used to detect the displacement of any conductive target, they are optimized and factory calibrated for use with aluminum.

The next task was to integrate these sensors into a suitable down-hole package for measuring as many components of strain and tilt as possible. We have completed three systems capable of measuring three components of horizontal strain, the vertical strain, and two orthogonal tilts. Two of these are permanently installed, or "grout-in" systems, and one is a removable instrument intended for short-to-intermediate term deployments. While there are many design similarities, there are enough differences in implementation between these two systems to necessitate the separate descriptions provided in the following sections.

2.2.2 Grout-In Multi-Component Eddy Current Strain and Tilt System

Two "grout-in" eddy current strain and tilt systems were designed, fabricated, assembled, and permanently deployed during this project. The main components are shown in Figure 2.8, which are housed in two main "Instrument" and "Electronics" packages. Dividing the system in this manner is intended to isolate the passive instruments and their eddy current sensors in the lower package from the active, heat dissipating electronics in the upper package. Wires and cables from the instrument packaged are delivered to the supporting electronics through a small hole in the "Feedthrough Cap", which is sealed during assembly to eliminate convective airflow between packages.

Each package is housed in a 4.5-inch (11.4 cm) diameter, 0.25-inch (0.635 cm) thick, 6061 aluminum alloy tube. The Version 1 system has 24-inch (61 cm) long packages, whereas the Version 2 is 34 inches (86 cm) long, resulting in total lengths of 50.5 inches (128 cm) and 70.5 inches (179 cm), respectively. The aluminum is treated with a sulfuric acid based anodizing technique known as Type III or "hard" anodizing that results in an extremely durable corrosion resistant coating that appears to eliminate the volatile reaction observed between the expanding grout and bare aluminum. This is also what gives the instruments their very dark brown or nearly black exterior color.

Four double o-ring bore seals are used to secure the package interiors from water infiltration. The top cap contains one penetration into the electronics package to deliver power and receive data from the instrument through wires housed in a 3/8 trade size liquid-tight conduit, as well as three non-penetrating 1/4"-20 tapped holes for lifting eyes. The bottom cap has one 1/2"-13 bottom-tapped hole for attaching additional weight to counteract any buoyancy forces during deployment.

The assembled instruments are centralized in the borehole by two sets of three vertical springs separated around the upper and lower pressure case packages by 120°. These are simply 1/2" (1.3 cm) wide, 1/16" (0.16 cm) thick strips of anodized aluminum that span the lengths of each package that are bowed outward to push the instrument off the borehole wall during deployment. This ensures that there is a uniform annulus of grout around the instrument and that the horizontal strain measurements are made concentric with the borehole.

2.2.2.1 Transducer Integration

The lower instrument package contains all of the strain and tilt measurement devices. The two orthogonal tiltmeters are based on a simple physical pendulum that measures the two horizontal tilt axes (roll and pitch) of the borehole package, whereas the horizontal and vertical strain gauges measure the deformation of the instrument pressure case itself. These two systems also differ in that it was not possible to arrange a differential measurement for the strains, but was trivial for the tilts.

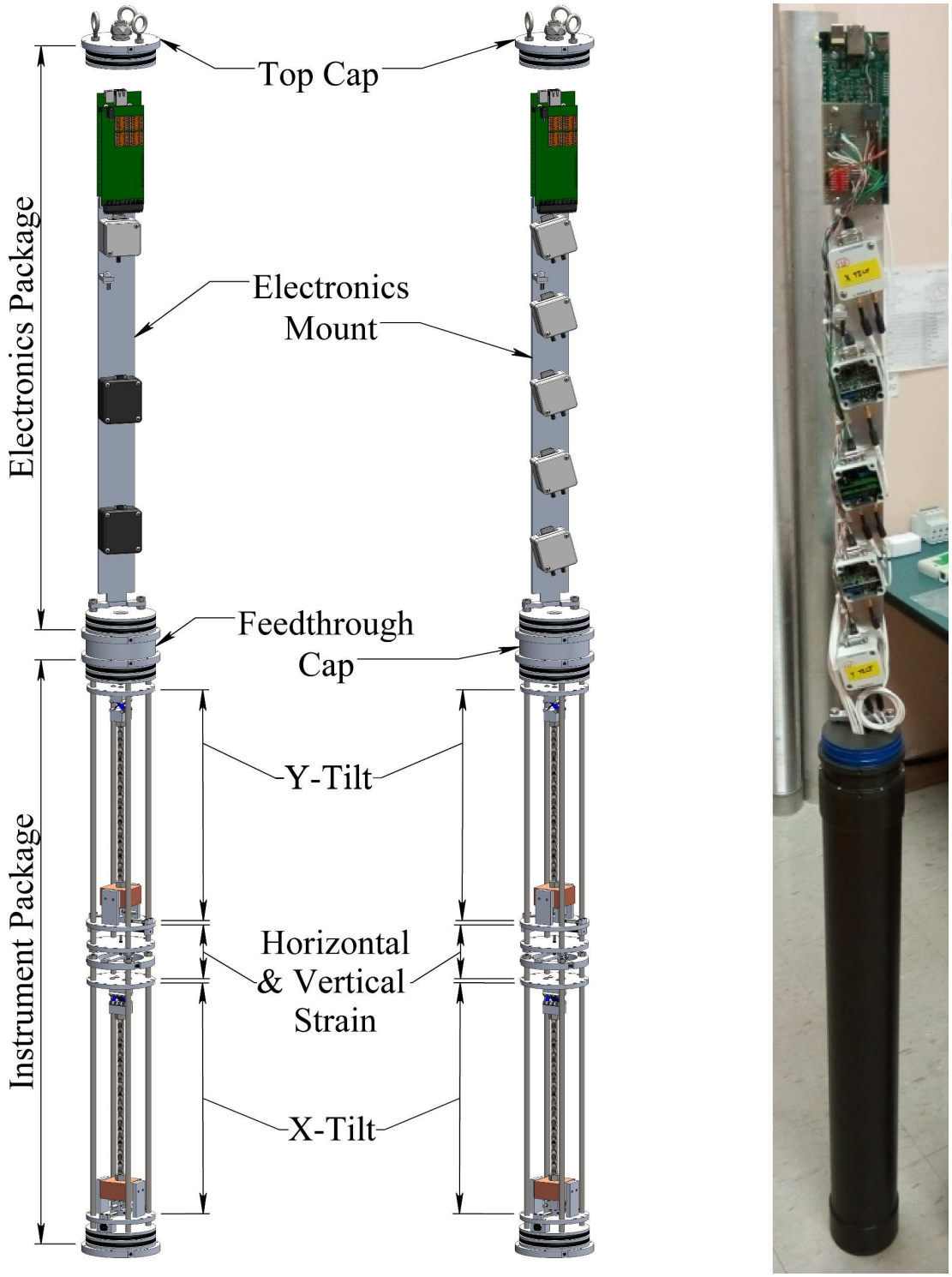

Figure 2.8: CAD renderings of the Version 1 (left) and Version 2 (center) grout-in instruments. A photograph of the Version 2 borehole package is shown on the right. Note that the Version 1 rendering has been stretched to match the length of the Version 2 instrument for illustration purposes. The centralizer springs have also been omitted for clarity.

2.2.2.1.1 Tiltmeters

Figure 2.9 shows the major design elements of the tilt measurement system, which is based on a physical pendulum. The hinge is assembled from four pieces of 0.005-inch (0.13 mm) thick blue-tempered 1095 spring steel arranged in a crossed pattern to eliminate any off-axis tilting or twisting. A length of 3/8"-16-inch (∼9.5 mm diameter) threaded rod is used to connect the hinge assembly to a 110 copper mass, which was chosen for its high density and excellent electrical conductivity. This allows the mass to be magnetically dampened via a pair of nickel plated, Grade N42 neodymium magnets (K&J Magnetics, Inc. BX0X03DCS) located on each side of the mass, resulting in an over-damped harmonic oscillator. While this significantly distorts its phase response, we were not interested in its dynamic performance for the quasi-static deformations under investigation in this project.

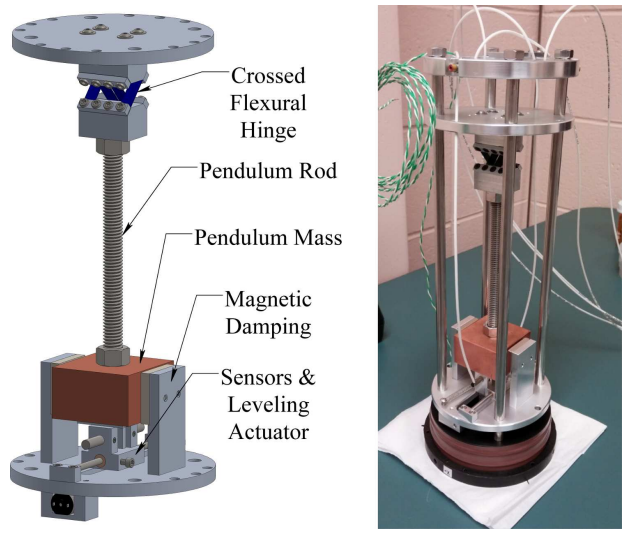

Figure 2.9: Diagram and photograph of the Version 1 physical pendulum tiltmeter used in the grout-in instrument. Note that the ring mount containing the three horizontal displacement transducers are also shown connected to the top of the tiltmeter in the photograph.

Integrating eddy current sensors into a tiltmeter required finding an innovative way to "zero-out" the transducers given their very small (1 mm) dynamic range. Pendulum type tiltmeters used in borehole applications are often leveled in situ by rotating a separate container containing the pendulum within the borehole package (Franz, 1983; Hunter et al., 2002). While this is optimal for preserving the linearity of the hinge for high-frequency measurements (e.g., seismic), like the over-damping it was not a concern for the long period measurements made during this project. Therefore, a much simpler sensor mount actuator system was developed (see Figure 2.10) to move the differential sensor pair in range of the aluminum sensor target attached to the bottom of the pendulum mass. While not technically a "leveling" system, this screw motor system serves a similar purpose in that it allows for the target to be re-centered between the eddy current sensors for package tilts up to ±10° and ±8.5° for the Version 1 and 2 instruments, respectively, due to their differing base lengths.

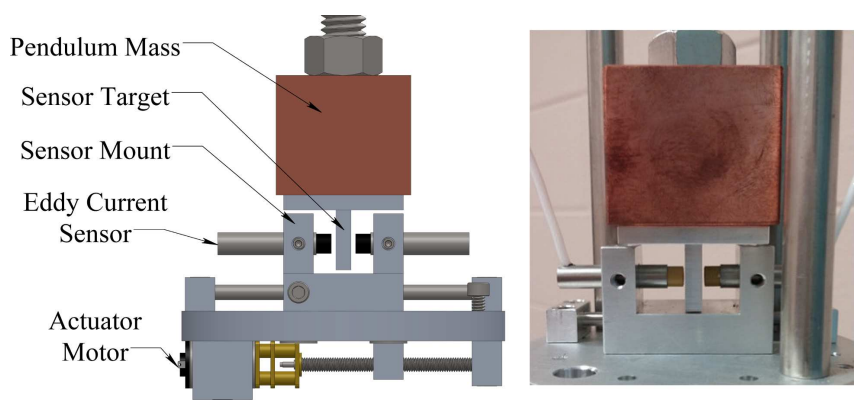

Figure 2.10: Closeup diagram and photograph of the tiltmeter sensing system showing the eddy current sensor actuator pack, which includes the sensor mount, eddy current sensors, and leveling actuator motor. The aluminum sensor target is attached to the bottom of the pendulum mass.

Several other features were added to the tiltmeter leveling system to improve its ease if use and mechanical stability. A linear potentiometer (Bourns PTA6043-2015CPB103) was added to each tiltmeter leveling actuator to measure the absolute tilt offset as well as prevent actuator overrun (Figure 2.11a). The resistance of the 20 kΩ potentiometer was converted to a voltage via a half-bridge or voltage divider circuit and calibrated so that the absolute tilt could be reported and recorded

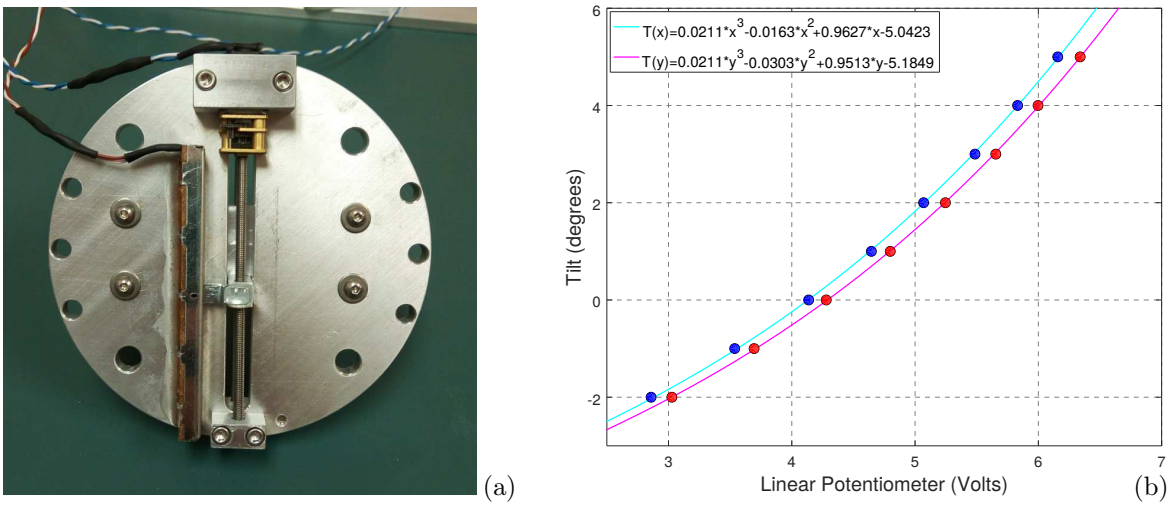

Figure 2.11: (a) Photograph of the underside of the tiltmeter sensor mount showing the threaded rod of the leveling actuator with accompanying linear potentiometer. (b) Calibration curves for the absolute tilt as a function of the half-bridge resistance-to-voltage output.

during a leveling operation (Figure 2.11b). This output also allows the leveling to be stopped prior to the limit of the actuator and preventing damage to the screw motor and sensor mount. An anti-backlash spring (Jones Spring Co. 2129) was added between the mounting plate and the sensor mount to prevent stick-slip motion during leveling and creep during sustained measurement.

The nominal tilt resolution was estimated based on the manufacturer's specifications and the length of each pendulum rod. The Version 1 system has a length of approximately 7 inches (∼17 cm), whereas the Version 2 is 12 inches (30 cm) long. Given the 0.1 nm resolution of the differential transducers, these systems should be capable of resolving tilts of 3 to 6×10^{-10} radians, which was predicted to be more than adequate for this project. While the Version 1 system used the Kaman DIT-5200L, two-channel differential system with two pairs of 15N-003 sensors, we chose to use the Micro-Epsilon eddyNCDT 3703 with two pairs of U1 sensors given their lower cost and better noise performance in situ that was not observed in laboratory comparisons. This required minor modifications to the sensor target and actuator mount, but not a substantial improvement in performance due to other factors (see Section 2.2.2.3).

2.2.2.1.2 Strainmeters

Integrating the single-ended eddy current transducers for strain sensing was fairly straight-forward since the instrument package is directly coupled to the formation via the grout. This implied that the strain measurements could be made by monitoring the deformation of the instrument package itself. Several initial designs included a differential measurement in the vertical direction for optimal resolution. However, the push-pull nature of the eddy current transducer bridge (Figure 2.7b) made this impossible for the horizontal strains. It would have been possible to have one of the two sensors set at a fixed distance while the other measured the radial deformation along one azimuth, or for the sensor pair to be oriented orthogonally (e.g., 0° and 90°). Unfortunately these ideas were roundly discouraged by the application engineers from both sensor manufacturers.

The design of the horizontal strain measurement scheme was the same for both instrument versions and is shown in Figure 2.12. The main sensor mount is an aluminum ring mounted to the top of the x-axis tiltmeter

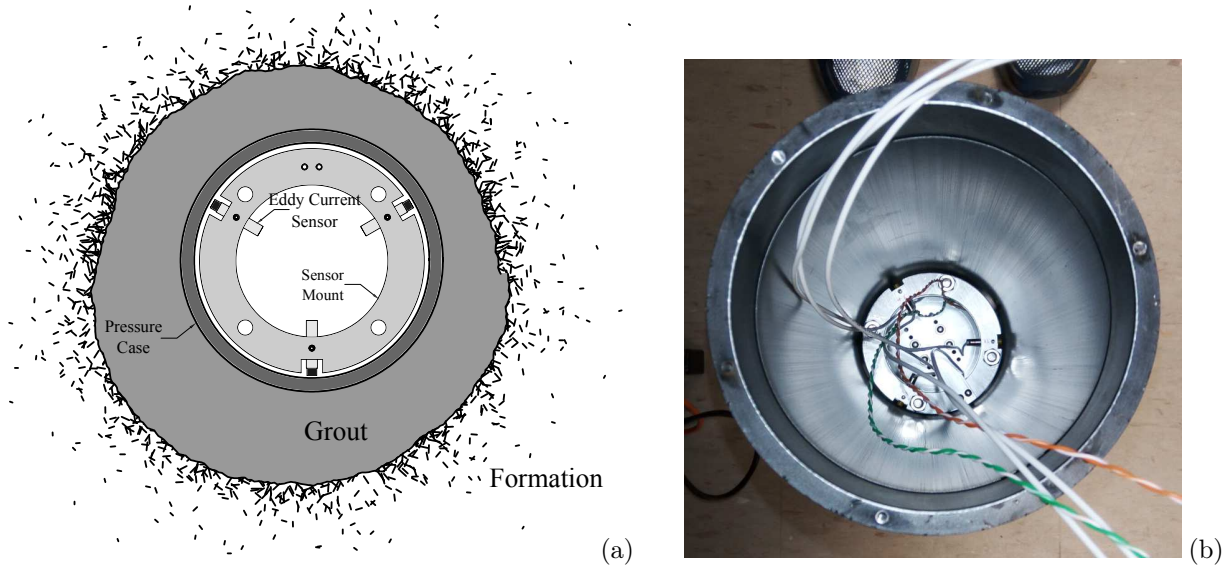

Figure 2.12: (a) Schematic representation of the deployed horizontal strain sensing system showing the sensor mount, instrument package pressure case, grout, and formation. (b) Photograph looking down into the instrument package pressure case showing the horizontal sensors and sensor mounts. Note that the sensor mount is also pictured in Figure 2.9.

assembly that is installed in the bottom of the lower instrument package. This ring has three through holes separated by 120° to accommodate each eddy current sensor body, as well as set screws to firmly secure them in place during assembly. A square notch in the ring was required at the end of each transducer to prevent "inductive loading" of the mount itself that can negatively impact the performance of the sensor.

Positioning, or "zeroing" the eddy current sensor heads was one of the most challenging aspects of integrating these ultra-high resolution transducers. This is due to their very limited 0.5 mm dynamic range, which implies that they must be located as close to 0.25 mm from their target in order to measure both positive and negative displacements. The expanding grout mixture further complicates this issue since it would be optimal to have the sensors be as close to 0.25 mm as possible after installation and curing. This turned out to be impossible in practice since simply putting the assembled instrument on its side (e.g., during transport) moved the sensor mount ring off center enough to disrupt the time spent positioning the sensors during assembly. Fortunately, this 0.25 mm over the 0.1 m baseline implies a total strain range of 2,500 microstrain, which exceeds the expected compression from the grout and is many orders of magnitude larger than the anticipated operating range of the instrument.

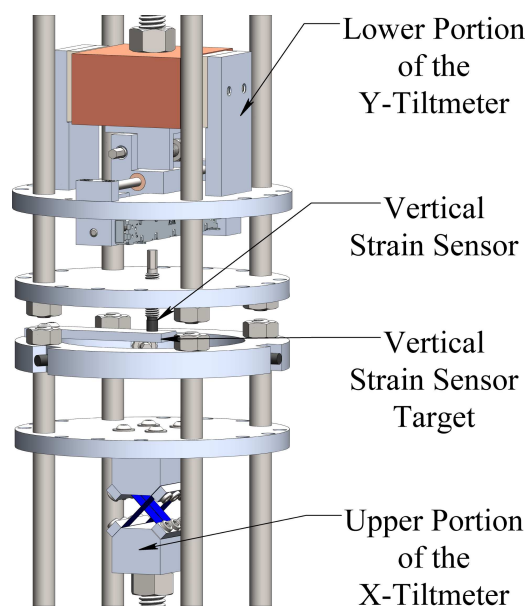

Figure 2.13: Schematic representation of the vertical strain sensing design as installed between the upper and lower tiltmeters.

While the horizontal strain design was identical in concept between the Version 1 and 2 systems, they differed in the brand of sensor used. The Version 1 system used a Kaman SMT-9700 three-channel, single-ended system with a triplet of 15N-003 sensors. This resulted in a more compact integra-

tion (see Section 2.2.2.2 for more details), however, there was evidence of this system being outperformed by their competitor's system (see Section 2.2.2.3). Therefore we decided to use one Micro-Epsilon eddyNCDT 3702 dual-channel, and one 3701 single-channel system all with U1 sensors for the Version 2 horizontal strain measurements. This only required very minor modifications (i.e., M5-0.8 tapped holes rather than 0.150" through-holes) to the horizontal sensor mounting ring.

The same vertical strain measurement design was also used for both instrument versions, and is shown in Figure 2.13. A key design feature of the instrument package is that the lower, or x-axis tiltmeter is inserted from the bottom and the upper, or y-axis tiltmeter is inserted from the top. However, there is no physical connection between the upper and lower tiltmeter assemblies other than where they attach to the top and bottom of the lower pressure case. While this most likely diminishes the mechanical stability of the lower instrument package components, it does easily allow for the vertical deformation of instrument package pressure case to be monitored as a displacement between the bottom of the upper tiltmeter and the top of the lower tiltmeter. One Micro-Epsilon eddyNCDT 3701, single-channel system with one U1 sensor was used in both instruments.

There are several issues that need to be confronted with this conceptually simple vertical measurement scheme. The first is determining the base length of the strain measurement since the entire instrument is undergoing deformation, however, only the displacement of the lower package is being measured. This will be addressed during the in situ calibration presented in Section 2.2.2.3. The other is the very low vertical compliance of the pressure case. While some attempts were made at increasing this in the Version 1 system, no method proved to be effective and this was abandoned in the Version 2 design. It turned out, however, that this was not an issue since the vertical strain recordings on the Version 2 system have proven to be the most robust of all the eddy current system measurements.

2.2.2.2 Supporting Electronics

The major obstacle to integrating commercial eddy current sensor systems was bundling all of the various electronic components into a robust, and unserviceable down-hole package. This includes the mounting of the requisite signal conditioning electronics for each eddy current system, an Analog-to-Digital Converter (ADC), an electronic compass, and a main board to host the leveling motor controller and all the routing between the other components. The electronics mounts for both instrument versions are shown in Figure 2.14.

Accommodating the supporting electronics was less of a challenge for the Version 1 system. This was in large part due to the difference in the channel packaging between the two eddy current system manufacturers. For example, Kaman offers their single-ended systems in 1, 2, and 3-channels per signal conditioning board (SMT-9700). However, Micro-Epsilon only has one single-ended sensor per board (eddyNCDT 3701) since discontinuing their dual single-ended system (eddyNCDT 3702). Kaman also has single and dual channel options for their differential systems (DIT-5200L), which was ideal for an orthogonal pair of tiltmeters. This resulted in only needing to package three signal conditioners for the Version 1 system: one SMT-9700, one DIT-5200L, and one eddyNCDT 3701. However, the Version 2 system only uses Micro-Epsilon transducers, which meant mounting a total of five signal conditioners: two 3703 differential systems for x and y tilts, one 3701 for the vertical strain, and one 3701 and one 3702 for the three horizontals. (We were able to procure one used 3702 system.)

While more compact, the Kaman systems required more electrical support than the Micro-Epsilon systems. Both the SMT-9700 and DIT-5200L models operate at a tightly-regulated 15 ± 0.1 Volts, the latter requiring bipolar power (i.e., $\pm$15V), whereas the Micro-Epsilon systems require a very manageable 9–36V uni-polar power supply. Most standard solar systems operate at multiples of 12V, therefore 15V systems required external voltage conversion either up-hole, necessitating additional wires running down-hole, or

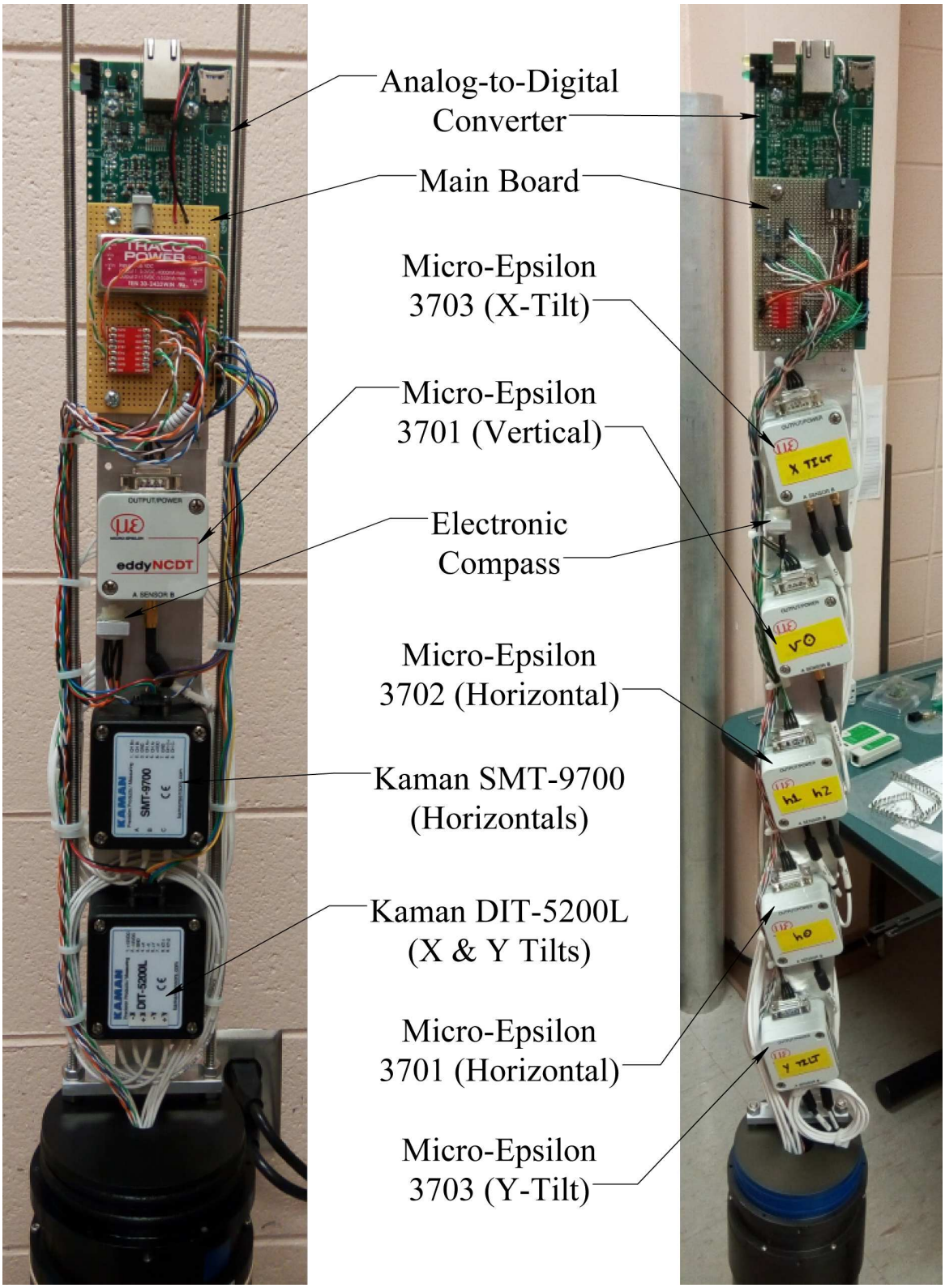

Figure 2.14: Photographs of the Version 1 (left) and Version 2 (right) electronics mounts.

conversion down-hole leading to more heat dissipation next to the sensors. Either case requires expensive, high-quality DC-to-DC conversion and additional power.

Different power and cabling schemes were implemented in each instrument version. The Version 1 system was supplied a single +12V input and the ±15V and +5V DC-to-DC conversion was performed down-hole via a Traco Power TEN 30-2432WIN, the 5V being required by the ADC, electronic compass, and leveling motor controller. While this meant increased down-hole heat generation, it avoided any potential low voltage issues related to cable losses on the 15V and 5V lines. The Version 2, Micro-Epsilon only system did not require 15V, and was supplied on +12V and +5V lines provided by an up-hole DC-to-DC converter (XP Power DDC1524S05). We also found that additional voltage regulation of the +12V line (via a XP Power DDC1524S12) was needed to prevent noise from the solar battery charge controllers from leaking into the displacement signals despite the manufacturers' claims of robust internal voltage regulation.

Other supporting hardware such as the ADC, main board and electronic compass are also housed in the upper electronics package. While a number of ADCs were tested for digitizing the displacement transducer voltages, the LabJack T7-Pro OEM was chosen because of its 24-bit resolution, Ethernet output, and simple ANSI C based application programming interface. It also can accept single-ended and differential analog inputs and has multiple digital inputs and outputs for controlling the tiltmeter leveling actuators. A Dinsmore R1655 (The Robson Company, Inc.) was used to azimuthally orient each system in situ, which required lab calibration (see Figure 2.15).

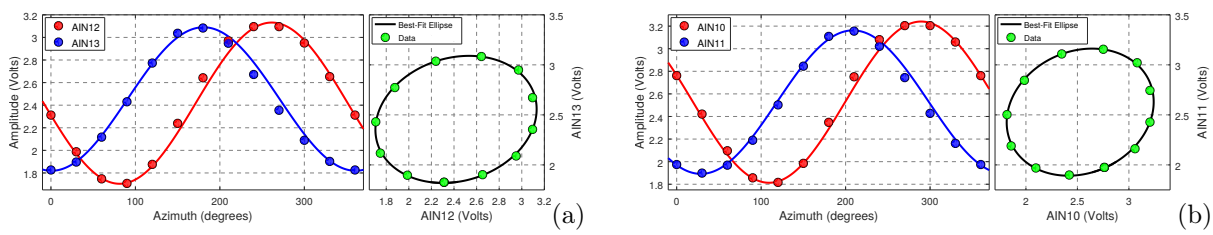

Figure 2.15: Electronic compass calibration curves for the (a) Version 1 and (b) Version 2 grout-in instruments. Each compass outputs a sine and cosine curve whose ratio is the tangent of the compass azimuth.

The final major component of the electronics package is the custom main board that routes all of the inputs and outputs from the other supporting electronics. This includes the DC motor controller (SparkFun Dual TB6612FNG, ROB-14451) for the tiltmeter leveling actuators. Two half-bridge and one full-bridge circuit convert the resistances from the two tiltmeter actuator potentiometers and instrument package thermistor (BetaTHERM 30K6A1B) to single-ended and differential voltages, respectively.

Details of the up-hole supporting electronics such as the solar hardware and telemetry are presented in Section 4.2.2.

2.2.2.3 Field Observations

A number of time and frequency domain observations have been made leading up to and following the installation of both the Version 1 and 2 instruments. However, the post-deployment field observations are the most critical for evaluating whether the performance of these instruments will be satisfactory for monitoring the deformations anticipated by the proposed injection tests. The first assessment is observing the initial post-installation grout curing. This is followed by an evaluation of a longer duration record in both the time and frequency domain to identify any obvious noise and drift issues and most importantly determine if the instruments are in fact recording geophysically meaningful signals (e.g., teleseismic event waveforms and solid Earth tides). Tidal analyses can then be used to calibrate and orient each strain and tilt gauge

relative to the theoretical solid Earth tides, after which comparisons can be made to other instruments.

It is essential to note that *in-situ calibration can only be done successfully if the given instrument gauge is is capable of measuring the solid Earth tides.* While the displacement-voltage calibration of each eddy current sensor was performed by the manufacturer and verified in the lab, the strain-displacement relationship can only be, at best, *inferred* before installation since it is difficult and often impractical to predict the relationship between the observed gauge strain and the formation strain (Gladwin and Hart, 1985; Hart et al., 1996). Therefore, the following initial time and frequency domain observations are shown in units of *displacement*, which is the linearized voltage output of a given eddy current sensor's signal conditioner. Results of the fully processed (Section 2.4) and in-situ calibrated data are presented in Section 2.5.

We expect a characteristic time-evolving behavior immediately following installation that starts with the initial exothermic reaction from the grout that is ideally followed by each of the strain gauges going into compression. Figure 2.16 shows time series plots of both the Version 1 and 2 instruments in the two weeks following installation. All strain and tilt components show responses to the temperature induced by the grout's initial exothermic reaction. While the x and y tiltmeters seem to level off after a few days, the strain gauges in the Version 1 instrument start behaving in an unpredictable manner with multiple correlated creep events. Fortunately the 0°, 240°, and vertical strain gauges all appear to be in compression at the end of two weeks. The Version 2 response appears to be much more well behaved, however, a significant 1 cylcle-per-day (CPD) noise source emerges shortly after deployment. This was determined to be a voltage regulation issue related to the solar charge controller and was remedied by installing an additional external regulator in the up-hole electronics enclosure during a visit several months later. It appears that only the 0° and vertical strain gauges have gone into compression at the end of this time period, and further examinations of the data are needed to assess the functionality of each instrument's components and the success of each installation.

Figure 2.17 shows an approximately year long tilt and strain time series several months following the initial grout cure shown in Figure 2.16a. The tilt time series (Figure 2.17a) reveals a fairly stable x-tilt signal but a relatively large drift in the y-tilt signal where it appears to go off scale, or "clip" at about day 500. Several attempts have been made to re-level this tiltmeter, however, this effect is likely caused by an electrical malfunction in either the signal conditioning electronics or ADC channel since the y tiltmeter is nowhere near its ±450 micron limit. The strain time series (Figure 2.17b) seem to be operating normally with the exception of the large drift in the 120° and stochastic behavior of the 240° strain gauges.

While the time series reveal some of the larger scale behaviors, it is not immediately obvious whether any of the Version 1 instrument components are capturing any geophysical data. This is much more evident in the frequency domain (Figure 2.18) where the solid Earth tides are present in some gauges and absent from others. For example, it is readily apparent that only the x-tilt, 120° and vertical strain components are performing as expected since they are the only signals with a discernible tidal response. The remaining gauges (e.g., the y-tilt, 0° and 240° strains) appear to be capable of measuring at least the M2 tide since their spectral levels do not exceed the peak magnitudes observed by the properly functioning gauges.

Similar time and frequency domain plots of the Version 2 system deployed at the North Avant Field site in Oklahoma are shown in Figures 2.19 and 2.20, respectively. While there is clear evidence that the solid Earth tides are present in both tilt time series (Figure 2.19a), the x-tilt suffers from sporadic creep events not present in the y-tilt time series. The strain time series (Figure 2.19b) is more complex. The vertical strain appears to be in an ongoing state of increasing compression and is fairly stable aside from several thermal transients following power outages (e.g., days 315 and 360). However, the exact behavior of the 120° and 240° horizontal gauges are obscured by several large correlated excursions, and the 0° gauge goes off scale for several hundred days before reemerging around day 540.

Magnitude spectra of the Version 2 instrument (Figure 2.20) show an improved performance and overall success rate compared to the Version 1 instrument. Both tilt gauges (Figure 2.20a) appear to be performing as expected with a tidal signal-to-noise ratio (SNR) of about 4–5 at 1 CPD and 12–15 at 2 CPD, which

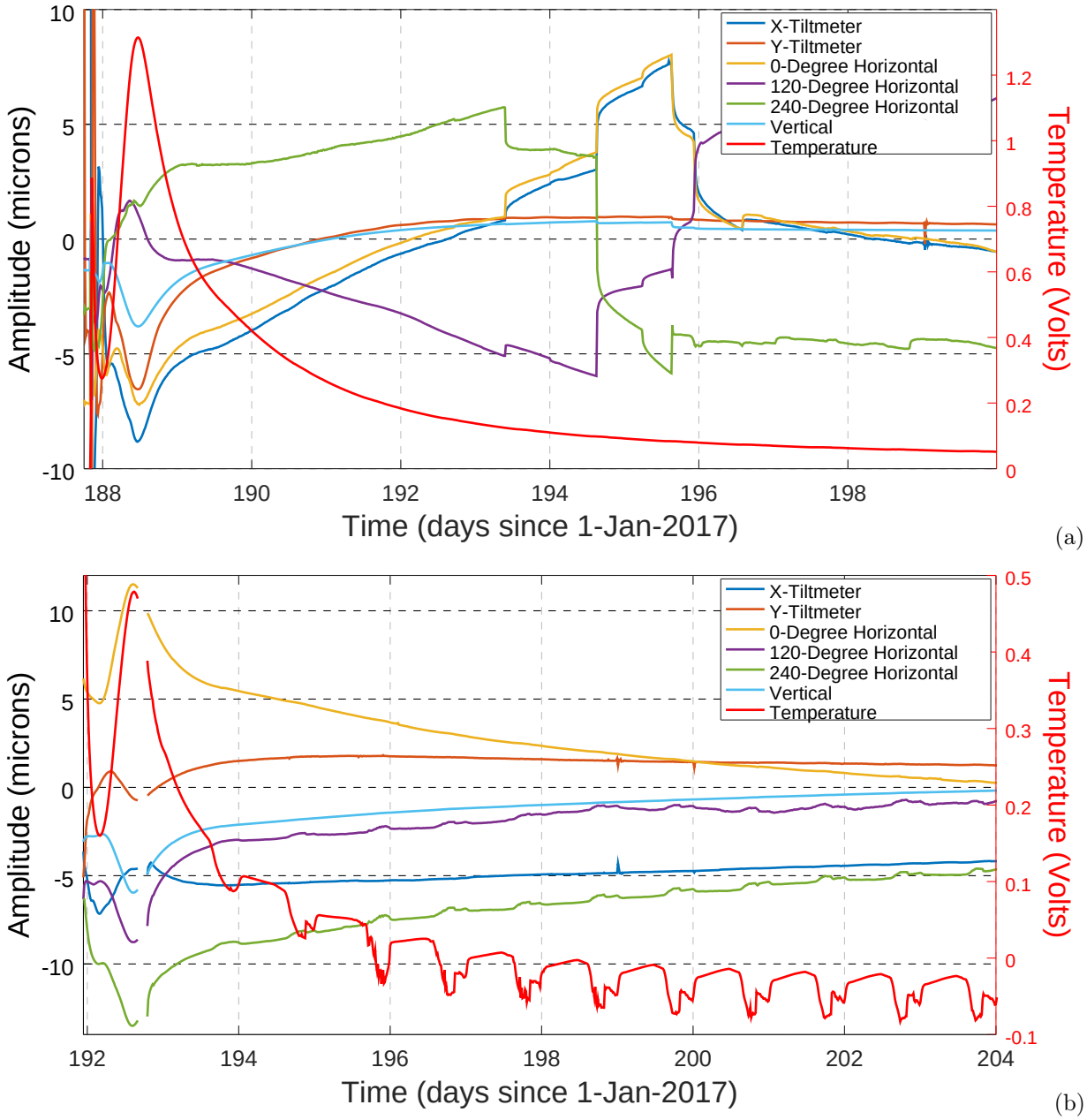

Figure 2.16: Time series plots of the grout cure for the Version 1 (a) and Version 2 (b) eddy current strain and tilt systems deployed at the Simpson Station, SC, and North Avant Field, OK, respectively. The temperature is in uncalibrated units of voltage from the output of the bridge circuit used to measure the resistance from the thermistor included in each instrument package. Note that the mean of each time series has been artificially offset for plotting purposes.

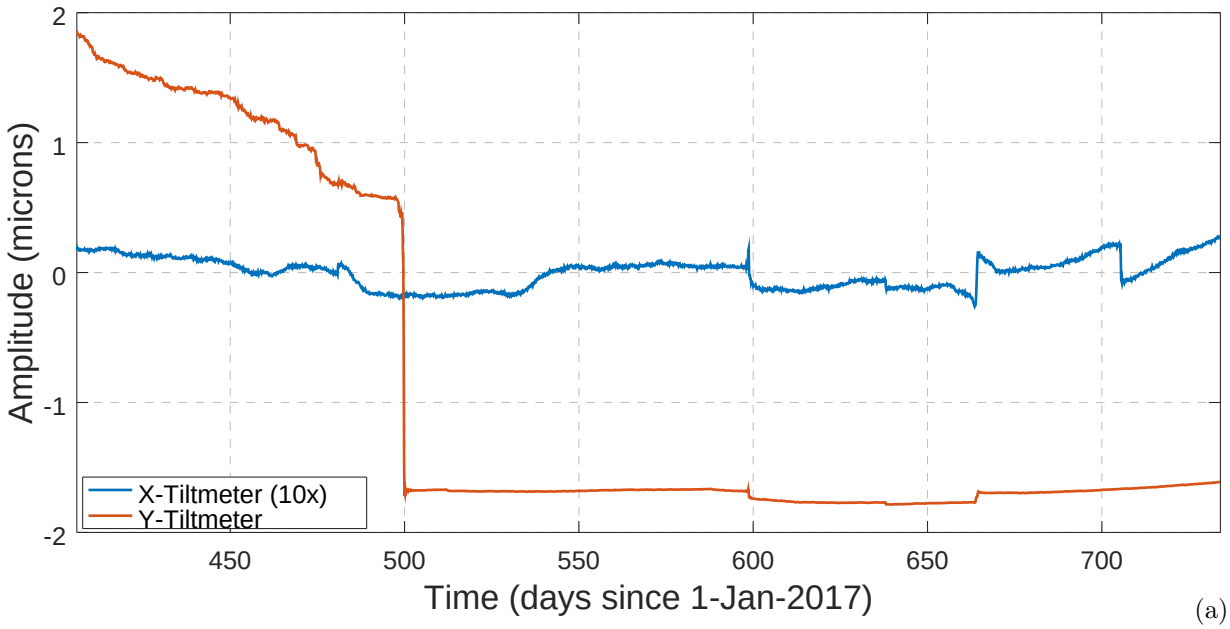

(a)

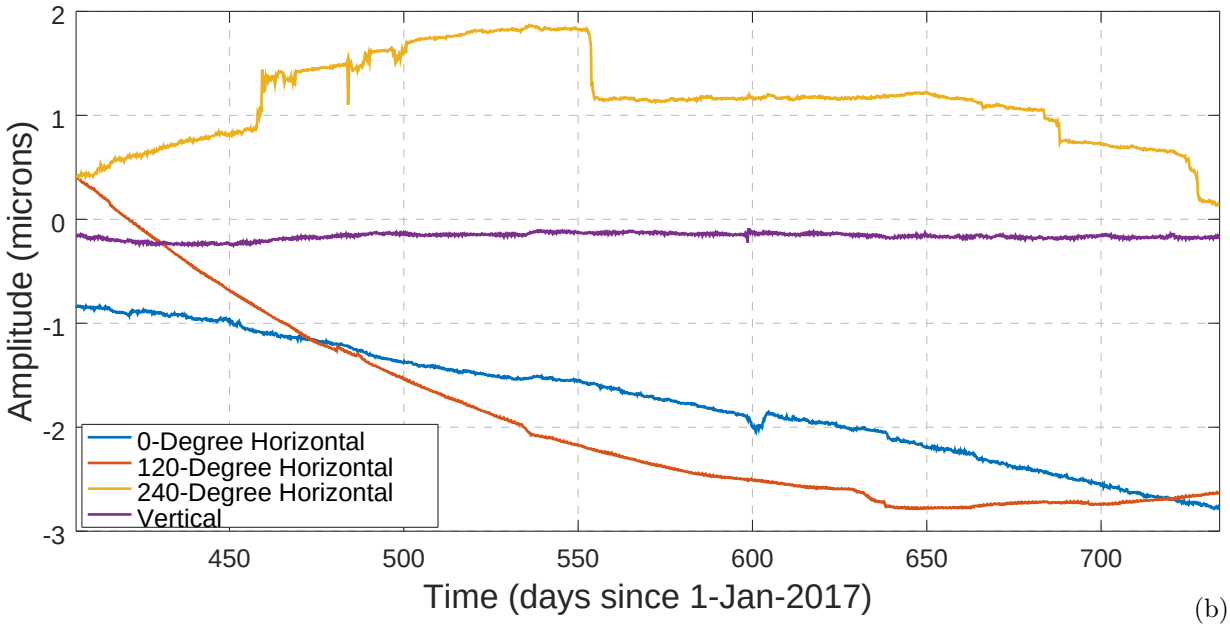

(b)

Figure 2.17: 330-day tilt (a) and strain (b) time series plots following the grout cure for the Version 1 eddy current strain and tilt system deployed at the Simpson Station, SC. Note that the mean of each time series has been artificially offset for plotting purposes.

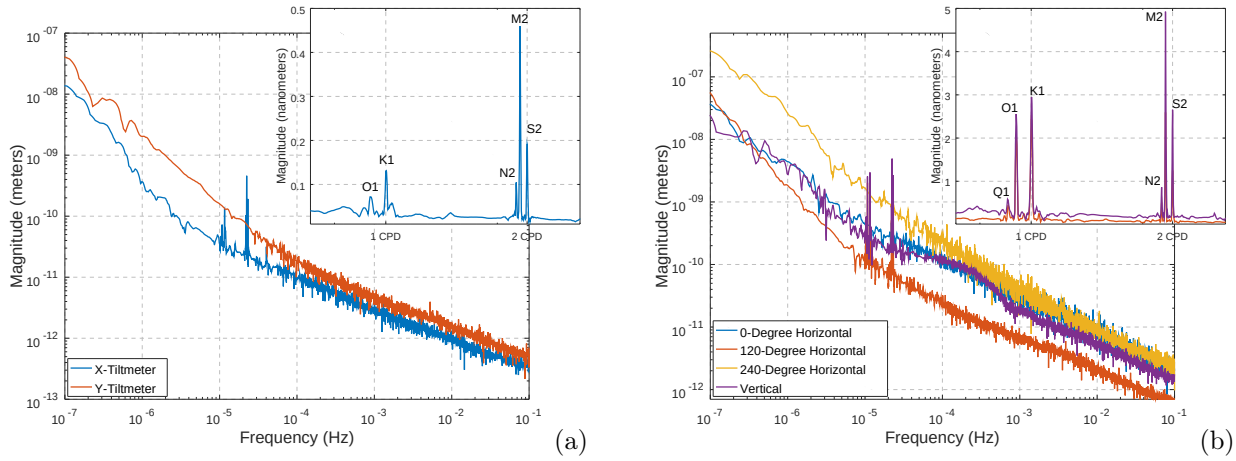

Figure 2.18: Magnitude spectrum estimates using the 330-day tilt (a) and strain (b) data from Figure 2.18. Inset plots are included for each highlighting the tidal band the six major tidal constituents: Q1, O1 and K1 near 1 CPD, and N2, M2 and S2 near 2 CPD.

is comparable to the x-tilt gauge in the Version 1 instrument (Figure 2.18a). The main difference is in their performance above ∼10,000 seconds (10^{-4} Hz), where the Version 2 system levels off just below ∼0.1 nm, whereas the Version 1 system continues downward at a rate of approximately $1/f$ to about 5×10^{-13}. It is important to observe, however, that the M2 tidal response is a full order of magnitude larger on the Version 2 instrument most likely due to the longer base length and higher resolution Micro-Epsilon eddy current sensor, and that the $1/f$ decline in the Version 1 spectra is a tell-tale sign of electrical circuit and not environmental noise.

The strain spectra (Figure 2.20b) show that three of the four strain gauges are capable of measuring geophysically meaningful signals. Like the 0° and 240° gauges in the Version 1 instrument, the 120° gauge in the Version 2 instrument appears to be recording only noise despite being on-scale. This is unlike the 0° gauge, which is definitely clipped during most of the observation period (despite being adjusted to be in the center of its operating range during assembly), but is able to very clearly record the tides when on scale.

The data presented above convincingly demonstrates that commercial non-contact eddy current displacement transducers can be successfully integrated into a permanent, grout-in package similar to a Gladwin strainmeter. While there is considerable room for improvement, the functioning gauges exceed their design goals and appear to be capable of measuring the same signals as commercial geodetic strain and tilt systems. Most importantly they appear to be capable of resolving the deformations anticipated by the proposed injection tests.

2.2.3 Removable Multi-Component Eddy Current Strain and Tilt System

One removable eddy current strain and tilt system was developed during this project. While it shares many design elements with its permanently installed counterpart, the removable instrument differs substantially in complexity (Figure 2.21). It also consists of two pressure case packages that house the main sensing components and supporting electronics, but was designed to operate in smaller, HQ-sized (96 mm diameter) boreholes. The outer diameter is 3.25 inches (8.2 cm) with 24-inch (61 cm) long packages like the Version 1 grout-in instrument. It also uses 0.25-inch (0.635 cm) thick, Type III anodized aluminum tubing, with a total assembled length of 51 inches (129.5 cm). Each package is also sealed with double bore o-rings with end caps that admit a 3/8 trade size conduit fitting through the top cap and 1/2"-13 bottom tapped hole

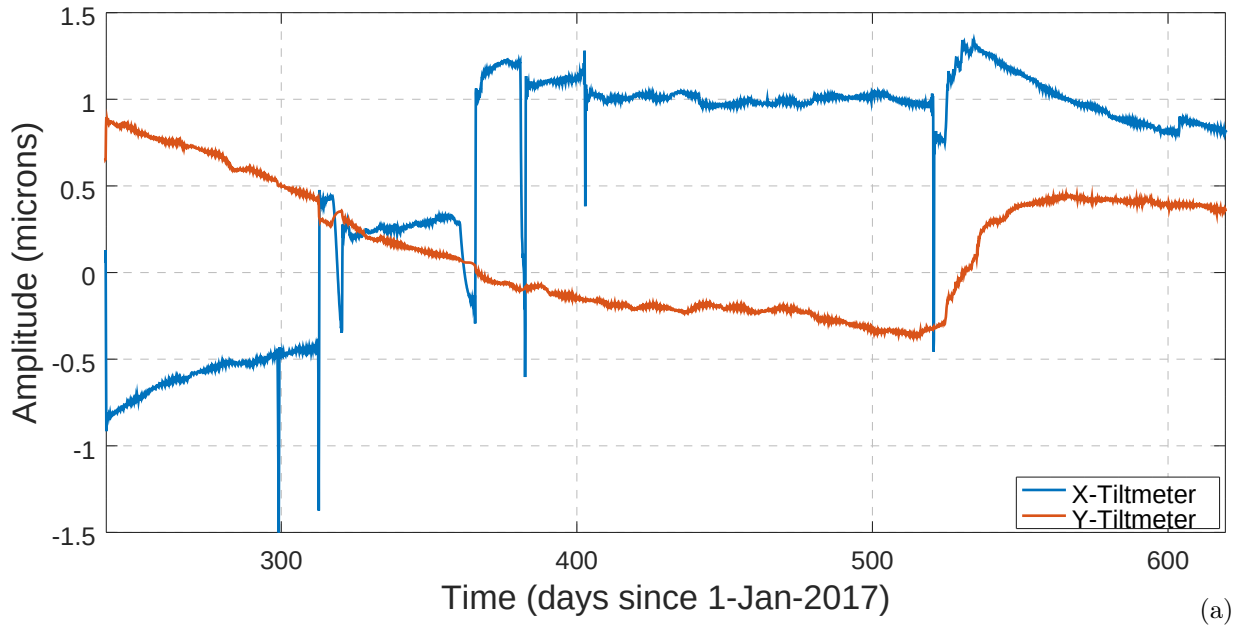

(a)

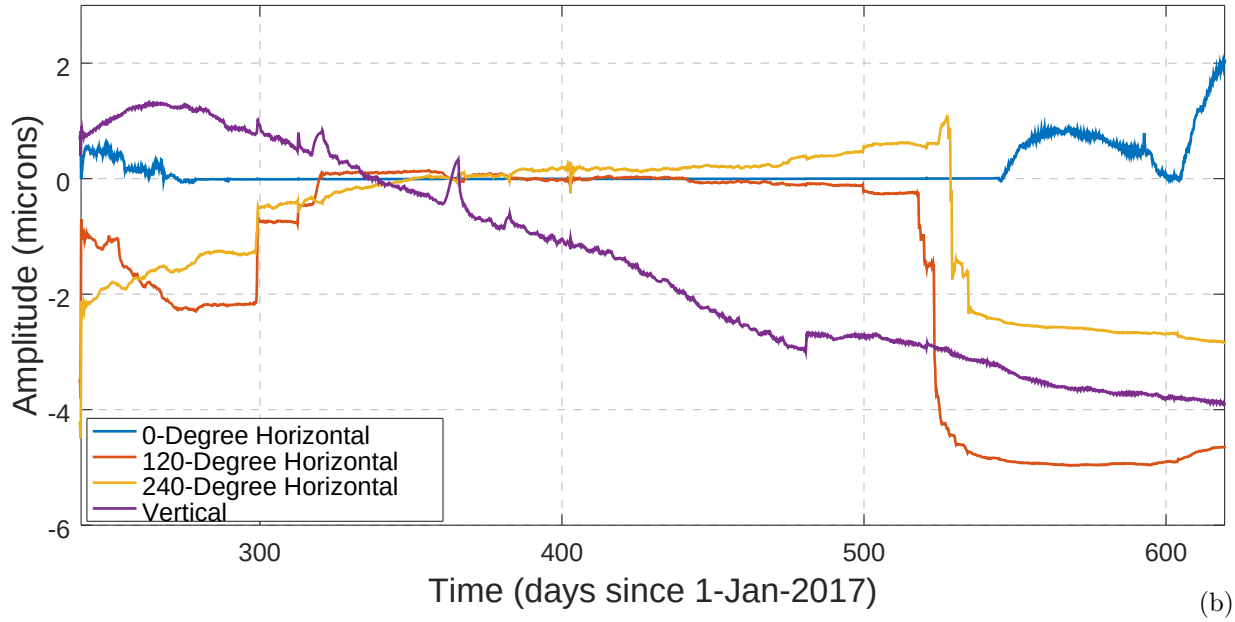

(b)

Figure 2.19: 380-day tilt (a) and strain (b) time series plots following the grout cure for the Version 2 eddy current strain and tilt system deployed at the North Avant Field, OK. Note that the mean of each time series has been artificially offset for plotting purposes.

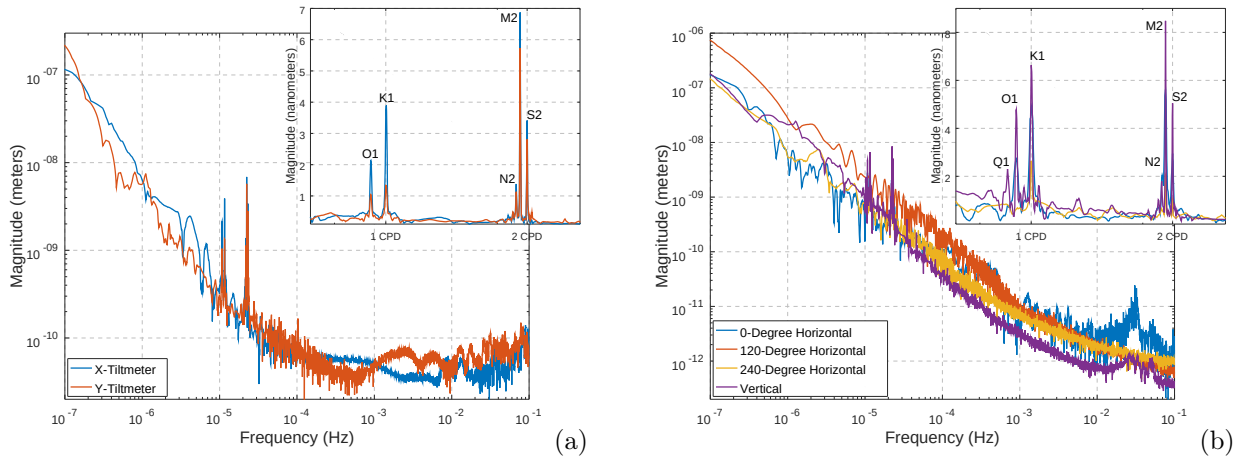

Figure 2.20: Magnitude spectrum estimates using the 380-day tilt (a) and strain (b) data from Figure 2.20. Inset plots are included for each highlighting the tidal band the six major tidal constituents: Q1, O1 and K1 near 1 CPD, and N2, M2 and S2 near 2 CPD.

in the bottom cap. The top cap also includes three 1/4"-20 bottom tapped holes for lifting eyes, however, the package can also be raised and lowered via the conduit.

The removable instrument obviously differs from the permanent versions in that it can be relocated between and even during injection tests. This is made possible in part to the upper and lower clamping mechanisms that consist of two fixed and one movable plate that is driven by a lever arm connected to large gear motor through a double o-ring sealed shaft. The three clamping plates have a radius that matches the inner diameter of the casing in which it is deployed, and the two fixed plates are set before installation. Therefore, the instrument is centered through the action of the movable clamping arm. The drive current is monitored during installation to manage its outward force and prevent damage to the motors and gear reducers.

These and the details to follow may be best understood in the context of the instrument's deployment procedure. Consider a borehole completed with an electrically conductive casing (e.g., steel or treated aluminum) that is coupled to the formation with expanding grout. The fixed upper and lower clamping plates are set to correspond to the inner diameter of the casing, and the movable clamping arms are fully retracted. The instrument is then lowered to the desired depth and the movable clamping arms are extended to secure it in the borehole. Once set, the tiltmeters can be leveled in a manner identical to the permanently installed instrument. However, the horizontal transducers must be moved up to the casing to within roughly one-half the 0.5 mm range of the sensors. Furthermore, the instrument package must be vertically compliant to monitor axial deformation. These are the two main challenges that must be addressed when undertaking this type of integration.

2.2.3.1 Transducer Integration

Non-contact eddy current sensors are ideal for measuring borehole deformation since the sensors themselves have no mechanical interaction with the casing. However, their limited dynamic range required that they be moved into very close proximity to the casing to make deformation measurements. It is this action that makes the sensor integration substantially more challenging for strain monitoring, and is where the permanent and removable instrument designs diverge considerably. Fortunately, both tiltmeters were able to remain nearly identical to the permanently installed instrument.

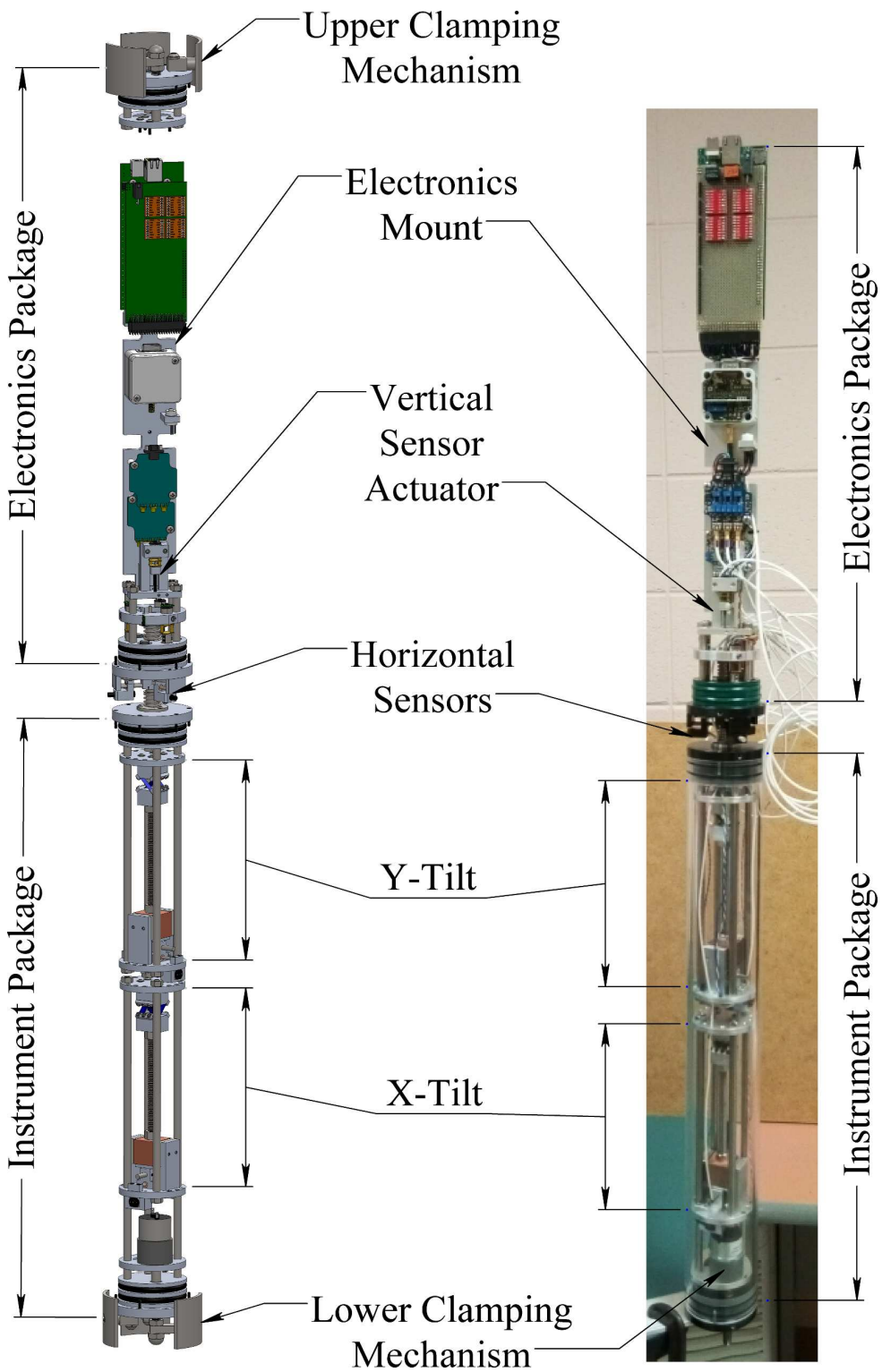

Figure 2.21: CAD realization and photograph of the removable eddy current strain and tilt system pointing out some of the main design elements discussed in greater detail in the following sections.

2.2.3.1.1 Tiltmeters

There are few differences in the tiltmeter designs between the permanent and removable eddy current systems. They are both crossed-flexural physical pendulums with magnetic damping and employ the same movable eddy current sensor mount and leveling actuator. In fact, Figure 2.10 is actually a photograph of the removable instrument tiltmeter pendulum mass and actuator assembly. This system uses the Kaman DIT-5200L differential transducer system with 15N-003 sensors like the Version 1 grout-in instrument.

The primary difference is the range over which the tiltmeters are able to be leveled. This is due to the narrower inner diameter of the instrument package (only 2.75 inches, or ∼7 cm), which is only partially offset by the shorter 6.7 inch (17 cm) base length. Therefore, these tiltmeters can only be re-leveled within a ±4.8° range. This also required the use of a shorter linear potentiometer (Bourns PTA1543-2015CPB103). A top view photograph of the leveling actuator and their potentiometer calibration curves are shown in Figure 2.22.

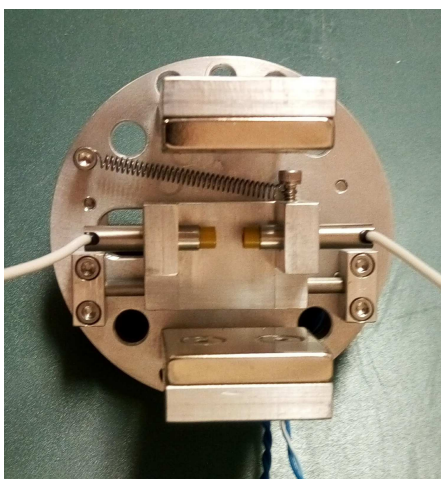

(a)

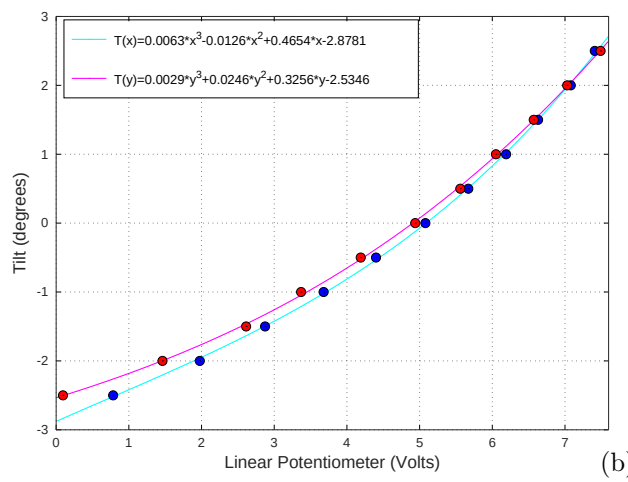

(b)

Figure 2.22: (a) Photograph of the top side of the tiltmeter sensor mount showing the magnetic dampers, along with the leveling actuator guide rod and anti-backlash spring. (b) Calibration curves for the absolute tilt as a function of the half-bridge resistance-to-voltage output.

2.2.3.1.2 Strainmeters

Integrating high-resolution, non-contact eddy current sensors into a robust down-hole package for multi-component strain measurement was the primary instrumentation challenge faced during this project. The vertical strain was perhaps the most straightforward since it can be made by measuring the distance between the upper and lower clamps. However, it cannot be done in a similar manner to the grout-in instrument since the axial stiffness of the assembled instrument would be much higher than the friction between the clamps and the borehole casing, leading to stick-slip motion and creep. Our approach was to increase the vertical compliance by having a non-rigid connection between the upper and lower instrument packages.

Figure 2.23 shows a cross-sectional view of the connection between the main upper and lower pressure case packages. The central element is the feedthrough shaft that penetrates the top of the instrument package and the bottom of the electronics package. Its bottom flange rigidly attaches to the lower pressure case and is sealed with two bore o-rings. The main shaft of the feedthrough passes through into the upper pressure case and captures the bottom cap between a pair of springs and an aluminum clamp collar that prevents the

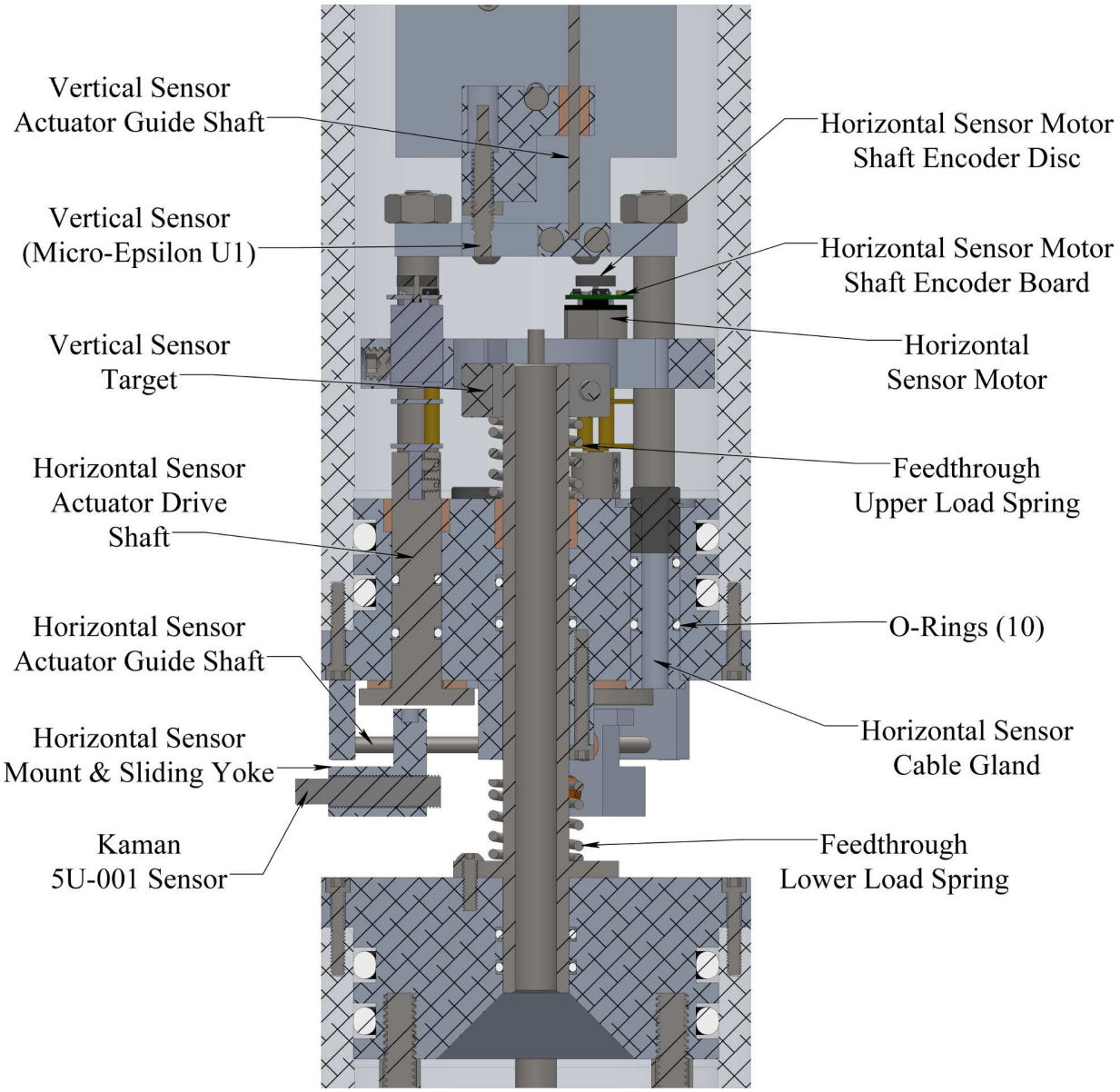

Figure 2.23: Cross-sectional view of the removable eddy current system centered around the penetration between the lower instrument package and upper electronics package where the horizontal and vertical displacement measurements are made.

two packages from fully separating and also serves as the vertical sensor target. It is also sealed with a pair of o-rings and is guided with an oil-impregnated sleeve bearing. This arrangement allows the two pressure cases to "float", or slide up and down axially approximately 0.25 inches (∼6 mm). The vertical strain is therefore measured as the change in displacement between these two main instrument packages.

The vertical strain sensor and actuator is fixed to the bottom of the lower pressure case and measures the amount the feedthrough shaft protrudes into the electronics package (Figure 2.24). The actuator is required to pull back the sensor and prevent its tip from colliding with the target during deployment. This system also includes a linear potentiometer (Bourns PTA2043-2015CPB103, not shown) to avoid motor overrun during retraction, as well as an anti-backlash spring like the tiltmeter actuators. It is the only measurement made with the Micro-Epsilon (eddyNCDT 3701) brand sensor like the Version 1 grout-in system.

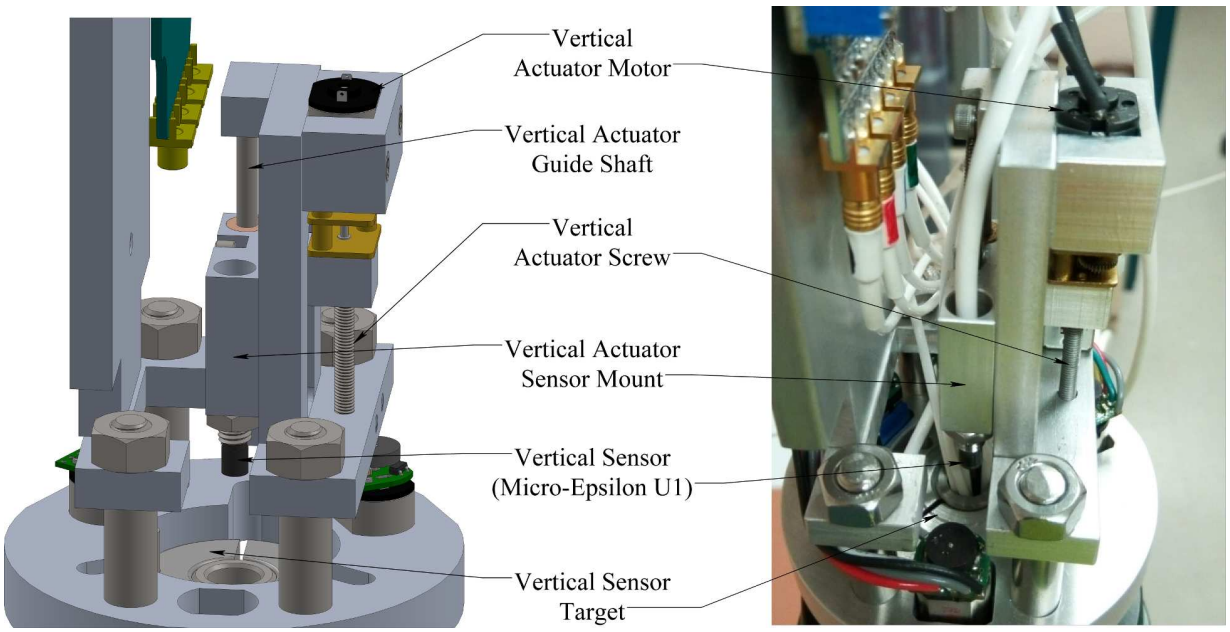

Figure 2.24: CAD realization and photograph of the removable eddy current vertical strain sensor and actuator (in its retracted position).

The first issue faced during the integration of the horizontal sensors was the survivability of the sensors themselves. This is because there was really no way to arrange the horizontal strain measurements without having something mechanically attached to the borehole casing or having the sensors operate in an open borehole environment. Engineers at Kaman Precision Products suggested using a modified version of their 5U-001 sensors since they have the same precision as the 15N-003 sensors used in the Version 1 grout-in instrument, but are housed in a very rugged polyether-ether-ketone (PEEK) plastic. These, as with all the eddy current sensors used in this project, are connected to RG316, RG174 or RG188 coaxial cable with polytetrafluoroethylene (PTFE, or Teflon^{TM}) insulation, making them ideal for hazardous environments as long as no leaks develop between the sensor body and cable.

The next complication was preventing the horizontal sensors from being damaged during deployment and yet still be able to have each end up within 0.25 mm from the borehole casing to make the highest possible strain measurement. This naturally required some sort of actuator since it would have been unfeasible to complete a borehole with such a tight tolerance such that a simple low-friction guide could be used to prevent the sensor tips from scraping inside the casing. The ∼0.1 base length (i.e., borehole diameter) and 1 nm resolution of the single-ended sensors meant that double-digit nanostrain resolution would be only just unattainable. Therefore, using longer range sensors that could be fixed at a safe location farther back

(i.e., greater than 0.25 mm) would mean sensors with a resolution less than the original design goal of the instrument.

Moving the horizontal strain gauges into position required exploring various actuator options. Linear motion was the most reasonable choice, however, most linear motors often require more space than their range of motion and cannot operate in a borehole environment. It proved to be impossible to design a system with a reasonable range of translation that could both accommodate the length of the sensor body itself and the length of the linear motor while still fitting into an instrument package with a 3.25-inch cross section. Furthermore, a sealed linear penetration would create a pressure differential between the pressure case and the wellbore thereby creating a system that would be susceptible to pressure changes in the wellbore.

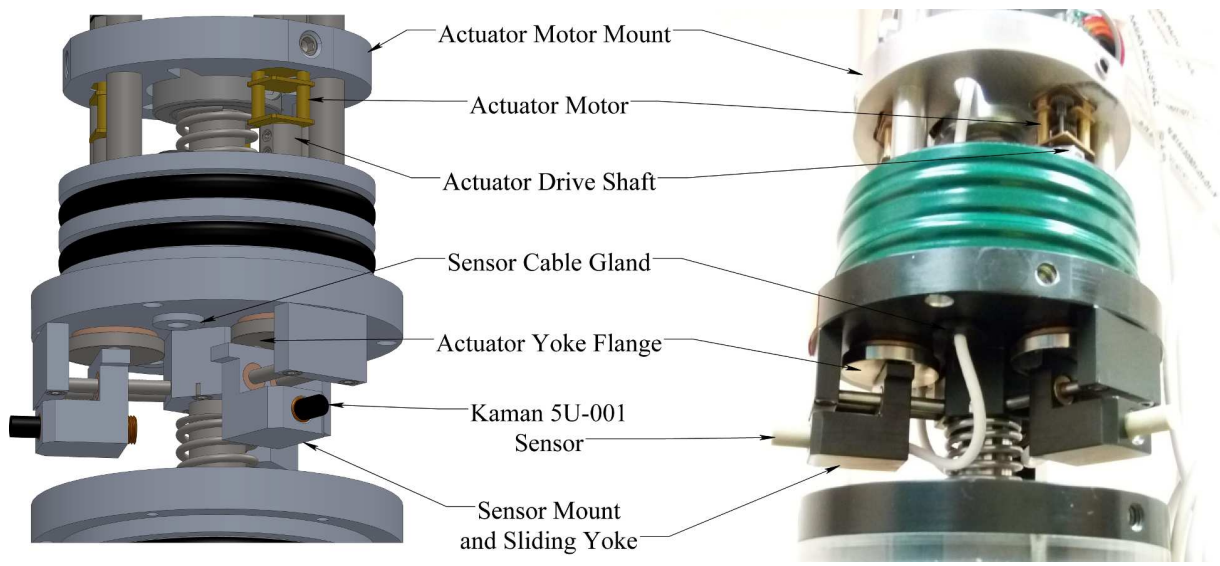

Figure 2.25: CAD realization and photograph of the removable eddy current horizontal strain sensors and actuators.

Rotary-to-linear motion seemed like the most logical path forward, and the Scotch yoke mechanism was chosen for its simplicity and minimal number of moving parts. Figures 2.23 and 2.25 both illustrate some of the key elements of this particular implementation. The main concept behind the Scotch yoke is a slot that is driven forward and backward by an off-center pin on a rotating platform. In this case the actuator drive shaft is turned by a small gear motor. The drive shaft exits the bottom cap of the electronics package through a pair of o-ring seals and terminates in a 7/8-inch (22 mm) diameter flange. A 1/8-inch (∼3 mm) diameter dowel pin is pressed into this flange at a 5/16-inch (8 mm) radius that drives a slot in the bottom of the sliding yoke that is also the sensor mount. Thrust washers and sleeve bearings are used between all contact surfaces to ensure proper alignment and smooth motion. The resulting actuator can safely retract the eddy current sensor behind the edge of the pressure case cap during deployment and extend to accommodate boreholes of up to 4.56 inches (11.6 cm) in diameter.

There were several outstanding issues dealing with the Scotch yoke horizontal actuation mechanism. One was safely passing the sensor cable from the borehole environment into the electronics package. Part of the issue was sealing to the PTFE insulation on the sensor coaxial cable. This was accomplished by first etching the cable insulation with a sodium-based solution (Acton Technologies FluoroEtch®), and then potting it in a high-strength, low permeability, low-viscosity epoxy (Henkel Loctite Stycast 1264). However, it was undesirable to pot this cable directly into the pressure case cap itself since that would have made this penetration very difficult to service in the event of a sensor failure. Therefore, the individual cables were potted into three separate removable cable glands, which were also sealed with double-bore o-rings. A small

flange lip prevents the glands from sliding through the bottom cap, and a small external snap ring is used to secure them in place within the electronics package.

The final obstacle deals with the repeated sinusoidal action of the Scotch yoke mechanism. For example, it is trivial to rotate the yoke such that the horizontal sensors appear fully retracted before deployment as well as to deploy them to some distance (e.g., 0.25 mm) from the borehole casing since the sensor itself can be used for feedback. However, it is not obvious how far to retract the sensors before extraction from the borehole since the actuator can rotate indefinitely (i.e., there is no firm stopping point). This was solved by attaching shaft encoders to the backside of each horizontal actuator motor. These particular motors have a 1000:1 gear reduction (Pololu Item #3057) that can accept a 12-counts-per-revolution hall effect sensors (Pololu Item #3081) that can be read via the digital inputs on the LabJack T7-Pro OEM data acquisition board, which implies over 5,000 digital counts when deployed in a 4-inch diameter borehole casing. This was deemed to be more than adequate to safely retract the horizontal sensors before removal.

The resulting vertical and horizontal actuators are complex, but accomplish their respective tasks while integrating the highest possible resolution sensors. Each actuator has feedback for interactive monitoring. Both the floating pressure cases and Scotch yoke mechanisms are immune from wellbore pressure changes, making it possible to operate in open and closed boreholes during injection. The mechanisms are robust enough to operate reliably over multiple deployments and everything is serviceable.

2.2.3.2 Supporting Electronics

The added mechanical complexity of the removable instrument compared to the permanent versions also translated to a commensurate increase in complexity of the supporting electronics. Figure 2.26 shows the electronics mount for the removable instrument and its main components. While the result was a more compact integration, the number of total connections and interconnections was over an order of magnitude higher. A total of 61 analog and digital inputs and outputs were required to connect all of the sensing and feedback systems to the main board, which were then routed to other subsystems such as motor controllers, bridge circuits, and the ADC.

Like the Version 1 grout-in instrument, the removable uses both Kaman and Micro-Epsilon sensors. Both the Kaman SMT-9700 3-channel single-ended and DIT-5200L dual differential signal conditioning boards were able to be extracted from their enclosures. This allowed for them to be placed in a partially overlapping configuration to save space. Unfortunately, the boards for the Micro-Epsilon eddyNCDT systems like the eddyNCDT 3701 used for the vertical are soldered into their enclosures and cannot be easily extracted. Unlike the permanent instrument, however, there was no room on the back side of the mounting tray to coil up any surplus coaxial cabling due to the number of wires running to the input/output header. Therefore, each eddy current sensor cable had to be shortened, which also meant that each sensor had to be re-calibrated to accommodate the different impedance of their new cable length.

The main board, as its name suggests, is the primary routing hub for the entire electrical system. This begins with taking the +12V input from the up-hole solar system and converting it to a regulated ±15V (Traco Power TDN 5-2423WI) and +5V (Traco Power TDN 5-2411WI) power supply for the eddy current signal conditioners and ADC. A critical difference between this instrument and its grout-in predecessors is that the half-bridge circuits (used to monitor the tiltmeter and vertical actuators), motor controllers, and Dinsmore R1655 electronic compass are powered by the Digital-to-Analog Converter (DAC) of the LabJack T7-Pro OEM board. Additional circuits like the clamping motor current monitor and horizontal actuator shaft encoders are also powered on demand by the DAC to limit power consumption since these systems are inactive during strain and tilt monitoring.

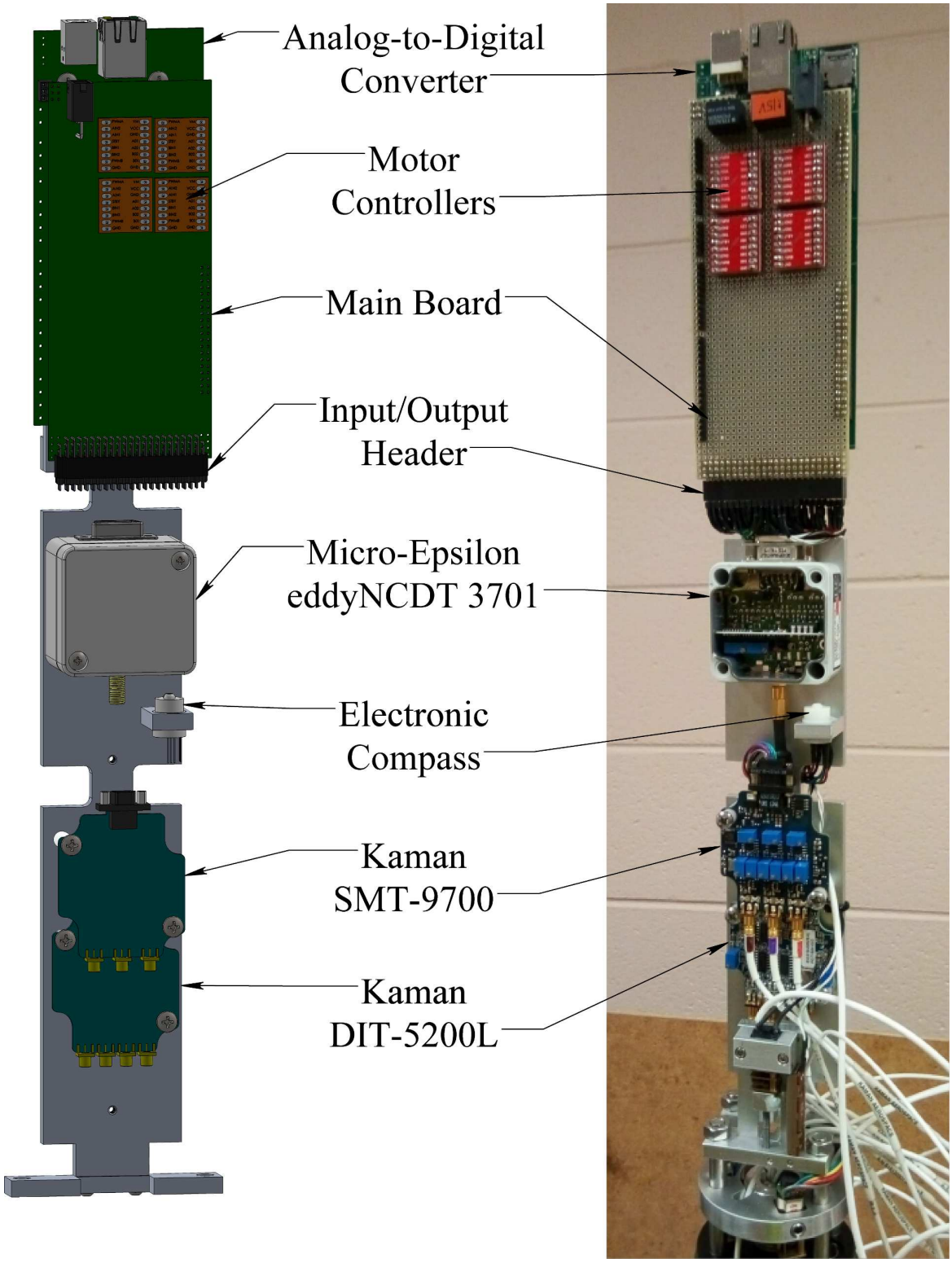

Figure 2.26: Electronics mount for the removable instrument showing its main components. Note that the photograph was taken before shortening the eddy current sensor coaxial cables.

2.2.3.3 Field Observations

There have yet to be field trials of the removable instrument due to the substantial time investment required to assemble and mechanically and electrically debug this system. Field tests also require the grouting of an aluminum casing to the formation, which has yet to be successfully executed. While this is likely to be more difficult in deeper formations, field tests are planned in shallow boreholes at our local field site where shallow pumping tests have been underway for several years.

2.3 Optical Fiber Areal Strainmeter

Optical fiber strainmeters provide an inexpensive and passive way to monitor subsurface strains at a resolution far beyond electromagnetic systems like the Gladwin or the eddy current systems described above. The two single-component areal (or circumferential) strainmeters deployed during this project were based on previous work by DeWolf (2014), and yielded the highest fidelity subsurface strain measurements ever recorded. The following theoretical development is based on DeWolf et al. (2015), and is followed by a detailed description of the down-hole package and interrogator designs.

2.3.1 Optical Fiber Interferometry

The measurement principle used in the optical fiber strainmeters is the optical fiber Michelson interferometer. Figure 2.27 shows the most basic implementation wherein a light source of an arbitrary initial polarization state is injected into one of the four arms of a 2×2 fused optical fiber coupler where the light is split into two paths. After propagating down their respective paths, the two light rays reflect off mirrors (retroreflectors) and return back through their same paths and recombine at the 2×2 coupler to form interference fringes.

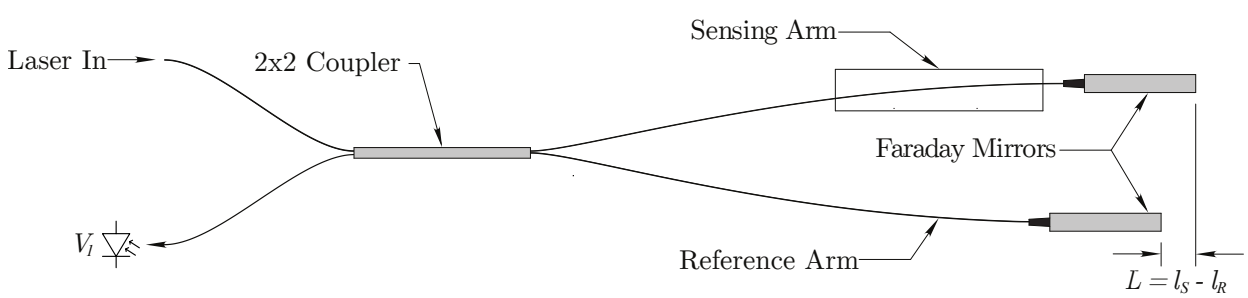

Figure 2.27: Schematic of a basic optical fiber Michelson interferometer using a single 2×2 coupler and photodetector.

The total optical phase of coherent, monochromatic light propagating in an optical fiber can be expressed as

$$\theta = \frac{2\pi n l}{\lambda} \tag{2.2}$$

where the index of refraction $n = c/v$ is the ratio of the speed of light in air c and the speed in the material v, l is the path length, and λ is the wavelength. The optical phase shift ϕ is related to the difference between the optical phase of the light propagating in the sensing arm θ_S and reference arm θ_R, respectively, as

$$\begin{aligned}\phi &= \theta_S - \theta_R \\ &= \frac{2\pi n}{\lambda}\left(l_S - l_R\right) \\ &= \frac{2\pi n L}{\lambda},\end{aligned} \tag{2.3}$$

where $L = l_S - l_R$ is the physical length difference between the two interferometer arms.

The intensity at the output of the 2×2 coupler as seen by the output (voltage) V_1 of the photodetector can be expressed as

$$V_1 = u_1 + v_1 \cos\left(2\phi\right) \tag{2.4}$$

where u_1 is the DC offset, v_1 the fringe amplitude, and the factor of 2 is a result of the reflection (i.e., the light travels through its path twice). Therefore, changes in the optical path length difference nL between the sensing and reference arms of the interferometer manifest themselves as changes in the output voltage of the photodetector. However, there are two main limitations to this technique addressed below.

One well known difficulty with optical fiber interferometers is decreased fringe contrast caused by differential polarization changes. This occurs after the light is split in two since each pathway is then subjected to different environmental conditions (strain, temperature, pressure, etc.), and these can alter the birefringence and therefore the state of polarization in one arm relative to the other. The amplitude of the (returned) interfering light, the fringe contrast, depends upon this relative polarization state of the two returning beams; in the extreme, with orthogonal polarizations, the returning beams do not interfere with each other.

A simple remedy to employ a pair of optical components known as a phase-conjugating, or Faraday mirrors, first used in fiber interferometers by Kersey et al. (1991). These consist of a Faraday rotator (typically a rare-earth magnet surrounding a high Verdet constant optical material) and a plane mirror. This creates a non-reciprocal reflection that rotates the polarization state of the incoming light by 90°, forcing what had been the component of the electric field propagating along the fast axis (low n) to propagate back to the coupler along the slow axis (high n) and vice-versa. The result is return-beams restored to their original polarization (rotated by 90°) and nearly perfect fringe contrast as long as the polarization perturbations do not occur faster than the propagation time. Faraday mirrors are compact and inexpensive, and can be used in place of the retroreflectors in Figure 2.27.

The second obstacle relates to the bidirectional phase ambiguity shown in equation (2.4). Consider the case where the output intensity is a maximum, i.e., where the optical phase is $\phi = \pi/2$, or optical path length difference $nL = \lambda/2$. An increase or decrease in L results in a decrease in intensity seen by the photodetector, thereby making it impossible to discriminate between expansive and contractive path length changes.

One method involves exploiting the evanescent waveguide properties of the coupler used to split and recombine the two interferometer arms. Fused optical fiber couplers are fabricated by grinding down or melting the cladding between a pair of adjacent fibers such that light "leaks" from one waveguide to the other when fused together. In addition to the amplitude being split, there is also a phase shift induced in proportion to the distance between the waveguides and the wavelength of light. For an ideal 3 dB 2×2 coupler (50/50 splitting ratio), the light in the second fiber is phase-shifted by 180°; unfortunately this provides no new information since it is just -1 times the original. However, in an evenly split 3×3 fused coupler the other two fibers undergo a 120° phase shift. Therefore, for a (polarization-insensitive) optical fiber Michelson interferometer using a 3×3 coupler (Figure 2.28), there are three fringe signals 120° phase-shifted from each other. It is then possible to take advantage of this for the recombined light returning from

the sensing arms for resolving directional fringe information. Sheem (1980) was among the first to publish results of a fiber optic gyroscope using 3×3 couplers, and there have been many dozens of other published works using this technique in Michelson and Mach-Zehnder optical fiber interferometers.

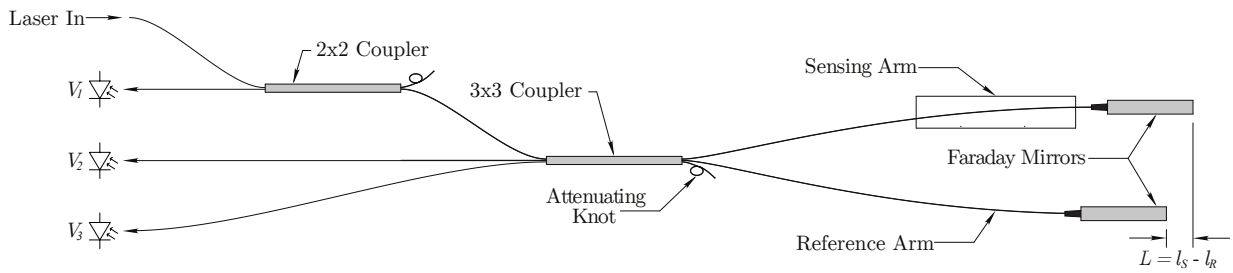

Figure 2.28: Schematic of the optical fiber Michelson interferometer using a 3×3 coupler with a 2×2 coupler tap and triple photodetector detection scheme.

The optical fiber interferometers used during this project employ a real-time digital signal processing system was developed to extract the optical phase difference ϕ from all three phase-shifted interference fringe signals output by the 3×3 coupler. This method was adapted from Todd et al. (2002), wherein equation (2.4) is extended to accommodate all three outputs as

$$V_1 = u_1 + v_1 \cos(2\phi + \theta_1) \tag{2.5}$$
$$V_2 = u_2 + v_2 \cos(2\phi + \theta_2) \tag{2.6}$$
$$V_3 = u_3 + v_3 \cos(2\phi + \theta_3) \tag{2.7}$$

where θ_i $(i = 1, 2, 3)$ represents the optical phase shift of each output relative to the input. These three relationships can be inverted to compute the phase using the relationship

$$\phi = \frac{1}{2} \arctan\left(\frac{s_1 V_1 + s_2 V_2 + s_3 V_3}{c_1 V_1 + c_2 V_2 + c_3 V_3}\right) \tag{2.8}$$

where c_i and s_i are coefficients related to u_i, v_i, and θ_i, which in practice are determined by a nonlinear least-squares fit to a known modulation input (Schliep and Hereth, 1992). This phase estimate is linearly proportional to the strain in the fiber, and is therefore the desired output.

It is important to note that only two fringe signals, e.g., equations (2.5) and (2.6), are required to unambiguously estimate the optical phase difference (Sheem, 1980). However, the three-fringe demodulation scheme has the very important advantage that the phase estimate is independent of the laser power. Semiconductor lasers require a stable supply current to maintain a fixed wavelength (and optical path difference or apparent strain signal: see equation (2.3)), but their output efficiency is a very strong function of temperature. It is common practice to regulate the temperature of the laser using a thermo-electric device such as a Peltier cooler in a control loop with a thermistor to sustain a constant laser output power. However, this temperature control increases the total power consumption by as much as factor of four, which translates to additional solar panels and batteries in remote deployments. Furthermore, two-fringe demodulation methods such as the one developed by Zumberge et al. (2004) require a fairly elaborate and computationally intensive real-time parameter estimation scheme to track the parameters u_i and v_i to prevent phase distortion caused by small laser output changes that occur even with active temperature stabilization. The obvious disadvantage of the three-fringe approach are the additional optical components (2×2 coupler) and electronics (photodiode and digitizer channel). However, these additional components allow for a more simple, passive, and lower-power demodulation system.

2.3.2 Down-Hole Package Design

The fundamental design principle behind the Optical Fiber Areal Strainmeter (OFAS) down-hole package is a cylinder, or mandrel, wrapped with optical fiber that is coupled to the formation. This coupling (e.g., expanding grout) transmits strain from the formation to the mandrel which in turn changes the length of the fiber wrapping that is continuously measured using laser interferometry. Many versions of this operating principle have been used in optical fiber hydrophones and (Bucaro et al., 1977; Rashleigh, 1985) aero-acoustic sensors (Bucaro et al., 1979; Zumberge et al., 2003) for decades, however, to the best of our knowledge was first attempted in a borehole by DeWolf (2014).

Figure 2.29 shows the basic construction of the OFAS developed during this project. The main outer package is a 47.25-inch (120 cm) long piece of 4-inch (nominal), Schedule 5, 304 stainless steel pipe measuring 4.5 inches (11.4 cm) in diameter with a 0.083-inch (0.2 cm) wall thickness, which implies an inner diameter of 4.334 inches (11.0 cm). This is capped at both ends with 0.5-inch (1.3 cm) thick discs with central 1/2"-13 threaded through holes on each end to accommodate adjustable centralizers, and three 1/4"-20 threaded holes in the top cap for lifting eyes. The upper centralizer rod is hollow to allow light to enter and leave the main optical fiber cable (Fiber Instrument Sales FBSMTACCABLE4).

Details of the internal construction are shown in Figures 2.29 and 2.30, which in cross section are a series of three nested cylinders. The outermost cylinder is the aforementioned 4-inch nominal pipe made from stainless steel since it must be durable to survive deployment and non-reactive to the borehole environment and expanding grout. The middle cylinder is a thin aluminum sleeve measuring 4.214 inches (10.7 cm) ID, 4.026 inches (10.2 cm) OD, 0.094-inch (0.2 cm) wall, by 44.375 inches (112.7 cm) long, which started out as 4-inch nominal, Schedule 40 pipe whose OD was turned down. A shallow (0.01 inches, or 0.3 mm deep) helical groove was cut into the outer diameter of this cylinder at 20 threads-per-inch ($\sim$1.3 mm spacing) to guide and protect the optical fiber. The innermost cylinder is a 3-inch nominal, Schedule 80, 304 stainless steel pipe measuring 3.5 inches (8.9 cm) OD, 2.9 inches (7.4 cm) OD, 0.3 inch (0.76 cm) wall, with a length matching the sensing mandrel.

These two inner cylinders are the sensing and reference mandrels are each wrapped with $\sim$265 meters of optical fiber (Corning ClearCurve® ZBL), and form the sensing and reference arms of the interferometer. A narrow 0.125-inch (3.2 mm) wide slot was cut into each cylinder 3.87 inches (9.8 cm) from the bottom and 0.93 inches (2.4 cm) from the top to allow the ends of the wrapped fibers to penetrate from the tube outer diameters into the central volume (shown in Figures 2.29 and 2.30a). The distance between these fiber penetrations is 1 meter, which was the intended sensing interval for the instrument.

The instruments required careful assembly given the fragility of the optical fibers and the weight of the mandrels. The sensing mandrel was set over the reference mandrel, the penetration slots aligned, and ends centralized and epoxied closed approximately 0.5 cm from each end. After curing, the fiber ends were fed into the central volume and the slots sealed to form an air tight volume between the inner diameter of the sensing mandrel and outer diameter of the reference mandrel. Faraday mirrors (OZ Optics FOFM-21P-1550-9/125-S-60-X-0.25-0.5) were spliced on to the bottom ends and 2×2 and 3×3 couplers (Gould Fiber Optics PSK-002121 and PSK-002122) were spliced on the top ends of the emerging fibers in a manner identical to Figure 2.28. The ends of these couplers were spliced to the main input/output fiber cable, and all loose fiber and components secured to the inner diameter of the reference mandrel using a fast bonding cyanoacrylate adhesive.

A key feature of the OFAS construction is its completely potted interior (Figure 2.30b) and welded exterior. This was accomplished by inserting the paired mandrels into the outermost cylinder along with a 2-inch-by-2-inch (5.1 cm) square bar of 1018 steel for counter-ballast and volume filling. The remaining interior was filled with a low exothermic, low viscosity epoxy (Henkel Loctite Stycast 1264) up to the point where all the interior components were submerged. After curing, the top cap was welded on and the remaining volume was filled with epoxy, including the annulus between the fiber cable and centralizer rod.

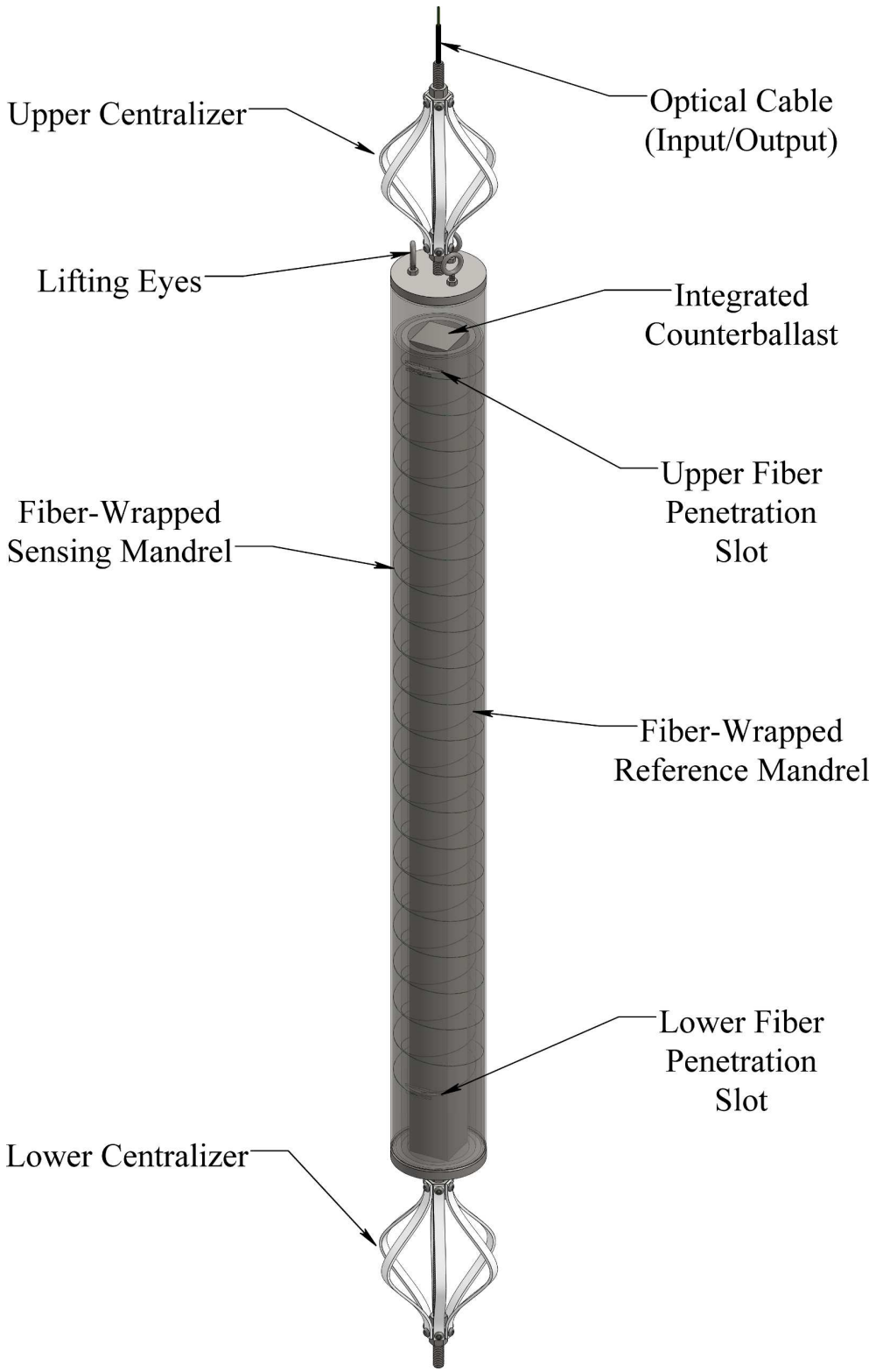

Figure 2.29: Diagram highlighting the major components of the final Optical Fiber Areal Strainmeter design deployed at the North Avant Field in Oklahoma.

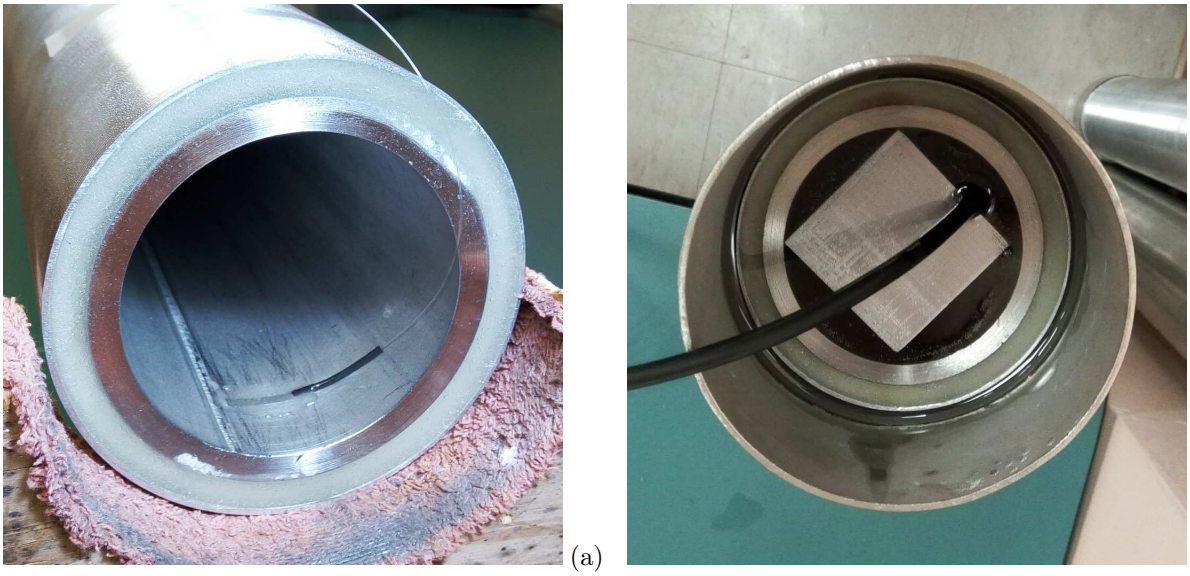

(a) (b)

Figure 2.30: Photographs of the areal strainmeter mandrels. (a) The thin aluminum, fiber-wrapped outer sensing mandrel over the exterior with the thick stainless steel, fiber-wrapped reference mandrel. (b) Top view of the fully potted internal construction showing the previous mandrels embedded in the outer-most stainless steel cylinder and 2-inch-by-2-inch square steel counter-ballast.

The completed instrument is a completely passive, extremely robust down-hole areal strainmeter with very high ($\sim 10^{-15}$ nε) resolution. The final density was approximately 4.5 g/cm^3, which is over twice the density of the grout and was therefore highly likely to sink and stay submerged during curing. However, any sensing head is not very useful without the required opto-electronics to "read-out" or interrogate the optical path length of the embedded fiber.

2.3.3 Interrogator Design

The optical fiber sensor interrogator is the active counterpart to the passive down-hole sensing component. Its purpose is to transmit coherent, monochromatic laser light to the down-hole optics and demodulate the returning interference fringes into an optical phase signal linearly proportional to the formation strain. Each of the components needed to do this are described in the following paragraphs.

Our most recent Version 3 interrogator is shown in Figure 2.31, and consists of a power distribution system, laser driver, laser diode, photodetection system, and ADC. The power distribution board was developed in-house, and is capable of accepting an unregulated voltage from 9–36V and converts it to a regulated +5V (Traco Power TDN 5-2411WI) for the ADC and photodetection system, and +12V (Traco Power TDN 5-2412WI) for the laser driver. The laser system is a combination of four components: a distributed feedback laser diode (e.g., Optilab DFB-4G-DM-1550), 14-pin butterfly laser mount (ModularOne MOT_BTSCK_HS-T), laser current source/driver (Thorlabs LD1100), and custom laser-driver-to-laser-mount adapter board. Electrical engineers at Clemson University also developed a photodetection system capable of reading up to three separate interferometers. Each channel consists of three InGaAs photodiodes (Bitline Systems PD-A-25-9-1-N), operational amplifiers (ON Semiconductor LM258NG), and potentiometers (Bourns 3296W-1-203LF) for adjusting the gain. These are all mounted on a daughterboard whose header plugs directly into the ADC (LabJack T7 OEM, the 16-bit version of the T7-Pro used in the eddy current systems).

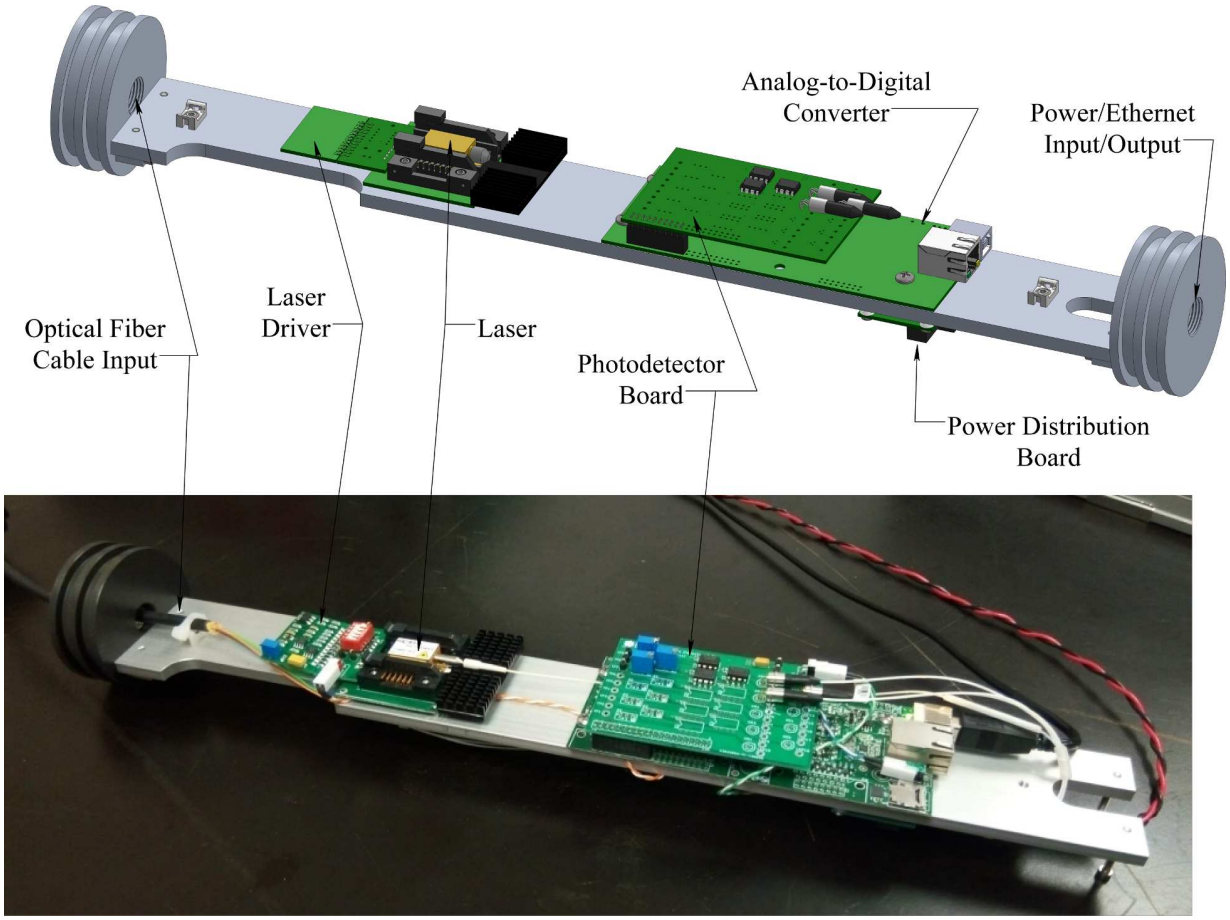

Figure 2.31: CAD realization and photograph of the Version 3 optical fiber Michelson interrogator with the outer pressure case sleeve removed.

There were several motivations for packaging the interrogators into a cylindrical pressure case with cable exits on each end. The main purpose for the pressure case packaging is so that the interrogator can also be deployed in the borehole, albeit much closer to the surface (normally ∼5 m). At this depth the temperature is sufficiently stable to run the laser without active thermal regulation, which translates to a massive (3–4×) power savings, and is also why the laser is thermally connected to the aluminum pressure case. While it is less than ideal to terminate optical and electrical connections in the field, the interrogator must be serviceable. The pressure case outer cylinder is held over the component tray and end caps using a pair of internal snap rings. This allows for the pressure case cover to be removed with the cables attached by simply sliding it over one end or the other. Furthermore, the interrogator itself can be readily replaced without changing any up-hole or down-hole hardware.

We have successfully deployed two Version 3 interrogators with each of the two OFASs in this project. Earlier versions were replaced due to reliability issues related to their hand-made quality. Data are transmitted via Ethernet from the ADC, logged at each station computer, and telemetered to Clemson University. Details of the deployments will be covered in Section 4.2.3.

2.3.4 Field Observations

Time and frequency domain observations of the OFAS performance have also been performed similar to those made for the eddy current strain and tilt systems presented in Section 2.2.2.3. Both the Version 3 and 4 systems were successfully deployed and calibrated in-situ (see Section 2.4) and therefore are presented in units of strain rather than their native units of radians of optical phase change (i.e., equation (2.8)). However, comparisons to other instruments are suppressed until Section 2.5.

While there is no grout cure time series for the North Avant Field areal strainmeter (see Section 4.2.3.2), the Simpson Station installation record is shown in Figure 2.32. This plot has a very clear initial compressional trend while lowering the instrument into the grout, followed by the temperature increase from the grout's exothermic reaction, and concludes by going into permanent compression just before day 130, indicative of a successful installation. The remaining time series data for both OFASs is not as informative as the eddy current systems since it contains multiple data gaps where the is similar to the post-cure time series in that it is dominated by an increasing compression signal.

Frequency domain plots are shown in Figure 2.33 for both installations. The Simpson Station spectra do not have the same resolution as the North Avant Field instrument due to a large data gap and shorter overall deployment period (see Section 4.2.3.1), however, they both have a similar and very characteristic response. Both spectra indicate a clear tidal response that is much better resolved in the North Avant Field installation both in terms of frequency and SNR. Unlike the eddy current systems, there is an obvious response to teleseismic surface waves with periods ranging from 10 to 50 seconds (2×10^{-2} to 1×10^{-1} Hz).

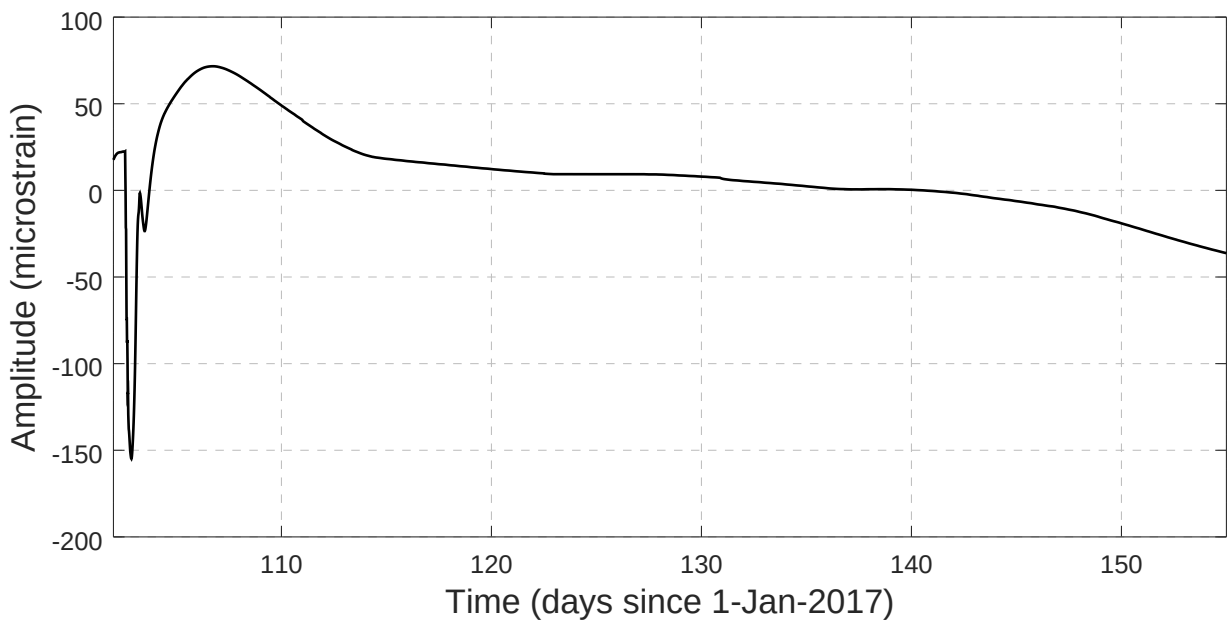

Figure 2.32: 52-day time series of the installation of the first OFAS at the Simpson Station, SC. The initial ∼175 με compression is from the instrument descending in the water column and eventually into the grout, followed by a sharp rise from the grout's exothermic reaction. While the strainmeter appears to be in permanent compression after only about a week, the best evidence of a successful grouting is that it remains in compression after the ∼4–5 week cure time.

2.4 Data Processing

Borehole strainmeters and tiltmeters are designed to respond to changes in the deformation of the rock formation to which they are coupled. However, not all of the observed deformations are related to the signals of interest, i.e., the strains related to injection tests performed during this project. Furthermore, the relationship between the instrument response (in its native units), or "gauge" strains or tilts, and the desired formation strains and tilts is best done in-situ. So while it is possible to directly observe the injection signals in the raw strain and tilt records, it is necessary to "process" these data before interpreting them using the modeling frameworks developed in Chapter Three and implemented in Chapters Four and Five. This procedure includes eliminating extraneous geophysical signals like changes in surface loading from barometric pressure fluctuations (e.g., atmospheric tides and meteorological events), re-scaling or calibrating the data to match the predicted solid Earth tides, removing the solid Earth tides, and discarding any long-period background signals (detrending).

Each of these tasks are described in the following sections and are modeled from the processing procedures established by Hodgkinson (2006) at UNAVCO and Langbein (2010) at the United States Geological Survey.

2.4.1 Barometric Pressure Fitting and Removal

Some of the clearest signals observed in the raw strain records are the result of barometric pressure changes from the passing of convective storms. However, the primary influence on subsurface deformation measurements is the diurnal and semi-diurnal loading and unloading of the ground surface from atmospheric tides. This effect can confound the observed solid Earth tides that are used to calibrate the instrument (Section 2.4.2), but can also be used to independently estimate important geophysical properties such as the Young's modulus of the formation.

Several methods can be used to estimate and remove the influence of the barometric pressure on the strain and tilt records. One powerful, non-parametric technique is to examine the cross spectrum between the barometer and deformation signals using an empirical transfer function estimate (ETFE). Figure 2.34 is an example of an adaptive multi taper ETFE based on the method of Riedel and Sidorenko (1995) between the vertical strain record at AVN3 from the Version 2 eddy current system and the barometric pressure

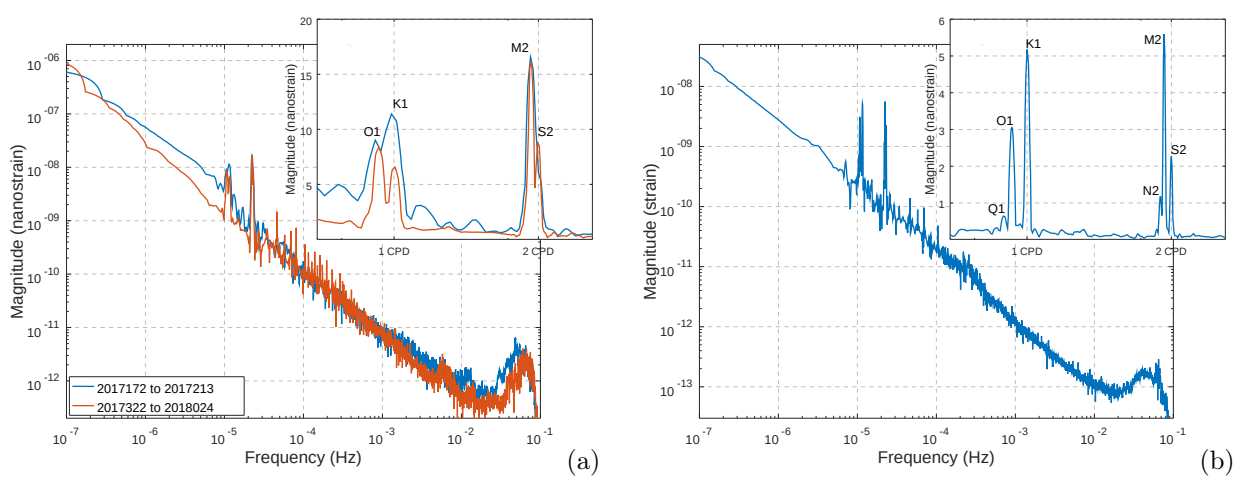

Figure 2.33: Magnitude spectrum estimates from the (a) Simpson Station, SC, and (b) North Avant Field OFAS installations. Inset plots are also included highlighting the 1 and 2 CPD tidal bands.

recorded a short distance away at AVN4 using a commercial Vaisala WXT520 combination weather station. This type of ETFE yields estimates of the magnitude-squared coherence as well as the magnitude and phase of the relationship between the two records as a function of frequency. These relationships can be quite complex, but the example shown in Figure 2.34 shows a strong coherence (or spectral correlation) approaching 0.9 at 2 CPD (2.3×10^{-5} Hz) with a transfer function magnitude of about 3×10^{-10} m/Pa at a phase of approximately $-35°$ (or $145°$ after accounting for the fact that the sign of the barometric pressure was reversed before computing the ETFE). While there is non-negligible coherence at 0.5 and 1 CPD (5.8×10^{-6} and 1.2×10^{-5} Hz) and above 2 CPD, the magnitude is $\sim 10\times$ less and almost perfectly out of phase.

ETFEs like the one shown in Figure 2.34 can be very useful for exploratory data analysis purposes, and can also be used to perform a full coherence-weighted, frequency-dependent correction to remove the barometric pressure signal from strain or tilt data (Crawford and Webb, 2000). However, in practice it can be difficult to obtain an ETFE that is both detailed enough to discriminate between effects at neighboring frequencies and also smooth enough to not introduce additional noise into the resulting signal (i.e., over-correction). Therefore the barometric pressure corrections performed on the data in this project were performed using a simple linear least-squares fit, which is more than adequate for most cases.

An example of removing the barometric loading from the vertical strain signal using linear least-squares is shown in Figure 2.35. There is a clear anti-correlation between the strain and pressure time series in Figure 2.35a for the large, several-day-long excursions. These appear to have been successfully removed in Figure 2.35b, where the residual time series shown in red contains mostly the solid Earth tides and a 3-day-long injection test starting on November 28th, 2017 (day 332).

2.4.2 In-Situ Calibration

The in-situ calibration of borehole strainmeters is a very well known issue. While it seems trivial to measure a displacement over a given base length (e.g., diameter of a borehole), relating this to the formation strain turns out to be very challenging due to any number of issues such as the mismatch between the material properties of instrument and the formation (Gladwin and Hart, 1985), small scale heterogeneities near the instrument (Hart et al., 1996) and residual stresses caused by drilling (Brudy and Zoback, 1999). Developers like Micheal T. Gladwin, the inventor of the Gladwin Tensor Strainmeter (Gladwin, 1984), have invested considerable effort in designing instruments that attempt to match the formation properties such that the measured gauge strains are a direct reflection of the formation strains (Gladwin and Hart, 1985). Unfortunately this ends up being ineffective in many cases (Roeloffs, 2010), and several accepted methods have been developed to calibrate strainmeter in-situ by comparing the instrument response to the predicted solid Earth tides (Roeloffs, 2010; Hodgkinson et al., 2013; Qiu et al., 2013). This is the method used to calibrate both the strain and tilt instruments used in this project.

The basic procedure is to estimate the magnitudes and phases of the two largest tidal constituents from the data and compare them to the values predicted by theory. This obviously requires that the tides are present in the data, which was an issue for some of the individual eddy current gauges in both the Version 1 and 2 instruments (see Section 2.2.2.3). We used the software program `ertid` to compute the theoretical strain and tilt tides, which is a component of the SPOTL (Agnew, 2012) and NLOADF (Agnew, 1997) software packages. This program, written in Fortran 77, uses astronomy, gravitational theory and the bulk elastic properties of the Earth to estimate the deformation at a given geographic location on the Earth's surface and is widely used by researchers in the geodetic community for tide prediction and removal.

A linear least-squares method similar to Pawlowicz et al. (2002) is used to extract the magnitudes and phases of the O1 and M2 tidal constituents from both the observations and predicted waveforms. While it is trivial to derive calibration factors for single-component instruments like the vertical and areal strain gauges (i.e., the average ratio between the predicted and observed amplitudes at O1 and M2), a joint-

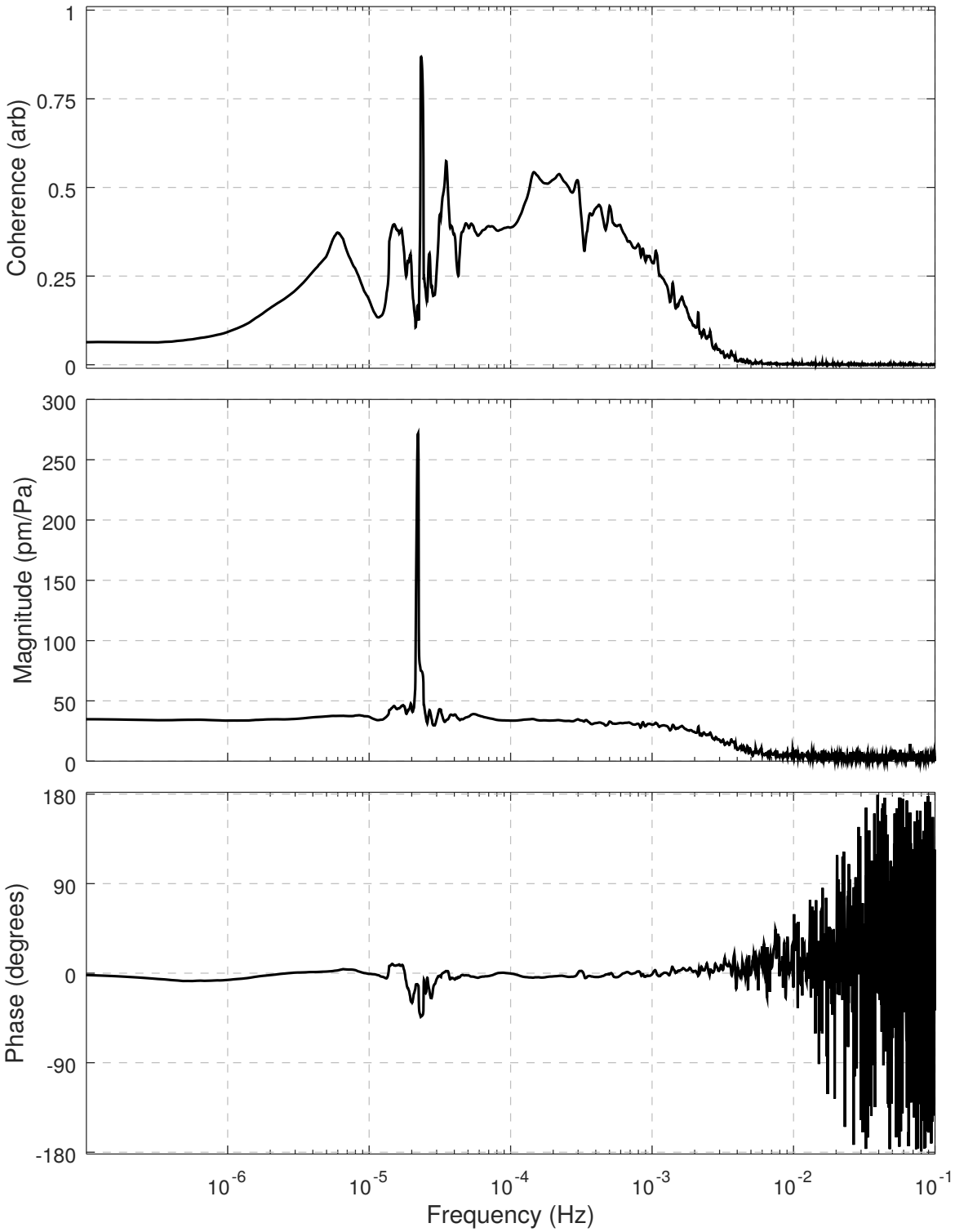

Figure 2.34: Adaptive multi taper empirical transfer function estimate of the vertical strain and barometric pressure recorded at the North Avant Field in Oklahoma showing the magnitude-squared coherence (top) and transfer function magnitude (center) and phase (bottom) as a function of frequency. Note that the sign of the barometric pressure signal was reversed prior to estimating.

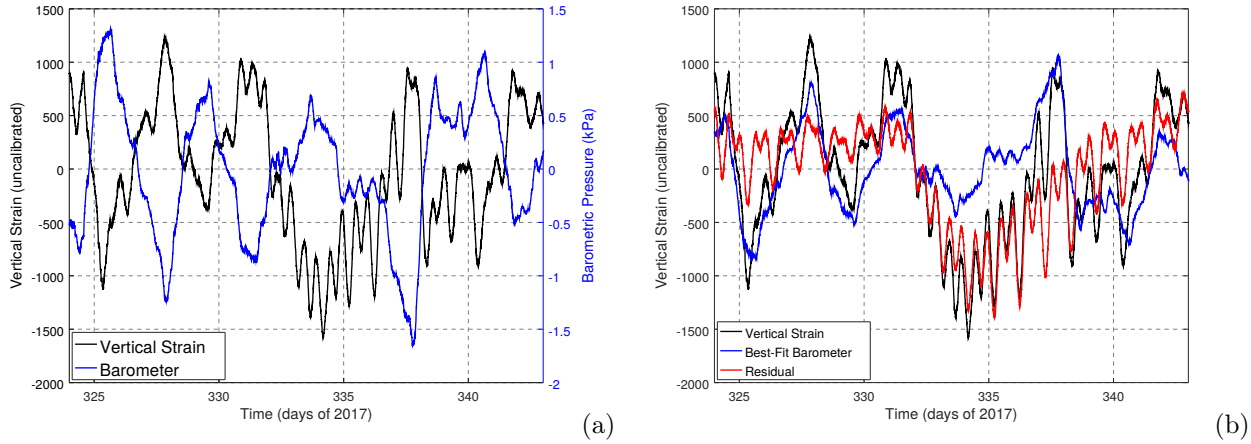

Figure 2.35: (a) Plot of the vertical strain (black) and barometric pressure (blue) over a 20 day period at the North Avant Field, OK. (b) Vertical strain record from (a) along with the best-fitting barometric pressure (blue) and their residual (vertical strain minus the best-fitting barometer in red).

inversion approach was used to determine both the calibration factor *and* orientation of the multicomponent instruments. This approach reduces to a system of linear equations that can be solved for a range of azimuths using the strain transformation relationship (Timoshenko and Goodier, 1951)

$$e(\theta) = \frac{1}{2}(\varepsilon_{xx} + \varepsilon_{yy}) + \frac{1}{2}(\varepsilon_{xx} - \varepsilon_{yy})\cos\theta + \varepsilon_{xy}\sin\theta \tag{2.9}$$

where e is the gauge extension along a given direction θ, and ε_{xx}, ε_{yy}, and ε_{xy} are the normal and shear strains. A similar transformation can be used for the tilts using

$$\begin{aligned} \omega_{EW} &= \omega_x \cos\theta - \omega_y \sin\theta \\ \omega_{NS} &= \omega_x \sin\theta + \omega_y \cos\theta \end{aligned} \tag{2.10}$$

where ω_x and ω_y are the measured x and y tilts and ω_{EW} and ω_{NS} are the tilts rotated into east-west and north-south geographic coordinates, respectively. Therefore the observed O1 and M2 magnitudes and phases for the strains and tilts are compared to the theoretical values until an angle θ is found that minimizes the squared error.

Figure 2.36 shows the joint in-situ calibration results for the Version 2 eddy current strain and tilt system deployed at the North Avant Field, OK. While the 120° gauge was unable to record the tides (see the magnitude spectra in Figure 2.20b), the joint inversion procedure yields very good results for the x-tilt, 0° and vertical strains at an orientation of 182 ± 17 degrees clockwise from north. It turns out that there is no azimuth that fits the y-tilt particularly well, which also happens to be the case for the commercial tiltmeter in the nearby borehole AVN4. It is unclear why we were unable to fit the 240° horizontal strain gauge data, and this remains an active area of investigation.

This in-situ tidal calibration procedure was applied to all of the strain and tilt data excluding the Gladwin strainmeter since the calibrated data from this instrument is provided by UNAVCO.

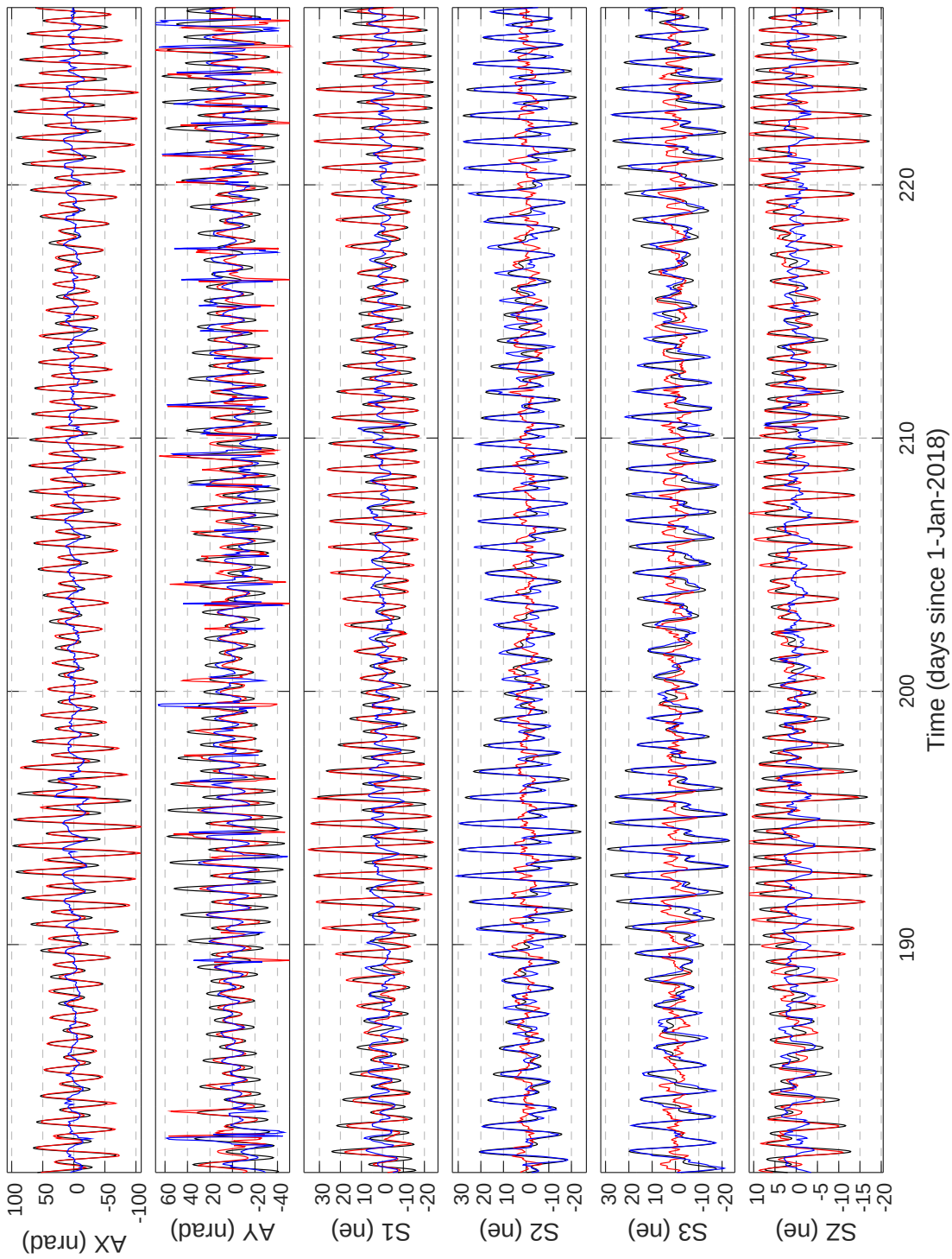

Figure 2.36: Joint in-situ calibration results for all six components of the Version 2 eddy current strain and tilt system deployed at the North Avant Field, OK. "AX" and "AY" denote the x and y tilts, "S1", "S2" and "S3" denote the 0°, 120° and 240° horizontal strains, respectively, and "SZ" denotes the vertical strain (this follows the SEED convention found in Ahern and Dost (2012)). The theoretical data are shown in black, the best-fit observations in red, and their residual in blue. Note that the observational data have been high-pass filtered.

2.4.3 Tide Fitting and Removal

Tide fitting is a routine practice for Earth and ocean tide removal. There are many commercial and open-source software packages, however, we have found through previous experiences that a simple linear least-squares approach like what is used in the `T_TIDE` package from Pawlowicz et al. (2002) is more than adequate. This assumes a time series model $x(t)$ of the form

$$x(t) = b_0 + b_1 t + \sum_{k=1}^{N} \left[A_k \cos(2\pi f_k t) + B_k \sin(2\pi f_k t) \right] \tag{2.11}$$

where b_0 and b_1 represent the offset and drift components, respectively, and A_k and B_k are the "in-phase" and "quadrature" terms for the kth tidal constituent at a frequency of f_k. The amplitudes M_k and phases P_k for each frequency are calculated using the well-known relationships

$$\begin{aligned} M_k &= \sqrt{A_k^2 + B_k^2} \\ P_k &= \tan^{-1}\left(\frac{B_k}{A_k}\right) \end{aligned} \tag{2.12}$$

A total of 24 tidal constituents, 12 diurnal and 12 semi-diurnal, were selected from the the largest amplitude deformation tidal constituents contained in the software program `tidhar`, which is also included in both the SPOTL (Agnew, 2012) and NLOADF (Agnew, 1997) packages.

An example of tide removal is shown in Figure 2.37 using the same time series as in Figure 2.35 but with the barometric pressure removed and in-situ tidal calibration factor applied. This shows a near complete removal of tidal energy throughout the record segment and reveals smaller non-tidal fluctuations as well as an even more clear injection signal. The tided and de-tided time series are often presented together in this manner to provide an immediate scale reference for the size of non-tidal anomalies.

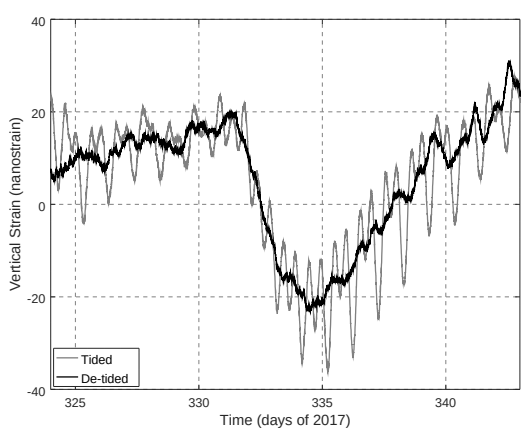

Figure 2.37: Calibrated vertical strain time series before and after tide removal. An artificial offset has been applied for plotting purposes.

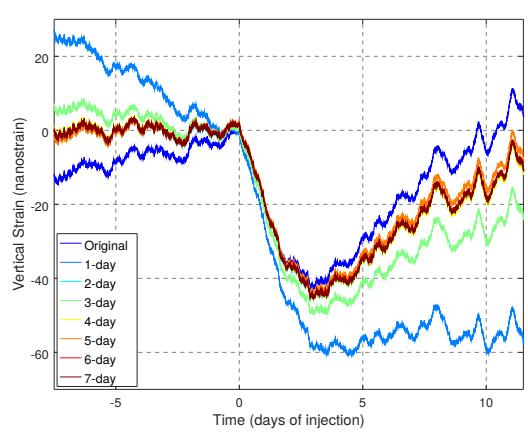

Figure 2.38: Vertical strain time series with varying lengths of initial trends removed. This approach appears to converge for periods beyond ∼4 days.

2.4.4 Trend Fitting and Removal

Removing any large-scale background trends is the final step in reducing the deformation time series to focus on the injection signal for modeling and interpretation. While the pre-processed Gladwin data provided by UNAVCO includes a best-fit borehole relaxation trend model based on the work of Roeloffs (2005), there are no well established guidelines or best practices for removing secular trends from deformation time series.

The approach taken for the data analyzed and interpreted in Chapters Four and Five of this report was to offset and remove a linear trend from the data. This procedure starts with setting each strain, tilt and pressure time series record to zero at the start of the injection, making it easy to visually identify the effect of the injection signal. A line is fit to the time series from $t = 0$ up to a week preceding the start of injection. While the choice of 7 days is somewhat arbitrary, Figure 2.38 shows that this is enough time to produce consistent and adequate trend removal for the majority of the time series used in this report.

2.5 Instrument Performance Assessment

The time series and magnitude spectra presented in Sections 2.2.2.3 and 2.3.4 are explorations of the raw data to show whether the installation was successful, check for basic functionality and determine which sensors capable of monitoring the anticipated deformations. Data from these successful installations can then be processed using the methods described above (Section 2.4) and used for modeling and interpretation (Chapters Four and Five). However, it is also critical to assess the performance of the instruments developed during this project relative to the commercial systems to evaluate their costs and benefits and potential for future developments.

2.5.1 Tiltmeter Performance

Each eddy current strain and tilt system included an orthogonal pair of physical pendulum tiltmeters, however, only the Version 2 system is colocated with a commercial tiltmeter. The eddy current system is located in borehole AVN3, approximately 25 meters from the Applied Geomechanics (now Jewell Instruments) LILY tiltmeter in borehole AVN4 at the North Avant Field in Oklahoma. The nominal resolution of the Version 2 eddy current tiltmeters is approximately 3×10^{-10} radians, whereas the LILY is reported to have about an order lower resolution at $< 5 \times 10^{-9}$ radians.

However, the actual in-situ performance is a function of frequency, which is perhaps best quantified by examinging their frequency spectra shown in Figure 2.39. Both tiltmeter records have been rotated into east-west (Figure 2.39a) and north-south (Figure 2.39b) coordinates using equation (2.10). The primary difference is that the Eddy Current System (ECS) is out-performed at short periods above about 10,000 seconds (10^{-4} Hz), which is most likely due to a combination of electronic and mechanical noise (e.g., aliased ringing from the pendulum's free period). The ECS system appears to be match or exceed the LILY in the tidal band from just above 1 CPD down to about a 1 week period. While the SNR in the 2 CPD tidal band appears to be higher for the ECS, the SNR is somewhat lower for the east-west (Figure 2.39a) at 1 CPD. This may be partially due to improper rotation, i.e., some of the over-estimated 1 CPD signal in the north-south record could actually be from the east-west record. The performance of the two tiltmeter systems appears to be similar at very low frequencies ($< 10^{-6}$ Hz).

The overall performance of the ECS tiltmeters appears to be more than adequate for the proposed several week long-period injection tests. While there is still some uncertainty in the orientation and calibration, the observed tidal amplitudes from both systems are consistent with one another and the predicted Earth tides.

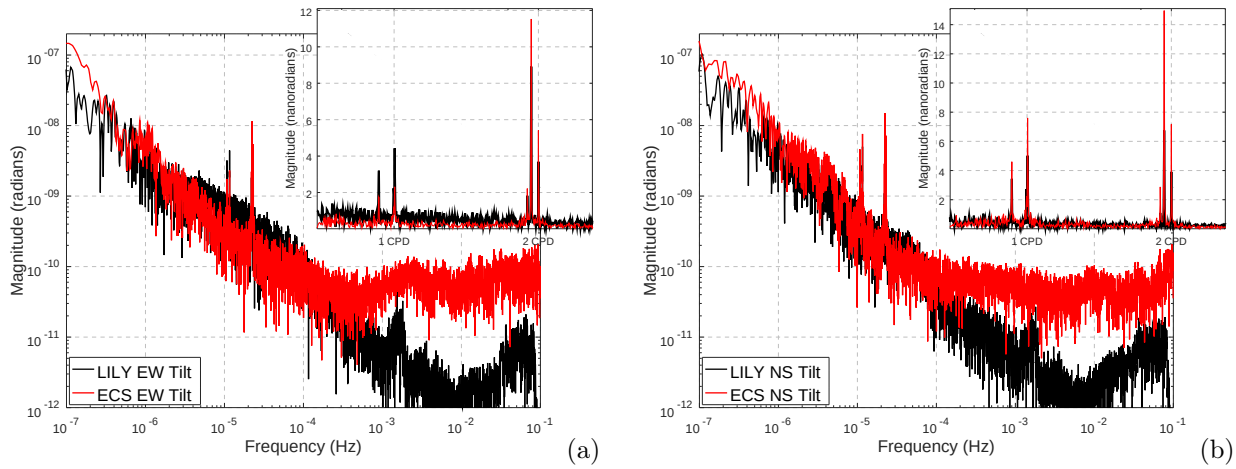

Figure 2.39: East-west (a) and north-south (b) tilt magnitude spectra comparing the LILY (black) to Eddy Current System (ECS, red) tiltmeters. Inset plot shows a closeup of the tidal band. Both instruments are located within ∼25 m at the North Avant Field in Oklahoma.

2.5.2 Horizontal Strainmeter Performance

A similar analysis to that in Section 2.5.1 was conducted on the ECS horizontal strain gauges. In this case, however, the two successfully calibrated ECS gauges (0° and 240°) are compared to the Gladwin Tensor Strainmeter (GTSM) using the east-west (ε_{xx}) north-south (ε_{yy}) and shear (ε_{xy}) rotated to the same orientation as the two ECS gauges using equation (2.9). Both the Version 2 ECS and GTSM are located about 12 m apart at the North Avant Field site in Oklahoma at a depth of ∼ 30 m.

Magnitude spectra comparing the 0° and 240° gauge strains are shown in Figures 2.40a and 2.40b, respectively. While the ECS gauges are clearly out-performed by the GTSM across the entire frequency band, they are capable of resolving the solid Earth tides with a SNR of at least 1 and up to ∼10 or 12. The 0° gauge (Figure 2.40a) over-predicts the amplitude of the O1 tide (just below 1 CPD) but under-predicts M2 (just below 2 CPD). This is in contrast to the 240° gauge (Figure 2.40b) that seems to match the M2 amplitude, but O1 is completely absent. There is a strong 1 CPD signal in both gauges that is only present in the 240° GTSM spectrum, which may be an indication of temperature-related noise or under-corrected barometric pressure.

Both functioning ECS horizontal strain gauges are capable of resolving the solid Earth tides and therefore should be capable of measuing injection strains. While the ECS gauges have a higher overall noise level (lower SNR), this was fully anticipated given that the GTSM capacitance gauges are at least an order of magnitude higher resolution than the commercial single-ended eddy current sensors used in the ECS horizontal gauges.

2.5.3 Vertical Strainmeter Performance

The lack of a commercial vertical strainmeter at the Simpson Station or North Avant Field makes it impossible to make a direct comparison to the ECS vertical strain gauge. However, assuming a Poisson solid ($\nu = 0.25$) for a traction-free half space, the vertical strain is $-1/3$ the areal strain (DeWolf, 2014). Therefore, we compared the ECS vertical strain to the re-scaled GTSM areal strain, the results of which are shown in Figure 2.41.

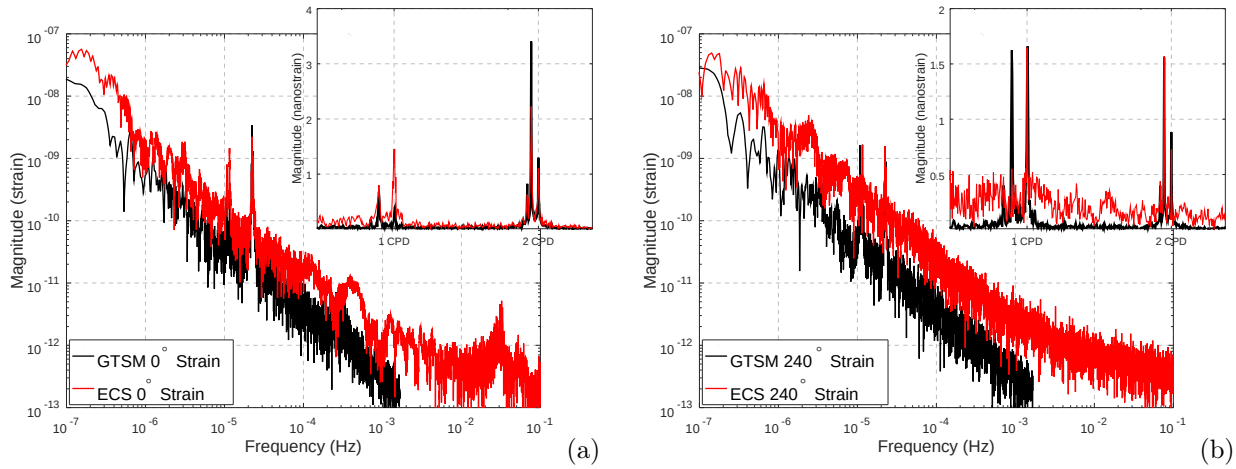

Figure 2.40: 0° (a) and 240° (b) horizontal strain magnitude spectra comparing the Gladwin Tensor Strainmeter (GTSM, black) to the Eddy Current System (ECS, red) strain gauges. Inset plot shows a closeup of the tidal band. Note that the GTSM spectra is truncated at 600 seconds ($1.\overline{6} \times 10^{-3}$ Hz) since this twice the sampling period (Nyquist frequency) of the processed data provided by UNAVCO.

The performance of this single-ended sensor exceeds that of its horizontal counterparts. It very closely matches the GTSM at the four main tidal peaks and appears to resolve the 2 CPD Earth tides with nearly the same SNR. Unlike the tiltmeters, the two spectra converge above about 2 CPD, but do start to pull apart at lower frequencies (below 2 CPD). This gauge exceeds our design goals and expectations by performing nearly as well as the GTSM, which is more than adequate for resolving vertical strains induced by injection tests.

2.5.4 Areal Strainmeter Performance

The final comparison is between the areal strain from the GTSM and the Optical Fiber Areal Strainmeter (OFAS). Figure 2.42 shows the magnitude spectra from both instruments, which appear to be almost perfectly in agreement. One exception is a larger 1 CPD signal on the OFAS that is about 2–3 times larger than that of the GTSM, which may be due to an under-corrected barometer, thermal noise or perhaps some vertical strain coupling (i.e., the areal strainmeter is actually a *volumetric* strainmeter) and remains an active topic of investigation. However, it is clear that the strain monitoring capabilities of the North Avant Field OFAS are at least as reliable as the GTSM across all frequency bands and should be more than effective for injection strain measurements.

2.5.5 Final Instrument Assessment

The eddy current strain and tilt systems developed for this project have all been successful in that we have integrated commercial non-contact eddy current sensors into a borehole package capable of measuring multiple components of strain and tilt. The performance of the eddy current systems has exceeded design goals based on the predicted strain rates from injection tests. While the horizontal strain gauges were expected and observed to be about an order of magnitude more noisy than the Gladwin Tensor Strainmeter gauges, they were able to clearly record and be calibrated against the solid Earth tides in most cases.

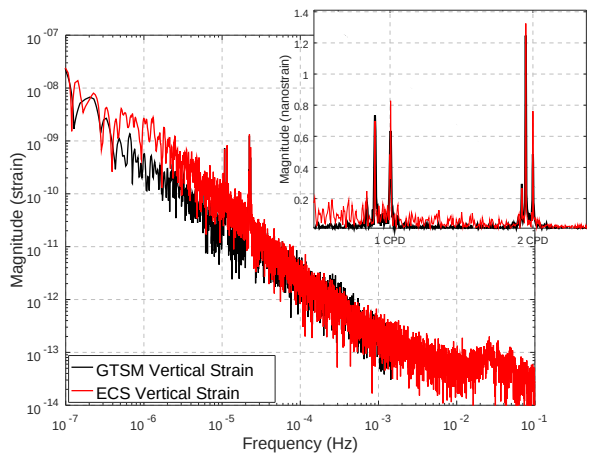

Figure 2.41: Vertical strain magnitude spectra comparing the re-scaled areal strain from the Gladwin Tensor Strainmeter (GTSM, black) to the Eddy Current System (ECS, red) vertical strain gauge. Inset plot shows a closeup of the tidal band.

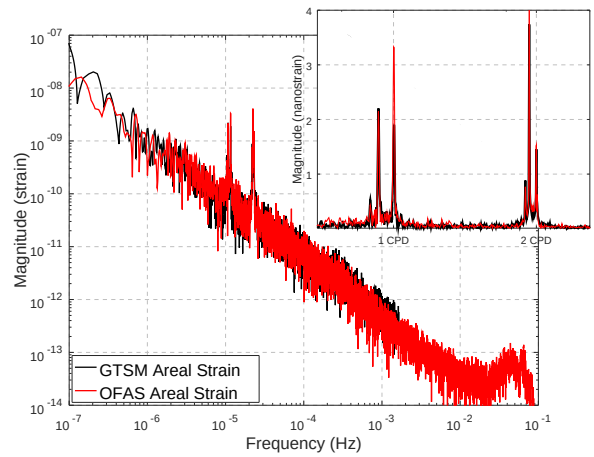

Figure 2.42: Areal strain magnitude spectra comparing the the Gladwin Tensor Strainmeter (GTSM, black) to the Optical Fiber Areal Strainmeter (OFAS, red). Inset plot shows a closeup of the tidal band.

Two optical fiber areal strainmeters were developed initially as an inexpensive, low-risk way to evaluate our grouting procedure and competency of the installation. However, they ended up demonstrating that optical fiber borehole strainmeters can match the performance of a state-of-the-art borehole strainmeter. While the OFAS is only a single-component, this same measurement principle is currently being adapted to resolving the *complete* strain tensor (i.e., horizontals *and* vertical) at a fraction of the cost and about $2,000\times$ higher resolution.

There are always improvements that can be made despite the success of these developments. The Eddy Current Systems did suffer from failed gauges (e.g., the y-tilt, 0° and 240° in the Version 1, and the 120° in the Version 2 instruments) and have ongoing creep issues. While exact nature of these failures are not well understood, it is clear that the very limited dynamic range of the eddy current sensors is problematic in terms of keeping them within their optimal operating range. In fact the best performing gauge is the 0° sensor in the Version 2 system when it is on scale since it is operating at the very edge of its range. This non-linearity could be taken advantage of by installing the horizontal gauges on actuators similar to the removable system. Creep events are most likely a result of residual stresses between their constituent components (Otero, 2009) that would be significantly reduced by designing the instrument from as few parts as possible, like for example the folded pendulum design of Acernese et al. (2008) and physical pendulum design of Zumberge et al. (2018).

2.6 Data Management and Availability

Multiple sources of data were gathered throughout this project including strain, tilt, wellhead pressures and injection rate as well as supporting meteorological data. This required aggregating data from both commercial and project-developed instruments into a suitable database, transmitting it to several backup locations on and off campus, and making the data available to project participants and to the public. Each of these tasks are briefly summarized in the following sections.

2.6.1 Data Acquisition and Telemetry

The strain and tilt systems developed during this project all employ an independent modular data acquisition strategy. All of the eddy current and optical fiber interrogator packages use a discrete ADC (LabJack T7 or T7-Pro) that is queried by a DC-powered "station" computer located at each wellhead. These station computers are not only capable of recording data from any number of ADCs, but also data from other sources such as serial devices like combination weather stations, commercial tiltmeters, pressure transmitters, etc. This implies that each station computer serves as local data storage for all the data being produced at a given location.

Data acquisition software for all project and commercial systems are written in ANSI C and record data to a standard seismic database format. Originally data were recorded to the station computer hard drives in a rudimentary binary "blob" format and manually processed into a more user friendly format when requested. These software were later updated to record all incoming data natively to a standard established by the Federation of Digital Seismograph Networks (FDSN) known as the Standard for the Exchange of Earthquake Data, or SEED (Ahern and Dost, 2012). This was particularly desirable given our intent to make all incoming data publicly available through the Incorporated Research Institutions for Seismology's Data Management Center (IRIS DMC), which only accepts SEED data.

The SEED database standard consists of two main components: dataless SEED and miniSEED. Dataless SEED volumes contain metadata such as instrument locations, serial numbers, calibration factors, etc., that is manually maintained offline using free and open-source software maintained by IRIS. Data acquired in the field are recorded natively to miniSEED, which contains a short 64-byte header of station, channel, and timing information that is followed by a 4,032-byte data section containing the binary waveform information. So-called "full SEED" is simply the concatenation of both dataless SEED and miniSEED, and has been the standard used throughout the seismological and geodetic communities for decades.

Data collected at each computer are automatically transmitted to several locations once per day. Some sites consist of several station computers, however, only one station is equipped with a cellular modem (Sierra Wireless RV50). Data from other station computers are transmitted to a single "head node" at each field site that telemeters to a virtual data server hosted by Google Compute shortly after midnight UTC. These incoming miniSEED volumes are then pushed to the IRIS DMC and to a local data server at Clemson University. Separate physical and cloud backups are automatically made once the data are received by the local data server. All data connections and file transfers are encrypted.

While the handling of the raw data is automated, the processing (Section 2.4) is still currently done manually on an as-needed basis (e.g., for each injection test). Future plans are to provide real time data to IRIS and to automate the processing of the raw data.

2.6.2 Raw Data Availability

All raw data from this project (DE-FE0023313) and incoming data from ongoing research (DE-FE0028292) are publically available through the Incorporated Research Institutions for Seismology's Data Management Center (IRIS DMC). All data managed by Clemson University are aggregated through the International Federation of Digital Seismograph Networks (FDSN) Network Code 2J, which can be found through the following listing:

DeWolf, S. and Murdoch, L. C. (2016). *Clemson University Subsurface Deformation Monitoring Network*, International Federation of Digital Seismograph Networks, Dataset/Seismic Network, `http://www.fdsn.org/networks/detail/2J_2016/`, DOI: 10.7914/SN/2J_2016.

Metadata (dataless SEED) and waveforms (miniSEED) can be found via the IRIS MetaData Aggregator at:

`http://ds.iris.edu/mda/2J/`

This includes automated daily backups from AVN3, AVN4, SBF0, SBF1 and SBF2 and manual backups from WW11A, WW27, WW29 and WW60. 9A injection pressure and rate data are property of Grand Resources and are not made publically available through the IRIS DMC at this time. Past and ongoing data offerings are summarized in Table 2.1.

The Gladwin Tensor Strainmeter deployed in AVN2 is operated and maintained by UNAVCO, whose data are also made publically available under the FDSN Network Code PB. Metadata (dataless SEED) and waveforms (miniSEED) can be found via the IRIS MetaData Aggregator at:

`http://ds.iris.edu/mda/PB/AVN2/`

Table 2.1: Summary of past and ongoing project data offerings at the IRIS DMC.

Station	Instrument	Channel	Description	Backup
AVN3	Eddy Current Strain and Tilt System, Rev.02	VAX	x-Tilt	Daily
		VAY	y-Tilt	Daily
		VS1	0° Strain	Daily
		VS2	120° Strain	Daily
		VS3	240° Strain	Daily
		VSZ	Vertical Strain	Daily
		VKD	Temperature	Daily
AVN4	Optical Fiber Areal Strainmeter, Rev.04	AYX	x-Fringes	Daily
		AYZ	y-Fringes	Daily
		AYY	z-Fringes	Daily
		BS1	Areal Strain	Daily
	Vaisala WXT520 Combination Weather Station	VDO	Barometer	Daily
		VIO	Humidity	Daily
		VKO	Temperature	Daily
		VRH	Hail	Daily
		VRO	Rainfall	Daily
		VWD	Wind Direction	Daily
		VWS	Wind Speed	Daily
	Applied Geomechanics LILY Tiltmeter	LAX	x-Tilt	Daily
		LAY	y-Tilt	Daily
		LKD	Temperature	Daily
SBF0	Vaisala WXT520 Combination Weather Station	VDO	Barometer	Daily
		VIO	Humidity	Daily
		VKO	Temperature	Daily
		VRH	Hail	Daily
		VRO	Rainfall	Daily
		VWD	Wind Direction	Daily
		VWS	Wind Speed	Daily

continued on next page

continued from previous page

Station	Instrument	Channel	Description	Backup
SBF1	Optical Fiber Areal Strainmeter, Rev.03	AYX	x-Fringes	Offline
		AYZ	y-Fringes	Offline
		AYY	z-Fringes	Offline
		BS1	Areal Strain	Offline
SBF2	Eddy Current Strain and Tilt System, Rev.01	VAX	x-Tilt	Daily
		VAY	y-Tilt	Daily
		VS1	0° Strain	Daily
		VS2	120° Strain	Daily
		VS3	240° Strain	Daily
		VSZ	Vertical Strain	Daily
		VKD	Temperature	Daily
WW11A	In-Situ Rugged TROLL Pressure Logger	UDD	Pressure	Per Visit
		UKD	Temperature	Per Visit
WW27	In-Situ Rugged TROLL Pressure Logger	UDD	Pressure	Per Visit
		UKD	Temperature	Per Visit
WW29	In-Situ Rugged TROLL Pressure Logger	UDD	Pressure	Per Visit
		UKD	Temperature	Per Visit
WW60	In-Situ Rugged TROLL Pressure Logger	UDD	Pressure	Per Visit
		UKD	Temperature	Per Visit

2.6.3 Processed Data Availability

Processed data from the shut-in and three injection tests discussed in Chapters Four and Five can be found on the United States Department of Energy National Energy Technology Laboratory's Energy Data eXchange (EDX). This includes all available calibrated, de-tided, and de-trended strain, tilt, pressure and injection pressure and rate. These can be found via the following listings:

Murdoch, L. C., and DeWolf, S. (2019). 1A Shut-In: March 31 thru April 7, 2017. `https://edx.netl.doe.gov/dataset/1a-shut-in-march-2017`, DOI: 10.18141/1505373.

Murdoch, L. C., and DeWolf, S. (2019). 9A Injection: October 11 thru October 17, 2017. `https://edx.netl.doe.gov/dataset/9a-injection-october-2017`, DOI: 10.18141/1505374.

Murdoch, L. C., and DeWolf, S. (2019). 9A Injection: November 28 thru December 1, 2017. `https://edx.netl.doe.gov/dataset/9a-injection-november-28-2017`, DOI: 10.18141/1505375.

Murdoch, L. C., and DeWolf, S. (2019). 9A Injection: June 28 thru July 23, 2018. `https://edx.netl.doe.gov/dataset/9a-injection-june-2018`, DOI: 10.18141/1505376.

These files include the fully processed, "Level 2" data from the Gladwin Tensor Strainmeter in AVN2, which was accessed via their FTP site at:

`ftp://bsm.unavco.org/pub/bsm/level2/osageavn2bok2016`

References

Acernese, F., Giordano, G., Romano, R., De Rosa, R., and Barone, F. (2008). Mechanical monolithic horizontal sensor for low frequency seismic noise measurement. *Review of Scientific Instruments*, 79(7):074501.

Agnew, D. C. (1997). NLOADF: A program for computing ocean-tide loading. *Journal of Geophysical Research: Solid Earth*, 102(B3):5109–5110. http://dx.doi.org/10.1029/96JB03458.

Agnew, D. C. (2012). SPOTL: Some Programs for Ocean-Tide Loading. Technical Report 954322pg, University of California San Diego Scripps Institution of Oceanography. https://escholarship.org/uc/item/954322pg.

Ahern, T. K. and Dost, B. (2012). Standard for the Exchange of Earthquake Data (SEED) Reference Manual, Version 2.4. Technical report, Incorporated Research Institutions for Seismology. http://www.fdsn.org/media/_s/publications/SEEDManual_V2.4.pdf.

American Society for Testing and Materials (2010). Standard Test Method for Flow of Grout for Preplaced-Aggregate Concrete (Flow Cone Method). Technical Report C939-10, ASTM International.

Brudy, M. and Zoback, M. D. (1999). Drilling-induced tensile wall-fractures: implications for determination of in-situ stress orientation and magnitude. *International Journal of Rock Mechanics and Mining Sciences*, 36(2):191–215.

Bucaro, J. A., Carome, E. F., and Dardy, H. D. (1979). Fiber optic acoustic sensor. US Patent 4,162,397.

Bucaro, J. A., Dardy, H. D., and Carome, E. F. (1977). Fiber-optic hydrophone. *The Journal of the Acoustical Society of America*, 62(5):1302–1304.

Crawford, W. C. and Webb, S. C. (2000). Identifying and removing tilt noise from low-frequency (< 0.1 hz) seafloor vertical seismic data. *Bulletin of the Seismological Society of America*, 90(4):952–963.

DeWolf, S. (2014). *Optical Fiber Sensors for Infrasonic Wind Noise Reduction and Earth Strain Measurement*. Doctor of Philosophy in Oceanography, University of California San Diego. http://roger.ucsd.edu/record=b8191107~S9.

DeWolf, S., Wyatt, F. K., Zumberge, M. A., and Hatfield, W. (2015). Improved vertical optical fiber borehole strainmeter design for measuring earth strain. *Review of Scientific Instruments*, 86(11):114502.

Franz, K. L. (1983). Method and apparatus for zeroing a tilt meter mechanism. US Patent 4,397,098.

Gladwin, M. T. (1984). High-precision multicomponent borehole deformation monitoring. *Review of Scientific Instruments*, 55(12):2011–2016.

Gladwin, M. T. and Hart, R. H. G. (1985). Design parameters for borehole strain instrumentation. *Pure and Applied Geophysics*, 123(1):59–80.

Gladwin, M. T. and Wolfe, J. (1975). Linearity of capacitance displacement transducers. *Review of Scientific Instruments*, 46(8):1099–1100.

Hart, R. H. G., Gladwin, M. T., Gwyther, R. L., Agnew, D. C., and Wyatt, F. K. (1996). Tidal calibration of borehole strain meters: Removing the effects of small-scale inhomogeneity. *Journal of Geophysical Research: Solid Earth*, 101(B11):25553–25571.

Hodgkinson, K. (2006). Procedures for processing borehole strainmeter data. Technical report, UNAVCO. https://www.unavco.org/projects/project-support/borehole-services/lib/docs/BSM_Processing.pdf.

Hodgkinson, K., Langbein, J., Henderson, B., Mencin, D., and Borsa, A. (2013). Tidal calibration of plate boundary observatory borehole strainmeters. *Journal of Geophysical Research: Solid Earth*, 118(1):447–458.

Hunter, S. L., Boro, C. O., and Farris, A. (2002). Tiltmeter leveling mechanism. US Patent 6,370,784 B1.

Kaman Precision Products (2011). Inductive Technology Handbook. Technical Report 860214-001, Kaman Aerospace. `https://www.kaman.com/sites/default/files/Kaman_Applications_Handbook_WEB%20%281%29.pdf`.

Kersey, A. D., Marrone, M. J., and Davis, M. A. (1991). Polarisation-insensitive fibre optic Michelson interferometer. *Electronics Letters*, 27(6):518–520.

Langbein, J. (2010). Computer algorithm for analyzing and processing borehole strainmeter data. *Computers & Geosciences*, 36(5):611–619.

Office of Water (2012). Geologic Sequestration of Carbon Dioxide: Underground Injection Control (UIC) Program Class VI Well Construction Guidance. Technical Report EPA 816-R-11-020, United States Environmental Protection Agency.

Otero, J. D. (2009). *Development and characterization of an observatory-class, broadband, non-fedback, leaf-spring interferometric seismometer*. Doctor of Philosophy in Earth Sciences, University of California San Diego. `http://roger.ucsd.edu/record=b6621245~S9`.

Pawlowicz, R., Beardsley, B., and Lentz, S. (2002). Classical tidal harmonic analysis including error estimates in MATLAB using T_TIDE. *Computers & Geosciences*, 28(8):929–937.

Qiu, Z., Tang, L., Zhang, B., and Guo, Y. (2013). In situ calibration of and algorithm for strain monitoring using four-gauge borehole strainmeters (FGBS). *Journal of Geophysical Research: Solid Earth*, 118(4):1609–1618.

Rashleigh, S. C. (1985). Fiber optic sensors operating at DC. US Patent 4,495,411.

Riedel, K. S. and Sidorenko, A. (1995). Minimum bias multiple taper spectral estimation. *IEEE Transactions on Signal Processing*, 43(1):188–195.

Roeloffs, E. (2005). Long-term trends in borehole strainmeter and tiltmeter data. 2005 UNAVCO Strainmeter Short-Course, `http://www.unavco.org:8080/cws/straindata/Notesfrom2005class/detrend_long-term.pdf`.

Roeloffs, E. (2010). Tidal calibration of Plate Boundary Observatory borehole strainmeters: Roles of vertical and shear coupling. *Journal of Geophysical Research: Solid Earth*, 115(B6).

Schliep, F. and Hereth, R. (1992). Phase sensitive measurement technique for singlemode fibre directional couplers. *Electronics Letters*, 28(16):1538–1540.

Sheem, S. K. (1980). Fiber-optic gyroscope with [3×3] directional coupler. *Applied Physics Letters*, 37(10):869–871.

Timoshenko, S. and Goodier, J. N. (1951). *Theory of elasticity*. New York.

Todd, M. D., Seaver, M., and Bucholtz, F. (2002). Improved, operationally-passive interferometric demodulation method using 3×3 coupler. *Electronics Letters*, 38(15):784–786.

Zumberge, M. A., Berger, J., Dzieciuch, M. A., and Parker, R. L. (2004). Resolving Quadrature Fringes in Real Time. *Applied Optics*, 43(4):771–775.

Zumberge, M. A., Berger, J., Hatfield, W., and Wielandt, E. (2018). A three-component borehole optical seismic and geodetic sensor. *Bulletin of the Seismological Society of America*, 108(4):2022–2031.

Zumberge, M. A., Berger, J., Hedlin, M. A., Husmann, E., Nooner, S., Hilt, R., and Widmer-Schnidrig, R. (2003). An optical fiber infrasound sensor: A new lower limit on atmospheric pressure noise between 1 and 10 Hz. *The Journal of the Acoustical Society of America*, 113(5):2474–2479.

Chapter Three
Theoretical Analysis

In situ strain during injection results from coupling between the changing fluid pressure in the reservoir and the deformation of the solid framework of the reservoir and confining unit. Simulating this coupled process is an important aspect of designing in situ strain sensors, and inverting simulations is an equally important tool for interpreting strain data. The project developed new methods for analyzing strain signals, in addition to utilizing existing methods.

The typical approach for simulating strain during injection involves numerical solutions to coupled equations describing fluid pressure and deformation used in poroelasticity. This approach is versatile, but the execution time can be lengthy and this causes some applications to be cumbersome or infeasible. In response to this these limitations, we developed a new analytical solution to the deformation caused by a pressurized poroelastic inclusion. The new method can represent geometries that are much more realistic than existing analytical solutions and it is many orders of magnitude faster than numerical methods.

We have also developed a new stochastic inverse procedure designed to invert numerical solutions to 3D poroelastic problems. Stochastic inversion requires the execution of many simulations, which can be computationally intensive when applied to problems with long execution times. The stochastic inversion method developed for the project takes advantage of high throughput computing techniques to interpret strain signals using 3D numerical models.

During the course of the investigation we noticed that shallow normal strain signals were approximately functions of the logarithm of time. The pressure in the underlying reservoir has long been analyzed using analytical solutions to idealized scenarios that are expressed as "type curves". A fundamental pressure type curve is a function of logarithm of time, so we evaluated the feasibility of analyzing strain signals using methods similar to those used to analyze pressure type curves.

Planning the field project described in Chapter Four required preliminary simulations of the field site in order to anticipate the expected strain signal. This was done using both the new analytical solution and 3D numerical solutions.

3.1 Analysis of a Pressurized Poroelastic Inclusion Resembling a Reservoir

Injection causes the fluid pressure to increase in the vicinity of a well and this deforms the reservoir and overlying confining unit, and the injection wellbore itself. The region of increased fluid pressure, Δp, expands outward away from the wellbore and this causes the deformation field to change with time. The approach used in this project is to first analyze deformation overlying a pressurized region when Δp is spatially uniform (although it changes with time). This case is tractable in closed form and the results can be scaled so they approximate a wide range of cases. The developed forwarded model is then used for the first-order analysis of injection tests conducted at the North Avant Field as a part of this project.

3.1.1 Concepts

The pressurized reservoir will be represented by a sub-horizontal, poroelastic inclusion (Figure 3.1a) of uniform thickness, h, and characteristic lateral dimension, a, embedded in uniform matrix with low permeability. In the axisymmetric case (Figure 3.1b), a is the reservoir radius, but we do not assume any symmetry at this stage. However, the reservoir is assumed to be thin ($h/a \ll 1$), deep ($h/H \ll 1$), and uniformly pressurized by Δp, which represents the pore pressure *change* caused by the injection

process. At the North Avant Field, this assumption is approximately supported by the independent pressure measurements and is sufficient to fit the obtained strain data. More specifically, it turns out that in the area of the North Avant Field, the reservoir permeability may be high enough for the pressure to roughly equilibrate in the vicinity of the well.

The elastic properties of the reservoir are assumed to be homogeneous, but they can differ from the properties of the confining unit. The contrast between the properties of the reservoir and confining unit may be within two order of magnitude (or even more as discussed below). Most reservoirs considered for CO_2 storage are well represented by these conditions (Murdoch et al., 2016). The adopted approach allows some assumptions to be relaxed to provide results for more general conditions, such as variable h and Δp (Germanovich and Chanpura, 2002), and irregular shapes (Figure 3.1a). Although those analyses are beyond the scope of this project, this capability will be useful in the continuing work.

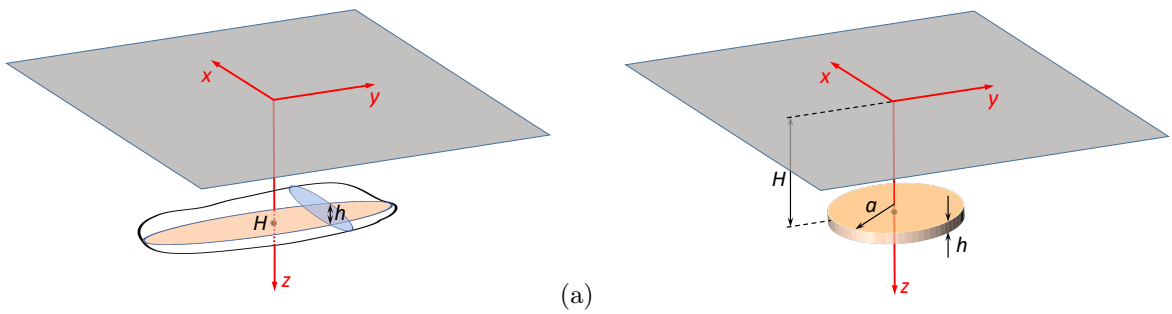

Figure 3.1: (a) Thin poroelastic inhomogeneity V of thickness $h(x, y)$ at depth $H \gg h$ in a half-space $z \geq 0$. (a) Thin cylindrical inclusion of the uniform thickness h at depth $H \gg h$ in a half-space $z \geq 0$.

Linear elastic poroelasticity (Detournay and Cheng, 1993; Wang, 2000) with the constitutive law

$$\sigma_{ij} = 2\mu\varepsilon_{ij} + \lambda\varepsilon_{kk}\delta_{ij} - \alpha\Delta p\delta_{ij} \tag{3.1}$$

will be used to describe the deformation. Here σ_{ij} and ε_{ij} are the stresses and strains, respectively, $\mu = E/[2(1+\nu)]$ and $\lambda = 2\mu/(1-2\nu)$ are the Lamé parameters, E is the Young's Modulus, ν is the Poisson's ratio, and α is the Biot-Willis coefficient. Suffixes i and j (and all other tensor indexes) take values of 1, 2, and 3, which correspond to the coordinate axes x, y, and z, respectively (Figure 3.1a). A repeated suffix is summed over the values of 1, 2, 3, and the Kronecker delta $\delta_{ij} = 1$ when $i = j$, and $\delta_{ij} = 0$ when $i \neq j$.

A reference value for deformation is the unconstrained volumetric strain caused by pressure change in the absence of surrounding material, the transformation strain, ε_0. The poroelastic, volumetric transformation strain is related to mechanical properties as

$$\varepsilon_0 = \alpha_1\Delta p/K_1 \tag{3.2}$$

where $K = (2\mu + 3\lambda)$ is the bulk modulus. Hereafter, subscript "1" denotes material properties of the reservoir, and the lack of subscript indicates material properties of the confining unit. Using (3.2), equation (3.1) can be rewritten as

$$\sigma_{ij} = 2\mu\left(\varepsilon_{ij} - \varepsilon_{ij}^T\right) + \lambda\left(\varepsilon_{kk} - \varepsilon_{kk}^T\right)\delta_{ij} \tag{3.3}$$

where $\varepsilon_{ij}^T = (\varepsilon_0/3)\,\delta_{ij}$. Therefore, the transformation strain ε_0 is a particular case of the Robinson-Eshelby stress-free strain (Robinson, 1951; Eshelby, 1957), which the inhomogeneity (reservoir) would undergone

in the absence of the matrix (confining unit). Hereafter, the term "inclusion" is reserved for a region in a homogeneous body, which undergoes the transformation strain. The inclusion and its surroundings (matrix) have the same elastic properties. When the region and the matrix have different properties, such a region is called an "inhomogeneity". This terminology was introduced by Eshelby (1957, 1959) and has become common in modern mechanics, e.g., Mura (2013) and Kachanov and Sevostianov (2018).

In constructing the forward mathematical model, we follow the Eshelby (1957) method of equivalent inclusion. This method reduces the inhomogeneity transformation to the transformation of a properly chosen "equivalent" inclusion. Specifically, the equivalent inclusion has the geometry identical to the original inhomogeneity, but its elastic properties are the same as those of the matrix. The transformation strains, ε^*_{ij}, in the inclusion, however, are not the same as the transformation strains, ε^T_{ij}, in the original inhomogeneity. They are adjusted to make the strains and stresses generated by the inclusion transformation equal to those generated by the transformation of the inhomogeneity (both in the inhomogeneity and in the matrix). Determining the equivalent transformation strains, ε^*_{ij}, effectively provides the solution of the original inhomogeneity problem, which is typically written in the form of

$$\varepsilon_{ij} = S_{ijkl}\varepsilon^*_{ij} \tag{3.4}$$

where S_{ijkl} is the Eshelby tensor. This tensor depends on the properties of the matrix and geometries of both inhomogeneity and matrix (host body), but not on the transformation strain and not on the inhomogeneity properties.

It turns out that for an *ellipsoidal* inhomogeneity in the *unbounded* matrix and with *uniform* ε^T_{ij}, the strains and stresses, generated by the transformation inside the inhomogeneity, are also uniform (Eshelby, 1957; Kachanov and Sevostianov, 2018). This simplifies the solution. Specifically, given ε^T_{ij}, the *normal* transformation strains in the equivalent inclusion can be found from the set of three linear algebraic equations, e.g., Mura (2013), as

$$2\mu_1\left(S_{ijkl}\varepsilon^*_{kl} - \varepsilon^T_{ij}\right) + \lambda_1\left(S_{kkmn}\varepsilon^*_{mn} - \varepsilon^T_{kk}\right) = 2\mu\left(S_{ijkl}\varepsilon^*_{kl} - \varepsilon^*_{ij}\right) + \lambda\left(S_{kkmn}\varepsilon^*_{mn} - \varepsilon^*_{kk}\right) \quad (i = j) \tag{3.5}$$

for ε^*_{ii} (no summation) while the *shear* transformation strain are defined explicitly by

$$\varepsilon^*_{ij} = \frac{\mu_1\varepsilon^T_{ij}}{\mu + 2\left(\mu_1 - \mu\right)S_{ijij}} \quad (i \neq j,\ \text{no summation}) \tag{3.6}$$

Thus, (3.4) reduces the inhomogeneity problem to determining S_{ijkl}. For a general ellipsoid, tensor S_{ijkl} has 24 non-zero components, 15 of which are independent. They are tabulated in the closed form (Mura, 2013; Kachanov and Sevostianov, 2018), and with adding the ellipsoid symmetries (e.g., oblate spheroid), the number of independent components of S_{ijkl} reduces.

3.1.2 Mathematical Model

Eshelby's approach has revolutionized mechanics of materials and has been also successfully applied in geological and geomechanical settings (e.g., Reches (1998); Rudnicki (2011); Meng et al. (2012); Guido et al. (2015); Zhang et al. (2019)). This approach is not universal, however. The difficulties of using (3.5) appear when the transformation strains are not uniform, the inhomogeneity shape is not ellipsoidal, or the host body has a boundary. Equations (3.5) and (3.6) are then replaced by a set of integral equations for ε^*_{kl}, which defeats the benefit of using (3.4) (e.g., Kachanov and Sevostianov (2018)).

In particular, the interpretation of our *shallow* measurements requires explicit including the earth surface in the analysis (Figure 3.1a). This is why we consider an inhomogeneity in the half-space (Figure 3.1a). Generalization of the Eshelby approach to a half-space scenario has been a subject of the ongoing effort and results are available for *inclusions* with transformation strains in a half-space (e.g., Mura (2013); Ru (1999); Davies (2003); Germanovich et al. (2012); Lyu et al. (2018); Zhang et al. (2019)). Most of them are based on using (directly or indirectly) a point source in a half-space as a Green's function (e.g., Mura (2013); Davies (2003); Lyu et al. (2018); Zhang et al. (2019) or on employing the method of complex variables (Muskhelishvili, 2013) to an inclusion in a half-plane (e.g., Ru (1999) and Germanovich et al. (2012)). Targeted numerical approaches have also been developed (Lehner et al., 2005; Mogilevskaya and Crouch, 2007; Chen, 2016), but little results are known for the *inhomogeneity* case (when the inhomogeneity and the half-space have different elastic properties).

To the best of our knowledge, all existing works on an inhomogeneity in a half-space involve numerical analysis as a major component. A notable exception is the paper by Dobrovolskii (2007). For the arbitrary contrast in elastic properties between the inhomogeneity and the half-space, he reduced the problem to a set of integral equations, which needs to be solved numerically. For weakly contrasting properties, however, he used a small parameter, which characterizes the difference in properties, and offered an asymptotic solution obtained by regular perturbations. In this work, the property difference is not necessarily small, but we have another small parameter available, that is, h/a. Although in the presence of half-space boundary, we lose the benefit of employing (3.4)–(3.6), we still have the advantage of the inhomogeneity being thin. This allows us to employ the asymptotic approach and still use the method of equivalent inclusion, albeit in the form that differs from (3.4)–(3.6).

The vertical deformation, ε_{zz}, of a thin horizontal pressurized reservoir *with elastic properties that may differ* from the confining unit follows from methods outlined in Germanovich and Chanpura (2002). They employed an asymptotic technique proposed by Movchan and Movchan (1995) and based on singular perturbations. Accordingly, they used different spatial scaling inside and outside the inhomogeneity and matched the inner and outer expansions (with respect to the small parameter h/a) on the inclusion boundary. As a result, they obtained the displacements and strains inside the inclusion.

Although Germanovich and Chanpura (2002) consideration was two-dimensional, the three dimensional analysis is similar and yields

$$\varepsilon_{zz} = \frac{\Delta h}{h} = \frac{2\mu_1 + 3\lambda_1}{2\mu_1 + \lambda_1}\varepsilon_{zz}^T \tag{3.7}$$

where the higher order terms are omitted, $\varepsilon_{zz}^T = \varepsilon_0/3$, and ε_0 is defined in (3.2). In the leading terms, strain changes that occur laterally along the reservoir are negligible, so (3.7) also represents the local volumetric strain in the reservoir. It is apparent from (3.7) that the volumetric strain in the reservoir is dominated by elastic properties of the reservoir. This is because equation (3.7) represents the first order asymptote with respect to the small parameter, h/a. Properties of the confining unit would appear in the second order, which contribution is small as long as the elastic properties of the reservoir and confining unit are constrained by $h/a \lesssim \mu/\mu_1 \lesssim a/h$ and $h/a \lesssim \lambda/\lambda_1 \lesssim a/h$. From a practical stand point, these constraints are not too important as nearly always $h/a \lesssim 10^{-2}$. This implies that the properties may differ by at least two orders of magnitude.

An important advantage of equation (3.7) is that it holds for both bounded and unbounded bodies. In general, the effect of the boundary appears through strains that would be in the homogeneous body on the inhomogeneity place (Germanovich and Chanpura, 2002). These strains are not present in (3.7) since we only consider changes caused by the pressure increment, Δp, and, therefore, the boundary is not loaded.

Equation (3.7) replaces relation (3.4) in the method of equivalent inclusion. By definition, the equivalent inclusion experiences the same deformation (3.7) as that of the inhomogeneity. Hence, swapping μ_1 and λ_1

in (3.7) with μ and λ, respectively, yields

$$\varepsilon_{zz} = \frac{\Delta h}{h} = \frac{2\mu + 3\lambda}{2\mu + \lambda}\varepsilon^*_{zz} \quad (\varepsilon^*_{zz} = \varepsilon^*_0/3) \tag{3.8}$$

where ε^T_{zz} was replaced with the equivalent transformation strain, ε^*_{zz}, that takes place in the equivalent inclusion (rather than the real transformation strain ε^T_{zz}, in the inhomogeneity). The equivalent volumetric transformation strain

$$\varepsilon^*_0 = \varepsilon^*_{kk} = \alpha \Delta p_* / K \tag{3.9}$$

is produced by the equivalent pressure, Δp_*. Similar to (3.7), all shear strains in the equivalent inclusion are negligible (because the inclusion is thin).

Hence, comparing (3.7) with (3.8) and taking into account that $K = (2\mu + 3\lambda)/3$, results in the relation

$$\varepsilon^*_0 = \frac{(2\mu_1 + 3\lambda_1)(2\mu + \lambda)}{(2\mu_1 + \lambda_1)(2\mu + 3\lambda)}\varepsilon_0 = \frac{3\alpha_1 (2\mu + \lambda)\Delta p}{(2\mu_1 + \lambda_1)(2\mu + 3\lambda)} \tag{3.10}$$

which replaces equations (3.5), (3.6) in the method of equivalent inclusion. Using then equations (3.2) and (3.9) in (3.10), finally arrive at

$$\Delta p_* = \frac{\alpha_1 (\lambda + 2\mu)}{\alpha (\lambda_1 + 2\mu_1)}\Delta p \tag{3.11}$$

An important conceptual step is to recognize that the analysis for the homogeneous case can be applied to the heterogeneous case by equating (3.7) and (3.8). This gives expression (3.10) for the equivalent pressure change, Δp_*, that should be used in the homogeneous case to account for contrasts in elastic properties between the reservoir and confining unit.

Owing to (3.2) and (3.10), when the pressure distribution, Δp, in the reservoir is known, ε_0 is known too and so are ε^*_0 and Δp_*. As discussed below, the deformation field caused by a thin pressurized reservoir *with elastic properties the same* as enveloping material can be determined in closed form.

Note that ε_0 in (3.7) does not need to be uniform. Hence, Δp does not have to be uniform either. Likewise, the region thickness, h, does not need to be constant (Figure 3.1a). For (3.7) to be asymptotically valid, however, h and Δp should not change abruptly along the inhomogeneity. Therefore, (3.7) needs to be revised, for example, near faults or compartmentalization boundaries, but it holds where $|\partial h/\partial x_i| \lesssim 1/\varepsilon$ and $\partial(\Delta p)/\partial x_i \lesssim \mu_1/h \quad (i = 1, 2)$.

3.1.3 Results

The analysis outlined above predicts the spatial distribution of strains and tilts as a function of material properties. The analysis can simulate the effects of transient pressure changes in the reservoir using some simplifying assumptions, as outlined below.

3.1.3.1 Strains and Tilts at the Measurement Location

Finding strains induced by the reservoir pressure distribution from (3.11) can be done by using the classic Mindlin and Cheng (1950a,b) result for a point source in a homogeneous elastic half-space. Using their solution as a Green's function, consider a region, V, that undergoes a volumetric transformation strain, $\varepsilon_0(x,y,z)$. The displacement vector at point $\mathbf{r} = \{x,y,z\}$ in the half-space $z \geq 0$ (Figure 3.1a) is expressed as

$$u_i(x,y,z) = u_i^0(x,y,z) + (3-4\nu)\, u_i^0(x,y,-z) + (-1)^\delta\, 2z \frac{\partial}{\partial z} u_i^0(x,y,-z) \tag{3.12}$$

where $i = 1$, 2, or 3, represent x, y, and z, respectively, and $\delta = 1$ for $i = 1,2$, while $\delta = 0$ for $i = 3$. The displacements

$$u_i^0(x,y,z) = -\frac{1}{4\pi}\frac{\partial \varphi_0}{\partial x_i} \tag{3.13}$$

would occur in the infinite space, $-\infty < z < \infty$, with region V at the same location in its lower half-space $z \geq 0$. The potential (Timoshenko and Goodier, 1951)

$$\varphi_0(x,y,z) = \frac{1}{3}\frac{1+\nu}{1-\nu}\int_V \frac{\varepsilon_0^*(\mathbf{r_1})\, d^3\mathbf{r_1}}{|\mathbf{r}-\mathbf{r_1}|} \quad (\mathbf{r_1} = \{x_1, y_1, z_1\} \in V) \tag{3.14}$$

where $\mathbf{r} = \{x,y,z\}$ is an arbitrary point in the half-space $z \geq 0$, and

$$|\mathbf{r}-\mathbf{r_1}| = \left[(x-x_1)^2 + (y-y_1)^2 + (z-z_1)^2\right]^{1/2}$$

with x_1, y_1, and z_1 being the integration variables inside V.

Differentiating (3.14) and using (3.12), we express tilts in the half-space

$$\omega_{ij} = \frac{\partial u_i}{\partial x_j} = \omega_{ij}^0(x,y,z) + A(\nu)\,\omega_{ij}^0(x,y,-z) + (-1)^\gamma\, 2z\frac{\partial}{\partial z}\omega_{ij}^0(x,y,-z) \quad (i \neq j) \tag{3.15}$$

through the corresponding tilts in the full space

$$\omega_{ij}^0 = \frac{\partial u_i^0}{\partial x_j} = -\frac{1}{4\pi}\frac{\partial^2 \varphi_0}{\partial x_i \partial x_j} \quad (i \neq j) \tag{3.16}$$

where $A(\nu) = 5-4\nu$ for ω_{xz} and ω_{yz}, and $A(\nu) = 3-4\nu$ for other tilts, while $\gamma = 1$ for ω_{zx} and ω_{zy} and $\gamma = 0$ otherwise.

As can be seen from (3.16), $\omega_{ij}^0 = \omega_{ji}^0$, and it can be shown that $\omega_{xy} = \omega_{yx}$. Shear strains in the half-space are then given by

$$\varepsilon_{ij} = \frac{1}{2}\left(\frac{\partial u_i}{\partial x_j} + \frac{\partial u_j}{\partial u_i}\right) = \frac{\omega_{ij}+\omega_{ji}}{2} \quad (i \neq j) \tag{3.17}$$

while normal strains in the half-space

$$\varepsilon_{ii}(x,y,z) = \varepsilon_{ii}^{0}(x,y,z) + (3-4\nu)\,\varepsilon_{ii}^{0}(x,y,-z) + 2z\frac{\partial}{\partial z}\varepsilon_{ii}^{0}(x,y,-z) \tag{3.18}$$

are expressed through the corresponding normal strains in the infinite space

$$\varepsilon_{ii}^{0} = \frac{\partial u_i^0}{\partial x_i} = -\frac{1}{4\pi}\frac{\partial^2 \varphi_0}{\partial x_i^2} \tag{3.19}$$

Note, there is no summation with respect to i in (3.18) and (3.19).

Therefore, finding displacements, tilts, and strains in the half-space with a region undergoing transformation strain is reduced to evaluating the integral in (3.14), which is a classic task of the potential theory. This project considers measurements in shallow boreholes, so the observation point $\mathbf{r} = \{x, y, z\}$ in (3.14) is outside of the integration domain (Figure 3.1a), and the integration is straightforward as there is no singularity in the integrand. In this case, it is often possible to differentiate under the integration sign in (3.14) (Peirce, 1902; Kellogg, 1929), which results in

$$\frac{\partial \varphi_0}{\partial x_i}(x,y,z) = \frac{1}{3}\frac{1+\nu}{1-\nu}\int_V \frac{\varepsilon_0^*(r_1)(x_i-\rho_i)\,d^3\mathbf{r_1}}{|\mathbf{r}-\mathbf{r_1}|^3} \quad (\mathbf{r_1} = \{x_1, y_1, z_1\} \in V) \tag{3.20}$$

The computations are further simplified if the pressure change distribution, Δp, is uniform. Then owing to (3.10), the transformation strain, ε_0^*, is also uniform and can be taken out of the integrals, which become independent of material properties and pressure distribution. For uniform Δp and canonical forms such as cuboidal or elliptical shapes, integrals such as (3.14) and (3.20) can be evaluated in closed form (e.g., Kellogg (1929), Germanovich et al. (2012) and Guido et al. (2015)).

3.1.3.2 Dependence on Material Properties and Normalization

Explicitly, equations (3.12)–(3.20) include only the Poisson's ratio, ν, of the confining unit. This is expected as they follow from the method of equivalent inclusion and represent a solution in a homogeneous host material. The reservoir properties, however, are included in the equivalent transformation strain, ε_0^*, that appears in (3.14) and (3.20) only in the term

$$\frac{1+\nu}{1-\nu}\varepsilon_0^* = \frac{2\mu_1 + 3\lambda_1}{2\mu_1 + \lambda_1}\varepsilon_0 = C_1 \Delta p \tag{3.21}$$

where

$$C_1 = \frac{3\alpha_1}{2\mu_1 + \lambda_1} = \frac{3\alpha_1(1+\nu_1)(1-2\nu_1)}{(1-\nu_1)E_1} \tag{3.22}$$

In other words, ε_0^* depends only on the combination, C_1, of three reservoir properties (E_1, ν_1, α_1) and is independent of the properties of the confining unit.

Therefore, to the first order (with respect to the small parameter, h/a, displacements and strains, caused by the pressure change in the reservoir, depend upon only two material parameters: 1) Poisson's ratio of the

confining unit and 2) the combination of reservoir properties, C_1. In other words, only these two material parameters are available for the inverse analysis, and the second order terms are needed to separate the individual properties E_1, ν_1, and α_1.

It is possible to determine E_1, ν_1, and α_1 individually, but this analysis highlights the difficulty that may be faced by the numerical modeling. In shallow environment, not only sensitive measurement techniques are required to register the small values of strains, tilts, and displacements, highly accurate numerical calculations are needed to interpret the measurement results.

This analysis also highlights the expectations of the analytical approach described above. To determine the reservoir Young's modulus, E_1, for example, it will be necessary to assume the values of the Poisson's ratio, ν_1, and Biot-Willis coefficient, α_1. Fortunately, α_1 is well constrained and is probably close to 1, while varying ν_1 within reasonable limits only affects E_1 by about 50% or less. Such an accuracy appears reasonably good given the analytical model does not have yet time dependence implemented explicitly. It can be used nonetheless to analyze transient deformation at least for some injection scenarios, such as conducted injection tests at the North Avant Field. This is addressed below.

The above discussion indicates that it will be instrumental to normalize (3.14) and all subsequent quantities in (3.12)–(3.20) by parameter ε_0^* defined in (3.2). The obtained results will be independent of the reservoir properties, and the only remaining material parameter will be the Poisson's ratio, ν, of the confining unit.

3.1.3.3 Simulated Transient Deformation

A simple approach to characterizing the deformation field far from the reservoir is to assume that injection increases the pore pressure in the reservoir, Δp, over a radial extent, a, which scales with the radius of an axisymmetric inclusion (Figure 3.1b). The magnitude of a relative to the depth of the reservoir, H, will affect the deformation field. When $a/H \gg 1$, deformation is relatively insensitive to depth, so the confining unit deforms like a thin plate. Whereas when $a/H \ll 1$, deformation is expected to change significantly with vertical distance from the reservoir, and it will resemble the deformation over a point source. The radial extent of the pressurized region expands outward, so a increases with time as $a \sim \sqrt{2D_1 t}$, where D_1 is hydraulic diffusivity. This implies that deformation of the confining unit will resemble that from *an underlying* point source early in an injection project, and it will progress toward deformation similar to a thin plate with time.

The magnitude of deformation measured by an instrument will depend on the location of the instrument and a/H at the time of the measurement, and it will also depend on the pressure change, Δp in the reservoir and mechanical properties of the reservoir and overlying formation (Section 3.1.3.2).

Deformations determined with the analytical model (Sections 3.1 through 3.1.3.1), will be asymptotically accurate in the confining formation at distances from the pressurized reservoir that considerably exceed the reservoir thickness. Most reservoirs are thin relative to their depth, so the results are accurate across most of the formation above the pressurized region. They are also accurate from the ground surface to below the reservoir at radial distances greater than a. The results (Figure 3.2) are normalized to ε_1, so they only include the Poisson ratio of the confining unit (Section 3.1.3.2), which was chosen $\nu = 0.25$ in this Section.

Deformation along a radial profile at shallow depth of $z = 0.1H$ (Figures 3.2a and 3.2b) and along vertical profiles at $r = a$ (Figures 3.2c and 3.2d) were calculated to evaluate the general distribution of strains and tilts. The results show that strains and tilts respond to pressurization in distinct patterns that depend on a/H, and the pattern is particularly well defined when a/H is large. In this case (e.g., $a/H = 2$ in Figure 3.2a), the radial strain is positive (tensile) over the pressurized region, but it decreases and becomes negative (compressive) at approximately $r = a$ (dashed red line in Figure 3.2a). Compressive radial strains occur at significant distances from the well $r \gtrsim a$. The vertical strain is compressive over the pressurized region

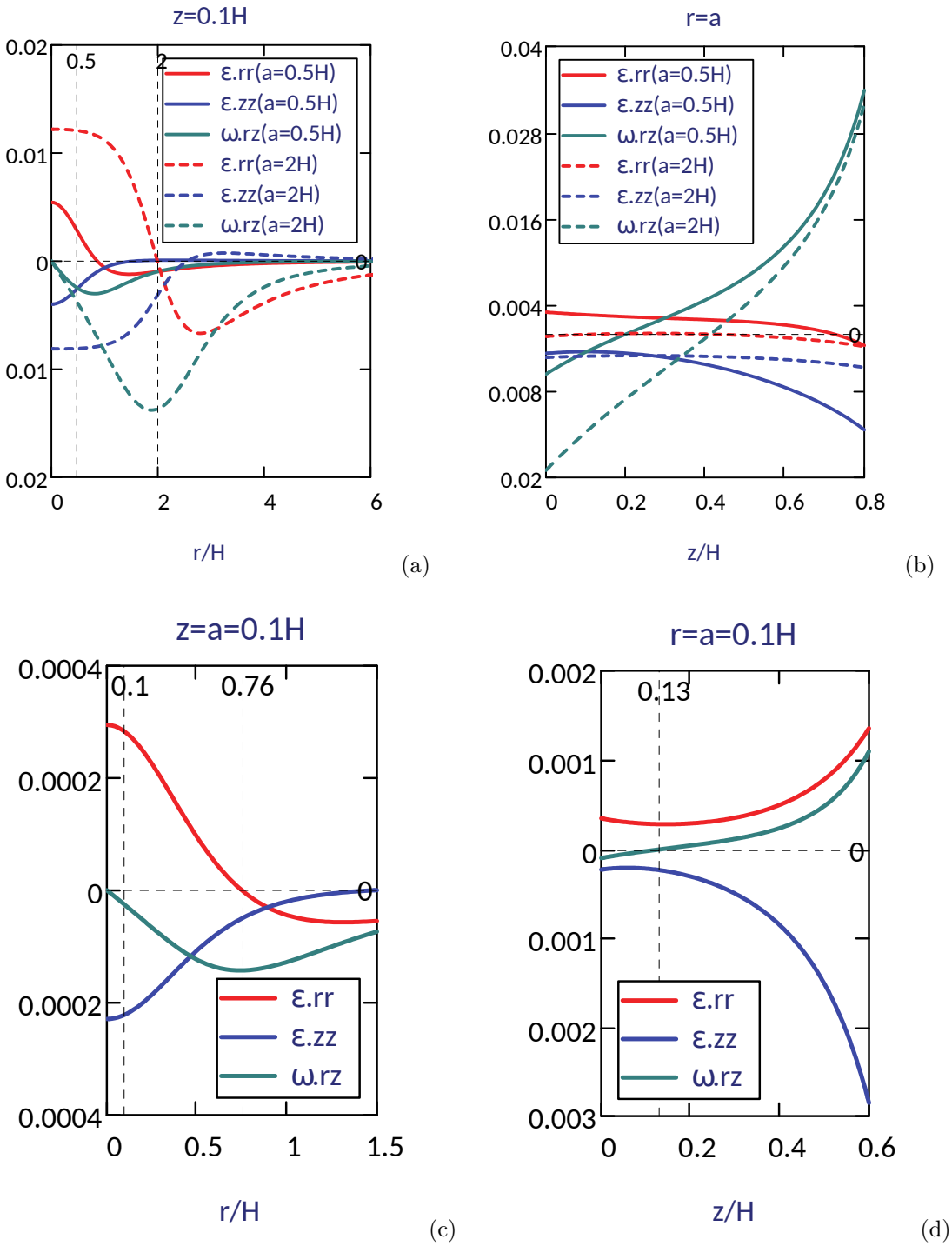

Figure 3.2: Strains, ε_{rr} and ε_{zz}, and tilt, ω_{rz}, normalized by the transformation strain, ε_0^*, in the equivalent inclusion (equation (3.10)) along radial and vertical lines for different values of a/H in the case of $\nu = 0.25$. (a) Radial profiles at shallow depth ($z = 0.1H$) for $a/H = 0.5$ and 2. (b) Vertical profiles at $r = a$ for $a/H = 0.5$ and 2. (c) Radial profiles at shallow depth ($z = 0.1H$) for a small or deep pressurized zone $a/H = 0.1$. (d) Vertical profiles at $r = a$ for a small or deep pressurized zone, $a/H = 0.1$.

$r < a$, but it goes to zero approximately at $r = a$, when $a/H = 2$ (dashed blue line in Figure 3.2a). The tilt ($\omega_{rz} = du_r/dz$), which could be measured with a borehole tiltmeter, is negative and reaches a maximum absolute value over approximately the edge of the pressurized region, $r = a$ (solid and dashed green lines in Figure 3.2a).

When the pressurized region is broad relative to its depth, the limits of the pressurized region are well defined by the deformation field (change in sign from tensile to compressive radial strain, significant decrease in vertical strain, and max in tilt), but this changes as the size of the pressurized region decreases. For example, when the pressurized region is $a/H = 0.5$, the radial strain changes sign at slightly less than $r \approx 2a$ (solid red line in Figure 3.2a). When the pressurized region is smaller or deeper (e.g., $a/H = 0.1$), the radial strain changes sign at an even larger distance ($r \approx 8a$) relative to the pressurized zone (red line in Figure 3.2c). The sharp reduction in vertical strain and change in sign of the tilt occur at roughly the same location as the change in sign of the radial strain for the different cases of a/H. The magnitude of the dimensionless strains also change significantly with a/H. For example, they are $\sim 10^{-4}$ when $a/H = 0.1$ (Figure 3.2c) and they increase to $\sim 10^{-3}$ to 10^{-2} as a/H increases to 0.5 or greater (Figures 3.2a and 3.2b).

Vertical profiles above the edge of the pressurized zone ($r = a$) show that the radial strain is tensile and vertical strain is compressive (Figures 3.2b and Section 3.1.3.2d). Tilt changes sign from negative at shallow depths to positive at greater depths, going to zero in the range of $0.15 < z/H < 0.3$.

A basic pattern of the strain distribution emerges from Figure 2, but in order to evaluate actual strains we turn to the example parameters $E = E_1 = 15$ GPa, $\nu = \nu_1 = 0.25$, $\alpha = \alpha_1 = 1$, and $\Delta p = 1$ MPa. We reviewed the properties of different formations (Murdoch et al., 2015), and we used properties typical of a depleted oil reservoir to conduct a baseline analysis. Owing to (3.10), the transformation strain in the equivalent inclusion is $\varepsilon_0^* = 1 \times 10^{-4}$. This indicates that the magnitude of strains at shallow depths will be 0.01 με (10^{-8}) when $a/H \approx 1$, but they will increase to 0.1 to 1 με (10^{-7} to 10^{-6}) as a/H increases to ∼0.5 or more. Increasing the stiffness of the reservoir to $E_1 = 30$ GPa yields $\varepsilon_0^* = 0.5 \times 10^{-4}$, which indicates the strains will change by a factor of 1/2 when the stiffness of the reservoir doubles. This can also be seen directly from (3.21), which shows that $\varepsilon_0^* \propto E_1^{-1}$.

3.1.4 Implementation

The analytical solution outlined above was originally implemented using the software Mathcad. That software was used to support and check the derivation, and it was a logical choice to obtain solutions to the resulting integrals. However, it is cumbersome to use the Mathcad software in applications involving external programming languages, like Fortran, Python, or Matlab. Moreover, the solution outlined above gives rise to a lengthy expression, which could limit implementation.

To address these limitations we have developed a Python implementation of the analytical solution (equation (3.20)). Analytical expressions were simplified and expressed as a set of mathematical functions, and integrals were approximated numerically. This runtime of this model was on the order of 0.5 milliseconds. The Python code is given in Appendix 3.A, and is available in NETL the code repository. We ran a series of inversions using this analytical solution as the forward model. The runtime of this model is brief and the number of parameters involved is low (2 and 3, respectively), so we used a simple Monte Carlo approach to explore the entire parameter space thoroughly and uniformly.

One inversion (Figure 3.3) used synthetic strain and displacement measurements taken from instruments assumed to be in a shallow boring above the inclusion, similar to our field site. The inclusion is referred to a "channel" in 3.3 because we assume it represents an alluvial channel deposit similar to the deposits at the North Avant Field field site. The width and length of the channel identified by the inversion are the correct width and length.

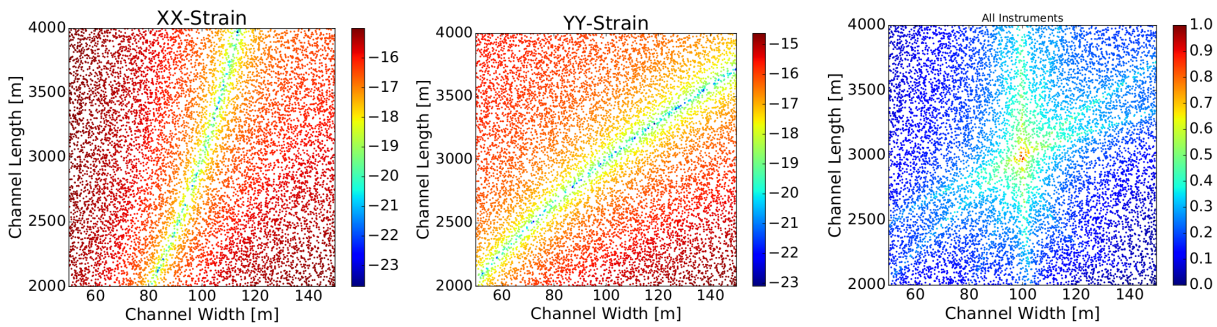

Figure 3.3: Data-model misfits for strain along the x-axis (left), strain along the y-axis (center) are shown as a function of the cuboid channel length and width. The posterior probability (right) combines information from both strain components.

The ability to identify the channel geometry was evaluated by calculating the data-model misfits as a function of the length and width of the channel. The inversion process identifies a band where the fit with synthetic ε_{xx} is good. Another band is identified when the fit with ε_{yy} is used. These bands indicate that there is some tradeoff when inverting using only one component of strain. However, a unique combination of width and length of the inclusion is identified when using both strain components (Figure 3.3). This suggests that indicate that the combination of several components of strain can resolve the width and length of the channel when the physical parameters are known.

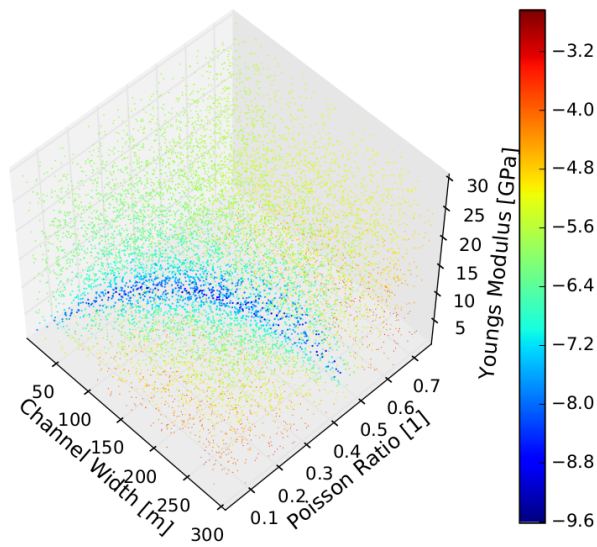

Figure 3.4: Data-model misfits for strain are shown as a function of the cuboid channel width, Poisson's ratio, and Young's modulus.

Another test case determined the misfit (Figure 3.4) for one geometric parameter (the channel width), and two physical parameters (Poisson's ratio and Young's modulus). We were able to identify a small, cone-shaped region of the parameter space that fit the data well. This result shows that the analytical solution can fit the data, but the analysis can indicate tradeoffs that constrain parameters to certain ranges. This type of non-unique result is common when interpreting the subsurface, and we expect that using the strain data will help tighten the constraints on range of identified parameters.

3.2 Inversion for Interpreting Numerical Poroelastic Analyses

We have developed a highly parallelizable inverse problem solver that uses several inversion algorithms in parallel, searching the parameter space broadly and thoroughly, then selecting the most promising models to fine-tune them iteratively until a solution emerges. This approach makes use of high-throughput computing to distribute computational effort over a large, heterogeneous set of compute nodes, which is necessary because 3D poroelastic problems of reservoirs can require tens of minutes to more than an hour to complete, and inversion problems can require many thousands of simulations.

The inverse problem solver includes three main components; 1) access to many compute nodes, 2) a set inversion algorithms, and 3) a centralized, highly structured database to retrieve and store the results of these simulations. These components would interact with the poroelastic forward model.

The compute nodes may be drawn from various resources such as OpenScience Grid (OSG), Amazon Web Services (AWS), or a university cluster computer. The inverse problem solver uses object-relational mapping to connect Python code (Oliphant, 2007), which is one of the more popular and well-supported scientific programming languages, with a MySQL database, which is a mainstay of many web services (Nuccio and Guerzoni, 2019). Storing inversion data in a relational database provides an efficient, scalable, easily managed method of storing the highly structured dataset necessary to support the various inversion algorithms.

The inverse problem solver provides a variety of standard options drawn from the inversion literature such as Monte Carlo (Metropolis and Ulam, 1949), Latin Hypercube (Stein, 1987), Markov chain Monte Carlo (McMC) (Hastings, 1970), gradient descent (Press et al., 2002), and genetic algorithms (Deb, 2002). However, it also allows one to combine these methods such that they can exchange information with each other and perform better than they would as stand-alone programs. We used an object-oriented approach to generalize the functions of an inversion algorithm (Figure 3.5), and to develop a set of methods implementing these functions. This allows future researchers to "inherit" these functions when developing and implementing their own inversion algorithms, making it easier to integrate new algorithms into this parallelized framework

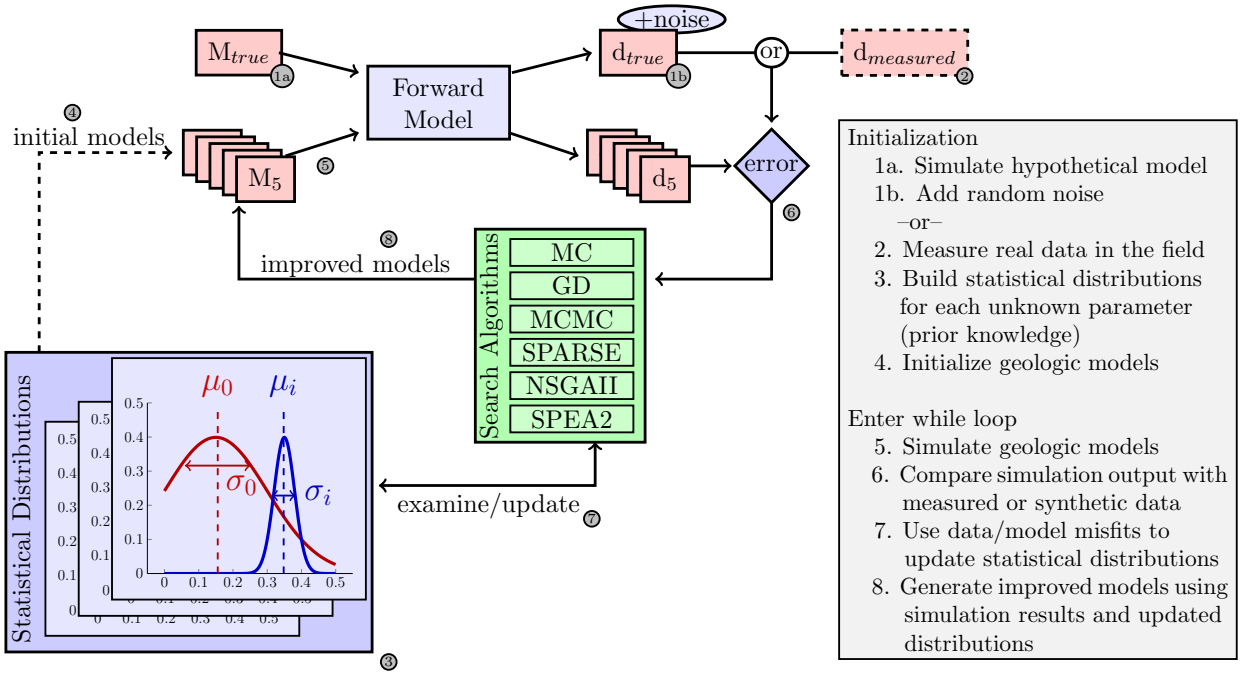

Figure 3.5: Illustration of parallel model calibration process. A hypothetical model M_{true} is run through the forward model to generate a synthetic dataset, d_{true}. Alternatively, field observations can be collected d_{measured}. A series of random models (M_i) are then generated based on our prior model (mean μ_0, variance σ_0) and evaluated by the forward model to produce simulated datasets (d_i) which are then compared to the measured or synthetic dataset. These comparisons are used by a variety of inverse algorithms including Monte Carlo (MC), Gradient Descent (GD), Markov Chain Monte Carlo (McMC), space-filling algorithms such as Latin Hypercube or Voronoi method (Sparse), genetic algorithms (NSGA-II, SPEA2). These algorithms use data-model comparisons to produce iteratively improved models and thereby reducing uncertainties and providing a better characterization of the posterior distribution (mean μ_i, variance σ_i).

without new users having to replicate or even fully understand the details of the process by which their simulations are distributed to the compute nodes.

We evaluated the performance of the various optimization algorithms, and we determined a combination of the Latin Hypercube and Non-dominated Sorting Genetic Algorithm II (NSGA-II) was ideal for this problem. One reason is that the data-fitting problem is often multi-modal, so a gradient-informed method such as Gradient Descent or McMC would often be at risk of finding a local minimum and neglecting the rest of the parameter space. Gradient methods are also sequential in nature, making parallelization more challenging. By contrast, the Latin Hypercube and NSGA-II methods are less sequential and can be used to quickly assemble a large number of models to suit the number of cores currently available. Since the runtime of the geomechanical simulation is so long, we found that distributing computational effort over a wide range of computational core was essential to completing the analysis in a reasonable time.

3.2.1 Database Design

The inversion code has each been implemented in Python using a modular, object-oriented approach that mirrors the structure of the database, with one class definition per database table (Figure 3.6). Classes and tables are synchronized using SqlAlchemy, a popular object-relational mapping software. This approach allows the use of external Python libraries such as `numpy` and `scipy` (math and statistics functions), `matplotlib` (graphics and visualization), and `boto` (AWS file transfer and job management).

An abstract class (Optimization) contains general definitions for all the basic operations that any inversion algorithm must be able to perform, while each specific inversion algorithm inherits these definitions and adds some distinct code detailing how these operations are to be performed.

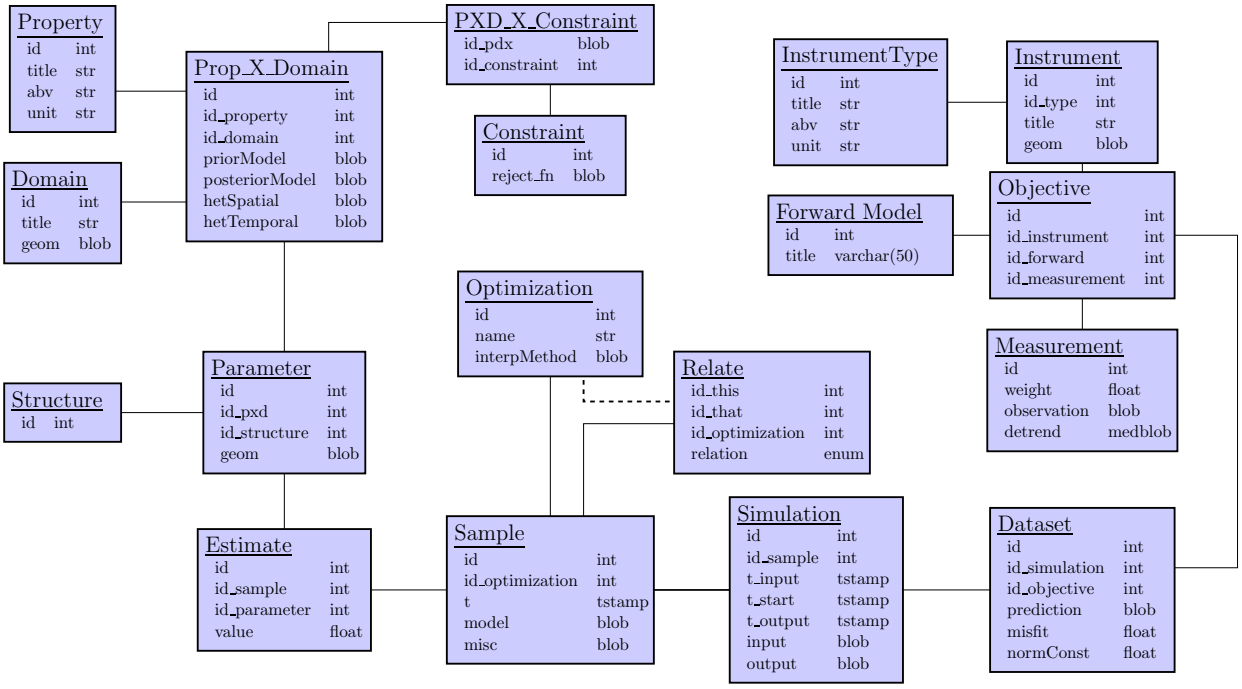

Figure 3.6: Entity-Relationship diagram for the inversion database. Blue boxes indicate tables in the database, while lines indicate the cardinality relationships between tables.

The physical properties of interest (i.e, density, permeability, compressibility) are listed in the Property table, and the physical domains of interest (i.e., distinct rock layers) are listed in the Domain table. The Prop_X_Domain table defines a particular Property of a particular Domain using a statistical distribution, the prior model. Two or more Prop_X_Domains may be related by the Constraint table, which contains a rejection function that tests whether a particular combination of parameter values is feasible for the forward model. This allows us to define the feasible parameter space as any arbitrary shape rather than simply as an n-dimensional hypercube. The Parameter table lists the unknown parameters in our particular inverse problem. It is conceptually similar to the Prop_X_Domain table, but remains a distinct table to allow for the special case of a tomography or imaging problem, where many parameters may describe a single pixel or voxel of a given structure but all have a common underlying statistical distribution.

The types of instruments installed in the field (i.e., pressure sensor, temperature probe, humidity etc) are listed in the InstrumentType table while specific instruments are listed in the Instrument table with their name and location. In general, each instrument corresponds to a distinct entry in the Objective table, however when there are multiple forward models available to attempt to simulate the behavior of an Instrument, there may be multiple Obective entries for a single Instrument. An Objective may relate to the Measurement table, where synthetic measurement is stored or where actual measurements from the field are periodically uploaded.

Once these database tables are populated, the inversion process can begin. The basic function of the Optimization object is to create an entry in the Sample table, create one entry in the Estimate table for each Parameter, use these estimates to build a set of input files in a format appropriate for the physics solver being used, then create an entry in the Simulation table and stores the input files in this table. The input files are then uploaded to the Amazon Simple Storage Service (S3) where it can be retrieved by any remote machine with both the appropriate credentials and the S3 object key, a string of characters which uniquely identifies that particular set of input files. The object key is then posted on the Amazon Simple Queue Service (SQS), another AWS service which maintains the integrity of the simulation queue. A variety of remote machines can then periodically check this queue to see if any new input files are available for evaluation, without the risk that any two compute nodes will be served the same S3 object key and thus duplicating one another's work or causing table locking by attempting to modify the same database entry simultaneously. Each compute node then uses their unique S3 object key to download the appropriate set of input files, uses them to run a (perhaps computationally intensive) physical simulation, and performs any necessary post-processing to extract the expected sensor responses from the larger output file. Since our sensors are generally relatively sparse compared to the scope of the simulated region, the post-processed summary file is generally much smaller. The raw simulation output files are then uploaded to long-term storage in an appropriate S3 bucket (or discarded if the storage cost is judged prohibitive), while the summary file is sent to short-term storage in a separate S3 bucket so it may be later downloaded by the head node. The head node then stores the simulated sensor predictions in the Dataset table. The prediction is compared to the field data stored in the Measurement table to arrive at a prediction-observation misfit.

Once prediction-observation misfits are available, each specific implementation of the Optimization object uses a unique strategy to interpret data-model misfits and assemble progressively better input files. These strategies are described in detail in the following section. Many of these strategies involve relating one Sample to another, so these relationships are defined in the Relate table.

3.2.2 Latin Hypercube

The Latin hypercube (Stein, 1987; Helton and Davis, 2003) is an n-dimensional generalization of the Latin square (Figure 3.7), a combinatorial puzzle where n different symbols are arranged in a table such that each symbol appears in exactly one column and exactly one row. The

1	2	3	4
2	4	1	3
3	1	4	2
4	3	2	1

Figure 3.7: The Latin Square.

Latin hypercube inversion method subdivides the parameter space into a regular grid of arbitrary grid size, and then samples from this grid such that each parameter is allowed to vary with respect to all other parameters. Latin hypercube methods are commonly used in experimental design where a large number of unknowns are being investigated using a limited number of experiments or simulations.

3.2.3 NSGA-II: Pareto Rank-Based Fitness, Elitism and Niche Formation

One of the inversion algorithms we relied upon heavily was the Non-dominated Sorting Genetic Algorithm II (NSGA-II) (Deb, 2002), a popular multi-objective genetic algorithm. Genetic algorithms randomly select solutions from a population and either combines their parameters or discards them depending on how well they fit the data. This process generally resembles natural selection in genetics. NSGA-II builds upon standard concepts of genetic algorithms using Pareto ranking, elitism and niching to explore the complex, high-dimensionality relationships that can exist between a parameter space and an objective space.

Elitism refers to the selection of a set of solutions that remain in the population regardless of any stochastic selection criteria that might otherwise remove them. Genetic algorithms have a stochastic random selection step that sometimes results in good solutions being discarded without being properly evaluated. NSGA-II uses elitism to preserve all rank 1 solutions, whether or not they are selected.

Niche formation uses clustering to prevent solutions from being too similar to each other and therefore ignoring promising areas of the parameter space. The NSGA-II algorithm uses a distance formula to penalize solutions that are too close to each other, promoting the further exploration of sparse areas along the rank 1 Pareto front.

Pareto ranking is one approach to characterizing misfit among multiple objectives. In an ideal optimization analysis, one unique set of model parameters would be identified that explain all data sets equally well. However, analyses using real data rarely achieve this ideal result. Consider an example where two datasets are used to evaluate a simulation. For poroelastic problems, one dataset could be the normal strain in the x direction, ε_{xx}, and the other could be ε_{yy}. The simulation predicts ε_{xx} and ε_{yy} at the location of a strain sensor in the field, and the root mean square (RMS) error is calculated as the misfit between the field data and a simulation. Then a set of simulations is conducted with different values of parameters and the data-model misfit is calculated for both ε_{xx} and ε_{yy} for each set of parameters. Some datasets will give a good fit to ε_{xx}, but a poor fit to ε_{yy}, whereas the opposite will be true for other solutions. One approach to evaluate the overall fit is to sum the RMS errors for all the datasets into a single value representing the overall error. The RMS error for each dataset can be multiplied by a parameter to weight the importance of that dataset in the overall error. One problem with this approach is the results are heavily dependent on the weighting parameters, which can be difficult to identify objectively. Weighting parameters are often selected based on judgment and experience, and this can introduce a bias in the results that is difficult to evaluate. Moreover, this approach overlooks the tradeoffs that are made between the misfit to each dataset.

The Pareto approach instead evaluates the data-model misfit using a ranking system that highlights tradeoffs. The ranking approach can be visualized by plotting the RMS misfit for ε_{xx} as f_1 on the abscissa and the misfit for ε_{yy} as f_2 on the ordinate (Figure 3.8). Solution 1 fits the ε_{xx} strain better than Solutions 2 and 3, whereas Solution 2 fits the ε_{yy} strain better than Solutions 1 and 3. Solution 1 is therefore the best in objective f_1 and second best in f_2 whereas Solution 2 is the best in f_2 and second best in f_1. Solution 3 is worse than both Solutions 1 and 2 in both f_1 and f_2 (Figure 3.8).

One way to visualize the relative ranking of the three solutions is to consider the colored rectangles defined by their position on the f_1 and f_2 axes (Figure 3.8). No other points plot in the pink rectangle defined by Solution 1, and no other points plot in the purple rectangle defined by Solution 2. However, Solution 1 and 2 plot in the green rectangle defined by Solution 3. This approach is used to define the Pareto ranking. Solutions like 1 and 2 that define rectangles containing no other points are Pareto rank 1, whereas solutions

that define rectangles that only contain rank 1 points are Pareto rank 2. This allows all the solutions to be ranked, and the Pareto ranking provides a basis for considering tradeoffs among solutions that fit the data well. In Figure 3.8b, several ranks are identified and color-coded. The *Pareto front* is the best tradeoff between the misfits, and the rank 1 simulations are the set of solutions that best represent the Pareto front. The approximate Pareto front is readily visualized using 2 objective functions, as in Figure 3.8b, and the concept is readily extended to multiple dimensions when more objective functions are used.

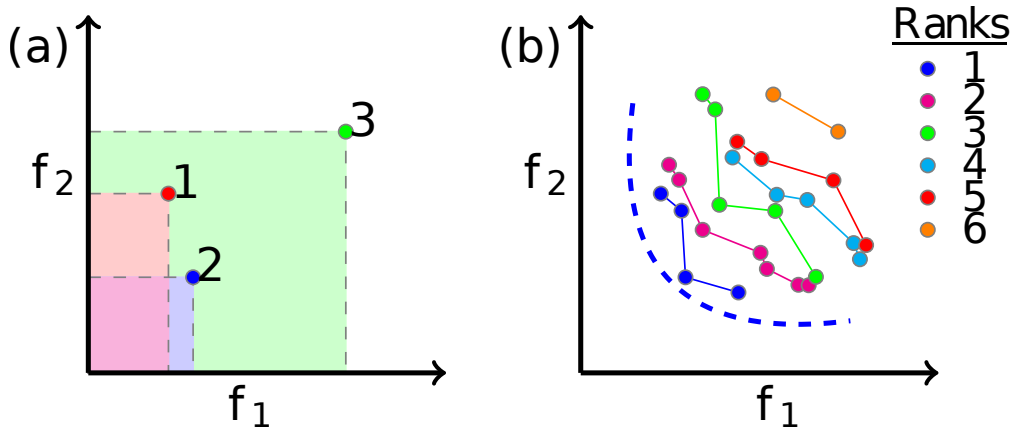

Figure 3.8: Illustration of Pareto optimality. (a) Results from three solutions plotted with respect to objective functions f_1 and f_2. Colored rectangles used to define Pareto Rank. (b) Pareto ranking used to characterize model-data misfit for a set of 26 simulations with different parameter sets.

3.2.4 Dynamic Parameterization of Heterogeneities

Distributions of material properties place a strong control on fluid flow. We are particularly interested in how strain data can be inverted to characterize the geometry of material heterogeneities that affect fluid flow or stress concentration. The possible geometry of geologic heterogeneities span a broad range, so it is typically necessary to adopt assumptions that narrow this range. One approach is the object-based method (Deutsch and Wang, 1996), where heterogeneities are specified as easily parameterizable shapes. For example a circular heterogeneity has three parameters, an x,y location and a radius. Three parameters can be quickly identified in many inverse problems, but a circular heterogeneity may lacks the necessary detail to fit the data adequately.

Another approach is where arbitrarily-shaped heterogeneities are constructed from a set of points, which are then adapted at each iteration. This method allows for a wider variety of geometries and may fit the data better, but requires more free parameters in the inverse problem and therefore a longer runtime. This is an example of a dynamic parameterization (Bodin and Sambridge, 2009), as the parameterization of the problem changes throughout the course of the inversion and is itself one of the unknowns to be inverted for. This is similar to the method of pilot points from Doherty (2003), drawn from the literature of geostatistics.

We combine these two approaches. Object-based inversions are used to quickly find a set of optimal models based on heterogeneities with simple geometric shapes. This set is then used as starting models for the more time consuming dynamic parameterization inversion. This efficiently finds irregular heterogeneities that best explain the data.

The field site for the project is underlain by permeable lenses that are equant to elongate in map view. We characterized these heterogeneities using object-based inversion for a circular geometry, and these results were then used to start an object-based inversion using elliptical geometries. The datasets from the circular

models along the Pareto front were mapped to the elliptical parameter space, so the search could take advantage of the results of the first step. This allows the more complex models to be evaluated in a narrower parameter space.

The third step is to use the dynamic parameterization approach. This approach starts with the elliptical models at the Pareto front, and then searches for improvements by adjusting the geometry and allowing it to deviate from the elliptical shape. Arbitrary "chunks" of permeable material are added or removed along the outer edge of the heterogeneity, and if these changes explain the data better or equivalently well they are accepted and further refined, leading to heterogeneities with complex irregular shapes. Characterizing heterogeneities in general might ordinarily be computationally intractable due to the huge number of free parameters, we use the results of the previous circular and elliptical inversions as starting models, allowing the inversion to start close to the right answer.

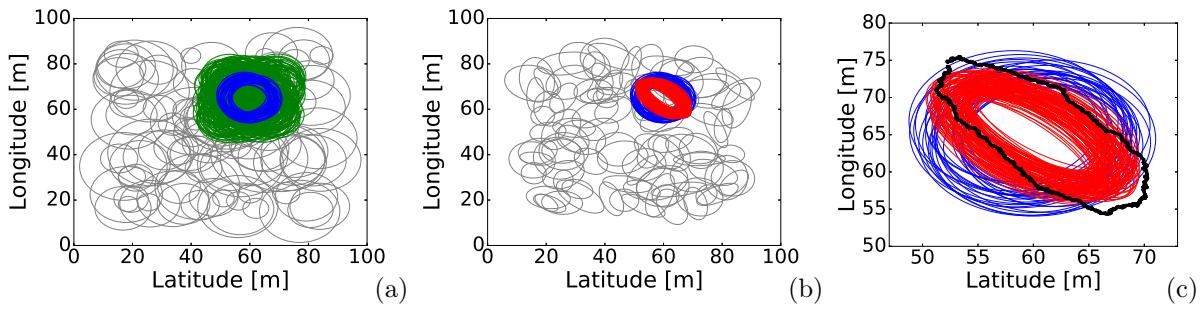

Figure 3.9: Three stage process for heterogeneity inversion. (a) Stage 1, heterogeneity assumed to be circular. Gray circles are from the Latin Hypercube search of the entire space, whereas green circles are from the genetic algorithm result, and blue circles are the best-fitting circular models; (b) Stage 2, heterogeneity assumed to be elliptical. Gray ellipses are the second-stage Latin Hypercube search, red ellipses are best fits found using the genetic algorithm. (c) Stage 3, heterogeneity assumed to be irregular. Blue and red ellipses are from (b) Black line is the irregularly shaped heterogeneity identified by the genetic algorithm as the final result.

3.3 Strain Type-Curve Analysis

In-situ pore fluid pressures during fluid injection or extraction have long been measured to estimate formation properties, or to indicate potential problems like the creation of fractures. One drawback to pressure monitoring is that the pressure signal is limited to the targeted reservoir or aquifer, so measurements require wells completed in the formation. These wells can be expensive to drill, and this limits the availability of pressure data, particularly for deep formations.

Changes in pore fluid pressure from injection or recovery deforms the enveloping formation. This strain field expands outward away from the well and it potentially reaches the ground surface. The strain field results from changes in fluid pressure in the subsurface, so it is possible that strain data could be interpreted to obtain information similar to that estimated from analyses of pore fluid pressure. Borehole strainmeters capable of measuring small deformations are available, and new designs are under development. It may be feasible to measure strains at shallow depths that result from injection into much deeper formations.

One approach to developing a useful method of interpreting strain data is to use numerical inversion of poroelastic numerical models, which are capable of simulating the strain field resulting from injection or extraction. Poroelastic simulations can be slow and many simulations can be required for numerical inversion, so simplified interpretation methods that provide initial parameter estimates can be useful. Moreover, numerical inversion may be impractical for some applications.

Transient pressure signals from hydraulic well tests have been analyzed using analytical solutions since long before the computing capabilities made numerical inversion feasible. Graphical methods of matching simulated values with observed data can be manipulated to estimate hydraulic diffusivity, transmissivity, and other parameters (Cooper and Jacob, 1946; Streltsova, 1988). Analytical solutions describing strain during well testing are limited, so the approach that served the interpretation of pressure signals for many decades has been unavailable for interpreting strain data.

We noticed that the strain signal predicted by numerical simulations resembled the shape of the pressure signal in analytical solutions used for well testing. The pressure and strain both could be approximated as a function of the logarithm of time after an initial period. We hypothesized that this similarity could be exploited to improve interpretation. The objective of this paper is to evaluate this hypothesis with the goal of simplifying preliminary analyses of strain data resulting from injection or extraction wells.

3.3.1 Analysis

Strain in the vicinity of an injection well will be analyzed using linear elastic poroelasticity (Detournay and Cheng, 1993; Wang, 2000). Conservation of momentum on the solid with Hooke's Law gives (Wang, 2000)

$$G\frac{\partial^2 u_i}{\partial x_k^2} + \frac{G}{(1-2\nu)}\frac{\partial \varepsilon_{kk}}{\partial x_i} = \alpha\frac{\partial P}{\partial x_i} \tag{3.23}$$

where u_i is displacement of the solid in the ith direction, G is the drained shear modulus, ν is the drained Poisson's ratio, ε is strain, and α is the Biot-Willis coefficient. Conservation of mass of the fluid at constant and uniform density leads to (Wang, 2000)

$$-\frac{\partial q_i}{\partial x_i} = \frac{1}{M}\frac{\partial P}{\partial t} + \alpha\frac{\partial \varepsilon_{kk}}{\partial t} \tag{3.24}$$

where q_i is the volumetric flux vector, p is the pore pressure, and M is the Biot modulus. The volumetric flux is

$$q_i = -\frac{k}{\mu}\frac{\partial}{\partial x_i}\left(P + \rho\, g\, x_3\right) \tag{3.25}$$

where k is the permeability, ρ is fluid density, μ is dynamic viscosity, g is gravitational acceleration, and x_3 is the upward coordinate.

Strain is given by

$$\varepsilon_{kk} = \frac{\partial u_k}{\partial x_k} \tag{3.26}$$

3.3.1.1 Geometry and Boundary Conditions

The geometry of the problem consists of a permeable aquifer or reservoir of thickness, b, overlain by a confining unit of thickness, d, and underlain by a confining unit of thickness, b_L. A well screen is assumed to fully penetrate the permeable aquifer and the volumetric flux is uniformly distributed over the well screen.

The permeability of the confining layer is small so leakage out of the aquifer is negligible. The lateral boundary is far from the well ($r_{max} = 100$ km) so there is no effect of the lateral boundary over the duration of the simulation.

The analysis is conducted using axial symmetry over $(r_{well} < r < r_{max}, -(d + b + b_L) < z < 0)$. The boundary conditions for (3.23) consist of zero normal displacement (roller) along the bottom and outer boundary, and along the inner boundary where it contacts the confining unit. The total stress is set equal to the fluid pressure where the inner boundary contacts the reservoir, and the total stress is set equal to zero at the ground surface. Boundary conditions for (3.24) assume zero normal pressure gradient (no flow) everywhere except where the aquifer intersects the inner boundary of the reservoir. The fluid flux is specified along the inner boundary.

3.3.1.2 Scaling

The characteristic strain is the transformational strain given by

$$\varepsilon_0 = \frac{\alpha P_c}{K} \tag{3.27}$$

where P_c is a characteristic pressure.

The characteristic length, L_c, is the depth to the top of the pressurized layer, so

$$L_c = d \tag{3.28}$$

The characteristic pressure during constant rate injection, Q, is

$$P_c = \frac{Q\mu}{kd} \tag{3.29}$$

The characteristic time is

$$t_c = \frac{L_c^2}{D_{hs}} \tag{3.30}$$

where the horizontal hydraulic diffusivity in the reservoir is taken as:

$$D_{hs} = \frac{T}{S_s b} = \frac{k}{\mu\left(\frac{1+\nu}{3K(1-\nu)} + \frac{\varphi}{K_f}\right)} \tag{3.31}$$

and the bulk modulus is

$$K = \frac{2G(1+\nu)}{3(1-2\nu)} \tag{3.32}$$

and the uniaxial specific storage, S_s, defined as (Wang, 2000)

$$S_s = \frac{1}{K_v} + \frac{\varphi}{K_f} \tag{3.33}$$

which assumes incompressible grains. The uniaxial bulk modulus, K_v, is related to the bulk modulus as (Wang, 2000)

$$K_v = \frac{3K\left(1-\nu\right)}{1+\nu} \tag{3.34}$$

Transmissivity of the reservoir is

$$T = \frac{kb\gamma}{\mu} \tag{3.35}$$

The dimensionless time, pressure change, strain, and coordinates follow respectively as

$$t^* = t/t_c \tag{3.36}$$

$$\Delta P^* = \Delta P/P_c \tag{3.37}$$

$$\varepsilon^* = \varepsilon/\varepsilon_0 \tag{3.38}$$

and

$$r^* = \frac{r}{L_c};\ z^* = \frac{z}{L_c};\ x^* = \frac{x}{L_c};\ y^* = \frac{y}{L_c} \tag{3.39}$$

3.3.1.3 Comparison to Porous Media Solution

The poroelastic analysis is compared to analytical and numerical solutions where storage change is assumed to be proportional to pressure change, which is the typical assumption for the analysis of hydraulic well tests. The porous media analysis is conducted using the same geometry and boundary conditions as the poroelastic analysis. The porous media analysis uses the uniaxial specific storage (equation (3.33)).

The analyses were compared to the late-time drawdown in a confined reservoir, which is given by (Cooper and Jacob, 1946)

$$\Delta P = \frac{\ln\left(10\right)Q\mu}{4\pi kb}\log\left(\frac{2.25Tt}{r^2S_sb}\right) = \frac{\ln\left(10\right)P_c}{4\pi b^*}\log\left(2.25t_p^*\right). \tag{3.40}$$

Taking the product of time and the derivative of time yields

$$t\frac{d\Delta P}{dt}\frac{1}{P_c} = t^*\frac{d\Delta P^*}{dt^*} = \frac{1}{4\pi b^*}, \tag{3.41}$$

where $b^* = bL_c$. So,

$$4\pi b^* t \frac{dP}{dt} \frac{1}{P_c} = 1, \tag{3.42}$$

and

$$t_p^* = t^* \frac{1}{r^{*2}} \tag{3.43}$$

The results indicate that the pressure predicted using the poroelastic analysis is within a few percent of the pressure predicted by the porous media analysis (Figure 3.10a) when the uniaxial specific storage coefficient is used.

The scaled, semi-log derivative of both solutions increases and approaches unity (Figure 3.10b), which is consistent with equation (3.42). The approach to unity occurs over roughly an order of magnitude in time, between approximately $1 < t_p^* < 10$.

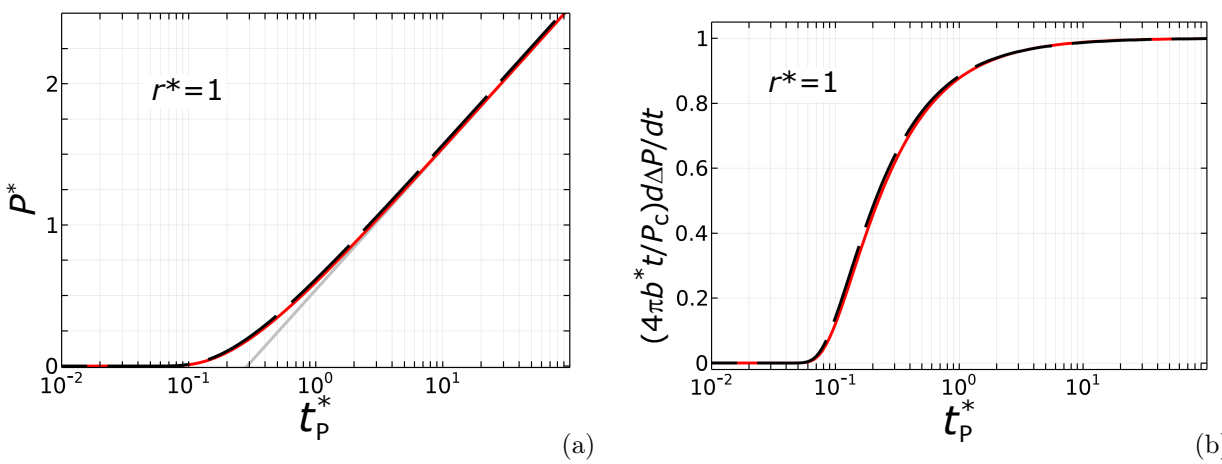

Figure 3.10: (a) Dimensionless pressure as a function of dimensionless time. Red line is porous media analysis using uniaxial specific storage equation (3.33), dashed line is poroelastic analysis, gray line is based on equation (3.40). (b) Scaled semi-log slope of reservoir pressure according to equation (3.42) for analysis assuming porous medium with uniaxial specific storage (red) and poroelastic analysis (black dashed).

3.3.2 Strain Transients

The normal strain components increase in magnitude as a function of time during injection. At shallow depths, the horizontal strain increases (becomes more tensile) and becomes an approximate log function of time, similar to the pressure in the reservoir. At radial distances greater than approximately $r^* > 1$, the radial strain decreases as the formation is initially compressed, but then the sign reverses and it becomes tensile with increasing time (Figure 3.11). The vertical strain is compressive and it also increases as a log function of time (Figure 3.11).

The analyses were conducted using three different depths ranging down to roughly $d/2$. The results indicate that the shapes and magnitudes of the normal strains are only slightly sensitive to depth within the zone that was evaluated ($0.05 < r^* < 2.5$; $-0.06 < z^* < -0.46$). Tilt is highly sensitive to depth, however,

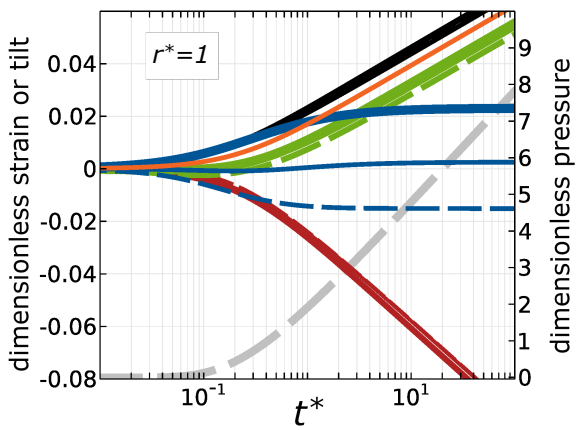

Figure 3.11: Dimensionless strain, tilt and pressure as functions of time at different depths at $r^* = 1$. Thick line is at $z^* = 0.06$, thin line is $z^* = 0.26$, dashed line is at $z^* = 0.46$. Gray dashed line is pressure in the reservoir. Red line is vertical strain, green is radial strain, black is circumferential strain, blue is tilt, orange line is average horizontal strain.

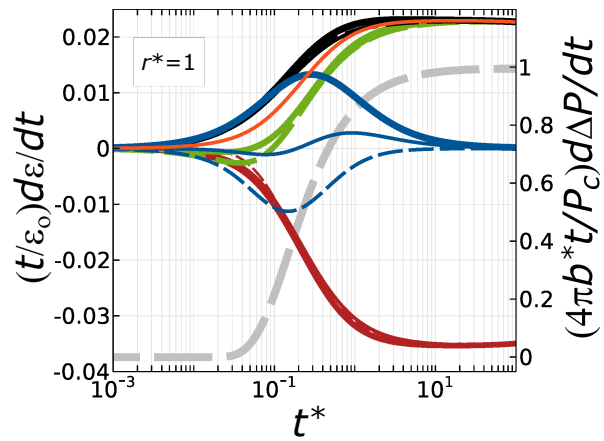

Figure 3.12: Semi-log slope of strain, tilt and pressure as functions of time at different depths at $r^* = 1$, based on data in Figure (3.11) . Thick line is at $z^* = 0.06$, thin line is $z^* = 0.26$, dashed line is at $z^* = 0.46$. Gray dashed line is pressure in the reservoir. Red line is vertical strain, green is radial strain, black is circumferential strain, blue is tilt, orange line is average horizontal strain.

changing sign over this depth range with tilts occurring away from the well at $z^* = 0.06$ and toward the well at $z^* = 0.46$, and tilts are negligible at the middle depth of $z^* = 0.26$ (Figure 3.11).

The semi-log slope of the scaled horizontal strains increase and becomes constant in the range of $1 < t^* < 10$ for $r^* < 2$ (Figure 3.12). Interestingly, the radial strain, ε_{rr}, and the circumferential strain $\varepsilon_{\theta\theta}$ follow the same semi-log slope (slope = 0.023). The average horizontal strain is

$$\varepsilon_h = \frac{\varepsilon_{rr} + \varepsilon_{\theta\theta}}{2} \tag{3.44}$$

and the semi-log slope of ε_h is the same as that of the radial and circumferential strains. The semi-log slope of the vertical strain (Figure 3.10) is steeper than that of the horizontal strains, and it also appears to be insensitive to depth within the evaluated interval. The results from Figure 3.12 indicate that

$$\frac{1}{\varepsilon_0}\frac{d\varepsilon_{rr}}{d\left(\log\left(t\right)\right)} = t\frac{\ln\left(10\right)}{\varepsilon_0}\frac{d\varepsilon_{rr}}{dt} = 0.023 \tag{3.45}$$

$$\frac{1}{\varepsilon_0}\frac{d\varepsilon_{\theta\theta}}{d\left(\log\left(t\right)\right)} = t\frac{\ln\left(10\right)}{\varepsilon_0}\frac{d\varepsilon_{\theta\theta}}{dt} = 0.023 \tag{3.46}$$

$$\frac{1}{\varepsilon_0}\frac{d\varepsilon_{zz}}{d\left(\log\left(t\right)\right)} = t\frac{\ln\left(10\right)}{\varepsilon_0}\frac{d\varepsilon_{zz}}{dt} = 0.035 \tag{3.47}$$

It follows that the transformation strain can be estimated from the strain data as

$$\varepsilon_0 = \frac{1}{0.023}\frac{d\varepsilon_{rr}}{d\left(\log\left(t\right)\right)} \tag{3.48}$$

$$\varepsilon_0 = \frac{1}{0.023}\frac{d\varepsilon_{\theta\theta}}{d\left(\log\left(t\right)\right)} \tag{3.49}$$

$$\varepsilon_0 = \frac{1}{0.035}\frac{d\varepsilon_{zz}}{d\left(\log\left(t\right)\right)} \tag{3.50}$$

The portion of the pressure and strain data that follows a semi-log straight line can be extrapolated backward in time to intersect the abscissa (Figure 3.13). When this is done with the pressure signal described by (3.40), the intersection occurs at

$$t_o = \frac{S_s b r^2}{2.25T} = \frac{r^2}{2.25D_{hs}} \tag{3.51}$$

and it follows that the hydraulic diffusivity can be estimated as

$$D_{hs} = \frac{r^2}{2.25t_o} \tag{3.52}$$

The normal strain data were extrapolated to the time when zero strain occurs, t_{oa}, and this time was compared to t_o determined from the pressure analysis at different radial distances. The strain was measured at shallow depth, $z^* = 0.06$, whereas the pressure was measured in the underlying aquifer at the same radial distance. Both times were determined by manually fitting a line to pressure or strain data determined using the numerical analysis (Figure 3.13).

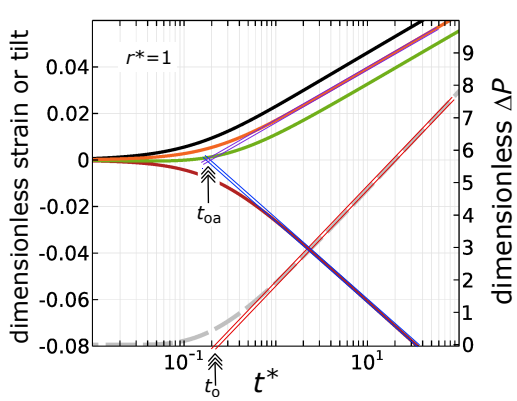

Figure 3.13: Dimensionless strain and pressure as functions of time. Lines fit to semi-log straight segments of vertical strain (red), areal strain (orange) and pressure (gray dash). Arrows point to t_o and t_{oa}.

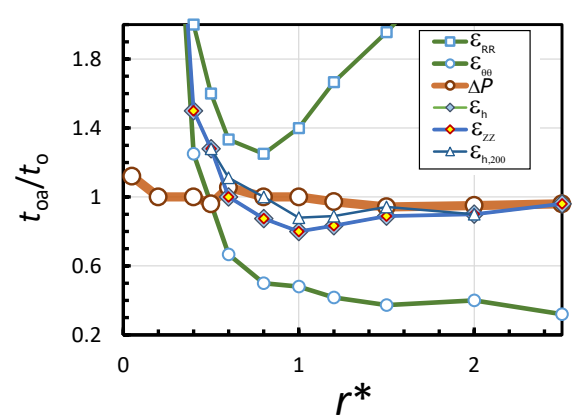

Figure 3.14: Ratio of the intercept time, t_{oa}, determined using strain data and t_o determined from pressure data as a function of r^*. Strain data determined at $z^* = -0.06$, except $\varepsilon_{h,200}$, which is at $z^* = -0.46$.

The results (Figure 3.14) indicate that t_{oa} determined from the strain data is similar to t_o from the pressure data in some cases. In particular, t_{oa} determined from the vertical strain and from the average

horizontal strain is within $0.8\,t_o < t_{oa} < t_o$ for measurement locations greater than approximately $r^* > 0.5$. Interestingly, the semi-log straight lines for the vertical strain and the average horizontal strain intersect at zero strain, so they give the same value of t_{oa} for all the cases that were evaluated. t_{oa} from radial strain is greater than t_o, whereas t_{oa} from the circumferential strain is less than t_o for $r^* > 0.5$. Values of t_{oa} are greater than t_o for normal strains in the vicinity of the well ($r^* < 0.5$).

3.3.3 Application

The analysis outlined above was applied to an injection test conducted at well 9A in the North Avant Field, Osage County, Oklahoma. Well 9A intersects the Bartlesville sandstone at a depth of 530 m and the sandstone is approximately 30 m thick. A 5-m-thick lens of coarse-grained sand occurs at the bottom of the formation and the well is completed in this lens. Similar lenses occur throughout the region and they are an important oil reservoir, so their location and thickness has been estimated by coring and well logs. The lens in the vicinity of Well 9A is approximately 1 km in lateral dimension (Figure 3.15), although the lateral extent is poorly constrained in several locations. Oil and water are pumped from the Bartlesville sandstone, and produced water is re-injected. Active wells are more than 1 km away and their rates were roughly constant during the test at 9A, so the other wells are assumed to have no effect on the injection test.

The well test was conducted by injecting produced water into well 9A for approximately 6 days. Injection rates decreased from 9×10^{-4} to 5×10^{-4} m^3/s, and 7×10^{-4} m^3/s was the average rate. The injection rate also varied on a 5 hour period. Variations in injection rate occurred because the water supply for the test was controlled by infrastructure associated with the operating oil field.

Water pressure was measured at three observations wells and at two, co-located borehole strainmeters at location AVN in Figure 3.15. The strainmeters are 215 m from well 9A, and monitoring Well 60 is approximately the same distance (235 m) from 9A. The strainmeters include a Gladwin strainmeter (Gladwin, 1984) and a new strainmeter designed for this project. The new strainmeter uses eddy-current sensors to measure horizontal and vertical strain, along with tilt. The Gladwin strainmeter measures the horizontal strain tensor. Both strainmeters were grouted into a 3-m-thick limestone bed at a depth of 30 m. Shale occurs below and above the limestone.

Pressure at Well 60 was measured with a submersible transducer (In-Situ Rugged TROLL), which was retrieved after the test. The pressure measurements were corrected for changes in barometric pressure, and adjusted for long-term trends. The Gladwin strainmeter was calibrated at the factory, and our strainmeter was calibrated in the lab. Both strainmeters were also calibrated in the field using Earth tides.

More information describing the North Avant Field and well tests is in Chapter Four.

3.3.4 Results

The results include analyses of the pressure signal at a depth of 530 m in the reservoir, and analysis of strain at a depth of 30 m from the AVN strainmeters.

3.3.4.1 Analysis of the Pressure Signal

Pressure at Well 60 increased as a function of time throughout injection and then decreased when injection ceased after approximately 5×10^6 s (Figure 3.16). The semi-log slope increased throughout injection, but the rate of increase diminished over $1 \times 10^5 < t < 2 \times 10^5$ s. We interpret this period to be the first semi-log straight segment of the test. Interaction between the pressure and lateral boundaries of the permeable lens

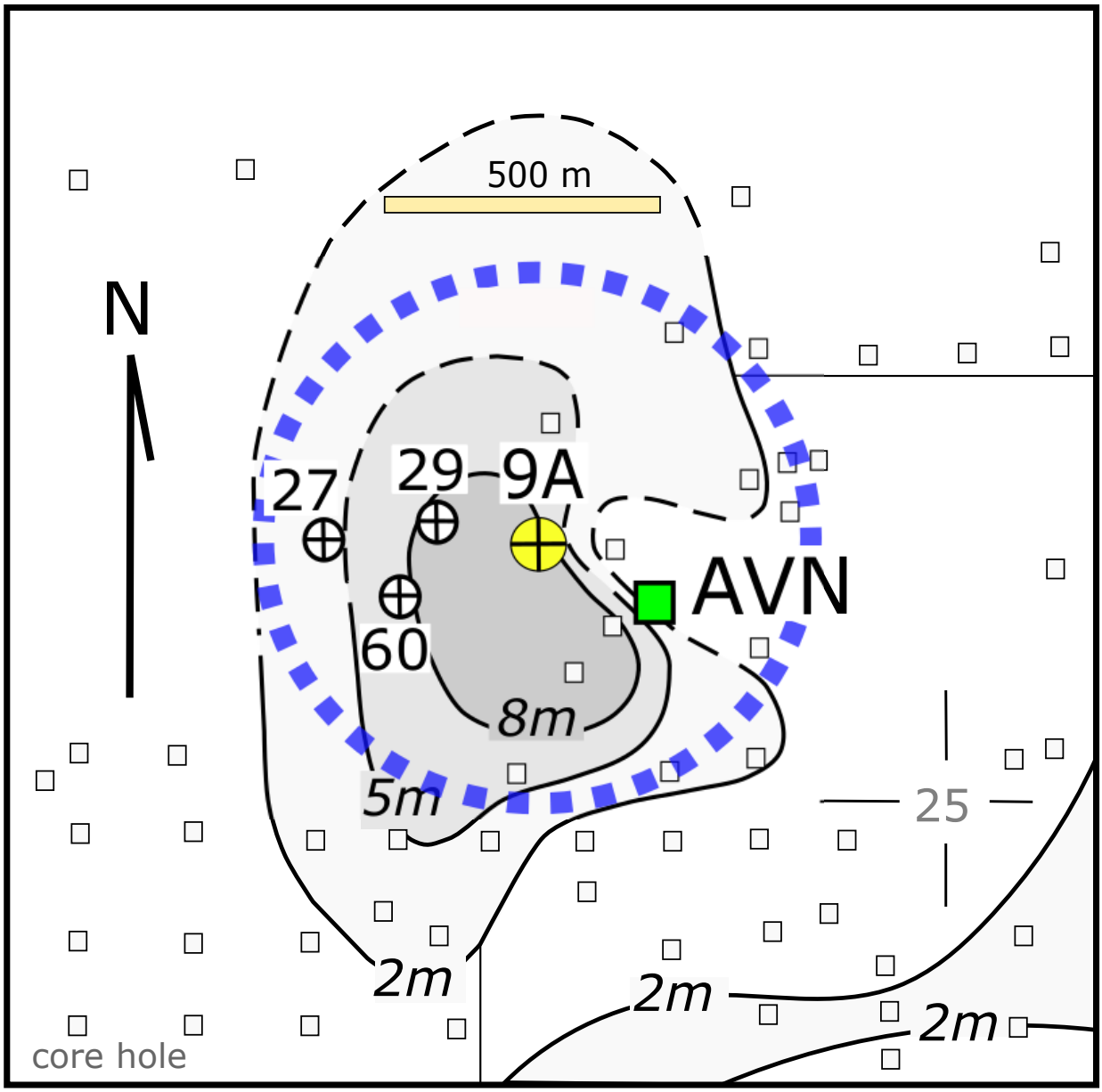

Figure 3.15: Location of the field test. Injection well 9A as yellow circle with cross, and pressure monitoring wells as white circle with cross. Shallow strainmeters at AVN. Contours are thickness permeable lens at base of Bartlesville sandstone in m, dashed where inferred. Purple dotted line is 500 m from well 9A. Open squares are locations of cores. "25" is center of Section 25 in T24N, R11E, in Osage County, OK, USA.

probably cause the semi-log slope to increase slightly over this period. The semi-log slope during this interval ranges from 2.6×10^5 Pa to 3×10^5 Pa, and 2.8×10^5 Pa is the average (Figure 3.16). The intercept is in the range $4.5 \times 10^4 < t_o < 5 \times 10^4$ s. The semi-log slope approximately doubles over $2.5 \times 10^6 < t < 3 \times 10^6$ s (marked by green line in Figure 3.16). This change in slope is assumed to result from interaction with the lateral boundary of the lens.

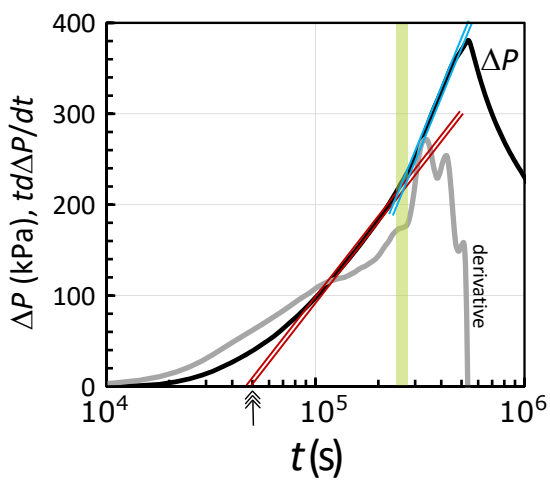

Figure 3.16: Drawdown, ΔP, and log derivative as functions of time at Well 60. Double red line is best fit to first straight section, double blue line is best fit to second straight section, green line is when slope changes. Arrow points to t_o.

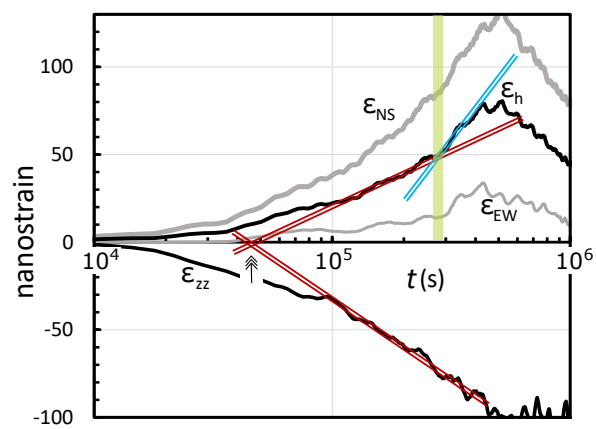

Figure 3.17: Strain at AVN2 as a function of time. Red double line is best fit to first straight segment, double blue line is best fit to second straight segment, green line is intersection of straight segments, blue arrow points to t_{oa}.

The results of the pressure signal indicate that the hydraulic diffusivity is $D_h = 0.5 \pm 0.03$ m^2/s, according to equation (3.52). Using equation (3.40) with the semi-log slope and the estimate of D_h gives the permeability as $k = 1 \pm 0.1 \times 10^{-13}$ m^2 . These values for k and K are within the range expected for the reservoir, which helps to confirm the interpretation of the pressure record. Those data indicate that the characteristic pressure is $P_c = 1.3 \times 10^4$ Pa, based on (3.29).

Interaction with a circular boundary causes the semi-log slope to increase. According to Streltsova (1988), the distance to the boundary of a circular lens enveloped by a much lower permeability material with a centrally located well can be estimated as

$$L_b = 1.5\sqrt{D_h t_b} \tag{3.53}$$

where t_b is the time when the semi-log straight lines intersect. Using $D_h = 0.5$ m^2/s gives $530 < L_b < 590$ m for the range of times indicated in Figure 3.17.

The isopach map (Figure 3.15) indicates the lateral extent of the permeable lens is 500 to 600 m from 9A to the south and east, and the lateral extent is poorly constrained by cores to the west and north. It seems feasible that the change in slope in the pressure record from Well 60 is a result of interaction with lateral boundaries of the permeable lens. Moreover, it suggests that t_b and D_h can be used to estimate the lateral extent of the lens, if cores or well logs were unavailable, for example.

3.3.4.2 Analysis of the Strain Signal

The horizontal strains become more tensile, whereas the vertical strain becomes more compressive with time (Figure 3.17), as predicted by the theoretical analysis (Figure 3.11). The slope of the plot increases with time, rather than becoming constant as in Figure 3.11. Scrutiny of the record indicates that the horizontal and vertical strains approach an approximately semi-log strain line over $1 \times 10^5 < t < 2 \times 10^5$ s. This is the same time interval identified as the first semi-log straight line on the pressure record from Well 60. The semi-log slope of the horizontal strains approximately doubles at $2.5 \times 10^5 < t < 3 \times 10^5$ s, which is the same time when the semi-log slope changes in the pressure record.

The semi-log slope of the average horizontal strain, ε_h, is 65 to 75 nε, and the slope of the vertical strain is $\varepsilon_{zz} = 95$ to 105 nε. The transformational strain follows from these slopes using equations (3.48) through (3.50), which gives

$$\varepsilon_0 = 3,000 \pm 200 \text{ n}\varepsilon \text{ from } \varepsilon_h$$
$$\varepsilon_0 = 2,900 \pm 200 \text{ n}\varepsilon \text{ from } \varepsilon_{zz}$$

Measurements of ε_h and ε_{zz} are from two instruments in different boreholes. They give essentially the same result for the transformational strain.

The first straight-line segments of the strain records were extrapolated to intersect the abscissa and t_{oa} was determined for both ε_h and ε_{zz}. The fitting and extrapolation were done manually. The results indicate that the intercept is in the range $4.5 \times 10^4 < t_{oa} < 5 \times 10^4$ s for analyses of both ε_{zz} and ε_h.

This finding is consistent with the theoretical analyses in Figure 3.13 where the semi-log straight lines fit to ε_h and ε_{zz} intersect at the abscissa in all the plots. The theoretical results indicate that the ratio t_{oa}/t_o is approximately equal to unity for $r^* > 0.5$ (Figure 3.14). The AVN strainmeters are approximately $r^* = 0.4$, but the data indicate that $t_{oa}/t_o \approx 1$ for this case. This suggests that it may be feasible to use shallow strain data to estimate t_o at radial distances slightly closer to the well than indicated by the idealized analysis used here.

3.3.5 Discussion

This is the first time to our knowledge that normal strain data has been used to estimate the properties and basic structure of a reservoir. The results indicate that the strain data give values of hydraulic diffusivity and location of a lateral boundary that are similar to results from a monitoring well. These results are consistent with theoretical analyses, and are based on simple interpretation of the data.

An important implication is that the strain data were measured at a depth of 30 m whereas the pressure data were measured in the reservoir at 530 m depth. This suggests that shallow strain data may provide characterization information that previously required the use of deep monitoring wells.

Gladwin strainmeters used for this work are currently unavailable, but we are developing new optical strainmeter instruments that promise to take their place. We have tested an optical fiber strainmeter next to the Gladwin strainmeter and they give essentially the same results for ε_h. Importantly, the new optical fiber strainmeter is based on a simple, robust design that can be constructed for a modest cost – a small fraction of the cost of drilling a well to 500 m, for example.

Strain measurements were interpreted using simple methods in order to demonstrate the information content in the data. We envision that simple methods, like the ones described here, could be used as a starting

point for more comprehensive analyses made using numerical inverse methods. Future characterization efforts may replace one monitoring well drilled into a formation with many shallow strainmeters, which could provide a rich data set for characterizing the structure of reservoirs used for carbon storage, hydrocarbon production, or other applications.

Tiltmeters have been used to measure deformation in the vicinity of reservoirs, but the tilt signal differs significantly from the normal strain. Tilt changes rapidly at the onset of injection, but it slows and the dimensionless tilt rate is smaller than that of the normal strains when $t^* \approx 0.2$ (Figure 3.12). As a result, it appears that the tilt signal is not amenable to the simple interpretation outlined here. Moreover, the tilt signal goes to zero and changes sign with depth, which further complicates acquisition and interpretation. The tilt signal appears to be useful, but a good monitoring strategy would be to include it along with measurements of normal strain.

3.3.6 Conclusions

Normal strains measured at shallow depths (30 m) over a 500-m-deep reservoir can be used to estimate properties using a simple approach similar to the one used to estimate properties from pressure measurements in monitoring wells. Theoretical analyses provide the basis for the approach, and it is validated by field data measured during an injection test in an oil-bearing confined aquifer. Estimates of hydraulic diffusivity derived from the shallow strain data are essentially the same as estimates made using pressure data from a monitoring well. The strain data can also be used to estimate the transformational strain, which in this case is 3,000 nε for two different strain data sets measured using different strainmeters. Using a characteristic pressure of 13 kPa gives a shear modulus of the formation of $K \approx 5$ GPa, according to equation (3.27). This value is in the range of measurements made on sandstone in the laboratory (Wang, 2000). The shallow strain data appear to respond to a lateral heterogeneity in the reservoir, suggesting the approach has the potential to contribute to the characterization of reservoir structure. Strainmeters used for this work were installed for a small fraction of the cost of drilling a monitoring well into the reservoir. This suggests that shallow strain data could reduce costs and/or improve resolution during characterization and monitoring aquifers or reservoirs for resource recovery or storage.

3.4 Analysis of Expected Strains at the North Avant Field Site

Field testing at the North Avant Field site will involve fluid injection into a reservoir while monitoring deformation using strainmeters and tiltmeters. The field tests conducted for the project were the first time strainmeters were used to monitor effects of injection, so the magnitude of the strain and the best locations for strainmeters were difficult to anticipate. To help plan the field tests, we utilized a combination of analytical and numerical models to predict the expected strain signal resulting from injection into well 9A at the North Avant Field. The reservoir at the North Avant Field includes high permeability sand lenses that are several hundred meters to several km in maximum dimension and that range from equant to elongate in plan view. These permeable lenses are inferred to have been deposited by a river flowing with high energy, and so locally they are called High Energy Channels (HEC). We are interested in how the permeable channels might affect the strain signal, so they were included in the analyses. The permeable lenses will be referred to as HECs, following local terminology. More information about the North Avant Field is given in Chapter Four.

The analytical models were developed based on complex potentials using conformal mapping, as described in Section 3.1. Numerical models were created using Comsol, a commercial finite element software package. The analytical models were used to simulate relatively simple geometries and to verify the numerical models. More geometrically complex scenarios of fluid injection at well 9A were modelled numerically to predict the expected strains for certain conditions.

3.4.1 Verification of Simulations with Analytical Solution

We developed analytical methods suitable for solving problems related to deformation that include complex shapes able to represent subsurface structures (Section 3.1) and (Germanovich and Chanpura, 2002; Germanovich et al., 2012)). This approach considers subsurface regions as pressurized inclusions, with deformation resulting from the pressure change. The analytical solution uses methods of complex potentials (e.g., Muskhelishvili (2013) and Germanovich et al. (2012)) and described in more detial in Section 3.1.

The numerical model was verified by investigating the deformation induced during pressurization of an ellipse in a homogeneous medium under plane strain conditions (Figure 3.18). An ellipse with dimensions $a = 400$ ft and $b = 25$ ft is embedded within an elastic solid. It is centered at a depth of 1,700 ft within an infinite half-space for the analytical model and within a medium 400,000 ft wide and 200,000 ft deep for the numerical model. In the numerical model, the ellipse is a highly permeable ($k = 1,000$ mD) poroelastic material and the confining medium is a non-permeable solid-elastic material. Initial pressure is zero and the center point of the ellipse was kept as a constant $p = 118$ psi. The elastic medium has no pressure. The Young's modulus $E = 10$ GPa, Poisson's ratio $\nu = 0.25$, and Biot-Willis coefficient $\alpha = 0.7$. For numerical models, the density $\rho = 2,500$ kg/m^3 and porosity $\varphi = 0.1$. Steady-state solutions were calculated for both models.

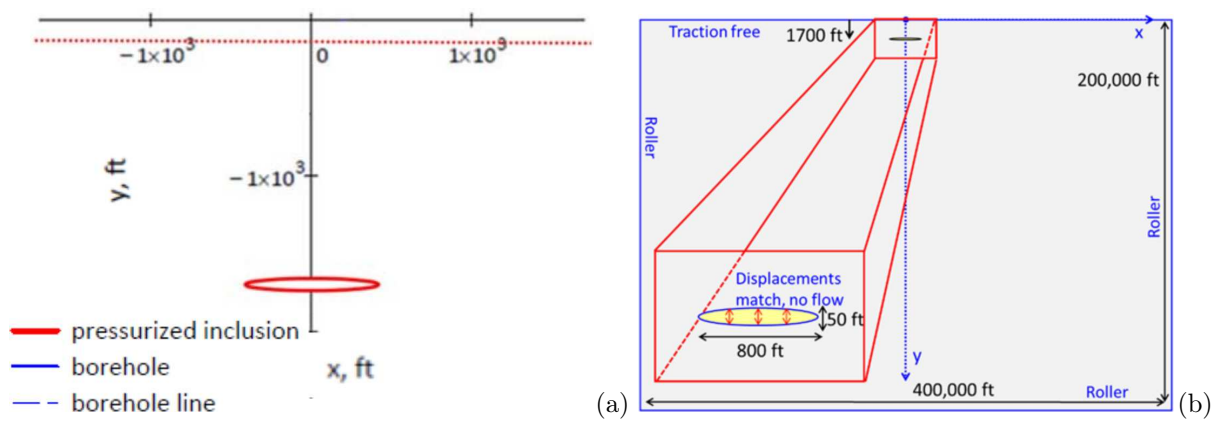

Figure 3.18: Geometry of a pressurized ellipse within an elastic medium, where red is the pressurized zone. (a) Analytical geometry of ellipse within an infinite half-space. (b) Geometry used for the numerical model.

This analysis confirms the validity of the numerical technique. The strain tensor matched for both the numerical and analytical models. The pressurized inclusion pushes the overburden upward and outward away from the injection site (Figure 3.19a). The calculated deformations are within ∼5% for the two solutions. Surface uplift is at a maxima at the origin (0.12 mm, 5×10^{-4} ft) and decreases gradually to ∼0.1 mm at 1,200 ft away from the center of the ellipse.

More realistic simulations can only be solved numerically, however, this analysis serves as a benchmark to the more complex models below. The HEC has a permeability two orders of magnitude greater than the overlying reservoir and several orders of magnitude greater than the confining layers. This analysis represents a simplified scenario where all fluid injection is contained within a HEC that is elongated in one direction.

3.4.2 Injection at 9A

Injection will occur in the HEC at well 9A. The injected fluid will raise the local pore pressure, which results in a pattern of deformation in the overburden that depends on the underlying permeability structure

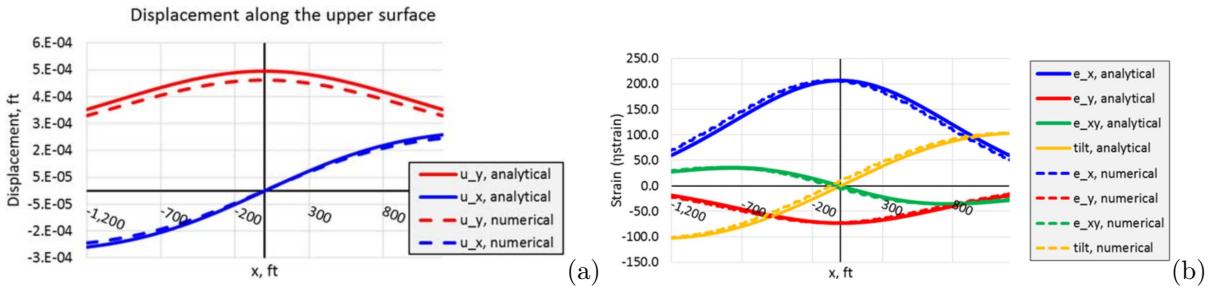

Figure 3.19: Comparison of analytical and numerical solutions of a pressurized ellipse. (a) Displacements along the surface. (b) Strain and tilt (du/dy) at a depth of 150 ft from the upper surface.

in the HEC. We developed 2D and 3D models to evaluate the effects of HEC geometry on the deformation pattern.

3.4.2.1 2D Model of HEC Inclusion

Strain resulting from injection into an HEC lens was evaluated in 2D using analytical and numerical models. Alluvial channel sands, like HECs, are likely to be much longer than they are wide, approaching plane strain conditions, such as those used in the analytical solution. In addition, three cases of different shapes of reservoirs were evaluated numerically (Figure 3.20). In one case, a single homogeneous reservoir 105 ft thick is at a depth of 1,735 feet (Figure 3.20a). The permeability of the reservoir $k = 80$ mD and porosity $\varphi = 0.25$. In the second case, a quarter-ellipse 30 ft thick and 1,000 ft wide is at the base of a 75-ft-thick reservoir (Figure 3.20b). A rectangular channel with identical length and wide replaces the quarter-ellipse for the third case (Figure 3.20c). For the second and third cases, reservoir properties are $k = 10$ mD and porosity $\varphi = 0.15$ and channel properties are $k = 1,000$ mD and porosity $\varphi = 0.25$. The K_v/K_h ratio is always 0.75 within the reservoir and channel. The permeability $k = 0.01$ mD and porosity $\varphi = 0.15$ is assigned to the confining unit. Elastic properties are uniform through the model ($E = 15$ GPa, $\alpha = 0.75$, $\nu = 0.23$, $\rho = 2,500$ kg/m^3). The well is a line of constant pressure $p = 275$ psi along the left boundary of the reservoir. Constant hydrostatic pressure is maintained at the far extent of the reservoir (right side of model). There is no flow across all other boundaries. The upper surface is traction free and all sides use roller boundaries ($u_\perp = 0$). Boundary conditions are summarized in Table 3.1. Initial conditions assume hydrostatic pressure and zero displacements. The model was run to simulate injection for 10 days, which is the same as the planned for the field tests.

Table 3.1: Boundary conditions used in these analyses.

Boundary	Fluid Flow	Elasticity
Upper Surface ($z = 0$)	pore pressure, $p = 0$	traction free, $\sigma_{ij} = 0$
Bottom Surface	impermeable, $dp/dz = 0$	roller, $u_z = 0$
Outer Verical of Confining Layer	pore pressure, $p = 0$	roller, $u_r = 0$
Left Vertical of Reservoir	pore pressure, $p = 275$ psi	roller, $u_r = 0$
Right Vertical of Reservoir	hydraulic head, $h = 0$	roller, $u_r = 0$

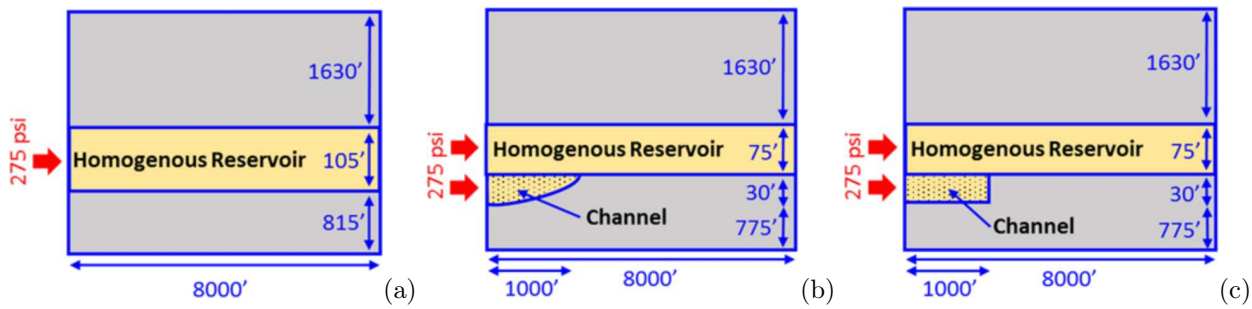

Figure 3.20: Geometry (not-to-scale) of the HEC at the base of the anisotropic reservoir (not to scale). (a) Case of a homogenous reservoir ($k = 80$ mD and porosity $\varphi = 0.25$). The HEC ($k = 1,000$ mD and porosity $\varphi = 0.25$) is modeled as an (b) quarter-ellipse and (c) rectangle at the base of a reservoir ($k = 10$ mD and porosity $\varphi = 0.15$).

Tilt is always positive at the monitoring depth (Figure 3.21a). Tilt does not occur directly over the injection site, increases rapidly until it reaches a maximum, and then decreases to zero far from $x = 0$. The maximum tilt signal occurs between 1,000 and 2,000 ft in all cases. After two days, the maximum tilt rate exceeds $\sim 1\times10^{-6}$ when the HEC is included in the simulation. This is more than 30% larger than the maximum tilt at the same time for the simulation of a single homogeneous reservoir and over three orders of magnitude greater than the resolution of our instruments. The magnitude of the strain signals increase with time at shallow depths. Strains increase rapidly for the first day, after which the strain rate continues to increase slowly. Figure 3.21b displays the strain after 10 days of injection. The overburden is dragged outward near the well ($\sim$2 $\mu\varepsilon$) by the pressurization of the reservoir and compressed vertically ($\sim$1 $\mu\varepsilon$). The magnitude of normal strains is greatest near the well and approaches zero near $x = 2,250$ ft, where the overburden is then compressed laterally ($\sim$0.5 $\mu\varepsilon$) and expands vertically ($\sim$0.5 $\mu\varepsilon$). The HEC causes the strain signal to increase $\sim$30% near the well and decrease more rapidly as the distance from the well increases.

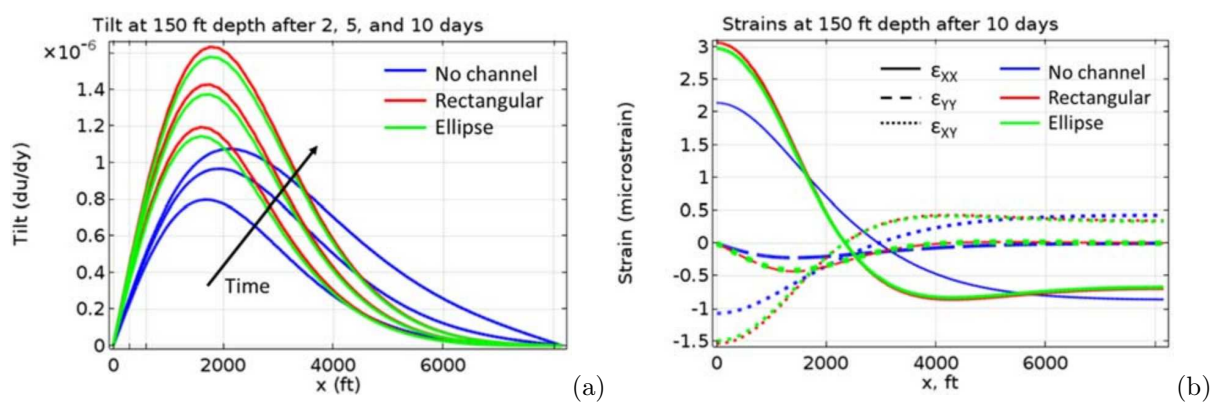

Figure 3.21: Comparison between injection into a homogeneous reservoir and a reservoir with a HEC at the base. The tilt and strain at a depth of 150 feet is plotted after a time period of 10 days.

The analysis shows strain and tilt signals are orders of magnitude greater than the resolution of the strainmeters. The strain signal is greatest near the well and the tilt signal is greatest between 1,000 to 2,000 ft from the well.

3.4.2.2 3D Model of Deformation Pattern

Current geologic models infer the maximum dimension of the HEC to be 1–2 km (∼1 mile). Injection is unlikely to occur near the center of the HEC, causing an asymmetric pattern in the strain distribution. A 3D poroelastic model of finite channel dimensions tests how the strain and tilt signal varies due to the channel size and shape. This simulation is used to determine locations of optimal deformation signals to drill the monitoring wells.

We model deformation during injection into a cuboidal HEC (5,280 ft long, 2,000 ft wide, and 30 ft thick) underlying a 75-ft-thick reservoir. The base of the HEC lies at a depth of 1,735 ft. Injection at constant pressure $p = 275$ psi occurs 1,320 ft from the $+y$ border of the channel (Figure 3.22a). There is initially hydrostatic within all domains. The upper surface is traction free, and all other sides are roller boundaries. Fluid pressure is held constant and equal to initial conditions at the far field end of the reservoir. There is no flow across all other boundaries. The mesh has ∼600,000 degrees of freedom. The fluid flow properties for the reservoir are $k = 10$ mD and porosity $\varphi = 0.15$, $k = 1,000$ mD and porosity $\varphi = 0.25$ for the HEC, and $k = 0.01$ mD and porosity $\varphi = 0.15$ is assigned to the medium. The K_v/K_h ratio is always 0.75 within the reservoir and channel. Elastic properties, estimated from similar formations, are constant through the model ($E = 15$ GPa, $\alpha = 0.75$, $\nu = 0.23$, $\rho = 2,500$ kg/m^3). The model was run for 10 days, the same as the planned scenario during injection into at 9A.

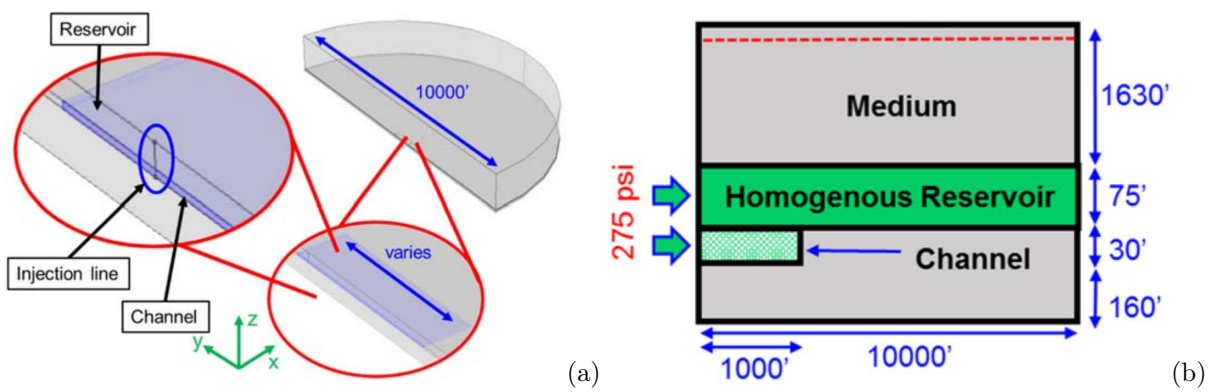

Figure 3.22: (a) 3D geometry of fluid injection at the center of a 5,280 ft long, 2,000 ft wide, and 30 ft thick HEC at the base of a 75 ft reservoir. (b) $x - z$ cross-section of the model at $x = 0$. The red dotted line is the depth of monitoring. Elastic properties are identical in all domains, but flow properties vary (see Table 3.2).

Table 3.2: Material properties for the model shown in Figure 3.22.

Domain	Permeability (mD)	Porosity
Medium	0.01	0.15
Reservoir	10	0.15
Channel	1,000	0.25

In general, the deformation pattern (Figure 3.23) follows the border of the underlying HEC. Strain and tilt signals are on the order of 1×10^{-6}. All strain magnitudes are greatest directly above the injection point and are greater above the HEC than outside the HEC. Vertical strains are negative (compressive) everywhere. The magnitude of the tilt is large slightly outside the HEC boundary, with the greatest values occurring at the boundary closest to the injection well. The tilt is small over the well and at distances greater

than twice the depth of injection (∼3,500 ft). These plots show that the strain tensor is greatest near the well and tilt signals are greatest slightly outside of the HEC boundary. Therefore, instrument locations must be near enough to the well to record the strain, but not too close as to not record the tilt.

The orientation of the HEC boundary results in some of the monitoring locations being closer to the HEC border than others. The temporal variations of strain and tilt are plotted at three monitoring locations (Figure 3.24). Monitor locations near the HEC border are modelled at points (750 ft, 0, -150 ft) and (150 ft, 750 ft, -150 ft). The second point is an additional distance $x = 150$ ft to reduce any potential model boundary effect. All signals are on the order of $\sim 0.5 \times 10^{-6}$, except for tilt measurements that are parallel to the nearest channel border. Locations around the nearest HEC borders have lateral strains that are always positive, vertical strain is always negative, and tilts are always positive (tilt away from the well). Differences in strain signals between the two points are small, however, the tilt signals suggest these can be used to determine where HEC borders lie. Both points are near a HEC border, one along the x-axis and the other along the y-axis. Tilt parallel to the HEC border is 50% to 100% less than tilts perpendicular to the border.

At an additional point that lies towards the center of the HEC is inspected (Figure 3.24c), the strain signals are similar to the two points. The z component of the displacement in the y-direction (tilt ∼0.25 μrad) is negative in this location. This shows that the tilt towards the center of the HEC may change direction. The behavior of the tilt signal around the injection point shows the geometry of the HEC.

3.4.3 Identifying Locations for Strain Instruments

An axisymmetric model of injection into a homogeneous reservoir was developed to predict optimal locations of strain signal. Geologic data in the vicinity of well 9A was applied to a model of constant injection into a homogeneous reservoir confined within a horizontal medium. The reservoir is 105 ft thick and lies at a depth of 1,630 ft. The permeability within the reservoir is $k = 80$ mD and porosity $\varphi = 0.25$, and the confined layers have a permeability $k = 0.01$ mD and porosity $\varphi = 0.15$. Injection occurs uniformly along the wellbore (radius $r = 6$ inches) at a constant pressure $p = 730$ psi and the hydraulic head in the reservoir is held constant 8,000 ft away from the well. This is the scenario of injection into the Bartlesville sandstone if no heterogeneities are present in the subsurface. The model is run for 10 days to calculate the resulting deformation during the injection process. The objective of the field demonstration is to evaluate strain data from shallow wells (hundreds of feet) to monitor fluid injection at greater depths (greater than 1,500 ft). We determine zones of maximum strain and tilt signal within the axisymmetric model to conclude where to place the monitoring wells.

The analyses show that injection pressurizes the reservoir and pushes it outward (away from the well), dragging the confining layers with it. At shallow depths, strain signals within the overburden are greatest near the well and decrease to negligible values at radial distances greater than several 1,000 ft (Figure 3.25). At the wellbore, the magnitude of tilt is always zero because of the symmetry assumed for the problem. The tilt signal increases with radial distance and reaches a maximum where the radius is approximately equal to the depth of the reservoir.

Normal strain generally decreases whereas tilt increases when the radial distance is less than the well depth. A good location for the instruments will be where these to trends are roughly balanced, providing relatively high strains and tilts. The approach we took was to characterize the magnitude of the strain signal using the sum of the absolute value of the volumetric strain and the absolute value of tilt. The volumetric strain is the sum of the 3 normal strains. The representative strain determined this way was calculated at various locations and times (Figure 3.25c and 3.25d).

The representative strain increases by approximately four times from 2 to 10 days and the location of maximum signal moves radially outward as time increases. The maximum signal is at approximately $r = 500$ ft after 2 days of injection and it moves to $r = 1,000$ ft after 10 days. The gradient in the representative strain

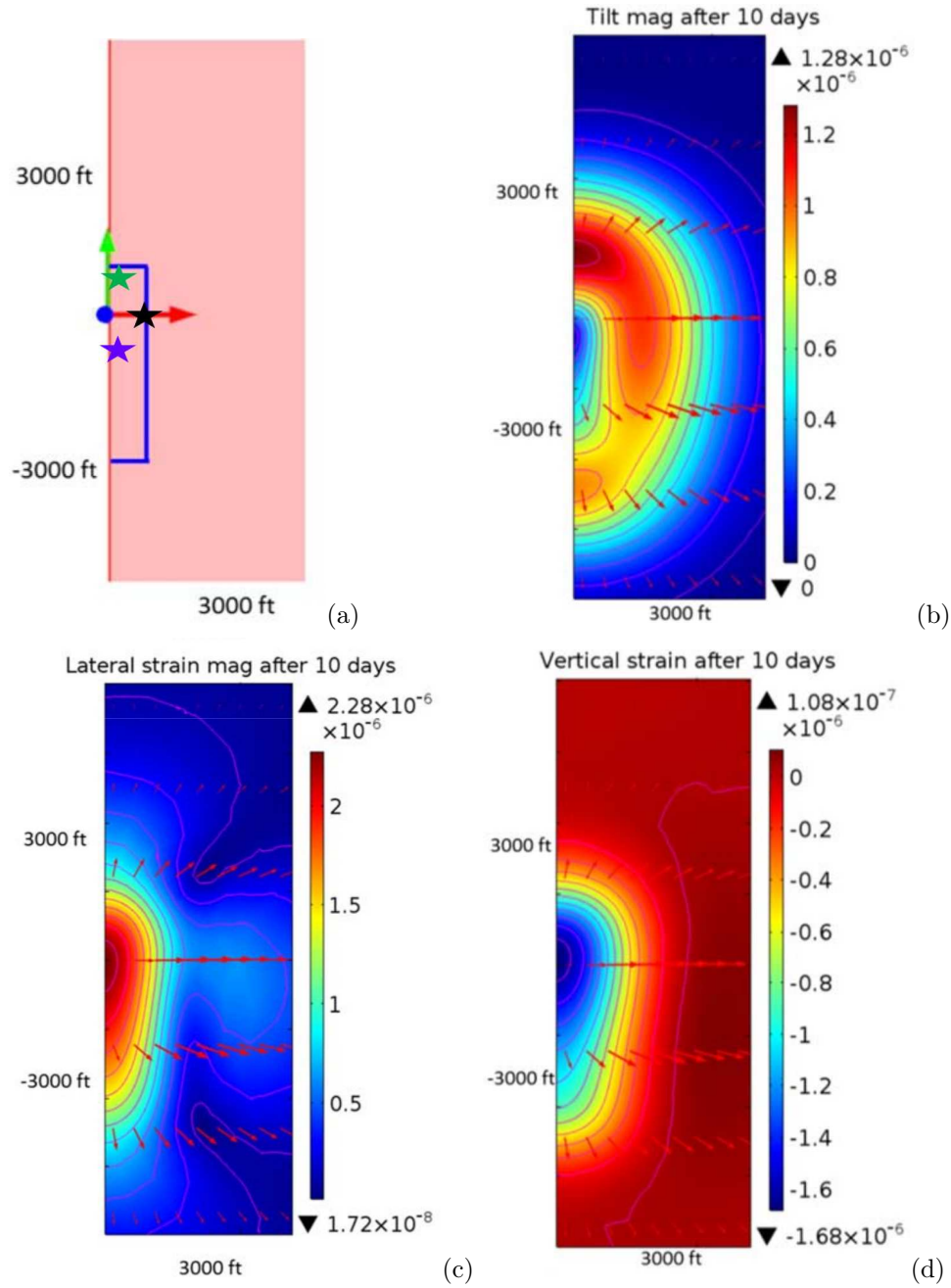

Figure 3.23: Plots of deformation at the monitoring depth (x,y,z = 150 ft) near the injection site after 10 days. The cross-section corresponds to the dotted red line in Figure 3.22b. The blue circle is the injection line and the blue line is the outline of the HEC. (b) Magnitude of tilt, $\sqrt{(du/dz)^2 + (dv/dz)^2}$. Arrow surface shows the direction of deformation. (c) Magnitude of lateral strain, $\sqrt{\varepsilon_x^2 + \varepsilon_y^2}$. (d) Vertical strain. Arrow lines are the displacement field tilts are always positive (tilt away from the well). Differences in strain signals between the two points are small, however, the tilt signals suggest these can be used to determine where HEC borders lie. Both points are near a HEC border, one along the x-axis and the other along the y-axis. Tilt parallel to the HEC border is 50% to 100% less than tilts perpendicular to the border.

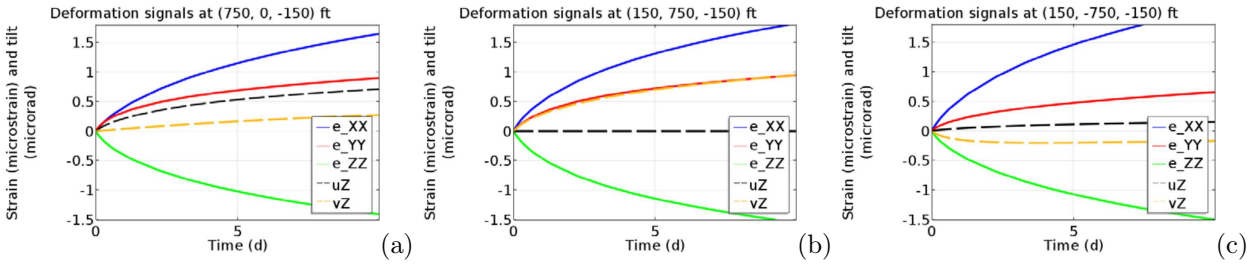

Figure 3.24: Temporal variations in strain and tilt signals at three monitoring points. (a) Black star in Figure 3.23a at (750, 0, -150) ft. (b) Green star in Figure 3.23a at (150, 750, -150) ft. (c) Purple star in Figure 3.23a at (150, -750, -150) ft. These monitoring points are the black stars on Figure 3.23a. Normal strains are solid lines and tilts are dotted lines.

is quite flat, however, so the strain anywhere in the range $500 < r < 1,000$ ft is within 5% of the maximum value throughout the time period of $2 < t < 10$ days. The range of radial distances of $500 < r < 1,000$ ft appeared to be best suited for the strain instruments.

Along vertical profiles, tilts and strains are greatest at the depth of the reservoir and they generally decrease upward. The tilt signal is negative at large depths and increases towards the surface reaching zero at depth between 350 ft and 400 ft. The tilt changes sign and becomes more positive above that depth range (Figure 3.25). The vertical strain also reaches a minimum and then increases slightly in close proximity to the ground surface.

The representative strain was determined at $r = 500$ ft and $r = 1,000$ ft at 2, 5, and 10 days and plotted as functions of depth (Figure 3.25c). The total signal strength increases with time, and the signal is at a minimum between depths of $300 < z < 450$ ft. The representative strain increases above that depth range.

The analysis indicates that strain instruments at the North Avant Field should be located at a radial distance between 500 ft and 1,000 ft from the well and at depths either above 300 ft or below 450 ft. The shallow depth range would be much less expensive, so that seems to be the best alternative. The analysis indicates that the strain increases as the ground surface is approached. However, the degree of fracturing and chemical alteration will increase as the ground surface is approached. Ground water flow and temperature changes will also increase nearer to the surface. The depth where these effects become important will depend on the local conditions, but they will likely diminish significantly below 100 ft depth.

We narrowed the optimal radial distance to between 600 ft and 800 ft, and we used a target depth of approximately 120 ft to 180 ft for design purposes. These guidelines provide a range, and then site specific factors will be used to pick the actual location. Factors such as access to the location and proximity to surface features are important constraints on specific locations in plan view. Well logs provide information on specific depth intervals for the instruments.

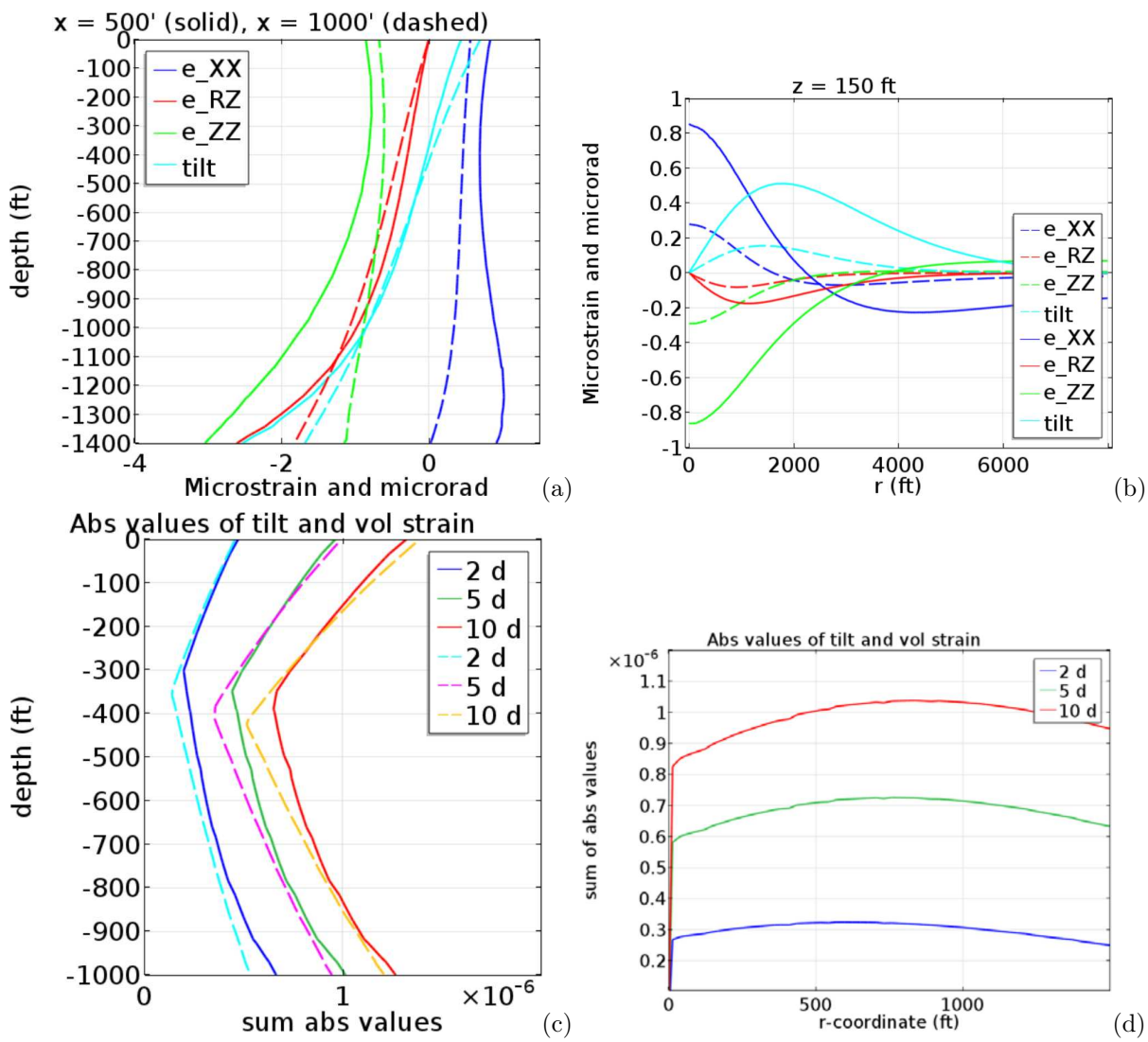

Figure 3.25: (a) Vertical profiles above the reservoir at radial distances $r = 500$ and 1,000 ft from well. (b) Strain and tilt profiles at a depth $z = 150$ ft. Solid line is the signal after 2 days and dashed line is the signal after 10 days. (c) Representative strain (sum of tilt and volumetric strain magnitudes) at $r = 500$ ft (solid line) and $r = 1,000$ ft (dashed line). (d) Representative strain at a depth $z = 150$ ft.

Appendix 3.A Python Implementation of the Cuboid Inclusion

The following is a Python implementation of the analytic solution to the pressurized inclusion problem detailed in Section 3.1.2.

```
import numpy as np
import math

class Cuboid3d:

  def __init__(self): pass

  def set_a(self,a): self.a = a
  def set_b(self,b): self.b = b
  def set_c(self,c): self.c = c
  def set_h(self,h): self.h = h

  def set_alpha(self,alpha): self.alpha = float(alpha)
  def set_nu(self,nu):       self.nu    = float(nu)
  def set_E(self,E):         self.E     = float(E)
  def set_delp(self,delp):   self.delp  = float(delp)

  def set_d0(self):          self.d0 = self.alpha * (1.0-2.0*self.nu) / self.E
     ↪  * self.delp

  def I_x_inf_cuboid(self,x,y,z):
    a = float(self.a)
    b = float(self.b)
    c = float(self.c)
    h = float(self.h)
    output = 0.0
    nh = 200
    delz1 = (2.0*c)/float(nh)
    for z1 in np.linspace(h-c,h+c,nh+1):
      term1 = float( ( (x+a)**2+(z-z1)**2+(y-b)**2)**0.5 + b - y )
      term2 = float( ( (x-a)**2+(z-z1)**2+(y-b)**2)**0.5 + b - y )
      term3 = float( ( (x-a)**2+(z-z1)**2+(y+b)**2)**0.5 - b - y )
      term4 = float( ( (x+a)**2+(z-z1)**2+(y+b)**2)**0.5 - b - y )
      output += np.log( (term1/term2) * (term3/term4) ) * delz1
    return output

  def I_y_inf_cuboid(self,x,y,z):
    a = self.a
    b = self.b
    c = self.c
    h = self.h
    output = 0.0
    nh = 200
    for z1 in np.linspace(h-c,h+c,nh+1):
      term1 = float(((y+b)**2+(z-z1)**2+(x-a)**2)**0.5+a-x)
      term2 = float(((y-b)**2+(z-z1)**2+(x-a)**2)**0.5+a-x)
```

```
      term3 = float(((y-b)**2+(z-z1)**2+(x+a)**2)**0.5-a-x)
      term4 = float(((y+b)**2+(z-z1)**2+(x+a)**2)**0.5-a-x)
      output += np.log( (term1/term2) * (term3/term4) ) * (2*c/float(nh))
    return output

  def I_z_inf_cuboid(self,x,y,z):
    a = self.a
    b = self.b
    c = self.c
    h = self.h
    output = 0.0
    na = 200
    for x1 in np.linspace(-a,a,na+1):
      term1 = ((z-(h-c))**2+(x-x1)**2+(y-b)**2)**0.5+b-y
      term2 = ((z-(h+c))**2+(x-x1)**2+(y-b)**2)**0.5+b-y
      term3 = ((z-(h+c))**2+(x-x1)**2+(y+b)**2)**0.5-b-y
      term4 = ((z-(h-c))**2+(x-x1)**2+(y+b)**2)**0.5-b-y
      output += np.log( (term1/term2) * (term3/term4) ) * (2*a/float(na))
    return output

  def Ip_x_z_inf_1_cuboid(self,x,y,z):
    a = self.a
    b = self.b
    c = self.c
    h = self.h
    output = 0.0
    nh = 200
    for z1 in np.linspace(h-c,h+c,nh+1):
      term1 = z-z1
      term2 = ((a+x)**2+(b-y)**2+(z-z1)**2)**0.5
      term3 = b-y+term2
      term4 = z1-z
      term5 = ((a-x)**2+(b-y)**2+(z-z1)**2)**0.5
      term6 = b-y+term5
      output += ( (term1/(term2*term3)+term4/(term5*term6)) * (2.0*c/float(nh)
          ↪ ) )
    return output

  def Ip_x_z_inf_2_cuboid(self,x,y,z):
    a = self.a
    b = self.b
    c = self.c
    h = self.h
    output = 0.0
    nh = 200
    for z1 in np.linspace(h-c,h+c,nh+1):
      term1 = z1-z
      term2 = ((a+x)**2+(b+y)**2+(z-z1)**2)**0.5
      term3 = b+y-term2
      term4 = z-z1
      term5 = ((a-x)**2+(b+y)**2+(z-z1)**2)**0.5
```

```
      term6 = b+y-term5
      output += ( (term1/(term2*term3)+term4/(term5*term6)) * (2.0*c/float(nh)
          ↪ ) )
    return output

  def Ip_y_z_inf_1_cuboid(self,x,y,z):
    a = self.a
    b = self.b
    c = self.c
    h = self.h
    output = 0.0
    nh = 200
    for z1 in np.linspace(h-c,h+c,nh+1):
      term1 = z-z1
      term2 = ((a-x)**2+(b+y)**2+(z-z1)**2)**0.5
      term3 = a-x+term2
      term4 = z1-z
      term5 = ((a-x)**2+(b-y)**2+(z-z1)**2)**0.5
      term6 = a-x+term5
      output += (term1/(term2*term3)+term4/(term5*term6)) * (2.0*c/float(nh))
    return output

  def Ip_y_z_inf_2_cuboid(self,x,y,z):
    a = self.a
    b = self.b
    c = self.c
    h = self.h
    output = 0.0
    nh = 200
    for z1 in np.linspace(h-c,h+c,nh+1):
      term1 = z1-z
      term2 = ((a+x)**2+(b+y)**2+(z-z1)**2)**0.5
      term3 = a+x-term2
      term4 = z-z1
      term5 = ((a+x)**2+(b-y)**2+(z-z1)**2)**0.5
      term6 = a+x-term5
      output += (term1/(term2*term3)+term4/(term5*term6)) * (2.0*c/float(nh))
    return output

  def Ip_z_z_inf_1_cuboid(self,x,y,z):
    a = self.a
    b = self.b
    c = self.c
    h = self.h
    output = 0.0
    na = 200
    for x1 in np.linspace(-a,+a,na+1):
      term1 = c-h+z
      term2 = ((c-h+z)**2+(b-y)**2+(x-x1)**2)**0.5
      term3 = b-y+term2
      term4 = c+h-z
```

```
      term5 = ((c+h-z)**2+(b-y)**2+(x-x1)**2)**0.5
      term6 = b-y+term5
      output += (term1/(term2*term3)+term4/(term5*term6)) * (2.0*a/float(na))
    return output

  def Ip_z_z_inf_2_cuboid(self,x,y,z):
    a = self.a
    b = self.b
    c = self.c
    h = self.h
    output = 0.0
    na = 200
    for x1 in np.linspace(-a,+a,na+1):
      term1 = c+h-z
      term2 = ((c+h-z)**2+(b+y)**2+(x-x1)**2)**0.5
      term3 = b+y-term2
      term4 = c-h+z
      term5 = ((c-h+z)**2+(b+y)**2+(x-x1)**2)**0.5
      term6 = b+y-term5
      output += (term1/(term2*term3)+term4/(term5*term6)) * (2.0*a/float(na))
    return -output

  def Ip_x_z_inf_cuboid(self,x,y,z): return self.Ip_x_z_inf_1_cuboid(x,y,z)-
      ↪ self.Ip_x_z_inf_2_cuboid(x,y,z)
  def Ip_y_z_inf_cuboid(self,x,y,z): return self.Ip_y_z_inf_1_cuboid(x,y,z)-
      ↪ self.Ip_y_z_inf_2_cuboid(x,y,z)
  def Ip_z_z_inf_cuboid(self,x,y,z): return self.Ip_z_z_inf_1_cuboid(x,y,z)-
      ↪ self.Ip_z_z_inf_2_cuboid(x,y,z)

  def u_x_inf_cuboid(self,x,y,z):
    nu = float(self.nu)
    d0 = float(self.d0)
    I  = self.I_x_inf_cuboid(x,y,z)
    term1 = (-1.0)/(4.0*math.pi)
    term2 = (1+nu)/(1-nu)
    return term1*term2*d0*I

  def u_y_inf_cuboid(self,x,y,z):
    nu = self.nu
    d0 = self.d0
    I = self.I_y_inf_cuboid(x,y,z)
    term1 = - (1.0)/(4.0*math.pi)
    term2 = (1+nu)/(1-nu) * d0
    return term1*term2*I

  def u_z_inf_cuboid(self,x,y,z):
    nu = self.nu
    d0 = self.d0
    I = self.I_z_inf_cuboid(x,y,z)
    term1 = - (1.0)/(4.0*math.pi)
    term2 = (1+nu)/(1-nu) * d0
```

```
    return term1*term2*I

  def up_x_z_inf_cuboid(self,x,y,z):
    nu = self.nu
    d0 = self.d0
    I = self.Ip_x_z_inf_cuboid(x,y,z)
    term1 = - (1.0)/(4.0*math.pi)
    term2 = (1+nu)/(1-nu) * d0
    return term1*term2*I

  def up_y_z_inf_cuboid(self,x,y,z):
    nu = self.nu
    d0 = self.d0
    I = self.Ip_y_z_inf_cuboid(x,y,z)
    term1 = - (1.0)/(4.0*math.pi)
    term2 = (1+nu)/(1-nu) * d0
    return term1*term2*I

  def up_z_z_inf_cuboid(self,x,y,z):
    nu = self.nu
    d0 = self.d0
    I = self.Ip_z_z_inf_cuboid(x,y,z)
    term1 = - (1.0)/(4.0*math.pi)
    term2 = (1+nu)/(1-nu) * d0
    return term1*term2*I

  def u_x_inf_image_cuboid(self,x,y,z): return self.u_x_inf_cuboid(x,y,-z)
  def u_y_inf_image_cuboid(self,x,y,z): return self.u_y_inf_cuboid(x,y,-z)
  def u_z_inf_image_cuboid(self,x,y,z): return self.u_z_inf_cuboid(x,y,-z)

  def up_x_z_inf_image_cuboid(self,x,y,z): return -self.up_x_z_inf_cuboid(x,y
      ↪ ,-z)
  def up_y_z_inf_image_cuboid(self,x,y,z): return -self.up_y_z_inf_cuboid(x,y
      ↪ ,-z)
  def up_z_z_inf_image_cuboid(self,x,y,z): return -self.up_z_z_inf_cuboid(x,y
      ↪ ,-z)

  def u_x_cuboid(self,x,y,z):
    nu    = self.nu
    term1 = self.u_x_inf_cuboid(x,y,z)
    term2 = self.u_x_inf_image_cuboid(x,y,z)
    term3 = self.up_x_z_inf_image_cuboid(x,y,z)
    return term1+(3-4*nu)*term2+2*z*term3

  def u_y_cuboid(self,x,y,z):
    nu    = self.nu
    term1 = self.u_y_inf_cuboid(x,y,z)
    term2 = self.u_y_inf_image_cuboid(x,y,z)
    term3 = self.up_y_z_inf_image_cuboid(x,y,z)
    return term1+(3-4*nu)*term2+2*z*term3

```

```
  def u_z_cuboid(self,x,y,z):
    nu    = self.nu
    term1 = self.u_z_inf_cuboid(x,y,z)
    term2 = self.u_z_inf_image_cuboid(x,y,z)
    term3 = self.up_z_z_inf_image_cuboid(x,y,z)
    return term1+(3-4*nu)*term2-2*z*term3

  def u_x_inf_image_cuboid(self,x,y,z): return self.u_x_inf_cuboid(x,y,-z)
  def u_y_inf_image_cuboid(self,x,y,z): return self.u_y_inf_cuboid(x,y,-z)
  def u_z_inf_image_cuboid(self,x,y,z): return self.u_z_inf_cuboid(x,y,-z)

  def up_x_z_inf_image_cuboid(self,x,y,z): return -self.up_x_z_inf_cuboid(x,y
      ↪ ,-z)
  def up_y_z_inf_image_cuboid(self,x,y,z): return -self.up_y_z_inf_cuboid(x,y
      ↪ ,-z)
  def up_z_z_inf_image_cuboid(self,x,y,z): return -self.up_z_z_inf_cuboid(x,y
      ↪ ,-z)

  def comp_sign(self,input):
    if input==0:          return 0
    if np.real(input)>0: return 1
    else: return -1

  def J_xx_cuboid(self,x,y,z,z1,a,b):
    if x==-a or y==-b: return 0
    term1 = self.comp_sign(x+a) * self.comp_sign(y+b)
    term2 = (z-z1)*((y+b)**2)**0.5
    term3 = ((x+a)**2)**0.5 * ( (x+a)**2 + (y+b)**2 + (z-z1)**2 )**0.5
    return term1 * math.atan( - term2 / term3 )

  def J_yy_cuboid(self,x,y,z,z1,a,b):
    if x==-a or y==-b: return 0
    term1 = self.comp_sign(x+a) * self.comp_sign(y+b)
    term2 = (z-z1)*((x+a)**2)**0.5
    term3 = ((y+b)**2)**0.5 * ( (x+a)**2 + (y+b)**2 + (z-z1)**2 )**0.5
    return term1 * math.atan( - term2 / term3 )

  def J_zz_cuboid(self,x,y,z,y1,d,a):
    if x==-a or z==d: return 0
    term1 = self.comp_sign(x+a) * self.comp_sign(z-d)
    term2 = ((x+a)**2)**0.5 * (y-y1)
    term3 = ((z-d)**2)**0.5 * ( (x+a)**2 + (z-d)**2 + (y-y1)**2 )**0.5
    return term1 * math.atan( - term2 / term3 )

  def I_xx_inf_cuboid(self,x,y,z):
    a = self.a
    b = self.b
    c = self.c
    h = self.h
    term1 = self.J_xx_cuboid(x,y,z,h+c,+a,-b)
    term2 = self.J_xx_cuboid(x,y,z,h-c,+a,-b)
```

```
    term3 = self.J_xx_cuboid(x,y,z,h+c,-a,-b)
    term4 = self.J_xx_cuboid(x,y,z,h-c,-a,-b)
    term5 = self.J_xx_cuboid(x,y,z,h+c,-a,+b)
    term6 = self.J_xx_cuboid(x,y,z,h-c,-a,+b)
    term7 = self.J_xx_cuboid(x,y,z,h+c,+a,+b)
    term8 = self.J_xx_cuboid(x,y,z,h-c,+a,+b)
    return term1-term2-term3+term4+term5-term6-term7+term8

  def I_yy_inf_cuboid(self,x,y,z):
    a = self.a
    b = self.b
    c = self.c
    h = self.h
    term1 = self.J_yy_cuboid(x,y,z,h+c,+a,-b)
    term2 = self.J_yy_cuboid(x,y,z,h-c,+a,-b)
    term3 = self.J_yy_cuboid(x,y,z,h+c,-a,-b)
    term4 = self.J_yy_cuboid(x,y,z,h-c,-a,-b)
    term5 = self.J_yy_cuboid(x,y,z,h+c,-a,+b)
    term6 = self.J_yy_cuboid(x,y,z,h-c,-a,+b)
    term7 = self.J_yy_cuboid(x,y,z,h+c,+a,+b)
    term8 = self.J_yy_cuboid(x,y,z,h-c,+a,+b)
    return term1-term2-term3+term4+term5-term6-term7+term8

  def I_zz_inf_cuboid(self,x,y,z):
    a = self.a
    b = self.b
    c = self.c
    h = self.h
    term1 = self.J_zz_cuboid(x,y,z,+b,h+c,+a)
    term2 = self.J_zz_cuboid(x,y,z,-b,h+c,+a)
    term3 = self.J_zz_cuboid(x,y,z,+b,h+c,-a)
    term4 = self.J_zz_cuboid(x,y,z,-b,h+c,-a)
    term5 = self.J_zz_cuboid(x,y,z,+b,h-c,-a)
    term6 = self.J_zz_cuboid(x,y,z,-b,h-c,-a)
    term7 = self.J_zz_cuboid(x,y,z,+b,h-c,+a)
    term8 = self.J_zz_cuboid(x,y,z,-b,h-c,+a)
    return term1-term2-term3+term4+term5-term6-term7+term8

  def eps_xx_inf_cuboid(self,x,y,z):
    nu = self.nu
    d0 = self.d0
    I = self.I_xx_inf_cuboid(x,y,z)
    term1 = -(1.0)/(4.0*math.pi)
    term2 = (1+nu)/(1-nu) * d0
    return term1*term2*I

  def eps_yy_inf_cuboid(self,x,y,z):
    nu = self.nu
    d0 = self.d0
    I = self.I_yy_inf_cuboid(x,y,z)
    term1 = -(1.0)/(4.0*math.pi)
```

```
    term2 = (1+nu)/(1-nu) * d0
    return term1*term2*I

  def eps_zz_inf_cuboid(self,x,y,z):
    nu = self.nu
    d0 = self.d0
    I = self.I_zz_inf_cuboid(x,y,z)
    term1 = -(1.0)/(4.0*math.pi)
    term2 = (1+nu)/(1-nu) * d0
    return term1*term2*I

  def XY_cuboid(self,x,y,z,a,b,d):
    term1 = d-z+( (x-a)**2+(y-b)**2+(z-d)**2 )**0.5
    term2 = d-z+( (x+a)**2+(y-b)**2+(z-d)**2 )**0.5
    return np.log(term1/term2)

  def YZ_cuboid(self,x,y,z,a,b,c,h):
    term1 = a-x+( (x-a)**2+(y-b)**2+(z-(h+c))**2 )**0.5
    term2 = a-x+( (x-a)**2+(y-b)**2+(z-(h-c))**2 )**0.5
    return np.log(term1/term2)

  def XZ_cuboid(self,x,y,z,a,b,c,h):
    term1 = b-y+( (x-a)**2+(y-b)**2+(z-(h+c))**2 )**0.5
    term2 = b-y+( (x-a)**2+(y-b)**2+(z-(h-c))**2 )**0.5
    return np.log(term1/term2)

  def I_xy_inf_cuboid(self,x,y,z):
    a = self.a
    b = self.b
    c = self.c
    h = self.h
    term1 = self.XY_cuboid(x,y,z,+a,+b,h+c)
    term2 = self.XY_cuboid(x,y,z,+a,+b,h-c)
    term3 = self.XY_cuboid(x,y,z,-a,-b,h+c)
    term4 = self.XY_cuboid(x,y,z,-a,-b,h-c)
    return term1-term2+term3-term4

  def I_yz_inf_cuboid(self,x,y,z):
    a = self.a
    b = self.b
    c = self.c
    h = self.h
    term1 = self.YZ_cuboid(x,y,z,+a,+b,+c,+h)
    term2 = self.YZ_cuboid(x,y,z,-a,+b,+c,+h)
    term3 = self.YZ_cuboid(x,y,z,+a,-b,-c,+h)
    term4 = self.YZ_cuboid(x,y,z,-a,-b,-c,+h)
    return term1-term2+term3-term4

  def I_xz_inf_cuboid(self,x,y,z):
    a = self.a
    b = self.b
```

```
    c = self.c
    h = self.h
    term1 = self.XZ_cuboid(x,y,z,+a,+b,+c,+h)
    term2 = self.XZ_cuboid(x,y,z,+a,-b,+c,+h)
    term3 = self.XZ_cuboid(x,y,z,-a,+b,-c,+h)
    term4 = self.XZ_cuboid(x,y,z,-a,-b,-c,+h)
    return term1-term2+term3-term4

  def eps_xy_inf_cuboid(self,x,y,z):
    nu = self.nu
    d0 = self.d0
    I = self.I_xy_inf_cuboid(x,y,z)
    term1 = -(1.0)/(4.0*math.pi)
    term2 = (1+nu)/(1-nu) * d0
    return term1*term2*I

  def eps_yz_inf_cuboid(self,x,y,z):
    nu = self.nu
    d0 = self.d0
    I = self.I_yz_inf_cuboid(x,y,z)
    term1 = -(1.0)/(4.0*math.pi)
    term2 = (1+nu)/(1-nu) * d0
    return term1*term2*I

  def eps_xz_inf_cuboid(self,x,y,z):
    nu = self.nu
    d0 = self.d0
    I = self.I_xz_inf_cuboid(x,y,z)
    term1 = -(1.0)/(4.0*math.pi)
    term2 = (1+nu)/(1-nu) * d0
    return term1*term2*I

  def Jp_xx_z_cuboid(self,x,y,z,z1,a,b):
    if x==-a or y==-b: return 0
    term1 = (x+a) * (y+b) * ( (x+a)**2 + (y+b)**2 )
    term2 = ((z-z1)**2 * (y+b)**2) + (x+a)**2 * ( (x+a)**2 + (y+b)**2 + (z-z1)
      ↪ **2 )
    term3 = ( (x+a)**2 + (y+b)**2 + (z-z1)**2 )**0.5
    return - term1 / ( term2 * term3 )

  def Jp_yy_z_cuboid(self,x,y,z,z1,a,b):
    if x==-a or y==-b: return 0
    term1 = (x+a) * (y+b) * ( (x+a)**2 + (y+b)**2 )
    term2 = ((z-z1)**2 * (x+a)**2) + (y+b)**2 * ( (x+a)**2 + (y+b)**2 + (z-z1)
      ↪ **2 )
    term3 = ( (x+a)**2 + (y+b)**2 + (z-z1)**2 )**0.5
    return - term1 / ( term2 * term3 )

  def Jp_zz_z_cuboid(self,x,y,z,y1,d,a):
    if x==-a or z==d: return 0
    term1 = (x+a)**2+(y-y1)**2+2.0*(z-d)**2
```

```
    term2 = ( (x+a)**2 + (y-y1)**2 + (z-d)**2 )**0.5
    term3 = (y-y1)*(x+a)
    term4 = ( (y-y1)**2 * (x+a)**2 ) + ( (d-z)**2 * ( (x+a)**2 + (y-y1)**2 + (
        ↪ z-d)**2 ) )
    return ( term1 / term2 ) * ( term3 / term4 )

  def Ip_xx_inf_z_cuboid(self,x,y,z):
    a = self.a
    b = self.b
    c = self.c
    h = self.h
    term1 = self.Jp_xx_z_cuboid(x,y,z,+h+c,+a,-b)
    term2 = self.Jp_xx_z_cuboid(x,y,z,+h-c,+a,-b)
    term3 = self.Jp_xx_z_cuboid(x,y,z,+h-c,-a,-b)
    term4 = self.Jp_xx_z_cuboid(x,y,z,+h+c,-a,-b)
    term5 = self.Jp_xx_z_cuboid(x,y,z,+h+c,-a,+b)
    term6 = self.Jp_xx_z_cuboid(x,y,z,+h-c,-a,+b)
    term7 = self.Jp_xx_z_cuboid(x,y,z,+h-c,+a,+b)
    term8 = self.Jp_xx_z_cuboid(x,y,z,+h+c,+a,+b)
    return term1-term2+term3-term4+term5-term6+term7-term8

  def Ip_yy_inf_z_cuboid(self,x,y,z):
    a = self.a
    b = self.b
    c = self.c
    h = self.h
    term1 = self.Jp_yy_z_cuboid(x,y,z,+h+c,+a,-b)
    term2 = self.Jp_yy_z_cuboid(x,y,z,+h-c,+a,-b)
    term3 = self.Jp_yy_z_cuboid(x,y,z,+h-c,-a,-b)
    term4 = self.Jp_yy_z_cuboid(x,y,z,+h+c,-a,-b)
    term5 = self.Jp_yy_z_cuboid(x,y,z,+h+c,-a,+b)
    term6 = self.Jp_yy_z_cuboid(x,y,z,+h-c,-a,+b)
    term7 = self.Jp_yy_z_cuboid(x,y,z,+h-c,+a,+b)
    term8 = self.Jp_yy_z_cuboid(x,y,z,+h+c,+a,+b)
    return term1-term2+term3-term4+term5-term6+term7-term8

  def Ip_zz_inf_z_cuboid(self,x,y,z):
    a = self.a
    b = self.b
    c = self.c
    h = self.h
    term1 = self.Jp_zz_z_cuboid(x,y,z,+b,+h+c,+a)
    term2 = self.Jp_zz_z_cuboid(x,y,z,-b,+h+c,+a)
    term3 = self.Jp_zz_z_cuboid(x,y,z,-b,+h+c,-a)
    term4 = self.Jp_zz_z_cuboid(x,y,z,+b,+h+c,-a)
    term5 = self.Jp_zz_z_cuboid(x,y,z,+b,+h-c,-a)
    term6 = self.Jp_zz_z_cuboid(x,y,z,-b,+h-c,-a)
    term7 = self.Jp_zz_z_cuboid(x,y,z,-b,+h-c,+a)
    term8 = self.Jp_zz_z_cuboid(x,y,z,+b,+h-c,+a)
    return term1-term2+term3-term4+term5-term6+term7-term8

```

```
  def epsp_xx_inf_z_cuboid(self,x,y,z):
    nu = self.nu
    d0 = self.d0
    I = self.Ip_xx_inf_z_cuboid(x,y,z)
    term1 = -(1.0)/(4.0*math.pi)
    term2 = (1+nu)/(1-nu) * d0
    return term1*term2*I

  def epsp_yy_inf_z_cuboid(self,x,y,z):
    nu = self.nu
    d0 = self.d0
    I = self.Ip_yy_inf_z_cuboid(x,y,z)
    term1 = -(1.0)/(4.0*math.pi)
    term2 = (1+nu)/(1-nu) * d0
    return term1*term2*I

  def epsp_zz_inf_z_cuboid(self,x,y,z):
    nu = self.nu
    d0 = self.d0
    I = self.Ip_zz_inf_z_cuboid(x,y,z)
    term1 = -(1.0)/(4.0*math.pi)
    term2 = (1+nu)/(1-nu) * d0
    return term1*term2*I

  def XY_z_cuboid(self,x,y,z,a,b,d):
    term1 = ( (x-a)**2+(y-b)**2+(z-d)**2 )**0.5
    return 1.0 / term1

  def Y_z_cuboid(self,x,y,z,a,b,d):
    term1 = ( (x-a)**2+(y-b)**2+(z-d)**2 )**0.5
    term2 = (d-z) / ( (a-x + term1) * term1 )
    return term2

  def X_z_cuboid(self,x,y,z,a,b,d):
    term1 = ( (x-a)**2+(y-b)**2+(z-d)**2 )**0.5
    term2 = (d-z) / ( (b-y + term1) * term1 )
    return term2

  def Ip_xy_inf_z_cuboid(self,x,y,z):
    a = self.a
    b = self.b
    c = self.c
    h = self.h
    term1 = self.XY_z_cuboid(x,y,z,-a,+b,h+c)
    term2 = self.XY_z_cuboid(x,y,z,+a,+b,h+c)
    term3 = self.XY_z_cuboid(x,y,z,+a,+b,h-c)
    term4 = self.XY_z_cuboid(x,y,z,-a,+b,h-c)
    term5 = self.XY_z_cuboid(x,y,z,+a,-b,h+c)
    term6 = self.XY_z_cuboid(x,y,z,-a,-b,h+c)
    term7 = self.XY_z_cuboid(x,y,z,-a,-b,h-c)
    term8 = self.XY_z_cuboid(x,y,z,+a,-b,h-c)
```

```
    return term1-term2+term3-term4+term5-term6+term7-term8

  def Ip_yz_inf_z_cuboid(self,x,y,z):
    a = self.a
    b = self.b
    c = self.c
    h = self.h
    term1 = self.Y_z_cuboid(x,y,z,+a,+b,h+c)
    term2 = self.Y_z_cuboid(x,y,z,+a,+b,h-c)
    term3 = self.Y_z_cuboid(x,y,z,-a,+b,h+c)
    term4 = self.Y_z_cuboid(x,y,z,-a,+b,h-c)
    term5 = self.Y_z_cuboid(x,y,z,+a,-b,h+c)
    term6 = self.Y_z_cuboid(x,y,z,+a,-b,h-c)
    term7 = self.Y_z_cuboid(x,y,z,-a,-b,h-c)
    term8 = self.Y_z_cuboid(x,y,z,-a,-b,h+c)
    return -term1+term2+term3-term4+term5-term6+term7-term8

  def Ip_xz_inf_z_cuboid(self,x,y,z):
    a = self.a
    b = self.b
    c = self.c
    h = self.h
    term1 = self.X_z_cuboid(x,y,z,+a,+b,h+c)
    term2 = self.X_z_cuboid(x,y,z,+a,+b,h-c)
    term3 = self.X_z_cuboid(x,y,z,+a,-b,h+c)
    term4 = self.X_z_cuboid(x,y,z,+a,-b,h-c)
    term5 = self.X_z_cuboid(x,y,z,-a,+b,h+c)
    term6 = self.X_z_cuboid(x,y,z,-a,+b,h-c)
    term7 = self.X_z_cuboid(x,y,z,-a,-b,h-c)
    term8 = self.X_z_cuboid(x,y,z,-a,-b,h+c)
    return -term1+term2+term3-term4+term5-term6+term7-term8

  def epsp_xy_inf_z_cuboid(self,x,y,z):
    nu = self.nu
    d0 = self.d0
    I = self.Ip_xy_inf_z_cuboid(x,y,z)
    term1 = -(1.0)/(4.0*math.pi)
    term2 = (1+nu)/(1-nu) * d0
    return term1*term2*I

  def epsp_yz_inf_z_cuboid(self,x,y,z):
    nu = self.nu
    d0 = self.d0
    I = self.Ip_yz_inf_z_cuboid(x,y,z)
    term1 = -(1.0)/(4.0*math.pi)
    term2 = (1+nu)/(1-nu) * d0
    return term1*term2*I

  def epsp_xz_inf_z_cuboid(self,x,y,z):
    nu = self.nu
    d0 = self.d0
```

```
    I = self.Ip_xz_inf_z_cuboid(x,y,z)
    term1 = -(1.0)/(4.0*math.pi)
    term2 = (1+nu)/(1-nu) * d0
    return term1*term2*I

  def eps_xx_inf_image_cuboid(self,x,y,z): return self.eps_xx_inf_cuboid(x,y,-z)
  def eps_yy_inf_image_cuboid(self,x,y,z): return self.eps_yy_inf_cuboid(x,y,-z)
  def eps_zz_inf_image_cuboid(self,x,y,z): return self.eps_zz_inf_cuboid(x,y,-z)
  def eps_xy_inf_image_cuboid(self,x,y,z): return self.eps_xy_inf_cuboid(x,y,-z)
  def eps_yz_inf_image_cuboid(self,x,y,z): return self.eps_yz_inf_cuboid(x,y,-z)
  def eps_xz_inf_image_cuboid(self,x,y,z): return self.eps_xz_inf_cuboid(x,y,-z)

  def epsp_xx_inf_image_z_cuboid(self,x,y,z): return -self.epsp_xx_inf_z_cuboid(x,y,-z)
  def epsp_yy_inf_image_z_cuboid(self,x,y,z): return -self.epsp_yy_inf_z_cuboid(x,y,-z)
  def epsp_zz_inf_image_z_cuboid(self,x,y,z): return -self.epsp_zz_inf_z_cuboid(x,y,-z)
  def epsp_xy_inf_image_z_cuboid(self,x,y,z): return -self.epsp_xy_inf_z_cuboid(x,y,-z)
  def epsp_yz_inf_image_z_cuboid(self,x,y,z): return -self.epsp_yz_inf_z_cuboid(x,y,-z)
  def epsp_xz_inf_image_z_cuboid(self,x,y,z): return -self.epsp_xz_inf_z_cuboid(x,y,-z)

  def omega_xy_cuboid(self,x,y,z):
    nu = self.nu
    term1 = self.eps_xy_inf_cuboid(x,y,z)
    term2 = (3-4*nu) * self.eps_xy_inf_image_cuboid(x,y,z)
    term3 = 2*z*self.epsp_yz_inf_image_z_cuboid(x,y,z)
    return term1+term2+term3

  def omega_xz_cuboid(self,x,y,z):
    nu = self.nu
    term1 = self.eps_xz_inf_cuboid(x,y,z)
    term2 = (3-4*nu) * self.eps_xz_inf_image_cuboid(x,y,z)
    term3 = -2*self.eps_xz_inf_image_cuboid(x,y,z)
    term4 = -2*z*self.epsp_xz_inf_image_z_cuboid(x,y,z)
    return term1-term2+term3+term4

  def omega_zx_cuboid(self,x,y,z):
    nu = self.nu
    term1 = self.eps_xz_inf_cuboid(x,y,z)
    term2 = (3-4*nu) * self.eps_xz_inf_image_cuboid(x,y,z)
    term3 = -2*z*self.epsp_xz_inf_image_z_cuboid(x,y,z)
```

```
    return term1+term2+term3

  def omega_yz_cuboid(self,x,y,z):
    nu = self.nu
    term1 = self.eps_yz_inf_cuboid(x,y,z)
    term2 = (3-4*nu) * self.eps_yz_inf_image_cuboid(x,y,z)
    term3 = -2*self.eps_yz_inf_image_cuboid(x,y,z)
    term4 = -2*z*self.epsp_yz_inf_image_z_cuboid(x,y,z)
    return term1-term2+term3+term4

  def omega_zy_cuboid(self,x,y,z):
    nu = self.nu
    term1 = self.eps_yz_inf_cuboid(x,y,z)
    term2 = (3-4*nu) * self.eps_yz_inf_image_cuboid(x,y,z)
    term3 = -2*z*self.epsp_yz_inf_image_z_cuboid(x,y,z)
    return term1+term2+term3

  def eps_xx_cuboid(self,x,y,z):
    nu = self.nu
    term1 = self.eps_xx_inf_cuboid(x,y,z)
    term2 = (3-4*nu) * self.eps_xx_inf_image_cuboid(x,y,z)
    term3 = 2*z*self.epsp_xx_inf_image_z_cuboid(x,y,z)
    return term1+term2+term3

  def eps_yy_cuboid(self,x,y,z):
    nu = self.nu
    term1 = self.eps_yy_inf_cuboid(x,y,z)
    term2 = (3-4*nu) * self.eps_yy_inf_image_cuboid(x,y,z)
    term3 = 2*z*self.epsp_yy_inf_image_z_cuboid(x,y,z)
    return term1+term2+term3

  def eps_zz_cuboid(self,x,y,z):
    nu = self.nu
    term1 = self.eps_zz_inf_cuboid(x,y,z)
    term2 = (1-4*nu) * self.eps_zz_inf_image_cuboid(x,y,z)
    term3 = 2*z*self.epsp_zz_inf_image_z_cuboid(x,y,z)
    return term1+term2+term3

  def eps_xy_cuboid(self,x,y,z): return self.omega_xy_cuboid(x,y,z)
  def eps_xz_cuboid(self,x,y,z): return ( self.omega_xz_cuboid(x,y,z)+self.
      ↪ omega_zx_cuboid(x,y,z) ) / 2.0
  def eps_yz_cuboid(self,x,y,z): return ( self.omega_yz_cuboid(x,y,z)+self.
      ↪ omega_zy_cuboid(x,y,z) ) / 2.0
```

The following is an example implementation of the `cuboid_inclusion.py` code presented above.

```
import cuboid_inclusion as ci

a = 400
b = 1000
c = 25
h = 1700
x = -300
y = 500
z = 150
delp = 118

alpha = 0.70
nu    = 0.25
E     = 1.0e10

a = a*0.3048
b = b*0.3048
c = c*0.3048
h = h*0.3048
x = x*0.3048
y = y*0.3048
z = z*0.3048
delp = delp*6894.76

cuboid = ci.Cuboid3d()

cuboid.set_a(a)
cuboid.set_b(b)
cuboid.set_c(c)
cuboid.set_h(h)

cuboid.set_alpha(alpha)
cuboid.set_nu(nu)
cuboid.set_E(E)
cuboid.set_delp(delp)

cuboid.set_d0()

print cuboid.u_x_inf_cuboid(x,y,z), -5.07886e-6
print cuboid.u_y_inf_cuboid(x,y,z), +6.53365e-6
print cuboid.u_z_inf_cuboid(x,y,z), -2.77194e-5

print cuboid.up_x_z_inf_cuboid(x,y,z), -2.59958e-8
print cuboid.up_y_z_inf_cuboid(x,y,z), +2.80107e-8
print cuboid.up_z_z_inf_cuboid(x,y,z), -8.88255e-8

print cuboid.u_x_inf_image_cuboid(x,y,z), -3.27602e-6
print cuboid.u_y_inf_image_cuboid(x,y,z), +4.48753e-6
print cuboid.u_z_inf_image_cuboid(x,y,z), -2.10287e-5
```

```

print cuboid.up_x_z_inf_image_cuboid(x,y,z), +1.47310e-8
print cuboid.up_y_z_inf_image_cuboid(x,y,z), -17.64929e-9
print cuboid.up_z_z_inf_image_cuboid(x,y,z), 5.99370e-8

print cuboid.eps_xx_inf_cuboid(x,y,z), +5.09677e-8
print cuboid.eps_yy_inf_cuboid(x,y,z), +3.78578e-8
print cuboid.eps_zz_inf_cuboid(x,y,z), -8.88255e-8
print cuboid.eps_xy_inf_cuboid(x,y,z), +5.02579e-9
print cuboid.eps_yz_inf_cuboid(x,y,z), +2.80107e-8
print cuboid.eps_xz_inf_cuboid(x,y,z), -2.59958e-8

print cuboid.epsp_xx_inf_z_cuboid(x,y,z), +2.46011e-10
print cuboid.epsp_yy_inf_z_cuboid(x,y,z), +1.58131e-10
print cuboid.epsp_zz_inf_z_cuboid(x,y,z), -4.04142e-10
print cuboid.epsp_xy_inf_z_cuboid(x,y,z), +3.56400e-11
print cuboid.epsp_yz_inf_z_cuboid(x,y,z), +1.46006e-10
print cuboid.epsp_xz_inf_z_cuboid(x,y,z), -1.72015e-10

print cuboid.eps_xx_inf_image_cuboid(x,y,z), +3.35970e-8
print cuboid.eps_yy_inf_image_cuboid(x,y,z), +2.63402e-8
print cuboid.eps_zz_inf_image_cuboid(x,y,z), -5.99370e-8
print cuboid.eps_xy_inf_image_cuboid(x,y,z), +2.70108e-9
print cuboid.eps_yz_inf_image_cuboid(x,y,z), +1.76493e-8
print cuboid.eps_xz_inf_image_cuboid(x,y,z), -1.47310e-8

print cuboid.epsp_xx_inf_image_z_cuboid(x,y,z), -1.44630e-10
print cuboid.epsp_yy_inf_image_z_cuboid(x,y,z), -9.94020e-11
print cuboid.epsp_zz_inf_image_z_cuboid(x,y,z), +2.44032e-10
print cuboid.epsp_xy_inf_image_z_cuboid(x,y,z), -1.75493e-11
print cuboid.epsp_yz_inf_image_z_cuboid(x,y,z), -8.62057e-11
print cuboid.epsp_xz_inf_image_z_cuboid(x,y,z), +8.59788e-11

print cuboid.u_x_cuboid(x,y,z), -1.02839e-5
print cuboid.u_y_cuboid(x,y,z), +1.38948e-5
print cuboid.u_z_cuboid(x,y,z), -7.52576e-5

print cuboid.omega_xy_cuboid(x,y,z), +2.54529e-9
print cuboid.omega_xz_cuboid(x,y,z), +2.50663e-8
print cuboid.omega_zx_cuboid(x,y,z), -6.33197e-8
print cuboid.omega_zy_cuboid(x,y,z), +7.11919e-8
print cuboid.omega_yz_cuboid(x,y,z), -3.47038e-8

print cuboid.eps_xx_cuboid(x,y,z), +1.04936e-7
print cuboid.eps_yy_cuboid(x,y,z), +8.14489e-8
print cuboid.eps_zz_cuboid(x,y,z), -6.65113e-8
print cuboid.eps_xy_cuboid(x,y,z), +2.54259e-9
print cuboid.eps_yz_cuboid(x,y,z), +1.82441e-8
print cuboid.eps_xz_cuboid(x,y,z), -1.91267e-8
```

References

Bodin, T. and Sambridge, M. (2009). Seismic tomography with the reversible jump algorithm. *Geophysical Journal International*, 178(3):1411–1436.

Chen, Y. (2016). Numerical solution of eshelby's elastic inclusion problem in plane elasticity by using boundary integral equation. *Engineering Analysis with Boundary Elements*, 68:17–23.

Cooper, H. H. and Jacob, C. E. (1946). A generalized graphical method for evaluating formation constants and summarizing well-field history. *Eos, Transactions American Geophysical Union*, 27(4):526–534.

Davies, J. H. (2003). Elastic field in a semi-infinite solid due to thermal expansion or a coherently misfitting inclusion. *Journal of Applied Mechanics*, 70(5):655–660.

Deb, K. (2002). A Fast and Elitist Multiobjective Genetic Algorithm: NSGA-II. *IEEE Transactions on Evolutionary Computation*, 6(2):182–197.

Detournay, E. and Cheng, A. H.-D. (1993). Fundamentals of poroelasticity. In *Analysis and design methods*, pages 113–171. Elsevier.

Deutsch, C. V. and Wang, L. (1996). Hierarchical object-based stochastic modeling of fluvial reservoirs. *Mathematical Geology*, 28(7):857–880.

Dobrovolskii, I. (2007). Problem on an inhomogeneity in a linearly elastic space or half-space. *Mechanics of solids*, 42(1):50–56.

Doherty, J. (2003). Ground water model calibration using pilot points and regularization. *Groundwater*, 41(2):170–177.

Eshelby, J. D. (1957). The determination of the elastic field of an ellipsoidal inclusion, and related problems. *Proceedings of the Royal Society of London. Series A. Mathematical and Physical Sciences*, 241(1226):376–396.

Eshelby, J. D. (1959). The elastic field outside an ellipsoidal inclusion. *Proceedings of the Royal Society of London. Series A. Mathematical and Physical Sciences*, 252(1271):561–569.

Germanovich, L. N. and Chanpura, R. A. (2002). Modeling thin inclusions in poroelastic medium by line discontinuities. In *IUTAM Symposium on Analytical and Computational Fracture Mechanics of Non-Homogeneous Materials*, pages 133–142.

Germanovich, L. N., Genc, G., Lowell, R. P., and Rona, P. A. (2012). Deformation and surface uplift associated with serpentinization at mid-ocean ridges and subduction zones. *Journal of Geophysical Research*, 117(B07103).

Gladwin, M. T. (1984). High-precision multicomponent borehole deformation monitoring. *Review of Scientific Instruments*, 55(12):2011–2016.

Guido, F. L., Antonellini, M., and Picotti, V. (2015). Modeling ground displacement above reservoirs undergoing fluid withdrawal/injection based on an ellipsoidal inhomogeneity model. *International Journal of Rock Mechanics and Mining Sciences*, 79:63–69.

Hastings, W. K. (1970). Monte Carlo sampling methods using Markov chains and their applications. *Biometrika*, 57(1):97–109.

Helton, J. C. and Davis, F. J. (2003). Latin hypercube sampling and the propagation of uncertainty. *Reliability Engineering and System Safety*, 81(1):23–69.

Kachanov, M. and Sevostianov, I. (2018). *Micromechanics of materials, with applications*, volume 249. Springer.

Kellogg, O. D. (1929). *Foundations of potential theory.* Verlag Von Julius Springer, Berlin. reprinted by Dover, New York, 1953.

Lehner, F., Knoglinger, J., and Fischer, F. (2005). Use of a Maysel integral representation for solving poroelastic inclusion problems. In *6th International Congress on Thermal Stresses*, pages 1–4.

Lyu, D., Zhang, X., Li, P., Luo, D., Hu, Y., Jin, X., Zhang, L., and Keer, L. M. (2018). Explicit analytical solutions for the complete elastic field produced by an ellipsoidal thermal inclusion in a semi-infinite space. *Journal of Applied Mechanics*, 85(5):051005.

Meng, C., Heltsley, W., and Pollard, D. D. (2012). Evaluation of the Eshelby solution for the ellipsoidal inclusion and heterogeneity. *Computers & geosciences*, 40:40–48.

Metropolis, N. and Ulam, S. (1949). The monte carlo method. *Journal of the American Statistical Association*, 44(247):335–341.

Mindlin, R. D. and Cheng, D. H. (1950a). Nuclei of strain in the semi-infinite solid. *Journal of Applied Physics*, 21(9):926–930.

Mindlin, R. D. and Cheng, D. H. (1950b). Thermoelastic stress in the semi-infinite solid. *Journal of Applied Physics*, 21(9):931–933.

Mogilevskaya, S. G. and Crouch, S. L. (2007). On the use of Somigliana's formulae and series of surface spherical harmonics for elasticity problems with spherical boundaries. *Engineering Analysis with Boundary Elements*, 31(2):116–132.

Movchan, A. B. and Movchan, N. V. (1995). *Mathematical modelling of solids with nonregular boundaries*, volume 3. CRC Press.

Mura, T. (2013). *Micromechanics of defects in solids.* Springer Science & Business Media.

Murdoch, L. C., Freeman, C. E., Germanovich, L. N., Thrash, C., and DeWolf, S. (2015). Using in situ vertical displacements to characterize changes in moisture load. *Water Resources Research*, 51(8):5998–6016.

Murdoch, L. C., Moysey, S., Germanovich, L. N., and Hughes, B. (2016). Proof-of-feasibility of using well bore deformation as a diagnostic tool to improve co2 sequestration. Technical Report 1240376, United States Department of Energy. DOI: 10.2172/1240376.

Muskhelishvili, N. I. (2013). *Some basic problems of the mathematical theory of elasticity.* Springer Science & Business Media.

Nuccio, M. and Guerzoni, M. (2019). Big data: Hell or heaven? Digital platforms and market power in the data-driven economy. *Competition & Change*, page 1024529418816525.

Oliphant, T. E. (2007). Python for scientific computing. *Computing in Science & Engineering*, 9(3):10–20.

Peirce, B. O. (1902). *Elements of the theory of the Newtonian potential function.* Ginn & Company, Boston, 3rd edition.

Press, W. H., Teukolsky, S. A., Vetterling, W. T., and Flannery, B. P. (2002). *Numerical Recipes in C++: The art of scientific computing.* Cambridge University Press, second edition.

Reches, Z. (1998). Tensile fracturing of stiff rock layers under triaxial compressive stress states. *International Journal of Rock Mechanics and Mining Sciences*, 35(4-5):456–457.

Robinson, K. (1951). Elastic energy of an ellipsoidal inclusion in an infinite solid. *Journal of Applied Physics*, 22(8):1045–1054.

Ru, C. Q. (1999). Analytic solution for Eshelby's problem of an inclusion of arbitrary shape in a plane or half-plane. *Journal of Applied Mechanics*, 66(2):315–523.

Rudnicki, J. W. (2011). Eshelby's technique for analyzing inhomogeneities in geomechanics. In *Mechanics of crustal rocks*, pages 43–72. Springer.

Stein, M. (1987). Large sample properties of simulations using latin hypercube. *Technometrics*, 29(2):143–151.

Streltsova, T. D. (1988). *Well testing in heterogeneous formations.* Exxon Monographs Series. Wiley.

Timoshenko, S. and Goodier, J. N. (1951). *Theory of elasticity.* New York.

Wang, H. F. (2000). *Theory of linear poroelasticity with applications to geomechanics and hydrogeology.* Princeton Series in Geophysics. Princeton University Press.

Zhang, X., Lyu, D., Li, P., Jin, X., Liaw, P. K., and Keer, L. M. (2019). A closed-form solution for the horizontally aligned thermal-porous spheroidal inclusion in a half-space and its applications in geothermal reservoirs. *Computers & Geosciences*, 122:15–24.

Chapter Four
Field Demonstration

The objective of this phase of the project is to evaluate the feasibility of measuring in-situ strains during injection. To meet this objective, strainmeters and tiltmeters were installed at field sites in South Carolina and Oklahoma. The South Carolina field site was used to test prototype instruments and develop field procedures. The Oklahoma field site is an operating oil field and it was used to monitor ground deformation in the vicinity of an injection well during a three injection tests and one shut-in test (Figure 4.1).

The settings of the two field sites are described below, followed by a description of the strain measuring instrumentation. Descriptions of the methods and observations during the field tests are also included in this chapter.

4.1 Settings of the Field Sites

Project activities were conducted at a field site underlain by biotite gneiss a few km east of Clemson University, and another site underlain by Pennsylvanian sedimentary rocks at the North Avant Field north of Tulsa, Oklahoma.

4.1.1 North Avant Field Site

4.1.1.1 Location

The North Avant Field is an oilfield in Tiers 23N and 24N, Ranges 11E and 12E in Osage, OK. The field spans a total of approximately 11 mi^2 in eastern Osage County, Oklahoma (Figure 4.1a). Wells in the North Avant Field produce oil from the Bartlesville Formation, a sandstone on the northeastern side of the Oklahoma platform of the Cherokee Basin.

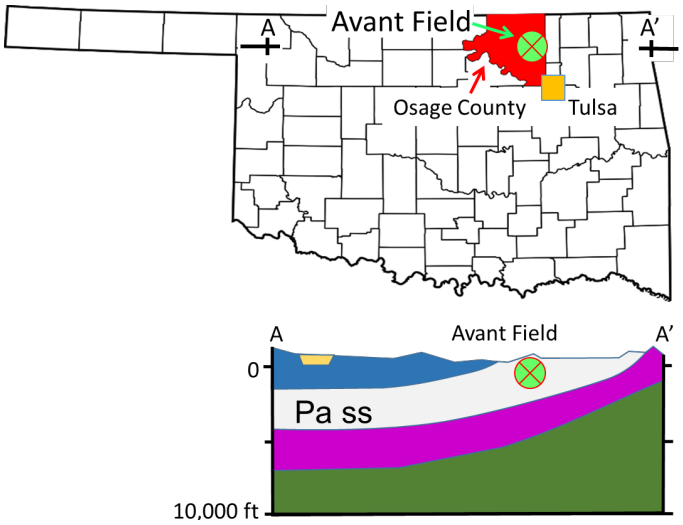

Figure 4.1: Location of the North Avant Field in Osage County, OK. Cross-section shows approximate location of the reservoir in Pennsylvanian age rocks. Mississippian age rocks in purple, Permian age rocks are blue.

The field site for the project is on the northwestern side of the North Avant Field in Township 24N, Range 11E, Sections 25 and 26. The site is approximately 1 km southwest of Wolco, OK. Injection tests used Well 9A, a vertical well completed in the Bartlesville Formation at 530 m (1,700 feet) depth. Topographic relief is less than several meters within approximately 100 m of well 9A. A North-South trending, shallow drainage occurs approximately 120 m west of well 9A where the upper reaches of Tucker Creek flow to the south. The elevation of well 9A is approximately 256 m (840 feet) above mean sea level (AMSL), and the Tucker Creek drainage is at approximately 240 m (790 feet) elevation. Property in the vicinity of well 9A and to the west is privately owned and is accessible to the project through our collaborator Grand Resources. Property including Tucker Creek and regions to the west are unavailable for drilling, although existing wells can be used for pressure monitoring.

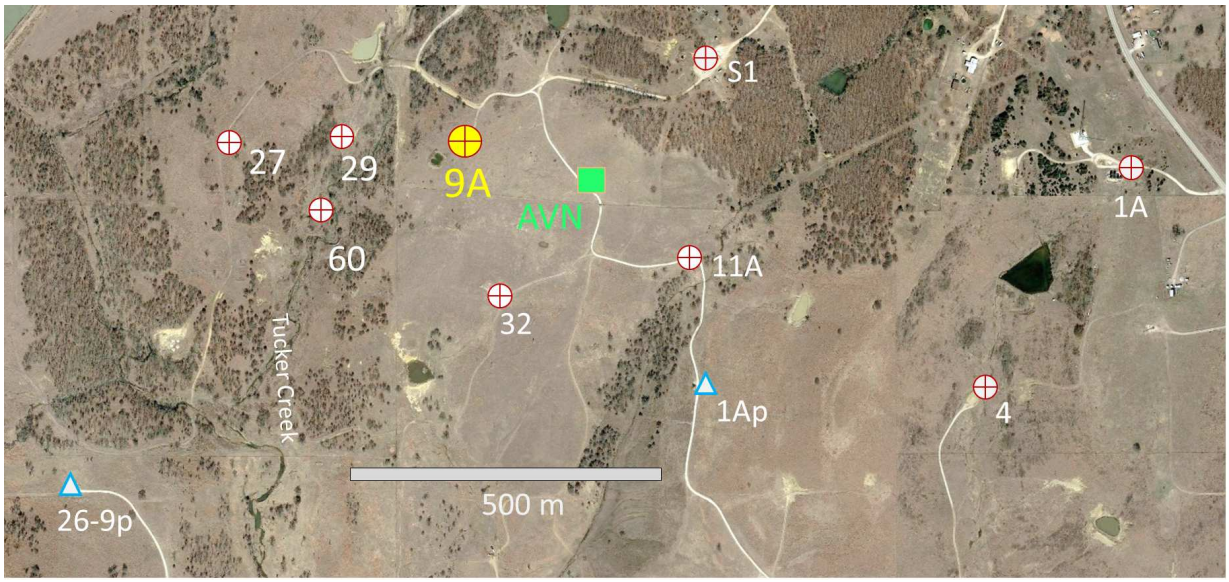

Figure 4.2: Vicinity of well 9A used for field testing in the North Avant Field, OK. Red circle with cross are wells in the reservoir used for pressure monitoring or injection, blue triangles are production wells.

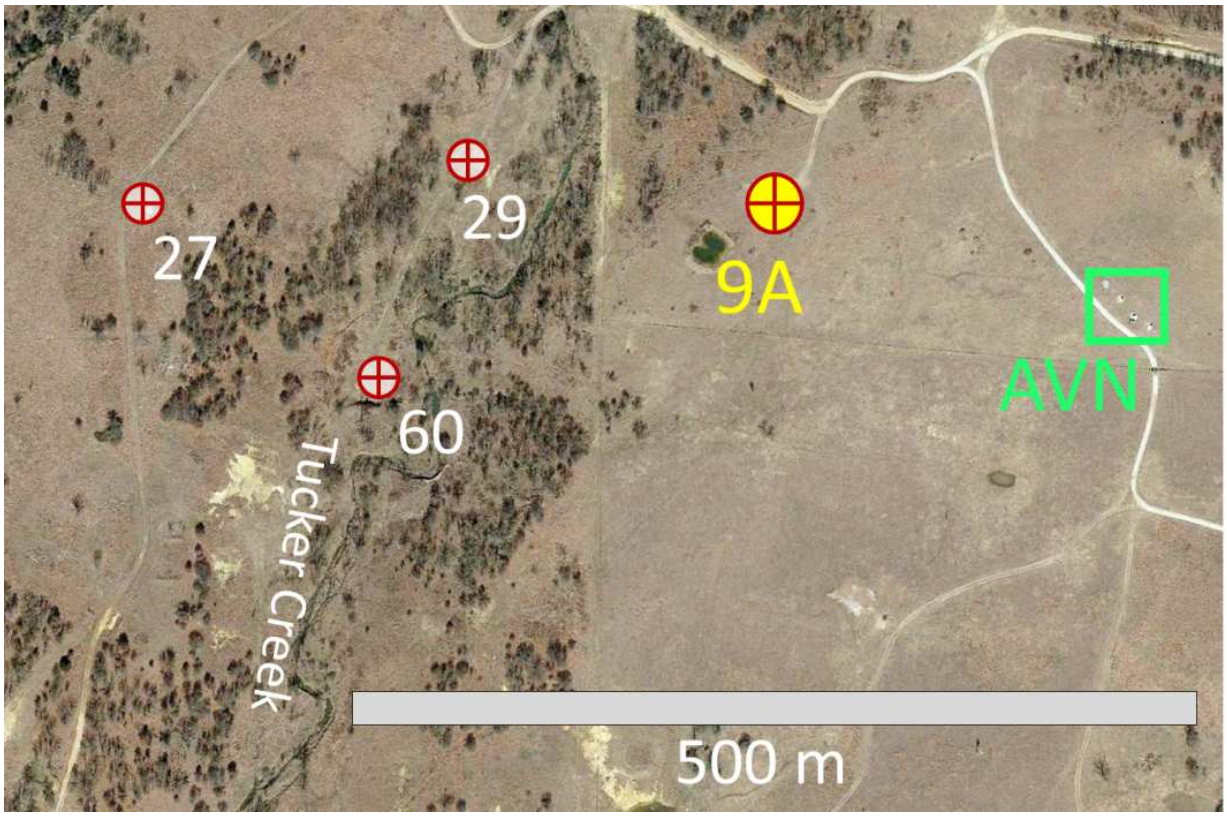

Figure 4.3: Enlarged view of scene in Figure 4.2 in vicinity of well 9A.

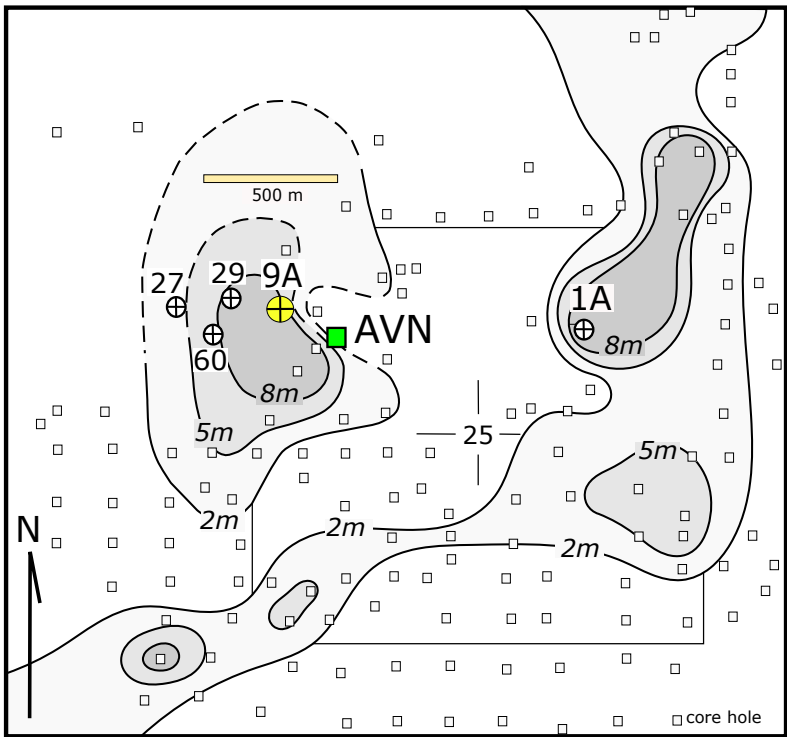

Figure 4.4: Map of vicinity of well 9A in the North Avant Field, OK. Strainmeters are at location AVN. Wells 27, 29, 60 used for pressure monitoring, cored holes as small squares. Well 1A is an injection well that was shut-in. Isopach shows thickness in meters of coarse-grained unit at base of Bartlesville sand interpreted from core, dashed where inferred. Border of Section 25 in T24N, R11E for location.

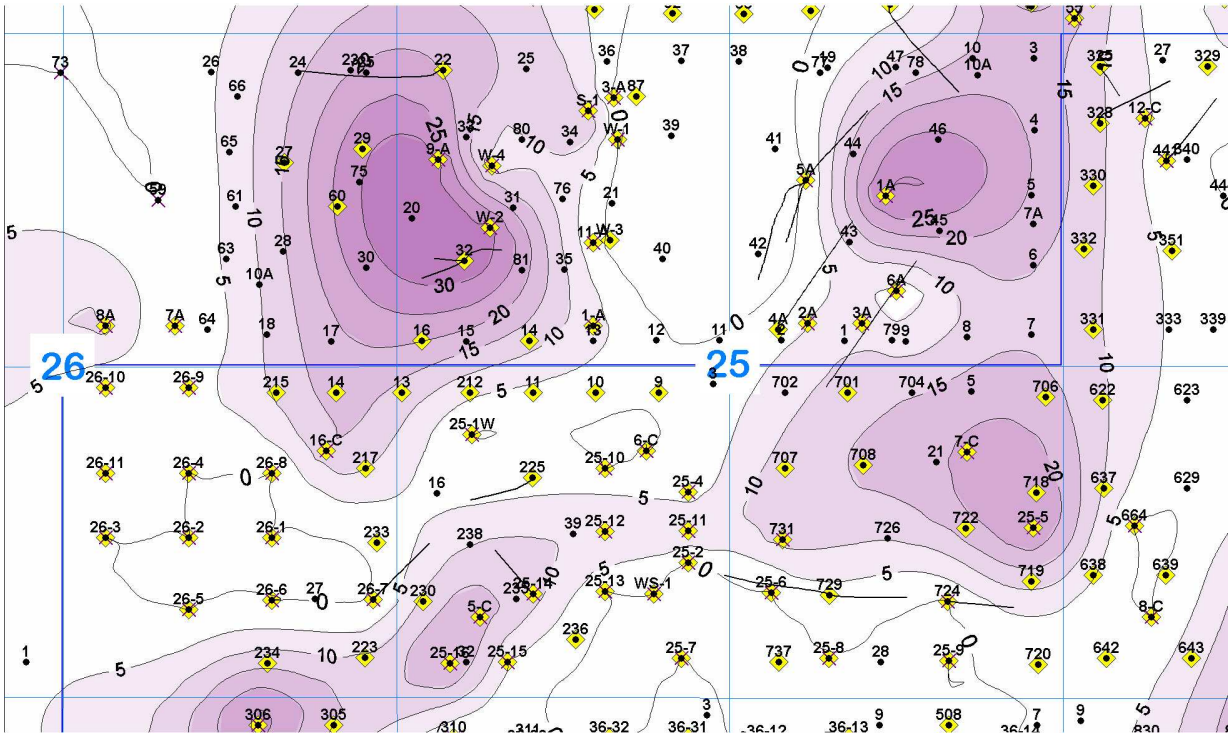

Figure 4.5: Map of vicinity of well 9A in the North Avant Field, OK. Well locations shown as points. Yellow points are cored boreholes. Black lines are horizontal wells. Isopach (in feet) of coarse-grained lens shown in purple. Numbers are sections in T24N, R11E. Section width is one mile, and North is upward.

Wells that were used for either recovery or water injection occur in the vicinity of well 9A (Figures 4.2, 4.3 and 4.4). Thirteen wells were completed within 300 m of well 9A. Wells #22, #29, #32 and #60 (Figure 4.5) have produced oil in the past several years, and were shut-in in January 2016, February 2015, October 2011 and July 2008, respectively. Horizontal wells were drilled in the vicinity of 9A at locations #22, which is approximately 250 m to the N–NW, and #32 (three laterals), which is 250 m to the S–SW (Figure 4.5). The other wells have been inactive for many decades.

4.1.1.2 Geology

The Bartlesville Formation is the major producing reservoir of the North Avant Field. It is part of the Boggy Formation of the lower Desmoinesian series of Pennsylvanian age. The formation extends north-south more than 450 km, and the width broadens from 10 km in the north to 120 km in the south. Bedding dips to the west-southwest at 1/100. It is inferred to consist of fluvial, incised valley-fill deposited in paleovalleys during a transgressional period. The Bartlesville Formation is 40 to 80 m thick within the paleovalleys and thins to less than 5 m outside paleovalleys.

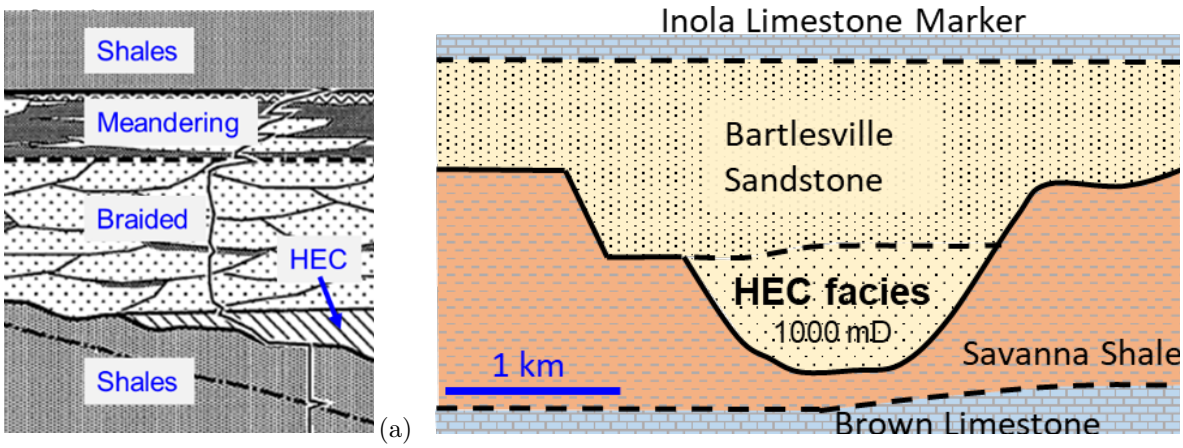

Figure 4.6: Idealized cross-sections through the Bartlesville Formation. a.) a meandering fluvial unit overlies the braided fluvial unit; b.) Coarse-grained lenses (HEC facies) cut into underlying shale. Modified from Ye et al. (1999).

Locally within the North Avant Field, the Bartlesville Formation is a medium to very-fine-grained sandstone that is moderately to poorly sorted (Obianyor, 2008). The grain size becomes finer upward through the thickness of the formation. The Bartlesville Formation includes two stratigraphic units characterized by different inferred environments of deposition (Figure 4.6). The upper unit includes bedforms typical of meandering fluvial facies, which is inferred to have been deposited during an upper transgressive system tract. The lower unit is a series of cross-bedded sands typical of sediments deposited in anabranching channels in a braided fluvial facies. This unit is typical of deposition during a lowland system tract. The braided fluvial unit lies below the meandering fluvial deposits. Minor splay and levee deposits, and floodplain mudstone lenses occur throughout the Bartlesville Formation (Obianyor, 2008).

Five cores were taken from an area 2 km from well 9A and used to characterize stratigraphy and make permeameter measurements (Obianyor, 2008). These data indicate that the braided fluvial unit is dominated by subangular to subrounded, moderate to well sorted, coarse to medium grained, channel-fill sandstones. This unit is 15 m thick with individual channel-fill thicknesses ranging from 1 to 5 m. Permeability ranges from 0.1 to 430 mD and porosity is between 0.15 and 0.27, according to measurements made on cores from the vicinity of well 9A. Average porosity is 0.18 and the geometric mean horizontal permeability is 35 mD.

The K_v/K_h ratio is between 0.07 and 0.8. Mud drapes are common and are assumed to create permeability baffles.

The meandering fluvial facies fines upwards from fine-grained sandstone at the base to very fine-grained sandstone to mudstone at the top. The thickness of this moderately sorted sandstone is approximately 13 m feet with individual channels ranging from 1 to 4 m thick. Permeability ranges between 0.01 to 130 mD with a geometric mean of 8 mD (Obianyor, 2008). Porosity varies between 0.1 and 0.2 with an average value of 0.16. It is composed of upper, lower, and middle channel-fill subfaces that have average porosities of 0.14, 0.17, and 0.16, respectively and permeabilities of 0.7, 13, and 6.7 mD, respectively. The K_v/K_h ratio is between 0.03 and 0.4.

There are high permeability zones within the braided fluvial facies of the Bartlesville Formation. These zones are elongate, approximately 300 m wide and 1,000 m long or more, and they typically trend approximately NE/SW (Figure 4.4). They consist of multiple, fining upward deposits of relatively coarse-grained sediments. These zones are referred to as "high energy channels" (HECs) because the coarse-grained sediment they contain is inferred to have been deposited in an environment where the water flow was rapid and thus at high energy. The HEC typically occur along the bottom of the braided fluvial facies of the Bartlesville Formation and are inferred to be multiple channel deposits localized within paleovalleys.

The HECs are the most productive oil bearing units in the Bartlesville Formation. The porosity of these zones is typically greater than 0.2. The permeability is greater than 100 mD, and it is approximately 1,000 to 2,000 mD in some locations (e.g. Figure 4.7). The HECs are embedded in sands with permeability several tens of mD, approximately 1 to 2 orders of magnitude less than the zones themselves. They are scattered within the braided facies and their location and extent are difficult to predict (Figure 4.4). Identifying the location of the HECs is important to oil production operations because more fluids occur within these channels compared to the adjacent, finer-grained sandstones. Characterizing HECs during CO_2 storage is also important because their storage capacity would be larger than in other units.

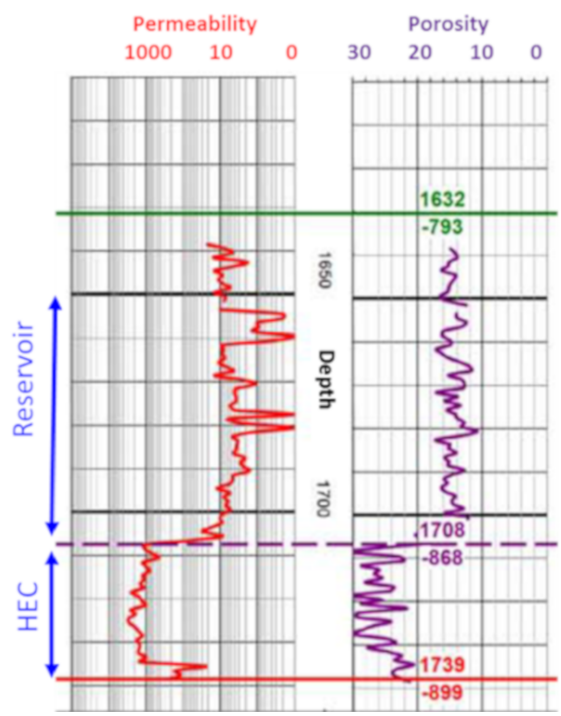

Figure 4.7: Distribution of permeability (milliDarcy) and porosity (percent) in the HEC and overlying Bartlesville sand reservoir from a well log in the North Avant Field. Vertical scale is in feet.

Production during water flooding suggests formation properties are highly heterogeneous. Geologic and permeability analysis indicates that well 9A intersects a NE-trending HEC, according to current interpretations from Grand Resources (Figure 4.7a). Linear interpolation of the HEC thickness from rock cores in the vicinity of 9A indicate that the HEC may extend 2 km. It is inferred to be 800 m wide, and up to 10 m thick.

The Bartlesville sandstone is underlain by the Drywood coal and claystones ranging from 2 to 4 m thick. These are absent in some cores, where the Bartlesville sandstone is directly underlain by the Savanna shale. In general, the Bartlesville Formation is overlain by a series of inter-bedded coals, sandstones, limestones, and mudstones that grades between facies.

The vicinity of well 9A is underlain by a 6-m-thick limestone layer at a depth of 45 m, according to cores from wells in the vicinity. This competent rock is the target depth for installing the monitoring equipment.

4.1.1.3 Production History

The North Avant Field has been in production since 1905. Primary recovery methods were used from 1905 to 1984 and secondary techniques were introduced afterwards. Gas re-injection was performed during the primary phase and waterflooding was initiated in 1984. Starting in 2004, horizontal well technology was implemented by Grand Resources to improve waterflooding. Cumulative oil production at North Avant Field from 1906 to 2001 exceeds 14,000,000 barrels. Production has focused to the south and east of 9A, with little production within a mile to the north or west of the injection well (Figure 4.3). Production is focused at locations where the where the HEC zones are inferred to be relatively thick, allowing for greater pumping rates.

The production of oil on the first day, termed the Initial Potential (IP), ranged from 4 to 240 bbls for wells in the vicinity of well 9A. Well 9A itself had the lowest IP, so it was switched to a water injection well to increase the reservoir pressure.

Water injection at well 9A was ongoing until October 12th, 2015, when it was shut-in occurred to allow the pressure field to return to more background pressure prior to project testing. The well was previously shut-in between mid-March and mid-September 2013. Otherwise, injection has been at a rate of approximately 750 bbl/day. The injection pressure was approximately 85 psi at the well head (Figure 4.8). Nearly 1,000,000 barrels of water have been injected at well 9A since the beginning of 2011.

Production wells occur in the vicinity of our monitoring locations, and were shut-in at the same time as well 9A. Wells 1Ap and 26-9p are production wells that were in operation during the field tests (Figure 4.2). Water and with oil were pumped from those wells at rates that were approximately constant during the well tests conducted for the project.

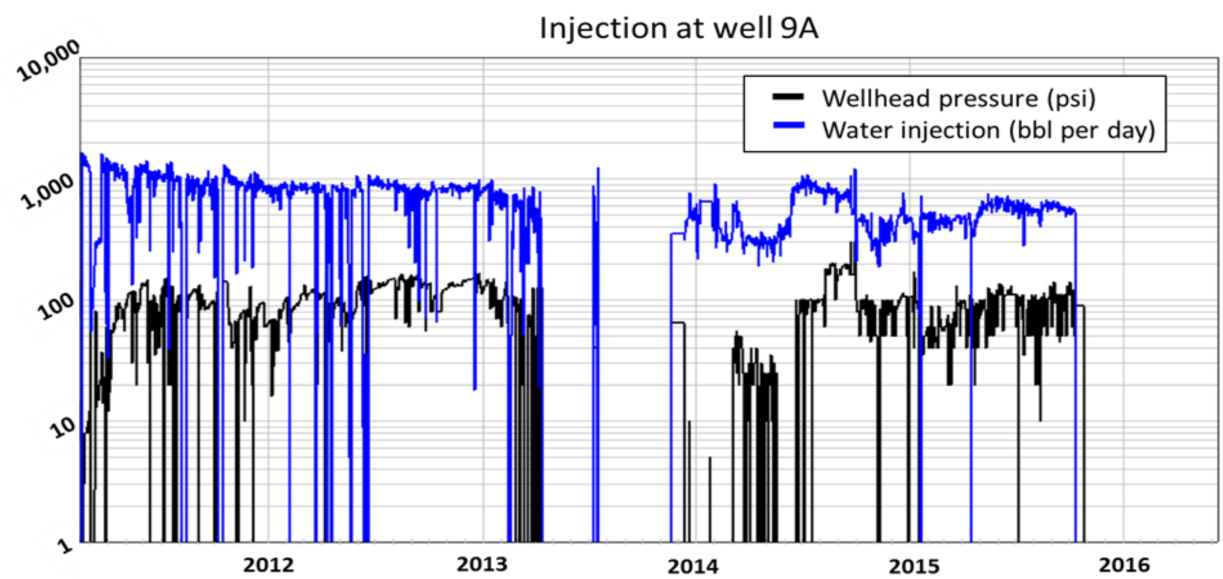

Figure 4.8: History of injection and wellhead pressure at well 9A in the North Avant Field, OK.

4.1.2 Clemson Field Site

The project used a research facility designated for hydromechanical testing the Simpson Station field site in Anderson County, South Carolina. The Simpson Station is a tract of land used for agricultural research by Clemson University, and our research facility is adjacent to the Bull Testing Facility at the Simpson Station, approximately 10 km east of Clemson University campus. Our facility is approximately $1,500$ m^2 ($\sim$0.4 acres), and it is adjacent to a 2,000 square-foot covered storage facility with electric power and water and a wireless data connection. A variety of investigations and studies have been performed at the site since the early 2000s. These studies included monitoring well installation, soil core sampling and excavations to observe and document soil characteristics.

4.1.2.1 Hydrogeologic Setting and Characterization

The field site is in the Piedmont physiographic province (34.670018°, −82.729311°). The field site is a 1,500 m^2 ($\sim$0.4 acres) plot adjacent to a 12 ha pasture, which is used for grazing. An electric fence surrounds the perimeter of the site to prevent interference from cattle. Ground cover and vegetation at the site consists of fescue grass and small shrubs. The topography is flat to slightly rolling with a shallow slope ($< 2\%$) to the northeast.

The soil profile at the site extends from the surface to approximately 3 m depth and is classified as the Cataula sandy loam soil series, which is characterized as a reddish, sandy, clayey silt. The B-horizon toward the bottom of the profile has a silty clay texture and a saturated hydraulic conductivity below the resolution of a Guelph permeameter, $< 10^{-9}$ m/s. The soil horizon grades into a biotite-gneiss derived saprolite to approximately 30 m, where it transitions into the fractured metamorphic parent rock. The saprolite has an ambient water content of 0.2–0.3 and the water table is at a depth of 9 m. A cross section of the site is shown in (Figure 4.9). Core samples taken in the saprolite reveal a high degree of heterogeneity and fabric similar to that of the metamorphic parent rock with high mica content. The texture of the saprolite ranges from a sandy loam to a loamy sand and has a reddish-brown appearance (5YR 5/6) with mottling throughout.

Shelby tube samples from two depth intervals were collected and submitted for laboratory analysis to determine estimates of the hydraulic and elastic properties of the saprolite. Triaxial tests were performed under partially and fully-saturated conditions to understand how the elastic properties changed as a function of saturation. Laboratory results indicate a Young's modulus of 60 MPa for partially saturated conditions and 50 MPa under full saturation. These values are similar to those found in previous investigations which range from 24 to 48 MPa. The loading curves from the most recent triaxial test are in Figure 4.10.

The triaxial tests also indicate a saturated hydraulic conductivity of 9.3×10^{-6} m/s, which is in agreement with the value obtained from numerical analysis of pumping test data (6.87×10^{-6} m/s). Estimates of the hydraulic conductivity of the saprolite from a series of Guelph permeameter tests indicate a slightly higher value of 0.8 to 3.5×10^{-5} m/s. Retention curve analyses were also performed on the Shelby tube samples and results indicate that the van Genuchten retention curve parameters (α and n) of saprolite are similar to that of silt, with an air-entry term (α) of 0.6 1/m and a pore size distribution term (n) of 1.31 (dimensionless).

4.1.2.2 Instrumentation and Ongoing Monitoring

The Simpson Station field site currently has five instruments installed in the saprolite in the shallow subsurface (< 12 m bgs) measuring vertical strain, as well as two strain sensors at over 45 m depth in the biotite-gneiss bedrock, including an electromagnetic eddy current instrument measuring multiple components of the strain tensor (vertical, horizontal and tilt) and an optical fiber areal strainmeter based on a Michelson

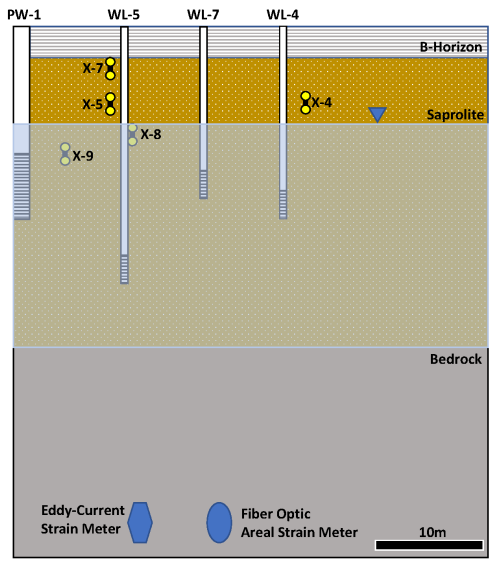

Figure 4.9: Geologic cross section and instrumentation of Simpson Station Field Site (Anderson County, SC).

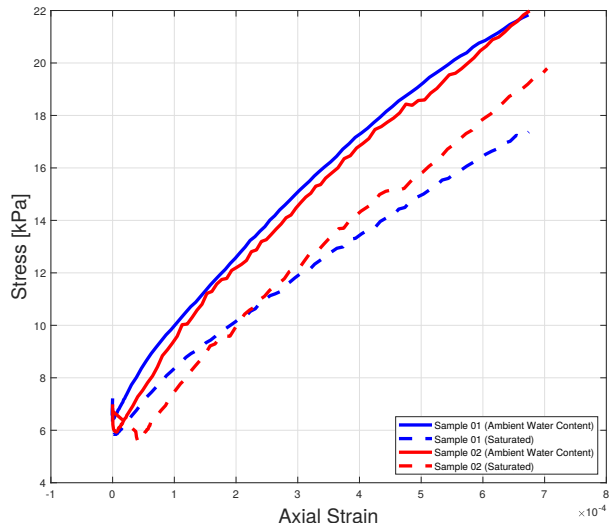

Figure 4.10: Stress as a function of strain during loading under partially and fully-saturated conditions.

interferometer. Locations of each of the instruments may be found in the Site Layout Map shown in (Figure 4.11). Additional measurements being made at the site include meteorological data (precipitation, wind speed and direction, barometric pressure and temperature) and hydrological data, including soil moisture, matric potential, evapotranspiration and water table elevation. These measurements are used to interpret the ambient strain signals, as well as to to correct the strain signals from pumping tests by removing the components associated with these ambient processes.

4.2 Instrumentation at North Avant Field

There have been a number of strain, tilt and pressure instruments deployed as a part of the injection monitoring effort around well 9A at the North Avant Field. Deployments began in September of 2016 with the drilling of two wells, AVN1 and AVN2, where the Gladwin Tensor Strainmeter (GTSM) was installed in the second well AVN2. This was followed in June of 2017 with the drilling of two more wells at AVN3 and AVN4, and installation of the Optical Fiber Areal Strainmeter in AVN4. Several commercial pressure transducers were also installed at this time in nearby wells 11A, 27, 29 and 60. Installation of the grout-in eddy current strain and tilt system occurred five weeks later in July of 2017 in borehole AVN3. This was followed by several subsequent trips to install supporting instruments such as a combination weather station and commercial 2-axis tiltmeter at borehole AVN4 in October, 2017.

4.2.1 Gladwin Borehole Tensor Strainmeter

The Gladwin Tensor Strainmeter (Gladwin, 1984) is the most widely deployed borehole strain monitoring instrument, and is the benchmark against which the project instruments were compared. It consists of four stacked capacitive displacement transducers that measure the diameter of the borehole along the azimuths 0, 30, 60, and 90 degrees to yield and over-determined estimate of the normal and shear strains. Data are recorded by a proprietary 24-bit ADC with a least-count (i.e., one digitizer step, or 2^{-24}) of 0.01 nanostrain.

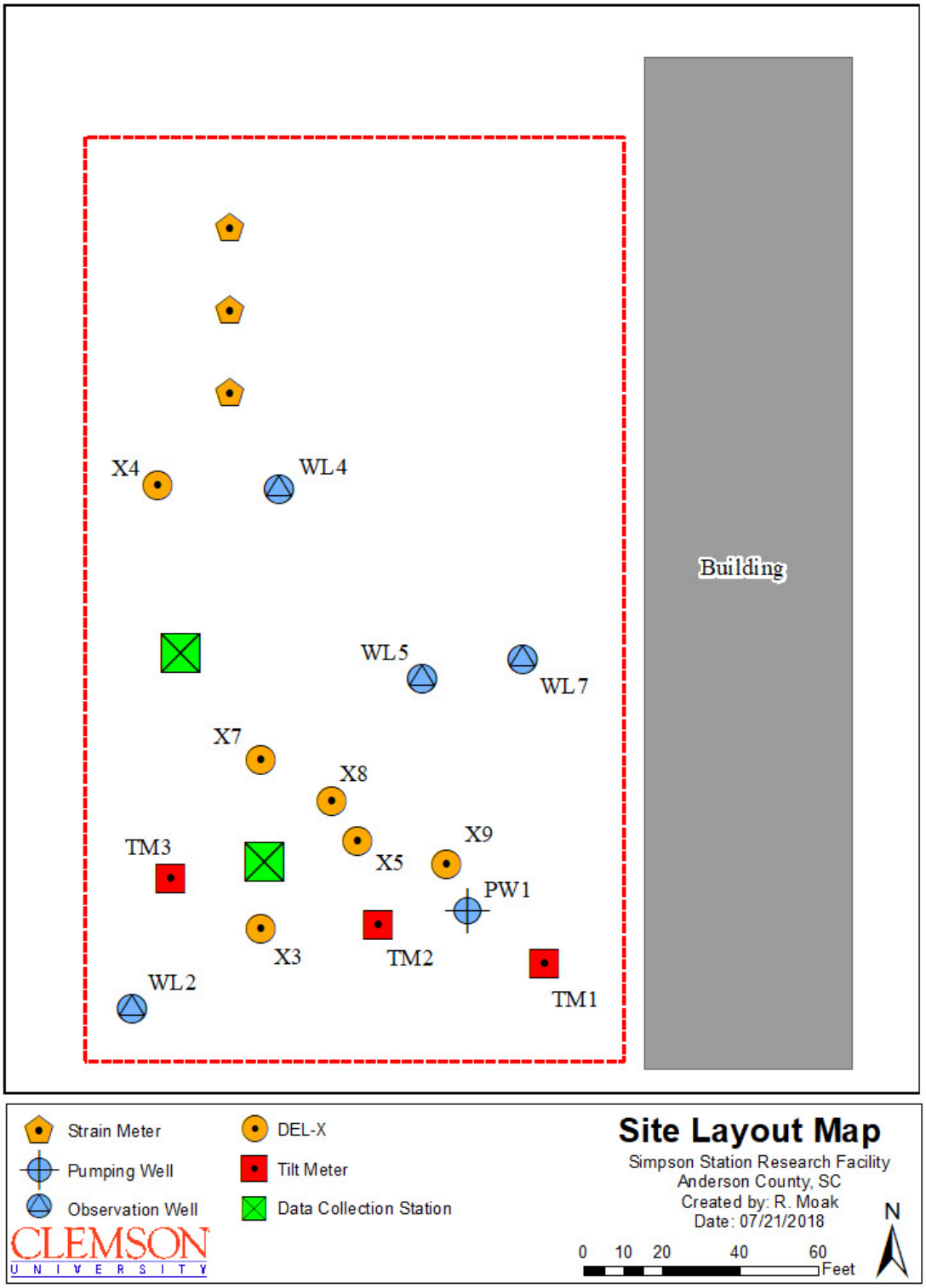

Figure 4.11: Simpson Station Site Layout Map.

UNAVCO had installed 89 of 100 GTSMs procured for the Plate Boundary Observatory and other projects prior to the deployment of #90 for this project (Figure 4.12a). They have since deployed the all of the remaining instruments. Details of the installation and background data are presented below.

4.2.1.1 Installation

Gladwin Tensor Strainmeter (serial number US90) was installed at the North Avant Field on September 8–13. The initial well location, AVN1 (36.532379°, −96.081191°) was determined during previous site visits and the goal was to drill and set casing to below an upper limestone layer at approximately 100 feet (∼30 m) and drill to a second limestone layer at around 200 feet (60 m) as predicted by existing logs from nearby wells. The initial hole was drilled using an 8-inch air hammer and 6-inch steel casing set and grouted at 115 feet (35 m). Drilling to the final depth of 240 feet (∼73 m) was done through this casing with a 6-inch air rotary bit to limit any potential fracturing in the install zone.

An underlying limestone layer was not encountered (Figure 4.13) so a second well, AVN2 (36.532120°, −96.081021°) was drilled the following day approximately 80 feet (∼25 m) southeast of AVN1. This was drilled in the same manner with casing set to 85 feet (26 m), and then drilled to a final depth of 100 feet (30 m). Well logs from this borehole (Figure 4.14) showed a competent limestone layer from 86–97 feet (26.2–29.6 m) where the instrument was installed the following day (September 10th, 2016).

The GTSM was deployed in a manner consistent with previous UNAVCO installations. Approximately 4 cubic feet (∼0.111 m^3) of expanding grout (BASF MasterFlow® 1206) was prepared and delivered to the bottom of the borehole using a dump bailer, resulting in a grout column of about 20 feet (∼6 m). The instrument (Figure 4.12a) was lowered through the grout to 96 feet (∼29.3 m), thereby centering the instrument within the limestone install zone. An additional 60 feet (18 m) of conventional grout was added to the borehole the following day to seal the remaining open hole and bring the cement to within 20 feet (6 m) of the surface.

Installation of the supporting infrastructure also began the day following the instrument deployment. This included burial of the surplus cable in a pit adjacent to the wellhead, and the pouring of a concrete pad foundation for the enclosure, or "doghouse" for the supporting electronics. The final day included the securing of the enclosure to the pad and installing the supporting electronics (Figures 4.12c and 4.12d) and solar panels. A barbwire fence was included around the perimeter to limit intrusion from grazing livestock. The completed installation is shown in Figure 4.12b.

4.2.2 Grout-In Eddy Current Strain and Tilt System

There were two versions of the grout-in eddy current strain and tilt systems completed and deployed during this project. Final assembly and initial borehole testing of the Version 1 eddy current strain and tilt system (shown on the left in Figure 2.8) was performed in March of 2016. This began with a shallow, 10-foot (3 m) deployment in a dry borehole located near the Clemson University L.G. Rich Laboratory in Anderson, SC. Testing and revisions were conducted in this borehole until September of 2016 after three new boreholes and supporting electronics were installed at the Clemson University Simpson Station in Central, SC.

The Version 2 instrument (shown in the center of Figure 2.8) was assembled, tested, and then deployed at the North Avant Field, OK, in mid-July of 2017 in borehole AVN3, approximately 40 feet (12 m) northwest of the GTSM in AVN2. This required a similar up-hole supporting electronics infrastructure as the Simpson Station installation for power and telemetry.

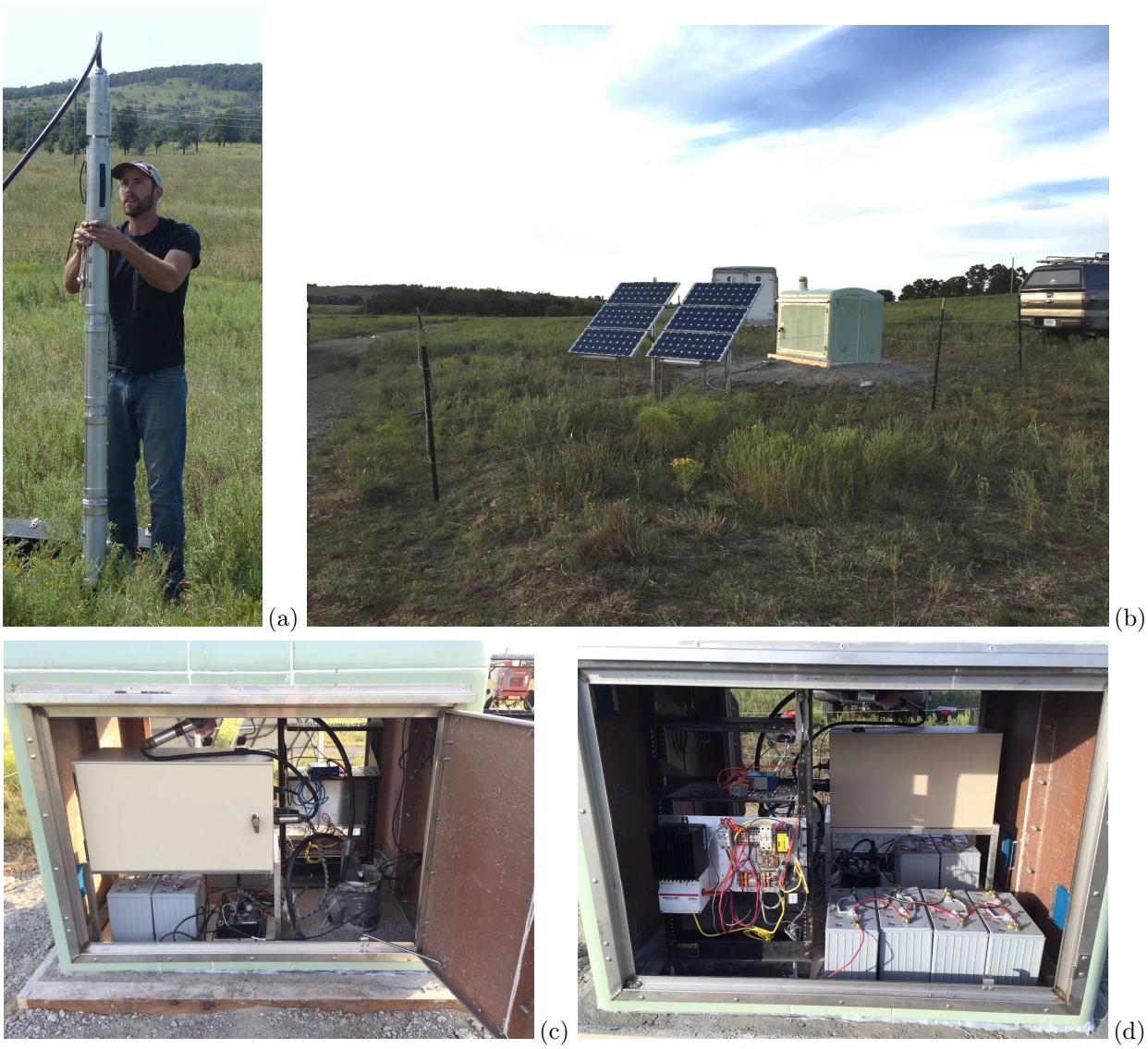

Figure 4.12: Photographs of the Gladwin Tensor Strainmeter installation in AVN2 at the North Avant Field. (a) The GTSM instrument before installation with a UNAVCO technician for scale. (b) Completed installation, including instrument "doghouse", solar panels, and cattle fencing. (c) GTSM doghouse interior facing west showing the main data acquisition system in the beige cabinet on the left, the borehole casing stickup on the right, and additional supporting hardware. (d) Doghouse interior facing east showing the main power distribution tray and battery storage.

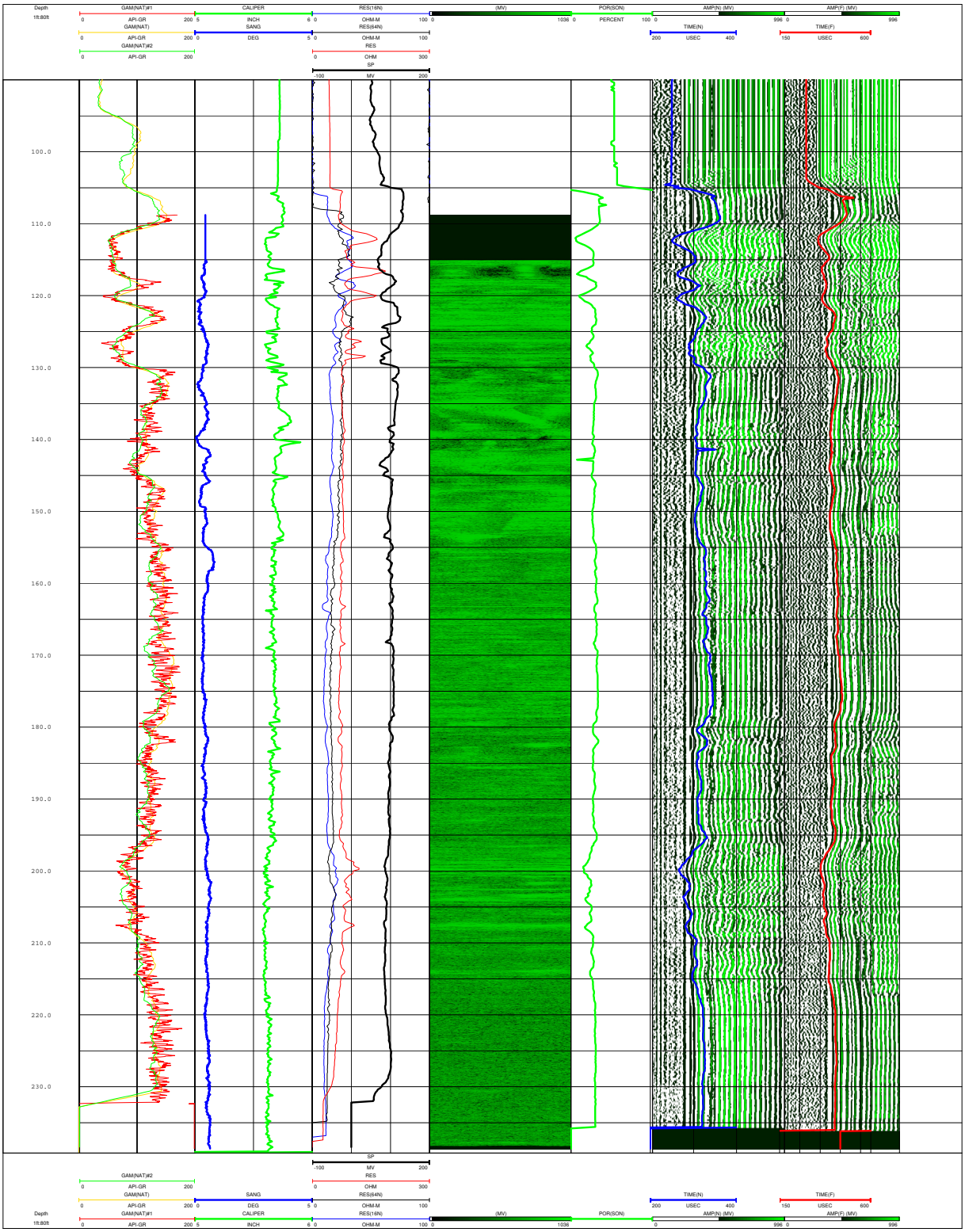

Figure 4.13: Well log from borehole AVN1 showing (from left-to-right) gamma, caliper, resistivity, video, sonic, and variable density logs.

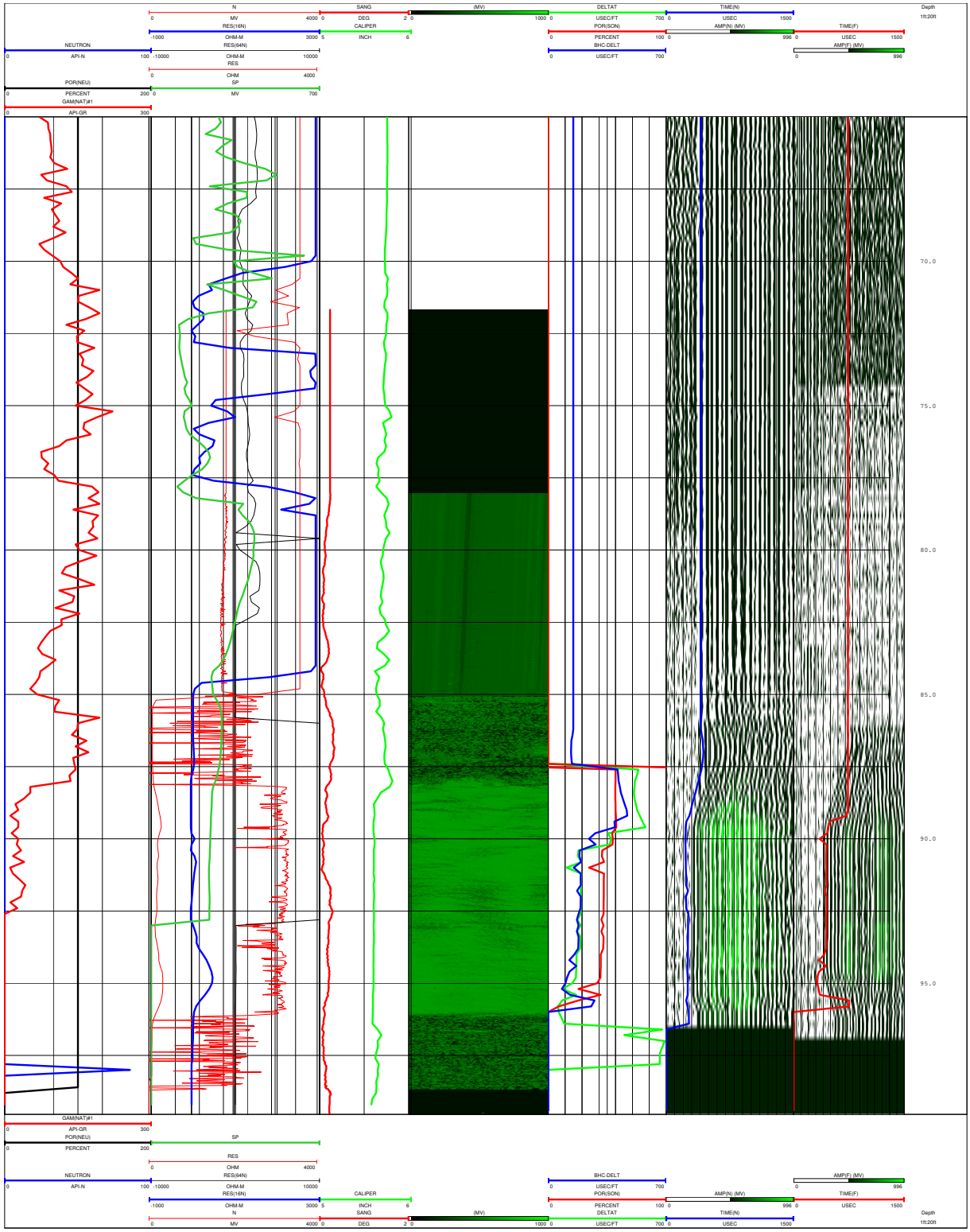

Figure 4.14: Well log from borehole AVN2 showing (from left-to-right) gamma, caliper, resistivity, video, sonic, and variable density logs.

4.2.2.1 Installation at the Simpson Station, SC

The three Simpson Station boreholes, SBF1–3 were drilled on June 17th, 2016 using an air hammer water well drilling rig. 6-inch PVC casing was set and grouted to a depth of 106 feet (∼32 m), which is roughly 10 feet (3 m) below the transition to competent bedrock (biotite gneiss), and the open hole (i.e., install zone) portion drilled to final depths of 150 feet (45.7 m). Video logs of the uncased well portions showed very smooth, un-fractured install zones in each well.

Three wellheads were completed with vaults and connected to a central "head node" (Figure 4.15). This included three flush-mounted well vaults with bolt-on covers that were placed over several feet of rock that filled a drainage hole surrounding each well stickup. A 2-inch (5 cm) diameter hole was drilled in each drainage hole to about a 10-foot (3 m) depth to penetrate the upper surface layer into the more porous underlying material, which provided excellent drainage. Each vault skirt was connected via 2-inch trade size plastic conduit to the bottom of an electrical enclosure (Hammond 1418N4J8) such that any cabling between the instruments and supporting electronics could be passed underground. Landscaping cloth was used to cover the drainage rocks and the well vaults were buried flush with the ground, resulting in a level ground surface for easy landscape maintenance.

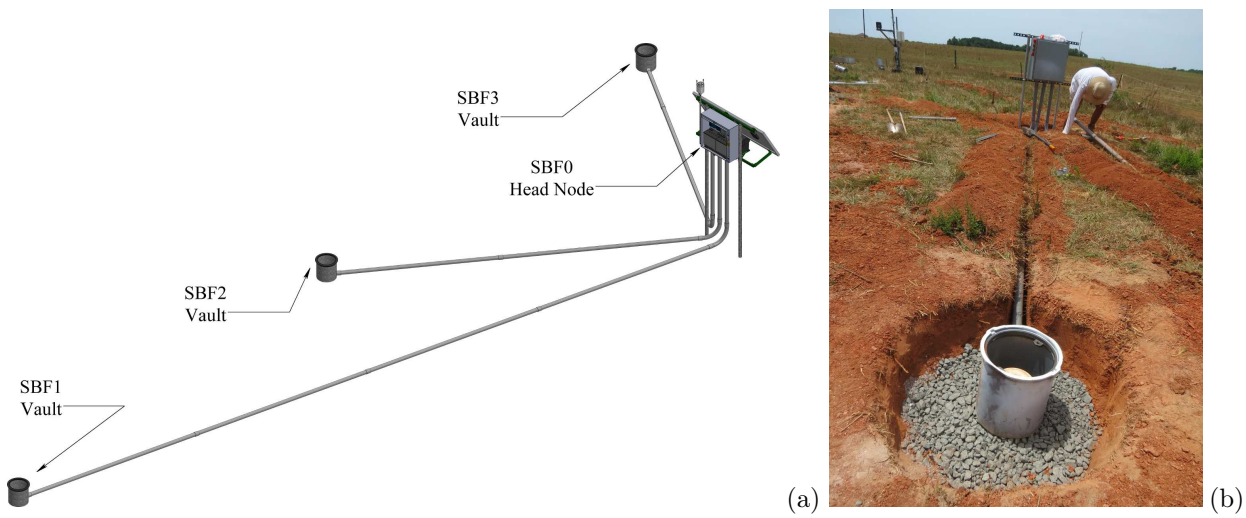

Figure 4.15: (a) Schematic layout of the Simpson Station well vaults and head node. (b) Photograph of the wellhead completion including well vault cover, conduit, and drainage rock.

Solar power and storage were added to the SBF0 head node in the weeks following the wellhead completions. Figure 4.16 shows the supporting hardware for the head node installation. This includes circuit breakers (Schurter AS168X-CB1G100) between the solar charge controller (Morningstar SS-20L-12V) and the 160 Watt solar panel (Solarland SLP160S-12), batteries (Duracell AGM24DC), and the output, or "load" that is distributed to the equipment that receives power via sets of DIN rail mounted terminal blocks. An additional 12 V power conditioner (XP Power DDC1524S12) is used to supply a well-regulated voltage to the eddy current strain and tilt system main board. Four (two internal and two external) 78 Amp-hour batteries were installed to power the total ∼1.3 Amp load for 240 hours (∼10 days).

A 12-Volt powered station computer (Compulab, or Fit-PC fitlet iA10) is used to perform the main data acquisition, time keeping, and file serving operations. It has two Ethernet ports, one of which is configured as a Dynamic Host Configuration Protocol (DHCP) client to the cellular gateway modem (Sierra Wireless RV50), and the other as a DHCP server to host Ethernet-based ADCs like the LabJack T7 boards used in the eddy current system. This DHCP server port is accessible through a five port Ethernet switch (Netgear

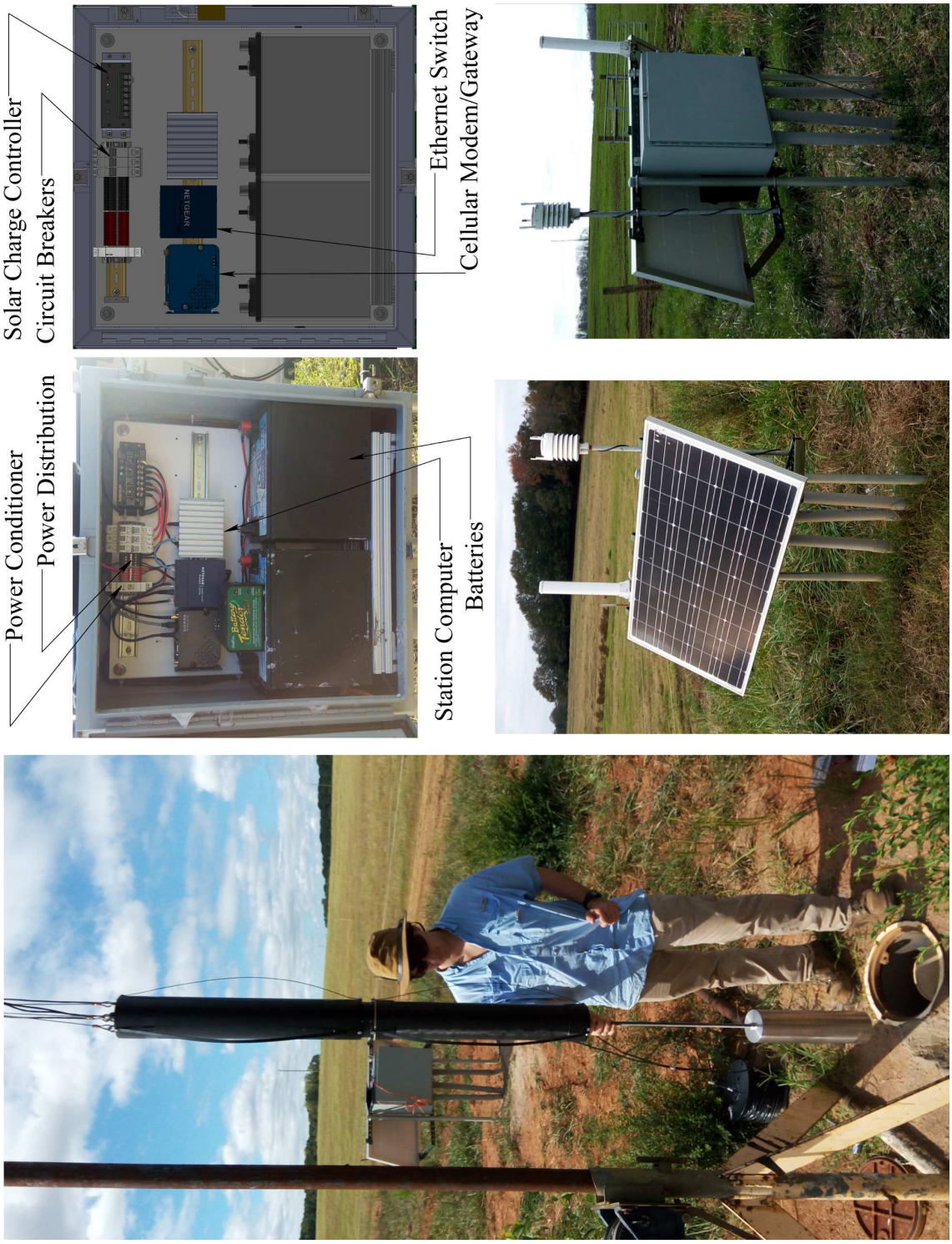

Figure 4.16: Installation of the Version 1 eddy current system showing the instrument before deployment into SBF2 (left), the inside of the SBF0 electrical enclosure (upper center and right), the south (bottom center) and north (bottom right) facing sides of the completed station.

GS105) to host as many DACs, and can be used to connect additional computers such as a field laptop during servicing operations. The fitlet iA10 also has a built-in RS232 serial port that is used to interrogate the combination weather station (Vaisala WXT520) mounted on a mast outside the enclosure, which provides wind speed and direction, outdoor temperature, barometric pressure, relative humidity, and rainfall and hail intensity measurements.

The Sierra Wireless RV50 gateway is used for outside communication and data telemetry. It is capable of both GSM and CDMA cellular service at up to 4G speeds. Service is provided by Verizon, a state-contracted provider with Clemson University. They also provide a static IP address to ensure reliable communications after network upgrades on their end and reboots and power failures at the site. An external 4G-compatible cellular antenna (MaxMostcom 4326574517) is also mounted outside of the electrical enclosure to maximize reception.

The Version 1 eddy current strain and tilt instrument was installed into the second borehole SBF2 (34.670173°, −82.729638°) at a depth of 145 feet (44.2 m), which was approximately 5 feet (1.5 m) from the bottom. The instrument ran at this depth prior to grouting for approximately 10 months where it underwent additional scrutiny and was extracted multiple times for improvements to the internal supporting electronics. Final grouting was performed on July 6th, 2017 using the same BASF MasterFlow® 1206 expanding grout as in the Gladwin installation at the North Avant Field. The grouting procedure was quite different, however, since the instrument counter-ballast had become stuck at the bottom of the hole after an extended period of testing. This required pumping the grout through a small, 0.5-inch (1.3 cm) diameter pipe that was inserted past the instrument in the annulus between the instrument and the borehole. The completion appeared to be successful, as evidenced by the grout curing curve previously shown in Figure 2.16. The initial estimate of the instrument's orientation was determined to be $62.35° \pm 0.04°$ using its internal electronic compass.

4.2.2.2 Installation at the North Avant Field, OK

Two additional boreholes were drilled at the North Avant Field on May 30th, 2017 to facilitate the installation of the two project strainmeters developed for this project. The first, AVN3 was drilled about 40 feet (∼12 m) northwest of the Gladwin strainmeter in AVN2, approximately halfway between AVN1 and AVN2. The second hole, AVN4 was drilled approximately 40 feet (12 m) to the southeast of AVN2. These were drilled by air hammer and cased to a depth of 80 feet (25 m) and drilled to a final depth of 100 feet (30 m) using a tri-cone air rotary bit in a manner identical to the Gladwin installation.

The Version 2 eddy current strain and tilt system was installed into borehole AVN3 (36.532214°, −96.081091°) at a depth of 91.5 feet (∼28 m) on July 10th, 2017. This was also performed using the same grout and dump bailer technique used to install the Gladwin strainmeter in 2016, and was also done with support from UNAVCO technician Wade Johnson. The initial estimate of the instrument's orientation was determined to be $204.8° \pm 0.2°$ using its internal electronic compass.

The up-hole infrastructure (Figure 4.17) was installed the following day after the grout had cured enough to release the support cable used to suspend the instrument in the grout column. The setup was very similar to the Simpson Station installation in that that it was designed to be the main communications hub, or "head node" for future installations. It contains the same station computer, cellular modem, and network switch configured in the same manner as the Simpson Station, and uses the same solar hardware and power conditioning devices. The station computer is also configured as a 802.11x wireless gateway and DHCP server that is delivered to a Hawking HAO9SIP mounted outside of the enclosure. A total of four (two internal and two external) 78 Amp-hour batteries were also installed capable of powering the measured 1.2 Amp load for 260 hours (∼10 days).

There are several key differences between the AVN3 and Simpson Station installations. The above ground enclosure for AVN3 was attached directly to the wellhead via a bolt-on flange, with the power and

communications cable passing up through the mount pedestal made of 3-inch nominal, Schedule 80 pipe. While there are gaskets between the wellhead and box flanges and the pedestal, the wellbore is not sealed to atmospheric pressure. The second difference addresses a runtime issue encountered with the LabJack T7 ADCs, which require power cycling if data acquisition is abnormally interrupted. Therefore, a 2-channel USB relay (Numato Labs RL20001) was installed to manually reboot the ADC before starting data collection.

The resulting above ground setup is robust and compact, and has required no maintenance so far. A barbed wire cattle fence had to be installed to prevent livestock from damaging the solar panel, which could be eliminated by using a taller pedestal. While this would make the setup and maintenance of the enclosure more difficult, it may be a better strategy for future installations.

4.2.3 Optical Fiber Areal Strainmeter

There were also two versions of the Optical Fiber Areal Strainmeter deployed during this project, with one at each field site. The first, Version 3 instrument was installed in borehole SBF1 at the Simpson Station, SC, whereas the Version 4 system was deployed in borehole AVN4 shortly after the second pair holes were drilled near AVN1 and AVN2 at the North Avant Field. Each preceded the installation of the eddy current systems at each site because of their low cost and simplicity, making them ideal for gaining valuable experience for subsequent field deployments of more complicated and expensive instruments like the eddy current systems. The Simpson Station instrument was particularly important since it was our first independent in situ verification of the expanding grout.

4.2.3.1 Installation at the Simpson Station, SC

The Version 3 Optical Fiber Areal Strainmeter was prototype instrument developed for the purpose of testing our deployment rigging and grouting procedures. This instrument was installed on April 12th, 2017 in borehole SBF1 (34.670245°, −82.729648°), at the same depth of 145 feet (44.2 m) as the eddy current system. The BASF MasterFlow® 1206 expanding grout was delivered to the bottom of the borehole using a 1.5-inch nominal diameter PVC tremie pipe. Approximately 4 cubic feet (∼0.111 m^3) was mixed and gravity fed into a large funnel mounted at the top of the tremie pipe. Specialized foam "pigs" were placed in the pipe before releasing the grout to push the water from the tremie pipe to limit mixing and separation as the grout descended. A second pig followed by a small volume of water was added following the grout to help push out grout in the pipe to limit mixing at the gout-water interface when the tremie pipe was withdrawn.

Figure 4.18: Photograph of the Version 3 areal strainmeter prior to installation in borehole SBF1.

An AC-powered optical fiber interrogator was used for several months following the deployment. This consisted of mostly benchtop equipment that was located inside of a machine building alongside the field site. The AC-powered setup was later replaced with a DC-powered, Version 3 Optical Fiber Sensor Interrogator on November 17th. This was packaged in a 3.25-inch (8.2 cm) diameter Type III anodized aluminum pressure case and deployed approximately 16 feet (5 m) below ground in the wellbore above the instrument, and was submerged about 5 feet (1.5 m) under water.

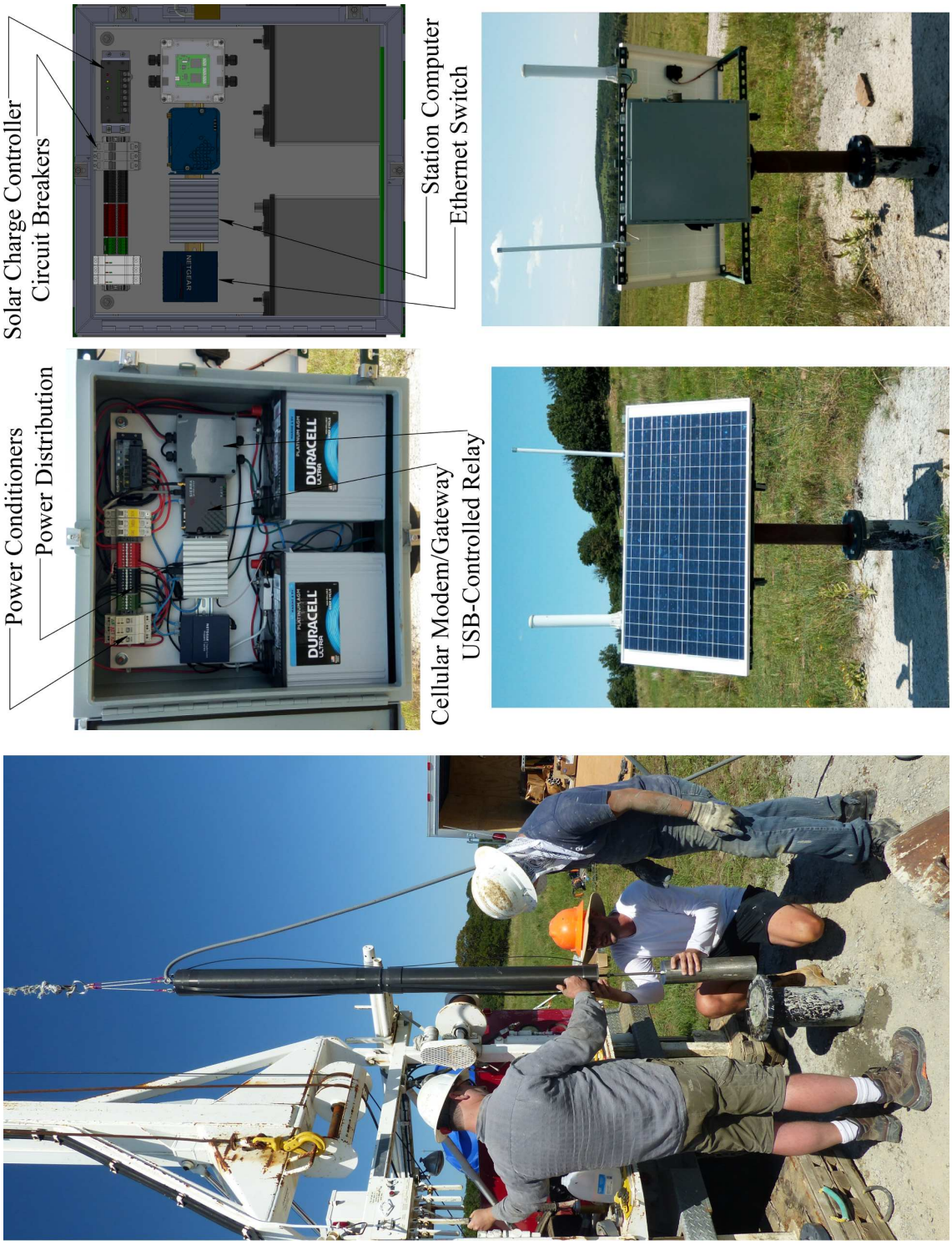

Figure 4.17: Installation of the Version 2 eddy current system at AVN3, showing the instrument before deployment (left), the inside of the main electrical enclosure (upper center and right), the south (bottom center) and north (bottom right) facing sides of the completed station.

Grout curing results show that this installation was successful (Figure 2.32), with the instrument going into compression after only about one week and the solid Earth tides appearing after the second week of operation. Data collection halted on May 14th, 2018 due to interrogator misbehavior that was later attributed to a small amount of water that had penetrated the pressure case cable gland.

4.2.3.2 Installation at the North Avant Field, OK

The Version 3 Optical Fiber Areal Strainmeter was the first instrument developed for this project to be installed at the North Avant Field. This was done on June 1st, 2017, in borehole ANV4 (36.532067°, −96.080908°), on the second day after drilling boreholes AVN3 and AVN4 (Figure 4.19). Grouting operations were performed by UNAVCO in a manner identical to the Gladwin and Version 2 eddy current systems, i.e., with a dump bailer containing 4 cubic feet of BASF MasterFlow® 1206 expanding grout. This instrument was also hung at a depth of 91.5 feet (∼28 m) for about 24 hours before completing the rest of the installation.

Supporting infrastructure and electronics were installed the day after grouting. A sealed 2-inch nominal PVC pipe was lowered to the top of the expanding grout column (about 80 feet, or ∼28 m). This was grouted in place with a volume sufficient to seal off the remaining 10 feet (3 m) of open borehole. The purpose of this pipe was to house a commercial Applied Geomechanics (now Jewell Technologies) LILY Self-Leveling Borehole Tiltmeter, however, this was not installed until a subsequent trip on October 27th, 2017. This is also when the Vaisala WXT520 combination weather station was installed.

The up-hole portion of the AVN4 installation is also shown in Figure 4.19. The design is consistent with other enclosures in that it contains batteries, solar charge controller, circuit breakers, power distribution, and USB-controlled relay system. It differs in that data telemetry occurs over standard 2.4 GHz 802.11x wireless with the AVN3 station computer (requiring an outdoor antenna mounted to the enclosure) where the data directory on AVN4 is mounted on AVN3 as a Network File System (NFS) such that AVN4 data are only transmitted through AVN3 during remote data requests. The AVN4 enclosure also contains a RS485-to-USB converter (US Converters AX101) to interrogate the commercial tiltmeter, as well as a weather station.

We were unfortunately unable to capture the grout curing process following the deployment of the Version 4 areal strainmeter. This was due to a short-circuit that occurred during the installation of the (Version 2) Optical Fiber Sensor Interrogator that was not able to be replaced until the visit five weeks later following the installation of the Version 2 eddy current system in June, 2017. Like the Simpson Station deployment, the hard anodized interrogator pressure case was deployed 5 m below the ground surface in the wellbore alongside the 2-inch casing for the commercial tiltmeter.

4.2.4 Wellhead Instrumentation and Pressure Monitoring

A number of commercial pressure loggers were installed in monitoring wells at the North Avant Field in the vicinity of the injection well 9A. This included wells "Wolco West" (abbreviated as "WW") 11A (36.531000°, −96.079513°), 27 (36.532752°, −96.087904°), 29 (36.533061°, −96.085770°), 30A (36.503614°, −96.082962°), and 60 (36.531791°, −96.086440°). These are autonomous pressure loggers manufactured by In-Situ, Inc., model Rugged TROLL 200 with a span of 250 feet of water (76 m, or roughly 0–750 kPa), resolution of 0.01% of the span (0.025 feet, 7.6 mm, or ∼75 Pa), and a burst pressure of roughly 150% of the span (368 feet, 112 m, or 1,100 kPa).

The main issue with employing autonomous pressure loggers is dealing with their deployment and periodic recovery to collect data. These also need to be installed in sealed wells such that there is no overflow during extended injection tests. The approach taken was to deploy the loggers on high-test, braided polymer line such that they could be raised and lowered using a hand-operated modified rod-and-reel system. A wellhead

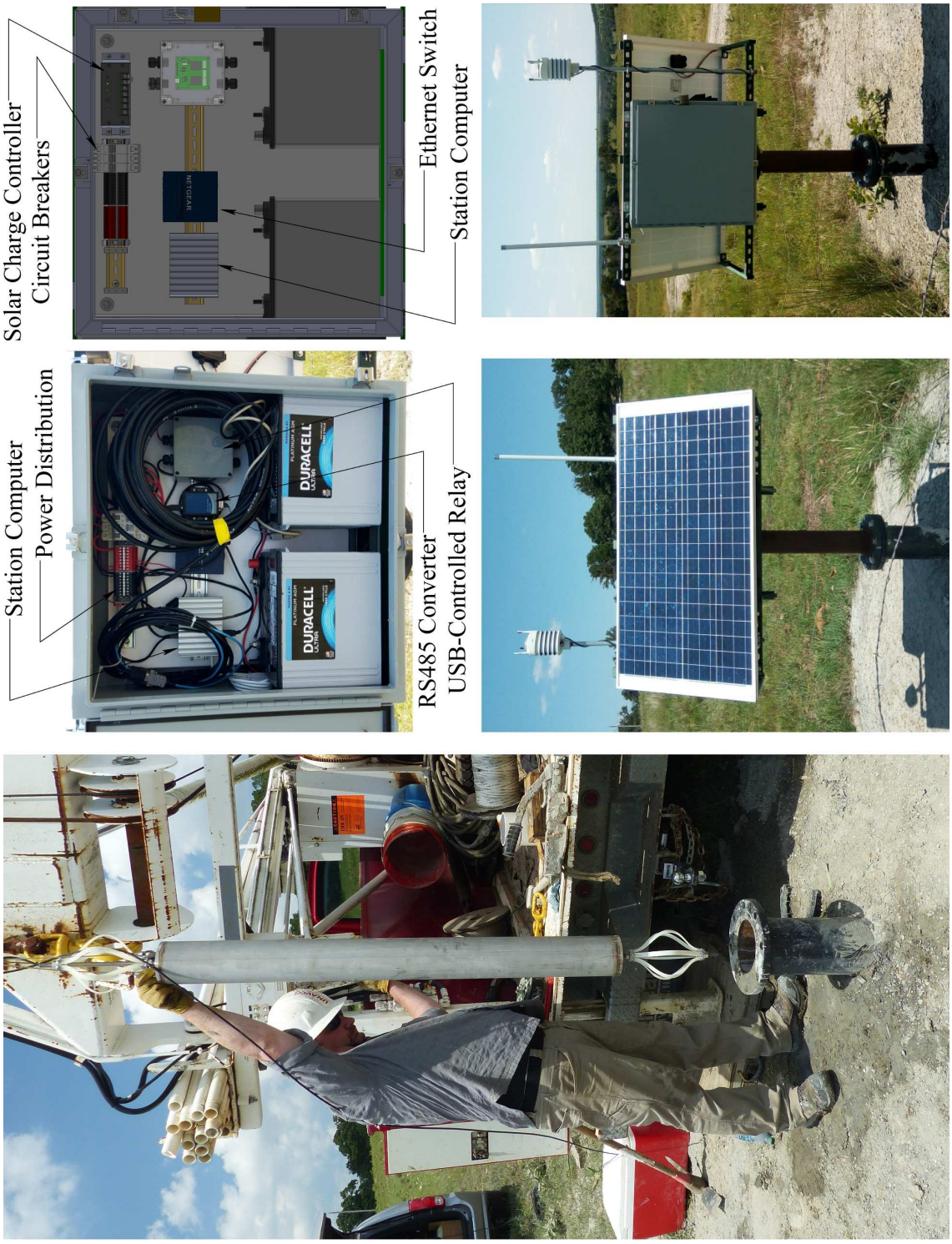

Figure 4.19: AVN4 areal strainmeter installation, showing the deployment (left), inside of the main electrical enclosure (upper center and right), the south (bottom center) and north (bottom right) facing sides of the completed station.

adapter was designed to accommodate this line and seal the well. The completed setup is shown in Figure 4.20, where a quick-release cam, or "banjo" fitting is used as the main wellhead entry point. The top portion of the quick release can be fully removed, and contains an eyelet that captures the end of the deployment line. This line terminates in a swivel-and-snap lock that can be easily connected to a take-up spool. A pressure gauge and release valve are also included to bleed off any gas pressure prior to entry.

Data are sampled in 5 minute intervals, and the logger can hold up to 120,000 records of pressure and temperature for a total run time of just over 200 days. The data are offloaded via a USB port located under the pressure logger cap that connects to the deployment line, which has been done periodically during site visits.

4.3 Strain During Transient Well Tests

Field demonstrations of strain during injection were done at sites near Clemson, South Carolina, and Wolco, Oklahoma, in 2017 and 2018. The Clemson field site was used to test prototype strainmeters. That site is readily accessed by the project team, so it was used for shakedown tests of instrument functionality. The Clemson site is underlain by metamorphic rock, which is significantly different from the rock used for CO_2 storage, so it was unsuitable for a full-scale demonstration. A full-scale demonstration of strain measurement during injection was conducted at the North Avant oil field in northeastern Oklahoma. The North Avant Field includes production and injection into Pennsylvanian sandstone, which is similar to formations suitable for CO_2 storage.

4.3.1 Well Tests at the North Avant Field

Strain data was obtained at the North Avant Field from the time the Gladwin strainmeter was installed in September 2016. Additional strain data became available when the Eddy Current strainmeter and Areal strainmeter were installed in the summer of 2017. Pore pressure measurements at monitoring wells began in the summer of 2017. Some weather measurements were initiated in September 2016 with the installation of the Gladwin strainmeter, and additional measurements from a weather station became available in August 2017. Most of the instruments have been operational most of the time since they were installed, although there have been a few temporary outages.

The primary strain data of value to this project consists of measurements made during four periods from April 2017 through July 2018. Six injection episodes were monitored at well 9A between July 2018 and July 2018, and three of them are suitable for analysis. Tubing on well 9A was modified in September 2017 by Grand Resources. Details of the injection process may have been affected by the tubing during injection tests conducted prior to the modification. Data from those tests show a clear strain response, but they will not be analyzed because of uncertainty related to the injection data.

Another episode of injection occurred from February through April 2018. This is the longest period of injection during the project, and it produced strong strain signals. The injection rate was erratic during this period because of fluctuations in the availability of water from elsewhere in the well field that were beyond our control. The erratic injection rate complicated the interpretation process, so we decided to defer interpretation of this injection period to a later date and it is not included here.

Scott Robinowitz at Grand Resources noticed a strain signal during early April, 2017 that was coincident with a week-long shut-in at well 1A, which is approximately 900 m west of the AVN strainmeters. This period was prior to injection planned for the project. We investigated this signal and it is both distinct from the signals during later injection tests at well 9A, and consistent with the strain signal expected to occur during a shut-in. We call this the "1A shut-in" dataset.

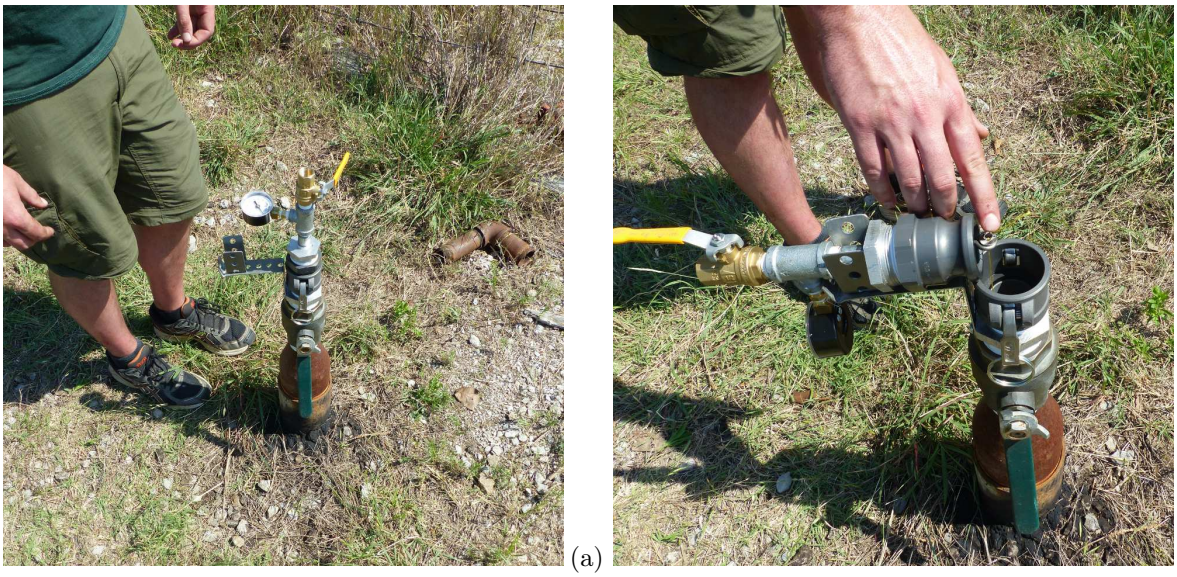

(a) (b)

(c) (d)

Figure 4.20: Photographs of the well pressure logger installations. (a) The sealed wellhead with pressure release valve (yellow handle) and pressure gauge. (b) Quick-release cam fitting separated with the male end resting in its holder, as well as the eyelet holding the line connected to the down-hole pressure logger. (c) Extraction of the pressure logger using a modified rod-and-reel system. (d) Successful removal of the pressure logger.

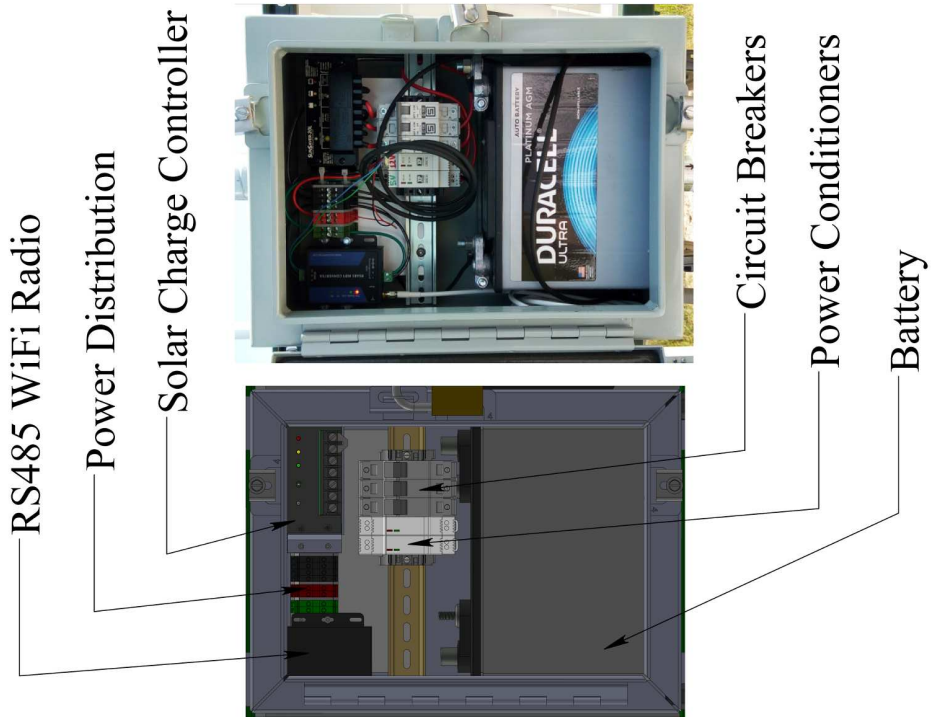

Figure 4.21: WW27 wellhead installation, which is an example of a remote pressure transmitter showing the inside of the main electrical enclosure (left and center left), the south (center right) and north (right) facing sides of the completed station.

Tests with data suitable for analysis occurred in April 2017 (1A shut-in), Oct. 2017, Nov. 2017, and June 2018. The duration of the injection tests range from 3 days to 20 days. Data generated during the tests include

- Gladwin: 3 components of horizontal strain
- Eddy Current: 3 components of horizontal strain, vertical strain, two components of tilt
- Areal: Sum of principle horizontal strains; 2× the average horizontal strain
- Pressure: Pressure in monitoring wells completed in the Bartlesville sand in vicinity of 9A
- Wellhead: Injection rate and positive pressure at the wellhead.

Data availability varied from test to test given the installation schedule and the timing of visits to offload pressure logger data (Table 4.1). Strain data were recorded during all four tests. Pressure in monitoring wells was measured using downhole transducers that measured absolute pressure and recorded it in memory within the transducer. The transducers were suspended on low-stretch polymer cable slightly below the water level in the well at the time of the test. The water levels ranged from 100 to 150 m below the ground surface at the beginning of the tests. The span of the pressure transducers was 0.6 MPa and they could resolve approximately 0.6 kPa. Pressure data were recorded every 5 minutes prior to, and during the tests. Pressure data from the March test are unavailable.

Table 4.1: Data measured during field tests.

Active well	Start Date	Gladwin Horizontals	Eddy Current Horizontals	Eddy Current Tilt	Optical Fiber Areal	Pressure	Weather
1A Shut-in	Apr. 2017	Y	N	N	N	N	N
9A Inject	Oct. 2017	Y	Y	Y	N	Y	N
9A Inject	Nov. 2017	Y	Y	Y	Y	Y	Y
9A Inject	Jun. 2018	Y	Y	Y	Y	Y	Y

Injection pressure and rate were measured with a pressure transducer and turbine flowmeter at the wellhead (Table 4.2). An electronic data acquisition system was used to record the data every 5 minutes, and it was also recorded manually by field personnel each day. The electronic data acquisition system was functioning during most of the test periods. There were brief periods when the well data acquisition system was being serviced and the manually recorded data were used.

Table 4.2: Specifications of injection and shut-in tests conducted at the North Avant Field from April 2017 to July 2018.

Active well	Start Date	Inject (days)	Recover (days)	Rate (bbl/day)	Wellhead Pressure (psi)
1A Shut-in	Apr. 2017	-	7	800–1,000	–
9A Inject	Oct. 2017	6	7	300–800	20–50
9A Inject	Nov. 2017	3	6	300–700	30–60
9A Inject	Jun. 2018	24	20	350–550	5–20

The injection rate varied during all the tests, but the degree of variability differs (Table 4.2). The injection rate decreased from approximately 700 bbl/d to 300 bbl/d during the tests in 2017, and it increased and decreased between 50 and 500 bbl/day. The most consistent rate was obtained during the June 2018 tests when the rate decreased from approximately 500 bbl/d to 400 bbl/d over 25 days. The rate dropped off at the end of the July test. The variability in the injection rate occurs because the injected water is derived from the water supply system at the well field. Produced water from elsewhere in the field is stored in several tanks, and pumps are used to pressurize a pipe network that delivers the produced water to multiple injection wells. This causes periodic fluctuations in the pressure and rate as the storage tanks fill and drain with periods of 4 to 6 hrs. For example, this caused the pressure to vary with an amplitude of approximately 30 psi, and the rate to vary by 150 to 200 bbl/d over a 4 to 5 hr period during the Oct 2017 test (Figure 4.25). The amplitude of rate variation was slightly less (100 bbl/day) but the average period was more variable and slightly longer (6 hrs) during the November 2017 test (Figure 4.29). There are longer term pressure fluctuations in response to changes in production rate and other factors.

Injection tests through April 2018 were conducted using gravity drainage from elevated storage tanks, which is the standard practice for injection at the North Avant Field. Grand Resources reconfigured well 9A with an injection pump for the June–July 2018 test. That is why the injection rate during that test is more consistent then during earlier tests. A production well was shut off at the end of the June 2018 test and this reduced water available to the injection pump. This is why the injection rate decreased sharply for the last few days of the June 2018 test.

The bottom-hole pressure at the beginning of testing was approximately 500 psi, and the static water level was approximately 500 ft below ground. The water level in well 9A rises quickly and the wellhead pressure is positive within an hour after the start of injection. The wellhead pressure was maintained above a few psi, and less than approximately 130 psi, during the injection tests.

Data from the field tests were processed prior to analysis. A description of the data processing procedure is given with examples in Section 2.4, but in general, the process begins with the removal of background trends in the strain and pressure data. This was done by fitting a first-order or second-order polynomial to the data before and after the test. Results from the polynomials were subtracted from the observed pressures or strains.

Effects of earth tides and barometric pressure were removed from the Gladwin data using standard data processing methods to produce "Level 2" data by UNAVCO. Similar methods were used to process the tilt and strain data measured using the eddy current instrument, the areal strainmeters, and the LILY tiltmeter. Earth tides create periodic variations in strain and tilt data that are similar to strains or tilts calculated theoretically. These periodic fluctuations are readily apparent in nearly all the strain data, and the presence of the tidal signal is used to confirm that the instruments are functioning properly. The observed data were corrected by subtracting the calculated strains or tilts. Barometric pressure effects were characterized by correlating background strain and barometric pressure during periods of no injection. This correlation was used to estimate the strain caused by barometric pressure during injection, and this strain was subtracted from the observed strain. The size and complexity of the strain data sets were then reduced by averaging the data over a window of 4 hrs. This reduced much of the periodic fluctuation evident in the data, but it preserved some of the variations that appear to be responses from changes in injection rate.

4.3.1.1 Shut-In Test at Well 1A

Well 1A in the North Avant Field was used to inject produced water at a roughly constant rate of approximately 1,000 bbl/day during winter and spring 2017. The well was shut-in for maintenance on 31 March 2017 and restarted again on April 7th, 2017. Well 1A is approximately 1,100 m east of well 9A, and 900 m east of the AVN strainmeters.

Horizontal strain was observed to change abruptly at the time of the shut-in. The EW strain increased and reached a maximum of 130 nε after 7 days. Positive strain is tensile, and the well is approximately due east of the strainmeter, so these data indicate tensile strain in a radial direction relative to the well. The strain in the NS direction, or the circumferential strain, reached a maximum of 60 nε after 7 days (Figure 4.22). The average horizontal strain was approximately 70 nε (not shown). The shear strain is essentially zero (Figure 4.22). This would occur if NS and EW were principle directions, which is consistent with the geometry.

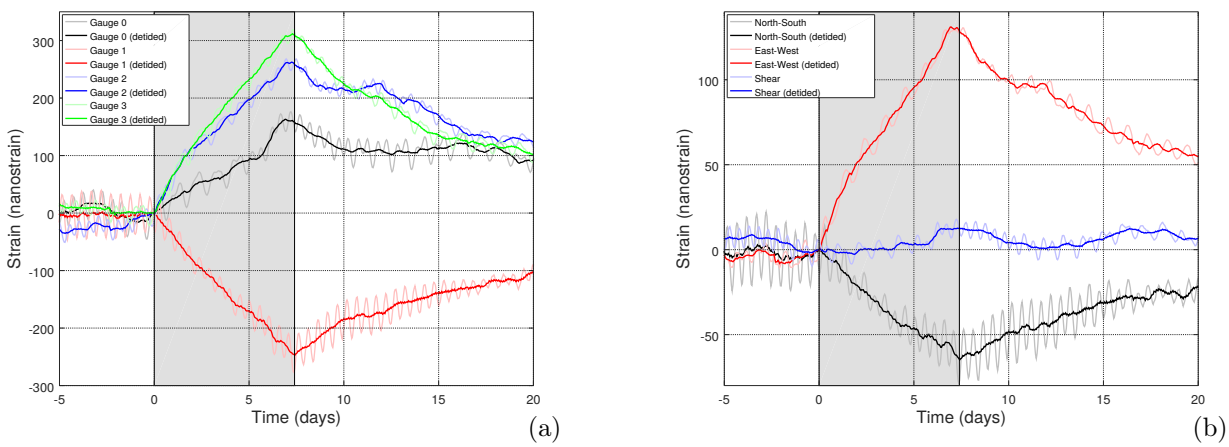

Figure 4.22: Strain data from Gladwin strainmeter at AVN2 following shut-in of well 1A, North Avant Field, OK. Shut-in occurred during gray band. Day 0 is 31 March 2017. Semi-transparent lines are raw data. Solid lines are data corrected for tides and barometric pressure (a) data measured by instrument gauges; (b) NS normal strain (black line), EW normal strain (red line) and EW shear strain (blue line).

The EW strain rate was 25 nε/day during the first few days after shut-in and then decreased to 15 nε/day. The NS strain rate decreases from 10 nε/day to 6 nε/day during the 7 days following shut-in.

For comparison, a strain rate of 8.6 nε/day is a rate of 10^{-13} ε/day. Strain rates from tectonic motion are localized around plate boundaries where they are in the range of 10^{-15} nε/day to 10^{-14} nε/day (Kreemer et al., 2014).

The orientation of the principle horizontal strains is aligned with the cardinal compass directions (Figure 4.23). The orientation may rotate slightly in the counterclockwise direction during shut-in, as indicated by the increase in the shear strain with time (Table 4.2), although this is a small effect. Primarily, the principle strains are oriented toward the well that was shut-in to cause the strains.

The relative magnitudes of radial tensile strain and a lesser compressive strain is the expected signal during shut-in, according to our simulations. As a result, it appears that the relative magnitudes and shapes of the

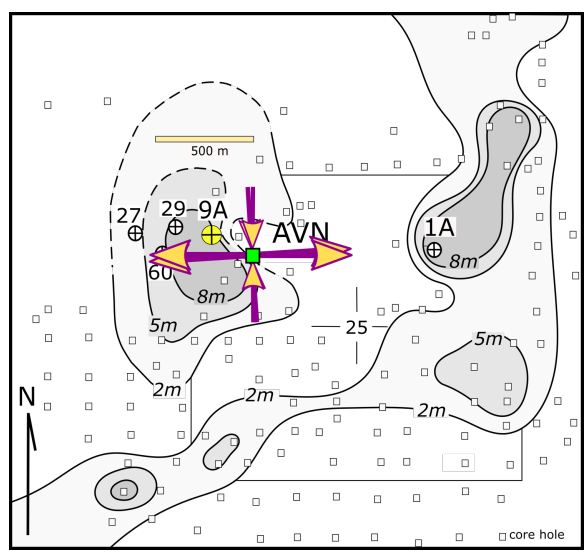

Figure 4.23: Principle horizontal strains (purple arrows) at AVN during shut-in at well 1A. Relative magnitudes shown as arrow length. Tensile strain aligned along radial direction (∼EW), compressive strain along circumferential direction (∼NS). Orientation rotates slightly during shut-in.

strain signal could be used to identify the source of the signal as a well being shut-in, and the direction of the principle strains could be used to identify the direction of the well.

4.3.1.2 Injection Tests at Well 9A

Testing at Well 9A commenced in July 2017 with several injection episodes lasting a few days to weeks. The eddy current and volumetric strainmeters were installed in June and early July 2017, and the initial injection tests were intended to evaluate functionality of the instruments, and operational capabilities of the injection system. Discussions with Scott Robinowitz identified several wells in the vicinity of 9A that were completed in the Bartlesville sandstone and the were accessible. These wells were unknown to us during initial planning of the injection tests, so we revised our plan to include pressure monitoring. Pressure transducers were installed in Wells 11A, 27, 29, and 60 during summer of 2017. The transducers store data internally, and they were recovered periodically to download the data.

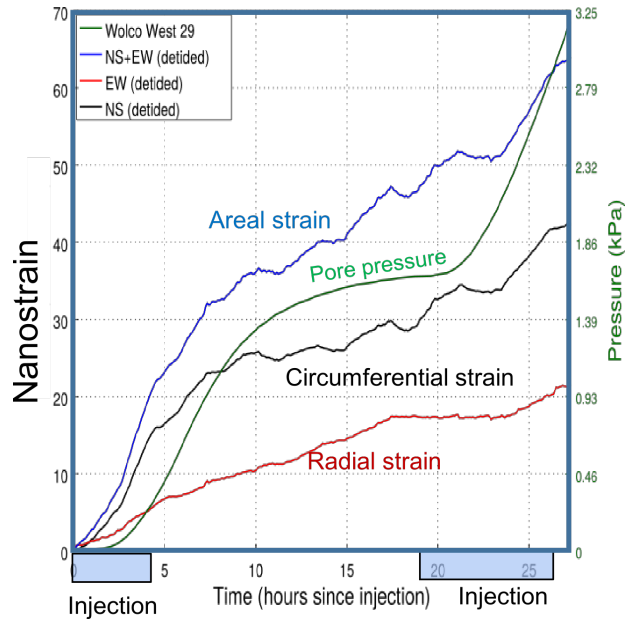

Figure 4.24: Strains measured at AVN and pressure at well 29 during shakedown injection tests in well 9A, North Avant Field, July, 2017.

The first shakedown injection test involved injecting water into well 9A for several 4 hours at approximately 1,000 bbl/day (∼30 gpm), 14 hrs of recovery and then 8 hrs of injection (Figure 4.24). Injection was accompanied by dilational strain at the Gladwin strainmeter. The NS strain (radial) increased at approximately 100 nε/day and EW strain at approximately 20 nε/day at the outset of injection. The strain rate decreased after shut-in and then increased again when injection resumed (Figure 4.24).

The pressure at monitoring well 29 was constant for a roughly 2 hrs and then increased by approximately 1,400 Pa. The rate of increase diminished several hours after shut-in and then increased again when injection resumed. The injection pressure follows a pattern that is similar to the normal strains, although the normal strains changed more rapidly early in the test than the strains at well 29 (Figure 4.24).

Addition injection tests were conducted in August 2017. The duration of injection was increased to several days and then to 1 week. Normal strains increased during injection and decreased during recovery, a pattern consistent with the initial tests, and consistent with expectations based on simulations. Operational data were identified by Grand Resources that suggested some of the injected water may have flowed into a formation overlying the Bartlesville sandstone. The well completion was modified to ensure that all the injected water flowed into the Bartlesville sandstone in September, 2017. We decided use injection test data prior to September 2017 as indicators of functionality, but not as candidates for analysis.

4.3.1.2.1 October 2017 Injection Test

The October injection test began on October 11th, 2017, and lasted for approximately 6 days. The average injection rate was approximately 600 bbl/d at the outset, but it decreased to approximately 400 bbl/d over the first day and it remained between 350 and 400 bbl/d (10 gpm to 12 gpm) for the remainder

of the test (Figure 4.25). The average rate decreased from 400 bbl/d to 350 bbl/d during the last day of the test 4.25. The injection rate varied by 100 bbl/d to 200 bbl/d over a period of 4 hr to 5 hr throughout the test. The water injection system at the North Avant Field is supplied from tanks that are filled periodically from production wells. The periodicity in the injection rate is inherited from the field-wide water injection system. The period of fluctuation is short compared to the duration of the test (Figure 4.25).

The injection pressure rapidly increased to approximately 140 kPa (20 psi) at the wellhead. The injection pressure fluctuated by ±70 to 140 kPa (10 to 20 psi) following the fluctuations in injection rate (Figure 4.25).

The horizontal strain data in Figure 4.26a were obtained from the Gladwin strainmeter, whereas the vertical strain and tilt data were obtained from the eddy current instrument. Baseline trends were removed, and the data were corrected for barometric pressure and Earth tide effects. The horizontal strain data were rotated to give strains the NS and EW direction and the EW shear strain (Figure 4.26b).

The NS and EW strain increased at the start of injection and continued to increase until approximately the end of injection (Figure 4.26b). The EW strain decreases slightly before the end of injection (Figure 4.26), probably in response to the slowing of the injection rate. The vertical strain decreased at the start of injection and it stayed approximately constant after injection ceased.

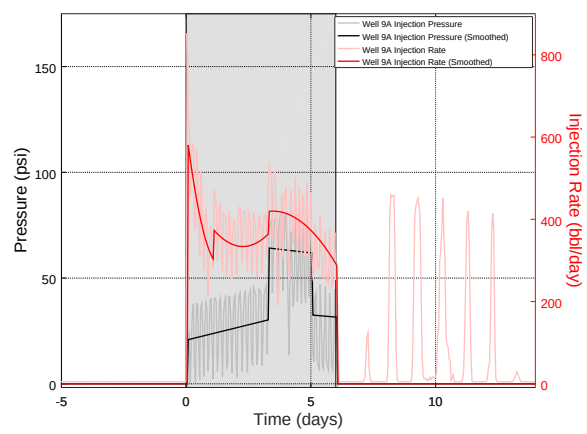

Figure 4.25: Wellhead pressure (black) and rate (red) during October 2017 injection test at well 9A. Injection occurred during gray band. Day 0 is October 11th, 2017. Semi-transparent lines are raw data. Solid lines are processed with high frequency removed. Pulses of injection rate after day 6 are artifacts. The well was shut-in during this time.

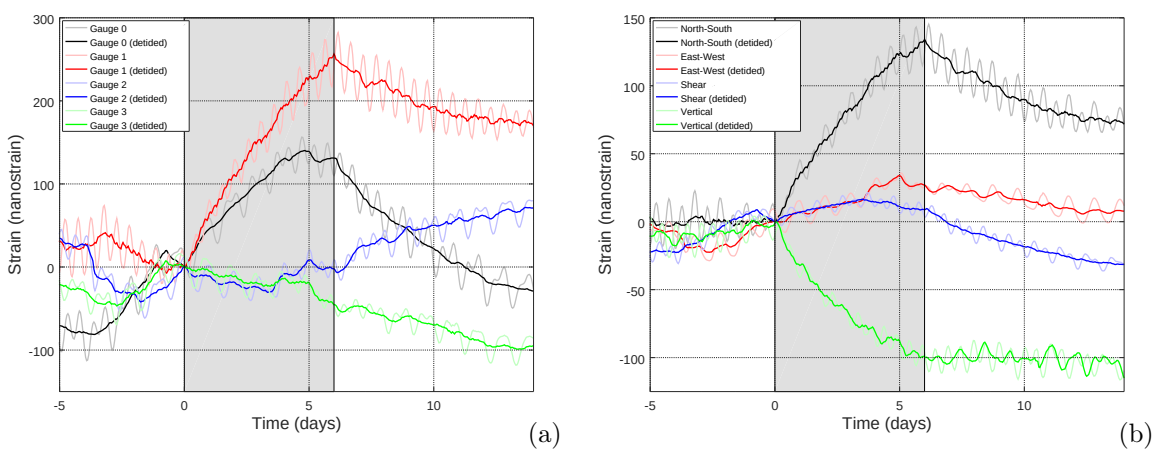

Figure 4.26: Strain data from Gladwin strainmeter at AVN2 during the October 2017 injection test at well 9A, North Avant Field, OK. Day 0 is October 11th, 2017. Semi-transparent lines are raw data. Solid lines are data corrected for tides and barometric pressure. Background trends removed. (a) data measured by instrument gauges; (b) NS normal strain (black line), EW normal strain (red line) and EW shear strain (blue line). Vertical strain from eddy current instrument (green line).

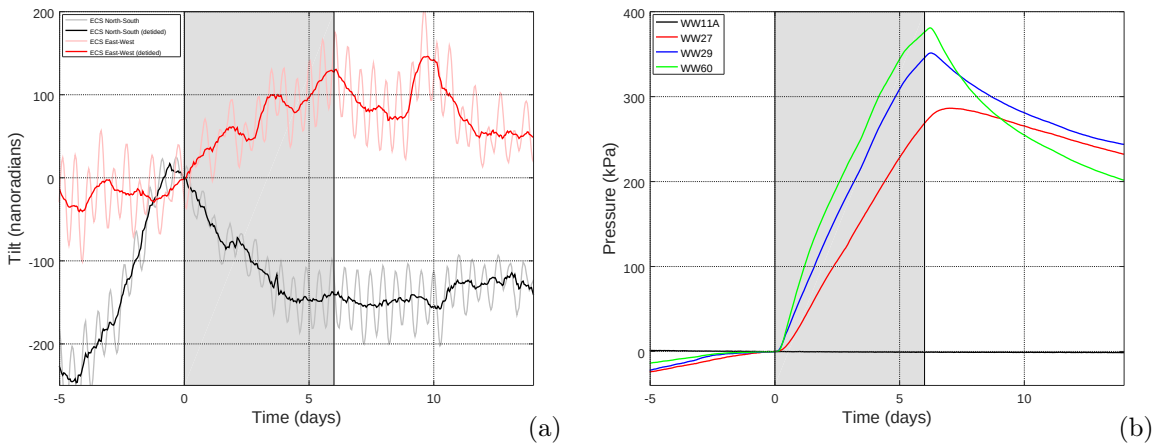

Figure 4.27: Tilt and well pressure data from the October 2017 injection test at well 9A, North Avant Field, OK. Day 0 is October 11th, 2017. Semi-transparent lines are raw data. Solid lines are data corrected for tides and barometric pressure. Background trends removed. (a) tilt in NS direction (red) and EW direction (black) measured using eddy current instrument. (b) pressure change at monitoring wells. Well 27 (red), well 29 (blue), well 60 (green), well 11A (black).

Strain rates during the test are largest at the start of the test and decrease with time, and they are generally in the range of tens of nε/d. The largest rate is in the NS direction and it starts at 30 nε/d and decreases to 15 nε/d. The EW rate is considerably slower, approximately 7 nε/d. The vertical strain rate is similar in magnitude, but opposite in sign, to the NS rate. It starts at approximately -30 nε/d and goes to -10 nε/d (Figure 4.26).

The tilt signal in the EW direction increased, whereas the tilt in the NS direction decreased at the start of injection at rates between 15 and 25 nrad/d (Figure 4.27). A positive EW tilt indicates tilting toward the E, whereas a negative NS tilt indicates tilting toward the S. The magnitude of the EW tilt is approximately 0.6 of the NS tilt. This indicates a tilt azimuth to the southeast. The tilt is roughly constant after injection stops.

Pore pressures increased during injection and decreased during shut-in at three monitoring wells (Well 27, 29, and 60), whereas the pressure was unchanged in Well 11A (Figure 4.27).

The pressure signal caused by injecting or pumping from a uniform, confined reservoir at a constant rate is becomes a logarithmic function of time after an initial early-time period. As a result, pressure data from well tests are commonly plotted with semi-log axes on the abscissa to compare to type curves for idealized reservoir conditions. In some cases, the slope and abscissa intercept of the straight line segment can be used to estimate reservoir properties.

The pressure, average horizontal, and vertical data from October 2017 were plotted on semi-log axes, and the results indicate two semi-log straight segments on four of the five plots (Figure 4.28). The exception is the vertical strain, where the second straight segment is absent. The first straight segment occurs approximately between 10^5 and 2.3×10^5 s to $\sim 4 \times 10^5$ s. The segments on the pressure plot are approximately parallel with time intercepts that range from $6 \times 10^4 < t_o < 12 \times 10^4$ s (Table 4.3). The plots are slightly curved over this interval, so the lines are determined approximately. There are also straight segments on the semi-log plot of strains over approximately the same time intervals as those of the pressure plots. The lines from the first segments for ε_h and ε_{zz} intersect at zero strain at $t_{oa} = 5 \times 10^4$ s, slightly less than t_o from Well 60.

The semi-log slopes of the pressure signals range from 275 to 300 kPa/log cycle, whereas the semi-log slopes for the horizontal strain is 50 nε and the vertical strain is 75 nε (Table 4.3).

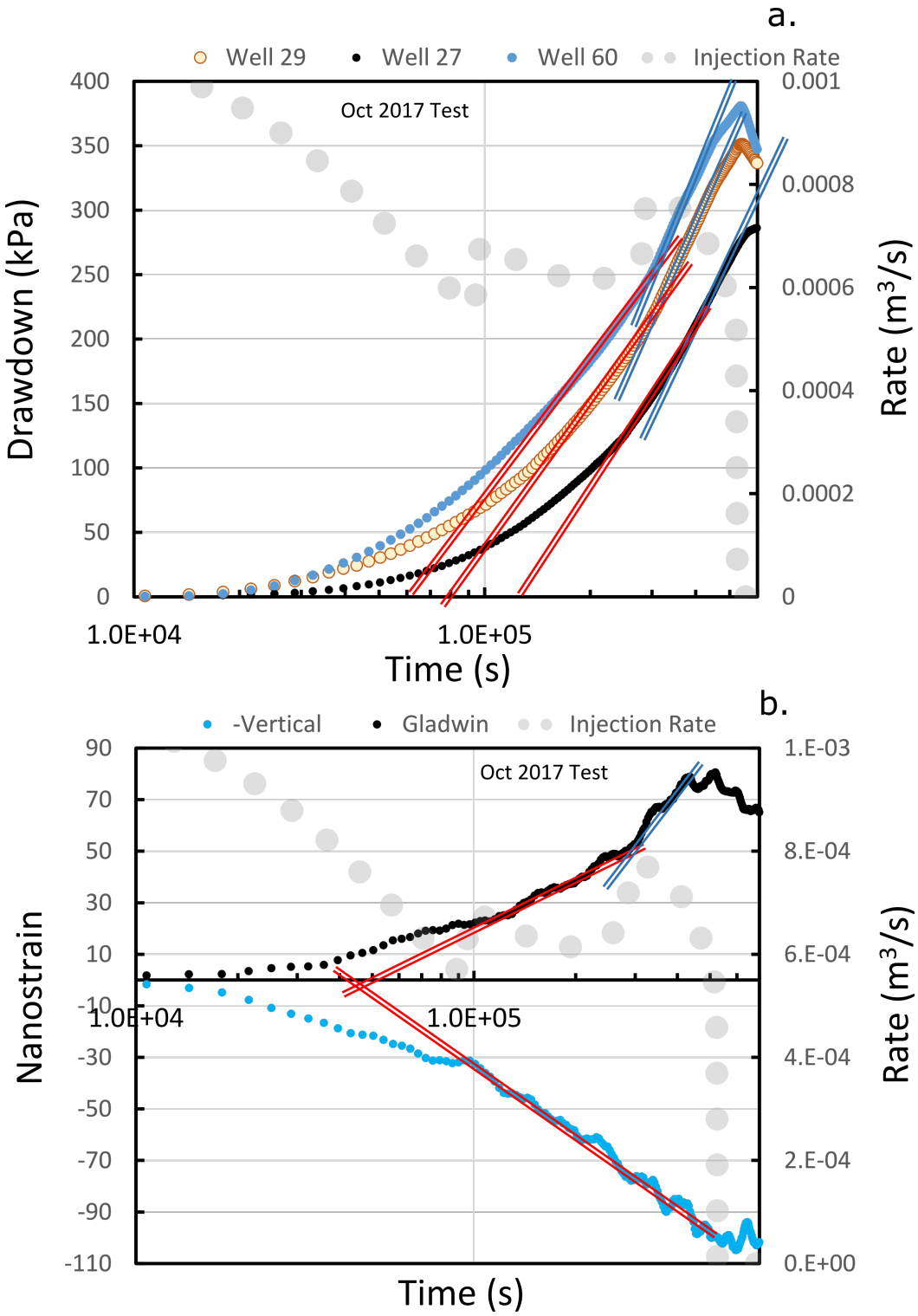

Figure 4.28: Pressure and strain as functions of log time for the October 2017 injection test. (a) pressure at wells 27, 29 and 60. First semi-log straight segment as double red line, second segment as double blue line. (b) Average horizontal strain (areal strain/2) determined using Gladwin strainmeter with semi-log line segments.

4.3.1.2.2 November 2017 Test

Injection during the November 2017 test began on November 28th, 2017, and lasted for 3 days (Figure 4.29). The injection rate was approximately 600 bbl/d at the start of the test and decreased to approximately 300 bbl/d at the end of the test. Fluctuations of 100 bbl/d about a mean rate occurred with a period of 5 to 6 hr as a result of interactions with the well field water supply.

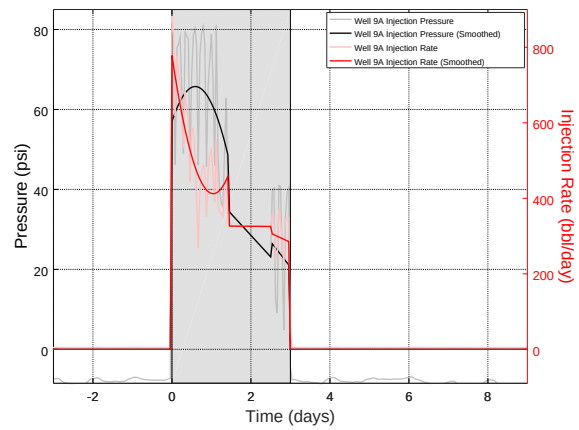

Figure 4.29: Wellhead pressure (black) and rate (red) during November 2017 injection test at well 9A. Injection occurred during gray band. Day 0 is November 28th, 2017. Semi-transparent lines are raw data. Solid lines are piece-wise splines fit through data.

The NS strain and EW strain both increased at the start of injection, whereas the vertical strain decreased (Figure 4.30), a pattern that resembles the observations during the October 2017 test. The NS strain rate decreased from 50 nε/d at the beginning to 15 nε/d at the end of the test. The EW strain rate was approximately 10 nε/d, whereas the vertical strain rate changed from -20 nε/d to -10 nε/d during the test.

Both the LILY and the Eddy Current tiltmeter were active during the November test, and this resulted in two tilt signals from the AVN location (Figure 4.31a). The tilt signals increase to approximately 50 nrad to 100 nrad during the test, but the directions are significantly different. For example, the NS and EW tilt components from the EC tiltmeter both decrease by 50 nrad during the first day of the test and then increase to approximately zero. This indicates that the tilt vector reaches a maximum of 70 nrad toward the SW after 1 day of injection and then the tilt returns to the original. The tilt from the LILY tiltmeter is a similar magnitude after 1 day of injection, but the vector is oriented to the NE. The tilt magnitude continues

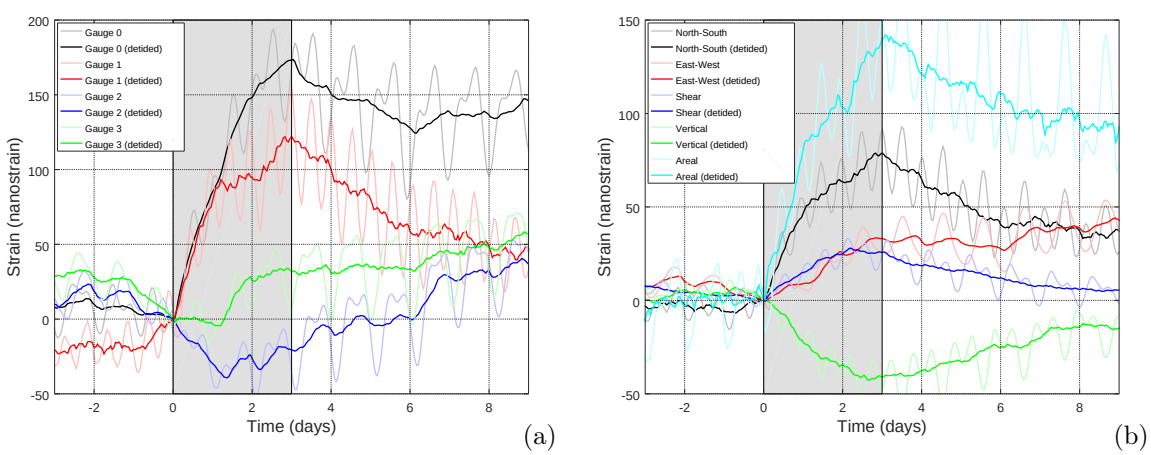

Figure 4.30: Strain data at AVN during the November 2017 injection test at well 9A, North Avant Field, OK. Day 0 is November 28th, 2017. Semi-transparent lines are raw data. Solid lines are data corrected for tides and barometric pressure. Background trends removed. (a) data measured by Gladwin instrument gauges; (b) NS normal strain (black line), EW normal strain (red line) and EW shear strain (blue line). Vertical strain from eddy current instrument (green line).

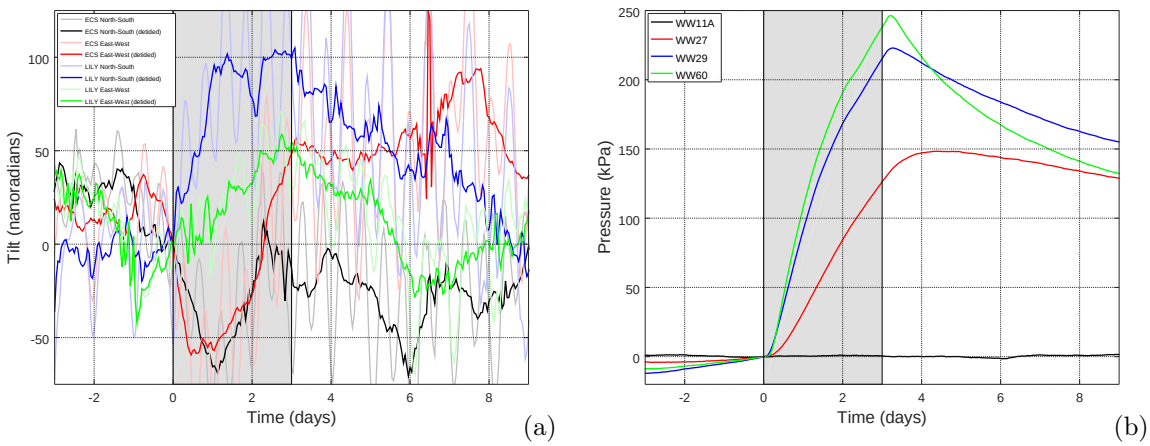

Figure 4.31: Tilt and well pressure data from the November 2017 injection test at well 9A, North Avant Field, OK. Day 0 is November 28th, 2017. Semi-transparent lines are raw data. Solid lines are data corrected for tides and barometric pressure. Background trends removed. (a) Tilt in NS direction (red) and EW direction (black) measured using eddy current instrument. (b) pressure change at monitoring wells. Well 27 (red), well 29 (blue), well 60 (green), well 11A (black).

to increase during injection and then it decreases after injection, according to data from the LILY tiltmeter. These results are difficult to reconcile with each other.

The pressure at monitoring wells increased during injection and decreased during recovery (Figure 4.31b). The rates and resulting magnitudes are consistent with data from the October 2017 test.

The November 2017 test is the first test when data from the Optical Fiber Areal Strainmeter (OFAS) was available. These data were compared to the sum of the principle horizontal strains measured with the Gladwin strainmeter, and the results are strikingly similar (Figure 4.32). The difference between the two signals is less than 10 nε during injection. Both instruments indicate a brief period of decreasing strain lasting several hours at the beginning of day 2. The deviation between the instruments reaches a maximum of approximately 20 nε at day 6, roughly 3 days after injection stopped. This difference amounts to approximately 20 percent of the total signal magnitude (Figure 4.32).

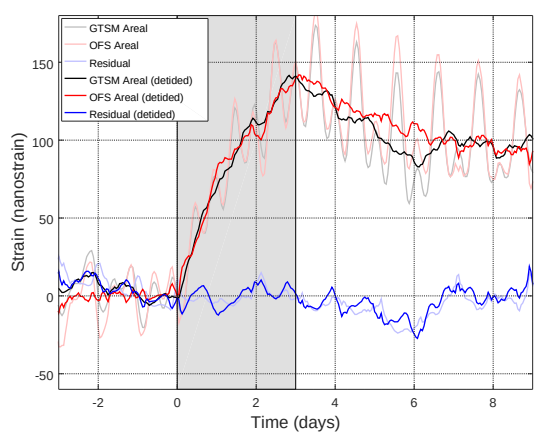

Figure 4.32: Comparison of areal strains during Dec 2017 injection test at well 9A. Injection occurred during gray band. Day 0 is November 28th, 2017. Semi-transparent lines are raw data. Areal strain measured with Optical Fiber Areal Strainmeter (OFAS) (red line), and with the Gladwin Tensor Strain Meter (GTSM) (black line). The residual (GTSM-OFAS) as blue line. Background trends removed.

We conclude that the areal strain measured with the optical fiber instrument developed for the project is essentially identical to the areal strain measured by the Gladwin strainmeter (Figure 4.32).

On semi-log axes, the pressure and strain signals are curved at early time and then are approximately straight starting between 5×10^4 and 8×10^4 s (Figure 4.33). A second straight segment with a steeper

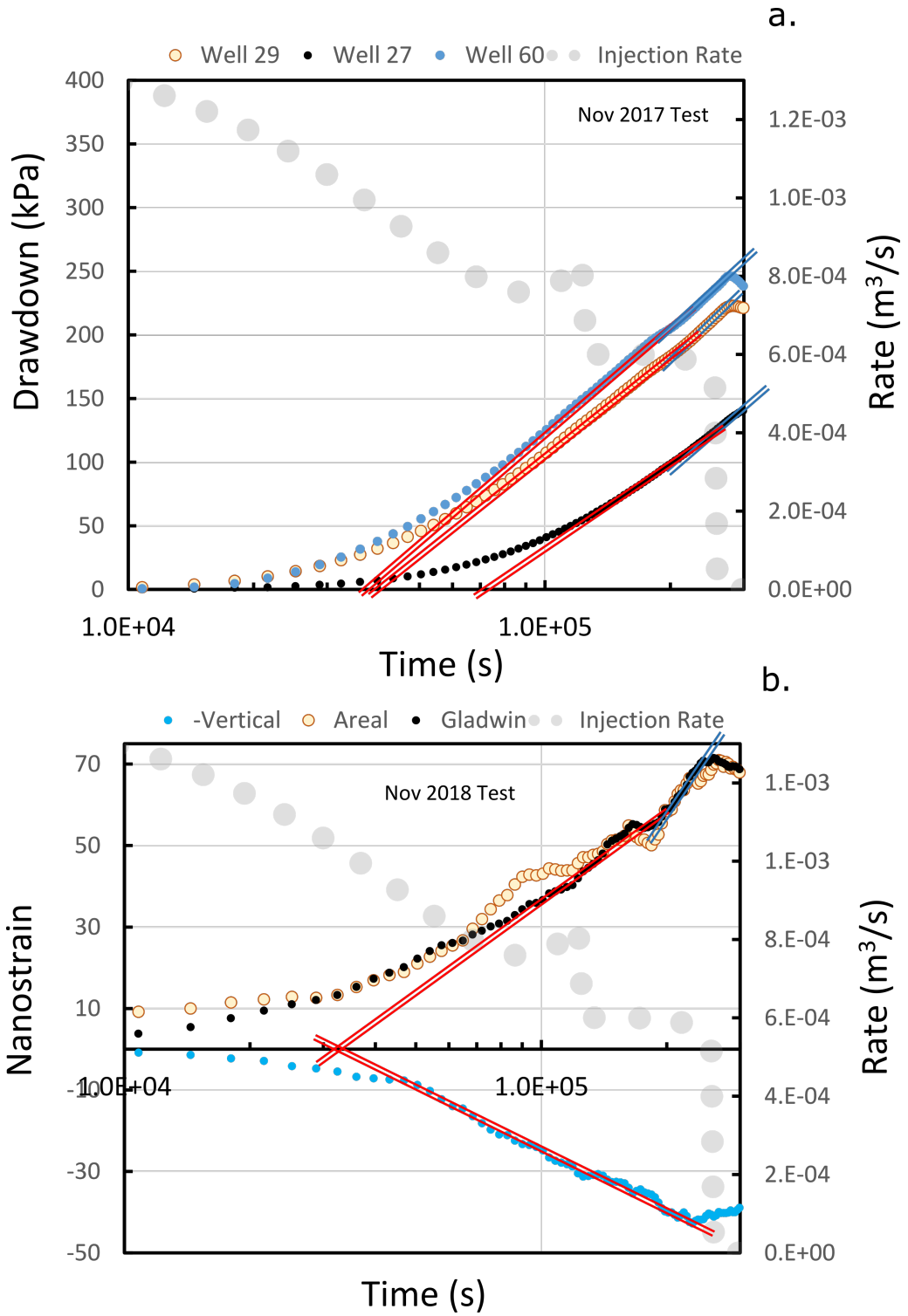

Figure 4.33: Pressure and strain as functions of log time from the November 2017 injection test. (a) pressure at wells 27, 29 and 60. First semi-log straight segment as double red line, second segment as double blue line. (b) Average horizontal strain (areal strain/2) determined using Gladwin strainmeter and the Optical Fiber strainmeter with semi-log line segments.

slope occurs at approximately 20×10^4 s. Interestingly, the vertical strain follows a single semi-log straight line–the slope of ε_{zz} does not increase at $\sim 20 \times 10^4$ s for the vertical strain as it does for the horizontal strains and the pressures. A similar response was observed in the vertical strain during the October 2017 test (Figure 4.28).

The intercept time t_o is approximately 4×10^4s for Wells 60 and 29 (Table 4.3). The intercept times, t_{oa}, for the both horizontal strains and the vertical strain are similar to each other, approximately 3.2×10^4 s, which is slightly less than t_o from data from wells 29 and 60 (Figure 4.28; Table 4.3).

The semi-log slopes for the pressure signal range from 225 to 275 kPa, which is similar to the slopes during the October test (Table 4.3). The magnitudes of the semi-log slopes of the strains are also similar to the magnitudes observed during the October test, except during the November test the slope of the $\varepsilon_{zz} < \varepsilon_h$, whereas during the October test $\varepsilon_h > \varepsilon_{zz}$ (Figure 4.28; Table 4.3).

The injection rate during both the October 2017 and November 2017 test decreased with time. A changing injection rate is known to affect the pressure signal measured in the reservoir, and we expect that it also affects the strain signal measured at shallow depth.

4.3.1.2.3 July 2018 Test

Injection during the July 2018 injection test began on June 28th, 2018, and lasted for 25 days. The injection rate was approximately 500 bbl/d (450–525 bbl/d) for the first 20 days. It decreased during the end of the test and dropped below 400 bbl/d on day 21. The rate dropped sharply to between 100 bbl/d and 200 bbl/d during the last 2 days of the test (Figure 4.34). The injection rate varied with a period of several hours, as it did during the earlier tests.

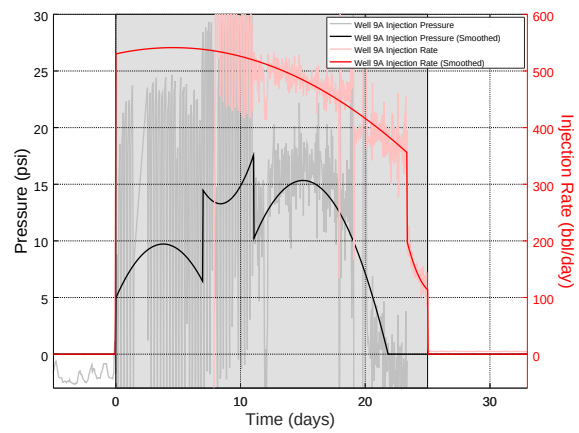

Figure 4.34: Wellhead pressure (black) and rate (red) during the July 2018 injection test at well 9A. Injection occurred during gray band. Day 0 is June 28th, 2018. Semi-transparent lines are raw data. Solid lines are piece-wise splines fit through data.

The strain signal is generally similar to the earlier tests, with extension in the horizontal plane and compression in the vertical. The NS strain increased faster than the EW strain, and the vertical strain decreased at a rate similar to the NS strain.

The strain rates also decrease with time, as in previous tests. The NS strain rate was 30 nε/d during the first few days of the July 2018 test (Figure 4.35), whereas it decreased from 50 to 15 nε/d during the 3 days of the November test (Figure 4.30) and it was 30 nε/d at the beginning of the October test (Figure 4.26). The NS strain increased to a maximum of 260 nε at day 22 (Figure 4.35), and it decreased thereafter following the drop in injection rate (Figure 4.34).

The EW strain rate started at approximately 10 nε/d during the July test, but the rate diminished after the first day (Figure 4.30). The EW strain fluctuates during most of the test and reaches a maximum of 30 nε at day 13. The EW strain decreased at the end of the test and reversed sign (Figure 4.34).

The vertical strain is compressive at a rate of approximately 30 nε/d during the first several days (Figure 4.30). The vertical strain rate diminished and even changed sign for a few days ($\sim$days 5–7). The vertical strain reached a maximum magnitude of -150 nε at day 22 and then diminished along with the other strain signals (Figure 4.30).

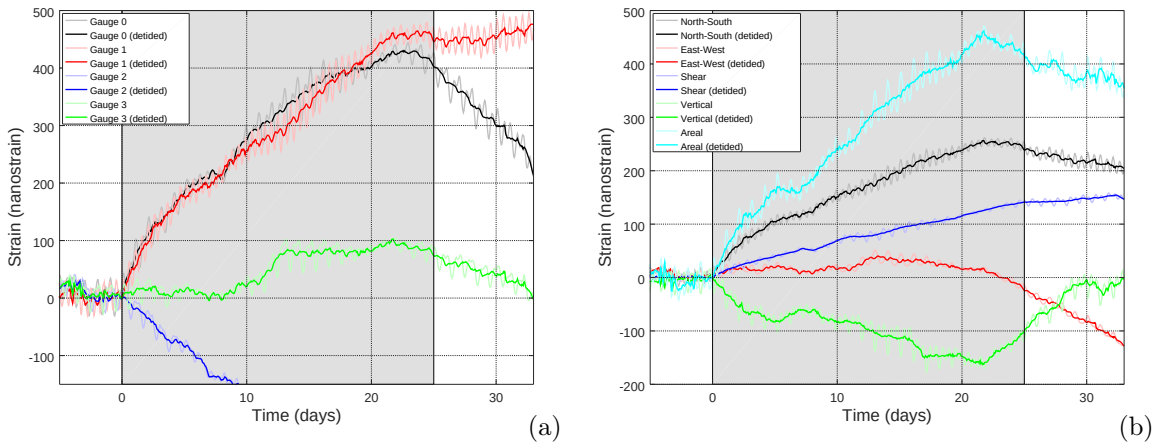

Figure 4.35: Strain data at AVN during the July 2018 injection test at well 9A, North Avant Field, OK. Day 0 is June 28th, 2018. Semi-transparent lines are raw data. Solid lines are data corrected for tides and barometric pressure. Long-term trends removed. (a) data measured by Gladwin instrument gauges; (b) NS normal strain (black line), EW normal strain (red line) and EW shear strain (blue line), Areal strain (cyan). Vertical strain from eddy current instrument (green line).

The slopes of all the normal strains decrease starting at approximately day 5 and then start increasing at day 7.

Tilt signals were measured by the LILY and Eddy Current tiltmeters (Figure 4.31). Signals from both tiltmeters increase to 200 nrad over the first 5 days of the test (40 nrad/day). However, the tilt occurs in the opposite direction–the LILY tiltmeter indicates tilt to the north, whereas the Eddy Current tiltmeter indicates tilt primarily to the south. In both cases, the tilting rate abruptly changes sign between days 5 and 6. The magnitude of the normal strains also decreases during this time. The tilt signals increase or become roughly constant between days 10 and 20, and then they decrease at the end of the test (Figure 4.31).

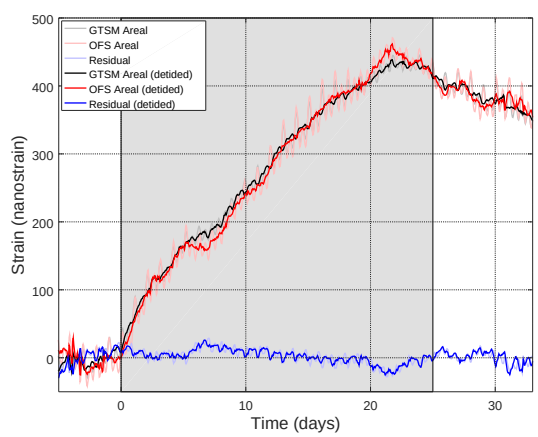

Figure 4.36: Comparison of areal strains during July 2018 injection test at well 9A. Injection occurred during gray band. Day 0 is June 28th, 2018. Semi-transparent lines are raw data. Areal strain measured with the Optical Fiber Areal Strainmeter (OFAS) (red line), and with the Gladwin Tensor Strain Meter (GTSM) (black line). The residual (GTSM-OFAS) as blue line. Long-term trends removed.

The pressure in the reservoir increased with time along a trend that is similar to the other tests (Figure 4.31). A brief decrease in pressure occurs during day 8 in the record for Well 29 and the slope of the pressure decreases in the record for Well 27 (Figure 4.31). This brief change in pressure appears to occur one to several days after the change in strain and tilt. The pressured decreases during the last day of the test, apparently in response to the decrease in injection rate. The transducer in Well 60 was damaged so data from that well are unavailable.

The areal strain measured using the Gladwin strainmeter is essentially identical to the areal strain measured with the Optical Fiber strainmeter (Figure 4.36). The strain rate decreases between days 5–7

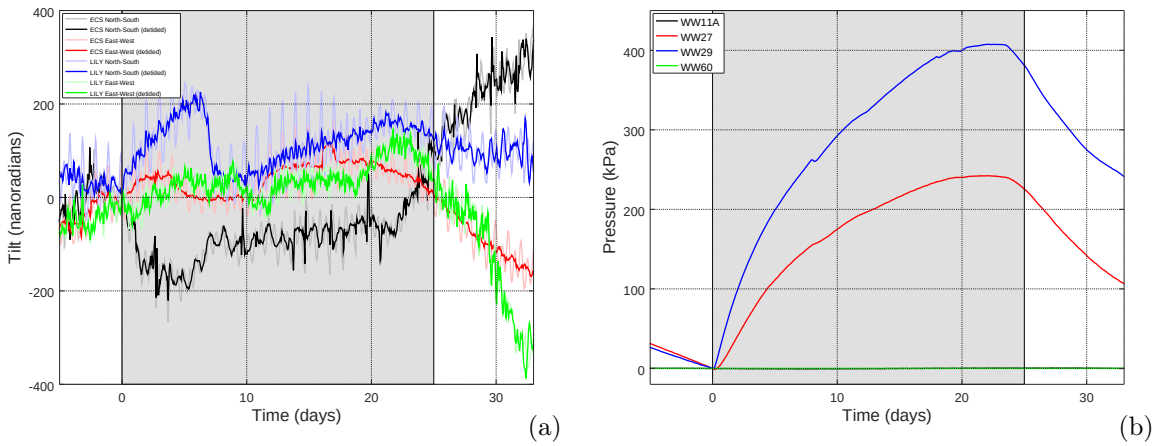

Figure 4.37: Tilt and well pressure data from July 2018 injection test at well 9A, North Avant Field, OK. Day 0 is June 28th,2018. Semi-transparent lines are raw data. Solid lines are data corrected for tides and barometric pressure. Long-term trends removed. (a) tilt in EW direction (red) and NS direction (black) measured using eddy current instrument, EW tilt with the LILY (green) and NS tilt with LILY tiltmeter (blue). (b) pressure change at monitoring wells. Well 27 (red), well 29 (blue).

according to both instruments, although the change in rate is greater in the OFS instrument than the Gladwin. The difference between the two signals is typically within 10 nε. The periodic fluctuations in the strain residual (blue line in Figure 4.36) are a result of diurnal variations in the Gladwin signal that persist after corrections have been applied. These variations are thought to be a result of temperature changes in the electronics of the Gladwin. This indicates that the signal from the Optical Fiber Strainmeter is not only essentially identical to the Gladwin signal, but it also lacks the small fluctuations that appear to be spurious in the Gladwin strain signal.

The semi-log plots of pressure and strain show two straight segments, on that begins at approximately 1.5×10^5 s (1.7 days) and another that begins at 7×10^5 s (8 days) (Figure 4.38a). The time intercept for the first segment of the data from Well 29 is approximately $t_o = 8 \times 10^4$ s. The time intercept for the average horizontal and the vertical strain are the same and equal to $t_{oa} = 5 \times 10^4$ s (Table 4.3; Figure 4.38).

The semi-log slope for the first segment of well 29 is 250 kPa, whereas it is slightly less (225 kPa) for well 27 (Figure 4.38b). The semi-log slopes for the strains are in the range of 70 to 80 nε (Table 4.3). In general, the values of intercept times and slopes for the first straight segment are similar to the earlier tests for both the pressure and strain signals. The intercept times and slopes for the second straight segment are greater than during the first one (Table 4.3; Figure 4.38).

4.3.1.3 Summary of Field Tests at North Avant Field

Four field tests were conducted at the North Avant Field, including both injection tests at well 9A and shut-in tests from Well 1A, and some overarching themes emerge from the results. The injection rate into Well 1A was approximately 1,000 bbl/d prior to shut-in, whereas the injection rates into well 9A were approximately half that rate, ~500 bbl/d. The duration of the shut-in test was 7 days, whereas injection occurred for between 3 and 25 days.

The pressure signals at three monitoring wells increased during injection following trends that become log functions of time. The distance between the injection well and the monitoring wells are 190 m, 270 m

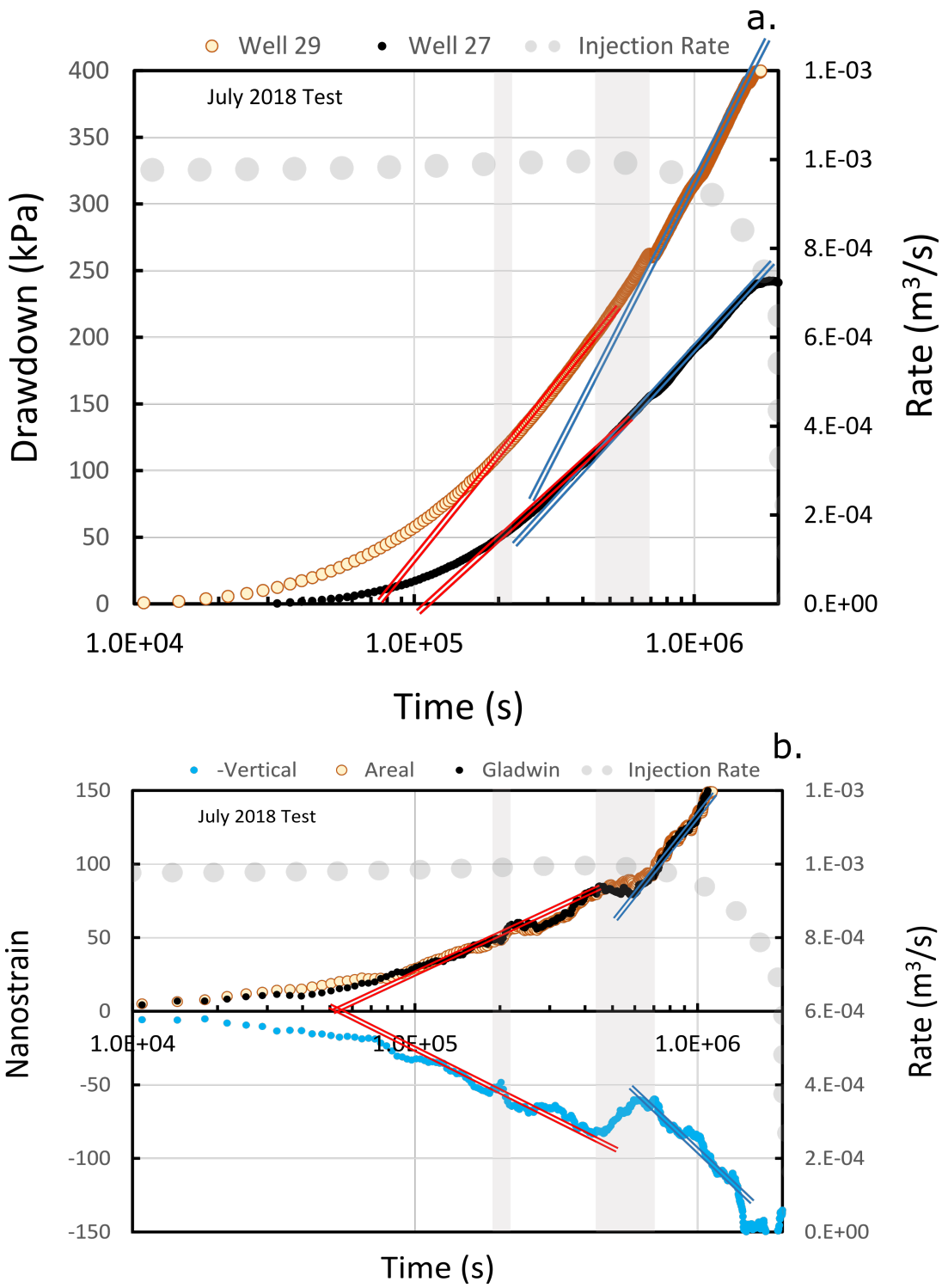

Figure 4.38: Pressure and strain as functions of log time, July 2018 injection test. (a) pressure at wells 27, and 29. First semi-log straight segment as double red line, second segment as double blue line. (b) Average horizontal strain (areal strain/2) determined using Gladwin strainmeter and the Optical Fiber strainmeter with semi-log line segments.

and 370 m. The slope of the first semi-log line segment ranged from 200 to 300 kPa, depending on the well and the test. A second semi-log straight line segment occurred during injection in most cases and the slope of the second segment was steeper than that of the first segment. Intercept times for the first segment from the closest monitoring point to the injection well range from $4.4 \times 10^4 < t_o < 7 \times 10^4$ s.

The pattern and magnitude of the normal strain signal were consistent among the different tests. The radial strain at AVN was tensile during both the injection into well 9A and shut-in at well 1A. The circumferential strain was compressive during 1A shut-in and tensile during 9A injection. Vertical strain was compressive during injection, and the vertical strain instrument was not available for the shut-in test.

Strain rates were largest at the start of injection or shut-in and they decreased with time. The maximum normal strain rate averaged during the first day was typically 30 nε/d and it decreased with time to 10 nε/d during the tests. The magnitude of the minimum horizontal strain was 0.5 to 0.2 of the maximum strain. This resulted in maximum strains of on the order of 10^{-7} ε.

The normal strains are approximate functions of the log of time, similar to the pressures. The semi-log slope of the first segment ranged from 50 to 85 nε. The semi-log slopes of the normal strains increase, and the semi-log slope of the second line segment was 140 to 220 nε. The intercept times for the first segment ranges from $3.2 \times 10^4 < t_{oa} < 5 \times 10^4$ s, which is slightly less than the intercept times for the closest monitoring well. The intercept time for the monitoring wells increases with distance from the injection well, and the distance to the two closest monitoring wells is similar to the distance to the strainmeters.

The hydraulic diffusivity can be estimated using the intercept time as $D_{hs} = r^2/2.25\, t_o$. The hydraulic diffusivity was calculated using either t_o or t_{oa} from Table 4.3, and this give seven estimates for the hydraulic diffusivity during the first straight segment D_{h1} using pressure data and strain data, and seven estimates for the D_{h2} during the second segment (Table 4.4. The results show that the mean value for D_{h1} calculated using the pressure data ($D_{h1} = 0.56$ m^2/s) is nearly identical to the value calculated using the strain data ($D_{h1} = 0.54$ m^2/s). The standard deviation is approximately 0.2 m^2/s.

Hydraulic diffusivity for the second straight segment is less than for the first, and the mean D_{h2} from the pressure data is similar to the mean from the strain data. A decrease in the hydraulic diffusivity is consistent with the well intersecting a permeable lens.

The results indicate that simple analyses of the shallow strain data could be used to estimate hydraulic diffusivity of the reservoir and the results would be similar to estimates made using pressure measurements from monitoring wells in the reservoir.

Areal strain measured using the optical fiber strainmeter developed for the project were essentially identical to the areal strain measured using the Gladwin strainmeter. Areal strains also change as a function of the log of time, and it gives similar results to those cited above. We conclude that the optical fiber strainmeter gives valid strain data, and those data can be used to estimate hydraulic diffusivity.

Table 4.3: Data determined from pressure and strain time series.

		t_o or t_{oa} ($\times 10^4$ s)	ΔP_{s1} (kPa)	$\Delta\varepsilon_{01}$ (ε)	t_{02} ($\times 10^4$ s)	ΔP_{s2} (kPa)	$\Delta\varepsilon_{02}$ (ε)	r (m)	Q (m^3/s)
October 2017									
	Well 29	8	400	-	16	600	-	190	1.1–0.6
	Well 60	6	350	-	16	600	-	270	
	Well 27	12	350	-	18	550	-	370	
	Gladwin	4.5	-	60	16	-	200	220	
	Vertical	4.5	-	90	-	-	90	210	
	Areal	n/a							
November 2017									
	Well 29	4	260	-	6	325	-	190	1.3–0.6
	Well 60	3.5	275	-	6	320	-	270	
	Well 27	7	230	−9	300	-	370		
	Gladwin	3.2	-	70	9	-	180	220	
	Vertical	3.2	-	50	4	−50 210			
	Areal	3.2	-	70	9	-	140	230	
July 2018									
	Well 29	7	250	-	18	400	-	190	1.0–0.8
	Well 60	n/a						270	
	Well 27	11	200	-	18	250	-	370	
	Gladwin	5	-	90	30		250	220	
	Vertical	5	-	90	30		170	210	
	Areal	5	-	90	30		250	230	

Table 4.4: Hydraulic diffusivity estimated from pressure and strain time series.

		D_{h1} pressure (m^2/s)	D_{h1} strain (m^2/s)	D_{h2} pressure (m^2/s)	D_{h2} strain (m^2/s)
October 2017					
	Well 29	0.36		0.10	
	Well 60	0.54		0.27	
	Gladwin		0.51		0.14
	Vertical		0.47		0.39
November 2017					
	Well 29	0.40		0.20	
	Well 60	0.93		0.54	
	Well 27	0.87		0.61	
	Gladwin		0.67		0.24
	Vertical		0.61		0.49
	Areal		0.73		0.26
July 2018					
	Well 29	0.23		0.09	
	Well 27	0.51		0.28	
	Gladwin		0.43		0.07
	Vertical		0.39		0.07
	Areal		0.47		0.08
Mean		0.56	0.54	0.30	0.22
Standard dev		0.24	0.19	0.19	0.18

4.3.2 Well Tests at the Clemson Field Site

The Clemson field site was used to conduct shakedown tests of prototype strainmeters prior to deployment at the North Avant Field. The shakedown tests include an evaluation of strainmeter performance in response to natural fluctuations in barometric pressure and Earth tides, as well as their response to pumping or injection. Constant-rate pumping tests were intended to create loading similar to that encountered at the North Avant Field. Strain measurements were made under both saturated and partially saturated conditions, and with strain instruments in the vicinity of the water table, as well as deeper in bedrock. In addition to the strainmeters described in Chapter Two, this site also includes instruments called DEL-X extensometers, which are designed to measure vertical strain in soft sediments. This is significant because the DEL-X extensometers were deployed in the vicinity of the well screen used for the pumping tests. Results from the tests were analyzed by comparison to a fully-coupled poroelastic finite element model that accounted for partial saturation.

4.3.2.1 Field Site

The study site for the shallow strain investigation is located near Clemson, South Carolina in the Piedmont physiographic province. The site is underlain by biotite-gneiss derived saprolite from the ground surface to approximately 30 m depth and the water table is at a depth of 9 m. Beneath the saprolite is biotite-gneiss bedrock. Core samples taken in the saprolite reveal a fabric similar to that of the metamorphic parent rock with high mica content.

The hydraulic and elastic properties of the saprolite were estimated from Shelby tube samples. Triaxial tests were performed under partially and fully-saturated conditions to characterize how the elastic properties changed as a function of saturation. Laboratory results indicate a Young's modulus of 60 MPa for partially saturated conditions and 50 MPa under full saturation. The saprolite is soft compared to the underlying bedrock. The biotite gneiss is sparsely fractured, and we estimate the Young's modulus to be in the range of 30,000 to 40,000 MPa (30 to 40 GPa).

The saturated hydraulic conductivity of the saprolite is 9.3×10^{-6} m/s. Results also indicate that the van Genuchten retention curve parameters (α and n) of saprolite are similar to that of silt, with an air-entry term ($\alpha = 0.6$ 1/m and a pore size distribution term $n = 1.31$.

Three borings were made into the biotite gneiss. The borings were cased to approximately 30 m depth and were open to a depth of 45 m. Slug tests were conducted after drilling and the results showed that the rock in the vicinity of the open borings is tight. The response to the slug test was slow enough so it was probably controlled by leakage around the bottom of the casing, so we did use the data to estimate formation properties. We used a camera to inspect the walls of the borings and no significant fractures were visible. Based on these findings, we concluded that the vicinity of the borings was sparsely fractured and the flow rate produced by pumping the wells would be minor. The flow that did occur would likely be localized around the base of the casing, so we expected that pumping from the borings would have negligible effect on the pore pressure in the gneiss. As a result, we decided to use a well in the overlying saprolite for pumping tests.

The well used for the pumping tests is 0.1 m (4 inches) in diameter and is screened in saprolite from 12–18 m below ground surface (bgs). Drawdown was monitored in the pumping well, as well as in three monitoring wells at radial distances of 9, 16 and 19 m from the pumping well.

A series of three constant rate pumping tests were performed over the course of one week. Each test was conducted by pumping at a rate of 1.9×10^{-4} m^3/s (3 gallons per minute) for a duration of 2.5 hours. Vertical strain measurements during the pumping tests were made at four locations. The objective of the

tests was to characterize the hydraulic and deformation properties of the saprolite and estimate how this would affect the underlying gneiss at the depth of the strainmeters.

4.3.2.2 In-Situ Strain Measurement

Vertical strain at a resolution of better than 7 $n\varepsilon$ was measured during the pumping tests by an array of four DEL-X extensometers. The relative depth and location of each of the instruments is shown in Figure 4.39. The DEL-X is composed of two cylindrical anchors situated co-axially at the bottom of a well in frictional contact with the surrounding material (Figure 4.40). A rod is rigidly attached to the bottom anchor and extends up through the center of the top anchor. A thin tube prevents frictional contact of the rod with the surrounding soils. As the soil deforms, the anchors move and the relative displacement of each anchor to the other is measured between the top anchor and the inner rod with a Differential Variable Reluctance Transducer (DVRT). The high frequency electromagnetic signal from the DVRT is demodulated into an analog voltage and is then converted to a digital voltage with an Analog-to-Digital converter. In order to increase resolution and minimize electromagnetic noise and thermal effects on the strain signal, signal processing is performed down-hole in a waterproof electronics housing where the temperature is stable. The resulting digital voltage signal is sent to a data logger at the surface for recording.

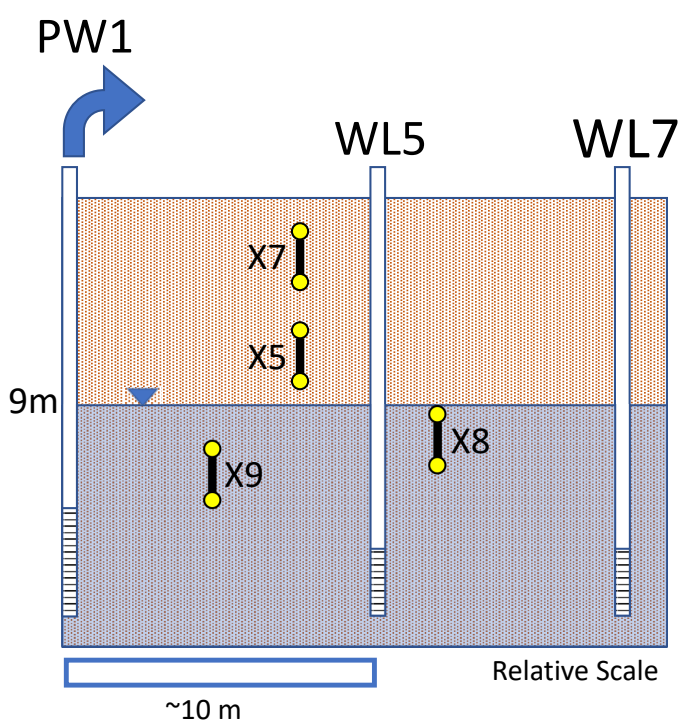

Figure 4.39: Site layout and relative location of extensometers and monitoring wells relative to pumping well.

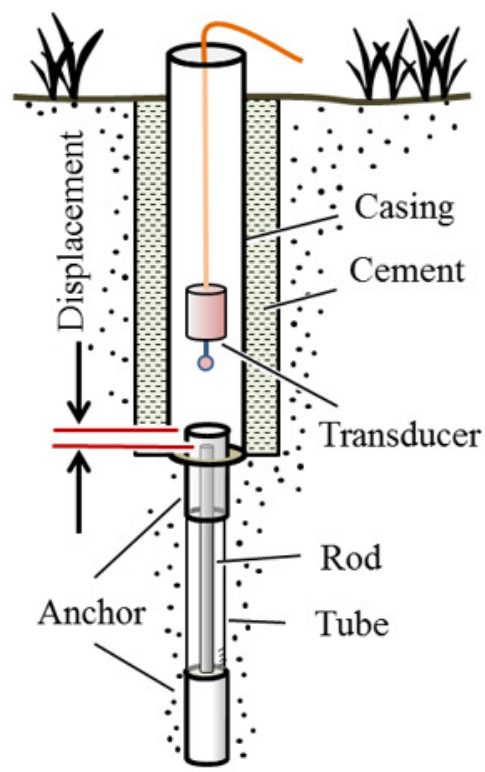

Figure 4.40: Schematic of installed DEL-X extensometer.

4.3.2.3 Field Observations

The results include data describing the fluid pressure, vertical strain and tilt.

4.3.2.3.1 Fluid Pressure

Three pumping tests were performed at the study site near Clemson, South Carolina. The tests were conducted for a duration of 2.5 hours with a rate of 1.9×10^{-4} m^3/s (3 gallons per minute). Pressure measurements were made in the pumping well (PW1), as well as in two monitoring wells at a radial distance of 9 m (WL5) and 16 m (WL7). Results from the test indicate an average drawdown of approximately 5 m in the pumping well and draw-downs of 11 and 6 cm were observed in monitoring wells WL5 and WL7, respectively (Figure 4.41). The pressure signal in the pumping well exhibited a steep decline for the first 30 minutes of pumping, followed by negligible drawdown for the remainder of the test. Drawdown signals observed in the monitoring wells exhibited a more gradual response with relatively high rates of decline for the first 100 minutes of pumping, followed by a gradual decrease in the rate of drawdown until the pump was shut off. The pressure signals from each of the wells during recovery ($t \geq 180$ min) is similar in shape to those observed during pumping ($t = 30$ to 150 min), but at a slightly slower rate.

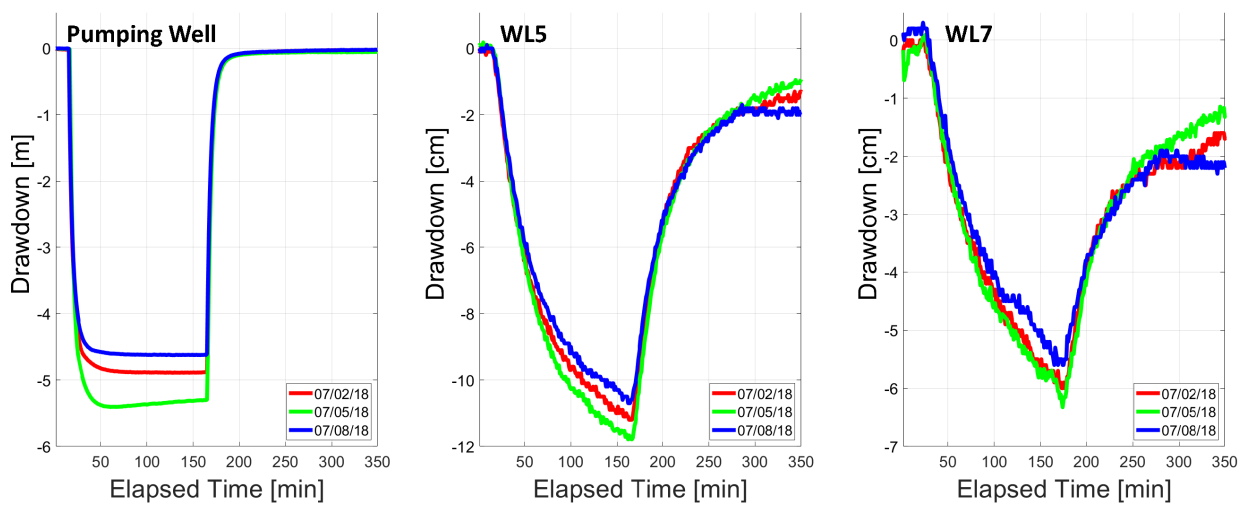

Figure 4.41: Water level response in pumping and observation wells from three pumping tests.

4.3.2.3.2 Vertical Strain

Vertical strain measurements were made in both the vadose and the saturated zone in response to pumping. All instruments recorded compressional strains during pumping and extension during recovery, with magnitudes of approximately 0.1 microstrain of compression observed in the vadose zone and 1–9 microstrain in the saturated zone where fluid pressure changes were significant. As can be seen in Figures 4.42–4.43, the signal to noise ratio is relatively high in the saturated zone compared to the vadose zone, where the magnitude of strain due to pumping is similar in scale to that of barometric pressure fluctuations. This effect is most noticeable in X5, which has been found to be more sensitive to barometric pressure than X7 in the ambient record. Both instruments in the saturated zone, X8 and X9, have also been found to be sensitive

to fluctuations in barometric pressure, but the magnitudes of strain produced during pumping were much greater than that of any background ambient effects, resulting in a much clearer signal. It should also be noted that the strain signals between the vadose and saturated zones had distinctly different shapes, with the saturated zone exhibiting a gradual compression throughout the test, similar to that of the pressure response in the observation wells, while the signal in the vadose zone was more rectangular in shape with rapid compression during the first 30 minutes of pumping, followed by negligible amounts for the remainder of the test. This rectangular shape closely resembles the shape of the drawdown curve in the pumping well.

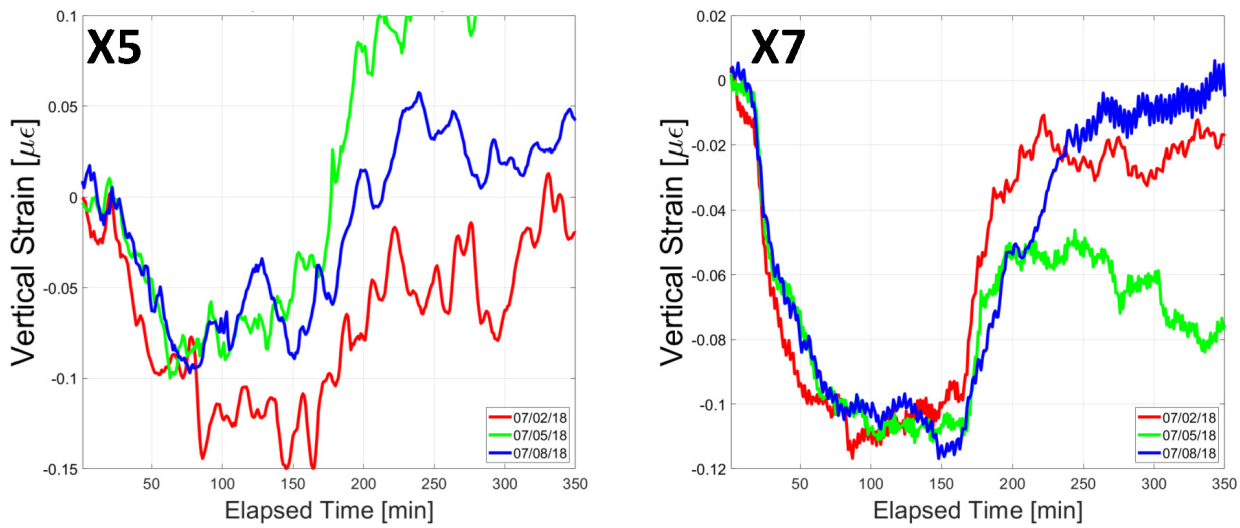

Figure 4.42: Vertical strain observed in the vadose zone in response to pumping.

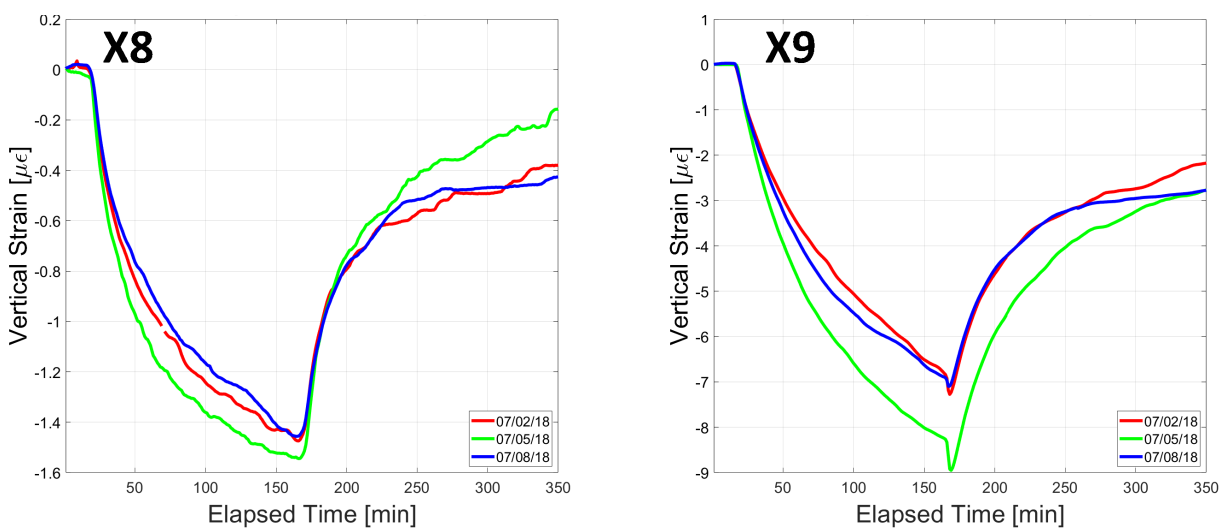

Figure 4.43: Vertical strain observed in the saturated zone in response to pumping.

Another interesting feature observed in the strain data was a sharp dip in the strain signal in X9 when the pump was shut off ($t = 180$ min). This Noordbergum-type effect was seen in the numerical simulation, which is covered in more detail in the following section.

4.3.2.3.3 Tilt

Tilt measurements in the vadose zone were also recorded during the pumping test with an Applied Geomechanics (now Jewell Instruments) LILY self-leveling borehole tiltmeter with a resolution of $sim5$ nanoradians. Measurements were made in 2-inch diameter PVC casing installed to a depth of approximately 3 m and a radial distance of 9 m from the pumping well. In an effort to match the modulus of the annular material with the saprolite, the wells were completed with sand, instead of cement. The tilt signal during pumping showed tilting toward the well and a recovery to its initial value after the pump was shut off. Comparison of the tilt signal to the calibrated numerical model showed a slight underestimation of the tilt magnitude by 1 micro-radian in TW2 and 3 microradians in TW1, but the shape observed in the model was quite similar to the field data (Figure 4.44). Interestingly, during model calibration, as the Young's modulus of the B-horizon was increased, the magnitude of the tilt signal also increased.

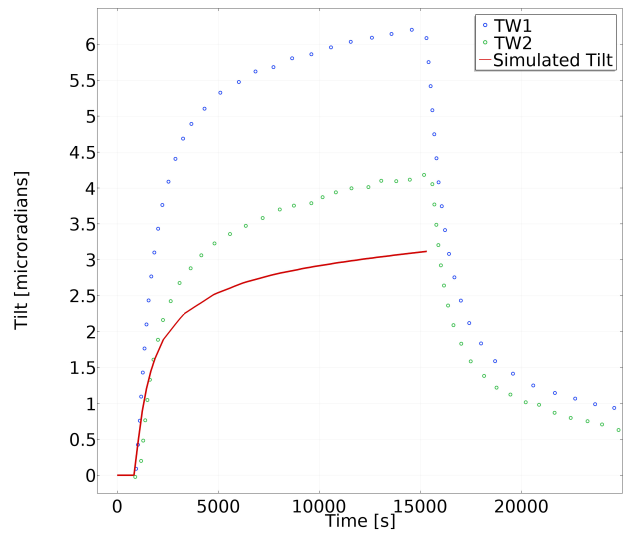

Figure 4.44: Tilt signal observed during pumping test.

4.3.2.4 Analysis

A fully-coupled poroelastic finite element model was constructed to analyze the strain signals from the field tests and ambient monitoring. Although core sample descriptions of the saprolite reveal a high degree of heterogeneity in both the structural fabric and the mineralogy, the material was assumed to be a homogeneous and isotropic elastic material. This assumption was made to establish a reference, as well as to formulate an understanding of the basic idealized poroelastic behavior of an unconfined aquifer system in response to pumping, surface loading and other stresses.

Methods for simulating the behavior of a fully-saturated, single phase poroelastic system were first developed by Biot (1941) and have been applied to a variety of problems. This method couples the fluid pressures obtained from Darcy's Law, with the strains calculated with Hooke's Law while satisfying the conservation of mass and momentum for both the fluid and the solid phases. In order to account for the effects of partial saturation observed at the study site, a modification of Biot's method was developed by using the Richards' equation to account for the fluid flow, instead of Darcy's Law. The deformation was coupled to the fluid pressure by including the volumetric strain rate ($\partial\epsilon_{kk}/\partial t$) obtained from Hooke's Law as a mass source term in the Richards' equation (4.1). Fluid-to-solid coupling was achieved by representing the fluid pressures (p) obtained from the Richard's equation

$$0 = \nabla \cdot (\rho q) + \rho(\frac{\Phi S_e}{\partial p} + \frac{\Phi S_e}{K_f})\frac{\partial p}{\partial t} + S_e \alpha_b \frac{\partial \epsilon_{kk}}{\partial t} \tag{4.1}$$

and the stresses in the solid using the Navier equation

$$\sigma_{ij} = 2G\epsilon_{ij} + \lambda\epsilon_{kk}\delta_{ij} - \alpha_b S_e p \delta_{ij} \tag{4.2}$$

where ρ is the fluid density, q is the volumetric flux, Φ is the porosity, K_f is the bulk modulus of the fluid, α_b is the Biot-Willis coefficient, σ_{ij} is the total stress and S_e is the effective saturation, which is defined as

$$S_e = \frac{\Theta - \Theta_r}{\Theta_s - \Theta_r} \tag{4.3}$$

where Θ is the volumetric water content, Θ_r is the residual water content, and Θ_s is the saturated water content.

A three layer model was constructed to simulate fluid pressure changes and deformation of the Simpson Station field site in response to pumping and other stresses. The top layer has a thickness of 2 m and represents the soil B-horizon, the saprolite was represented by the middle layer and is 28 m thick and the bedrock was specified for the bottom layer with a thickness of 20 m. Each layer was assumed to be homogeneous and isotropic for both the hydraulic and elastic material properties. Values used for the Young's modulus were 150 MPa for the soil horizon, 65 MPa for the saprolite and 30 GPa for the bedrock. A Poisson's ratio of 0.3 was used for the soil and the saprolite and a value of 0.2 was assumed for the bedrock.

4.3.2.4.1 Forward Model Results

A fully-coupled poroelastic finite element model was used to to interpret the data obtained from the pumping tests, as well as to understand the hydraulic and mechanical behavior of an unconfined aquifer in response to pumping. Results from the analysis indicated the sharp pressure drop observed near the well screen at the beginning of pumping produced compressional vertical strains locally and extensional strains above and below the well screen (Figure 4.45a). Additionally, the tilts predicted by the model shortly after the onset of pumping showed tilting away from the well at the top of the screen and tilting towards the well below. After 3 hours of pumping, the pressure and compressional vertical strain fields expand outward from the well, while extensional strains are observed in the vadose zone and directly beneath the well in the saturated zone (Figure 4.45b). The tilt field after 3 hours of pumping expands slightly, with additional tilting toward the well in the shallow vadose zone. As pumping continues, only compressional strain is observed in the saturated zone and each of the fields increase in magnitude and expand away from the well (Figure 4.45c).

The forward model was verified and calibrated by comparison to pressure and vertical strain data obtained from the pumping tests. The simulated pressure and strain signals were fit to the data by adjusting the elastic and hydraulic material properties of the formation, as well as the pore fluid compressibility. Material properties adjusted to fit the data included the Young's modulus E, the intrinsic permeability (k), and the van Genuchten retention curve parameters, α and n. The simulated curves for both pressure and strain fit the data quite well during pumping, but deviated slightly during recovery (Figure 4.46). This effect is likely due to hysteresis in the retention curve parameters during imbibition.

4.3.2.4.2 Sensitivity Analysis

A series of parameter sweeps were conducted with the forward model to determine the sensitivity of the pressure and strain signals to each of the parameters used to fit the data (Figures 4.47–4.51). The strain signal in the saturated zone was found to be sensitive to all of the model parameters, with the exception of the intrinsic permeability on the strain in X8, which showed little change for a range of permeability values. The simulated pressure signal in observation well WL5 appeared only to be sensitive to the permeability of the formation and the pore fluid compressibility.

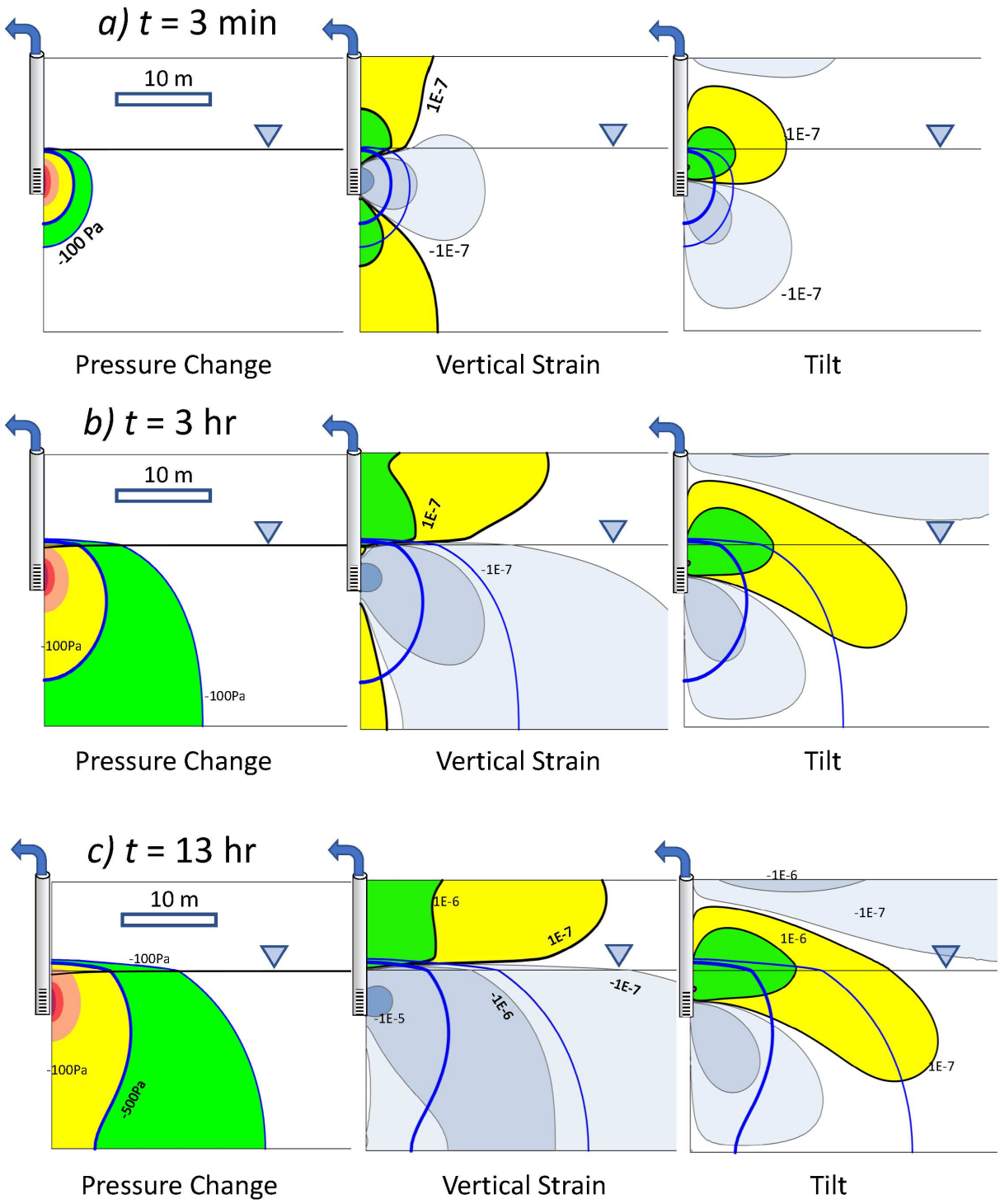

Figure 4.45: Cross-sections of pressure change, vertical strain, and tilt as functions of time during pumping. Axial symmetry assumed. Triangle is the water table. Colors are negative pressure change or positive strain or tilt, gray tones are negative (compressive) strain, or negative tilt (tilt away from the well).

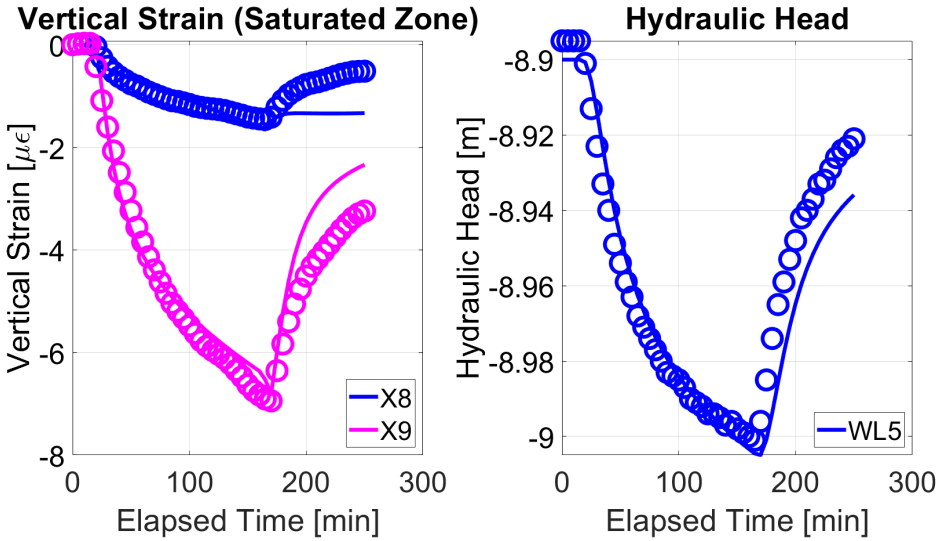

Figure 4.46: Vertical strain (left) and hydraulic head (right) for observations (circles) and simulation results (lines) from X8 and X9 and monitoring well WL5.

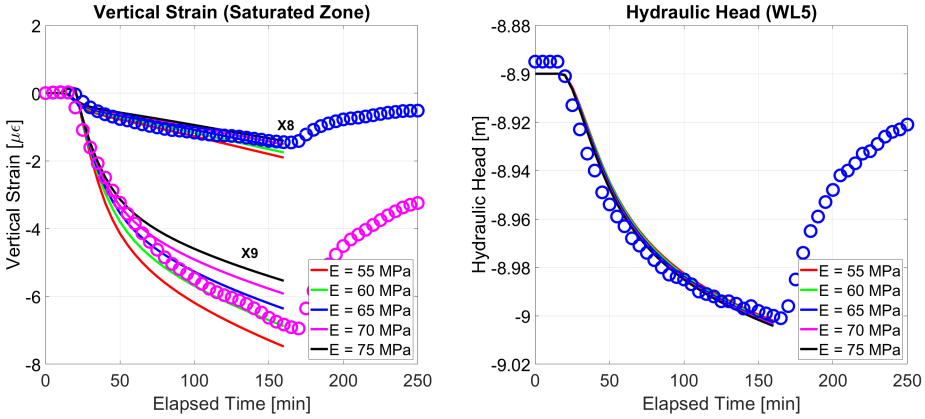

Figure 4.47: Vertical strain (left) and hydraulic head (right) for observations (circles) and simulation results (lines) from X8 and X9 and monitoring well WL5 for different values of Young's Modulus, E.

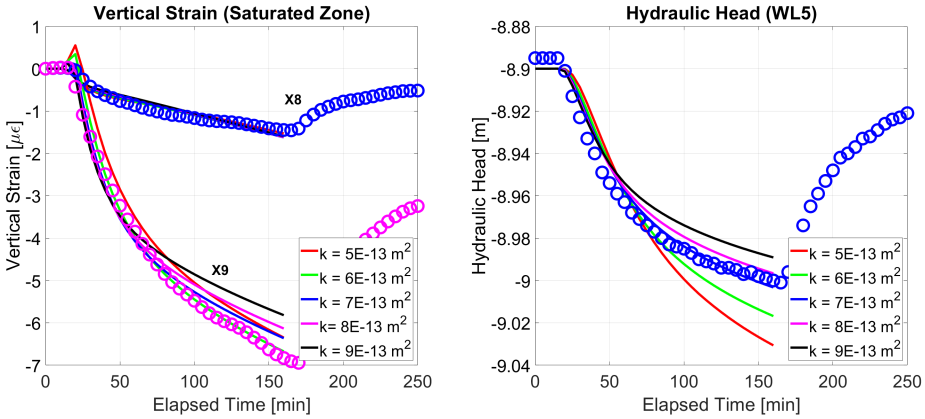

Figure 4.48: Vertical strain (left) and hydraulic head (right) for observations (circles) and simulation results (lines) from X8 and X9 and monitoring well WL5 for different values of intrinsic permeability, k.

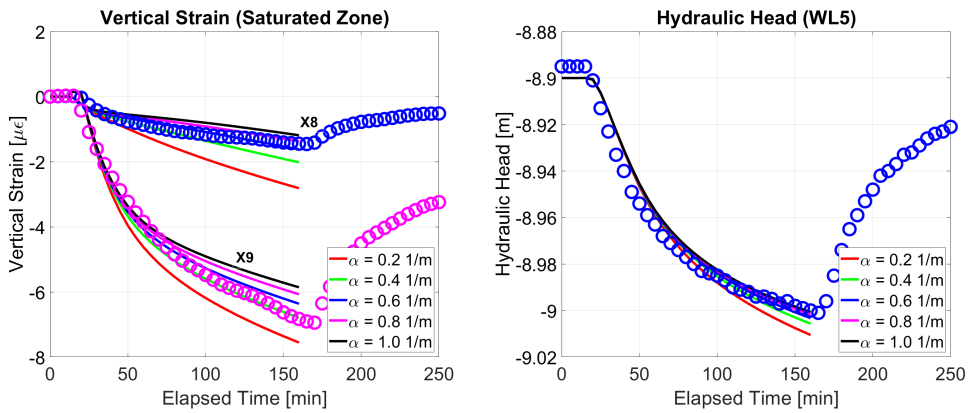

Figure 4.49: Vertical strain (left) and hydraulic head (right) for observations (circles) and simulation results (lines) from X8 and X9 and monitoring well WL5 for different values of van Genuchten retention curve parameter, α.

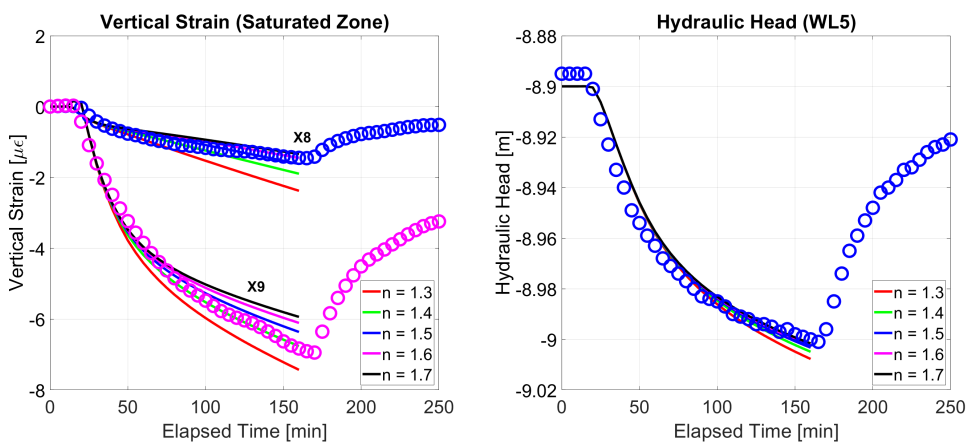

Figure 4.50: Vertical strain (left) and hydraulic head (right) for observations (circles) and simulation results (lines) from X8 and X9 and monitoring well WL5 for different values of van Genuchten retention curve parameter, n.

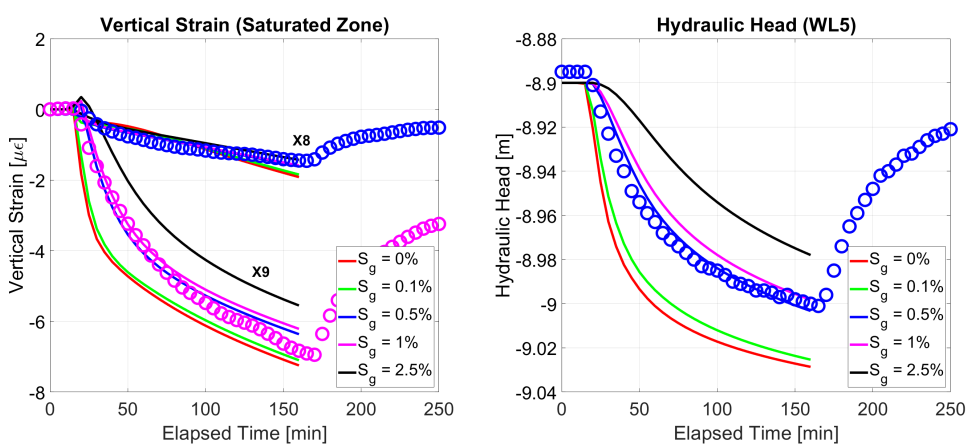

Figure 4.51: Vertical strain (left) and hydraulic head (right) for observations (circles) and simulation results (lines) from X8 and X9 and monitoring well WL5 for different values of pore fluid compressibility using equivalent gas saturation, S_g

4.3.2.5 Summary of Results from Clemson Field Tests

Vertical strain and fluid pressure measurements were made in a shallow, unconfined saprolite aquifer in response to pumping. These tests were conducted to gain a better understanding of how formations behave mechanically to induced changes in pore pressure, as well as to determine the feasibility and potential advantages of using strain measurements as a tool for CO_2 injection monitoring. The strain measurements for the current study were made at a resolution of better than 7 nanostrain with a series of four DEL-X extensometers we have developed and deployed at our Simpson Station field site near Clemson, South Carolina. Results from the pumping tests indicated that a repeatable, compressive strain signal could be measured in both the vadose and saturated zones. Interpretation of these signals through the use of a fully-coupled poroelastic finite-element model with partial saturation indicates that the strain signal is required for model calibration, due to the fact that the pressure signal is insensitive to the Young's modulus and van Genuchten retention curve parameters.

Further analysis of the mechanical behavior of the formation was conducted through interpretation of two-dimensional cross-sections of the vertical strain and tilt fields during pumping. The distribution of these fields from changes in pore pressure creates a complex signal that evolves with time and may be used to gain insight about the presence of heterogeneities in the distribution of material properties, as well as of the pore fluid. It should also be noted that vertical strain and tilt occurs and may be measured outside of the pumped formation in regions where little to no pressure change is observed. This capability would be especially advantageous when characterizing and monitoring deep formations, where monitoring well installation is expensive or in partially saturated settings where pore pressure measurements are not feasible. This study finds that high resolution strain measurements serve as an invaluable tool for poroelastic model calibration and for characterizing formation behavior in response to large changes in pressure, where mechanical deformation may be large and have important implications.

References

Biot, M. A. (1941). General theory of three-dimensional consolidation. *Journal of Applied Physics*, 12(2):155–164.

Gladwin, M. T. (1984). High-precision multicomponent borehole deformation monitoring. *Review of Scientific Instruments*, 55(12):2011–2016.

Kreemer, C., Blewitt, G., and Klein, E. C. (2014). A geodetic plate motion and Global Strain Rate Model. *Geochemistry, Geophysics, Geosystems*, 15(10):3849–3889.

Obianyor, E. (2008). *Permeability anisotropy related to meandering fluvial facies architectural elements in the Bartlesville sandstone of North Avant Field Osage County, Oklahoma.* Master of Science in Geosciences, University of Tulsa.

Ye, L., Kerr, D., and Yang, K. (1999). Facies Architecture of the Bluejacket Sandstone in the Eufaula Lake Area, Oklahoma: Implications for Reservoir Characterization of the Subsurface Bartlesville Sandstone. In Schatzinger, R. A. and Jordan, J. F., editors, *Reservoir Characterization–Recent Advances*, AAPG Memoir 71, pages 29–44. American Association of Petroleum Geologists.

Chapter Five
Interpretation of Field Tests at the North Avant Field

The objective of this phase of the project is to evaluate the interpretation of strain and pressure data measured at the North Avant Field in 2017 and 2018. Four methods of interpreting strain were evaluated ranging from a simple, graphical method to a complex, numerical calculation. The four methods include the strain type curve method, manual calibration of a 3D numerical model, numerical inversion of an analytical solution to a pressurized poroelastic inclusion, and stochastic inversion of a 3D numerical model.

The four methods use strikingly different mathematical models to calculate strains and find parameters that represent the observed data. The methods were evaluated at different times during the project, by three different groups of project team members, so they represent reasonably independent interpretations of the data. The interpretations methods provide estimates of hydraulic and mechanical properties, as well parameter distributions in the form of reservoir heterogeneity. Each method provides a somewhat different set of parameters, but there is overlap between the methods so intercomparison is feasible.

In general, the comparison indicates that the strain interpretation methods generate sets of parameters and heterogeneities that a similar to each other, and that are similar to expectations about the reservoir based on geologic conditions and characterization work conducted in the North Avant Field. The results from the individual interpretations are presented in the following pages.

5.1 Strain Type Curve

The hydraulic diffusivity can be estimated using the intercept time as $D_{hs} = r^2/2.25t_o$ as described in Section 3.3. The hydraulic diffusivity was calculated using either t_o or t_{oa} from Table 4.3, which gives seven estimates for the hydraulic diffusivity calculated using first straight segment D_{h1} from the pressure data and strain data, and seven estimates for the D_{h2} during the second segment (Table 5.1). The results show that the mean value for D_{h1} calculated using the pressure data ($D_{h1} = 0.56$ m^2/s) is nearly identical to the value calculated using the strain data ($D_{h1} = 0.54$ m^2/s). The standard deviation is approximately 0.2 m^2/s.

Hydraulic diffusivity estimated from the second straight segment is less than from the first segment, and the mean D_{h2} from the pressure data is similar to the mean from the strain data. A decrease in the hydraulic diffusivity is consistent with a response from the outer boundary of the permeable lens.

The semi-log slope of the strain time series can be used to estimate the transformational strain, according to 3.3. This yields transformational strains over the range $1.4 < \varepsilon_0 < 3.6$ $\mu\varepsilon$, with a mean of $\varepsilon_0 = 2.7 \pm 0.8$ $\mu\varepsilon$ (Table 4.3).

The transmissivity and permeability of the formation can be estimated using the Cooper-Jacob analysis (Cooper and Jacob, 1946), which requires assuming the extent of the reservoir is infinite and the pumping rate is constant. This analysis uses the pressure type curve equivalent of the analysis used for the strain. Applying this approach to the first straight line segment gives the mean transmissivity as $T = 5.6 \times 10^{-6} \pm 1.8 \times 10^{-6}$ m^2/s. Assuming the lens is 5 m thick and the fluid viscosity is 10^{-3} Pa·s, yields an estimate of permeability of $k = 130 \pm 40$ mD (Table 4.3).

5.2 Manual Calibration using 3D Numerical Model

Strain caused by injection was evaluated by comparing observed responses to simulations using a configuration similar to the field site. Parameters were adjusted until the results of the simulations resembled the

Table 5.1: Parameters estimated from pressure and strain time series using log type curve analyses.

		D_{h1} pressure (m^2/s)	D_{h1} strain (m^2/s)	D_{h2} pressure (m^2/s)	D_{h2} strain (m^2/s)	Transformational strain ($\mu\varepsilon$)	T ($m^2/s \times 10^{-6}$)	k (mD)
October 2017								
	Well 29	0.20		0.10			3.6	75
	Well 60	0.54		0.20			4.1	85
	Well 27	0.51		0.34			4.1	85
	Gladwin		0.48		0.13	2.6		
	Vertical		0.44		0.39	2.6		
November 2017								
	Well 29	0.40		0.27			5.5	
	Well 60	0.93		0.54			5.2	
	Well 27	0.87		0.68			6.2	
	Gladwin		0.67		0.24	3.0		
	Vertical		0.61		0.49	1.4		
	Areal		0.73		0.26	3.0		
July 2018								
	Well 29	0.23		0.09			7.2	148
	Well 27	0.55		0.34			9.0	186
	Gladwin		0.39		0.07	3.9		
	Vertical		0.36		0.07	2.6		
	Areal		0.43		0.08	3.9		
Mean		0.53	0.51	0.32	0.22	2.7	5.6	127
Standard dev		0.26	0.14	0.20	0.18	0.8	1.8	41

data (Figure 5.1). Comparing the simulations and the data for different values of parameters was used to develop some heuristics on factors affecting deformation during injection.

The configurations of the simulations consist of 2D axisymmetric, and 3D models. Preliminary analyses indicated that observed pressure could only be explained by a reservoir that was bounded laterally. This is consistent with the geologic model of the site, which recognizes discrete lenses of high permeability material deposited in alluvial channels as an important, hydrocarbon-bearing facies. As a result, the configurations of both simulations include a permeable lens of finite length underlying a laterally extensive layer representing the Bartlesville sandstone. In the axisymmetric model, the permeable lens is a circular disk, whereas it has a rectangular shape in the 3D model.

Preliminary analyses were conducted with the axisymmetric model (Figure 5.2). It became apparent that some of the observations were controlled by the locations of the boundaries of the lens. The symmetry of the axisymmetric model limited the ability to explain some of the observations, so the analysis focused on refining the 3D model. A layer representing the limestone bed containing the strainmeters was included in the 3D model, but it was omitted from the 2D simulations.

Boundary conditions were set up to represent the injection scenario (Figure 5.3). The well was represented as an edge with a specified injection rate. The injection rate schedule was simplified by omitting the periodic fluctuations in Figure 5.1.

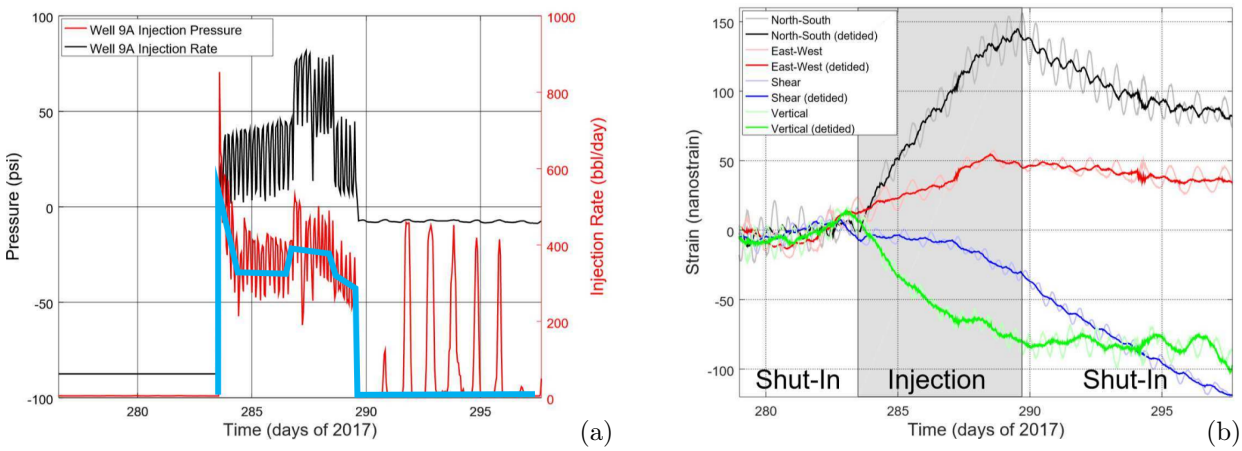

Figure 5.1: Pressure and injection rate during well 9A injection test in October 2017 (upper). Blue line is the rate used in the simulation. Normal strain, shear strain, and areal strain from Gladwin strainmeter at AVN2, vertical strain from Eddy Current instrument from October 2017 injection test (lower).

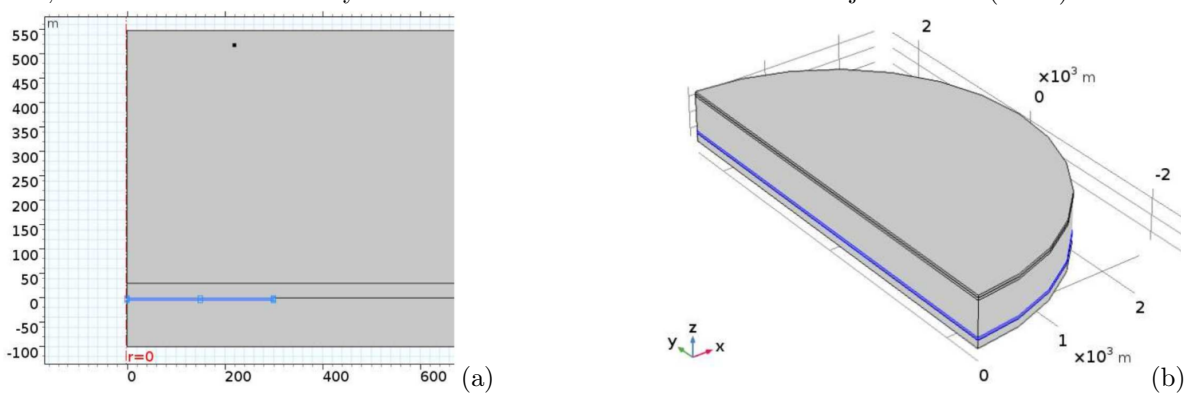

Figure 5.2: Configurations of the simulations. (a) axisymmetric model. Permeable lens in blue. Bartlesville sand is layer with a bottom an elevation of $z = 0$. Strain measurements at black point. Lateral extent is 10 km. (b) 3D model with well (not visible) midway along the front face.

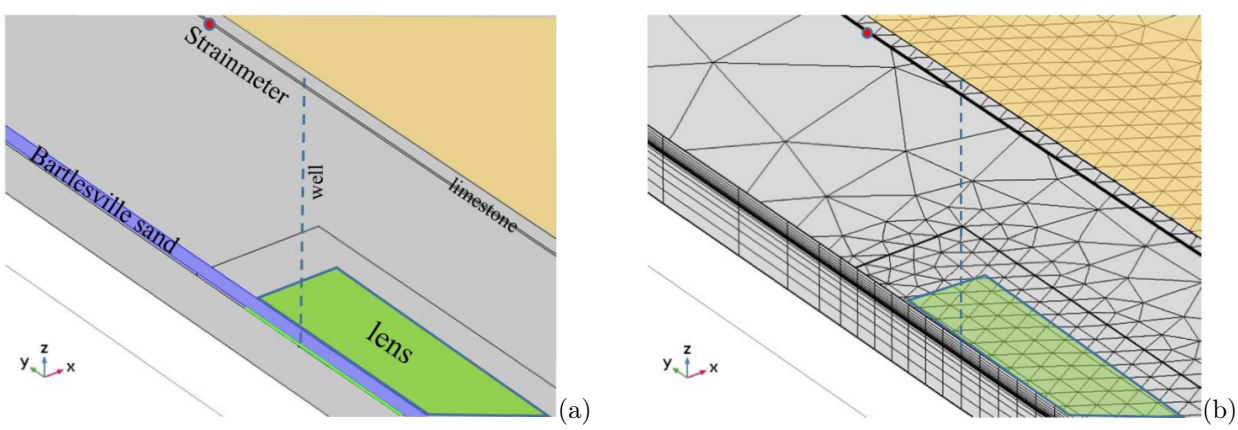

Figure 5.3: Configuration (a) and FEM mesh (b) used in 3D model. Permeable lens (green) under Bartlesville sand (purple). Strainmeter (red dot) in a limestone layer at 30 m depth. Path of the well is shown as a dashed line.

5.2.1 Results

Parameters were adjusted manually and the results were recorded in a database. The effects of the parameters on the simulated results were evaluated, and values of the parameters were adjusted to reduce the residual between the observed data and the simulated values. Results from the analyses of the October 2017 test are shown in the Figures 5.4 through 5.10 below.

Findings from a preliminary analysis of the October 2017 test include:

1. The results from the calibrated axisymmetric model (Figure 5.4) show that the magnitude of normal strains at shallow depth decreases with distance from the well and is generally in the range of 10^{-7} (100 nε). The spatial distribution of the normal strains depend on the location of the underlying lateral boundary of the permeable lens, which is the thin rectangular box at $z = 0$.

2. The permeable lens becomes pressurized during the injection test and the pressure propagates upward by roughly 10 m into the overlying Bartlesville sandstone at the end of injection (Figure 5.5). Pressure continues to move upward during recovery, and this will affect both the rate of pressure decrease and the strain during recovery. Pressure would move radially outward if the lateral extent of the radial lens was greater and the permeability of the overlying unit was lower.

3. The maximum absolute values of the strains typically occur at the end of injection, and they decrease thereafter. ε_{NS} and ε_{zz} are the largest observed strains with max values of 140 nanostrain and 80 nanostrain. The max value of ε_{EW} is approximately 50 microstrain. Horizontal shear strain during injection is approximately several tens of nanostrain, and similar values are predicted for the tilt. Fluid pressure in well 29 increased with time during injection and reached a maximum value of 3×10^5 Pa (3 bars).

4. The axisymmetric model was adjusted to match the injection pressure and the maximum horizontal strain, ε_{NS}. The model is able to simulate the transient pressure and ε_{NS} strain reasonably well (Figure 5.6). It overestimates the EW and vertical strain (Figure 5.6). The horizontal shear stress is zero in the axisymmetric model, so this component cannot be evaluated with the axisymmetric model.

5. When the axisymmetric model is used, the observed vertical strain, ε_{zz}, and ε_{EW} (radial strain) are approximately one half of the simulated strains. More specifically, ε_{zz} observed is 0.6 of the simulated and ε_{EW} is approximately 0.45 of the simulations (Figure 5.6).

6. The magnitude of the strain is controlled primarily by the magnitude of the pressure change in the formation and the elastic modulus of the permeable lens. The magnitude of the strain appears to be roughly proportional to p/E. This is consistent with scaling using the transformational strain.

7. Observations of pressure change in monitoring well 29 early in the test indicates that the hydraulic diffusivity is approximately 1 m^2/s. This is consistent with expectations based on the experience of the wellfield operator, Grand Resources.

8. The shape of the pressure with time plot differs from what is expected from a reservoir of infinite extent– the pressure during injection would decrease more rapidly in an infinite reservoir than indicated by the data. The pressure is consistent with a reservoir bounded by a lateral decrease in permeability (or hydraulic diffusivity). As a result, the pressure record is sensitive to both the hydraulic diffusivity and the distance and characteristics of the boundary. This implies that the strain record will also be affected by the hydraulic diffusivity and the geometry of the permeable lens.

9. The 3D model is able to simulate the correct magnitudes of the normal strains and the horizontal shear strain (Figure 5.7). The primary difference between the 2D and 3D models is the lack of symmetry of the permeable lens in the 3D model.

10. Parameters determined using the 3D numerical model are summarized in Table 5.2.

11. The relative magnitude of the horizontal normal strains cannot be explained by a reservoir that is symmetric around the well, but it can be explained by the presence of a boundary of the permeable lens that occurs between the injection well and the downward projection of AVN2 (Figure 5.7). The presence of a boundary in the underlying reservoir between the injection well and the monitoring location reduces the magnitudes of the EW relative to the NS strain.

12. The relative magnitude of the vertical strain can be explained by increasing the elastic modulus of the material containing the strainmeter. The strainmeter is completed in limestone, which is stiffer than the enveloping shale, so this result is consistent with the geology. Calibration using barometric loading suggests that E of the limestone layer is 42 GPa. This is larger than expected, but it also gives results for the vertical strain that are consistent with observations (Figure 5.7).

13. Increasing E of the permeable lens causes the shallow strain magnitude to decrease (Figure 5.8). Doubling E of the permeable lens (making the lens stiffer) reduces the shallow strain by a factor of 0.5 to 0.7, whereas reducing E (softening) of the lens increases the strain by a factor of 1.5 to 2 (Figure 5.8).

14. Increasing E (stiffening) of the confining unit causes the shallow strain magnitude to increase (Figure 5.9). This is the inverse of the response to a change in E of the permeable lens . The effect of changing E of the confining unit is smaller than a similar change in E of the lens (compare Figure 5.8 to 5.9). Increasing E of the confining unit tends to increase the difference between ε_{NS} and ε_{EW}. However, this effect is modest and unable to explain the observed differences between these components of strain.

15. Reducing the distance to the closest boundary of the reservoir reduces the strain and increases the pressure at the observation well, but these changes are small compared to the effect of increasing the distance to the boundary (Figure 5.10). Increasing the distance to the boundary to beyond the distance to AVN increases the strain and reduces the pressure. Increasing the distance to the boundary increases the magnitude of the EW strain relative to the NS strain to greater than the observations.

Table 5.2: Summary of parameters estimated by manually fitting 3D poroelastic model to data from October 2017 injection test, and from calibration using barometric pressure.

			3D Manual	Baro
Youngs Modulus	Lens	E (GPa)	2	
	Bartlesville	E (GPa)	8	
	Confining	E (GPa)	2.9	
	Instrument	E (GPa)		42
Poisson's ratio		ν	0.26	
Permeability	Lens	k (mD)	500	
	Bartlesville	k (mD)	5	
	Confining	k (mD)	0.01	
	Lens Thickness	m	5	
Fluid Compressibility	Bartlesville	B (1/GPa)	11.0	
	Lens	B (1/GPa)	3.5	
Hydraulic Diffusivity	Lens	$D_h(m^2/s)$	0.6*	
	Bartlesville	$D_h(m^2/s)$	0.004*	
Distance to boundary	1	m	80	
Distance to boundary	2	m	150	
Distance to boundary	3	m	500	

* derived from other data

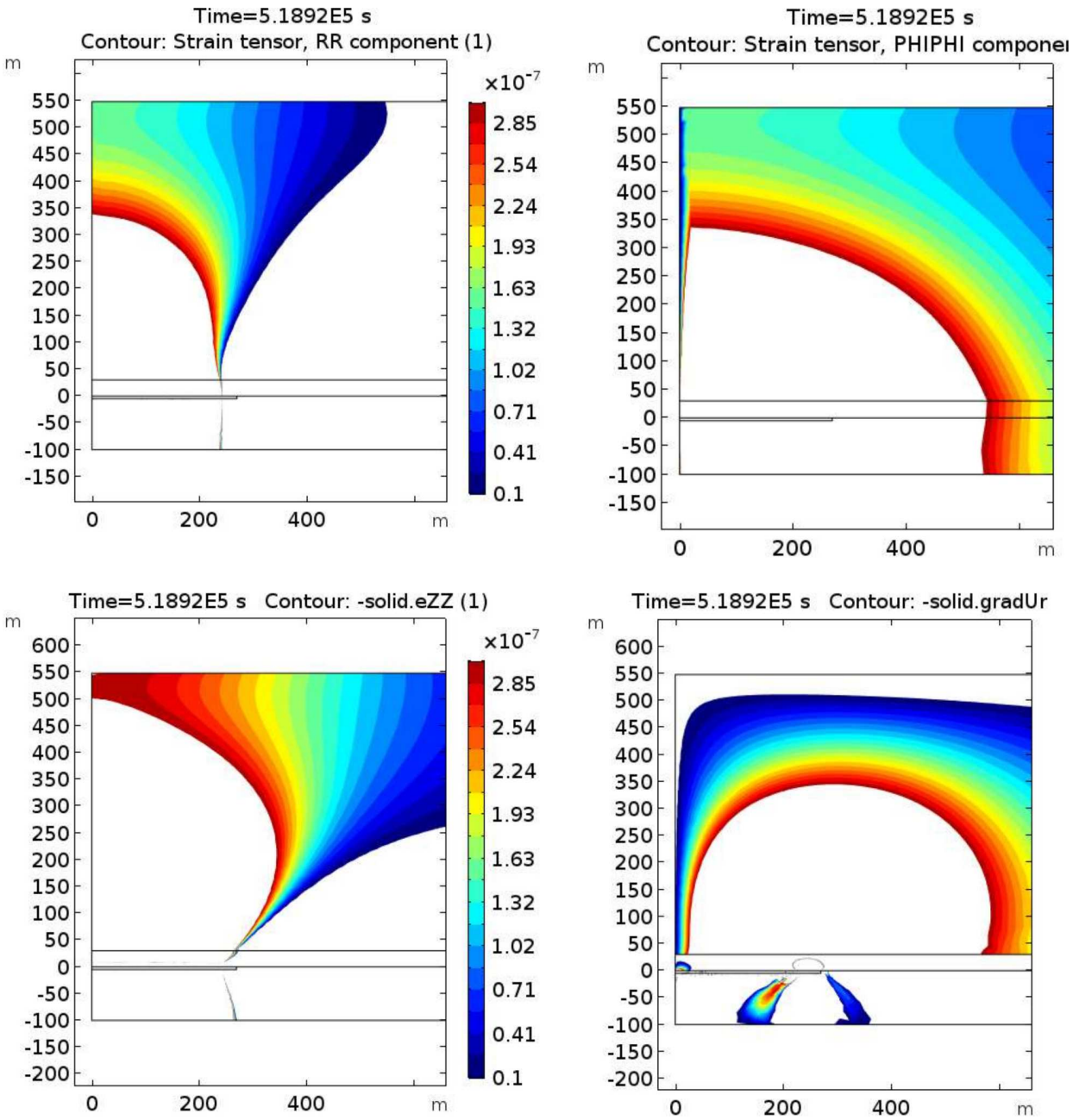

Figure 5.4: Strain distributions at the end of injection. Axisymmetric model calibrated to match the transient NS strain (component "PHIPHI"). Component "RR" is the EW strain, "eZZ" is the vertical strain, "gradUr" is tilt. Same scale used in all the plots.

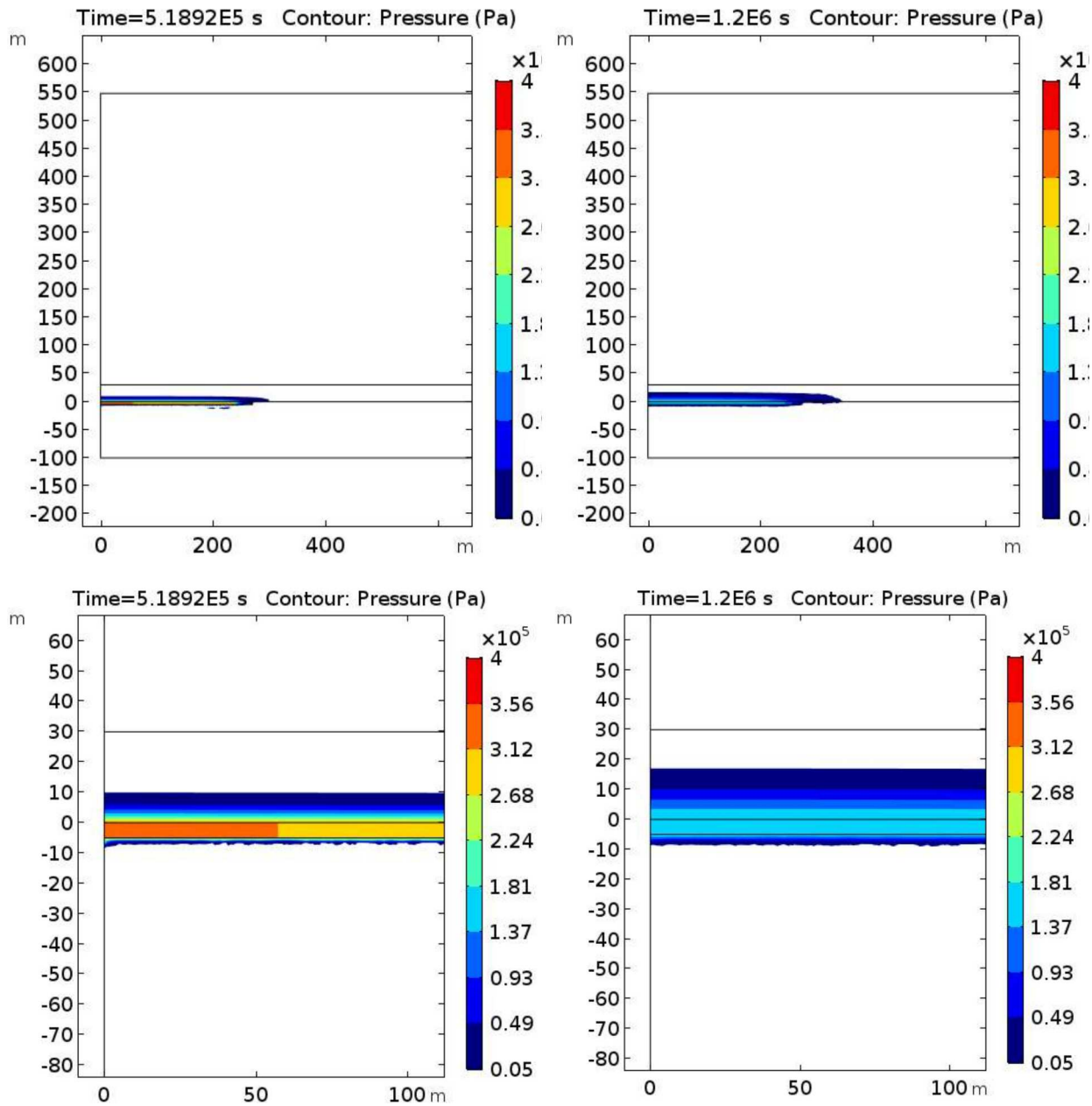

Figure 5.5: Pressure distribution at the end of injection (left side) and at the end of the simulated recovery period (right side). Geometry that includes full depth in upper row, enlarged area in lower row.

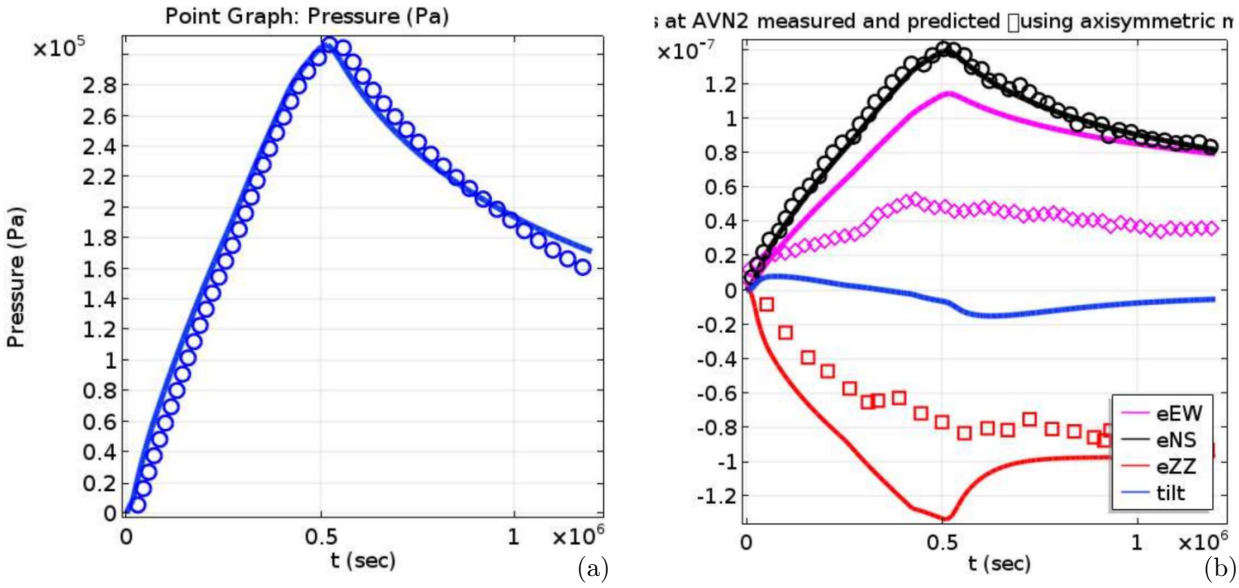

Figure 5.6: Pressure at well 29 and strain at AVN2 measured during October 2018 test. Simulation results from axisymmetric model shows as lines.

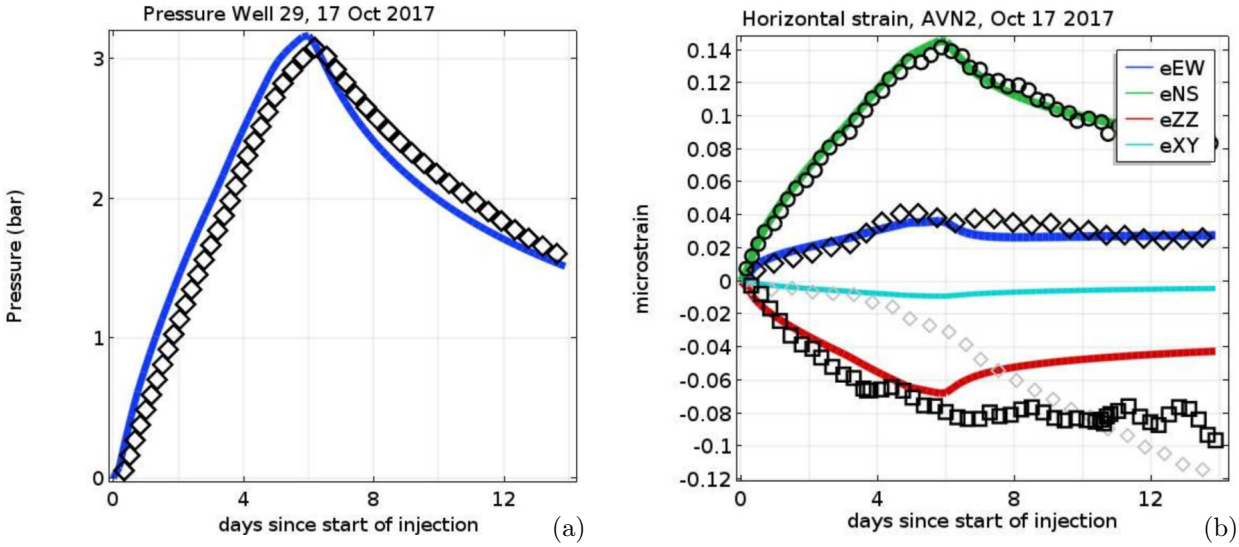

Figure 5.7: Pressure at well 29 and strain at AVN2 as functions of time (points), and results from 3D simulation (lines).

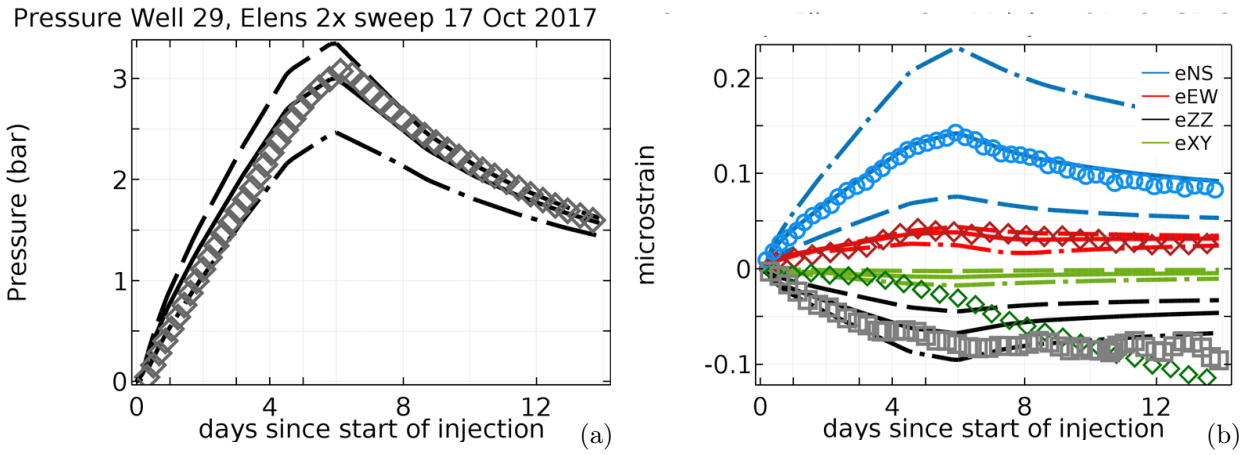

Figure 5.8: Simulated pressure (a) and strain (b) for different values of Young's Modulus of the permeable lens: Solid line: $E_{lens} = 2$ GPa, Dashed line: $E_{lens} = 4$ GPa; dash-dot line: $E_{lens} = 1$ GPa

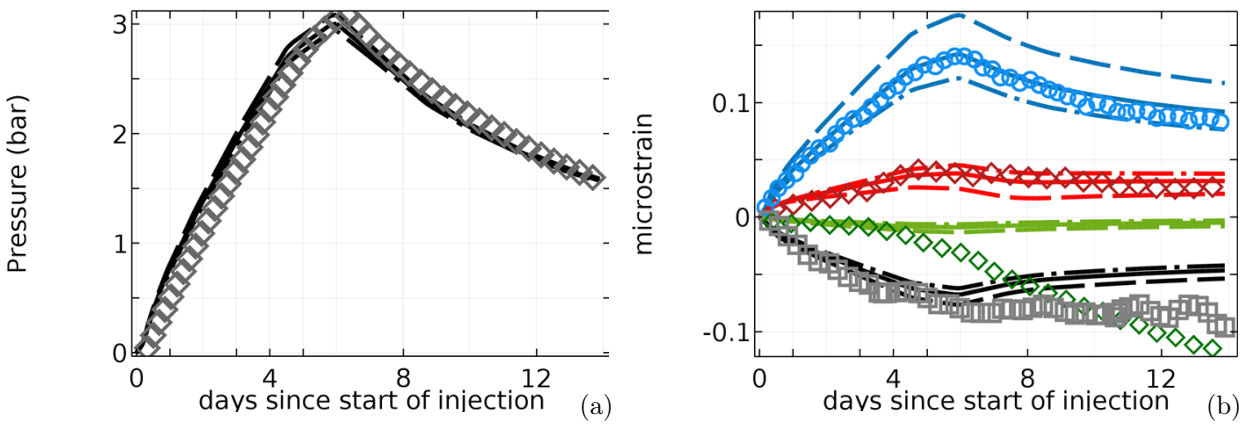

Figure 5.9: Simulated pressure (a) and strain (b) for different values of Young's Modulus of the confining unit: Solid, $E_{confining} = 2.9$ GPa, Dashed $E_{confining} = 5.8$ GPa; dash-dot line $E_{confining} = 1.95$ GPa

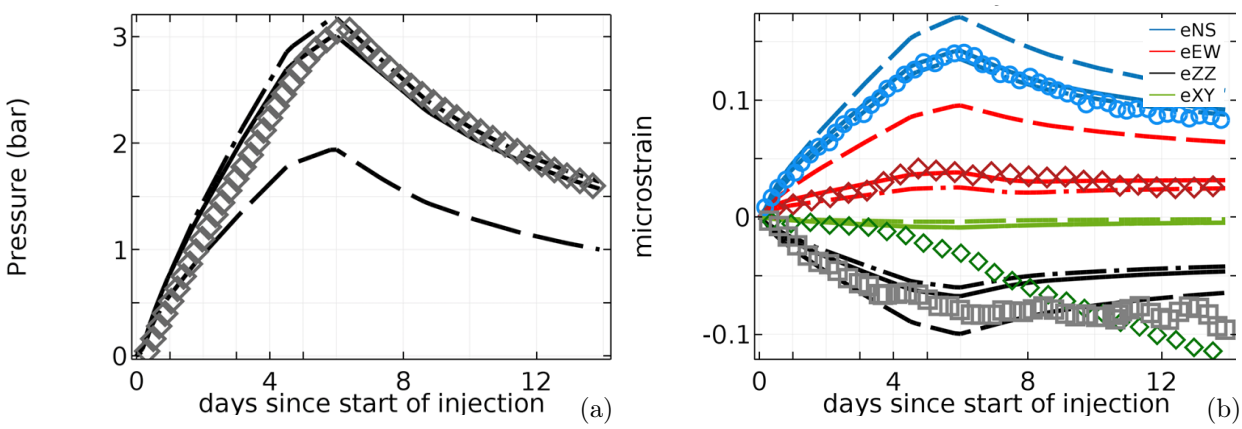

Figure 5.10: Simulated pressure (a) and strain (b) for different values distances to the closest boundary of the lens. Solid line: $L_{boundary} = 80$ m, Dashed line: $L_{boundary} = 500$ m; dash-dot line $L_{boundary} = 40$ m.

5.3 Inversion of Analytical Solution to Poroelastic Inclusion

5.3.1 Introduction

To simulate injection tests at the North Avant Field, we employ the conceptual model shown in Figure 5.11. The reservoir is represented by a uniformly pressurized region, which is modeled by a thin, horizontal, cuboidal inhomogeneity (Figure 5.11a)

$$V = \{-a \leq x \leq a,\ b \leq y \leq b,\ h - c \leq z \leq h + c\} \tag{5.1}$$

where (x, y, z) are the local coordinates employed in equations (3.12)–(3.21) to describe the deformation process. The origin of coordinate set (x, y, z) is at the center of symmetry of the reservoir projection to the ground surface, which is depicted by the light brown rectangle in Figure 5.11. The coordinate set (x', y', z'), also shown in Figure 5.11, is *global* with x' and y' axes pointing geographic North and East, respectively, and with the origin at the wellhead of the injection well 9A. Pressure measurements were generally taken in wells 27, 29, and 60. The strain-tilt measurements were taken in the closely located wells. At the scale of the drawing in Figure 5.13, these wells are shown as one location, AVN.

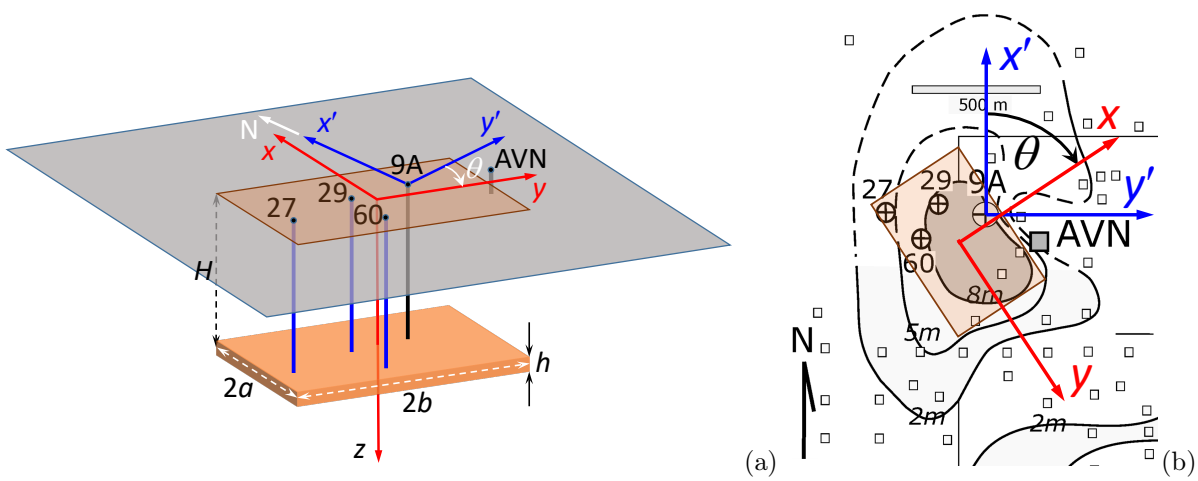

Figure 5.11: (a) The reservoir model and (b) the field test area at the North Avant Field. Coordinate system (x', y', z') is centered at the injection well 9A with x' and y' pointing North and East, respectively. Reservoir pressure during the injection was measured in wells 27, 29, and 60. Strain and tilt measurements were conducted in the shallow, closely located wells shown as one well, AVN. Light brown rectangular is the reservoir projection onto the ground surface. Equations (3.4)–(3.13) describe deformation in the coordinate system (x', y', z') with the center of symmetry of the rectangular.

The local coordinates are employed in equations (3.12)–(3.21) to describe the deformation process while the measured data are reported in global coordinates. The two coordinate sets are related by

$$\begin{cases} x = x' \cos\theta - y' \sin\theta + x_0 \\ y = y' \cos\theta + x' \sin\theta + y_0, \\ z = z' \end{cases} \quad \begin{cases} x' = x \cos\theta + y \sin\theta + x'_0 \\ y' = y \cos\theta - x \sin\theta + y'_0 \\ z' = z \end{cases} \tag{5.2}$$

where x_0, y_0 are the local coordinates of well 9A. In the (x', y', z'), the origin of the (x, y, z) set has coordinates $(x'_0, y'_0, 0)$. Global coordinates of wells shown in Figure 5.11 are given in Table 5.3.

The inverse analysis determines x'_0 and y'_0 along with the reservoir orientation, θ, and dimensions, $2a$, $2b$, and h (Figure 5.11a). The analysis also aims at determining the mechanical properties of the reservoir and confining unit. As detailed in Section 3.1.4, however, there are only two material parameters available to the first order analysis adopted in Chapter 3. That is, the Poison's ratio, ν, of the confining unit and the combination, C_1, of reservoir properties, E_1, ν_1, and α_1 (equation (3.21)). The reservoir Biot-Willis coefficient is assumed to be $\alpha_1 \approx 1$, which is a relatively well constrained value. The reservoir Poisson's ratio is assumed to be $\nu_1 \approx 0.25$, as a representative value. Then, the only remaining property is the reservoir Young's modulus, E_1, which is also determined using the inverse analysis.

Data from injection tests at the North Avant Field in October and November of 2017 were analyzed using the inverse analysis.

Table 5.3: Depth and global coordinates of wells shown in in Figure 5.11.

Well	y' (m)	x' (m)	Depth (m)
9A	0	0	532
AVN	210	-65	30
27	-370	-27	-532
29	-190	18	-532
60	-238	-127	-532

5.3.2 October and November 2017 injections

Measurements are described in detail in Chapter Four and summarized in Figure 5.12 for the injection test that took place in October 2017. Figure 5.12a shows the pressure response in wells 27 (red line), 29 (blue line), and 60 (green line) to the injection into well 9A. As a reference, the injection rate is also shown in Figure 5.12a (orange line), but it is not included in the forward model (equations (3.12)–(3.21)). The rate does affect the reservoir pressures in the current model, although the pressures will be computed based on the pressure diffusion equation in the future. Here we used instead the pressure obtained from the measurements in wells 27, 29, and 60. As stated in Section 3.1, we assumed that at each instance, the reservoir pressure change is uniform, but changes with time as shown in Figure 5.12a.

Using the least-squares method and the Levenberg-Marquardt algorithm (e.g., Aster et al. (2018)), we fitted the strain data shown in Figure 5.12b (dotted lines) to the strains computed based on equations (3.12)–(3.21) (solid lines). The best fits were obtained with the pressure dependence on time measured in well 60 (green line in Figure 5.12a). Fits shown in Figure 5.12b correspond to this pressure. Parameters estimated as a result of the inverse analysis are given in Table 5.4.

Figure 5.13a shows the relative locations of wells 9A, 27, 29, 60, and AVN (dots) and the reservoir boundary (thick line) estimated by inversion from the October 2017 data. The reservoir depth at the North Avant Field is known ($H = 533$ m) and did not change in the computations. The host rock Young's modulus is not reported in Table 5.4 as it does not affect the results in the first order (i.e., when the reservoir is thin).

Similar results were obtained for the November 2017 injection (Figure 5.14 and Table 5.4). The corresponding plots are shown in Figure 5.14 and the inverse analysis results are given in Table 5.4. For the sake of comparison, pressure dependence on time and injection rate in November 2017 are shown in Figure 5.14a together with those in October 2017.

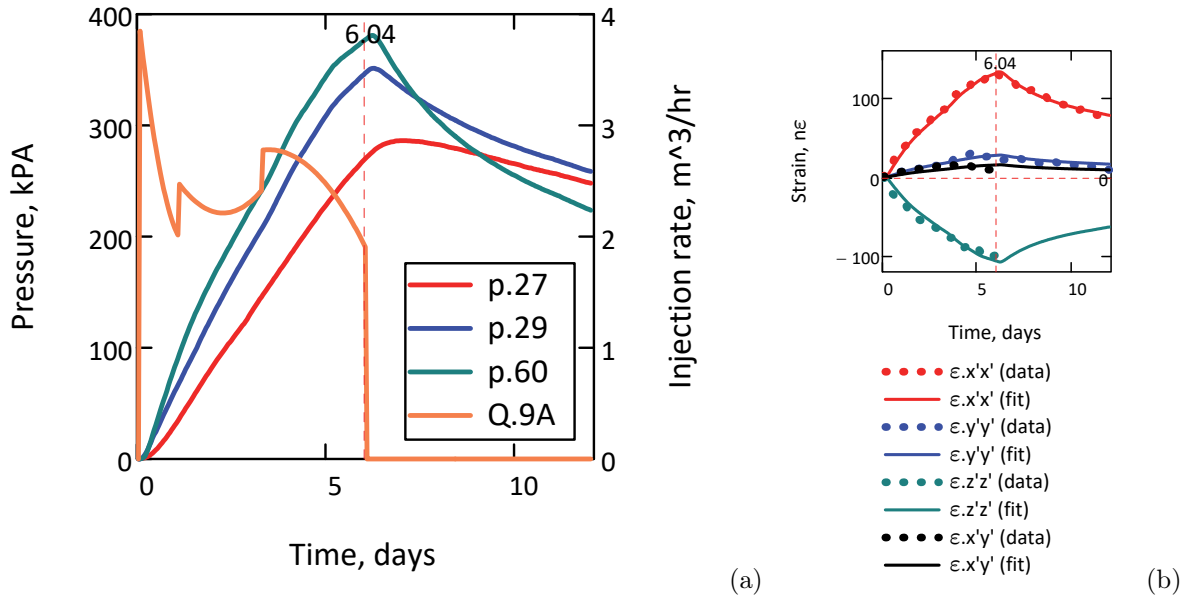

Figure 5.12: Data and the best fit of the theoretical model for October 2017 injection. (a) Reservoir pressure change (left axis) measured in wells 27, 29, and 60. The injection rate, measured in well 9A, is shown on the right axis. (b) Strain data obtained during the North Avant Field injection test in October 2017 (doted lines) and the best fit of the theoretical model (solid lines).

Table 5.4: Parameters providing the best fit of the theoretical model to the October 2017 and November 2017 injection data. The corresponding figure numbers are indicated in parentheses. The row order follows the order of appearance in the main text, where all the details are given. Parameter $d = \max(a, b)$, so c/d is the largest of two aspect ratios, c/a and c/b.

Injection	$2a$ (m)	$2b$ (m)	h (m)	c/d	h/H	E_1 (GPa)	ν_2	x_0' (m)	y_0' (m)	x_0 (m)	y_0 (m)	θ (°)
Oct 2017 (Figure 5.12b)	601.8	556.5	8.6	0.015	0.016	3.04	0.40	-4.8	-210.3	117.1	174.8	-32.5
Oct 2017 (Figure 5.14b)	472.4	481.4	8.4	0.018	0.016	2.99	0.23	-52.2	-187.6	122.1	151.7	-23.3
Oct 2017 (Figure 5.15a)	660.5	510.8	12.5	0.025	0.024	4.26	0.40	-16.0	-189.3	-44.7	184.7	18.4
Nov 2017 (Figure 5.15b)	582.7	565.8	9.2	0.016	0.017	3.96	0.28	-54.6	-168.8	105.5	-154.3	-17.4
Nov 2017 (Figure 5.16)	752.2	563.1	40.1	0.071	0.075	14.9	0.40	-2.2	-225.6	78.2	211.6	-19.7

5.3.3 Discussion

The agreement between predicted and observed in Figure 5.12b and Figure 5.14b is rather remarkable in view of the simplified assumptions used to formulate the model. As the injection rates were similar in October and November 2017, the main difference between these injections is their durations. The injection phase in November was approximately half the duration of that in October, which is consistent with the pressure response being higher in October than in November. The rates of pressure increase were similar in

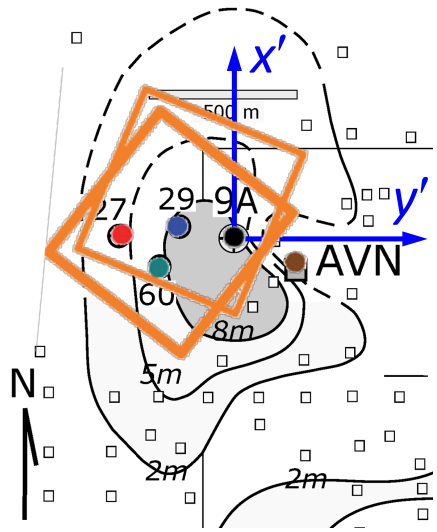

Figure 5.13: Boundaries of the permeable inhomogeneity determined by inverse analysis for October (bold orange line) and November (thin orange line), which provide the best data fits (Table 5.4, first and fourth rows, respectively). Borehole locations are shown by dots in the horizontal cross-section $z = h$. The dot colors correspond to the colors in Figure 5.12a and Figure 5.14a. The reservoir boundaries determined in the inverse analysis (Table 5.4) are overlaped with the test area at the North Avant Field (Figure 5.11b).

both injections, which indicates that the reservoir had enough time to return to the baseline between the injections. As follows from Table 5.4, $c/a \approx h/H \approx 0.015$. Hence, the main model assumption of reservoir being thin ($c/a \ll 1$) and deep ($h/H \ll 1$) is consistent with the results of the inverse analysis.

Most results from the inverse analyses are consistent with each other, and with independent estimates. For example, the Young's Modulus estimated for the reservoir rock ranges over $E_1 \simeq 3$ to 4 GPa. This is less than values of E_1 reported for sandstone, which is typically in the range of $10 < E_1 < 40$ GPa, but it is more typical of the value of E_1 for poorly lithified sand or mudstone (e.g., Murdoch et al. (2015), Table 2.4-1). Most of the published values of E_1 estimated for rocks are from measurements made on samples in the laboratory, whereas the values determined here are in-situ, and it seems possible the measurement scale could account for differences in E_1.

The analysis indicates that the horizontal dimension of the horizontal lens is approximately 450 to 650 m and it thickness is $\simeq$8 to 13 m. Lateral boundaries of the permeable lens have been estimated from core data and they are consistent with the range estimated from the inversion (Figure 5.13).

Inversions results from the two tests both indicate a boundary of the permeable lens that occurs between the injection well and the AVN strainmeters (Figure 5.13). The relative magnitude of the two horizontal normal strains is sensitive to the location of this boundary. A poor fit to either $\varepsilon_{x'x'}$ or $\varepsilon_{y'y'}$ occurs if there is no boundary between well 9A and AVN.

The value of the drained Poisson's ratio, $\nu_2 = 0.40$ of the confining unit determined from the October 2017 is fairly high. Such a value of the Poisson's ratio is possible though. For example, $\nu_2 \approx 0.42$ was measured by the static loading of specimens of cryptocrystalline amygdaloidal basalt citepxu2015. For rocks similar to the North Avant Field (claystone, shale, and sandstone) a value of $\nu_2 \approx 0.40$ was reported by citetgercek2007 and citetsayers2013, but it corresponds to the higher end of the Poisson's ratio for such rocks. A value of the Poisson's ratio of this magnitude could also be explained if the deformation of the confining unit was not completely drained at the injection test timescale. This mechanism appears to be plausible as the confining unit is mostly composed of porous, but tight, rocks such as shales. Nevertheless, at the moment, it is difficult to conclude on the final value of ν, because another best fit (Table 5.4, November 2017 injection), resulted in a more characteristic value (e.g., Gercek (2007); Sayers (2013)) of $\nu_2 = 0.28$.

Our results indicate the value of Poisson's ratio of the host rock may be sensitive to the strain data used in the inversion. Let us, for example, use only the horizontal strains in the inverse analysis. The obtained

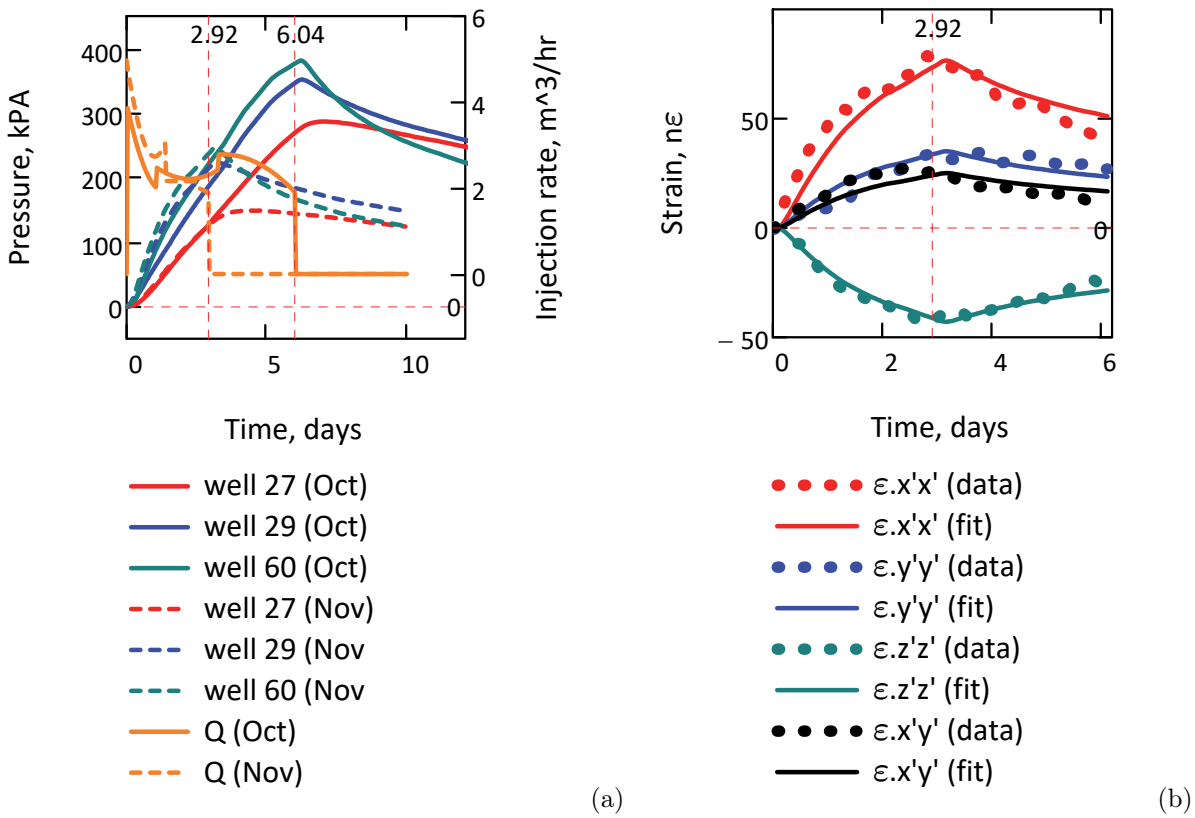

(a) (b)

Figure 5.14: Data and the best fit of the theoretical model for November 2017 injection. (a) Reservoir pressure change (left axis) measured in wells 27, 29, and 60. The injection rate, measured in well 9A, is shown on the right axis. For the sake of comparison, pressures registered in the same wells during the October 2017 injection are shown by dashed lines. (b) Strain data obtained during the North Avant Field injection in October 2017 (doted lines) and the best fit of the theoretical model (solid lines).

best fit is still good (Figure 5.15a) and most of the estimated parameters (second row in Table 5.4) are reasonably close to the previous results (first row in Table 5.4), but now we arrive at a considerably different Poisson's ration of the confining unit, $\nu_2 = 0.23$. The latter is much closer to the value of $\nu_2 = 0.28$ inferred from the November 2017 test (third row in Table 5.4). Yet employing three strain components (Figure 5.15b) yields again $\nu_2 = 0.4$.

The analysis used the pressure in the monitoring well as the pressure in the reservoir, but which of the three monitoring wells was used to determine the pressure had little effect on the results. This is demonstrated in Figure 5.15b (and third row in Table 5.4), which shows the best fit using the mean of pressures measured in wells 27, 29, and 60 (Figure 5.12a).

The analyses indicate consistent results for the geometry and location of the permeable lens, and for the Young's Modulus of the lens. Values of Poisson's ratio are more variable, although they remain within a plausible range. Future analyses will be used to further constrain the uncertainty in the estimated parameters.

Finally, it should be noted that based on the core data, the reservoir thickness in the inverse analysis was restricted to 15 m, which represents a lower, more permeable, part of the Bartlesville formation. If this constrain is removed, the inverse analysis shows another local minimum. The corresponding fit is still excellent (Figure 5.16a). While the horizontal extend of the permeable region has not changed considerably

(Figure 5.16a and fifth row in Table 5.4), the reservoir thickness is now 40 m. This is expected as the estimated Young's modulus of the reservoir rock is now $E_1 = 14.9$ GPa, which is within the range of petroleum sandstones (e.g., Sayers (2013) and Murdoch et al. (2015)). Thus, essentially, the increase in E_1 from 3 GPa to nearly 15 GPa is compensated by the thickness increase from 8.6 to 40 m (and by some increase of the lateral dimensions; Table 5.4). It seems possible to better constrain E_1 once more boreholes become available for measurements in the future.

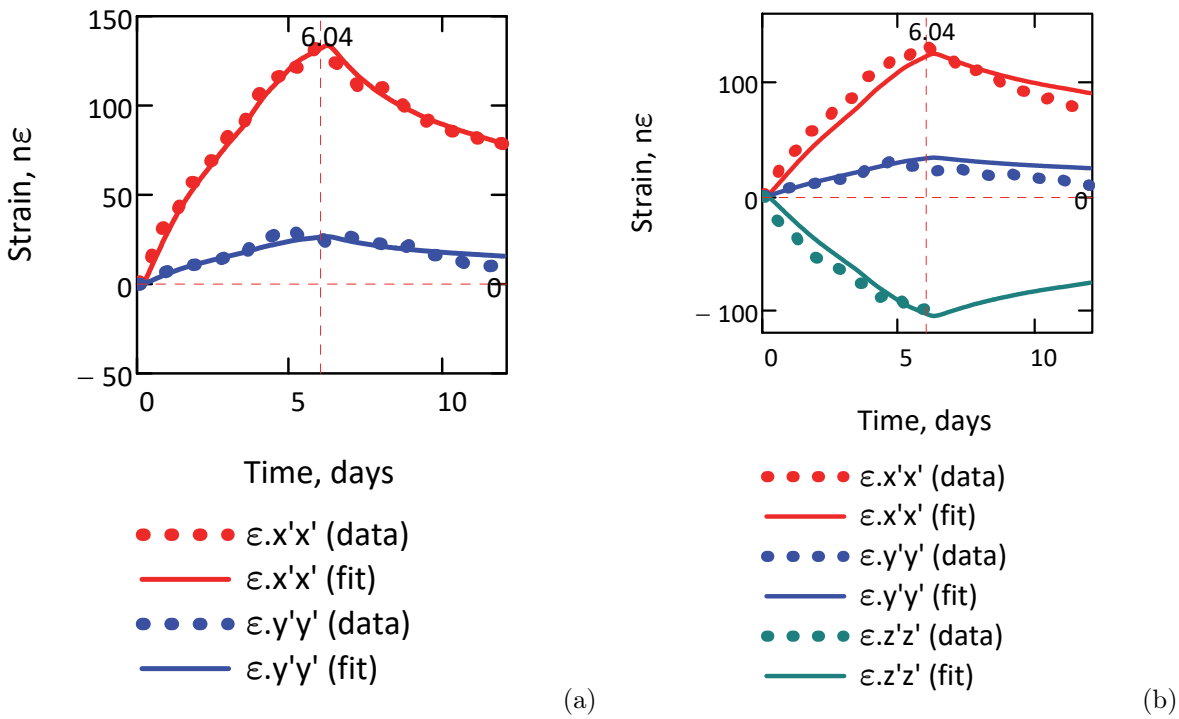

Figure 5.15: The best fits of the theoretical model to the strain data for October 2017 injection. The inverse analysis was conducted (a) based on two strain components and pressure measured in well 60 (green line in Figure 5.12a and second raw in Table 5.4) and (b) based on three strain components and the mean of pressures measured in wells 27, 29, and 60 (Figure 5.12a and third row in Table 5.4).

5.4 Stochastic Inversion with 3D Poroelastic Model

Stochastic inversion was conducted by applying the methods described in Section 3.2.4 to field data measured at the North Avant Field. The analysis includes inversion of data from the well 1A Shut-in and the October 2017 injection test at well 9A, and an evaluation of results using data from the November 2017 and July 2018 tests.

5.4.1 Inversion Methodology

In this section a numerical forward model is developed to approximate the hydromechanical behavior of the field site, and an inverse problem is defined in order to calibrate this hydromechanical model to measured strain and pressure datasets, and to infer the structure and material properties of the subsurface. The general inversion approach used is described in more detail in Section 3.2.

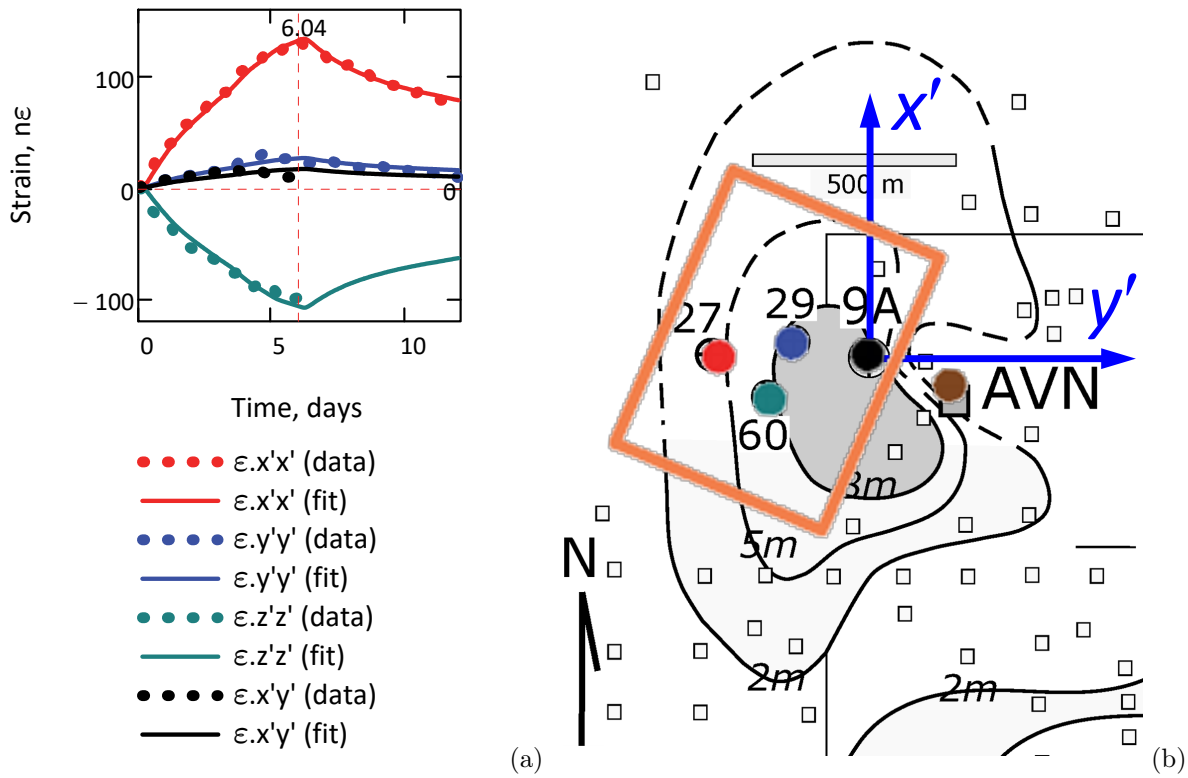

Figure 5.16: (a) The fits of the theoretical model to the strain data for October 2017 injection based on a different local minimum compared to Figure 5.12b. The inverse analysis was conducted (a) based on all four strain components and pressure measured in well 60 (green line in Figure 5.12a). (b) Boundaries of the permeable inhomogeneity determined by inverse analysis for the October 2017 injection (orange line). Borehole locations are shown by dots in the horizontal cross-section $z = h$. The dot colors correspond to the colors in (a). The reservoir boundaries determined in the inverse analysis (Table 5.4) are overlapped with the test area at the North Avant Field (Figure 5.11b).

5.4.1.1 Forward Model

The forward model is a poroelastic finite element partial differential equation solver called Geocentric (White and Borja (2008, 2011)), which simulates fluid flow and rock deformation. For this analysis, we assumed four horizontal layers (Figures 5.17 and 5.19), an upper (500 m thick) and lower (100 m thick) confining unit, a permeable confined unit representing the Bartlesville sandstone (27 m thick), and a discontinuous layer underlying the Bartlesville formation to represent the high-permeability lenses (5 m thick). The model space is 16 km by 16 km, where the outer region is coarsely meshed and a smaller interior region (4 km by 4 km) that is much more finely meshed (Figure 5.18). The side boundaries are defined by fixed pressure and a mechanical roller, meaning that the displacement normal to the boundary is zero. The lower boundary is zero flux, and a mechanical roller. The upper boundary is no flow and zero total stress.

Well geometries are defined explicitly as a cylindrical shell with a smaller, concentric cylinder inside. T he outer shell represents the casing and has a bulk modulus and permeability approximating that of steel ($E = 200$ GPa, $\kappa = 10 \times 10^{-99}$ m^2), while the inner core represents the inner diameter of the well and has as low a bulk modulus and high a permeability as is computationally possible ($K = 3$ GPa, $\kappa = 1 \times 10^{-8}$ m^2). The well casing is screened within the permeable lens, and has a permeability of $\kappa = 1 \times 10^{-8}$ m^2. A

flux is specified along the top surface of the inner cylinder, corresponding to the measured volumetric flow injected into each well.

The computational mesh consists of free quadrilateral elements over a region approximately 4 km across embedded in a larger domain of rectangular elements (Figure 5.18). The free quad elements wrap around the wells. The mesh is swept vertically to create prismatic elements in 3D.

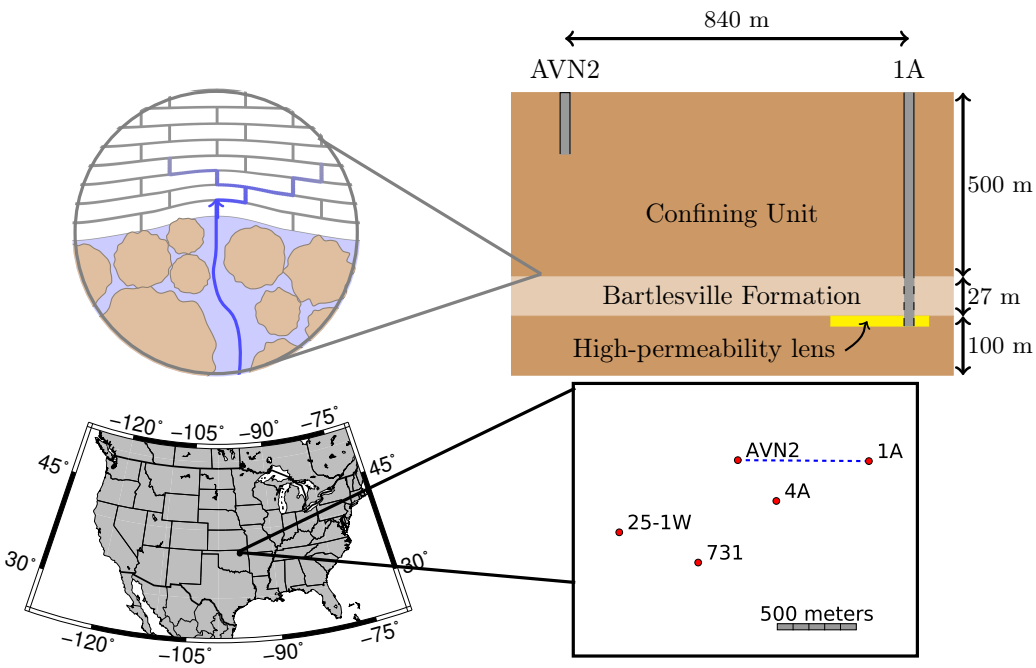

Figure 5.17: Location and conceptual model of the field site for 1A Shut-in test. Cross-section on top shows stratigraphy with contrasts in permeability (circle) and locations of well 1A and Gladwin strainmeter at AVN2. Location map of field site with wells included in the model.

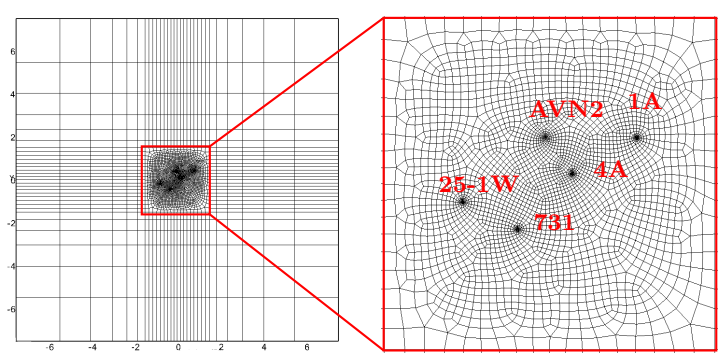

Figure 5.18: Computational mesh in plan view for entire model (left) and finely meshed region around well (inset).

The shut-in test at well 1A test involved four separate injection wells and one observation well, so the mesh is refined around these five locations (Figure 5.18). Simulating all four injection wells simultaneously was computationally intensive, and therefore we simulated the strain response of each well individually and used superposition to sum the contributions from all four wells. The validity of the superposition was tested

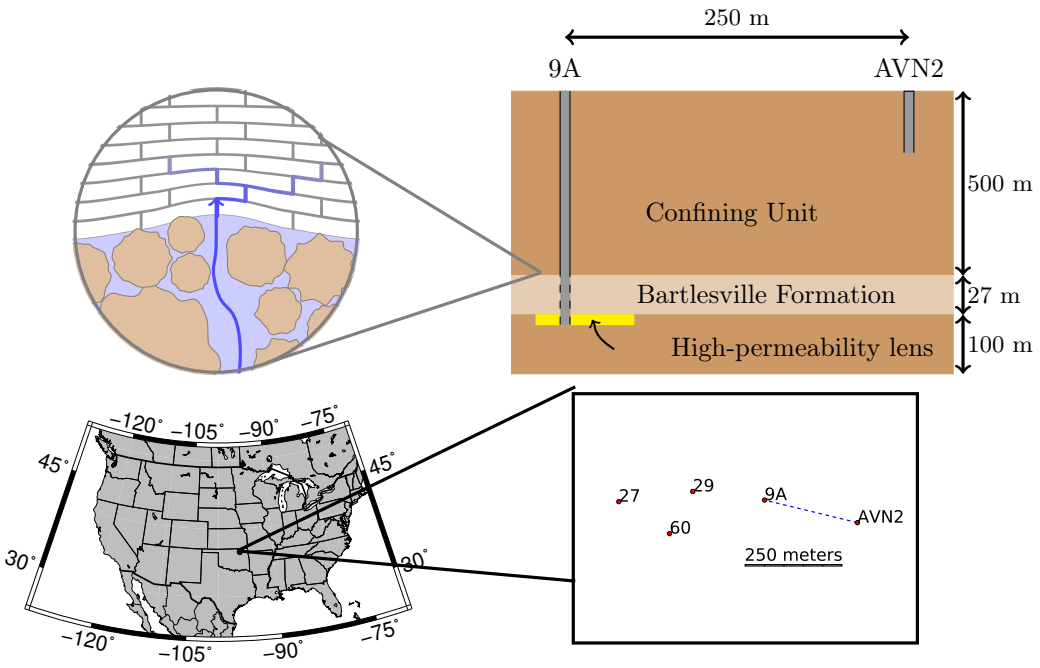

Figure 5.19: Location and conceptual model of the field site for 9A pumping test. Cross-section on top shows stratigraphy with contrasts in permeability (circle) and locations of well 9A and Gladwin strainmeter at AVN2. Location map of field site with wells included in the model.

by simulating two wells jointly using a mesh refined at three points (two injection wells and one observation well). Then those same two wells were simulated separately using a mesh refined at only two points (injection well and observation well). Results from the two separate simulations were superimposed and compared to results from the simulation that included both wells together. The results (Figure 5.20) are nearly identical, but the superposition simulation ran much faster. As a result, the analysis was conducted using superposition of strains from individual wells.

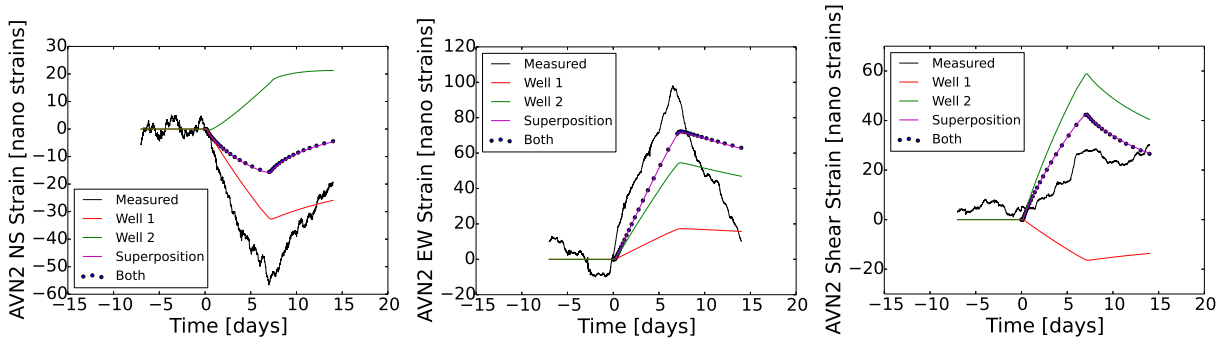

(a) (b) (c)

Figure 5.20: Measured and simulated strains as functions time. Effects of wells 1 and 2 simulated individually (red and green), and their superposition (magenta), along with effects of both wells simulated simultaneously (dotted), and compared to field data (black). (a) NS strain, (b) EW strain and (c) shear strain.

5.4.1.2 Inversion Process

Inversion was conducted by assuming a geometry for the permeable lens and then searching the parameters space for sets of parameters that fit the observed strains and pressures. The search methodology used Latin Hypercube sampling of the overall parameter spaced followed by a more localized search using NSGA-II, a genetic algorithm. The geometry of the permeable lens was initially assumed to be circular. In the inversions involving the well 9A injection tests, we also used lens geometries that were elliptical and irregular. Details of the methodology are given in Section 3.2.

The geology of the field site includes heterogeneities and preferential flow pathways at a fine scale, which would require a large number of free parameters resulting in a computationally intractable data-fitting problem. We therefore made a set of simplifying assumptions in order to reduce the problem to a manageable number of parameters. We assume that the confining unit, lens and Bartlesville formation are internally homogeneous, that their Poisson's ratios and porosities are fixed and known ($\nu = 0.25, \phi = 0.2$), that their grain moduli are that of quartz (K_s = 42.9 GPa), and that the pore fluid was single-phase water (K_f = 2.15 GPa). We assumed a continuous hydromechanical volume, with no faults or fractures to accommodate or localize strain. We also assume that the lens intersects the injection well. This results in a data-fitting problem with nine unknown parameters; the permeability and bulk moduli of the lens, Bartlesville formation and confining units, and the geometry of the lens in terms of its centroid location (x, y) and radius.

5.4.2 Stochastic Inversion of 1A Shut-in

During the 1A shut-in field test, we assumed the lens was circular. The inversion generated a total of 47,907 parameter sets, and 5,490 unique parameter sets defined models that could explain all three strain data sets (Figure 5.23) within an assumed measurement uncertainty of EW strain, $\varepsilon_{EW} \pm 25$ nε, NS strain, $\varepsilon_{EW} \pm 15$ nε, shear strain, $\varepsilon_{xy} \pm 10$ nε. Pressure data were unavailable for this test. Tilt data was available, but was neglected from this analysis because data from the LILY and Eddy current tiltmeters were difficult to reconcile with one another (see Section 4.3.1.2.1).

The overall data fit of each simulation is calculated as the sum (equation (5.3)) of the misfits for each of the strain time series weighted by the magnitude of the data noise (σ_n) as

$$WS = \sum_{i=1}^{6} \frac{\sum \left(d_i - f_i(m)\right)^2}{\sigma_{n,i}} \tag{5.3}$$

The data noise is estimated by fitting a high-order polynomial to the time series data (Figure 5.21), and taking the sum of squared errors between the noisy data and the smooth polynomial. The weighted error of each simulation is plotted as a function of two parameters, cycling through the 36 possible pairs of 9 parameters to characterize the error structure of the 9-dimensional parameter space being explored (Figure 5.24).

The distribution of simulations with small error is multi-modal, with a band of low error occurring in the range of $k = 10^{-14}$ to 10^{-13} for all values of the lens permeability. (blue dots on right side of Figure 5.24). Another region of low error (blue dots) occurs where the confining unit permeability is in the range of $10^{-17} < k < 3 \times 10^{-16}$, and the permeability of the lens is relatively high ($3 \times 10^{-13} < k < 10^{-12}$). This distribution indicates that a reasonable data fit can occur for a relatively impermeable confining only if the lens itself is permeable, but if the confining unit is permeable then the fit is insensitive to the lens permeability.

The inversion identified a small set of parameters that fit the NS and EW strains well, as indicated by a Pareto front with an "L" shape (yellow points on the lower left of Figure 5.26a). Similar shapes also occur for the other parameter sets (yellow points in Figures 5.26b and 5.26c) indicating small sets of parameters that fit the data with little tradeoff.

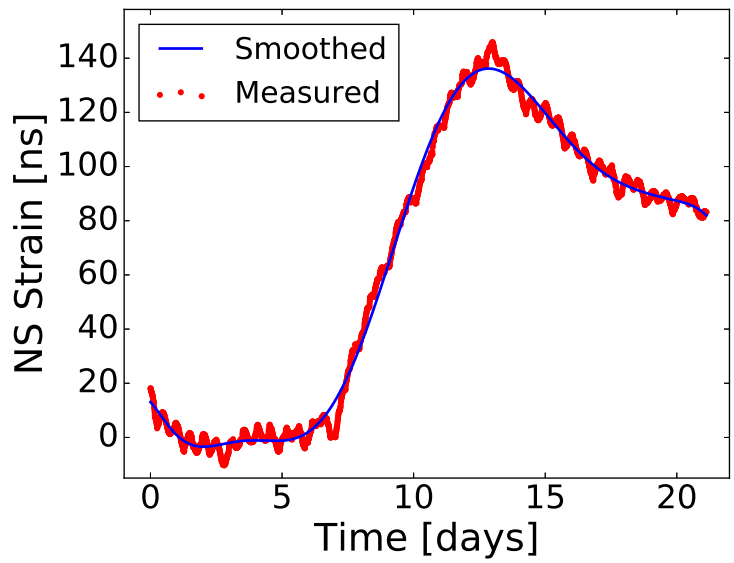

Figure 5.21: Measured NS Strain (red) and high-order polynomial fit (blue) as functions of time.

These results are encouraging, but they include parameter sets with a confining unit permeability that is fairly high (the band on the right side of Figure 5.24). The confining unit is shale and the permeability is expected to be low, so the parameter sets with high confining unit permeability are inconsistent with the expected geologic conditions. As a result, we evaluated the parameter sets when the high permeability confining unit data was omitted. The Pareto front that requires the confining unit to be relatively impermeable is more rounded and sparse than when all the data are included (black dots on Figure 5.26). This indicates more tradeoff and a poorer fit to the data when the confining unit permeability is low.

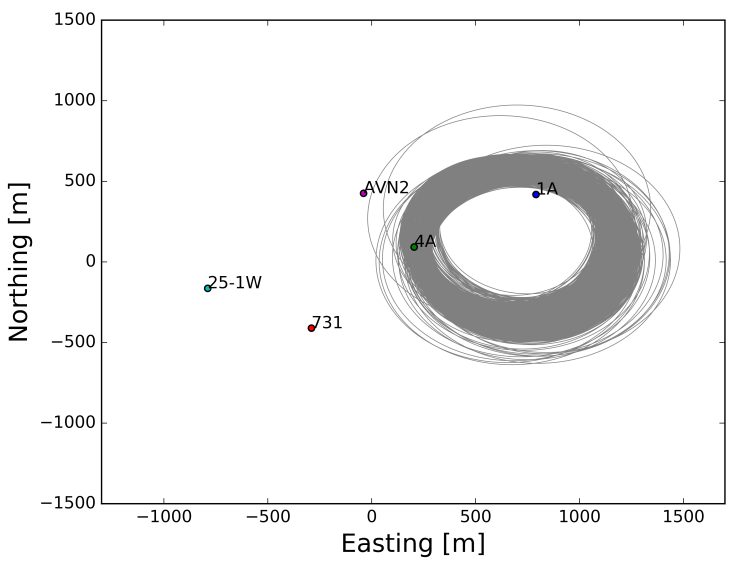

Figure 5.22: Lens geometries of the best-fitting models from 1A Shut-in test. Assuming low permeability confining unit. These lenses correspond to the black lines in Figure 5.23.

One reason for a decrease in the data fit occurs when injection resumes on day 14 (Figure 5.23). The observed strain decreases sharply at this time, but the simulated strain with an impermeable confining unit decreases only slightly. The mismatch that occurs when injection resumes on day 14 appears to be the reason why the models with an impermeable confining unit fit more poorly than the models with a more permeable confining unit.

Assuming that the permeability of the confining unit is low constrains the problem to a single uni-modal set of 661 solutions (Figure 5.25), whose lens geometries and physical properties are shown in Figures 5.22 and 5.27. These results indicate the log permeability in meters squared of the lens is 200 to 1,500 mD, Bartlesville sandstone is 10 to 1,000 mD, and the confining unit is 0.03 to 1 mD. The bulk modulus of the lens is $E = 2$ to 4 GPa, the Bartleseville sand is $E = 12$ to 16 GPa and the confining unit is $E = 20$ to 25 GPa (Figure 5.27).

The extent of the lens intersected by well 1A is 800 to 1,000 m and the centroid is to the southwest of well 1A (Figure 5.22). For comparison, the isopach map of the lens thickness (Figure 4.4) suggests that the lens extends approximately 500 m to the northeast, but the extent to west is limited to less than 100 m.

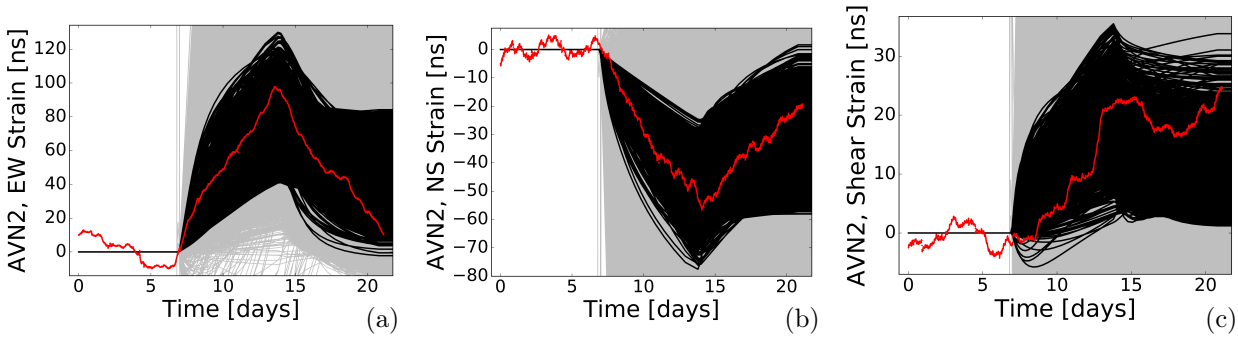

Figure 5.23: Strain as a function of time for 1A Shut-in Test. Measured strain data (red), simulation results (gray). Best-fitting simulation results in black.

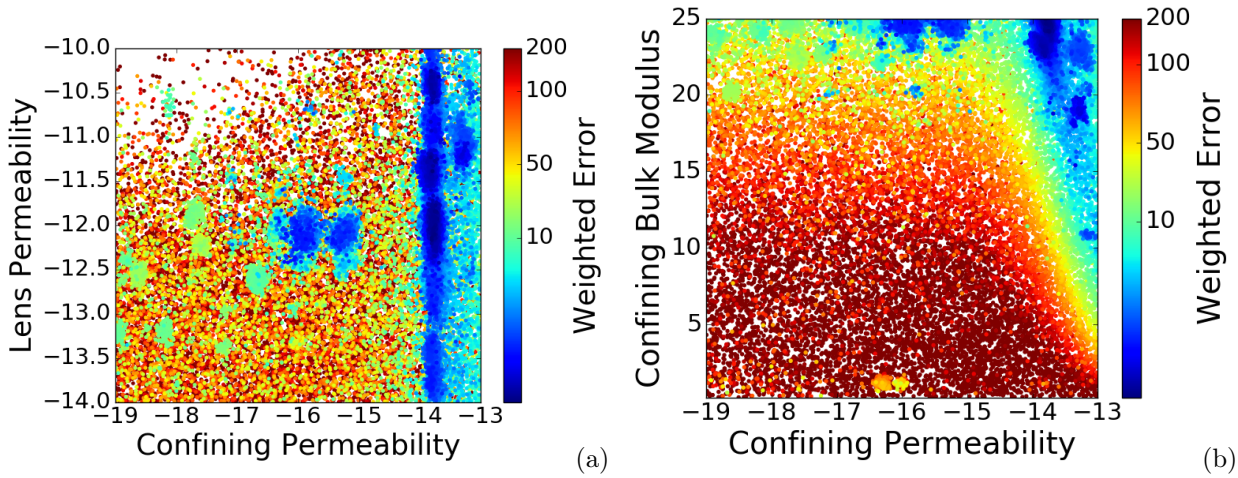

Figure 5.24: The weighted error (equation (5.3)) of each simulation as a function of (a) the confining unit permeability and lens permeability, and (b) the confining unit permeability and confining unit bulk modulus. Blue points correspond to the black lines in Figure 5.23. Note that this plot projects a 9-dimensional parameter space to a 2-dimensional plane, and therefore some of the variation shown is due to the other 7 parameters.

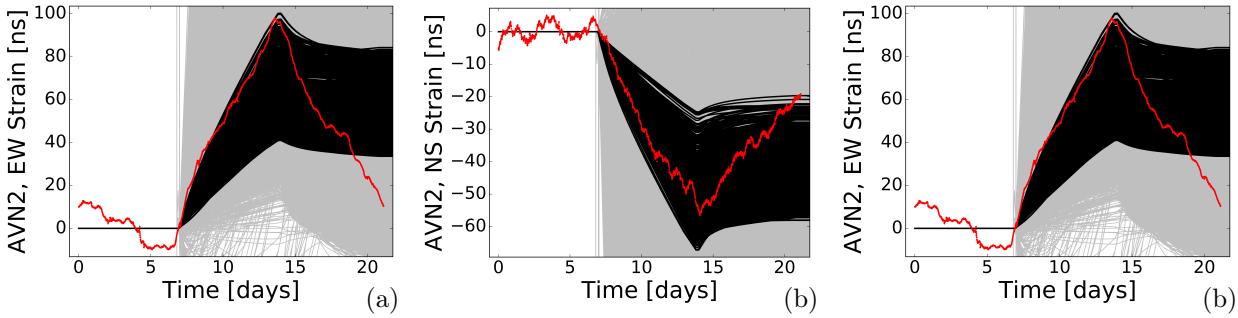

Figure 5.25: Strain as a function of time for impermeable confining unit parameter sets for 1A Shut-in Test. Measured strain data (red), simulation results (gray). Best-fitting simulation results in black.

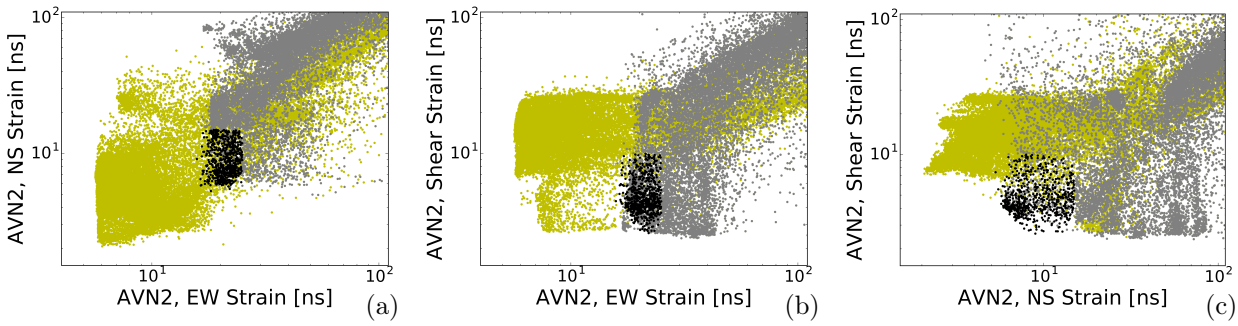

Figure 5.26: Data-model misfits for pairs of strain components (Pareto plots) with (a) East-West strain against North-South, (b) East-West against shear strain, and (c) North-South strain against shear for 1A Shut-in test. Yellow dots indicate models where the confining unit has a high permeability (greater than 10^{-15} m^2), gray dots indicate models where the confining unit has a lower permeability, and black dots indicate models with low confining unit permeability and also fit the measured data within the selected error bounds (corresponding to black lines in Figure 5.25).

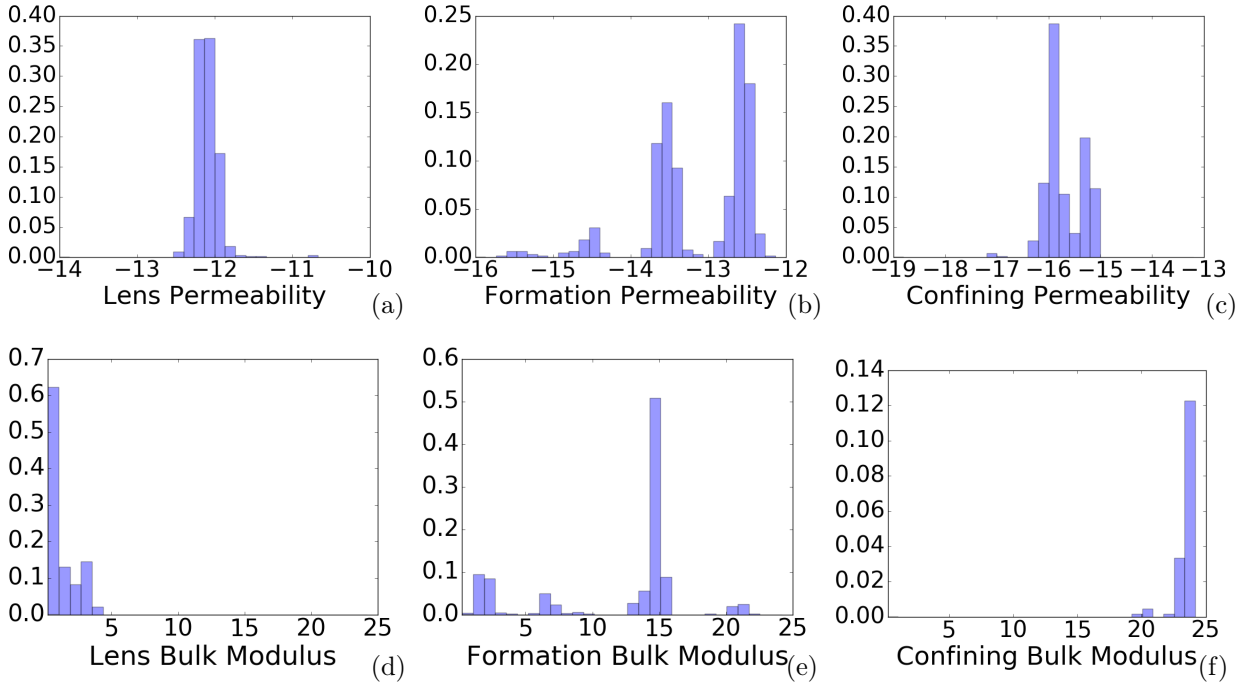

Figure 5.27: Histograms of the best-fitting parameters for low permeability confining unit from 1A-Shut-in test. Permeability as log base 10 m^2. Bulk moduli are in GPa.

5.4.3 Stochastic Inversion of 9A Injection Test, October 2017

All three stages of the inversion 1) circular lens; 2) elliptical lens; 3) irregular lens (e.g., Section 3.2.4) were used during the analysis of the October 2017 9A injection test. A total of 67,310 simulations were conducted to analyze the October 2017 injection test, they were distributed roughly evenly between the three stages. A total of 23,850 simulations were conducted during the last stage, and this ultimately resulted in 1,886 parameter sets that fit the data well using an irregular lens. During the first and second stages sets of both the circular (Figure 5.28) and elliptical (Figure 5.29) lens geometries were identified that fit all available data sets within the measurement error. Many different models were found early in the inversion that would fit all three strain components, but it was more difficult to find models that also explain the pressure signals. Figures 5.28 and 5.29 show subsets of the good fitting parameter sets.

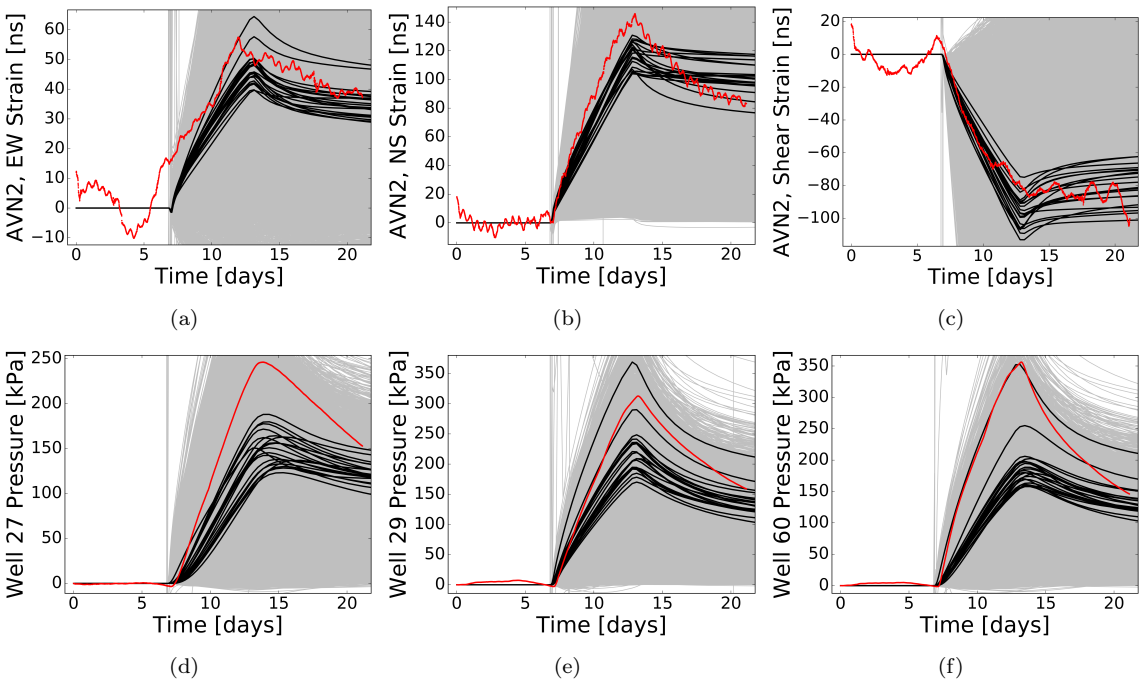

Figure 5.28: Strain at AVN2 and pore pressure at monitoring wells as functions of time during October 2017 injection test at well 9A. Lens geometries are assumed to be circular. Field data shown in red, simulation results shown in grey. The best fitting simulations shown as black lines ($n = 20$).

5.4.3.1 Results for Lenses with Circular and Elliptical Geometries

Pareto plots (Figure 5.30) show the tradeoffs between the different objective. For example the trade-off between East-West strain (ε_{EW}) and vertical strain (ε_{zz}) components shows sharp corner, or an "L" shape, near the origin (Figure 5.30a). The lower edge of this plot indicates the best fitting models for vertical strain all have a RMS misfit of approximately 6 nε, whereas the left-most edge indicates the best fitting models for EW strain all have a misfit of ~9 nε. The sharp corner in the lower left are models that fit both the EW and vertical strains well. This indicates minimal trade-off between EW and vertical strains.

The lower left corner of the plot of vertical strain ε_{zz} as a function of NS strain (ε_{NS}) is beveled compared to the sharp corner in the plot of ε_{zz} vs ε_{EW} (Figure 5.30b). The best fitting models for ε_{zz} have misfit of 6 nε, but they have a misfit of greater than 12 nε in ε_{EW}. The models that best fit ε_{EW} have a misfit of ~3

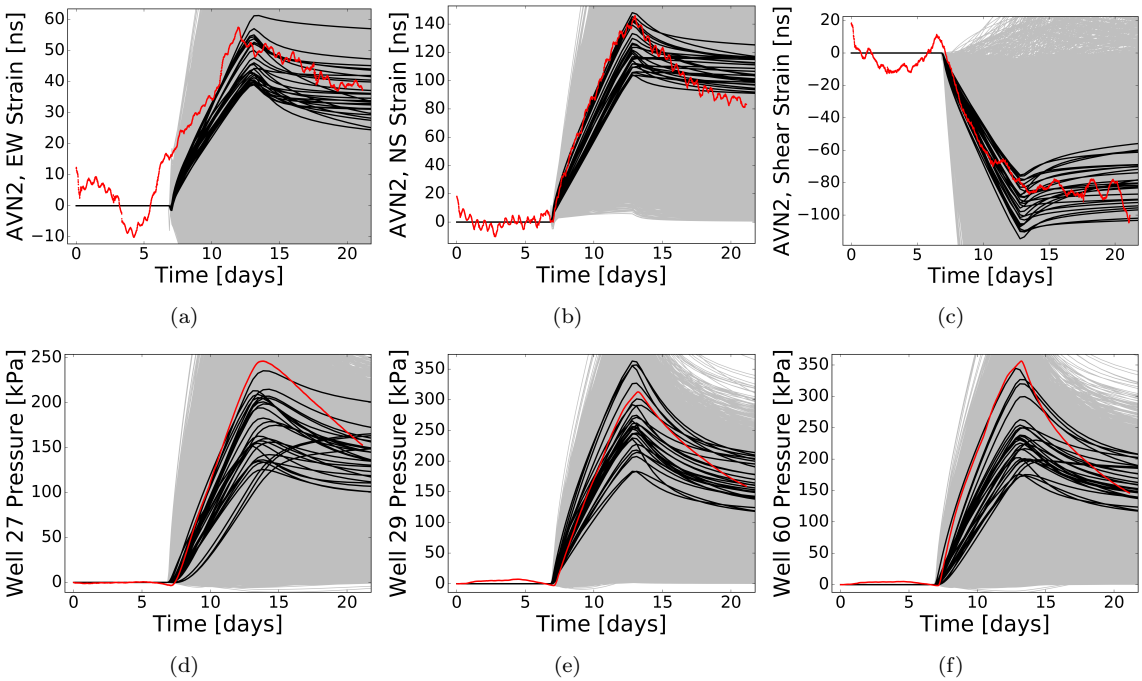

Figure 5.29: Strain at AVN2 and pore pressure at monitoring wells as functions of time during October 2017 injection test at well 9A. Lens geometries are assumed to be elliptical. Field data shown in red, simulation results shown in grey. The best fitting simulations shown as black lines ($n = 27$).

nε, but these models have a misfit of ∼10 nε. This is manifested by the sloping edge in the lower left corner of the cloud of red dots (Figure 5.30b). This means that there is a tradeoff between the ε_{EW} and ε_{zz}, so that among the best fitting models (∼10 to 12 nε), fitting one strain component marginally better requires fitting the other marginally worse.

There is an even larger trade-off between pressure in Well 27 and ε_{NS} (Figure 5.30c). A best misfit of ε_{NS} of 3 nε has a misfit more than 100 kPa in pressure, whereas the best misfit in pressure is 3 kPa and it occurs with a strain misfit of 40 nε. A similar result occurs for the pressure in well 60 and 40 nε.

The trade-off between pressure and strain occur even though the Non-dominated Sorting Genetic Algorithm II (NSGA-II) algorithm is explicitly designed to identify simulations along the leading edge of the trade-off surface and make random combinations and mutations of them, filling in gaps. However, the trade-offs involving pressures were often difficult to sample densely. This may indicate that pressure is more sensitive to parameters, so that a slight mutation to a model along the trade-off surface results in a very different pressure signal causing only small changes in the strain data.

The misfits of models with circular and elliptical lenses were similar, but the models with elliptical lenses were better able to balance the trade-off between strain and pressure objectives. This is illustrated in (Figure 5.30) where the blue dots representing the elliptical lenses are closer to the origin than the red dots representing the circular lenses in most cases. This is probably because the lens geometry could be better approximated by an ellipse than a circle.

The pressure and strain data are obtained from much different depths, and at much different drilling costs, so we were interested in evaluating the case where only the strain data were used to estimate parameters. This could represent an test that was conducted when a strainmeter was installed before a monitoring well was available. This evaluation was done by calculating the weighted sum of the RMS error for different

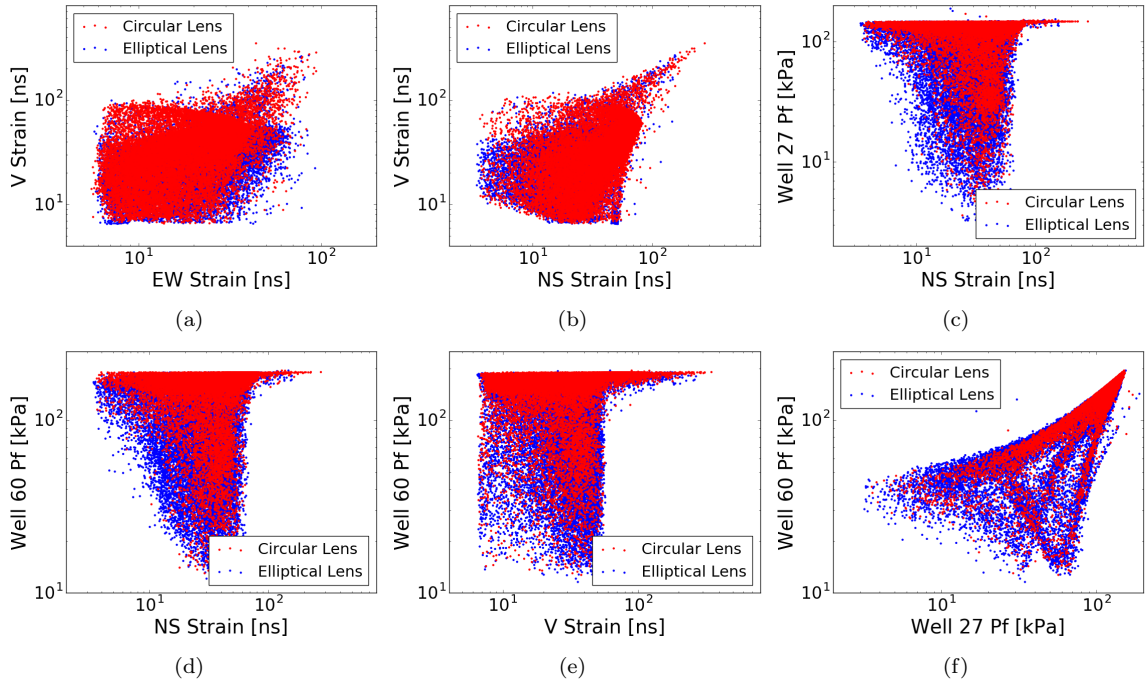

Figure 5.30: Data-model misfits (Pareto plots) of pairs of objectives that include strains and pore pressure for inversion of October 2017 injection at well 9A. Red dots indicate circular lens, blue dots indicate elliptical lens.

parameters when using only the strain data, and then comparing the results to findings when the strain data were used with pressure data from wells 29, 27 and 60 (see equation (5.3)). The porosity and Poisson's ratio are the least sensitive parameters, so they are neglected in the evaluation. The results are displayed as distributions of parameters, as well as weighted errors for pairs of parameters for the two cases, strain and pressure, and strain data alone (Figures 5.31 and 5.32).

The parameter distributions obtained when assuming the circular lens geometry for permeabilities of the Bartlesville formation, lens and confining units are approximately unimodal, as is the confining unit bulk modulus (Figures 5.31). The bulk moduli of the lens and formation are multi-modal. These distributions are characterized by single mode on the histograms along the diagonal, and by clusters of blue points on the weighted error plots (Figure 5.31). One cluster of blue occurs on plots using two unimodal parameters, whereas several clusters occur on plots using multi-model parameters.

The parameter distributions obtained when using the strain data alone are broader than when the pressure data are also used, but the modal values are similar. This is illustrated by comparing the red and purple bars on the histograms, and by comparing the distributions on the weighted error plots. The layout of the plots is symmetric about the diagonal, like a symmetric matrix. In all cases, a modal value determined using strain data alone is also a modal value when strain and pressure are used. For example, compare the plots of the bulk modulus and permeability of the confining unit in the upper left corner of Figure (5.31). The modal values identified by using pressure and strain are approximately $k = 1.5 \times 10^{-18}$ m^2 and $E = 8$ GPa. The mode when the strain only is used is slighly greater, approximately $k = 3 \times 10^{-18}$ m^2 and $K = 8.5$ GPa. The permeability is distributed over approximately half an order of magnitude when using strain and pressure, and it is spread over approximately an order of magnitude when using strain alone. The distribution of the bulk modulus estimated using strain alone is also wider (ranging over $5 < K < 18$ GPa) than when using strain and pressure ($7 < K < 9$ GPa).

The other parameters estimated using the strain only data are generally similar to those estimated using strain and pressure, but there are some differences. For example, the bulk modulus of the lens is estimated with a primary mode of 2 GPa, but there are secondary model 7 and 10 GPa, and a few models are in the 15 to 20 GPa range. When the pressure data are included, the results are two modes of equal magnitude at 5 to 8 GPa and 16 GPa. The bulk modulus using strain only is less than using strain and pressure, but both datasets estimate moduli that are spread over 10 GPa or more. The results for the bulk modulus of Bartlesville formation are spread over a similar range when assuming the lens is cicular.

The circular lens geometry estimated by the inversion is approximately 550 m in diameter with a centroid approximately 100 m west of well 9A (Figure 5.33a). The lens extends approximately 100 m to the east and the boundary occurs between well 9A and AVN2. Distances to boundaries to the north, south and west of well 9A are summarized in Table , along with parameter estimates.

The analyses that assumed an elliptical geometry started with parameters from the good fitting analyses that assumed a circular geometry, and it also did a search of the parameter space using Latin Hypercube. The effects of changing the geometry of the lens is illustrated by comparing Figures 5.33 and 5.32). The parameter distributions are quite similar, although the modal permeability of the lens is slightly greater for the elliptical lens (k = 250 mD) than for the circular one (k = 100 mD). The bulk moduli values are multi-modal, as they are with the circular geometry. The mode of the bulk modulus for the lens with both strain and pressure is in the same range as the mode for the strain only case, approximately 2 to 3 GPa. In contrast, the mode for the strain and pressure using a circular lens was larger (K = 6 to 8 GPa), whereas for the strain only it was 2 to 3 GPa (Figures 5.33 and 5.32). It is unclear if these differences are meaningful, however, because the bulk moduli span similar ranges all four cases.

The major axes of the best fit ellipses are EW and approximately the same dimension as the diameter of the best-fit circular lenses (approximately 550 m). The minor axes are approximately 400 m.

5.4.3.2 Results for Lenses with Irregular Geometries

After identifying the best-fit ellipses and circles, we allowed the lens geometry to deviate into irregular forms in order to better fit the data. This resulted in 1886 parameter sets that fit the data well (Figure 5.34). The results from the inversion using the irregular geometry are able to reduce the tradeoffs between strains and pressures. For example in Figure 5.35c, the misfits for the irregular-shaped lenses are much closer to the origin than those for the circular or elliptical models, and they for a sharp corner. This indicates that the assumption about the lens shape place an important role in the ability of the algorithm to jointly fit both the East-West strain and well 27 pressure data. This reduction in tradeoff also occurs for other datasets that include strain and pressure (Figure 5.35). The tradeoff for the Pareto plots that only include strains are improved slightly, but their tradeoffs are limited when using the elliptical or circular lenses.

Two of the models that fit the data well are summarized in Figure 5.36. The geometries both include a continuous zone roughly 500–600 m in EW and 300–400 m NS. They also both include sinuous zones approximately 50 m wide extending up to several 100 m to the NE (Figure 5.36). This finding is consistent with the geology of the North Avant Field where coarse-grained lenses are interpreted to be fluvial channels along a NE/SW trend (Section 4.1.1.2).

The distributions of the parameters for the inversion that assumed irregular geometries are narrower than those for inversions using circular or elliptical geometries. The modes of the parameters are resemble results from the elliptical case. For example, the permeability modes are: lens (k = 100 to 200 mD), Bartlesville formation (0.1 mD), and confining unit (0.003 mD). The bulk moduli modes are lens (K = 3 GPa), Bartlesville formation (K = 15 GPa) and confining unit (K = 10 GPa) (Table 5.5).

A representative lens geometry was calculated from the set of best fitting models. The representative

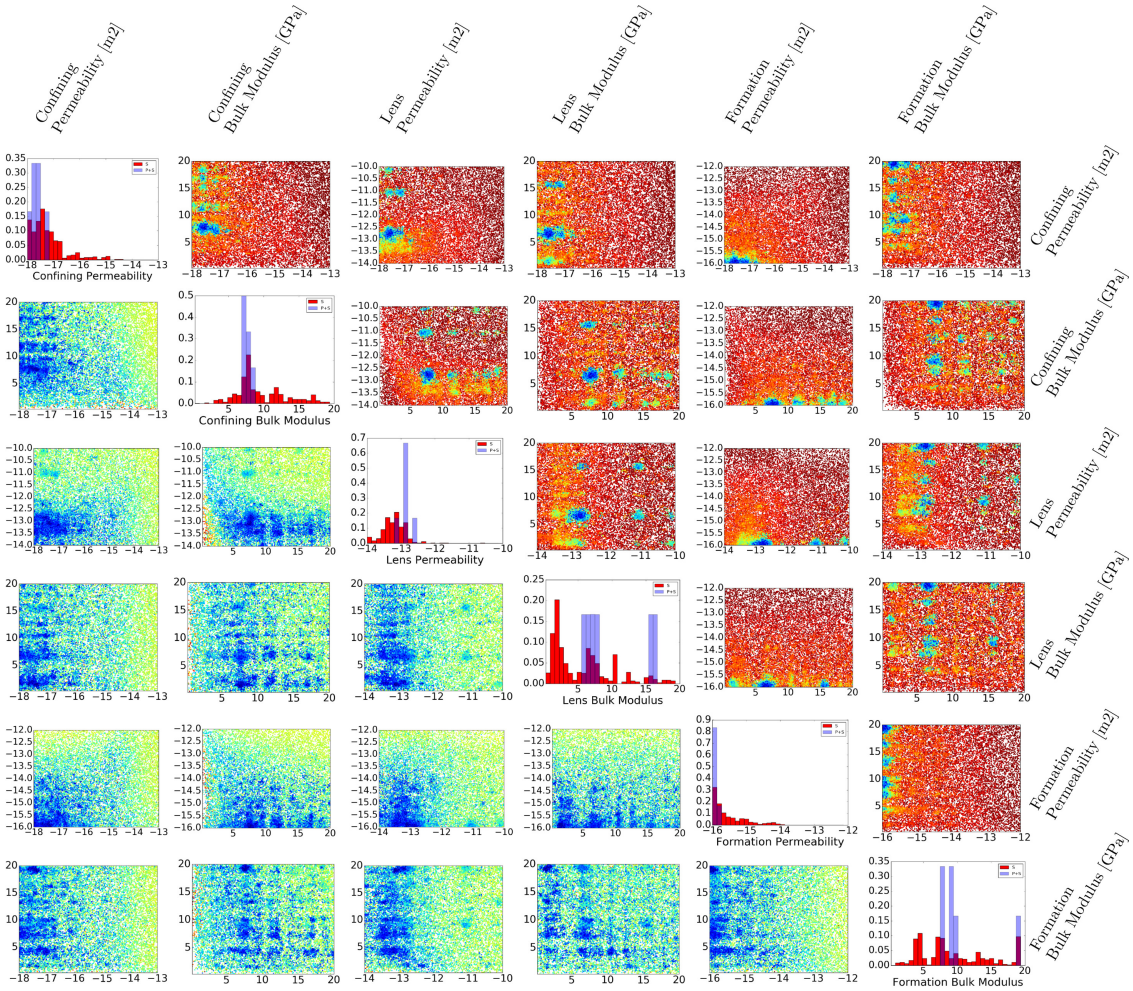

Figure 5.31: Inversion results from October 2017 injection test using pressure and strain data, and using strain data alone. Lens geometries are assumed to be circular. Histograms along the diagonal show distributions of parameters when using strain data alone (red bars) and when using strain and pressure (purple bars). Other plots show weighted RMS errors as functions of pairs of parameters (blue is low error, red is high error). 15 plots in upper right calculate errors using 3 strains and 3 pressures, whereas 15 plots in lower calculate errors using 3 strains.

geometry was determined by weighting each model of the best-fitting 1,886 models according to how well it fits all six datasets (Figure 5.37). Each mesh element that contained a lens was assigned the weighting factor for that model and the values for all the elements were summed. This provides an approximation of the likelihood that the lens occurs in a mesh element. The result is a lens geometry that is similar in size to the one identified using an elliptical lens, except it extends further north (Figure 5.37 and Table 5.5).

5.4.3.3 Differences in predicted strain and pressure fields

The best-fit models can can also be used to predict the full pressure and strain fields. In Figures 5.38, 5.39, a random selection of 120 of the 1,886 best-fit models are re-run and the full finite element output file

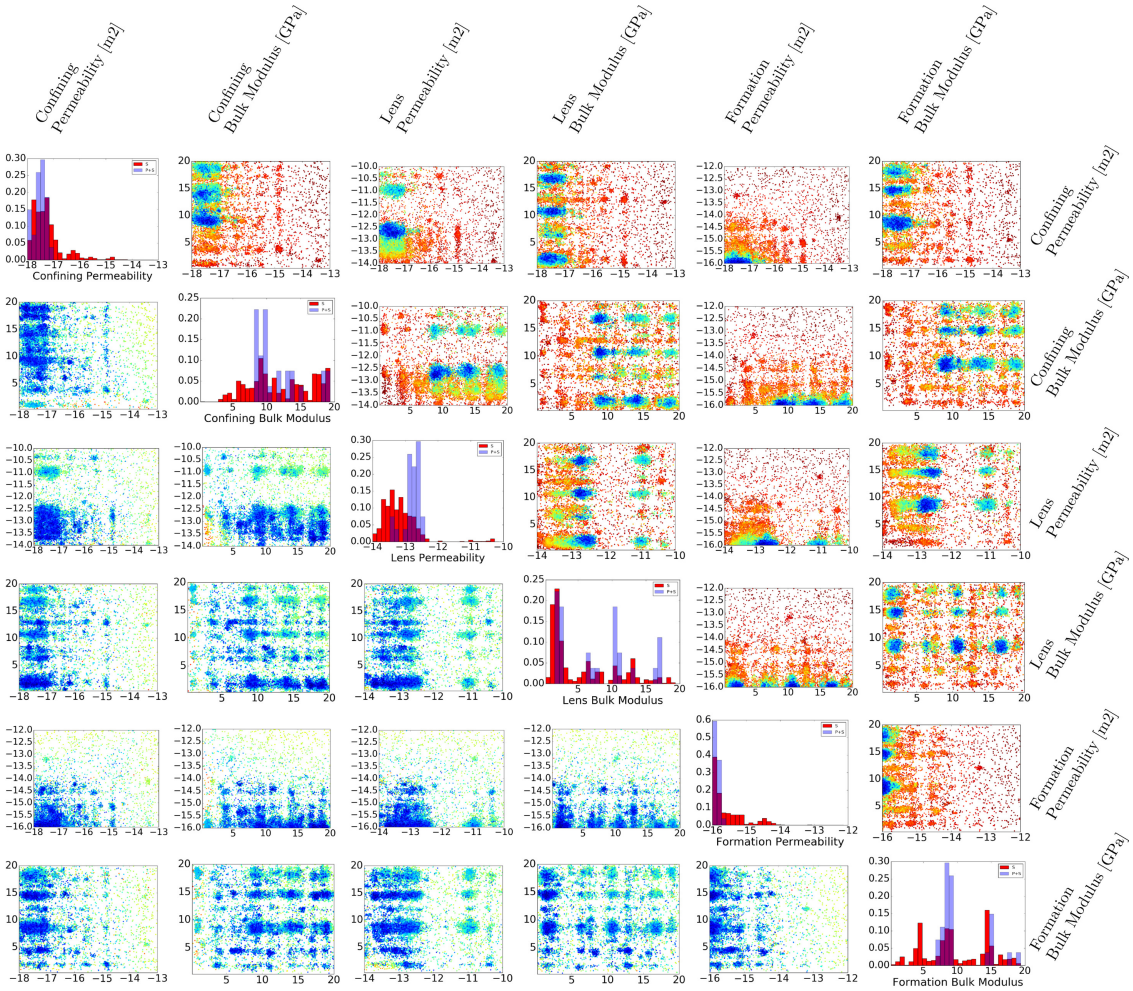

Figure 5.32: Inversion results from October 2017 injection test using pressure and strain data, and using strain data alone. Lens geometries are assumed to be elliptical. Histograms along the diagonal show distributions of parameters when using strain data alone (red bars) and when using strain and pressure (purple bars). Other plots show weighted RMS errors as functions of pairs of parameters (blue is low error, red is high error). 15 plots in upper right calculate errors using 3 strains and 3 pressures, whereas 15 plots in lower calculate errors using 3 strains.

is retained rather than the instrument responses alone.

Results from the suite of the best-fit simulations from the Oct 2017 test presented above consistently match observed data at the locations of the observations (strain at AVN and pressure at wells 27, 29 and 60), but the differences are larger in other locations. Results from 120 simulations selected at random from the suite of 1,886 best-fit model were compiled and the difference between the maximum and minimum predicted value was determind at each mesh element.

The results show that the simulations of normal strain are consistent (small maximum difference) in the vicinity of AVN2, but the difference between simulations increases to the northwest of AVN2 (Figure 5.38). An exception is the shear strain, but this is because the shear strain is small and is likely affected by drift that is not included in the simulations.

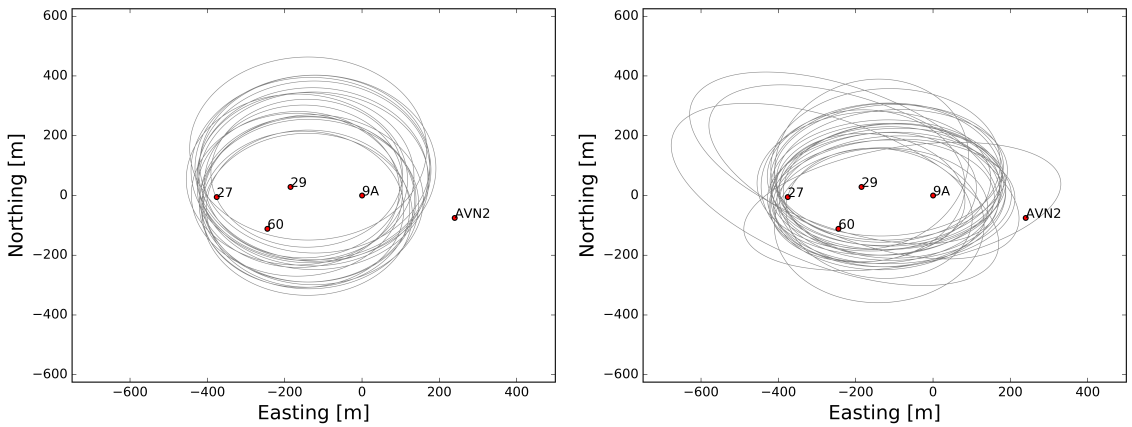

(a) (b)

Figure 5.33: Best-fitting lens geometries from the inversion of the October 2017 injection test at well 9A are shown for circular (left) and elliptical (right) lens geometries.

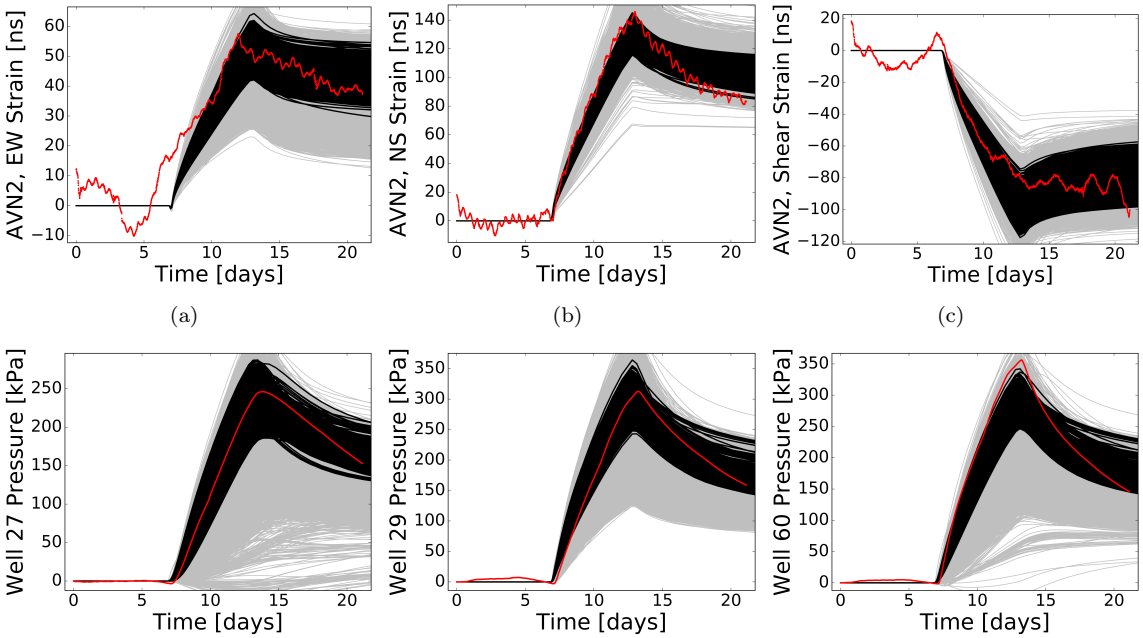

(a) (b) (c)

(d) (e) (f)

Figure 5.34: Strain at AVN2 and pore pressure at monitoring wells as functions of time during October 2017 injection test at well 9A. Lens geometries are allowed to be arbitrarily-shaped. Field data shown in red, simulation results shown in grey. The best fitting simulations shown as black lines ($n = 1,886$).

The maximum fluid pressure occurs at the end of injection during the Oct. 2017 test, and the pressure is predicted by to be greater than 500 kPa within a few 100 m of the well (Figure 5.39). The maximum difference between the 120 randomly selected simulations is relatively small in a region roughly 600 m EW by 300 m NS. This is the same region identified as the most likely lens geometry (Figure 5.37). The maximum pressure difference increases significantly outside of the most likely lens geometry. This occurs because the

Table 5.5: Summary of parameters estimated using Stochastic optimization applied to 9A injection test at North Avant Field from October 2017.

Parameter	Location	units	Circular	Ellipse	Pilot
Bulk Modulus	Lens	K (GPa)	6-8	2-3	3
	Bartlesville	K (GPa)	8-10	8-10	15
	Confining	K (GPa)	7-9	8-10	10
Permeability	Lens	k (mD)	100	250	100-200
	Bartlesville	k (mD)	0.1	0.1	0.1
	Confining	k (mD)	0.003	0.003	0.003
Poisson's ratio	All		0.26	0.26	0.26
Thickness	Lens	m	5	5	5
Fluid Compressibility[a]	assumed	B (1/GPa)	0.45	0.45	0.45
Hydraulic Diffusivity[d]	Lens	D_h (m^2/s)	1.0	0.9	0.8
Distance to boundary	E	m	100	150	180
Distance to boundary	N	m	200	200	500
Distance to boundary	S	m	150	150	200
Distance to boundary	W	m	400	400	400

[d] derived from other data

[a] assumed

set of 120 simulations includes some geometries that are larger than the most likely geometry.

The analyses of maximum differences identifies areas where strains or pressures are poorly constrained by the models that fit the available data. These results could serve to identify areas where additional measurements of strain or pressure could have the most benefit. For example, the results in Figure (5.38) indicate that another strainmeter several 100 m north of well 29 could provide data that would significantly reduce variability in predictions. This is important because it provides a quantitative way to evaluate the best locations for additional measurements.

5.4.4 Predicting Future Injection Tests

Predictive performance was evaluated by using parameters from a suite of 1,886 of the best-fiting models from the October 9A test (Section 5.4.3) to predict observations from injection tests during November 2017 and July 2018. No additional calibration was done prior to the simulations.

5.4.4.1 Simulation of 9A Injection Test, November 2017

The suite of results form an envelop that is able to predict the normal strains during injection quite

well (Figures 5.40,5.41). The maximum strain at the end of injection is within the envelop from the best-fit simulations at AVN2. The vertical strain at AVN3 is slightly overestimated, and the areal strain at AVN4 is slightly underestimated, but these results are within 20 percent of the envelope (Figure 5.40). The error increases during recovery after injection stops, but the simulations are consistent with the observations, and in some cases (e.g., AVN2 EW strain) the observations are probably affected by drift that is unrelated to injection. Similarly, the predicted pressure data are within 20 percent of the simulated envelope (Figure 5.41).

The observed tilt signal deviates significantly from the predicted tilts (Figure 5.42). However, the simulations also explain tilts poorly during the calibration simulation using the Oct 2017 injection data, so it is unsurprising that the simulation predict tilts during the Nov. 2017 test poorly. The observed tilt signal during both tests is roughtly the same magnitude as the predicted response, but it deviates erratically and it is difficult to identify a systematic response to pumping from the tilt data (Figure 5.42).

5.4.4.2 Evaluation of 9A Injection Test from July 2018

The best-fit models from the October 9A test (Section 5.4.3) were re-run using the pumping schedule from the July 9A test, in order to predict the strain, pressure and tilt behavior of the July 9A test.

These simulations predict strains and pressures well for the first few days, then systematically overestimated both strains and pressure at later times (Figures 5.43,5.44). This may because the pressure change during the July test interacts with geologic structures further from the injection well than it does during shorter tests in Nov. 2017 and Oct. 2017. For example, the results from the inversion of the Oct. 2017 test infer that the permeable lens is roughly 500 m in maximum dimension, but the lens may actually be larger than this and the predicted results are uncertain to the northwest of well 9A. A permeable lens that is larger than expected would explain why the pressures and strains are less than expected. It is also possible that uncertainty related to the injection rate may contribute to the differences between predicted and observed results for the July 2018 test.

5.4.5 Summary

Four methods were used to interpret strain, or strain and pressure data generated during injection tests at the North Avant Field. The methods used different forward models to represent the strain field, and different inversion methods to estimate parameters.

5.4.5.1 Strain Type Curve

The strain type curve method assumes that the normal strain at shallow depths can be approximated as a function of the logarithm of time. This assumption is consistent with observations for the average horizontal strain and the vertical strain. The inversion process involves manually fitting a straight line to the strain data. It is the easiest interpretation method we evaluated.

The results indicate that the 0-strain intercept time ranges from 3.5×10^4 s to 6×10^4 s, and the semi-log slope is approximately 50 to 80 nε. The intercept times indicate the hydraulic diffusivity is approximately $D_h = 0.5$ m^2/s, which is essentially the same as the result using pore pressure data (Table 5.1). The permeability estimated from D_h is approximately

$$k = \frac{D_h \mu}{K} \tag{5.4}$$

Assuming the bulk modulus is in the range of $2 < K < 10$ GPa, and $\mu = 0.001$ Pa·s, gives an estimate of the permeability as $50 < k < 250$ mD. This range is consistent with measurements of cores from the area, and it is consistent with estimates of permeability from analysis of the pressure data (e.g. Table 5.1).

The semi-log slope indicates that the mean transformational strain is $\varepsilon_0 = 2.7 \pm 0.8$ $\mu\varepsilon$. Assuming a hydraulic diffusivity of $D_h = 0.5$ m^2/s, this estimate of transformational strain can be used to estimate the Biot-Willis coefficient by rearranging with equation (3.27) to get

$$\alpha = \frac{\varepsilon_0 d D_h}{Q} \tag{5.5}$$

This indicates that the Biot-Willis coefficient is in the range 0.7 ± 0.2 (Table 5.6). This estimate is consistent with laboratory values given by Wang (2000). This approach appears to be one of the only methods for estimating α in-situ.

The semi-log slope of the average normal strain as a function of time increases at approximately 20×10^4 s, and a similar change in slope occurs in the pressure data. The change in slope could be caused by interaction with a boundary in the reservoir. If this is the case, the boundary is estimated to be approximately 500 m away from well 9A (Figure 5.47).

5.4.5.2 Pressurized poroelastic inclusion

This approach assumes the observed pressures measured in monitoring wells adequately characterize the pressure distribution in the permeable lens. It uses an analytical solution derived for the project with a gradient descent parameter estimation method to minimize error between simulated and observed strains.

The results demonstrate that the approach can explain the observed strains during the October and November tests quite well. The results indicate that Young's modulus is approximately 3 GPa to 4 GPa, and Poisson's ratio is 0.28 to 0.4 (Table 5.6).

The analysis indicates that the permeable lens is 500 m to 600 m in maximum dimension–sum the E and W distances, or the N and S distances to a boundary in Table 5.6. The center of the lens is west of well 9A, and the eastern boundary of the lens is approximately 120 m east of well 9A (Figure 5.46). This result places a permeability boundary on the lens between the injection well 9A and the strainmeters located at AVN2. The lens geometry is smaller than that indicated by strain type curve method (500 m radius). One explanation for this difference is the strain-type-curve method only estimates one dimension (radius), whereas the geometry of the inclusion is characterized by 4 lengths and an angle. Nevertheless, the sizes are remarkably similar in light of the differences in the method used to estimate them.

5.4.5.3 Manual fitting of a 3D poroelastic numerical model

Parameter values used in a 3D poroelastic model were adjusted manually to explain the data, and to provide some insights into controls on the strain signal. The geometry of the 3D model includes the Bartlesville sandstone, and overlying confining layer, and an underlying permeable lens with a rectangular shape.

The results indicate that the observed strain and pressure data (at well 29) can be explained with a Young's modulus of the lens of 2 GPa, which is in the range estimated by the pressurized inclusion. The moduli of the overlying Bartlesville sandstone and confining units are larger (8 GPa and 2.9 GPa,

respectively). The results indicate that the permeability of the lens is approximately 500 mD, and the the overlying Bartlesville sandstone is significantly tighter (Table 5.6).

The fluid compressibility was adjusted during the manual fitting in order to match the observed data after injection stopped (Table 5.6). The fluid pressure and strain decrease too slowly when the baseline fluid compressibility is used, but increasing the compressibility cause the pressure and strain to decrease more rapidly and match the data. A baseline compressibility equal to the water compressibility was used for the other simulations, but a larger compressibility is justified because the reservoir is known to contain some natural gas in the vicinity of well 9A.

The hydraulic diffusivity calculated from the permeability and compressibilities is approximately 0.6 m^2/s, which is essentially the same as the results from the strain and pressure type curve analyses (Table 5.6).

The permeable lens was assumed to be rectangular, and the results indicate that the major axis is roughly EW and 580 m long, whereas the minor axis is 300 m long (Figure 5.47). A boundary of the permeable lens occurs 80 m east of well 9A, and the centroid occurs to the west of well 9A, according to the manual fitting (Table 5.6). The geometry of the rectangular lens inferred from the 3D numerical model is slightly longer and narrower than the one determined using the analytical solution, but the differences are within several tens of percent. The distance to the closest boundary to the east of well 9A is remarkably similar to the result from the analytical solution (Table 5.6).

5.4.5.4 Summary from Stochastic Inversions

The stochastic inversion method developed in Section 3.2 was applied to strain and pressure observations during shut-in and injection tests at the North Avant Field using a poroelastic model consistent with the geologic setting of the field. The inversion resulted in parameter datasets describing the properties and geometries of reservoir and confining unit.

The results demonstrate that stochastic inversion methods can be applied to in-situ strain data measured at shallow depths to generate parameter sets (Table 5.6) and geometries (Figure 5.47) that are consistent with the expected geologic conditions.

The analysis that considers only strain measured from the shut-in of a nearby well (well 1A) estimated a median permeability of 600 mD. This is within the expected value for permeable lenses at the base of the Bartlesville sand in the area (Figure 4.7). The shut-in analysis identified two modes for the permeability of the Bartlesville sand, 25 and 250 mD. These values are within the permeabilities measured on cores taken from the Bartlesville sand in the area (e.g. Section4.1.1.2).

The shut-in analysis identified two cases for the permeability of the confining unit, one with a permeability that is approximately 10 mD and another where it is 0.1 mD. We expect that the lower value of permeability is the correct case because the confining unit is shale, but field data on the permeability of the confining unit are unavailable.

The inversion of the October 2017 injection test at well 9A yielded estimates of parameters and heterogeneities that are also within the values expected from the geologic setting. The results are more tightly constrained than the results from the 1A shut-in test. Inversions from the October 2017 test indicate the permeability of the lens is approximately 100 mD, whereas that of the Bartlesville sand is 0.1 mD and that of the confining unit is 0.003 mD. Well 9A intersects a different permeable lens from the one intersected by well 1A (Figure 4.4), so stratigraphic variablity may account for the differences in permeability. The results from the stochastic inversion is within the range of permeabilities identified by the other inversion methods (Table 5.6).

Estimates of Young's modulus of the permeable lens are similar to slightly larger than the results from the other inversion methods (Table 5.6). The stochastic inversion provides estimates of the Young's modulus that are several times stiffer than that of the permeable lens, in the range of 15 GPa to 35 GPa. These larger values of elastic modulus are within the range expected for well lithified rock (Wang, 2000).

The inversion process yielded estimates of the geometry of the permeable lens that are similar to each other, and generally consistent with the interpolated core data (Figure 5.46). All of the estimated geometries include a boundary between the injection well and the strainmeters at AVN. The core data indicate that the southern boundary of coarse-grained lens occurs south of the boundaries estimated by the inversion. The core data shown in (Figure 5.46) indicates that the coarse-grained sediment at the base of the Bartlesville sand extends further south than indicated by the inversion results. It is possible that there is a lateral permeability change in the coarse-grained lens that affects the inversion results, but is not resolved by the core data.

Using data from the 9A pumping test, we found that supplementing shallow-well strain data with in situ pressure measurements yielded improved results with lower uncertainties, but a qualitatively similar understanding of the system. We also found that simplifying assumptions about the geometry of geologic structures had a strong influence on the results of the inversion. The fit with the observed data improved with the complexity of the geometry assumed for the inversion, and the approach of using geometries of increasing complexity (circle→ellipse→irregular).

The results of the stochastic inversion provide an approach for prediction that could be used to support design or risk management decisions. The approach involves conducting predictions using all the parameter datasets for models identified by the inversion that fit the available data. This may include predictions from hundreds of models. This results in a set of predictions that embody both the best available estimate, and the uncertainty in the estimate of strains, pressures, and potentially other variables. The results outlined here demonstrate this approach (e.g. Figures 5.38 through 5.45).

5.5 Conclusion

Four independent methods of interpreting strain signals were evaluated using data from the North Avant Field. They give results that are generally consistent with each other, and with independent information characterizing the subsurface. The hydraulic diffusivity of the reservoir in the vicinity of well 9A is approximately 0.5 m^2/s and the permeability is betweeen 100 and 500 mD. This is consistent with measurements of permeability from cores taken in the vicinity of well 9A, and it is consistent with analyses of pressure transients using standard well testing interpretation methods. Analysis of strain from a shut-in at well 1A indicates slightly greater permeability, in the range 300 to 1,000 mD, with a mode of 600 mD. The specific capacity (injection rate/pressure) of well 1A is greater than at well 9A, and as a result, it is a preferred well for injecting produced water. This is consistent with the permeability of the formation in the vicnity of well 1A being greater than in the vicinity of well 9A.

The four methods of analysis indicate that Young's modulus of the reservoir is between 2 and 6 GPa. We conducted triaxial laboratory tests on small core samples of the Bartlesville sandstone from the North Avant Field and found that the Young's modulus was approximately 10 GPa. The small cores were obtained from larger cores stored in a core library operated by Oklahoma Petroleum Information Center (OPIC). The most well indurated sections of the larger core were preferentially selected for the smaller cores, so the samples we tested likely represent the strongest, and stiffest, rock in the formation. The simulations assumed a uniform modulus across the formation, and it seems reasonable that softer interbeds not represented by core samples cause the average Young's modulus to be softer than determined by laboratory tests. As a result, the range of elastic moduli seem to be a reasonable estimate of field conditions, even though it is softer than measurements made on selected cores.

Some of the interpretation methods, like the pressurized poroelastic inclusion, only provide estimates of elastic properties, whereas the strain type curve method provides estimates of hydraulic properties. These estimates are internally consistent using relationships like equation (5.4). The range of Young's modulus of $2 < E < 6$ GPa is consistent with a range of permeability of 100 to 250 mD using (5.4), $D_h = 0.5$ m^2/s, and typical values for porosity, bulk modulus of the fluid and Poisson's ratio.

None of the interpretation methods was able to provide insights from the tilt data. The data were obtained from two tiltmeters, and the result were more erratic than predicted by the analyses.

Strain interpretations all indicate the reservoir is bounded with a maximum dimension of 500 to 1,000 m. Cores and well logs indicate well 9A intersects a permeable lens at the base of the Bartlesville formation. An isopach map of the permeable lens indicates a feature that is roughly 1,000 m in extent, although data constraining the extent is sparse to the north and west (Figure 5.47). The extent of the permeable lens inferred from well data is consistent with the extents estimated from the strain measurements. The strain type curve method predicts the largest extent, but it is only capable of estimating a radial distance from the well. Results from the other methods are all remarkably consistent in both size and location. They indicate the maximum dimension is 500 to 600 m and the centroid is to the west of well 9A. The predicted sizes are somewhat smaller than the isopach map, but the differences are small and could be due to internal permeability structure independent of the isopach.

All the interpretations indicate that a boundary of the permeable lens occurs between well 9A and the strainmeters AVN. This interpretation occurs because the boundary is required to explain the relative magnitudes of the radial and circumferential horizontal strains. The boundary reduces the magnitude of the radial (EW) strain relative to the circumferential (NS) strain, which explains the field data.

Table 5.6: Summary of parameters estimated using Strain Type Curve, 3D poroelastic analytical solution to a pressurized inclusion, 3D poroelastic solution with manual parameter fitting, and 3D Poroelastic with stochastic parameter estimation. Interpretation methods applied to 9A injection tests at North Avant Field. Distance to boundary of the permeable lens in different directions from well 9A. These parameters are examples of values that fit the observed data using a particular forward model. Trade-offs between fitting multiple strain and pressure objectives will cause other parameter sets to also fit the data.

	Forward model		Strain	Poroelastic	3D Poroelastic	3D Poroelastic	3D Poroelastic
			Type Curve	analytical	Rectangle	Ellipse	Pilot
	Inversion		Graphical	Gradient	Manual	Stochastic	Stochastic
Parameter	Location	units					
Young's Modulus	Lens	E (GPa)		2	2	2-3,4-6	6
	Bartlesville	E (GPa)			8	17-22	33
	Confining	E (GPa)			2.9	17-22	33
Poisson's ratio		ν		0.23-0.4	0.26		
Biot-Willis		α	0.7 ± 0.2				
Permeability	Lens	k (mD)	100		500	250	150
	Bartlesville	k (mD)			5	0.1	0.1
	Confining	k (mD)			0.01	0.003	0.003
Thickness	Lens	m		7	5	5[a]	5[a]
Fluid Compressibility	Bartlesville	B (1/GPa)			11	0.45[a]	0.45[a]
	Lens	B (1/GPa)			3.5	0.45[a]	0.45[a]
Hydraulic Diffusivity[d]	Lens	$D_h(m^2/s)$	0.5	-	0.6	0.9	0.8
	Bartlesville	D_h (m^2/s)			0.004		
Distance to boundary	E	m	500	120	80	100	120
Distance to boundary	N	m	500	225	150	200	400
Distance to boundary	S	m	500	345	150	150	150
Distance to boundary	W	m	500	390	500	400	400

[d] derived

[a] assumed

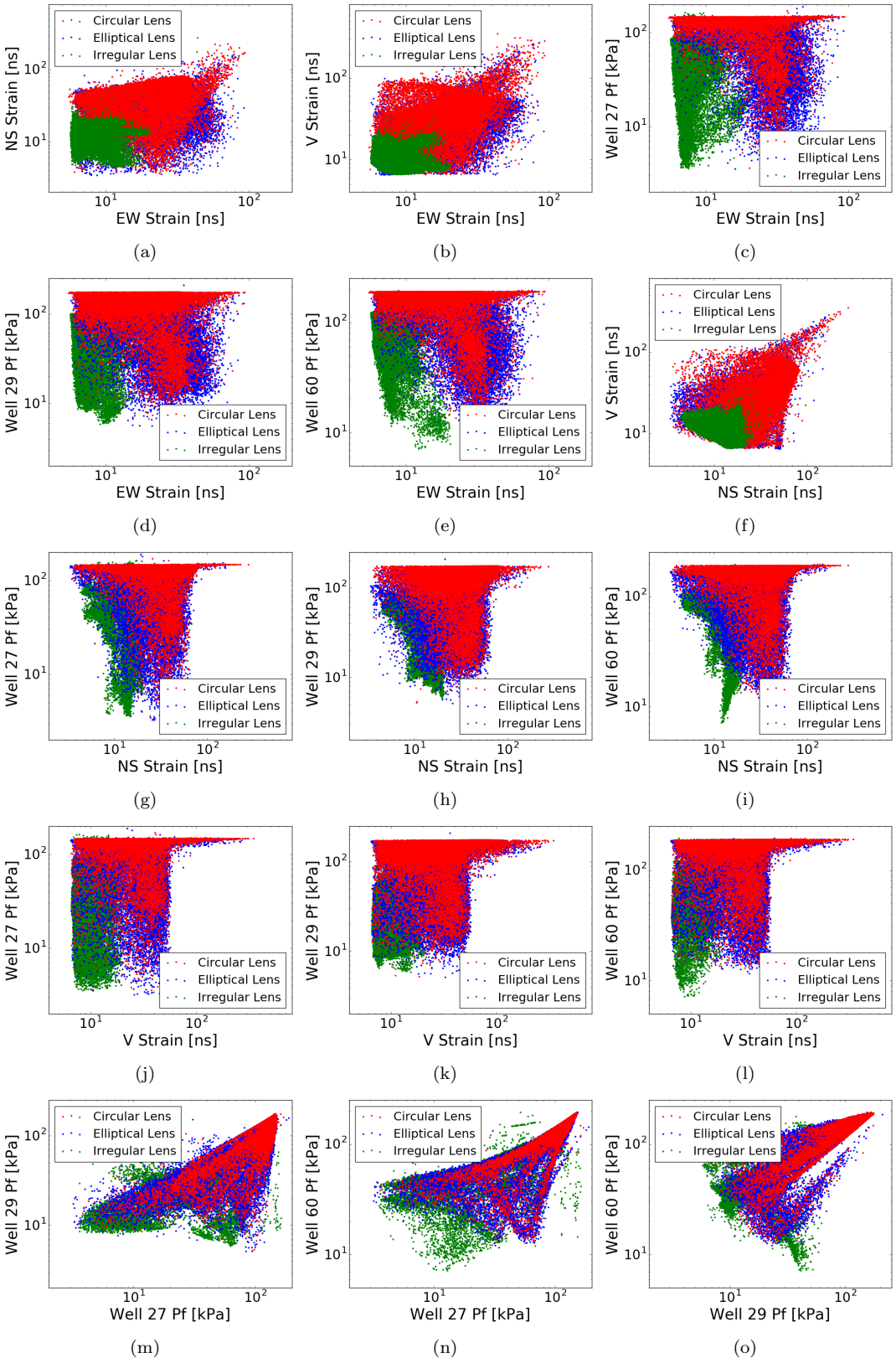

Figure 5.35: Data-model misfits (Pareto plots) for pairs of strain components for 9A pumping test. Red dots represent circular lenses, blue dots represent elliptical lenses, blue dots represent irregular-shaped lenses.

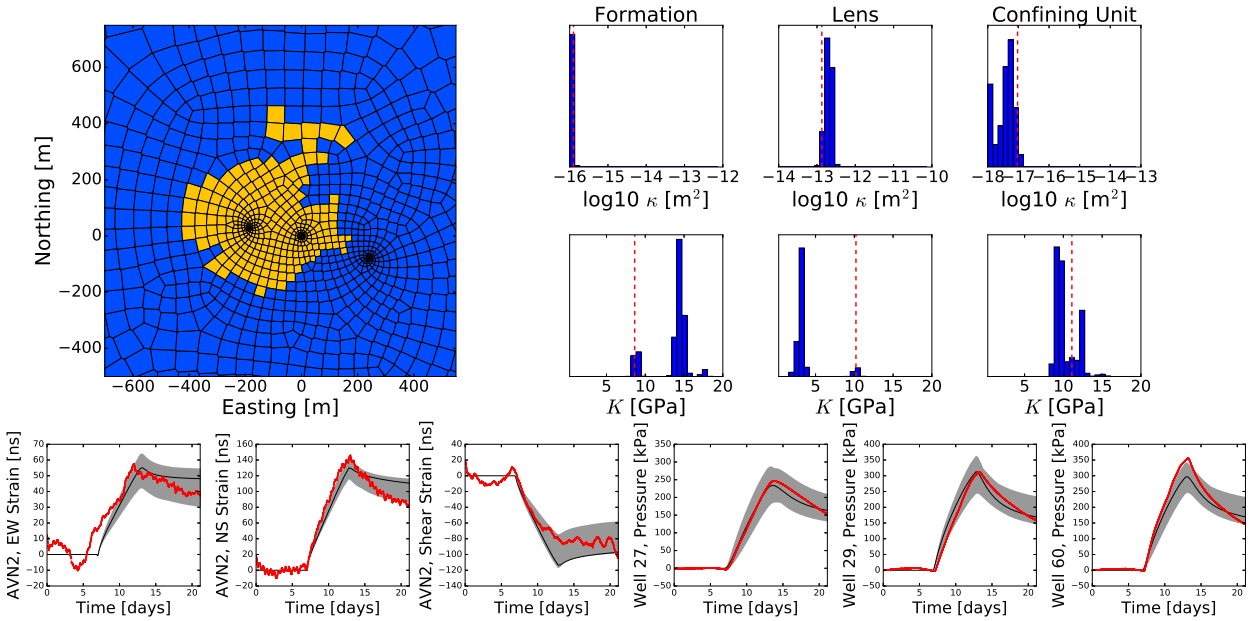

(a)

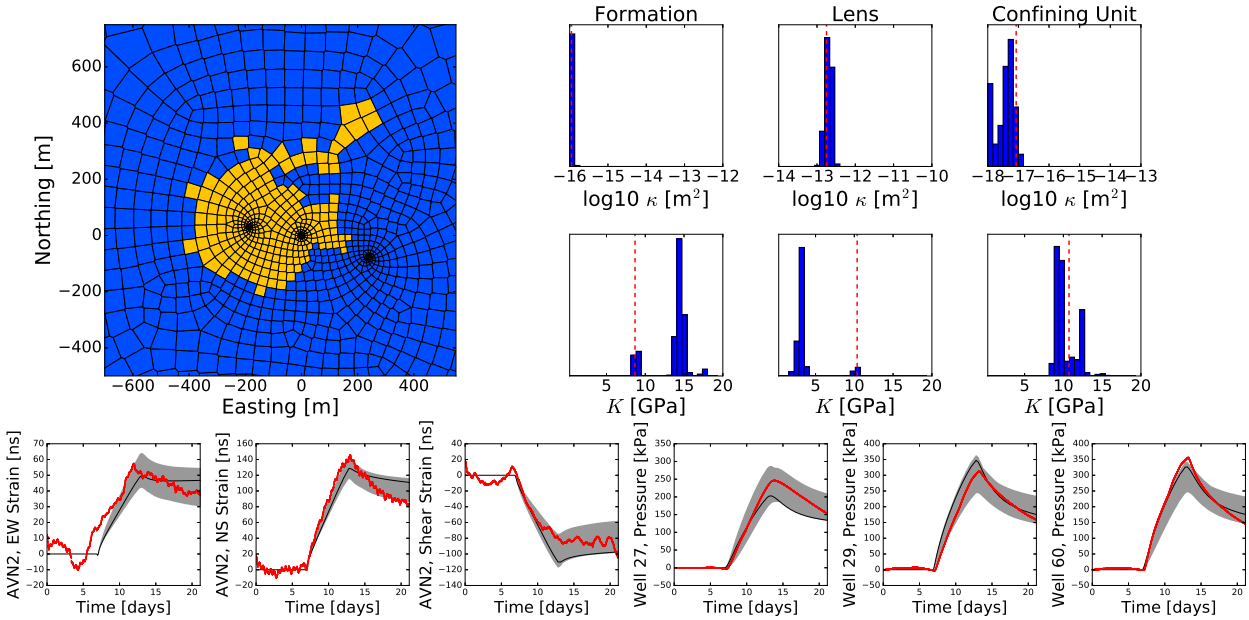

(b)

Figure 5.36: Results from two simulations (a) and (b) using irregular lens geometries for the inversion of the October 2017 injection test at well 9A. Each group shows the lens geometry in map view in the left corner. Parameters are shown in upper right corner, where red line represents the parameter value used in the particular simulation, and blue bars are the distribution of 1,886 best-fit models. Lower row shows data fit as black line, with gray lines representing 1,886 best-fit models.

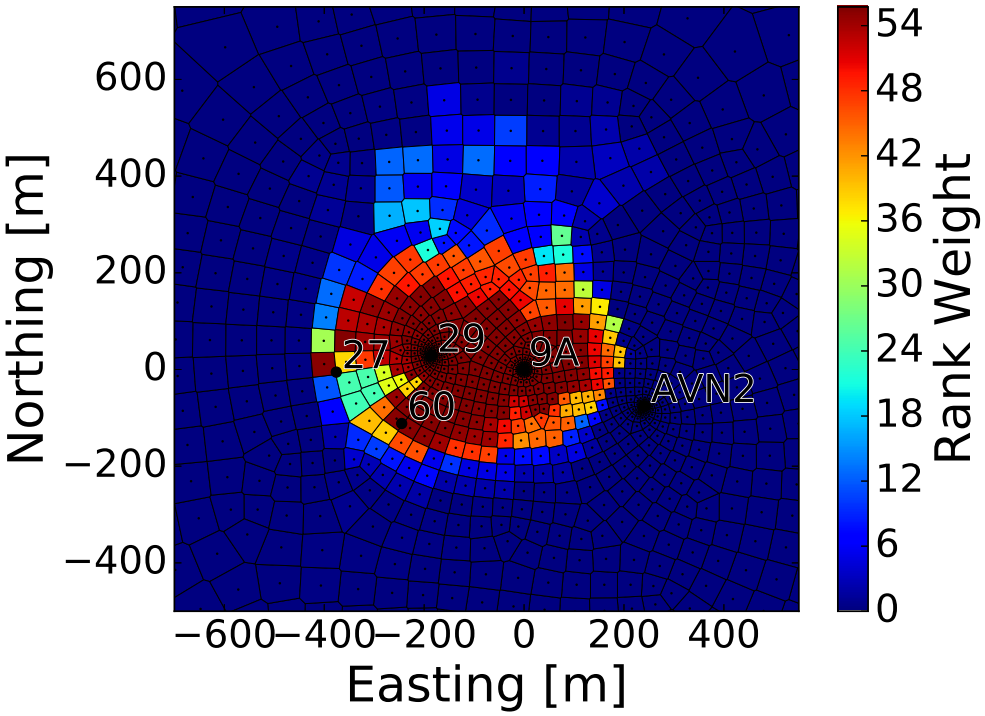

Figure 5.37: Estimated lens geometry. The 1,886 best-fit models are given a rank according to their weighted data misfit and the ranks are summed.

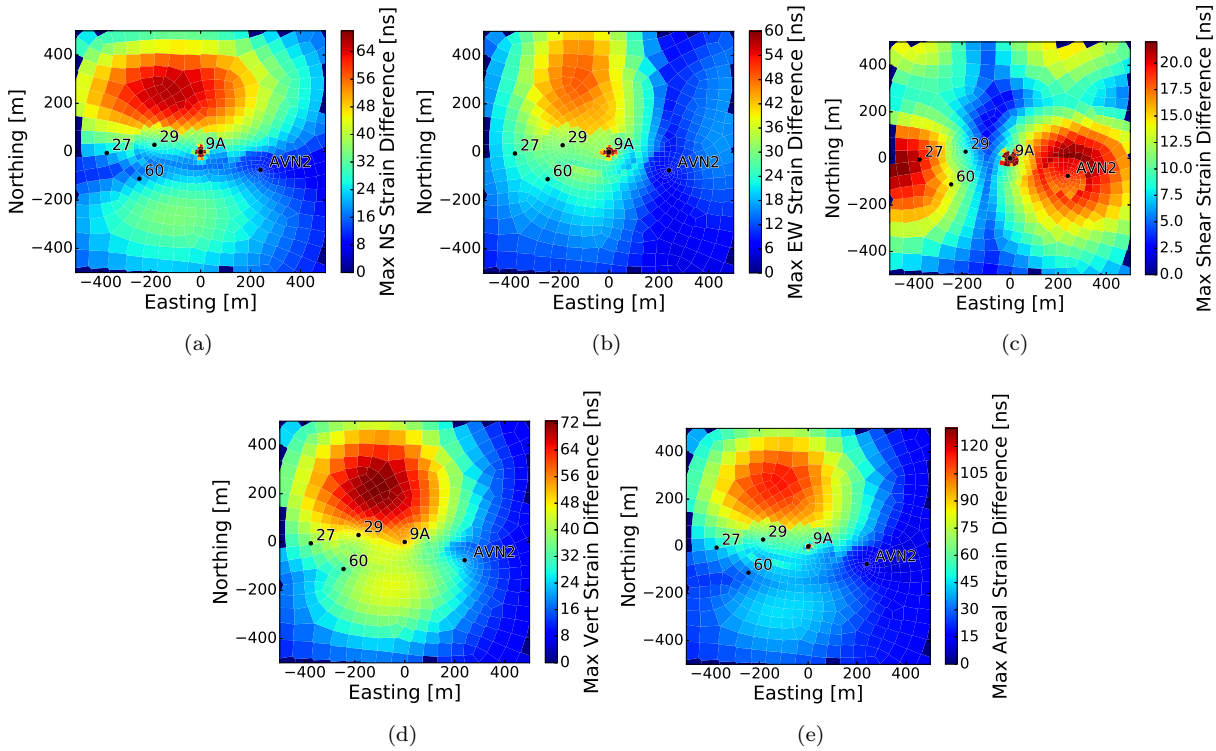

Figure 5.38: Map view distribution of maximum difference in predicted strains from random selection of best-fit models to the Oct. 2017 injection test at well 9A. For each mesh element the difference is computed between the highest and lowest strains predicted at each time step, and the magnitude of the largest model disagreement in the timeseries is shown as a color. For example in Figure 5.40a, the predicted strains disagree the most at around day 7, with a range of approximately 15–20 nanostrain. Therefore in subfigure (a), the AVN2 observation point shows a shade of blue corresponding to 15-20 nanostrains. North-South (a), East-West (b), shear (c), vertical (d) and areal (e) strain components are shown. Results are displayed in map view with the horizontal slice defined at a depth of 30 meters, the approximate depth of the currently installed strainmeters.

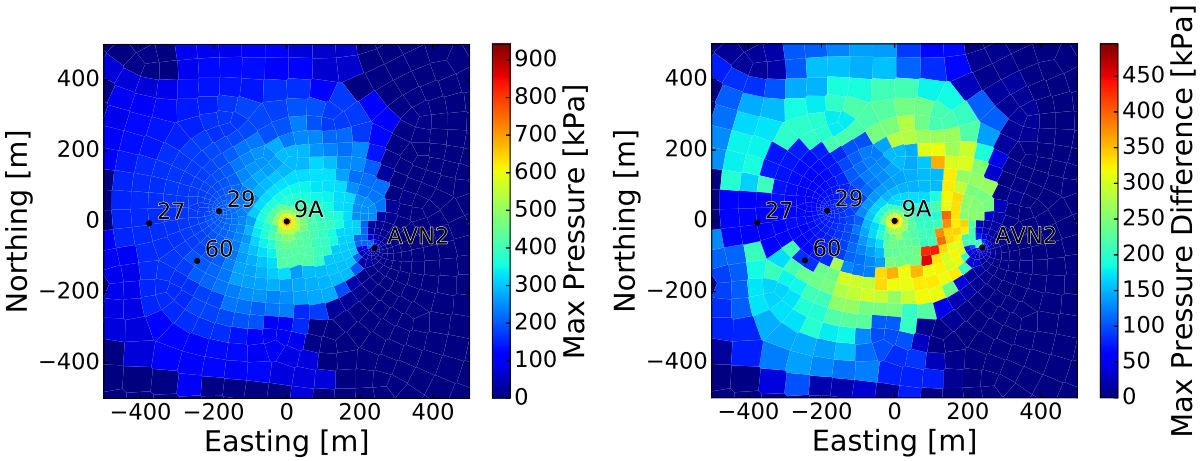

(a) (b)

Figure 5.39: Maximum fluid pressure (a) and maximum difference in fluid pressure (b) are shown as a function of position in map view. For each mesh element the difference is computed between the highest and lowest pressures predicted at each time step, and the magnitude of the largest model disagreement in the timeseries is shown as a color. For example in Figure 5.41a, the predicted strains disagree the most at around day 7, with a range of approximately 100 kPA. Therefore in this figure (a), the well 27 observation point shows a shade of blue corresponding to approximately 100 kPa. Horizontal slice is located in the vertical center of the permeable lens.

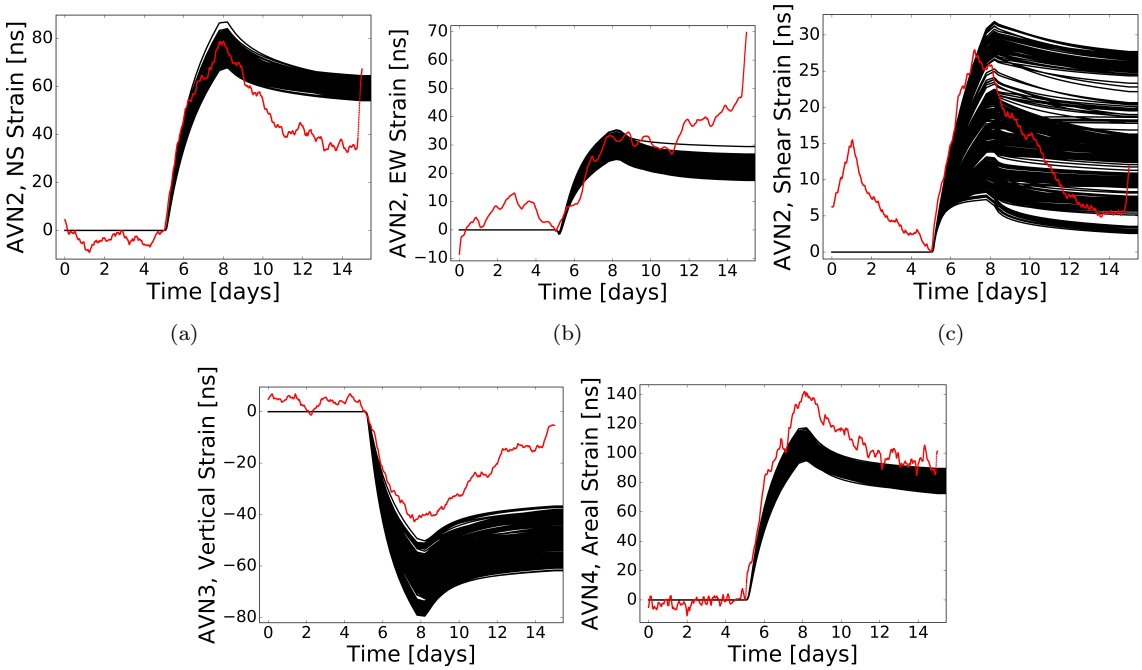

(a) (b) (c) (d) (e)

Figure 5.40: Strain components at AVN (North-South, East-West, shear) as functions of time for the November 9A injection test. Vertical strain at well AVN3, areal strain at AVN4. Simulation results are shown in gray and best-fit simulations are in black. Measured field data shown as red dots.

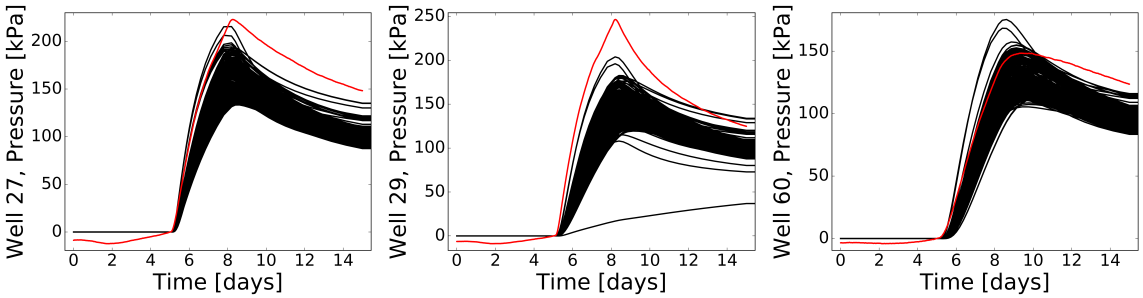

(a) (b) (c)

Figure 5.41: Pressure readings at wells 27, 29 and 60 as functions of time for the November 9A injection test. Simulation results are shown in gray and best-fit simulations are in black. Measured field data shown as red dots.

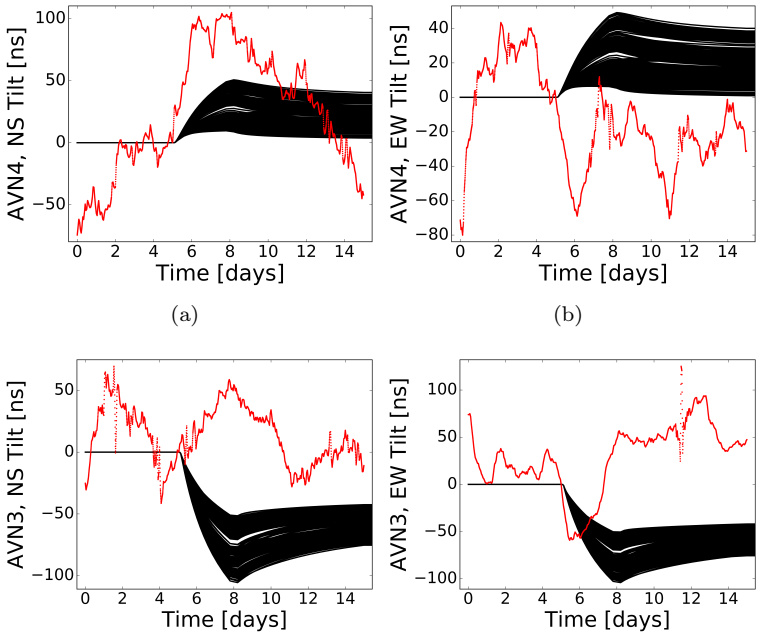

(a) (b) (c) (d)

Figure 5.42: Tilt components at AVN3 and AVN4 as functions of time for the November 9A injection test. Simulation results are shown in gray and best-fit simulations are in black. Measured field data shown as red dots.

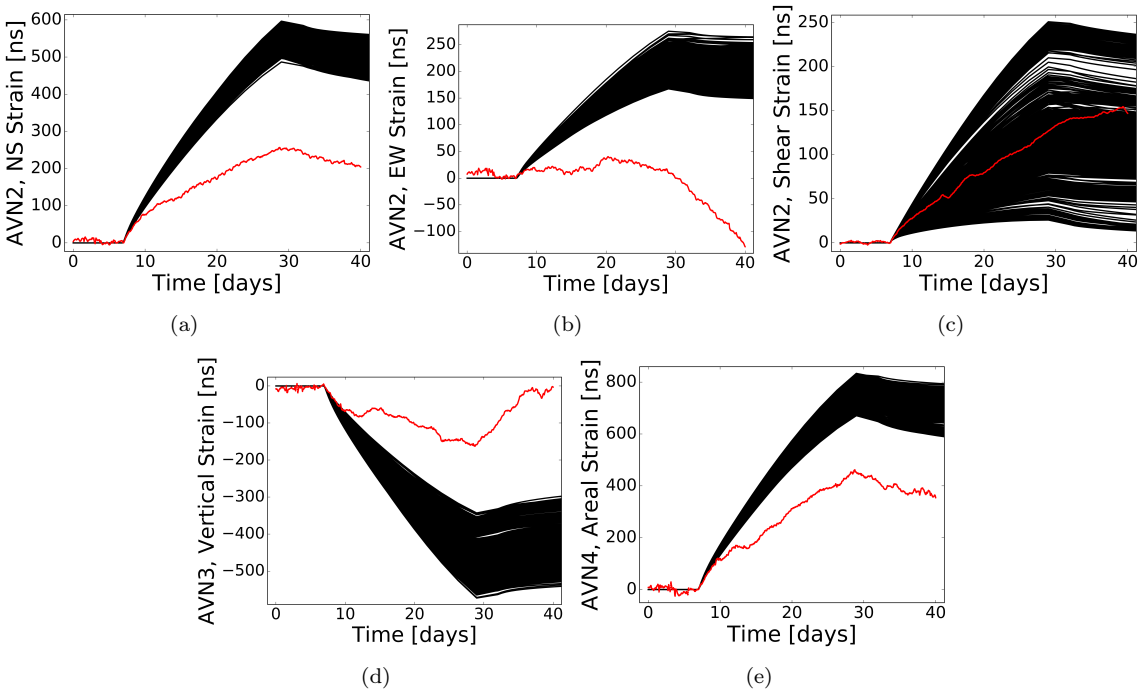

Figure 5.43: Strain components at AVN (North-South, East-West, shear) as functions of time for the July 2018 9A injection test. Vertical strain at well AVN3, areal strain at AVN4. Simulation results are shown in gray and best-fit simulations are in black. Measured field data shown as red dots.

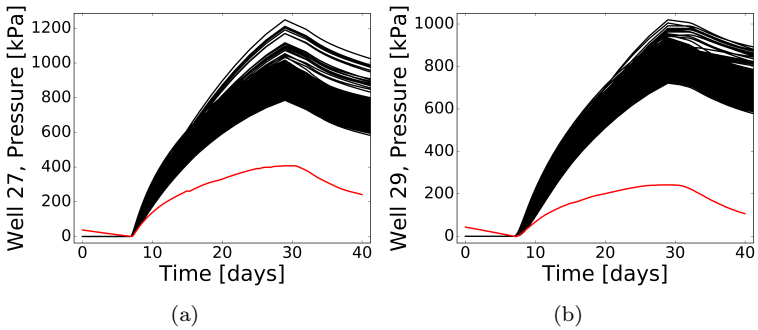

Figure 5.44: Pressure readings at wells 27, 29 and 60 as functions of time for the July 2018 9A injection test. Simulation results are shown in gray and best-fit simulations are in black. Measured field data shown as red dots.

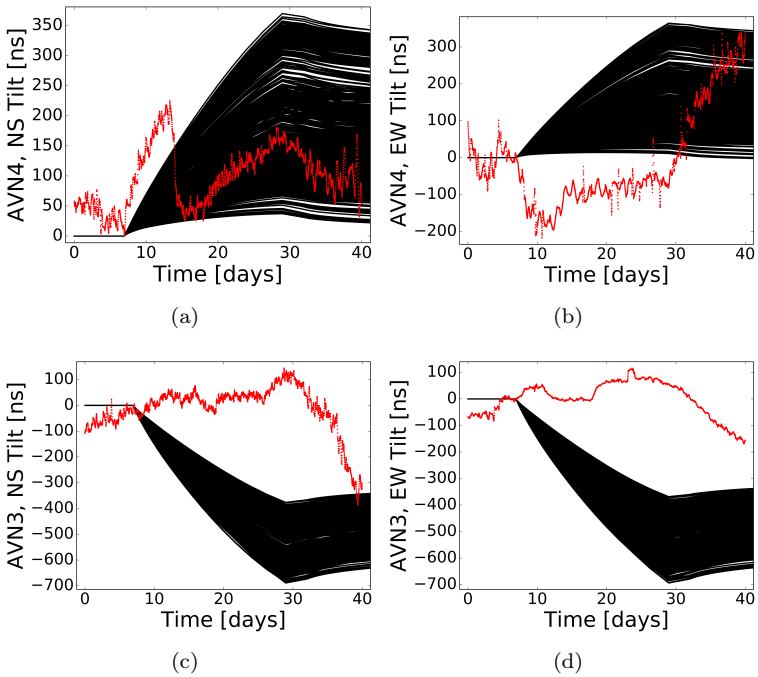

Figure 5.45: Tilt components at AVN3 and AVN4 as functions of time for the July 2018 9A injection test. Simulation results are shown in gray and best-fit simulations are in black. Measured field data shown as red dots.

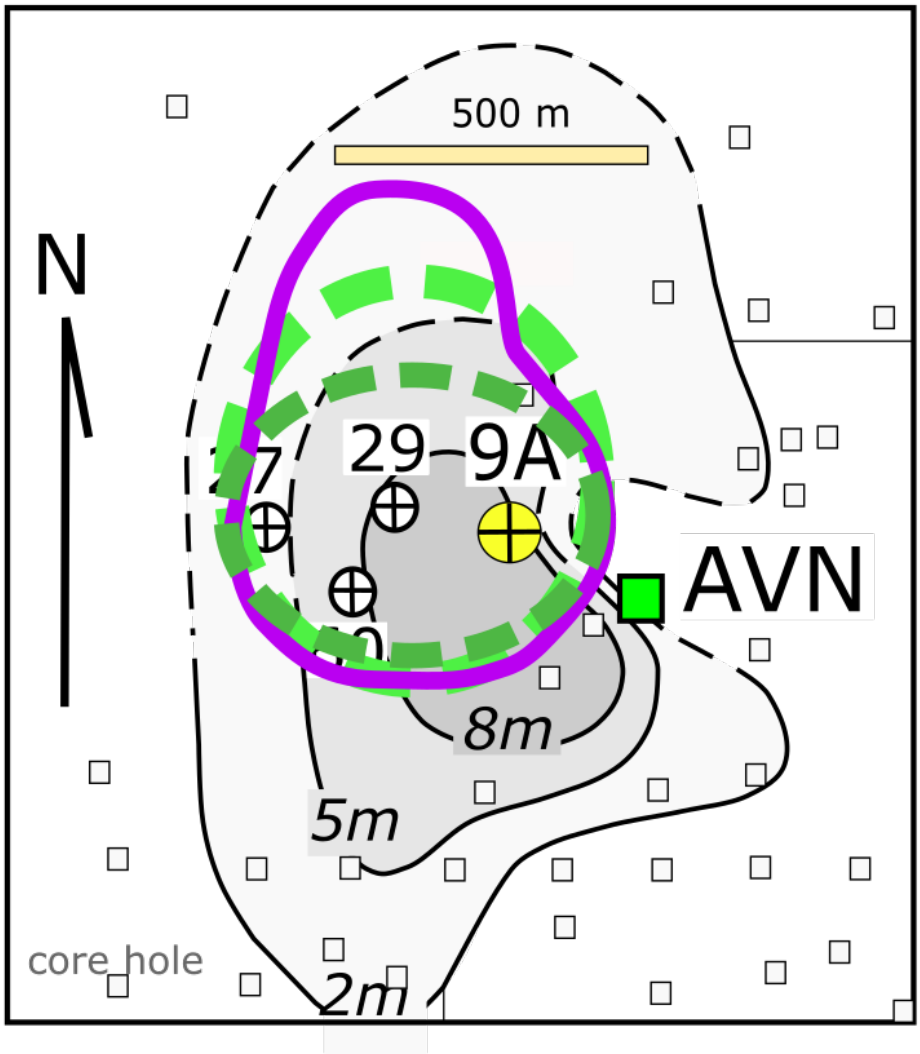

Figure 5.46: Summary of the extent of permeable lens in the vicinity of well 9A based on stochastic inversion of the October 2017 injection test.

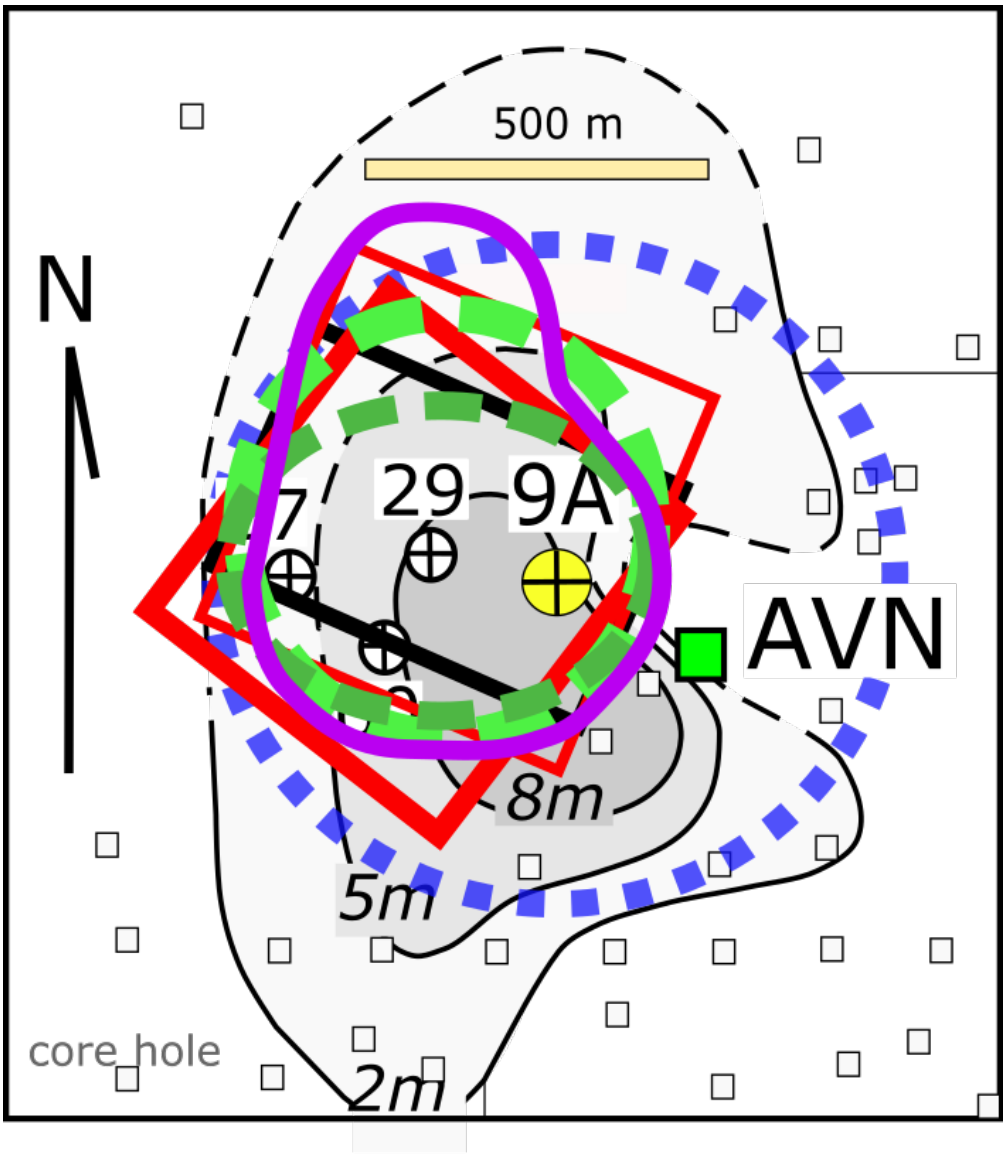

Figure 5.47: Summary of the extents of permeable lens in the vicinity of well 9A based on interpretations of injection tests at well 9A. Strain type curve: purple dotted line; poroelastic inclusion: thick red line from Oct. 2017 test, thin red line from Nov. 2017 test; manual fit of 3D poroelastic model: black line; stochastic inversion using circle: green dashed line; ellipse: dark green dashed line); or irregular geometry: purple line. Contours are the isopach in meters of the permeable lens identified in core or well logs, dashed where inferred.

References

Aster, R. C., Borchers, B., and Thurber, C. H. (2018). *Parameter estimation and inverse problems*. Elsevier.

Cooper, H. H. and Jacob, C. E. (1946). A generalized graphical method for evaluating formation constants and summarizing well-field history. *Eos, Transactions American Geophysical Union*, 27(4):526–534.

Gercek, H. (2007). Poisson's ratio values for rocks. *International Journal of Rock Mechanics and Mining Sciences*, 44(1):1–13.

Murdoch, L. C., Freeman, C. E., Germanovich, L. N., Thrash, C., and DeWolf, S. (2015). Using in situ vertical displacements to characterize changes in moisture load. *Water Resources Research*, 51(8):5998–6016.

Sayers, C. M. (2013). The effect of anisotropy on the Young's moduli and Poisson's ratios of shales. *Geophysical Prospecting*, 61(2):416–426.

Wang, H. F. (2000). *Theory of linear poroelasticity with applications to geomechanics and hydrogeology*. Princeton Series in Geophysics. Princeton University Press.

White, J. A. and Borja, R. I. (2008). Stabilized low-order finite elements for coupled solid-deformation/fluid-diffusion and their application to fault zone transients. *Computer Methods in Applied Mechanics and Engineering*, 197(49-50):4353–4366.

White, J. A. and Borja, R. I. (2011). Block-preconditioned Newton–Krylov solvers for fully coupled flow and geomechanics. *Computational Geosciences*, 15(4):647.